U.PORTO

FEUP FACULDADE DE ENGENHARIA
UNIVERSIDADE DO PORTO

EXPERIMENTAL STABILITY ANALYSIS OF GEOTEXTILE ENCAPSULATED-SAND SYSTEMS UNDER WAVE-LOADING

LUCIANA PAIVA DAS NEVES

Dissertação para Doutoramento em Engenharia Civil
na Faculdade de Engenharia da Universidade do Porto

PROGRAMA OPERACIONAL POTENCIAL HUMANO

UNIÃO EUROPEIA
Fundo Social Europeu

QUADRO DE REFERÊNCIA ESTRATÉGICO NACIONAL
PORTUGAL 2007.2013

JANEIRO 2011

ABSTRACT

The continuous population growth in the littoral has increased the volume of residential construction along the coastline enhancing the exposure to potentially hazardous damage to structures, as well as to economic activities. To help maintain safety of people and assets at acceptable levels many coastal defence schemes were developed. However, as neither the cause of erosion is eliminated, nor does the vulnerability/risk dissuade people from moving seawards and settling along the coast, it seems that the safety of highly populated coastal areas is compromised unless new approaches are considered.

In such context, the so-called soft coastal engineering techniques – hereby referred to those techniques that build with natural processes and rely on natural elements, such as sand, dunes, and vegetation, to prevent erosive forces from reaching the backshore – are set to play a bigger role in coastal protection, whilst any increase in vulnerability/risk is compensated with management and planning (*e.g.*, landwards reallocation of people and assets).

Partly due to the present interest in innovative techniques of coastal engineering, partly due to the potentialities and limitations of geotextile encapsulated-sand systems, the present investigation triggered with the aim to provide contributes to the knowledge available on the stability of geotextile encapsulated-sand systems under wave loading, with emphasis on the issues of scour development and more widespread beach lowering

Efforts in this research concentrated on the cross-shore component of sediment transport to study the response of a dune-beach system under erosional, accretionary, persistent erosional and conditions alternating between periods of erosion and accretion. Five models, corresponding to three erosion control systems with two configurations, one nearshore detached breakwater with four configurations and one non-protected beach and dune system as reference were taken for the investigation. The models were submitted to a total of ten different sea-states. Model characteristics were derived from the prototype dune-beach systems of *Estela* and *Figueira da Foz*.

At first the passive and active coastal defence schemes have been set-up to run on similar hydrodynamic and morphodynamic conditions aim to provide insights into the efficiency of each system in maintaining a beach and in protecting the shoreline. The differences in response of the cross-shore profile to the presence of the structure have been assessed with respect to *(i)* wave reflection off the structure; *(ii)* wave-induced pressure variations; and *(iii)* beach-profile evolution. The next step was to increase understanding of the response of the beach-profile under persistent erosional conditions and under periods of erosion followed by infilling and again erosion.

For the same wave conditions, a lowering of the beach levels in front of the passive coastal defence schemes was observed, with shoreline retreat as far as the established alignment and identical change in beach-profile shape. The beach-profile has respond to change in forcing wave conditions, erosional to accretionary, but the recovery occurred at much smaller rate. It was apparent that sediment transport removal from the beach was controlled by the position and elevation of the nearshore bar. The results showed that the submerged detached breakwaters were efficient in protecting the shoreline and in maintaining the beach; this efficiency has been achieved by retarding offshore movement of sediments, and also by trapping them in the upper beach.

The results from the laboratory measurements also indicate that the maximum scour depth under erosional waves decreased with an increase in the water depth at the structure and that it increased with waves breaking near the toe of the structure. They also suggest that the scour depth is dominated by the mechanisms of wave reflection off the structure and wave downrush flow on the exposed slope, which may be influenced by the bed and water levels at the structure during the period of higher energy forcing.

RESUMO

O contínuo crescimento da população no litoral aumentou o volume de construção residencial acentuando a exposição a danos potencialmente perigosos para as estruturas, assim como para as actividades económicas. Para ajudar a manter a segurança de pessoas e bens em níveis aceitáveis, variados esquemas de defesa costeira foram desenvolvidos. No entanto, como nem a causa da erosão é eliminada, nem o aumento da vulnerabilidade/risco dissuade as pessoas de se fixarem na costa, parece que a segurança de áreas costeiras altamente povoadas está comprometida.

Neste contexto, as designadas técnicas *soft* de engenharia – que se referem às técnicas que utilizam elementos naturais como a areia, as dunas e a vegetação, para evitar que as forças erosivas cheguem à pós-praia – são chamadas a desempenhar um papel mais importante na protecção costeira, enquanto o aumento da vulnerabilidade/risco é compensado com gestão e planeamento (por exemplo, a relocalização de pessoas e bens para áreas mais interiores).

Em parte devido ao interesse actual em técnicas inovadoras de engenharia costeira, em parte devido às potencialidades e limitações dos sistemas de confinamento de areia com geotêxteis, a presente investigação foi sendo desenvolvida com o objectivo de dar contributos para o conhecimento acerca da estabilidade destes sistemas sob a acção da agitação marítima, com ênfase nas erosões localizadas e no abaixamento do nível da praia.

Os esforços de investigação concentraram-se na resposta de um sistema praia-duna à componente transversal do transporte sedimentar, sob condições de erosão, de acreção, de erosão persistente e de períodos alternados de erosão e acreção. Foram testados cinco modelos, correspondendo a três sistemas de controlo de erosão dunar, com duas configurações, um quebramar destacado submerso com quatro configurações e um sistema de duna-praia não protegido, o qual serviu como referência. Os modelos foram submetidos a um total de dez estados diferentes de mar. O modelo teve como protótipo as características dos sistemas praia-duna existentes na praia da *Estela* e numa outra da *Figueira da Foz*.

No início, as estruturas passivas e activas de defesa costeira foram submetidas a condições hidrodinâmicas e morfodinâmicas similares com o objectivo de perceber a eficiência de cada sistema, tanto na protecção da linha de costa, quanto na manutenção da praia. As diferenças na resposta do perfil longitudinal da praia à presença da estrutura foram avaliadas em relação *(i)* à reflexão da agitação, *(ii)* às variações de pressão devidas à agitação, e *(iii)* à evolução do perfil da praia. O passo seguinte foi tentar compreender a resposta do perfil da praia sob condições de erosão persistente e a resposta a períodos alternados de erosão e de acreção.

Para as mesmas condições de agitação, foi observado um abaixamento do nível da praia em frente aos sistemas passivos de defesa costeira, com recuo da linha de costa até ao alinhamento estabelecido e idêntica variação do perfil de praia. O perfil de praia respondeu à alteração das condições de agitação, erosão para acreção, mas a recuperação ocorreu a um ritmo mais lento. Os resultados mostraram que a remoção de sedimentos da praia era controlada pela posição e elevação da barra submersa. As estruturas destacadas submersas foram eficientes na protecção da linha de costa e na manutenção da praia. Essa eficiência resultou da diminuição dos movimentos transversais de sedimentos, mas também da sua retenção na praia superior.

Os resultados das medições em laboratório indicam ainda que a máxima profundidade de erosão localizada diminuiu com o aumento da profundidade da água na estrutura e que aumentou com a rebentação perto do pé da estrutura. Os resultados sugerem que essa profundidade é dominada pela reflexão da agitação na estrutura e pelo refluxo no talude exposto, o qual pode ser influenciado pelo nível da praia e da água durante o período de maior energia.

RÉSUMÉ

La croissance continue de la population sur le littoral a augmenté le volume de construction résidentielle, ce qui accentue l'exposition aux dommages potentiellement dangereux pour les structures, ainsi que pour les activités économiques. Pour aider à maintenir la sécurité des personnes et des biens à des niveaux acceptables, différents schémas de défense côtière ont été développés. Néanmoins, étant donné que ni la cause de l'érosion est éliminée, ni l'augmentation de la vulnérabilité/risque dissuade les personnes de se fixer sur la côte, il semble que la sécurité des zones côtières hautement peuplées est compromise.

Dans ce contexte, les techniques d'ingénierie dites *soft* – qui font référence aux techniques qui utilisent des éléments naturels comme le sable, les dunes et la végétation, afin d'éviter que les forces érosives n'arrivent à l'après plage – sont appelées à jouer un rôle plus important dans la protection côtière, tandis que l'augmentation de la vulnérabilité/risque est compensée à travers la gestion et la planification (par exemple, la relocalisation de personnes et biens vers des zones plus intérieures).

En partie dû à l'intérêt actuel pour les techniques innovatrices d'ingénierie côtière, en partie dû aux potentialités et limitations des systèmes de confinement de sable avec des géotextiles, la recherche ici présentée a été développée avec l'objectif de contribuer pour la connaissance sur la stabilité de ces systèmes sous l'action de l'agitation maritime, en mettant l'accent sur les érosions localisées et l'abaissement du niveau de la plage.

Les efforts de la recherche se concentrent sur la réponse d'un système plage-dune à la composante transversale du transport sédimentaire, sous conditions d'érosion, d'accumulation, d'érosion persistante et de périodes alternées d'érosion et d'accumulation. Cinq modèles ont été testés, correspondant à trois systèmes de contrôle d'érosion dunaire, avec deux configurations, un brise-lames détaché submergé avec quatre configurations et un système de dune-plage non protégé qui a servi de référence. Les modèles ont été soumis à un total de dix états différents de mer. Le modèle a eu comme prototype les caractéristiques des systèmes plage-dune existants sur la plage de *Estela* et sur une autre de *Figueira da Foz*.

Au départ, les structures passives et actives de défense ont été soumises à des conditions hydrodynamiques et morphodynamiques similaires de façon à comprendre l'efficacité de chaque système, tant dans la protection de la ligne de côte, comme dans le maintien de la plage. Les différences dans la réponse du profil longitudinal de la plage à la présence de la structure ont été évaluées au niveau *(i)* de la réflexion de l'agitation, *(ii)* des variations de pression dues à l'agitation, et *(iii)* de l'évolution du profil de la plage. L'étape suivante a été d'essayer de comprendre la réponse du profil de la plage sous des conditions d'érosion persistante et la réponse à des périodes alternées d'érosion et d'accumulation.

Pour les mêmes conditions d'agitation, un abaissement du niveau de la plage en face des systèmes passifs de défense côtière a été observé, avec un recul de la ligne de côte jusqu'à l'alignement établi et identique variation du profil de la plage. Le profil de plage a répondu au changement des conditions d'agitation, érosion et accumulation, mais la récupération a eu cours à un rythme plus lent. Les résultats ont montré que le retrait de sédiments de la plage est contrôlé para la position et élévation de la barre submergée. Les structures détachées submergées ont été efficaces dans la protection de la ligne de côte et dans l'entretien de la plage. Cette efficacité a résulté de la diminution des mouvements transversaux des sédiments, mais aussi de leur maintien au niveau de la plage supérieure.

Les résultats des mesures en laboratoire indiquent également que la profondeur maximale d'érosion localisée a diminué avec l'augmentation de la profondeur d'eau de la structure et a augmenté avec le brisement au pied de la structure. Les résultats suggèrent que cette profondeur est dominée par la réflexion de l'agitation sur la structure et par le reflux sur le talus exposé, qui peut être influencé par le niveau de la plage et de l'eau durant la période de plus grande énergie.

ACKNOWLEDGEMENTS

I would like to express my deepest gratitude and appreciation to those who have contributed to the realization of this dissertation. First and foremost, I thank my advisors Professor Maria de Lurdes Lopes and Professor Fernando Veloso Gomes for providing me the opportunity to work on this project and for all the practical and intellectual guidance throughout my research. If it were not for their constructive direction, my task would have been dramatically heavier. To work with them was and it is to me surely a challenging, joyful and enriching experience, which I gratefully acknowledge.

My thanks also go to Professor Francisco Taveira Pinto for his unflagging support and guidance to my work. I have incorporated numerous of his stimulating ideas and interesting suggestions to my thesis, but have also been inspired by his personal qualities.

Appreciation is extended to all other faculty members and staff in the Hydraulics Laboratory and in the *Instituto de Hidráulica e Recursos Hídricos* for supplying various components of knowledge and help during this study. In particular, I would like to thank Mr. Aníbal for his help in the construction and many reconstructions of the model. Special thanks go to my colleagues and friends Paulo Santos, Joaquim Barbosa, Raquel Silva, Hugo Lopes, and Guilherme Paredes for their advice and commentary on various coastal related topics, but most especially for sharing the ups and downs of an experimental work. A special word of gratitude goes to my oceanographer friend, if life at the laboratory was as pleasurable as going to the beach, it was because of Luis Leite. I will always remember your engagement and companionship. Gratitude is due to Esmeralda Miguel for her friendship and assistance in innumerable essential details. Also I would like to thank Professor Francisco Piqueiro, Professor Paulo Santos and Eng. Elsa Carvalho for having replaced me in some of my classes, Ms. Paula Pinto for her help in the task of reviewing symbols and bibliography, Ms. Fátima Monteiro for her help in filling with sand the bags and Eng. Cristina Silva for reviewing the *resumé*.

The completion of this study would not be possible without the sponsorship by the *Fundação para a Ciência e a Tecnologia* through the POCI/FEDER programme (project reference: POCI/ECM/60807/2004), and also through the POPH/QREN programme (grant reference: SFRH/BD/22626/2005), support which is here gratefully acknowledged.

I deeply appreciate the materials offered by the companies NAUE and TENCATE and I thank Eng. Filipe Cascão at BBF Tecnologias do Ambiente (NAUE representative in Portugal) and at Geosin (TENCATE representative in Portugal) Dr. Filinto Oliveira and Eng. Jorge Vasconcelos, for their assistance in this respect. Also I would like to thank Estela Golf S.A. for the access to facilities and documents that were essential to design the physical model.

To my engineer friends, Ana Cristina, Cecília, and Carla, to my good-friends at Rampa Clube, particularly São and Raquel, to my weekend-nautical-birthday-gourmet-wii-pendulum-friends, to my team e11even, and to Luisinha, Inês, Sofia and Xanda goes a warm word of gratitude for those treasuring moments we share together through the years.

My final acknowledgement is reserved to those whom I owe the most, my family, specially my parents, Eduardo, Marisa and Bernardo, for their love, support, encouragement and patience through these years.

CONTENTS

LIST OF FIGURES

LIST OF TABLES

NOMENCLATURE AND ABBREVIATIONS

CAPITAL LETTERS

A ..... coefficient
..... immersed sediment buoyancy parameter
..... sediment scale parameter
..... wave amplitude
B ..... coefficient
..... parameter
..... width of sand-filled geotextile element
B_{crest} ..... crest-width
C ..... constant
C_c ..... curvature coefficient
C_D ..... drag coefficient
C_u ..... uniformity coefficient
D ..... diameter
..... particle size
D* ..... dimensionless particle parameter
D_{50} ..... median particle diameter
D_n ..... nominal diameter (where n is a % of the sample passed, *e.g.*, 10%, 30%, or 60%)
D_s ..... sieve diameter
E ..... time-averaged wave energy
..... Young's modulus
Eu ..... Euler number, proportional to the ratio of inertial force to pressure force
F ..... force
F* ..... mobility number (densimetric Froude, or Shields parameter)
F_D ..... drag forces
F_G ..... gravitational forces
F_L ..... lift forces
Fr ..... Froude number, characterizing the ratio of the inertial force to gravity force
F_S ..... upward seepage force
G ..... shear modulus
H ..... thickness or height of sand-filled geotextile element
..... wave-height
$H_{1/10}$ ..... highest one-tenth wave
H_{m0} ..... zeroth-moment wave-height
H_{mean} ..... mean measured wave-height
H_{min} ..... minimum measured wave-height
H_{rms} ..... root-mean-square wave-height
$\overline{H_s}$ ..... annual average significant wave-height
$H_{s,12}$ ..... significant wave-height that occurs 12 hours per year on average

K ..... hydraulic conductivity of water

..... modulus of bulk elasticity for gas mediums

K_{0w} ..... true bulk modulus of pore-water without air/gas

K_r ..... coefficient of wave reflection

K_t ..... coefficient of wave transmission

K_w ..... apparent bulk modulus of the pore-water

L ..... anti-nodes or loops

..... length of sand-filled geotextile element

..... representative unit length

..... wavelength

L_B ..... length of the breakwater

..... long basin axis

L_B* ..... dimensionless length of the breakwater

Ma ..... Sarrau-Mach number, characterizing the ratio of inertial force to elasticity force

N ..... number of waves during a test

N_F ..... ratio of prototype-to-model forces

N_L ..... ratio of prototype-to-model length

N_s ..... stability number

N_U ..... ratio of prototype-to-model velocities

N_{ws} ..... ratio of prototype-to-model sediment fall speed

R_c ..... crest freeboard (crest height above mean water level)

R_d ..... run-down

Re ..... Reynolds number, characterizing the ratio of inertial force to viscous force

Re* ..... grain size Reynolds number criteria

R_u ..... run-up

S ..... wave steepness

$S(f)$ ..... variance spectral density

S* ..... dimensionless fluid-sediment parameter

S_d ..... scour depth

SF ..... shape factor

S_{max} ..... maximum scour depth

S_r ..... degree of saturation (=1 for saturated soils)

S_s ..... specific gravity

St ..... Strouhal number

T ..... time scale of scour

..... wave-period

T* ..... normalized time scale

T_n ..... natural free oscillation period

T_p ..... peak wave-period

U ..... velocity

U* ..... critical velocity

UF ..... force output to supply measurements voltage

U_{fm} ..... friction-velocity

U_{RMS} ..... root-mean-square of horizontal velocity

U_x ..... local oscillatory velocity (or orbital bed velocity)

We ..... Weber number, proportional to the ratio of inertial force to capillary force

Y ..... exponent, function of the particle size and water temperature

SMALL CAPITALS

a ..... largest length scale associated with the particle
b ..... intermediate length scale associated with the particle
c ..... minimum length scale associated with the particle
c_1 ..... empirical constant
c_L ..... coefficient
c_T ..... coefficient
d ..... depth
$e_{x, y, z}$ ..... strains
f ..... frequency
g ..... gravitational acceleration (~9.81m/s^2)
h_c ..... water level above the crest of the structure
i ..... imaginary unit, $i = \sqrt{-1}$
k ..... coefficient of permeability
k_s ..... non-dimensional roughness height
k_s^+ ..... grain size Reynolds number to equivalent sand roughness height
k_α ..... factor that take into account the effect of the lateral bed slope (α)
k_β ..... factor that take into account the effect of the longitudinal bed slope (β)
m ..... exponent
..... parameter
m_h ..... moments of wave spectrum
n ..... level of turbulence
..... nodes
..... number of nodes along the long basin axis
..... porosity
p ..... porosity
..... wave-induced pore-pressure
p_0 ..... absolute pressure
p_A ..... percentage of filling with respect to cross-section area
p_H ..... percentage of filling with respect to height
p_{max} ..... maximum pore-pressure
u'_b ..... time-averaged near-bed velocity at initiation of motion
$u'_{c,b}$ ..... near-bed velocity fluctuation at initiation of motion
u'_{rms} ..... standard deviation of u'(t)
u_{crit} ..... critical current velocity
$\bar{u}_m$ ..... mean velocity
w ..... vertical seepage velocity
w_s ..... sediment fall speed (or fall velocity, or settling velocity)
x ..... distance to shoreline
x* ..... dimensionless distance of the breakwater
x_{80} ..... surf zone width
z ..... depth below the bed surface

SUBSCRIPTS

0 ..... as subscript denotes deep-water
..... as subscript denotes horizontal bed

b ..... as subscript denotes breaking
c ..... as subscript denotes critical
eff ..... as subscript denotes effective
i .....as subscript denotes incident
..... as subscript denotes incipient
m ..... as subscript denotes model
p ..... subscript denoting peak
.....subscript denoting prototype
r ..... as subscript denotes reflected
s .....subscript denoting significant
.....subscript denoting significant
ss ..... as subscript denotes supporting structure
t ..... as subscript denotes transmitted
w .....subscript denoting water

SYMBOLS

α .....breakwater slope
.....coefficient
.....lateral bed slope
.....quantity related to the water temperature
β ..... beach slope
.....coefficient
.....longitudinal bed slope
.....quantity related to the water temperature
.....slope angle of the support of the tube
γ .....peak enhancement factor (or shape factor)
.....quantity related to the water temperature
.....specific weight
δ .....parameter
Δ ..... relative density (or buoyancy) of the tube
ΔP .....pressure difference(s)
ε .....quantity related to the water temperature
.....volume expansion
ε_1 .....broadness factor
ε_2 .....narrowness factor
η ..... lift (F_L) to drag forces (F_D) ratio
..... ripples height
θ ..... direction of incident wave
.....lateral bed slope
λ .....characteristic length
..... ripples length
μ .....fluid's dynamic viscosity
υ ..... kinematic viscosity
ρ .....density
ρ' ..... sediment immersed relative density (or immersed sediment buoyancy)

σ ..... coefficient

..... surface tension

σ_{Hs} ..... standard deviation of the significant wave-height

σ_L ..... lift stress acting on the particle

τ^* ..... dimensionless critical bed-shear stress at incipient motion

τ_b ..... bed-shear stress acting on particle

τ_c ..... Shields parameter

τ_c^* ..... time averaged dimensionless critical bed-shear stress

$\tau_c^{*'}$ ..... dimensionless critical bed-shear stress fluctuation

ϕ ..... angle of internal friction (or angle of repose of single grains)

..... friction coefficient between the tube and the foundation

χ ..... overtopping energy

..... wave absorption correction factor

ξ ..... breaker parameter, surf similarity parameter or Irribarren number

ω ..... angular frequency

Ω ..... Gourlay parameter

$\forall$ ..... particle's defining volume

ACRONYMS

LIDAR ..... LIght Detection and Ranging

BAW ..... German Federal Waterways Engineering and Research Institute

PA ..... Polyamide

PE ..... Polyethylene

PET ..... Polyester

PP ..... Polypropylene

PVC ..... Polyvinylchloride

CEN ..... European Committee for Standardization

ISO ..... International Organization for Standardization

LWI ..... *Leichtweiß* Institute for Hydraulic Engineering and Water Resources

DEC ..... Department of Civil Engineer

FEUP ..... Faculty of Engineering of the University of Porto

SWL ..... Still-Water Level

SHRHA ..... Hydraulics, Water Resources, and Environment Division

PIV ..... Particle Image Velocimetry

MSL ..... Mean Still-water-Level

FDEP ..... Florida Department of Environmental Protection

WD ..... Water Depth

DWA ..... Dynamic Wave Absorption

GSC ..... Geotextile Sand-filled Containers

GND ..... ground

I/O ..... input/output

EPP ..... Equivalent Paddle Position signal

DIP ..... Demand Input Position

FFT ..... Fast Fourier Transform

ABBREVIATIONS

ca. ..... circa
e.g. ..... example given
i.e. ..... from the latin *id est*, that is
viz. ..... from the latin *videlicet*, namely
vs. ..... versus

1. INTRODUCTION

1.1. Background and aim of the work

Eroding shorelines are, around the world, shaping and modifying the coastal landscape. Most of those landscape transformations are natural responses to various physical processes, either at a time scale of days (*e.g.*, between tides) or of years (*e.g.*, global climate change); however, the actual human development along the coast is very often incompatible with the natural dynamics of coastal systems. Such development is an end result of a lack of sustainable spatial planning (*e.g.*, by allowing urbanisation and infrastructures too close to the sea), in turn converting the natural phenomena of coastal erosion into a problem with increasing consequences, and ultimately leading to requirements for coastal defence.

The coastal engineering and management practice focus of attention is thus primarily on the maintenance of the safety of people and assets at an adequate level of protection, ensuring a low level of exposure to potentially hazardous damage to structures, as well as to economic activities. Yet protection is virtually at the same level of importance as the preservation of the natural dynamics of coastal processes to the extent that it secures the space necessary for survival (*i.e.*, the necessary space so that people living near the coast take advantage of its great abundance without suffering from enhanced exposure to erosion and/or floods); as even the most extensive and massive coastal defence scheme is not able to control the sea in the long-term under certain severe hydrodynamic conditions and, in such conditions, to protect the hinterland areas (*e.g.*, low-lying areas).

Over the last decades, the predominance in investment priorities have been toward the former aspect, maintaining the safety of people and assets at an adequate level of protection, and less toward the latter. However, in spite of such investment, the basic conflict (*i.e.*, space scarcity) remains. This does not mean that those investments (*e.g.*, in building groynes and seawalls) were not indispensable in several cases, quite on the contrary, but rather that they have not always had the anticipated morphodynamic impact. To take an example, it is common for beaches located further downdrift coastal protected areas to suffer from increased erosion due to sediment supply shortage. What is more, in various locations, coastal structures did not hamper human development along areas at risk, but have had quite the opposite effect while being illusive with respect to the actual coastal erosion and/or flooding vulnerability.

Despite the prevalence (and very often the inevitability) of such remedy measures, change in coastal practice is on the way, as neither is reasonable to expect causes for sediment supply shortage to fade away, nor to expect the trend of continuous population growth in the littoral (*i.e.*, the actual volume of residential construction, as well as economic activities) to halt. Issues such as the anticipated impact of structures on coastal processes are becoming more and more decisive in coastal engineering and management. In fact, it is not just finding a solution to a specific problem but critically looking at the wider picture to arrive at a technically and environmentally appropriate design.

However, with less and less sand available as a result of many human activities (*e.g.*, river regulation works, damming, harbour breakwaters, maintenance dredging, and sand mining), in addition to the serious impact coastal protection has had on the natural coastal dynamics, it seems that the safety of highly populated coastal areas is compromised unless innovative (and more environmentally friendly) approaches are implemented.

With the environment interest being more present in decision-making, the so-called soft coastal engineering techniques – hereby referred to those techniques that build with natural processes and rely on natural elements, such as sand, dunes, and vegetation, to prevent erosive forces from reaching the backshore – are set to play a bigger role in coastal protection; whilst any increase in vulnerability/risk is compensated with management and planning (*e.g.*, landwards reallocation of people and assets). Examples of such techniques are, for instance, the artificial infill of a beach with sand, but also coastal structures incorporating geotextile encapsulated-sand elements.

Geotextile encapsulated-sand elements can be used in a wide range of types of structures such as groynes, seawalls, artificial reefs, and perched beaches. Roughly the applications of geosystems in coastal engineering fall in two categories: closed systems, or open systems. The first category concerns closed forms/units (bags, tubes, containers, mattresses, etc.) filled with sand, gravel or mortar and made of geotextiles or water-tight geosynthetics, such as geomembranes and/or special composite systems. The second category of applications is a geosynthetic anchored at both edges with the ability to retain water or soil.

Although the concept of wrapping sand in a geotextile is not innovative – actually it goes back to the fifties (see, *e.g.*, Bezuijen and Vastenburg, 2008) – it was only in recent years that attention has turned to the use of these materials on a larger scale; whereas before it has been mostly applied on temporary and emergency works. It has also been used effectively as hidden components of structures, in shallow water with low wave energy and tidal regimes, on projects where there is no risk to life or property in the event of failure, on projects with regular inspections and maintenance, and in complement to artificial sand nourishments. Yet, despite the many advantages, generally recognized, geotextile encapsulated-sand elements are seldom alternative to more conventional materials. The explanation for this lays on the fact that there is a lack of proper design criteria in comparison with rock or concrete (see, *e.g.*, Bezuijen and Vastenburg, 2008; Pilarczyk, 2000). Indeed, contrary to research on conventional materials (*e.g.*, concrete units) there has been no systematic research on the design and stability of geosystems. Recent past research on a number of selected products, namely at the Leichtweiβ Institute in Germany (see, *e.g.*, Oumeraci and Recio, 2009; Recio, 2007; Recio and Oumeraci, 2007a, 2007b, 2007c; and Oumeraci *et al.*, 2002) and at DELTARES in The Netherlands (see, *e.g.*, van Steeg and Vastenburg, 2010; and van Steeg and Breteler, 2008), has, however, improved the knowledge available on the stability of geotextile encapsulated-sand systems under wave loading. Yet, considerable research still needs to be performed (Recio, 2007), even on the very basics.

The limitations of the geotextile itself are additional points of concern, especially for exposed applications the aspect of the material may be indeed a major limitation. They can be punctured and abraded effortlessly by vandals, and debris; their life-expectancy after extended exposure to UV-radiation is not clear; and they are difficult to construct to precise alignment and crest elevation.

Yet, some significant research and developments have been achieved at the level of the materials – *i.e.*, the significant advances made with respect to the long-term performance of geotextiles (additives and stabilizers against UV-radiation, coating against abrasion, etc.) – and of the assessment of the durability and life-time prediction (accelerated testing, standards, etc.), also contributing to the growing popularity of these systems.

Partly due to the present interest in innovative techniques of coastal engineering, partly due to the potentialities and limitations of geotextile encapsulated-sand systems, the present investigation triggered with the aim to provide contributes to the knowledge available on the stability of geotextile encapsulated-sand systems under wave loading, with emphasis on the issues of scour development and more widespread beach lowering. Such contributes will in turn provide insights to the efficiency of different geotextile encapsulated-sand systems in maintaining a beach and in protecting the shoreline.

The failure of structures due to scour is a recognized problem (Wallis *et al.*, 2009), depending on the spatial extent, scour may lead to an overall degradation of the bed or to local scour holes (CIRIA *et al.*, 2007). While the former may lead to the gradual dislocation of the foundation and decrease the geotechnical stability of the

structure (Oumeraci, 1993); increased water depths due to scour may increase the hydraulic loading in front of the structure (CIRIA *et al.*, 2007). Both the aspects clearly illustrate how big a threat is scour to the stability of coastal structures in general.

Recent years have witnessed a rapid development of the knowledge of flow and scour processes around marine structures, particularly those with simple geometries such as pipelines, and piles (Sumer and FredsØe, 2002). The scour problems around coastal defence structures incorporating geotextile encapsulated-sand systems have not received the same kind of attention. To date research was able to bring about some developments on the stability of geotextile encapsulated-sand systems under wave loading (see, *e.g.*, van Steeg and Vastenburg, 2010; Oumeraci and Recio, 2009; van Steeg and Breteler, 2008; and Recio, 2007), but to author's knowledge still no information is available for the assessment of scour around those structures.

This thesis summarizes the motivation, challenges and results of the author's research contributions to the incorporation of geotextile encapsulated-sand systems in coastal engineering, with emphasis on their application at more exposed hydraulic conditions (*i.e.*, high wave energy with large water-level variations), as is on the Portuguese west coast. The research programme makes use of prototype monitoring and physical movable-bed model test series carried out at the Hydraulics Laboratory of the Faculty of Engineering of the University of Porto to compare cross-shore profiles under accretive and erosive wave conditions, for different layouts with different geotextile materials in active and passive coastal defence structures. The research motivation is based on the belief that the search for innovative solutions in coastal engineering, specifically for those that build-with-nature, must be made urgently, and that it is still possible to bring about improvement in the understanding of the processes and mechanisms responsible for the stability and performance of sand-filled geosystems under wave loading.

The present work is a contribution to that knowledge. It will not cover all unresolved issues but rather focus on a main objective with implications for practice, which relate to the instability caused by scour, and the consequences of more widespread beach-lowering.

A different but complementary focus is to sketch the background against which the decision for one type of scheme/material should be made (*e.g.*, hydrodynamic and morphologic conditions, installation, etc.), with emphasis on its application at more exposed hydraulic conditions.

1.2. Outline of the thesis

As referred already, the present thesis summarizes the author's research and development work on the incorporation of geosynthetics and geosystems in coastal engineering defence systems, carried out at the Hydraulics Laboratory (LH) of the Department of Civil Engineering (DEC) of the Faculty of Engineering of the University of Porto (FEUP). The main text of the thesis is divided into six chapters, which cover the following aspects:

Chapter 1 is constituted by the present chapter, which introduces the topic of the present contribution and briefly illustrates its relevance to state-of-the-art knowledge and to practice. It explains the motivation for this research, the strategy to meet its scientific objectives, and the structure of the contents.

Chapter 2 introduces the general background to the topic. The content is divided into two main sections and has been kept concise and focused. The first section gives a brief description on the impact of coastal engineering works in coastal processes, emphasizing the response to the equilibrium lost due to changes with impact on the dominant agents (*e.g.*, waves, currents, sediments), and the types and functions of coastal structures. Focus is also given to factors that have to be fulfilled by a certain material when incorporated into a specific coastal defence structure. The second one discusses aspects concerning the use of geosynthetics in various coastal engineering applications, based on Portuguese and worldwide experiences.

Chapter 3 covers the literature survey on different aspects related to the main goals of the present research and is divided into four sections and a summary. The first section provides an overview of the most relevant properties of geosynthetics in coastal engineering applications and briefly describes the state-of-the-art knowledge on the hydraulic performance and structural stability of geotextile sand-filled containers under wave loading. The following deals with scaling requirements for movable bed wave models, and introduce the shortcomings of this type of models due to scale effects. The third one presents the principle mechanisms of the cross-shore component of sediment transport and the ensuing morphologic changes. The last section is an attempt to identify the hydrodynamic processes causing scour in front of sloping structures, highlighting its potential impact on the stability of the structure, and to understand the dominant response mechanisms of the bed sediments.

Chapter 4 describes the experimental set-up used for the analysis reported in Chapter 5. The description and problem definition in this chapter take the outputs from examples of application (discussed in Chapter 2), the hydrodynamic processes causing scour in front of sloping structures (discussed in Chapter 3) and the hydraulic performance and structural stability of geotextile encapsulated-sand systems under wave loading derived in Chapter 3. The key features of the instruments used in the experimental set-up are also summarized in this chapter. Special attention is given to the miniature pore-pressure sensors and respective DAQ-system, which have never been used at FEUP hydraulics laboratory outside the present research. The basic principles of data-processing for each measuring technique and the methodology used for the investigation are presented.

Chapter 5 presents the results of the experimental research conducted in the frame of the present dissertation. A systematic study on scour development and more widespread beach lowering around sand-filled geosystems was conducted based measurements in a coastal sediment physical model. Various erosion control system layouts were studied aim to provide insights into the efficiency of each system in maintaining a beach and in protecting the shoreline. For this purpose different models of active and passive coastal defence structures have been set-up to run on similar hydrodynamic and morphodynamic conditions. The intercomparison carried out on the hydrodynamic and morphodynamic output produced by each scheme focused on the scour and deposition patterns over the test period evaluated on the parameters deep-water wave characteristics (H_0, L_0), reflection coefficient (K_r), and wave-induced pore-pressures. The next step was to increase understanding of the response of the beach under persistent erosional conditions and under periods of erosion followed by infilling and again erosion.

Chapter 6 summarizes the main conclusions of the thesis and presents suggestions for future research.

2. GENERAL BACKGROUND TO THE TOPIC

2.1. Introduction

The continuous population growth in the littoral has increased the volume of residential construction along the coastline enhancing the exposure to potentially hazardous damage to structures, as well as to economic activities. To help maintain safety of people and assets at acceptable levels many coastal defence schemes were developed. This chapter discusses main general aspects concerning the use of geosynthetics in various applications in coastal engineering, from erosion causes to worldwide examples of the application.

2.2. Shoreline protection and beach control structures

2.2.1. Coastal erosion

Utilisation of the coast increased dramatically during the 20th century and this trend is virtually certain to continue through the 21st century (Nicholls *et al.*, 2007). It has been estimated that 23% of the world's population lives both within 100km distance and less than 100m above sea level, and population densities in coastal regions are about three times higher than the global average (Small and Nicholls, 2003). This migration has become a true invasion of the coast, putting tremendous pressure on a scarce natural resource (Kamphuis, 2000).

The potential for conflict increases in direct proportion to the number of persons depending on coastal zones, especially those linked to competition for space.

Coastal systems are naturally dynamic systems, subject to morphological change that operate on different time and spatial scales (see *e.g.*, Comissão Europeia, 2006; Cowell *et al.*, 2003a, 2003b). Coastal systems respond as well to equilibrium lost due to changes with impact on the dominant agents (*e.g.*, waves, currents, sediments).

Each coastal environment reflect thus the interaction between anthropogenic factors (*e.g.*, change in natural flow conditions), and natural ones (*e.g.*, sea level rise), see *e.g.*, Mangor (2004), Veloso-Gomes *et al.* (2004b), and Comissão Europeia (2006). It also reflects the inputs and outputs affecting the system and neighbouring systems. In the manner of sediment transport, the response, inside a sedimentary cell, to all the inputs, outputs and interactions is of erosion when the sea encroaches upon the land due to sediment shortage or conversely, of accretion. Figure 2.1 indicates some of the inputs, outputs and elements of the simplest of coastal zone sub-systems, a short beach section between two structures, placed more or less perpendicular to the shore.

Both phenomena erosion and accretion are natural, have always existed (and will exist) and throughout History have shaped coastlines. This is an obvious statement, but a consensus view is more difficult to obtain in practice, especially in the case of erosion. Evidence demonstrate that pressures, impacts and conflicts, especially human-induced ones, are resulting in an accelerating difficulty in reconciling the safety of people and assets with natural coastal processes (Figure 2.2) and therefore, coastal erosion is essentially regarded as a problem of increasing intensity.

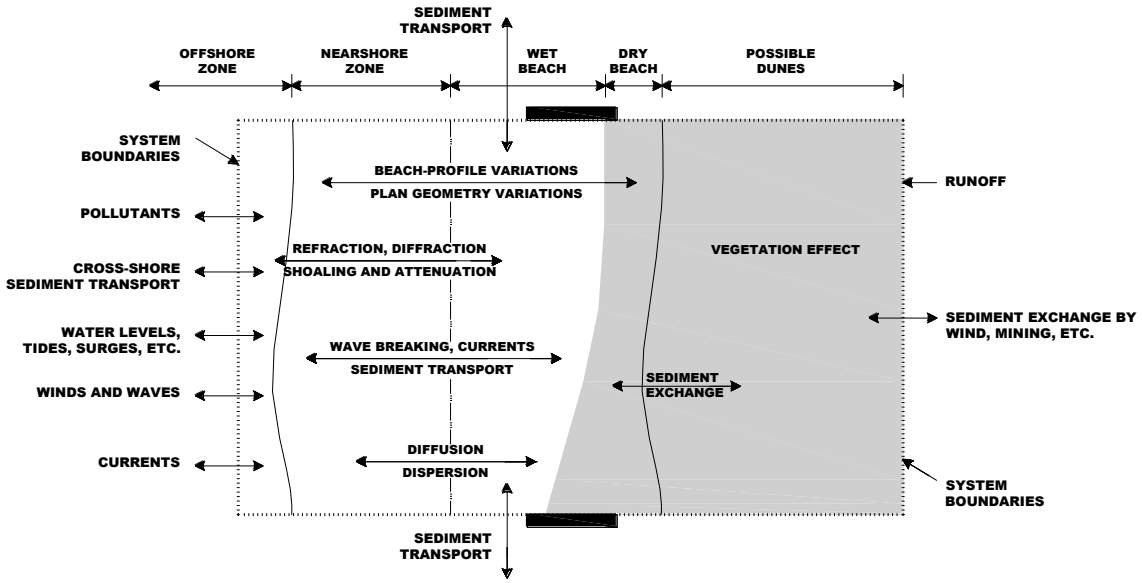

Figure 2.1: Main inputs, outputs and elements inside a sedimentary cell, a short beach between two structures (adapted from Kamphuis, 2000).

Figure 2.2: Shoreline retreat: protection structures in front of *Cortegaça* (photo by DRAOT).

2.2.2. Preventing shoreline erosion and flooding of the hinterland

Coastal defence schemes cover several types of applications, although the most common one is preventing shoreline erosion and flooding of the hinterland. This chapter describes a range of structures built to protect and prevent beach erosion. It also provides a brief overview on the advantages and the limitations of the options in scope, as summarized in Table 2.I.

Along the Portuguese coast, the most commonly used structures are the groynes and the seawalls. Other more unconventional coastal protection schemes include beach nourishment (*e.g.*, the case of the recent intervention on *Costa da Caparica*), and dune erosion control systems. Some examples are shown in Figures 2.3 to 2.6. Structures other than the ones included in Table 2.I, are built with objectives such as sheltering of harbour basins and harbour entrances against waves, stabilization of navigation channels at inlets, and protection of water intakes and outfalls.

It will become clear that there are no absolute rules, nor definitive solutions to protect the coast and the shore against the erosive forces of waves, currents and storm surges. Often for one shore to accrete, one is eroding downdrift. In other areas, remedial measures are no longer efficient due to modifications to sediment sources. In a given situation, the option for one type of structure, or for a combination of two or more, is always a compromise between the specificity of the problem being solved (persistent erosion at the shoreline, flooding of low-lying areas, etc.), the morphological conditions (the shoreline type and the beach-profile type), and the land-use (residential, recreational, agricultural, etc.), against the anticipated impact of structures on coastal processes. Those impacts are well dealt in numerous textbooks (*e.g.*, the several volumes of the Coastal Engineering Manual; and Mangor, 2004) from which a concise review is given.

Table 2.I: Description and function of coastal structures in scope
(modified from USACE, 2008).

Structure Type	**Description**	**Function**
Groynes and artificial headlands (Figure 2.3)	Structure generally constructed on a beach perpendicular to the shore. Groynes are typically built as rubble mound structure, but they can also be constructed in other materials, such as concrete units, geosystems, etc. The use of geosynthetic filters are a common application as well.	Intercepts (reduces) the longshore transport of sediments and traps beach material.
Seawalls and revetments (Figure 2.4)	Protective structure normally placed on embankment or profiled fill material. Geosynthetics can replace stone filters but can as well be used to build the whole structure or just the core.	Reinforces some part of the beach profile and protects low-lying areas against flooding.
Detached or reef breakwaters (Figure 2.5)	Structure generally constructed parallel to, but not connected to, shore. Typically is a rock mound structure, with or without concrete armour layers. Geosynthetics can replace stone filters but can as well be used to build the whole structure or just the core.	Reduces wave heights at the shore and longshore transport of sediments.
Submerged sills or berms	Structure generally constructed parallel to shore at the beach toe. It is a structure similar to a reef breakwater built nearshore.	Retard offshore movement of sediment by trapping it in the upper beach.
Beach nourishment and dune construction (Figure 2.6)	Artificial infill of beach and dune material. The core of the dunes can be reinforced with geosynthetic-encapsulated sand.	Artificial infill of beach and dune material to be eroded by waves and currents.
Scour protection	Protection at toe of structure, with *e.g.* rock or geotextile sand-filled containers.	Provides resistance to erosion caused by waves and currents and prevents undermining of the structure.

Figure 2.3: *Espinho* beach groynes
(photo by INAG).

Figure 2.4: Seawall at Granja beach
(photo by Google maps).

Figure 2.5: Detached breakwater at *Aguda* beach
(photo by Google maps).

Figure 2.6: Beach nourishment of Vale do Lobo beach
(photo by DRAGAPOR – Dragagens de Portugal, S.A.).

Groynes can be placed in single, in groups – the so-called groyne fields – or in association with other coastal structures, namely seawalls, detached breakwaters, and beach nourishment. Groynes are usually straight and perpendicular to the shoreline, although zigzag shapes as well as straight ones with Y-, T- and L-shaped heads have been used. Groynes can be permeable or impermeable. They can be classified as emerged, submerged or sloping depending on the crest elevation against water level and variation of elevation across the crest, and might also be classified as long or short depending on how far across the surf zone they extend.

The effect of a single groyne is accretion of the beach on the updrift side and erosion on the downdrift; both effects extend some distance from the structure (USACE, 2008). Groynes effectiveness is strictly related to the volume of sediments transported by the littoral drift current. Figure 2.7 shows a typical beach configuration with groynes and examples of conventional cross-sections.

The partial entrapment of sediments will normally impact the shoreline dynamic equilibrium downdrift, as the net longshore sediment transport is no longer adequate to provide with sufficient backfill material to the beaches. This is their principal and most important disadvantage. Moreover, groynes cannot prevent cross-shore transport of sediment.

When placed in groups along a shoreline, extra attention should be given to the terminal groyne and the construction sequence. Conveniently the construction sequence should permit an appropriate infilling of the beach against the dominant incoming waves, while permitting as well an analysis of the shoreline alignment following groyne construction. The spacing of groynes, as well as their individual permeability, length, height and orientation are the most important parameters in terms of effects of a groyne system on current flow patterns. Because of the expected lee side erosion, some cross-groyne transport is beneficial for obtaining a well-distributed retaining effect along the coast.

Groynes can consist of sand-filled geotextile fabric bags and tubes. Some examples are introduced later in section 2.3.

A headland combines the effects of groynes and detached breakwaters and at the same time, minimizes some of the disadvantages of groynes and breakwaters (Mangor, 2004). Headlands, which are smooth structures built from the coastline over the beach and some distance out on the shoreface, work by partly blocking the longshore transport.

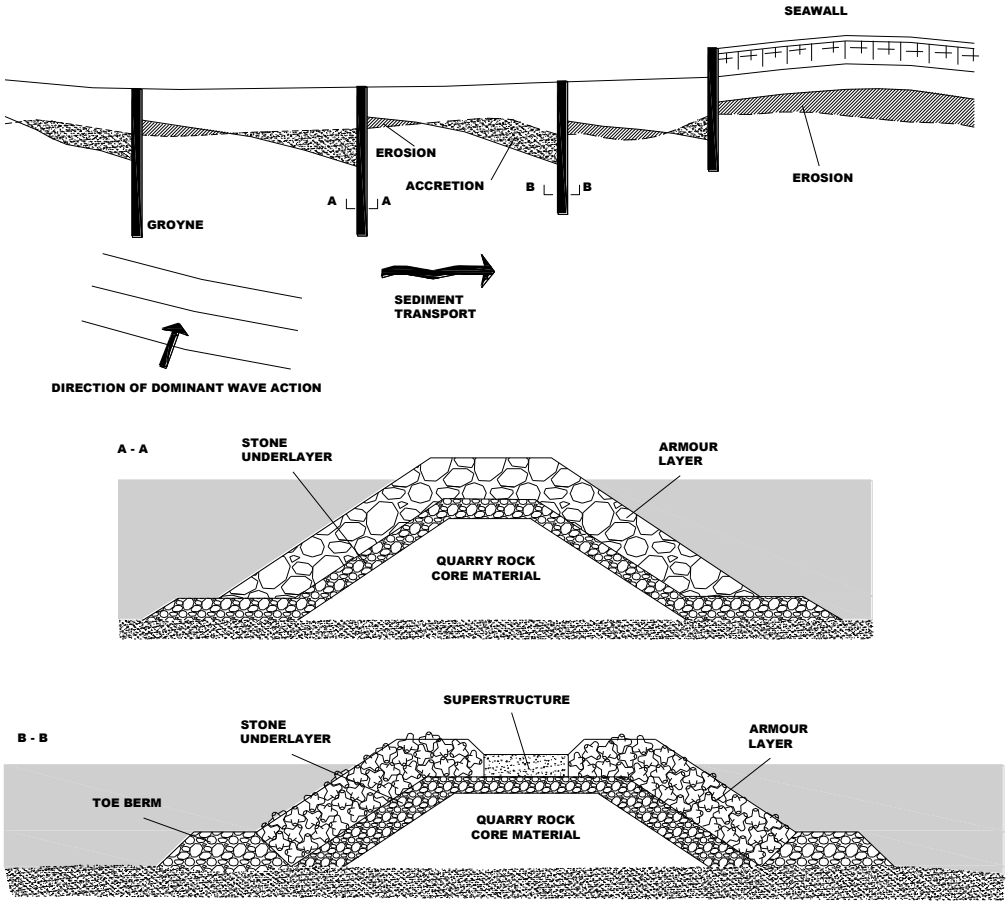

Figure 2.7: Shoreline development for a groyne field, and examples of conventional cross-sections (modified from USACE, 2008).

Seawalls and revetments differ by function but they are often similar in construction. Some authors (see, *e.g.*, Mangor, 2004) distinguish a seawall from a revetment by the protection against coastal flooding. In the U.S. Army Corps of Engineers the functional distinction is made between seawalls and revetments for the purpose of assigning project benefits (USACE, 2008). However, in most of the available technical literature there is no distinction whatsoever between the two and they are dealt as synonyms.

A seawall is an onshore parallel structure constructed at the coastline in the alignment one wishes to fix. It is a passive structure, which protects urban seafronts and promenades against erosion and coastal flooding caused by wave action, storm surges and currents, but will not arrest the ongoing erosion in the coastal profile. They are often used at very exposed locations where a high level of protection is required and limited space is available.

Seawalls are generally very massive slopping stone or concrete structures that can be smooth, stepped-faced or curved-faced, and can be also permeable or impermeable (Figure 2.8). Typically the beach in front of a seawall will in most cases disappear due to increased wave reflection caused by the seawall. Steeper seabed profiles are therefore expected in front of such structures which in turn will allow larger waves to reach it. Figure 2.2 clearly illustrates this effect, the shoreline has retreat as far as the established urban seafront line of defence and further retreat will implicate loss of the houses on the top of the small capes protruding from the natural coastline which have in time developed. Seawalls are prone to become instable by scour, and by wave slamming, run-up, and overtopping.

A revetment is, just as a seawall, onshore parallel structures. Revetments are built to protect scarp edges, dune or cliff toes, etc., against erosion by wave action, storm surges and currents. Revetments are typically slopping stone or concrete permeable structures but can also consist of sand-filled geotextile containers, tubes, and mattresses.

Big sand bags, which are used both in seawalls and revetments and differ from containers and tubes in size, are mostly used as emergency protection.

Factors that would contribute to increase the stability of onshore parallel structures are the presence of a stable rock foreshore and the capacity of the system to accommodate displacements of individual units of the structure, reshaping and differential settlements, etc., without failure.

Detached breakwaters are non-shore-connected nearshore breakwaters with the principal function of reducing beach erosion. Detached breakwaters are typically parallel or close to parallel structures built inside or outside the surf-zone. Like groynes, they can be placed in single, in groups or in association with other coastal structures, namely groynes, and beach nourishment. They can be classified as offshore, coastal or beach depending on their location in regard to the surf-zone (Figure 2.9).

By reflecting and dissipating some of the incoming wave energy, detached breakwaters partly provide wave shelter behind it. They as well generate diffraction currents at the heads of the structure, which transport sediments to the sheltered area in the lee side of the structure. These diffraction currents are important and occur even when there is no significant longshore transport and so the use of such detached structures is convenient in such cases (Taveira-Pinto, 2001). The sand accumulation pattern behind a detached breakwater can form a smooth salient in the shoreline or a tombolo connecting the breakwater to the beach (Figure 2.10); these accumulations are due to change in flow velocity in the vicinity of the structure and depend on the type of breakwater and parameters such as length, and distance to shoreline.

The definition parameters characterizing detached breakwaters and accumulation forms referred to in Figures 2.9 and 2.10 are the ones proposed in Mangor (2004). The most important parameters are L_B, length of the breakwater; x, distance to shoreline; x_{80}, surf-zone width, as approximately 80% of the transport takes place landwards of this line. These parameters can be transformed into dimensionless length and distance $L_B^*=L_B/x$, length relative to distance to shoreline, and $x^*=x/x_{80}$, distance relative to surf-zone width.

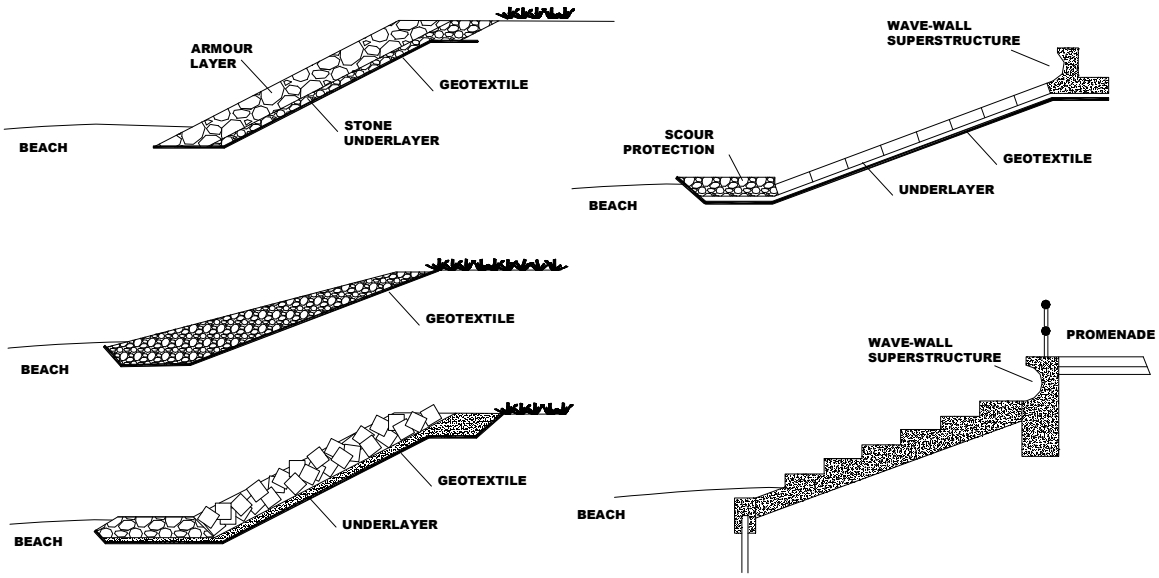

Figure 2.8: Examples of conventional cross-section of seawalls
(modified from USACE, 2008).

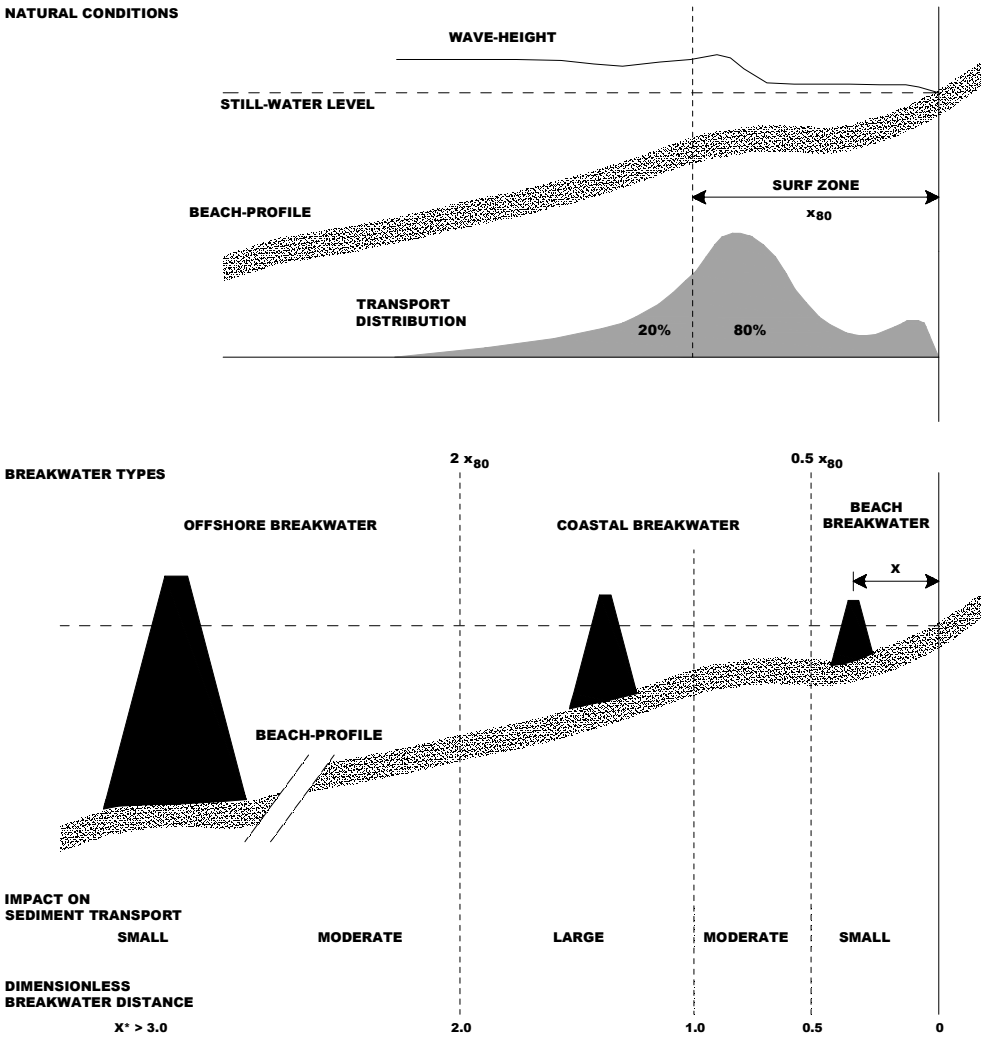

Figure 2.9: Types of detached breakwaters
(adapted from Mangor, 2004).

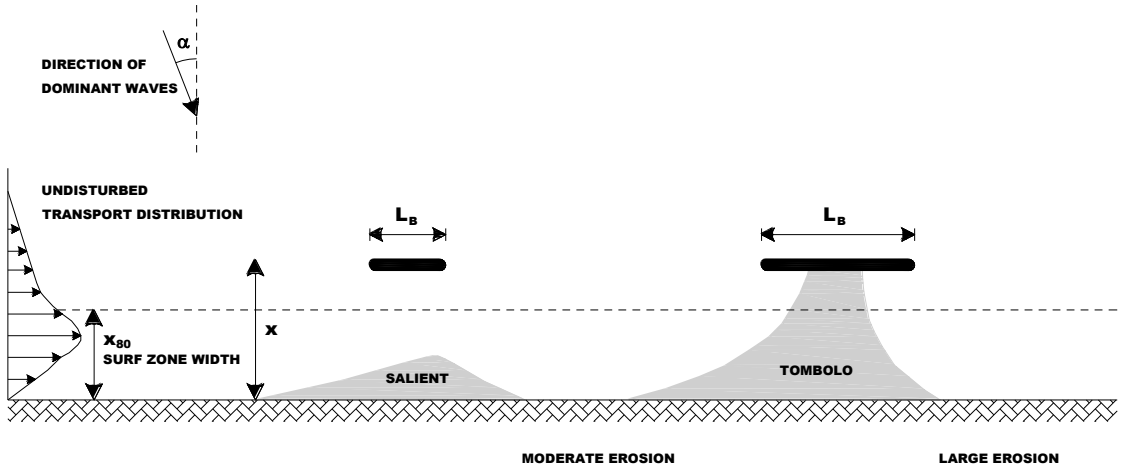

Figure 2.10: Definition of parameters characterising detached breakwaters and accumulations forms (adapted from Mangor, 2004).

Mangor (2004) suggests that when the dimensionless breakwater length L_B* is less than approximately 0.6 to 0.7, a bell-shaped salient in the shoreline will form in the lee of the breakwater, while a sand accumulation will connect the beach to the breakwater in a tombolo formation if that parameter is greater than approximately 0.9 to 1.0.

When placed in groups along a shoreline another parameter should be added to the latter – location relative to surf zone, length of the breakwater, and distance to shoreline – which is the spacing between breakwaters. To prevent the increasing of erosion that is anticipated downdrift the terminal structure in a series of detached breakwaters it is convenient to introduce a transition section where the breakwaters gradually are made smaller and placed closer to the shoreline. A groyne or a seawall can be placed downdrift a detached breakwater field as additional protection.

Detached breakwaters are regarded as effective structures in reducing erosion, building up beaches using natural littoral drift and holding artificially nourished sand; yet their design is difficult when large water-level variations are present, as is the case on the Portuguese coastline where the tidal range can be up to 4m.

Reef breakwaters are coast-parallel, long or short submerged structures built with the objective of reducing the wave action on the beach by forcing wave breaking over the reef (USACE, 2008).

Submerged detached breakwaters are aesthetically more appealing than emerged ones but are less efficient in accumulating sand in the lee side. Besides the above-mentioned parameters, low-crested breakwaters design introduces two additional ones, the crest freeboard and the crest width.

The main reasons for selecting a reef breakwater instead of a detached breakwater may be linked to less damaging visual impacts; less expensive construction costs; lower impact on coastal sediment transport; better water circulation behind the breakwater; and more favourable conditions for marine life growth. However, there are some shortcomings to reef breakwaters namely a submerged breakwater can be dangerous for small craft navigation; the overtopping discharges initiates local currents, which can be dangerous for swimmers; a low-crested structure provides only partial attenuation of the wave action as well as partial shore and coastal protection. The other main disadvantage is linked to proper design and is similar to the difficulty in optimizing emerged detached breakwaters design in areas with large water-level variations. The efficiency of a submerged structure with respect to the attenuation of both waves and littoral transport and with respect to shore protection very much depends on the design crest freeboard, the wave conditions and the water-level. This means that if there is considerable tide and storm surge the structure will end up being rather high or rather low relative to the normal water-level.

Detached and reef breakwaters are normally built as rubble-mound structures constructed as a homogeneous pile of stone or concrete armour units (see, *e.g.*, USACE, 2008) however, fill-containing geosystems (*e.g.*, sand-tubes and sand-containers) have grown in interest in the past recent.

A submerged sill is a special version of a reef breakwater built nearshore. It is used to retard offshore sand movements by introducing a structural barrier at one point on the beach profile so that the beach behind it becomes a perched beach as it is at higher elevation and is thus wider than the adjacent beaches. Submerged sills are also used to retain artificial sand nourishments (*e.g.*, the Copacabana beach project).

The main disadvantage of this structure is that it may also interrupt the onshore sand movement, *i.e.* the sand that is moved from the upper part of the beach profile to deeper water during extreme conditions may be irreversible lost. A higher sill would minimize the sand loss but with adverse and undesirable consequences. Under more extreme wave conditions wave-breaking can lead to significant mass transport over the sill, and to the formation of dangerous and difficult to predict current circulation patterns; while in calmer conditions it may result in stagnant water and poorer water quality.

Beach nourishment is a technique of artificial infilling of beaches with sediment of preferably the same, or larger, grain size and density as the natural beach material (see, *e.g.*, USACE, 2008). It may be a remedy or a preventive solution of shoreline protection to replace a deficit in the sediment budget over a certain stretch or, eventually, to create a wider beach. It can be divided into three types (see Figure 2.12): backshore nourishment which consists in the strengthening of the upper part of the beach by placing nourishment on the backshore or at the foot of the dunes; beach nourishment which is the supply of sand to the shore to increase the recreational value and/or to secure the beach against shore erosion by feeding sand on the beach; and shoreface nourishment which is the supply of sand to the outer part of the coastal profile, typically on the seaside of the bar. It may be applied as a stand-alone solution or, as seen before, combined with other structures.

Beachfills are costly solutions of difficult design, both for the variety of parameters involved in the design (*e.g.*, areas of lending, wave energy levels, characteristics of borrow material, understanding of the beach-profile response to individual and sequence of events, nourishment methods) and for the long-term maintenance effort that it requires.

A more detailed description of methods, design and long-term maintenance of beach nourishments can be found in texts dedicated to this topic like those from USACE (2008), Creed *et al.* (2000) and Dean and Yoo (1994).

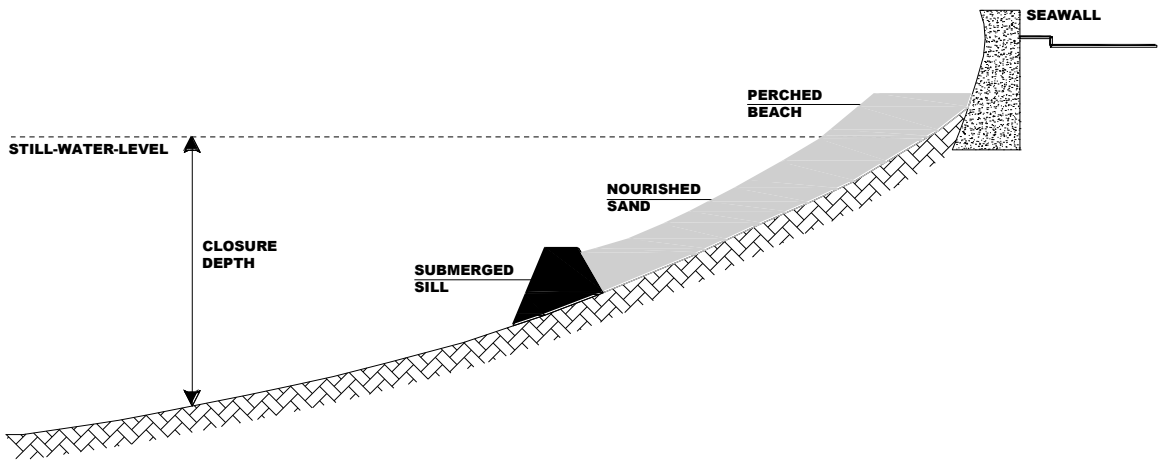

Figure 2.11: A sketch of a perched beach consisting of a beach fill (nourished sand) supported by a submerged sill (adapted from Mangor, 2004).

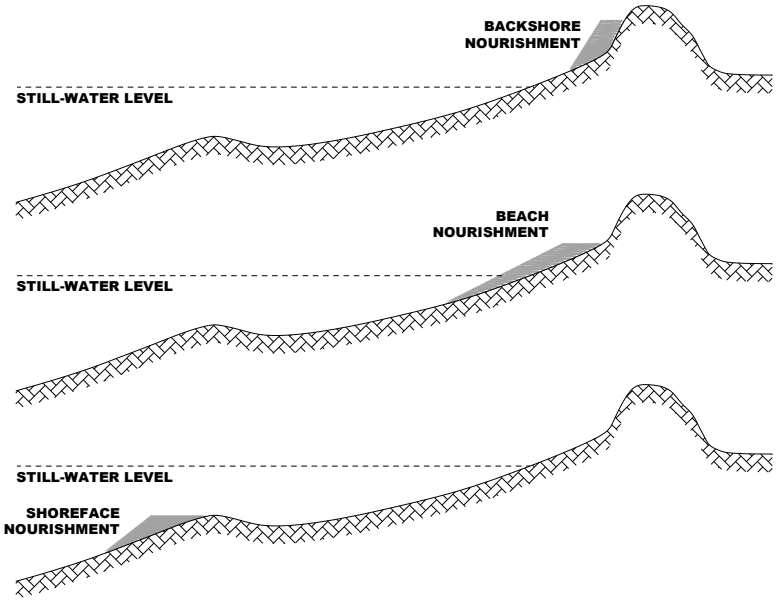

Figure 2.12: Principles in backshore nourishment, beach nourishment and shoreface nourishment (adapted from Mangor, 2004).

Dune construction is the piling up of beach quality sand to form protective dune fields to replace those washed away during severe storms (USACE, 2008). To help retain those dune fields it is common the plantation of dune vegetation and the placement of netting or snow fencing. In more severe cases, when some extra protection measures are necessary, it may be adequate to reinforce the sand dune core incorporating geotextile encapsulated-sand systems. Examples of dune reinforcement with geotextiles are given in the following section.

The instability caused by scour may require the use of a scour protection. It is commonly used in structures with foundations that rely on movable seabed that can be eroded by the action of waves and currents (*e.g.*, highly reflective structures). Typically it consists of a rock bed on stone or geotextile filter; however, several concrete block and mattresses systems with fixed design exist. Geotextile encapsulated-sand systems are often used as well.

The herein presented protective measures all concentrate on preventing the loss due to coastal erosion. However, as the cause of erosion is not eliminated, erosion may continue at the section being protected (*e.g.*, in a nourished beach) or in the neighbouring areas (*e.g.*, downdrift groynes). This means that to arrive at a technically and environmentally appropriate design, is crucial to roughly identify the causes of erosion and then to define the short to long-term requirements of protection in view of the acceptance of the impacts of that protection on coastal processes and how they will affect the system and neighbouring systems.

2.2.3. Considerations on materials in marine environment

In maritime construction works, either of erosion and scour prevention, or wave overtopping and flooding limitation, rock and concrete are commonly employed materials. Other materials, such the ones of interest to the scope of the present thesis – the geosynthetics, may also be used instead. This paragraph discusses general key considerations for materials in marine environment more detailed guidance on materials in coastal engineering can be found at CIRIA *et al.* (2007) and USACE (2008).

Factors that have to be fulfilled by a certain material when incorporated into a specific coastal structure concern primarily the achievement of functional requirements over time, along with other technical (*e.g.*, physical conditions, buildability, and maintenance), economical, environmental, and social considerations. Project constraints for any of the former requirements may also dictate aspects of design.

Structure lifetime and performance is linked to the choice of materials. Physical properties and strength, durability and degradation, adaptability, cost, handling requirements, available material sources, maintenance requirements and environmental impacts are the most relevant material considerations for use in design. It may help to examine past performance of a particular material in similar projects, as will become evident along the following section of this chapter.

System response that is the exercise of relating properties to functional requirements will be treated in Chapter 3, whereas this section deals with general consideration on material properties, individually or as a system, such as strength, durability, adaptability, and cost. Chapter 3 also provides specific guidance to geosynthetics properties and functions.

Material properties can be categorized as physical (*e.g.*, mass density), mechanical (*e.g.*, strength), geometrical, chemical and environmental (*e.g.*, aesthetic requirements). These properties evolve over the structure life cycle, depend upon site conditions (*e.g.*, loading intensity), and some depend upon each other (*e.g.*, strength properties can determine geometrical ones).

The extent to which the material loses performance quantifies durability, which is also influenced by degradation processes during handling and in-service.

Factors that affect a material's durability include its ability to resist abrasion, chemical attack and corrosion, marine biodegradation, wet/dry cycles, freeze/thaw cycles, and temperature extremes (USACE, 2008). Geotextile fabrics are very susceptible to weathering and must be protected against UV-light. Geotextiles are also fragile against mechanical impact and vandalism.

The term durability is also applied to refer the capacity of the project to continue functioning at an acceptable level even after the construction material has begun to degrade.

Project demands can force the use of a combination of different materials, for which compatibility should be assessed, as different materials may degrade at different rates and by different causes influencing structure durability. Such compatibility refers to both physical and chemical properties and is relevant in the extent of the additional induced stresses or component failure when not accurately considered.

Structure components in coastal engineering projects are often submitted to continual cyclic and impact wave loading. Materials, components, and structures with good flexibility will help absorb those loads up to the limit of fatigue failure, plastic deformation and crack formation. Complementarily, some structures can as well accommodate settlements and changes in slope without losing functionality and structural stability.

Material cost is another important design consideration. It includes actual material cost, transportation cost and special material handling requirements, and needs to be considered in terms of the project's life cycle, considering first costs, and projected maintenance expenses.

Finally, there are also considerations related with present and future material availability and material environmental impacts (*e.g.*, effects during construction, capacity to provide viable habitat, and present and future visual impacts).

Designers have quite as many aspects to consider when choosing a material as alternative materials to choose from. The use of each material brings additional advantages or disadvantages to the hydraulic performance and structural response of a coastal structure that have to be taken into consideration when designing protection works.

Chapter 3 of the present thesis is a complement to the more general considerations given along this paragraph, with respect to materials in marine environment.

2.3. Application of geosynthetics in coastal engineering

The first application of geosystems dates from the 50-ties of the last century (Bezuijen and Vastenburg, 2008). For instance, on the German North Sea coast sand-filled flexible tubes of plastic fabrics for long-range or temporary coastal protection purposes have been used since 1967 (Erchinger, 1993). Yet, it was only in the past recent that attention has turned to the use of these materials in permanent structures and as alternative to more traditional materials and systems.

A very important aspect of such turning links to the advantages those systems show relative to conventional coastal structures of rock or concrete units. Sand-filled geosystems made of flexible, high-tensile strength geotextiles are considered environmentally sound solutions (because they rely on a natural element and are able to slow down erosion with a limited and non-permanent impact on natural coastal processes), and are generally acknowledged by their cost-effectiveness, simplicity in placement and constructability.

Despite the advantages, for a more general application of geosystems in coastal engineering further investigation, experiments and practical experience at various climatic conditions are essential; as there is not only a lack of general valid design methods, but also the limitations of the geosystem itself are additional points of concern. Both the aspects will be referred to again in the following chapters, whereas in this section, a selected number of worldwide and Portuguese experiences with geosystems, either as closed forms/units or opens systems, is reviewed with respect to functional aspects, possible constructional and maintenance constraints, and performance.

A description on selected coastal protection structures using geosystems and troubles at design stage, during building or after construction is provided here. It is mainly intended to give a perception of what is happening in the field of geotextiles and geosystems in coastal engineering – *i.e.*, rapid development of the market with new products and an increasing number of conceptual ideas and actual examples – and to transmit pertinent information gained from existing projects. Eventually it will justify some of the enthusiasm around this topic, and thrown some light on those projects that were not a direct success.

As already mentioned along this chapter, geotextile encapsulated-sand elements can be used in a wide range of types of structures such as groynes, seawalls, artificial reefs, and perched beaches. Roughly the possible applications fall in two categories (see Figure 2.13): closed systems, or open systems. The first category concerns closed forms/units (bags, tubes, containers, etc.) filled with sand, gravel or mortar and made of geotextiles or water-tight geosynthetics, such as geomembranes and/or special composite systems. The second category of applications is a geosynthetic anchored at both edges with the ability to retain water or soil.

For the reason that it is not possible to comprehensively describe all possible applications in each category, and because this study is directed towards sand-filled geosystems, other applications such as geosystems filled with mortar, water-tight geomembrane tubes, dewatering systems, surface screens used to prevent the transportation of polluted sediments, will not be covered, not because they are less important but mostly because they are much beyond the scope of the present thesis.

Equally excluded from this overview is the application of geotextiles as filters (*e.g.*, in quay walls) since it is a common application with quite an extensive number of references in the literature. Yet, it is noteworthy the thorough list of studies performed in the 70-ties, 80-ties, and beginning of the 90-ties of the last century, on woven and non-woven geotextile filter design criteria included in Pilarczyk (2000).

In the manner of the worldwide experience on the application of geotextile systems there is some published and documented information, of which Pilarczyk (2000) has the most thorough review of geosynthetics and geosystems in coastal engineering and is still the reference book on this topic. CUR (2004), CUR (2006), and Saathoff (2003) are also invaluable references.

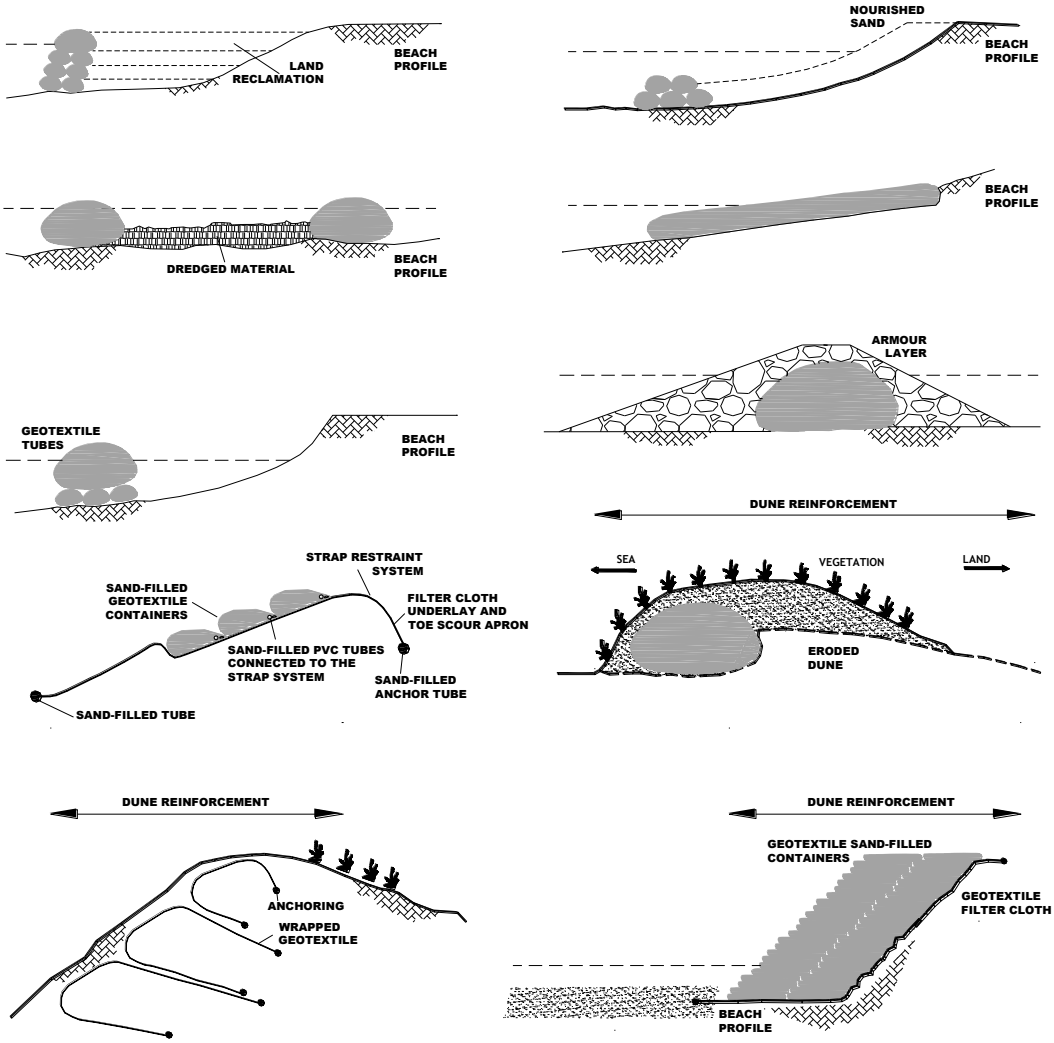

Figure 2.13: Some concepts on the application of geotextile encapsulated-sand elements (modified from Pilarczyk, 2000).

Commercial folders from manufacturer or supplier companies are usually interesting for ideas and start-up concepts. These are a catalogue of possible applications but very often solutions are purported there as the ultimate answer to protect the coast and the shore against the erosive forces of waves, currents and storm surge. Even if this were so, a more general application of geosystems to coastal engineering requires, as above said, further investigation, experiments and practical experience at various climatic conditions.

The case studies briefly described hereafter, were selected from the literature and reflect the comprehensive effort made by the author to get past performance indicators out of the most significant projects for which reliable monitoring data is available. When possible, information on hydrodynamic conditions is given also.

2.3.1. Worldwide experience

2.3.1.1. Geosystems to reinforce beaches and dunes

Dune systems are in many situations in an advanced state of degradation, and in several other have already disappeared. This fact is very negative, as dune systems are often the main protection against coastal flooding of the inland fields. The reduction of this protection is due not only to coastal erosion with subsequent effects of decrease in beach width and dune systems being further submitted to the direct wave run-up actions, but also to man-induced effects (*e.g.*, construction over dunes, public access through the dunes and trampling).

Given the importance of that protection with respect to coastal erosion, there is increasing awareness of the importance of stabilising, protecting, recovering and rehabilitating dune systems. Typically, this awareness is reflected in construction of surmount footbridges, planting of dune vegetation and placement of netting or fencing to help retain wind-blown sand normally trapped by mature dune vegetation.

Yet, in many locations those actions are not enough, and supplement measures of reinforcement have to be used. Such reinforcement may use geosystems, as, *e.g.*, wrapped-around geotextiles or sand-filled tubes/containers forming a backshore sill, submerged sills, and sand-filled tubes/mattresses placed transversely to the coastline and buried on the beach.

The following examples give a rough idea of the potentialities of geosystems in beach and dune reinforcement. They were chosen by concept representativeness – one example of a geotextile tube as a dune core, one example of a geotextile tube as a submerged sill, one example of an embankment of geotextile cushions, and one example of a revetment of geotextile sand-filled containers – and by the published and documented information about their performance.

The upper Texas coast was severely eroded during Tropical Storm Frances in September 1998, placing many beach houses along the Gulf shoreline of the southeast Texas coast in danger of being undermined or damaged during subsequent storms and gradual shoreline retreat. In response to this erosion and in an effort to prevent further storm damage to structures along the Gulf of Mexico shoreline, shore-parallel sand-filled geotextile tubes were installed (see, *e.g.*, Heilman *et al.*, 2008; Gibeaut *et al.*, 2003).

Between April 1999 and May 2000, approximately 12km of geotextile tube core dune projects were constructed along the Gulf of Mexico beaches of Galveston County (Heilman *et al.*, 2008). The projects consisted of the placement of geotextile tubes filled and encased with sand hauled from upland borrow pits. As shown in Figure 2.14 the geotextile tubes are placed along the back beach, and rest on a fabric scour apron that has sediment-filled anchor tubes along each edge. Final height of the restored dune generally ranged from 1.8 to 2.7m. Figure 2.15 show some views of the geotextile tube dune core.

The study by Gibeaut *et al.* (2003) provides a quantitative evaluation of those projects on the basis of observations made from May 2000 to March 2003. The monitoring consisted of six field surveys, including beach-profile monitoring and visual inspection of geotextile exposure and damage, three additional airborne LIDAR (LIght Detection and Ranging) surveys of the shoreline, and the compilation of wave and water-level data.

The above-mentioned study concludes that the geotextile tubes have been effective for temporary erosion control, but they may fail when exposed to direct wave attack. To prevent failure it is critical to keep the tubes covered with sand, to maintain a beach in front of them, and to repair holes in the fabric as soon as possible, all these actions require a significant effort.

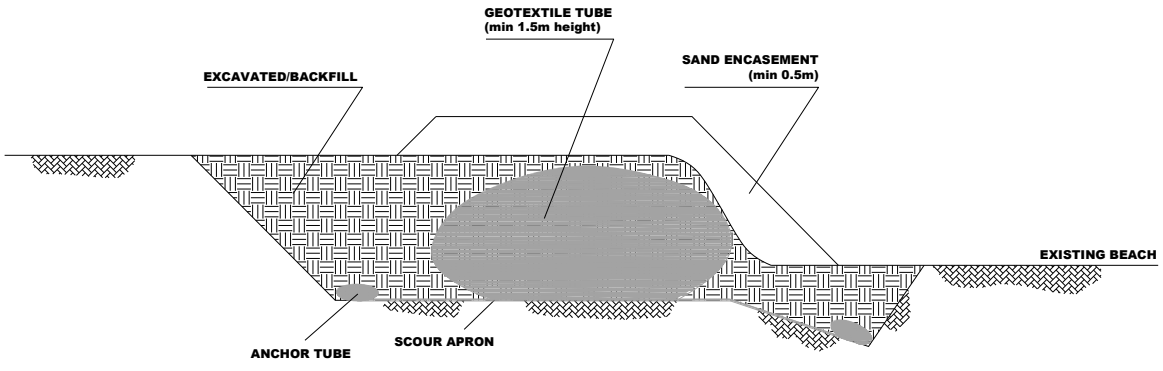

Figure 2.14: Schematic typical cross-section of the intervention along the Gulf of Mexico beaches of Galveston County (adapted from Heilman *et al.*, 2008).

Figure 2.15: Views of the geotextile tube dune core
(reproduced from Gibeaut *et al.*, 2003).

As of March 2003 no significant event with regard to storm surge and beach occurred and thus their effectiveness was untested (Gibeaut *et al.*, 2003).

During the study period, the geotextile tubes prevented the vegetation line from retreating landward of houses. However, those houses to which the vegetation line would have retreated were probably seaward of the natural line of vegetation at the time the tubes were installed. It is also important to note that, during storms, erosion and vegetation line retreat may occur landward of the geotextile tubes.

There has been some concern that the geotextiles tubes may eventually accelerate erosion downdrift. However, Gibeaut *et al.* (2003) states that as of March 2003, adjacent shorelines had not been demonstrably affected.

There has also been concern about the unnatural appearance of geotextile tubes, as they alter dramatically the geomorphology and sedimentary environment of the beach/dune system. Even when covered by vegetated sand they rise abruptly from the back beach.

This study also concluded that the beaches in front of the geotextile tubes are narrower than adjacent. Yet, it justifies it with the fact that the tubes were placed seawards the natural shoreline.

The more recent study by Heilman *et al.* (2008) summarizes initial lessons learned from the field monitoring and updates as of 2007 the conclusions stated in Gibeaut *et al.* (2003). Since spring 2003, annual wading-depth beach profile surveys have been conducted at the geotextile tubes locations and within adjacent areas. Additional surveys were conducted following major storms to assess erosion and beach recovery.

The data collected over a 8-year monitoring period in Galveston County beaches confirm that geotextile tubes can be a practical and relatively low-cost method of improving protection to coastal infrastructure without causing significant erosion of adjacent beaches.

In comparing beaches in Galveston County with and without geotextile tubes over approximately 8 years, no clear differences in shoreline change trends were observed Heilman *et al.* (2008). Geotextile tubes have thus provided adequate protection although with some substantial countermeasures such as additional periodic small-scale beach nourishment and dune restoration projects and repairing of damage to the tubes.

In the manner of localized erosion, the geotextile tubes did not cause sustained or permanent scour. Although some temporary localized scour occurred adjacent to the geotextile tubes, the post-storm recovery was generally similar for beaches with and without protection.

The study by Heilman *et al.* (2008) withdraws some more general conclusions with regard to the long-term performance of geotextile tubes. These authors recognize that geotextile tubes may have a limited life even with regular maintenance and anticipate maintenance on at least an annual basis in moderate wave climates. At sites that are subjected to frequent and rapid large-scale fluctuations in shoreline position, Heilman *et al.* (2008) affirms that geotextile tubes may be impossible to maintain for any useful duration.

Erchinger (1993) describes an interesting case on the German North Sea coast at the northwestern beach and the barrier dune of the island *Langeoog*. In 1971 this sea defence was severely eroded and had to restore by beach nourishment. To prevent the sand to be eroded away the beach-fill was bordered and stabilized at the seaside by geotextile sand-filled tubes. The characteristics of the geotextile tubes used in this intervention are shown in Table 2.II.

Approximately 3km of geotextile tube were installed at *ca.* of 60m in front of the eroded dune toe and some additional tubes were placed transversally to hinder longitudinal currents (Figure 2.16).

According to Erchinger (1993) the geotextile tubes worked well for some years until considerable parts of the tubes were sunk by the scouring effect of approaching swash channels and bars.

As occurs with other coastal structures, undermining of the foundation from scour is a major cause of failure in structures incorporating geosynthetic materials, so much so that failure to adequately safeguard the security of the foundation in relation to erosion can cause irreversible structural damage.

Erchinger (1993) also evaluated the durability of geotextiles from samples collected from buried and exposed tubes, to conclude that the tubes filled with sand can be used favourably on a long-term basis as long as they are protected from sunlight. For temporary use the geotextiles tubes are suitable unprotected, Erchinger (1993) concludes.

Table 2.II: Characteristics of the geotextiles tubes
(reproduced from Erchinger, 1993).

Raw Material	Tensile Strength (N/5cm)	Mass per Unit Area (g/m^2)
80% PP and 20% PE	90	500

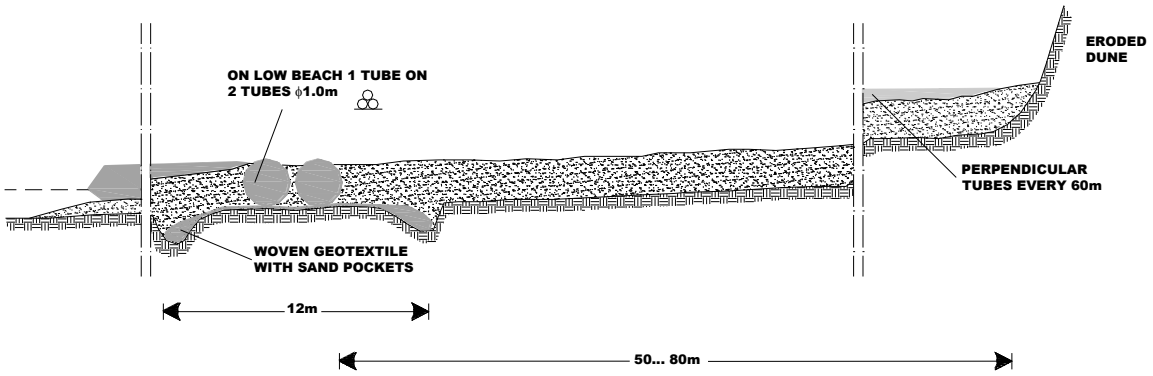

Figure 2.16: Cross-section of the intervention at the island *Langeoog*
(adapted from Erchinger, 1993).

Another well-documented example of geotextile containment for dune reinforcement is the protection system at the west coast of the island of Sylt (*Isles Schleswig-Holstein*), Germany. The *Schleswig-Holstein* islands belong to the sandy barrier islands of the North Frisian chain of the German *Wadden* Sea coast. Sylt is the most northern of the islands and its entire coast has been severely eroding since a long-time.

The average annual retreat at the west coast from 1870 to 1950 has been 0.9m per year but has increased during the past 35 years (Sistermans and Nieuwebhuis, 2002). An estimate of 1 million m^3 of sediment is lost every year, the majority of which through storm tides. Physical processes at the west coast of the island of Sylt may be summarized as follows (see, *e.g.*, Sistermans and Nieuwebhuis, 2002):

- The tide is semi-diurnal;
- Tidal ranges reach around 2m in the North Frisian region;
- Cross-shore transport through the gaps between barrier islands is mainly tide-induced;
- At the North Frisian Islands, wave action is generated by the alternately south-westerly and north-westerly winds;
- Long shore transport along the coast is mainly wave-induced and therefore also alternates in direction. This can be seen at Sylt, the island grows northward as well as southward by spit prolongation in both directions;
- Occasional storm surges can cause substantial erosion to the described dune cliffs at Sylt and cause some reshaping of the intertidal morphology;
- The storm surges mainly come from the west; therefore the western coast of Sylt is highly attacked and affected by storm surges.

A significant part of the island is heavily protected (because of the high economic values) and if it was not so the island would have wandered towards the east (see, *e.g.*, Sistermans and Nieuwebhuis, 2002). Up to 1985, when the region was designated as national park in recognition of the high ecological significance of the *Wadden* Sea, the strategy of protection has been characterized by a strong belief in engineering (hard) solutions for coastal defence follows, since then the approach to mitigate coastal erosion changed into trying to use more natural techniques and material (*e.g.*, beach fills). Hence, when in 1990 a series of storm tides caused severe erosion problems at the western coast of the island Sylt in Germany endangering the historical house *Kliffende* lying at the edge of a cliff, a new defence line was set-up consisting of sand nourishment combined with an integrated embankment of geotextile sand cushions (Figure 2.17), *i.e.*, sand wrapped into geotextile.

The installed geotextiles would have to provide a filter-effective protection against sediment wash-out and a reinforcement-effective stabilisation of the artificial dune.

A stability analysis was conducted by the BAW Germany (Federal Waterways Engineering and Research Institute) and was based on the decisive load case for possible deformations resulting from downdrift waves with the pore-water pressures acting from the inside of the structure (Lenze *et al.*, 2002). Outgoing waves with pore water pressures acting from the inside, which should rapidly be released towards the front of the construction, should be decisive for the stability and the possible deformation of the construction (see, *e.g.*, Pilarczyk, 2000).

To achieve the required relaxation towards the front of the construction, the fabric would have to meet good filtering with good drainage (*i.e.*, to match the permeability of the sand with the permeability and drainage effect of the fabric). Additional property requirements were high tensile strengths with elongations as low as possible, UV resistance, and abrasion resistance. Due to such requirements a project specific needle-punched composite material consisting of a polypropylene slit film woven (for permeability function) and a polyester non-woven (for drainage function) was specially manufactured.

The technical data of the composite material are presented in Table 2.III. The purposes of the non-woven component of the geotextile were to reinforce the embankment with a highly flexible and non-abrasive non-woven geotextile and to serve as UV protection to the polypropylene woven geotextile.

The cross-section of this protection system is shown in Figure 2.18; as seen the geotextiles hold and anchor the sand to a required position. The achieved total height of the construction was 8m with inclinations of 1:4 in the upper and 1:2 (V:H) in the lower cross-sectional area, further protected by 5m high sand nourishment at the foot of the dune. The embankment of geotextile sand cushions was constructed by first excavating a trench; then geotextiles overlapped by 1.5m were laid, filled with sand, and then folded back after sand compaction. The embankment was arranged layer by layer in the form of stairs. At a distance of 30m in front of the edge of the cliff the first cushion was installed 1m bellow the mean sea level.

Figure 2.17: Views of the dune reinforcement with wrapped-around geotextile sand cushions at the island Sylt (reproduced from NAUE FASERTECHNIK, 2000).

Table 2.III: Characteristics of the geotextile cushions (adapted from Pilarczyk, 2000).

	Woven Component	**Non-woven Component**
Raw Material	PP	PES
Mass per Unit Area	340g/m^2	620 g/m^2
Layer Thickness	-	6.6mm
Max. Tensile Strength **MD: machine direction** **CD: cross direction**	 80kN/m 80kN/m	 ≥ 12kN/m ≥ 18kN/m
$O_{90,w}$	0.33mm	0.15mm

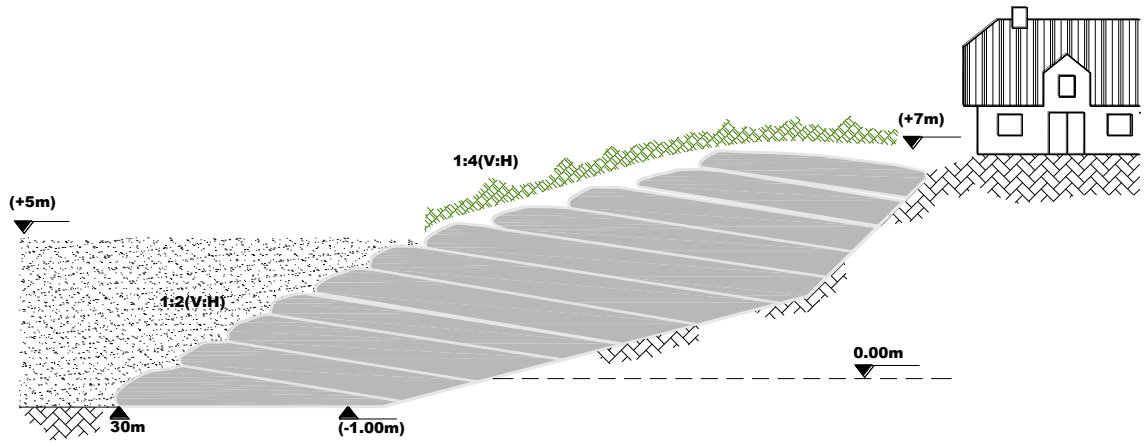

Figure 2.18: Typical cross-section at the island Sylt
(adapted from NAUE FASERTECHNIK, 2000).

The geotextile soft structure proved worthwhile several times during winter storms in 1993/94 and was exposed during these storm tides, but not damaged. These sand cushions even survived the second largest storm surge in December 1999, showing superior effectiveness compared to all other structures being used on the island (Lenze *et al.*, 2002). Compared with the year before, the storm tides which followed until the beginning of February 2000 resulted in the loss of more than 10m of the natural cliff area from the coast sections north and south of the *Kliffende* house together with the loss of the sandy beach (NAUE FASERTECHNIK, 2000). After these events, the geotextiles were in need of repair which was carried out in April 2000.

This structure has performed according to expectations and survived to storm-tide water levels of approximately MSL+4.5m in connection with waves 2.5m high and with a wave period of 5.5s (see, *e.g.*, Pilarczyk, 2000).

In 1996, severe erosion to the beachfront at Stockton beach had placed the Stockton Beach Surf Lifesaving Club in danger of collapse (see, *e.g.*, Restall *et al.*, 2002; and Saathoff *et al.*, 2007). Due to state government regulatory requirements an interim measure was the only rapid solution whilst a coastal management plan was finalised (Restall *et al.*, 2002). The geotextile sand container option was chosen because the structure provided an economical and user-friendly solution (Saathoff *et al.*, 2007).

Figure 2.19 show some views of the temporary erosion protection at Stockton beach, while the typical cross-section is shown in Figure 2.20.

Figure 2.19: Temporary protection at the Stockton beach, Australia
(reproduced from Saathoff *et al.*, 2007).

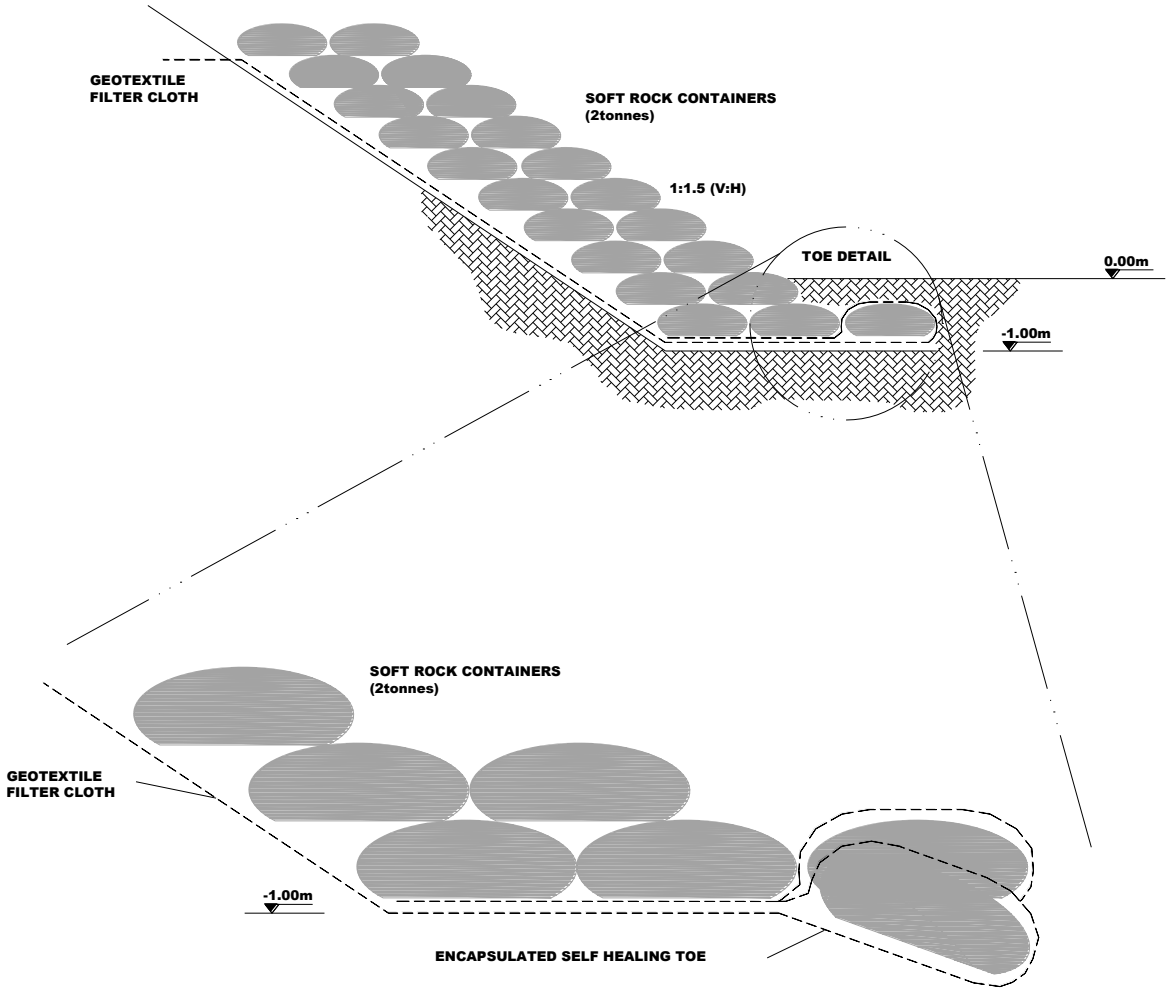

Figure 2.20: Typical cross-section of the revetment at the Stockton beach, Australia (adapted from Restall *et al.*, 2002).

The structure consists of 480 staple fibre non-woven geotextile containers each with a fill volume of 0.75m^3; typical dimensions when filled with sand 1.5m long, by 1.2m wide and 0.45m high. The achieved total height of the construction was close to 3m with inclinations of 1:1.5 (V:H). The structure toe was protected by an encapsulated self-healing toe.

This structure has performed above expectations and outlived the original design requirement of 6-months as after over 10-years in service it was still performing. Despite the "temporary" nature of the structure, the non-woven geotextile have withstood a number of storm cycles (Saathoff *et al*., 2007). To date, no "permanent" work has been carried out and further extensive works, using sand containers, have been proposed for the properties adjacent to the site (Restall *et al.*, 2002).

In December 2002 a dune erosion control system built with sand-filled tubes was installed along the *L'Amelie* beach, at the French Aquitaine coast. This dune system is immediately close to a stretch protected by a seawall and two groynes (Figure 2.21) which may be responsible for accelerating erosion problems to the shoreline on both sides of the protected stretch.

Figure 2.22 shows schematically the cross-section of the structure that consists of 3 levels of tubes on the northern beach and 2 levels on the southern beach, both with a cross slope of 15-20%. The structure is elevated by 40cm with reference to the beach level to prevent sand erosion at its toe.

Figure 2.21: Aerial view of the protection works at *L'Amelie* beach, March 1998
(reproduced from Artières *et al.*, 2004).

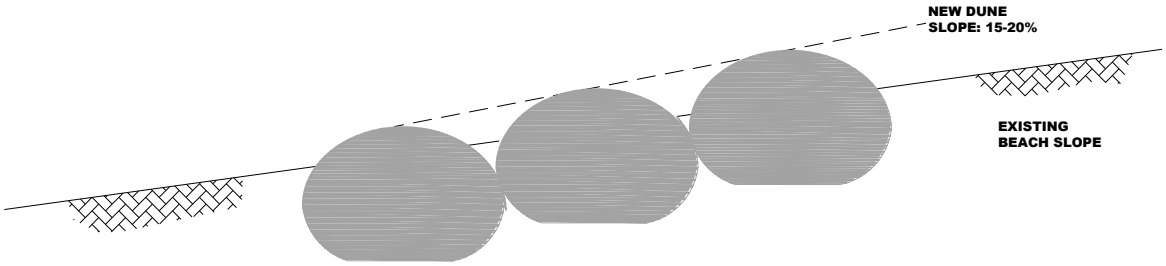

Figure 2.22: Schematic cross-section of tube structure installed at *L'Amelie* beach
(adapted from Artières *et al.*, 2004).

Figure 2.23: Views of the tube structure at *L'Amelie* beach
(reproduced from Artières *et al.*, 2004).

During installation of the tube breakwater on the northern beach, several storms of increasing strength occurred (Artières *et al.*, 2004). According to the authors, the first and weakest storm only removed 0.6m of sand at the toe of the lowest tube row. The second swell with waves of 2.5m occurred before the breakwater was totally finished, as the end which should be fixed inside the existing dune was not finished. The structure resisted, some tubes were deformed but without tears. The lowest rank sunk by scouring, apparently reaching an equilibrium position. The structure has resisted to a third and as of 2004 the last, storm event with 6m wave heights although with significant volumes of sediment being washed away, namely at the toe of the lowest tube row.

2.3.1.2. Multi-functional artificial reefs

Multi-functional artificial reefs (MFAR) constructed with sand-filled geotextile containers is in all probability the coastal protection structure incorporating geosynthetics that currently raise higher level of interest, as much to the technical point of view, as to the functional one.

Of these, the most noticeable example is the *Narrowneck* reef, located on the *Gold Coast*, *Queensland* – Australia. Besides *Narrowneck* there are other four reef examples: *Mount Maunganui* and *Opunake* both located on the coast of New Zeeland, *Boscombe* in Bournemouth – England, and *Kovalam* – India; there was another reef, *Prattes*, located in *El Segundo* California – United States of America, recently dismantled. More than twenty similar reef projects are now underway in New Zeeland, Australia, the USA and the UK, at stages ranging from feasibility study to tendering for construction (Black, 2004), there are as well as studies in other countries such as Dubai (see, *e.g.*, Mocke *et al.*, 2008; Smit *et al.*, 2009), Italy (see, *e.g.*, Franco *et al.*, 2009), Portugal (see, *e.g.*, Veloso-Gomes *et al.*, 2009; Oliveira and Marques, 2005), Spain (see ASR Limited construction newsletters at www.asrltd.com), and Fiji (see ASR Limited construction newsletters at www.asrltd.com).

The *Narrowneck reef* is the one providing the most useful performance indicators, as there has been comprehensive monitoring, since its completion in late 2000. Data on beach width, reef stability, geotextile container durability, marine ecology and surfing amenity is being collected.

The general perception is that the *Narrowneck* Artificial Reef has achieved objectives at a very competitive cost. Being those objectives to widen the beach and dunes along the Surfers Paradise Esplanade so as to increase the volume of sand within the storm buffer and also provide additional public open space; and to improve surf quality at *Narrowneck* by the construction of a submerged reef to stabilize nourished beaches.

The structural performance of the reef has been satisfactory, with ongoing improvements (Jackson *et al.*, 2007) and some additional minor sand nourishments of the beach. Despite a number of storm wave events, the reef has proven been effective in stabilizing the beach and a salient is generally present (Turner, 2006). For an average year, waves break on the reef ~50% of the time (Jackson *et al.*, 2007). It has also been observed that the reef interacts with the adjacent bar formations, creating more favourable natural conditions (Jackson *et al.*, 2007).

Monitoring clearly shows that the reef has resulted in a wider beach and reduced storm cut, thus fulfilling its primary objective (Jackson *et al.*, 2004). For the eight year period, August 2000 to July 2008, Blacka *et al.* (2008) concluded that at *Narrowneck* the underlying local beach width trend to date, since the completion of sand nourishment in mid 2000, has been a trend of modest net erosion of the order of -4.3 m per year (34 m over eight years). Still, the observed net result is more favourable in the lee of the reef compared to other sections of the beach.

In regards to durability, post-storm inspections indicate that containers are typically in good conditions.

A limited number of additional containers were placed across the crest of the Gold Coast reef in November – December 2001 (17 bags), November 2002 (10 bags) and January – August 2004 (15 bags), see, *e.g.*, Blacka *et al.* (2008). The placement of the additional containers in 2001 and again in 2002 was used to trim the crest level, and to fill the larger void spaces more generally across the reef structure (Turner, 2004).

A few other containers had to be replaced due to failure. Damage to the containers indicates failure originates from a number of sources, including the urethane trial coating (has tendency to crack), vandalism, boat anchors and wear/fatigue of the wider safety seams and square corners due to excessive marine growth (Jackson *et al.*, 2004).

Prattes reff was located offshore of *Dockweiler* Beach in *El Segundo*, California – EUA. The beach fronting the reef is approximately 60 to 120m wide depending on the tide and the season, it is partially backed by a ridge of low sand; the beach slopes gently from the base of the dunes until the back beach area meets the shoreface, which has a much steeper slope (see, *e.g.*, Borrero, 2001).

This experimental surfing reef was constructed in two phases: the initial phase, undertaken in September 2000, consisted of placing 110 sand-filled geotextile containers; the second phase of reef construction occurred in April 2001, when 90 additional bags were placed on top of original bags to increase the height and width of the structure. The reef site lies along a heavily protected shoreline. The project objective was to mitigate the impacts to recreational surfing engendered by the construction of a shore-perpendicular groyne at the *El Segundo* refinery during the winter of 1982-83 (Coastal Frontiers Corporation, 2008).

The results of the monitoring and reporting programme, required by the Surfrider Foundation, show that (see, *e.g.*, Borrero and Nelsen, 2003) *Prattes* reef had essentially no impact on the shoreline or offshore morphology. Surveys and dive inspections show that the crest height of the reef has steadily dropped affecting the wave breaking. According to Borrero (2002b), this was probably due to a combination of material loss due to ripped bags and settling.

Damage to the containers indicates failure originates from four sources, according to Borrero (2002a): tears starting at the fill hole and then spreading; tears starting at seams, then spreading; tears starting from wrinkles that first fray, then rip then spread; and, tears starting from tie wrap repairs or other cuts then spreading.

Due to its underperformance, *Prattes* reef was scheduled for removal in the fall 2008 by the Surfrider Foundation.

The monitoring results from the most recent projects, *Mount Maunganui*, located on the north east coast of New Zeeland, *Opunake*, located on the west coast of New Zeeland's north island, *Kovalam* located on the Arabian Sea, and Europe's first artificial reef, Boscombe, also known as Weights reef, are yet to be available, and therefore their structural and hydraulic performance with regard to the envisioned objectives is as yet unclear. Over time those results will provide new insights as to whether the multi-functional artificial reefs are able to provide sustainable solutions.

Conclusively, monitoring so far suggests that:

- The depicted examples of *Narrowneck* and *Prattes* demonstrate that the envisioned objectives were not thoroughly satisfied;
- The performance, measured from monitoring, reveal that the *Narrowneck* reef could not, by itself only, prevent erosion from going on whilst any effect of *Prattes* reef was merely elusive;
- Relevant issues harnessing performance like size, location, and crest height were roughly confirmed;
- The durability of the geotextile containers used in *Narrowneck* has demonstrated to be adequate.

2.3.1.3. Other examples of application

Oh and Shin (2006) and Shin and Oh (2007) presented various issues related to the construction of nearshore breakwaters with geotextile tubes at Young-Jin beach on the east coast of Korea, along which erosion is currently causing severe damage to shoreline scenic views and to public property (Figure 2.24).

Figure 2.25 show the implantation of the coastal defense scheme in plan and cross-section.

As of 2007 seaweed had already inhabited the surface of the submerged tubes. As for performance the shoreline accreted and eroded within a period of six-months although erosion was smaller when compared to the observed accretion and probably has accumulated around the tubes.

Figure 2.24: Erosion phenomena at the east coast of Korea
(reproduced from Shin and Oh, 2007).

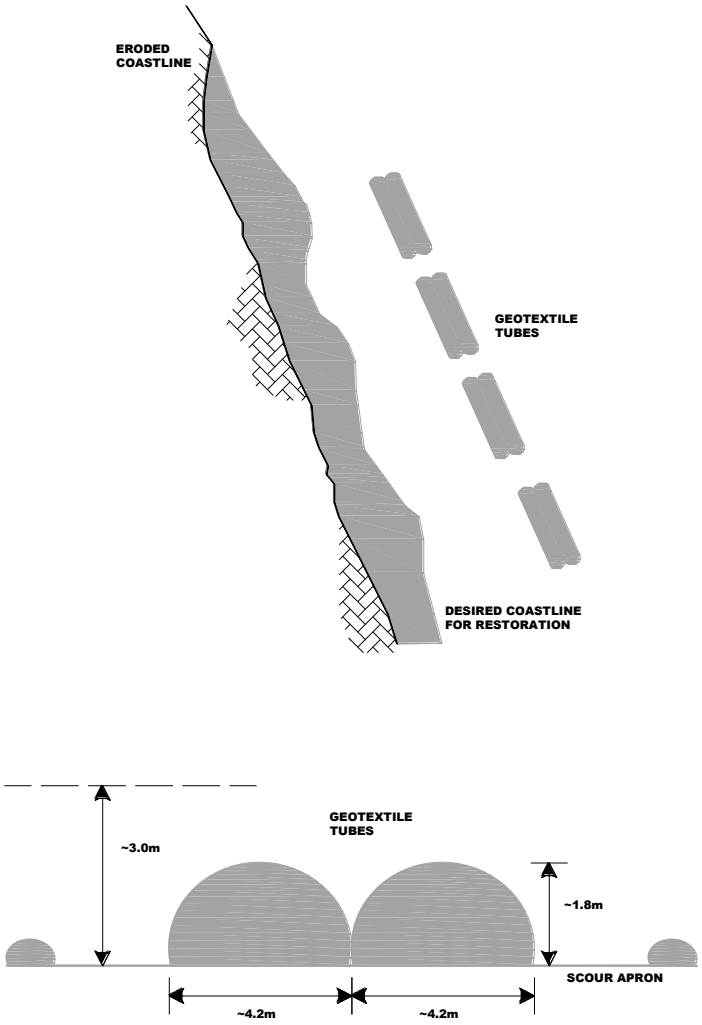

Figure 2.25: Layout and cross-section of the protection at Young-Jin beach
(adapted from Shin and Oh, 2007).

In Yucatan, Mexico, geotextile tubes are being used as submerged breakwaters to reduce the incident wave energy on the beach and prevent shoreline regression. This solution follow the recommendations of a Beach Rehabilitation Program, initiated in 2001 by the federal authorities from the Ministry of the Environment, which instigate the use of flexible structures capable of promoting sand accumulation without major impact on the longshore transport of sediments.

As of September 2005, 4km of tubes have been installed along the northern coast of Yucatan (see, *e.g.*, Alvarez *et al.*, 2007). Where required, in critical beach segments, the protection with geotextile tubes was supplemented with artificial sand nourishment.

As described in *e.g.* Restall *et al.* (2002), Saathoff (2003), and Saathoff *et al.* (2007) many of the worldwide examples of application of geotextiles in coastal engineering are located in Australia. One of those examples is the sand-filled geotextile groyne at Kirra beach.

In 1984, the Gold Coast City Council decided to install a temporary groyne at Kirra beach with an expected lifetime of at least 5 years during which a long-term solution for this seriously eroded area would be investigated and implemented (Pilarczyk, 2000). The temporary groyne would have to withstand exposed conditions of up to 5m deep-water waves, be easily removed and be compatible with intensive recreational activities.

Prior to the installation of the main groyne which was about 120m long, 12m wide at the base and 5m high, and consists of a number of stacked tubes of 1.2m in diameter in 5 layers (Figure 2.26), a smaller groyne of just 40m long by 1.2m high has been installed at another location because there was a need for a groyne in that location and to assess potential design and risks. The technical data of the UV stabilised non-woven staple fibre needle punched geotextile is presented in Table 2.IV.

Both Pilarczyk (2000) and Restall *et al.* (2002) present interesting comments on the performance of this groyne, that eventually was buried by a regional nourishment scheme commenced in 1990. The mentioned authors emphasize the problems with the vandalism and the inadequate head design and indentify these as major points of change/improvement in future projects. These problems have led to the almost total collapse of the seaward by 30m, whilst the rest of the structure although subjected to 2-2.5m breaking waves was still performing satisfactorily (see, *e.g.*, Pilarczyk, 2000). Restall *et al.* (2002), also refer to the significant impact of a single long tube can have in the overall integrity of the structure hinting at potential benefits of using smaller containers in order to isolate/mitigate damage.

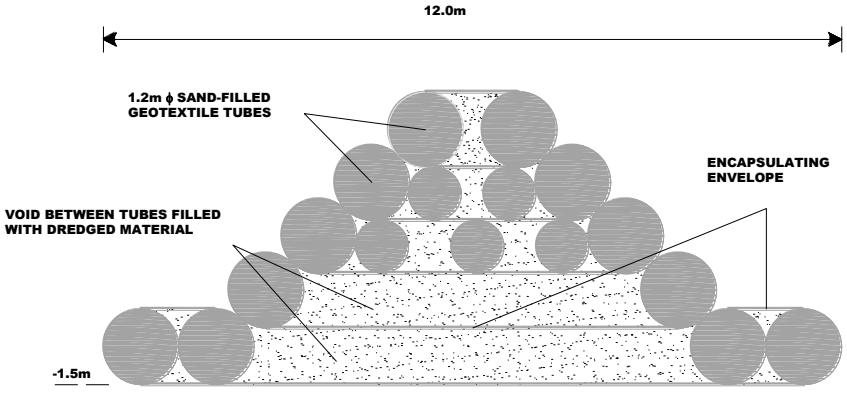

Figure 2.26: Cross-section of the sand-filled geotextile groyne at Kirra beach (adapted from Restall *et al.*, 2002).

Table 2.IV: Geotextile tube and geotextile envelope characteristics (adapted from Restall *et al.*, 2002 and http://www.naue.com).

Raw Material	Tensile Strength	Mass per Unit Area (g/m^2)	Thickness (mm)	CBR burst	Seam Strength
PET, PP White	65kN/m (Longitudinal) 38kN/m (Transverse)	1200	5.5	10kN at 60%	Min. 80% of base fabric

As described in Elko and Mann (2007), the Upham Beach in Florida was routinely (every four to five years) nourished since 1975 when in February 2003, the Florida Department of Environmental Protection (FDEP) issued a permit for the subject Upham Beach Geotextile T-Groin Project, which was intended to maintain the public beach and protect property along the beachfront, and included a beach fill approximately 250,000m^3 of sediment supplemented by the installation of five, temporary, geotextile T-shaped head groins.

Concerns about potential downdrift impacts have motivated the project to be constructed with geotextile tubes, as they are relatively easier to remove as compared to rock. The T-groins were designed to aid in the transition from a structured shoreline to an unstructured shoreline. To account for scour, the T-shaped heads (shore-parallel sections) of the groins were designed as stacked pyramid structures (Figure 2.27), providing sufficient depth and elevation for shore protection while maintaining the structural integrity of the T-groins (*i.e.*, prevent slumping). In an effort to enhance durability and to protect the fabric from UV-load, the top tube (which was above mean sea level) of the structure was sprayed with a polyurea coating after installation.

Overall, the T-groin project is performing as designed; according to Elko and Mann (2007), it has achieved the goal of maintaining a 12m wide beach with no downdrift impacts. Other interesting comments made by Elko and Mann (2007) concern fragility against vandalism (*i.e.*, by reporting an incident that occurred during installation) and observations with regard to installation (*i.e.*, by suggesting that "in the dry" would be the most successful construction method).

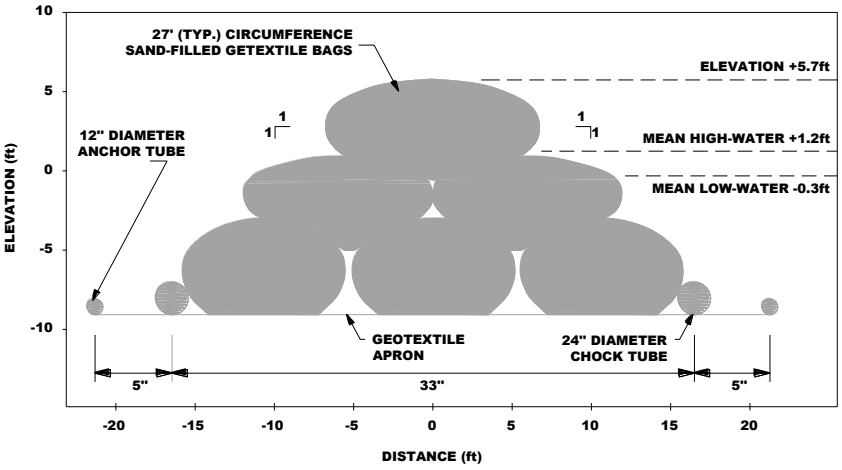

Figure 2.27: Cross-sectional view of the typical T-shaped head groin at Upham beach (adapted from Elko and Mann, 2007).

Figure 2.28: Photos taken from the roof of one of the condominiums 22 months after the 1996 and 2004 nourishment projects (reproduced from Elko and Mann, 2007).

2.3.2. Portuguese experience

Portuguese experience with the application of geosynthetics in coastal engineering is limited to their application as filters (*e.g.*, in harbour structures) – outside the scope of this thesis, and to some small emergency works and pilot prototype experiences which are summarized in the following sections.

2.3.2.1. Estela Golf course

The Estela Golf course is located in *Estela*, a municipality of *Póvoa do Varzim*, approximately 9km north of this city harbour and just south of a coastal protected area. It is situated along the north-western coast of Portugal in a 3km-long dune system. Dredging activities at the River *Cávado* and morphological changes in the river basin caused the decrease in the volume of sediments transported by the littoral drift. The completion of other groynes and seawalls, namely in the sand spit of *Ofir* and in the coast of *Cedo Bem* and *Apúlia*, further aggravate that reduction by retaining some more sediments.

The first documented intervention, done during the period of 1 to 12 April 1999, consisted of located reinforcement of the dune toe through mechanical ripping with sand from the frontal beach and consolidation of this sand deposit with wood piles and small 5kg sand bags, Figure 2.29 (Veloso-Gomes *et al.*, 2006a).

In October the same year a similar intervention was again required as the dune was showing advanced state of erosion with the erosion cliff very close to the golf course fence. Before the end of 1999/2000 winter two more interventions were needed, one in January and the other in March. These interventions were complemented by the installation of sand trap fences to enhance the aeolian effect on the dunes.

At the beginning of the 2000/2001 winter season, after the spring tides of September, the dune has almost been destroyed due to a storm-wave attack (see *e.g.* das Neves *et al.*, 2005; and das Neves, 2003). Persistent storms, generated by a very unusual case of consecutive events, caused a series of dune destruction events and compelled the execution of emergency dune repositioning works several times in the period from November 2000 to January 2001 (Figure 2.30).

December 2000 marked the beginning of the use of a new technique of coastal defence in association with sand ripping. This time a more solid reinforcement technique was essayed. The intervention was carried out in three stretches, of 350m, 70m and 50m, respectively, and consisted of placing a geotextile filter cloth and $1m^3$ sand containers along a 45º slope.

Figure 2.31 show some aspects of the execution of this technical solution – forming the dune platform through sand ripping, placing and anchoring the geotextile filter cloth and settling the sand containers. During October and December 2001 and May 2002, new sand containers were placed on the dune slope, but this time the geotextile filter cloth underlay was not placed.

Figure 2.29: Sand trap fences to enhance the aeolian effect on the dune of *Estela*.

Figure 2.30: Emergency intervention on the dune system of *Estela*, November 2000.

Figure 2.31: Views of the execution of the technical solution using geotextile sand containers on the dune system of *Estela*, December 2000.

A more detailed description of this case study in the period ranging from 1999 to 2003 can be found in das Neves (2003) and Veloso-Gomes *et al.* (2006a). Since then periodic interventions consisting of the piling up of beach sediment to the dune and replacement of tear, lost or displaced bags occur. Table 2.V summarizes the total cost of interventions per year from 1999 to 2009. The average cost per year is around 25,000.00€, 15% of which corresponds to material costs. The higher costs on Table 2.V are associated with years of more frequent storms regardless its intensity. This was the case in 2000/2001 and again in 2009.

Figure 2.32 show some recent images of the dune taken on the winter and spring 2009/2010. Estela Golf course case study will be again introduced in Chapter 4 of this thesis whilst describing prototype conditions to replicate in the physical experiments.

Table 2.V: Total cost of interventions from 1999 to 2009
(source: Estela Golf, S.A.).

Year	Cost (in Euros)	No. of bags (approx)
1999	27,433.88	-
2000	52,373.78	-
2001	44,570.12	2983
2002	16,736.00	1620
2003	20,085.40	1960
2004	8,681.00	660
2005	3,945.00	-
2006	9,853.50	1150
2007	9,837.00	150
2008	25,050.52	2637
2009	43,309.60	3212
Total	261,875.80	14372

Figure 2.32: Views of the *Estela* dune, March 2010.

2.3.2.2. Other experiences

This section provides an overview of other experiences with geosynthetics in coastal engineering along the Portuguese coast either as experimental projects – *Leirosa* and *Barrinha de Esmoriz* – *or* emergency work – *Lagoa de Óbidos*, and *São Bartolomeu do Mar*.

The installation of a pipeline in 1995 for the cellulose pulp and paper companies Celbi and Soporcel at *Leirosa* beach, municipality of *Figueira da Foz* forced the cut down of a dune system and have resulted in the progressive exposure of the dune system to wave attack, further enhanced by the weakening of nourishment from the updrift sediment sources,.

Since 2000 operations of dune construction – beach sand pilling up to the dune and planting of dune vegetation – were carried out on a regular basis. These operations have had limited success motivating the search for a better solution to strengthen the dune system, that would mitigate erosion and save maintenance costs. In February 2005, an experimental project with geotextiles has been installed over a stretch of approximately 120m (Figure 2.33), following a design concept similar to the one used to protect the *Kliffende* house at the island of Sylt (*i.e.*, sand wrapped around geotextile sheets). The cross-section of this experimental installation is shown in Figure 2.34. Maximum total height of the construction was 8m with inclinations of 1:2 (V:H); the beach level was +5.00m (MSL). The technical data of the needle-punched non-woven geotextile selected to this project is presented in Table 2.VI. Deep-water wave conditions at site has significant wave height, H_s, and wave peak period, T_p, values of 6.5m and 16s, accordingly.

Figure 2.33: Views of the installation of a dune reinforcement at *Leirosa* beach, February 2005.

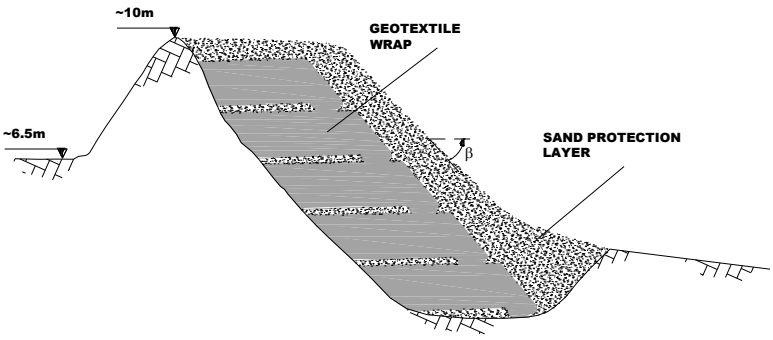

Figure 2.34: Cross-section of the dune reinforcement system of *Leirosa* (adapted from BBG, 2004).

Table 2.VI: Characteristics of the geotextile products installed at *Leirosa* (Source: NAUE GmbH & Co. KG).

	Terrafix® 1006
Raw Material	Polyester (PES), white
Mass per Unit Area	1000g/m^2
Thickness	5.3mm
Max. Tensile Strength **MD: machine direction** **CMD: cross machine direction**	 30N/m 50kN/m
Characteristic Opening Size	0.07 mm

According to the project design (BBG, 2004), structure foundation would be at +2.00m (MSL), and the sand-filled geotextiles would be overlapped by approximately 1.5m (perpendicular to facing). After sand compaction the geotextiles would be tied back, wrinkle free. To achieve an optimum frictional behaviour between the individual geotextile sand cushion BBG (2004) recommended the installation of a thin sand layer (approximately 0.10m) between two adjacent geotextile layers starting approximately 1m from the front face up to the end of each layer. Based on the given construction height (8m) and structure toe +2.00m (MSL), BBG (2004) suggested the use of 4 wraps with a length of 11.7m, and a final wrap at the slope crest with a length of 14.4m. At last, the structure toe was to be reinforced with 1.2m^3 sand-filled containers (200 units) and cover planted with marram grass.

Installed in February 2005, this structure has not totally performed according to expectations although it has been able to maintain the dune alignment. During the first years, the structure deflated in several places, apparently as a result of problems with construction, with sediment being washed away (Figures 2.35 and 2.36). The most serious problems arose from the jointing system, as the overlap seams assembled with hot air have doubtful soil tightness and are difficult (to say the least) to realize accurately in situ.

In 2008 the structure has been repaired with non-woven geotextile tubes (Figure 2.37). Figure 2.39 show some recent images of the dune taken on the spring 2010.

Figure 2.35: Aspects of the dune reinforcement system of *Leirosa*, March 2006.

Figure 2.36: Aspects of the dune reinforcement system of *Leirosa*, March 2007.

Figure 2.37: Views of the installation of non-woven geotextile tubes, June 2008.

Figure 2.38: Aspects of the dune reinforcement system of *Leirosa* in 2009, January (top panel), February (bottom left panel) and March (bottom right panel).

Figure 2.39: Aspects of the dune reinforcement system of *Leirosa*, April 2010.

The coastal lagoon of *Esmoriz* is a Natura 2000 site, located in the boundary between the municipalities of *Espinho* and *Ovar*. Because the lagoon catches water of poor quality from neighbouring streams its water has become contaminated with potential impact on the bathing water quality of the adjacent beaches.

To have some control over this situation and to avoid conflicts an experimental project of a fuse dique of 30m length made of wood and reinforced sand-filled containers has been installed in 2004 to maintain the contaminated waters of the coastal lagoon away from the sea.

In 2010 this experimental project had practically disappeared.

Besides these experimental projects, there are a few other emergency works carried out after severe storms that have used the same technique as in *Estela* namely big-bags filled with sand. Examples of such emergency work are located in *São Bartolomeu do Mar* (Figure 2.40), and *Óbidos* lagoon (Figure 2.41). The former was destroyed at the end of the first winter-season, whereas in *Óbidos* a permanent structure made with steel sheet-piles has been placed at the left bank.

Figure 2.40: Emergency work at *São Bartolomeu do Mar*, January 2003.

Figure 2.41: Emergency work at *Óbidos*, January 2004.

2.4. Concluding remarks

The first purpose of the considerations given along this chapter was to provide a background overview against which the option for one type of structure, or for a combination of two or more, is made.

It has become clear that sometimes the problem in hand requires the use of massive stone or concrete structures, and sometimes it involves leaving coastal systems to their natural dynamics. However, as neither the cause of erosion is eliminated, nor does the vulnerability/risk dissuade people from moving seawards and settling along the coast, maintaining the safety of people and assets at acceptable levels is becoming more and more expensive and technically more and more difficult to deliver.

For that reason the so-called soft engineering techniques – hereby referred to those techniques that build with natural processes and rely on natural elements such as sand, dunes, and vegetation to prevent erosive forces from reaching the backshore – are slowly but surely triggering interest whilst any increase in vulnerability/risk is compensated with management and planning, that is for instance the landwards reallocation of people and assets.

The anticipated impact of structures on coastal processes is becoming more and more decisive in coastal engineering and management. It is not just finding a solution to a specific problem but critically seeing the big picture to arrive at a technically and environmentally appropriate design.

Within this context the use of sand-filled geosystems in coastal engineering is growing in interest and is an application in full development as far as the materials, the applications and the design tools are concern.

The examples of application presented along this chapter have provided better insights into the successes and problems that may be of help in assessing the applicability and in the design of geotextile sand-filled systems for a specific problem in hand. This was the second purpose of this chapter, to derive general criteria of applicability and to assess the potential constraints based on the actual experiences.

Sand-filled geosystems have the decisive advantage over concrete or rock systems of being able to slow down erosion with a limited and non-permanent impact on natural coastal processes. So a good use for this type of system is a temporary structure, *e.g.*, in emergency works, or to learn the impacts of that protection on coastal processes and how they will affect the system and neighbouring systems.

These systems have been used successfully in shallow water and in low wave energy coasts with a low tidal range. They have as well been used successfully associated with regular artificial nourishment.

Their utilization as a permanent structure carries several implications. It has been seen that not exposed sand-filled geosystems have not deteriorated, but have sunk due to coastal processes becoming ineffective. As well, deformation may gradually induce change and variations in height and alignment along the structure with impact on structure performance under wave loading.

In the event of a storm, the structure may become exposed and thus durability against unpredictable UV exposition periods has to be foreseen. Exposed geosystems are an invitation to vandalism.

It has become clear that maintenance on a regular basis is anticipated. To expect otherwise may result in failure. It has also become clear that, except may be for very small projects, the installation needs an experienced contractor and/or supervision in order to ensure an optimal quality work. Negligence in materials and site preparation and positioning may lead to tearing of fabric and differential settlements, eventually causing collapse by excessive deflection, slumping and displacements. Seams and overlaps are always weaker than the original, non-connected fabric. They have to be kept to a minimum and pre-fabricated as much as possible.

Apart from weathering, a composite material that combines permeability/drainage properties with tensile strength is apparently the most suitable for this type of application. Permeability enables the free-flow of water which means that during the wave impacts, the wave forces are taken by the sand grains, and the geotextile is stressed only by the through flow of water. The pressure waves attenuate very rapidly in sand due to the air in the voids and in the water. Consequently, any liquefaction of sand is confined to the immediate vicinity of the sand face. Drainage is important during downrush flow and to prevent undercutting. During installation and handling the geotextile is submitted to significant mechanical stresses. During the filling process the mixture of soil particles flowing inside the tube causes abrasion of the internal side of the envelope. This abrasion is usually compensated by a sufficient thickness of the fabric. When the tube is inflated with the soil/water mixture, the internal hydraulic pressure applies a tensile force on the fabric. Physical properties of the material (*e.g.* structure, and mass per unit area) are also important. Material properties will be referred to again in the following chapter.

It seems that as long as the individual elements of the geosystem remain intact and firmly in place structures are effective. This is though difficult to achieve in practice. Several causes exist for failure of a geotextile structure but are usually related with overturning, sliding, deformation due to local scour, and forcing associated with waves – breaking waves, non-breaking waves, and waves propagating over the structure. Flanking erosion may as well induce instability.

Bigger elements are usually more stable but also more difficult to handle and more difficult to repair. Compartmentalisation may be significant in the overall stability while keeping damages as localised problems. Efficient compartmentalisation is a compromise between stability and overall vulnerability.

A thick and vegetated sand cover can partly compensate for a narrower beach. Because of the many uncertainties the use of these structures is preferable for low-risk-management coastal areas. For a more general application of geosystems to coastal engineering further investigation, experiments and practical experience at various climatic conditions is essential.

Chapter 3 of the present thesis is a complement to the more general considerations given along this chapter, with respect to the application of geosynthetics and geosystems in coastal engineering.

3. LITERATURE SURVEY AND STATE-OF-KNOWLEDGE

Has become clear in the previous chapter, geotextiles as containment systems in coastal engineering have been used successfully as temporary structures (in emergency works or to learn the impacts on coastal processes and how they will affect the system and neighbouring systems), in shallow water and in low wave energy coasts with a low tidal range. They have as well been used successfully associated with regular artificial sand nourishment. However, their utilization as a permanent structure in high wave energy coasts carries several implications and is so far unproven.

Some significant investigative efforts on the subject have commenced approximately one decade ago, namely in Germany, in the Netherlands, and in the United States of America, yet there is still considerable uncertainty in predicting the performance of geosystems under wave-loading, especially at more exposed hydraulic conditions.

In the present chapter, most especially in section 3.1, advances and limitations of current state-of-knowledge are highlighted. Emphasis is also given to important aspects related to material properties with respect to coastal engineering applications. For purposes of explaining how waves propagate into shallower water, and how they interact with coastal structures, a qualitative description of the forces acting within the nearshore zone (namely, the hydraulic response in terms of wave run-up and run-down and wave transmission and reflection) is given in section 3.1 as well.

Chapter 3 also consists of three additional sections, and a summary one. Such additional sections encompass the background topics addressed by the present thesis, namely the physical modelling of movable-bed models, the cross-shore component of sediment transport, and the development of scour around structures.

Aspects on how to scale similar flow conditions in model to those in the prototype, assumptions, and possible scale effects due to non-satisfied scaling between actual model properties and required model properties are described in section 3.2.

The second of those additional sections broadly describes changes in a beach-profile exposed to changing hydrodynamic conditions within the nearshore zone. It commence by a description of general considerations on sediment properties, the initiation of motion and the identification of transport processes. Bar morphology and short- and long-term changes of beach-profiles due to storms is then examined, along with effects of various parameters on the profile characteristics, including wave climate and sediment characteristics.

At last section 3.4 deals with aspects of scour around coastal structures with special emphasis on predicting local scour and more widespread beach lowering. Scour and beach lowering in front of coastal structures are topics of considerable relevance to coastal engineering practice due to their potential for causing damage to structures and even induce failure. They are also topics of considerable research interest as the hydrodynamic processes causing them have not yet been fully understood. Both the aspects, consequences and the mechanisms of scour in marine environment are covered in section 3.4. Liquefaction and wave-induced pore-pressures in sand bottoms are addressed as well in section 3.4.

The summary and conclusions drawn from the literature survey and current state-of-knowledge are given in section 3.5, and should be elucidative on both the originality and the relevance of the scope addressed by the present contribution.

3.1. Geotextiles in coastal engineering

The idea to use sand-filled containers in coastal engineering is over 50 years and though it has, potentially, many environmental and economical advantages, the number of existing applications is still very limited. This is mainly due to uncertainty about their medium- to long-term sustainability with respect to UV-light, weathering, mechanical loads and vandalism, and to the lack of proper design criteria. It is also link to uncertainty about their stability under wave-loading. A requirement for a proper application of geosynthetics in coastal engineering is thus a consideration of aspects which relate to the materials and to the hydrodynamic conditions. Both these issues are discussed below, while later along this thesis another aspect which relate to the installation is brought out in the discussion.

3.1.1. Introduction

Geosynthetics may be used for a number of purposes in coastal engineering, namely as a reinforcement, a filter or a separator (see Figure 3.1). They can as well be used in erosion control system. The choice of a material is influenced by the functional requirements to be performed over time, and is evaluated in regard to the material properties, which in the case of geosynthetics depend on the type of basic material and processing technology.

With respect to the former, five main polymers are used in the manufacturing of geosynthetics: Polyester (PET); Polypropylene (PP); Polyethylene (PE); Polyamide (PA), with the species PA6 and PA 6.6; and finally, Polyvinylchloride (PVC). The basic materials consist mainly of the elements carbon, hydrogen, and occasionally nitrogen and chloride (PVC); they are produced from coal and oil. Some characteristic properties are presented in Table 3.I.

The processing technology consists of melting the polymers in granular form followed by extrusion, and eventually spinning. During the melting before extrusion and during further processing, additives can be used as a way to improve the less favourable properties of the basic materials. Pigments can also be added. The final processing of the semi-manufactured products will provide the end products with distinctive characteristics. The most important end products are the woven fabrics and non-wovens, which together are called ‘geotextiles’. Woven fabrics and non-wovens are, as well, the most important end products with respect to applications in coastal engineering.

More detailed information on processing, manufacturing, and end-products can be found in various PhD and MSc thesis presented to FEUP (see, *e.g.*, Carneiro, 2009; Vieira, 2008; Pinho-Lopes, 2005; and das Neves, 2003), and in, *e.g.*, Pinho-Lopes and Lopes (2010), and Koerner (1999).

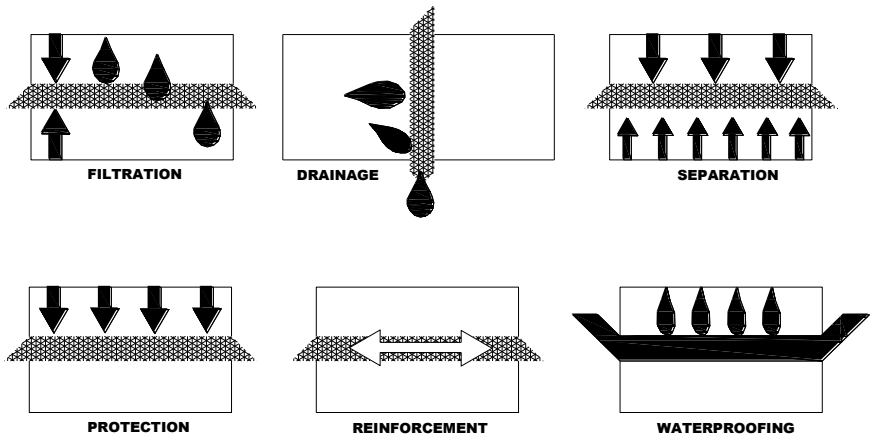

Figure 3.1: Major functions performed by geosynthetics
(adapted from ISO 10318:2005).

Table 3.I: Comparative properties of geosynthetics
(adapted from Pilarczyk, 2000).

Comparative Properties		**Polymer Group**			
		PET	**PA**	**PP**	**PE**
Strength		●	●	•	•
Elastic modulus		●	●	•	•
Strain at failure		●	●	●	●
Creep		•	●	●	●
Unit mass weight		●	●	•	•
Cost		●	●	•	•
Resistance to:					
UV-light	Stabilized	●	●	●	●
	Unstabilized	●	●	•	•
Alkalis		•	●	●	●
Fungus, vermin, insects		●	●	●	●
Fuel		●	●	•	•
Detergents		●	●	●	●

● high • low

3.1.2. Summary of geotextile properties

To effectively perform a given function, geosynthetics must possess a certain set of properties. These should be designated taking into account, on the one hand, the functionality requirements over the lifetime of work, and, on the other hand, the loads the geosynthetics will be subjected to during handling operations, storage and commissioning. Fortunately, the European (CEN) and International Standards (ISO) committees have devised tests and given the relevant tests and recommendations that should be used to define the properties required for the application in question.

Of particular interest to the scope of the present contribution is the standard ISO 13253:2000: Geotextiles and geotextile-related products - characteristics required for use in erosion control works (coastal protection, bank revetments). Such standard establishes the relevant characteristics of geotextiles and geotextile-related products for use in erosion control works, namely coastal protection, with the objective of avoiding migration of fine soil particles due to hydraulic gradients. It is important for producers, as it includes how geotextiles and related products should be described in specifications based on relevant characteristics according to use and how they should be determined. It also includes quality control procedures during production. The ISO 13253:2000 may as well be used by designers, and other final users in the definition of relevant functional requirements and terms of use.

Table 3.II includes the essential characteristics of geotextiles and geotextile-related products (hereafter referred to as geotextiles) in coastal erosion when used for purposes of filtration, separation, and/or reinforcement. Within this paragraph a discussion is made on the physical, mechanical, and hydraulic properties of geotextiles, while the next addresses the aspects related to durability with regard to weathering, and product life-time. Refer to the original reference for further detail on the scope of each standard included in Table 3.II, which is also treated extensively in Carneiro (2009).

Table 3.II: Characteristics of geotextiles and geotextile-related products according to functions and test methods (adapted from ISO 13253:2000).

Characteristics	**Test Method**	**Function**		
		Filtration	**Separation**	**Reinforcement**
1. Tensile test	ISO 10319:2008	●	●	●
2. Elongation at nominal strength	ISO 10319:2008	●	●	●
3. Tensile test for joints/seams	ISO 10321:2008	•	•	•
4. Static puncture test (CBR test)	ISO 12236:2006	•	●	●
5. Dynamic perforation test (cone drop test)	ISO 13433:2006	●	●	●
6. Friction characteristics	ISO 12957:2005 -1 and -2	•	•	■
7. Tensile creep and creep rupture behaviour	ISO 13431:1999	-	-	●
8. Damage during installation	ISO 10722:2007	●	●	●
9. Characteristic opening size	ISO 12956:1999	●	●	-
10. Water permeability	ISO 11058:2010	●	●	●
11. Durability	-	●	●	●
11.1 Resistance to weathering	ISO 12224:2000	●	●	●
11.2 Resistance to chemical weathering	ISO 12960:1998 ISO 13438:2004 ISO 12447:2001	•	•	•
11.3 Microbiological resistance	ISO 12225:2000	•	•	•

● high relevance • low relevance - no relevance

Table 3.III summarises common geotextile properties for use in coastal engineering applications, and the orders of magnitude for each property. The units on which the properties are usually given in, and some additional remarks are also referred to in Table 3.III.

A number of noteworthy observations may be drawn from the analysis of Tables 3.II and 3.III. For instance, some geotextile properties such as strength and elongation are derived from the basic materials (*i.e.*, polymers) and from the final processing which yields the shape of the end product (which governs, *e.g.*, permeability and soil tightness); while others such as creep are governed by the basic material only.

For filter or separation functions the geotextile has to be flexible, water-permeable and soil-tight as such relevant properties are the aperture size and shape, and the permittivity. Yet, as very often the material has to fulfill a main and a minor function, is possible that a geotextile with a filter function has to absorb tensile stresses. Soil reinforcement requests strong, relatively stiff and preferably water-permeable materials, thus governing properties are strength and stiffness although deformations and puncture may have a great impact on the admissible stresses.

Mechanical properties are important in those applications where the geotextile is required to perform a structural role. These properties are also very important when the geotextile is required to survive installation damage and localized stresses. Typically, PET-wovens are used in soil reinforcements, while PET-, PP-, PA-wovens or non-wovens are used as filters, drains and separators.

Table 3.III: Summary of geotextile properties.

Properties		Unit	Indicative Values		Remarks
			Woven	Non-woven	
Physical	Basic material	-	PET, PA, or PP	PET, PA, PP, or PE	-
	Mass per unit area	g/m^2	100-300	100-400	Some special fabrics may have a mass per unit area exceeding 1000 g/m^2. It can be a good indicator of cost, quality and several other properties such as tensile strength.
	Thickness	mm (or μm)	0.2-1.5	0.2-5.0	It is measured as the distance between the upper and the lower surfaces of the material at a specific normal pressure (generally 2.0kPa). It is an indicator of compressibility, and has a direct influence on the geotextile hydraulic and mechanic behaviour.
Hydraulic	Aperture size and shape (porometry)	mm (or μm)	0.05-1.5	0.06-0.15	Typically is expressed as O_{90}. It is a critical property in designing geotextiles as filters and as separators.
	Permittivity	s^{-1}	0.05-0.5	0.2-2.5	It may be defined as the volumetric rate of water flow per unit cross-sectional area, per unit head, under laminar flow conditions in a direction normal to the geotextile plane. It is a critical property in designing geotextiles as filters.
	Transmissivity	m^2/s	-	-	It depends on the geotextile thickness, and aperture size and shape. It is a critical property in designing geotextiles as drains.
Mechanical	Strength	kN/m	*Thick:* PET: up to 1500 PA: up to 800 PP: up to 250 *Tapes:* up to 250 *Multi-filament:* up to 800	PET: up to 40 *Others:* up to 20	It depends on the basic material and on the final processing.
	Creep and strain at break	%	*Thick:* PET: 10-20 PA: 20-30 PP: 10-20 *Tapes:* 10-20 *Multi-filament:* 20-30	PET: 20-40 *Others:* 25-75	It is the increase of strain under permanent loading; it is a very important factor in the geotextile medium- to long-term performance. It mostly depends on the basic material.
	Puncture survivability	-	-	-	It is the ability of the geotextile to elongate around protruding large angular particles without rupture or puncture. The degree of relevance of this property depends on the expected degree of damage with respect to installation.
	Friction at the interfaces	kN/m^2	-	-	It is a critical property in designing geotextiles as reinforcement, as the stability of reinforced soil is strongly related to the effectiveness of stress transference from soil (or other material) to reinforcement done through the interface. It depends on a large number of parameters such as the mechanical and physical properties of the soil and the geotextile, soil size, the geometry of the building, and the building process.

All the above mentioned aspects should be taken into consideration when evaluating the essential geotextile properties to withstand the functional requirements relative to a certain application. The next step is to assess durability and life-time performance requirements.

3.1.3. Durability and life-time performance

Under certain circumstances (*e.g.*, UV-load, hydrolysis, and chemical and/or biological attack), and in the course of time (*e.g.*, due to mechanical damage, fatigue, or creep), the properties of geotextiles can change unfavourably. Indeed much of the uncertainty with respect to geotextiles, in civil engineering in general, and in coastal engineering in particular, is related to durability – it is a well-known fact that geotextile fabrics are very susceptible to weathering and must be protected against UV-light – and life-time performance – there is a real concern about geotextiles, which links to their fragility against mechanical impact and vandalism.

The decay in resistance due to mechanical damage, weathering (most especially, raised temperature and ultraviolet radiation), chemical degradation, and biological degradation may result in the loss of performance, as a consequence of a loss in strength, and in functioning.

The extent to which the material loses performance quantifies durability, which is also influenced by degradation processes during handling and in-service. The term durability is also applied to refer to the capability of the project to continue functioning at an acceptable level even after the construction material has begun to degrade.

During application there is a great probability of mechanical damage. Also, storage and transport require special attention. What is more, depending on the location and accessibility to the geotextiles, there is a risk of vandalism. All such factors may lead to, *e.g.*, a reduction in tensile strength, leakage, tearing, crack formation, plastic deformation and differential stretching. These factors are relevant in the extent of the additional stresses or component failures they may induce and/or in the extent of their effect in losing functionality.

The environmental conditions specific to coastal engineering applications are propitiatory of the geotextiles' exposure to sunlight (duration and intensity) both in-service and at installation.

Raised temperature and ultraviolet radiation may have a negative effect on geotextiles because such ageing agents stimulate oxidation by which the molecular chains are cut off. Once this process starts, the molecular chains of the geotextile degrade continuously and the original molecular changes. Typically, when the geotextile is exposed to raised temperature and ultraviolet radiation for long time it becomes brittle and loses mechanical resistance. To reduce sensitivity to ageing, additives (*e.g.*, anti-oxidising agents and UV-stabilisers) can be used as a way to improve the less favourable properties of the basic materials. For instance, carbon black is indispensable for extending the life-time expectancy of geotextile materials. This has been clearly demonstrated in the recent investigation by Carneiro (2009).

Conveniently, according to the life-time expectancy and the basic material, the chemical resistance (ISO 12960:1998; ISO 13438:2004; and ISO 12447:2001) and microbiological resistance (ISO 12225:2000) should be tested. For instance, some geosynthetics like nylon (polyamide) and, to a lesser extent, polyester are sensitive to hydrolysis under wet conditions (*i.e.*, reaction to water). Moreover, reinforcing materials made of polyester are strongly attacked under high-alkaline conditions, whereas polypropylene can be attacked by some fungi.

Appendix B to standard ISO 13253:2000 presents generic aspects of durability against harmful effects. It provides guidance on maximum exposure times according to the application and the residual resistance after accelerated-ageing test (ISO 12224:2000), and establishes thresholds of resistance in regard to the basic material.

3.1.4. Overview on stability criteria for geosystems

In the previous chapters, sections, and paragraphs, several of the required planning and design procedures for coastal engineering projects have been described. For instance, Chapter 2, paragraph 2.2.2., provides specification of functional requirements for several coastal structures and possible geomorphological changes. Then, in paragraph 2.2.3., and later in the current chapter, key considerations on materials in marine environment and durability are discussed. Moreover, section 2.3. focus on alternative structure geometries and concepts. At last, this section deals with hydraulic responses and failure mechanisms.

The hydraulic responses are straightly connected with how waves propagate into shallower water, *i.e.* depth-induced wave transformation from the outer surf zone (waves start breaking) to the swash-zone (sand surface alternates between being emerged and submerged), and how they interact with coastal structures. Among those having greater relevance to the present contribution are: shoaling, breaking, run-up and run-down, overtopping, reflection, and transmission.

With respect to failure mechanisms one must distinguish between failure mechanisms related to external loads (*i.e.*, sliding instability; overturning instability; bearing instability; global instability; scour of the subsurface; and subsurface settlement), and internal failure mechanisms (*i.e.*, tearing of the geotextile; loss of fill material through the geotextile; and internal movement of the filling material).

Before proceeding to loading and responses in geosystems under wave-loading, some overall characterization of the phenomenon of wave transformation in shallow water is relevant.

Wave shoaling occurs when waves propagate from deep water into shallow region and may be described as gradually change in height as a result of the change in the rate of energy flux due to the reduction in water depth, even if no refraction takes place. Basically, the wave profile becomes steep and breaks at a certain depth when their height reaches a certain limit.

Wave breaking occurs when the horizontal fluid particle velocity at the surface of a crest exceeds the local phase speed of the crest (Smith *et al.*, 2009). Typically wave breaking has been classified into four types: spilling, plunging, collapsing, and surging (see, *e.g.*, USACE, 2008). Such classification follows the definitions proposed by Galvin (1968) for which Batjes (1975) – both cited in USACE (2008), proposed the breaker type transition values for plane slopes, as shown in Figure 3.2.

The breaker type refers to the form of the wave at breaking. It is influenced by deep-water wave characteristics (H_0, L_0) and bathymetry (beach slope, $tan\beta$), and may be correlated to the Irribarren number – also known as the surf similarity parameter or the break type parameter. For irregular waves the surf similarity parameter is defined as Eq. (3.1).

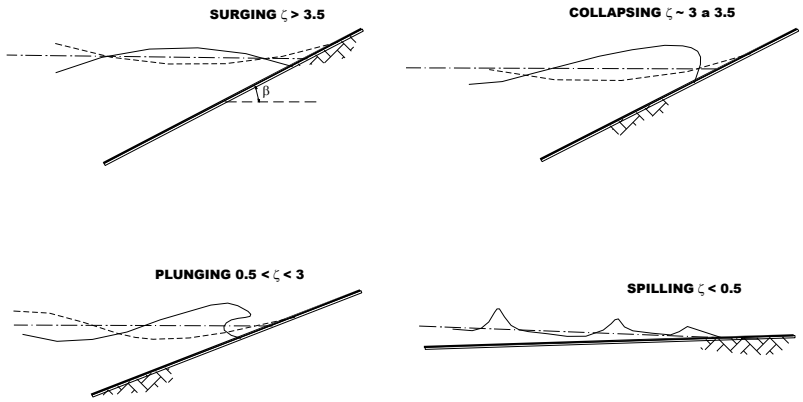

Figure 3.2: Wave breaker types in correlation to the surf similarity parameter (adapted from USACE, 2008).

$$\xi = \frac{\tan\beta}{\sqrt{\frac{H_0}{L_0}}} \tag{3.1}$$

where the deep-water wavelength, L_0, is given by Eq. (3.2). The ratio of wave-height to wavelength [Eq. (3.3)] is designated as wave steepness, $S_{0,p}$, in which the index 'p' designates the peak period.

$$L_0 = \frac{gT_p^2}{2\pi} \tag{3.2}$$

$$S_{0,p} = \frac{H_0}{L_0} = \frac{2\pi H_0}{gT_p^2} \tag{3.3}$$

In spilling breakers, the wave crest becomes unstable and cascades down the shoreward face of the wave producing a foamy water surface. In plunging breakers, the crest curls over the shoreward face of the wave and falls into the base of the wave. In collapsing breakers, the crest remains unbroken while the lower part of the shoreward face steepens and then falls, producing an irregular turbulent water face. In surging breakers, the crest remains unbroken and the front face of the wave advances up the beach with minor breaking.

The wave breaking causes run-up, R_u, and run-down, R_d, defined as the maximum and minimum water-surface elevation measured vertically from the still-water level (SWL), Figure 3.3. Overtopping occurs only if the run-up level, R_u, is higher than the freeboard of the structure, R_c, measured vertically from the still-water level (SWL) to the structure crest height.

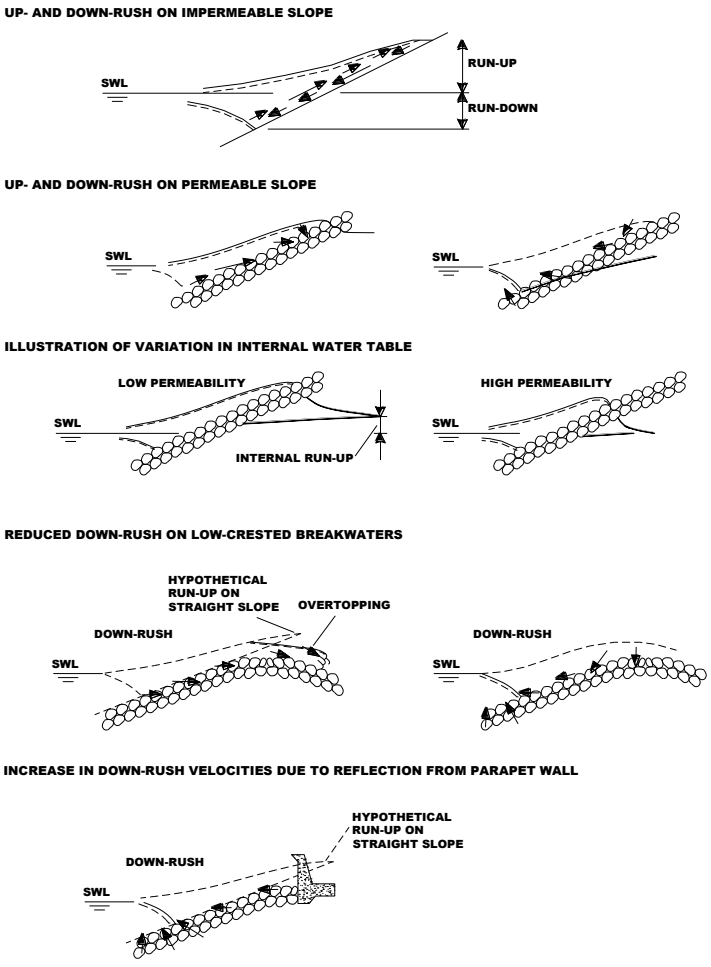

Figure 3.3: Illustration of run-up and run-down
(adapted from USACE, 2008).

In general incident wave energy can be partly dissipated by wave breaking, surface roughness and porous flow; partly transmitted leeward due to wave overtopping and penetration (if the structure is permeable); and partly reflected seaward (USACE, 2008). Typically, the part that is reflected seaward is quantified by the bulk reflection coefficient, K_r, as given by Eq. (3.4).

$$K_r = \frac{H_{sr}}{H_{si}} = \left(\frac{E_r}{E_i}\right)^{\frac{1}{2}} \tag{3.4}$$

where H_{sr} and H_{si} are the significant wave-heights of incident and reflected waves at that position.

Similarly to wave reflection, wave transmission can be characterised by a transmission coefficient, K_t, defined either as the ratio of transmitted to incident characteristic wave-heights (*i.e.*, H_{st} and H_{si}) or as the square-root of the ratio of transmitted to incident time-averaged wave energy (*i.e.*, E_t and E_i), as given in Eq. (3.5). Transmitted wave-periods are about half that of the incident waves (USACE, 2008).

$$K_t = \frac{H_{st}}{H_{si}} = \left(\frac{E_t}{E_i}\right)^{\frac{1}{2}} \tag{3.5}$$

The topics related to wave-structure interaction for conventional structures, such as rubble-mound breakwaters, are dealt extensively within the several volumes of the Coastal Engineering Manual but most specifically in Part VI-5, "Fundamentals of Design"; thus a fuller understanding of the hydraulic responses (*e.g.*, wave run-up, and wave reflection), and the loads and responses of such structures, can be gained from USACE (2008) and references cited therein. Later along this chapter wave transformation from the outer surf zone (waves start to break) to the swash-zone (sand surface alternates being emerged and submerged) is again introduced to describe sediment transport processes in the nearshore region.

With respect to wave-structure interaction for geosystems the list of available references is far less extensive (*i.e.*, number of publications), and far more limited (*i.e.*, usefulness of publications).

Yet, the book by Pilarczyk (2000) has covered developments which took place until late nineties, and is a valuable reference for a comprehensive understanding of geosystems in coastal engineering.

More recent studies on the stability of sand-filled geosystems under wave-load include:

- van Steeg and Vastenburg (2010) on large scale model tests on the stability of geotextile tubes;
- Oumeraci and Recio (2009) on geotextile sand containers for shore protection;
- van Steeg and Breteler (2008) on large scale physical model tests on the stability of geocontainers;
- Recio (2007) on the effect of deformations on the hydraulic stability of geotextile sand containers for coastal structures;
- Recio and Oumeraci (2007b) on the permeability of geotextile sand containers;
- Recio and Oumeraci (2007c) on the processes affecting the hydraulic stability of geotextile sand-filled containers;
- Oumeraci *et. al.* (2002) on the hydraulic stability of geotextile sand containers under wave loading; and
- Bezuijen *et al.* (2004), Bezuijen *et al.* (2002a, 2002b), and Bezuijen *et al.* (2000) on field and model tests on the placing accuracy and stability of geocontainers.

A brief summary of selected key results and conclusions drawn from the latter studies, which comprise the most commonly used sand-filled geosystems, namely *(i)* geotextile tubes (van Steeg and Vastenburg, 2010); *(ii)* geocontainers (van Steeg and Breteler, 2008; Bezuijen *et al.*, 2004; Bezuijen *et al.*, 2002a, 2002b; and Bezuijen *et al.*, 2000); and *(iii)* non-woven geotextile containers (Oumeraci and Recio, 2009; Recio, 2007; Recio and Oumeraci 2007b; Recio and Oumeraci, 2007c; and Oumeraci *et. al.*, 2002); the former book by Pilarczyk (2000), and some selected references are presented hereafter along this paragraph.

Overall, the results from the literature show that mode of placement (*i.e.*, overlapping, packing, and orientation with respect to the wave direction), filling-ratio, interface friction (*i.e.*, friction coefficients between structural elements and between these and its foundation), steepness of the slope, and wave conditions acting on the structure, represent important factors affecting the hydraulic stability.

van Steeg and Vastenburg (2010) investigated the stability of geotextile tubes and the possible migration of sand inside the tubes during wave attack by performing large scale physical model tests.

Seven structures consisting of geotextile tubes have been tested at large scale in the Delta flume of DELTARES. In four configurations, single placed tubes with varying filling percentages and sizes were tested. One configuration consisted of a single tube with a bar placed at the landward side to simulate a trench (Test Series F and T). Two other configurations consisted of two tubes placed behind each other and a so-called 2-1 stack (Test Series P); two tubes placed behind each other with a third tube on top (Test Series P). These configurations are shown in Figure 3.4, and the main dimensions are included in Table 3.IV.

Each structure was submitted to series of 1000 waves that would increase until failure occur (Table 3.V). The D_{50} of the sand used in the experiments is 194μm.

For all tests, irregular waves (JONSWAP, with a peak enhancement factor γ=3.3) were used. During tests, the wave characteristics were measured by means of three wave gauges in front of the structure, and the profile was determined using a mechanical profile tracker combined with hand measurements. The experiments were recorded in video from above, and with help of several marker points the displacements were determined by post-processing, as where the possible stretches in the geotextile. A penetrologger have been used to investigate geotechnical aspects of the sand and colour injections with ink allow the visualization of possible sand migration.

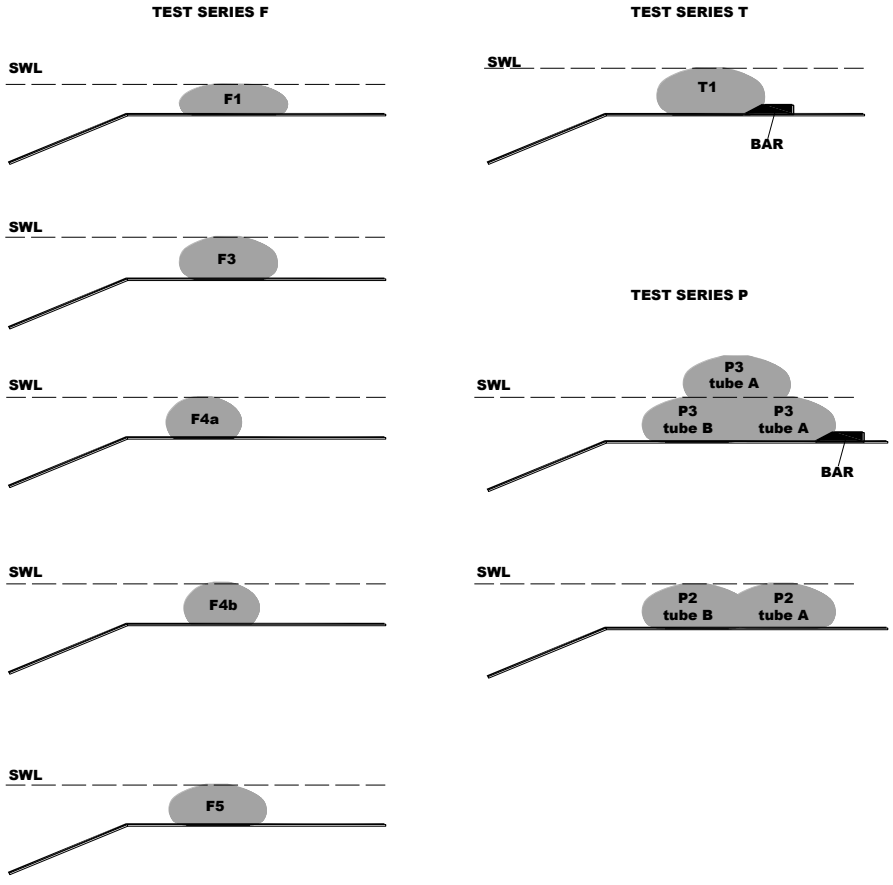

Figure 3.4: Configurations tested by van Steeg and Vastenburg (2010).

Table 3.IV: Overview of the main dimensions of the geotextile tubes used by van Steeg and Vastenburg (2010).

Series	Average Height, H (m)	Average Base-width, B (m)	Theoretical Diameter (m)	Percentage of filling with respect to	
				Height, p_H (%)	Cross-section Area, p_A (%)
F1	0.57	2.19	0.75	38	66
F3	0.79	2.04	0.75	53	80
F4	0.82	1.52	0.57	73	109
F5	0.74	2.02	0.76	48	72
T1	0.88	2.03	0.76	58	85
$P3_{avg}$	0.71	1.47	0.57	61	91
$P2_{avg}$	0.84	1.99	0.77	55	77

Table 3.V: Maximum measured wave conditions for each test series
(modified from van Steeg and Vastenburg, 2010).

Test	Water-level (m)	H_s (m)	T_p (s)	H_{max} (m)	$S_{0,p}$ (-)	$\xi_{0,p}$ (-)	N (-)
F1_10	4.22	1.283	5.330	1.610	0.029	2.35	75
F3_9	4.45	1.323	5.590	1.958	0.027	2.43	1034
F4_6	4.45	0.753	3.650	1.290	0.036	2.10	1021
F5_6	4.39	1.363	5.650	1.916	0.027	2.42	991
P2_4_t	4.46	1.381	5.630	1.840	0.028	2.39	568
P3_9	4.31	1.368	5.500	1.860	0.029	2.35	282
T1_9	4.42	1.497	6.364	2.126	0.024	2.60	2021

The overall conclusions drawn by van Steeg and Vastenburg (2010) may be summarized as follows:

- All the tested configurations failed due to the sliding mechanism;
- All single tubes have slide landwards;
- Two tubes behind each other (Test Series P2) did not significantly increase stability, as the tube at the landward side starts to shift due to a hydrostatic pressure caused by the water entrapped between the two tubes and the hydrodynamic water pressures at the landward side of the tubes;
- Placing two tubes behind each other with a third tube on top (Test Series P3) has resulted into a so-called slip circle failure mechanism during heavy wave attack; in the performed tests, the slip circle in landward direction was blocked by applying a fixed bar at the landward side of the tube which simulated a trench (for example formed due to settlement of the subsoil of the tubes or a commonly used dredged trench); at the seaside, such a bar was not placed resulting in a slip circle in seaward direction (see Figure 3.5);

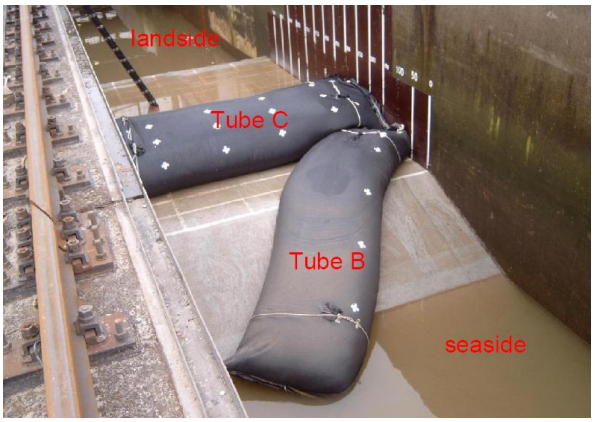

Figure 3.5: Geotextile tube after test P3_9
(reproduced from van Steeg and Vastenburg, 2010).

- Migration of sand within the tube was observed but did not cause any failure; although not guaranteed for larger tubes, it is likely that this mechanism is not dominant;
- Besides filling-ratio and density, parameters that should require attention are the shape of the element (depends partly on the elasticity, and partly on the thickness of the geotextile), the friction coefficient between the tubes and the friction coefficient between the tube and its foundation; and
- The deformation of the tubes is a function of the filling-ratio (a higher filling grade leads to less deformation) and may induce a loss of height.

Based on the experimental results, van Steeg and Vastenburg (2010) deduce a stability relation for single placed geotextile tubes expressed in terms of the base-width (B) and the height (H) of the tube, the slope angle of the support of the tube (β) as given in Figure 3.6, the friction coefficient between the tube and the foundation (ϕ), the significant wave-height (H_s) corrected with the amount of overtopping energy (χ), and the relative buoyancy of the tube (ρ') as given in Eq. (3.6), assuming that a maximum displacement of the geotextile tube of 5% of its width during a storm of approximately 1000 waves is acceptable. The stability relation is given by Eq. (3.7), with a correction factor for overtopping wave energy as given in Eq. (3.8) or Figure 3.7.

$$\rho' = \frac{\rho - \rho_w}{\rho_w} \tag{3.6}$$

$$\frac{\chi H_s}{\rho' \sqrt{BH}(\phi \cos\beta + \sin\beta)} \leq 0.65 \tag{3.7}$$

in which, K_t is the transmission coefficient, $K_{t,ss}$ is the transmission coefficient in a situation with only the supporting structure, $K_{t,ss+tube}$ is the transmission coefficient in a situation with the supporting structure and the tube, H_s is the significant wave-height, R_c is the crest freeboard, θ is the direction of incident wave, ξ is the breaker parameter as given by (3.1), and χ the wave absorption correction factor. The quantities ρ and ρ_w are the densities of the filling-material and the water, accordingly.

$$\chi = \sqrt{K_{t,ss}^2 - K_{t,ss+tube}^2} \tag{3.8}$$

$$K_t = \left(-0.3\frac{R_c}{H_s} + 0.75(1 - e^{-0.5\,\xi})\right)(\cos\theta)^{\frac{2}{3}} \tag{3.9}$$

where K_t has a minimum (0.075) and a maximum (0.8). In addition the following limitations apply: surf similarity parameter in the range of 1 to 3; θ in the range of 0º to 70º; and the crest-width (B_{crest}) to significant wave-height (H_s) ratio in the range of 1 to 4.

van Steeg and Vastenburg (2010) also refer that the stability relationship as given by Eq. (3.7) can be used for a structure consisting of two tubes placed behind each other because, as they observed during the experiments, the tubes will move apart from each other due to hydrostatic pressure.

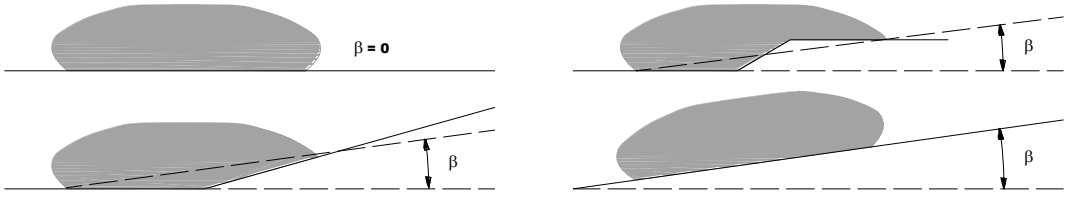

Figure 3.6: Determination of the slope angle of the support of the tube, β
(adapted from van Steeg and Vastenburg, 2010).

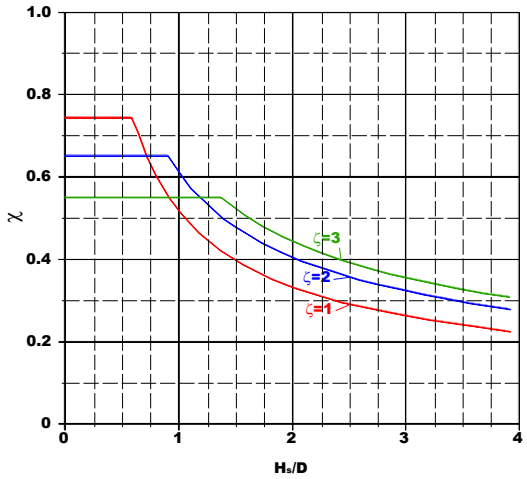

Figure 3.7: Design curve to determine χ,
assuming perpendicular wave attack and a water-level equal to the top of the tube
(adapted from van Steeg and Vastenburg, 2010).

van Steeg and Breteler (2008) had the same main objective as van Steeg and Vastenburg (2010), *viz.* determine the stability of geocontainers and the migration of sand in the geocontainers during wave attack through physical model tests. In addition, van Steeg and Breteler (2008) made an attempt to establish recommendations for the applicability of geocontainers.

The physical model tests have being carried out at large scale in the Delta flume of DELTARES, geometric model scale was 1:4. High-water, h_c/H_s in the range of 0.5 to 1.0, and low-water, h_c/H_s in the range of 0 to 0.5, conditions were tested (Figure 3.8), where h_c represents the water level above the crest of the geocontainers. The outer slope of the geocontainers had a slope of 1:2. The thickness of the geocontainers is 1.5-2.2m in prototype, and approximately 0.55m in model. The width of the geocontainers in model was 2.75m. The test programme consisted of three sub-programmes: *(i)* Test Series 1: high-water level, h_c/H_s=0.75 (top panel in Figure 3.8); *(ii)* Test Series 2: low-water level, h_c/H_s=0 (bottom panel in Figure 3.8); and *(iii)* Test Series 3: equivalent to Test Series 2 but two cuts are made to the geotextile (Figure 3.9).

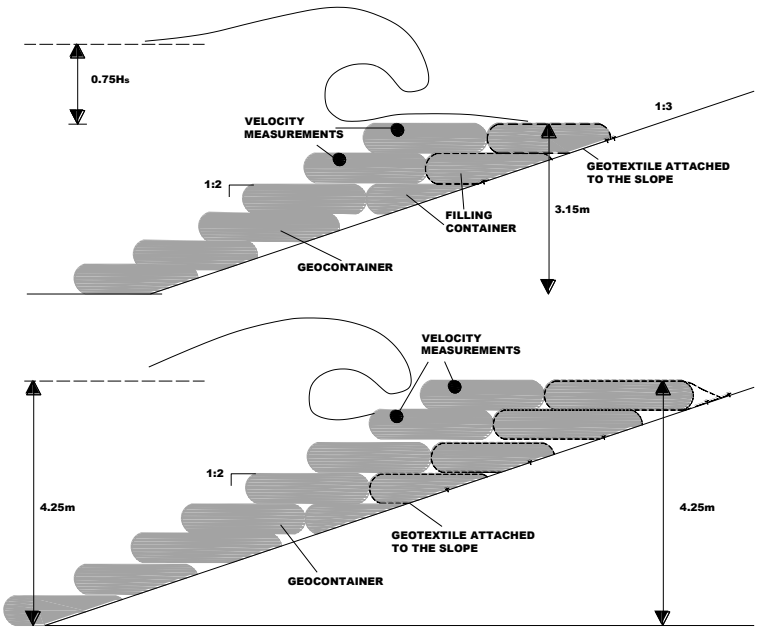

Figure 3.8: Tested cross-section, high-water level (top panel) and low-water level (bottom panel)
(adapted from van Steeg and Breteler, 2008).

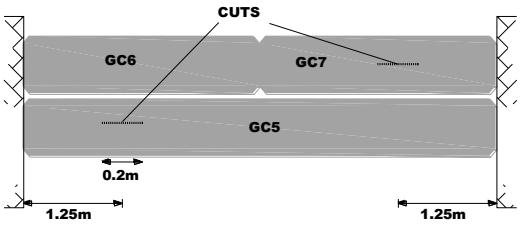

Figure 3.9: Test Series 3: location of cuts made to the geotextile
(adapted from van Steeg and Breteler, 2008).

For all tests, irregular waves (JONSWAP, with a peak enhancement factor γ=3.3 and a wave steepness of 3%) were used. During tests, the wave characteristics were measured by means of three wave gauges in front of the structure, and the profile was determined using a mechanical profile tracker. Sand movement inside the geocontainers was determined by measuring the water movement in the pores by means of six electro-magnetic flow devices. A penetrologger have been used to investigate geotechnical aspects of the sand. In Test Series 1 and 2, wave-height would increase until damage occurs, while Test Series 3 consists of only one test (Table 3.VI).

Table 3.VI: Measured incoming wave parameters, and stability number.

Test	**Water-level (m)**	**H_s (m)**	**T_p (s)**	**$S_{0,p}$ (-)**	**H_{max} (m)**	**ΣN (-)**	$\frac{H_s}{\sqrt{BH}}$
T1_2	4.05	1.19	5.09	0.029	1.72	2108	0.97
T2_5	4.25	1.34	5.36	0.030	1.92	9280	1.09
T3	4.25	0.91	4.35	0.031	1.52	965	0.74

Based on the experimental results, and some theoretical consideration van Steeg and Breteler (2008) drawn the following main conclusions and observations:

- For the tested configurations, the decisive failure mechanism has been the so-called caterpillar mechanism (refer to Figure 3.10 along with the explanation of such mechanism given bellow);
- The conditions at start of damage were H_s equal to approximately 0.76m, and 1.15m for a stack of geocontainers with the crest, respectively at, the water level and $0.75H_s$ under the water level;
- Stability of the geocontainers was found to be significantly lower than the stability of geocontainers in earlier (small) scale model tests; difference which may be explained by *(i)* the migration of sand caused a caterpillar mechanism of the geocontainers which contributed significantly to the instability of the geocontainers (has been previously observed by Venis, 1968); *(ii)* the presence of a 1:3 smooth slope above the geocontainers caused a wave rundown that might have affected the stability of the geocontainers;
- Small grains in the sand washed through the geotextile (estimated amount of 0% to 8% of the original volume of the geocontainer); with less volume of sand, more space is created for the remainder to move more freely, contributing to the caterpillar mechanism;
- The penetrologger measurements indicate that the porosity of the sand in the geocontainers is higher after wave attack; and
- A theoretical analysis show that the geotextile on the sides of the geocontainer might act as a cross brace therefore decreasing the caterpillar mechanism.

The caterpillar mechanism refers to the rotation that typically uplifts the containers and pulls them seawards as a result of external forces such as wave action or currents; forces which had the earlier effect of moving sand inside the containers, either by surface erosion (left panel in Figure 3.10), or by sliding surface reshape of a geocontainer (right panel in Figure 3.10).

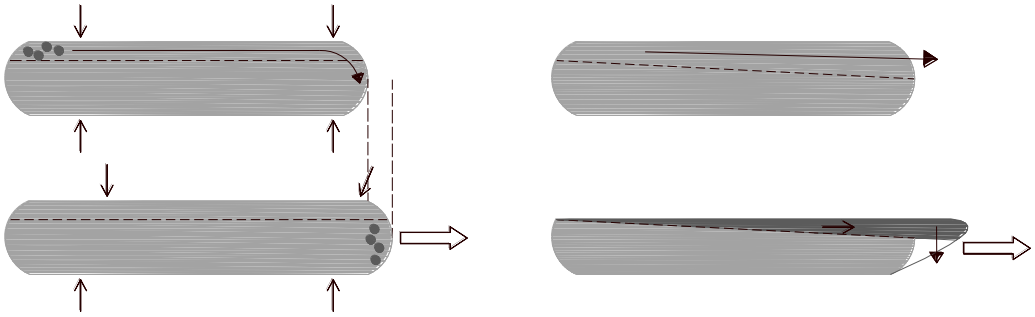

Figure 3.10: Caterpillar effect of a geocontainer; surface erosion (left panel) and sliding surface reshape (right panel) (adapted from van Steeg and Breteler, 2008).

Such sand movement inside the containers has been first described in Venis (1968), which investigations revealed that the loss of stability of sand containers differed from that of units that retain shape. Venis (1968) observed that before the bags as a whole began to move, the sand inside the bags shifted, causing considerable change in shape. Venis' investigations show further that considerable and sizeable influence by scale effects were likely to occur, which has motivated the tests to be repeated on a scale four times larger (*i.e.*, comparative tests were performed on scales 1:5 and 1:20). As seen in Figure 3.11, plotted results from various of Venis' tests evidence that from a point at which the sand in the containers start to shift, the critical current velocity, u_{crit}, set against the square root of container-length, $\sqrt{L}$, departs from Froude's scale-law; this could not be observed in the case of a material that would retain shape.

In more recent studies by researchers at the *Leichtweiß*-Institute for Hydraulic Engineering and Water Resources, the effect of the deformations of non-woven geotextile sand-filled containers (GSCs) on the hydraulic stability has been investigated, targeting the permeability of GSC-structures and its influence on the stability (Recio, 2007; Recio and Oumeraci, 2007b; and Oumeraci *et al.*, 2002), the wave-induced loads on the sand containers (Recio, 2007; Recio and Oumeraci, 2007c; Oumeraci *et al.*, 2002), the wave-induced flow on GSC-structures (Recio, 2007; Recio and Oumeraci, 2007c), the internal movement of sand in the containers and its effect on the stability (Recio, 2007, Recio and Oumeraci, 2007c), the variation of contact areas among neighbouring GSCs during wave action (Recio, 2007, Recio and Oumeraci, 2007c), the types of displacement of GSCs within a coastal structure (Recio, 2007, Recio and Oumeraci, 2007c), the influence of geotextile-friction between neighbouring containers, and finally the influence of boundary conditions on the stability (Recio, 2007; Recio and Oumeraci, 2007c). In addition, Recio and Oumeraci (2007a) did some numerical simulations on the stability of GSC-structures using a flow model (VOF) and two coupled structural models (FEM/DEM).

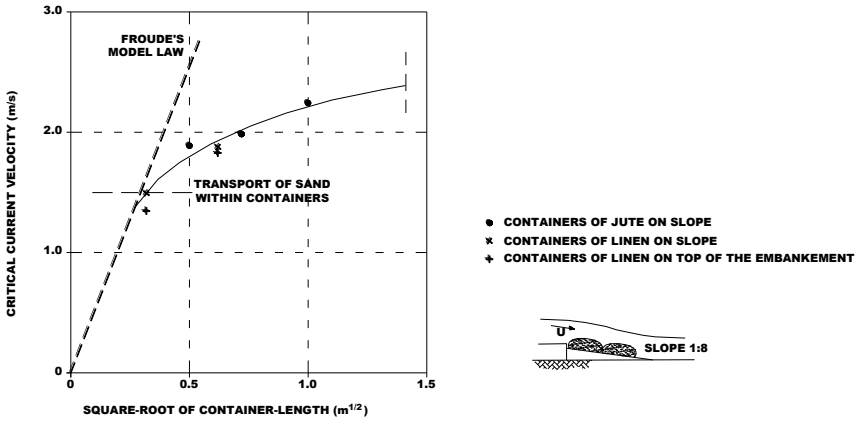

Figure 3.11: Critical current velocity *vs.* square root of bag-length, plotted from various tests (adapted from Venis, 1968).

A flapping geotextile (which refers to the free movement of the geotextile under cyclic load) may explain sand movement inside the element. In this respect, where there is chance of flapping, it is recommended that more curved shapes and more stiff geotextiles are used to refrain the geotextile from flapping. Therefore it may be concluded that higher filling-ratios can be positive in this respect, although at the expense of reducing contact areas between elements.

Recio (2007), Recio and Oumeraci (2007b), and Oumeraci *et al.* (2002) investigated the influence of the permeability of GSC-structures on the stability through basic permeability tests, and tests in wave-flume at two different scales.

In the basic permeability tests a total of eleven model alternatives, which differ in structure length and layout arrangement and size of containers, were tested. The sand containers used in the model tests were made of a non-woven geotextile with a permeability coefficient of k=1.1x10^{-1}m/s and sand with a median grain size of D_{50}=200μm, density of ρ_s=1800kg/m^3 and permeability coefficient of approximately k=1.1x10^{-4} m/s. Several structure geometries and two sizes of sand containers were tested (large: 0.45mx0.28mx0.11m, and medium: 0.35mx0.24mx0.09m) under at least three different hydraulic gradients. The measurements during the model tests focused on the in-outflow.

Detailed information on these tests is given by Recio and Oumeraci (2007b) and Recio (2007) and may be summarized as follows:

- The flow through GSC-structures essentially reduces to the flow through the size of the gaps (*i.e.* the size of the gap governs the overall permeability of the GSC-structure);
- The smaller the container, the smaller the permeability coefficient of the structure; this can be explained by the size and distribution of the gaps between containers, as a structure made with smaller containers will have more and smaller gaps, subsequently the friction losses of the gap flow will be higher;
- If only the permeability performance of the structure is important, then either longitudinal or transversal GSC-arrangements will provide similar total flows through the structure;
- The permeability of a GSC-structure (and thus the total flow through the structure) is considerably reduced, if there is a second layer of overlapped containers that obstructs the flow coming out of the gaps of the first layer; and
- The permeability coefficient of GSC-structures with elements parallel to the flow may vary from 8x10^{-3}m/s (medium containers) to 1.5x10^{-2}m/s (large containers).

Recio and Oumeraci (2007b) further analysed the data derived from the experiments conducted by Oumeraci *et al.*, (2002) in the large wave channel at the Coastal Research Centre of Hannover, to investigate the hydraulic stability of a GSC-revetment. The model consisted of a non-woven filter cloth and 150litre GSCs along a sand slope. After the model tests, the time required for the water to flow from behind the structure and the variation of water level before the structure *vs.* time were recorded, which allowed the calculation of the permeability coefficient, k, equal to 2x10^{-2}m/s.

Additional permeability tests with the larger containers used in the basic permeability tests (*i.e.*, dimensions equal to 0.45mx0.28mx0.11m) as revetment, were performed by Recio and Oumeraci (2007b) in the wave-flume of the LWI (small scale as compare to the experiments by Oumeraci *et al.*, 2002). In this case the estimate permeability coefficient was k=1.4x10^{-2}m/s.

Recio and Oumeraci (2007b) also study the influence of mode of placement of GSCs on the permeability of the overall structure. A smaller size of container (0.26mx0.13mx~0.05m), and three types of arrangements were tested; namely, containers placed longitudinally in the wave-flume; containers placed both longitudinally and transversally (interlaid); and randomly placed containers. A gravel structure was also tested for comparison.

From these experiments, Recio and Oumeraci (2007b) and Recio (2007) have concluded that the mode of placement considerably affects the permeability of the structure. The structure made of randomly placed containers has the higher permeability coefficient of the three tested structures, because the probability of the water flowing through the structure of finding a "direct" way (with large gap size) across it is higher than in the other two configurations. The smallest permeability coefficient is expectedly obtained for the containers placed interlaid in a way that the second layer blocks the gaps of the first layer of containers.

Another interesting result obtained by Recio and Oumeraci (2007b) and Recio (2007) is the comparison among the obtained permeability coefficients: the permeability of the sand material (k=1x10^{-3}m/s) is about ten times smaller than the permeability of the GSC-structure (k=1x10^{-2}m/s); moreover, the permeability of the GSC-structure (k=1x10^{-2}m/s) is approximately ten times smaller than the coefficient of a gravel structure (k=1x10^{-1}m/s).

These authors also conclude that randomly placed sand containers and longitudinally placed containers have similar permeability (randomly placed slightly higher than longitudinally). This can be explained because in the longitudinal containers, the water-flow has a direct way across the structure through the longitudinal gaps. However, these gaps are smaller than those that appear between randomly placed containers.

Each one of the three GSC-structures tested by Recio and Oumeraci (2007b) and Recio (2007) where then subjected to increasing regular wave-heights (varying from 0.08m to 0.24m). The wave period was maintained constant and equal to 2s. The structure was submitted to series of 100 waves that would increase of 0.04m in height from one series to the other until the structure collapsed (a rebuilt structure was re-submitted to the same wave run-segment for verification).

Recio and Oumeraci (2007b) and Recio (2007) concluded that, as expected, the structure with the lower permeability showed the lower resistance against wave action; and also that the higher permeability behind the first layer dissipates the pressures behind the structure, thus, providing higher hydraulic stability.

Within the same research programme the wave-induced flow near the GSC-revetment structure has been studied using Particle Image Velocimetry (PIV) techniques (see, *e.g.*, Recio and Oumeraci, 2007c). In another section of the model, an instrumented container with pressure gauges inside was used to record wave-induced pressures at three different elevations to still-water-level. Recio and Oumeraci (2007c) have also studied the internal movement of coloured sand inside a geotextile sand container, using a transparent permeable container.

From the PIV-measurements Recio and Oumeraci (2007c) have observed that vortices are generated between the containers (these may affect the stability of the containers), the main flow is essentially parallel to the revetment slope, and that the wave particles follow orbital trajectories until they reach the revetment, then the up- and downrush flow is divided into a main flow and local flow that is trapped between the containers.

Based on the pressure recorded inside the instrumented container, the horizontal and vertical components of the total wave force were obtained for each time during a wave cycle. Pressure measurements within the gaps between slope containers have shown that wave impact due to breaking and non-breaking waves are of shorter duration and thus less critical for the hydraulic stability than non-breaking waves rushing up and down the slope. The wave impact is significantly damped when propagating inside the gap.

The analysis of the video records of the movement of coloured sand inside a transparent permeable container has shown that (see, *e.g.*, Oumeraci and Recio, 2009):

- Noticeable sand movements occur only for larger waves that are capable to substantially move the front part of the container up and downward during the wave run-up and run down process. After about 30 wave cycles the internal sand movement decreases significantly due to the accumulated sand at the seaward front of the container;

- Due to the sand-fill redistribution at the seaward front of the container, the latter deforms thus offering a larger impact surface area to the mobilizing wave forces and reducing the contact area with neighbouring containers; and
- With the increased mobilizing forces and the decreased resisting forces, an incremental lateral seaward displacement of the deformed container occurs (pull out effect) which causes again the start of the internal sand movement in a similar way as during the first wave cycles.

These results have thrown some light on the influence that deformation likely has on the hydraulic stability of GSC-structures. It affects the hydraulic stability by reducing the contact area between GSCs and by increasing the drag and lift forces due to the increased exposed areas. Deformations also affect the crest height of a GSC-structure, as the sand-filled container height is reduced after placement under water and due to wave action.

Other interesting conclusions drawn by Recio and Oumeraci (2007c) via observation of the tests with the transparent container were: *(i)* during up-rush, vortices are formed in the areas between the containers and *(ii)* up- and downrush velocities induced by higher waves acting on the containers generate high turbulence next to the revetment. Researchers at LWI also observed that a wave breaking hitting directly on the revetment could generate a larger uplift deformation of the container than non-breaking waves.

Based on the experimental and numerical investigations at LWI, Recio (2007) derived stability formulae for GSCs which includes deformation factors for the two common modes of GSC failure (*i.e.*, sliding and overturning) and force coefficients (*i.e.*, drag coefficient, lift coefficient, and inertia coefficient).

Such formulation by Recio (2007), although relevant for having explicitly establish a dependency of the stability with deformation, is limited to, *e.g.*, one type of fabric (non-woven geotextile), specific geometrical conditions, and a container filling-ratio equal to 80%; further, it only considers stability against sliding and overturning.

Some of the most important contributions from earlier model investigations had already addressed issues like the degree to which the geotextile elements should be filled to provide maximum stability (see, *e.g.*, Venis, 1968); the influence of shape in stability (see, *e.g.*, Silvester, 1990; Leshchinsky, 1995; and DELFT Hydraulics (1975, 1973) also cited in Pilarczyk, 2000); the influence of wave steepness in stability (see, *e.g.*, Ray (1977) also cited in Pilarczyk, 2000); the influence of the slope steepness in stability (see, *e.g.*, Porraz (1979), also cited in Pilarczyk, 2000); and the influence in the stability by the overlapping (see, *e.g.*, Oumeraci *et al.*, 2002; and Jacobs and Kobayashi (1983), TEKMARINE (1982), and Porraz (1979), cited all in Pilarczyk, 2000). Yet, the correct quantification of each parameter to stability is not totally certain.

For instance, there is much uncertainty in regard to the optimum filling-ratio and it is still an open topic for investigation, even though its importance to stability has been acknowledged by several authors since many years; *e.g.*, Venis (1968) found in model that optimal results were obtained if the bags were filled to 80% of their capacity, the degree of filling which in the prototype was found to be most easily accomplished in the opinion of Venis (1968). However, it is not difficult to see that, optimum filling ratio should not be restricted to a percentage with disregard to other factors, such as geotextile properties and shape, structure layout, and filling material; despite some evidence to this respect a considerable number of studies reported in literature have been performed based only on the optimum filling ratio of 80%, as suggested by Venis (1968).

The mode of placement (*i.e.*, overlapping, packing, and orientation with respect to the wave direction) is an important factor affecting stability given its significance and relevance to the development of friction, which is mainly engendered by the contributing weight of overlaying elements, the length of contact areas, and the characteristics of the interfaces. To this respect structure geometry, particularly the steepness of the slope, is clearly also of great importance; it may be interesting to note that the majority of the experimental studies were performed in structures having a steep 1:1 slope.

Besides the already mentioned stability formulations by van Steeg and Vastenburg (2010) and Recio (2007), Wouters (1998) cited in Pilarczyk (2000) has developed a stability formula from the experimental data of Jacobs and Kobayashi (1983), TEKMARINE (1982), and Porraz (1979) – also cited all in Pilarczyk (2000) – that reads as Eq. (3.10). Similar formulations have been proposed by Oumeraci *et al.* (2002), as given by Eq. (3.11) and Eq. (3.12), for respectively crest and slope elements.

$$\frac{\mathrm{H}}{\Delta \mathrm{D_n}} = \frac{2.0}{\sqrt{\xi}} \tag{3.10}$$

$$\frac{\mathrm{H}}{\Delta \mathrm{D_n}} < 0.79 + 0.09\frac{\mathrm{R_c}}{\mathrm{H_s}} \tag{3.11}$$

$$\frac{\mathrm{H}}{\Delta \mathrm{D_n}} < \frac{2.75}{\sqrt{\xi}} \tag{3.12}$$

in which, H is the critical wave-height at the incipience of the damage (typically taken to be equal to the significant wave-height H_s), ξ is the breaker parameter as given by (3.1), D_n is the nominal diameter (equivalent thickness measured perpendicular to the slope), Δ is the relative buoyancy of the tube as given in Eq. (3.6), and R_c is the crest freeboard. The quantity $H/\Delta D_n$ is referred to as the stability number, N_s. There are a few other stability formulations which differ from the previous by not making the stability number depend on the breaker parameter, and by a different stability constant.

Bezuijen *et al.* (2004), Bezuijen *et al.* (2002a, 2002b), and Bezuijen *et al.* (2000) report investigations carried out with geocontainers in the field and in model to study the placing accuracy and geotechnical aspects focusing on, *e.g.*, the loading during opening of a slip barge, dimensions of geocontainer (*i.e.*, circumference, width and height), falling velocity, placing accuracy, impact loading, and stability in waves and currents. Most significant contributions given by this research to practical applications may be summarized as follows: *(i)* significant horizontal displacement is possible when a geocontainer is dumped on a flat bottom, whereas less displacement may be expect when the geocontainer is dumped on other containers instead; *(ii)* dilatancy of sand reduces the loading during impact, yet this loading is still considerable; *(iii)* measured vertical falling velocity corresponds reasonably well with the theoretical description; and *(iv)* placing accuracy is limited at water-depths higher than 15m.

3.1.5. Concluding remarks

The choice of a material is influenced by the functional requirements to be performed over time, and is evaluated in regard to the physical (*e.g.*, mass per unit area, and thickness), hydraulic, mechanical (*e.g.*, tensile strength), and durability properties of the fabric, which in the case of geosynthetics depend on the type of basic material and processing technology. Environmental requirements may also influence that choice.

Requirements of a geotextile regarding coastal erosion control are in essence soil-tightness and the care for a good application. Nevertheless, the geotextile (woven or non-woven) should ensure sufficient robustness to withstand, without being damaged, installation (*e.g.*, handling, and filling) and localizes stresses. When a geotextile is subject to certain circumstances (*e.g.*, UV-load, hydrolysis, and chemical and/or biological attack) over a period of time, the properties in the long-term should be considered. The durability requirements are established in the standards as follows: in regards to weathering resistance ISO 12224:2000; in regards to chemical weathering resistance ISO 12960:1998, ISO 13438:2004, and ISO 12447:2001; and in regards to microbiological resistance ISO 12225:2000.

Some geotextile properties such as strength and elongation are derived from the basic materials (*i.e.*, polymers) and from the final processing which yields the shape of the end product (which governs, *e.g.*, permeability and soil tightness); while others such as creep are governed by the basic material only.

For filter or separation functions the geotextile has to be flexible, water-permeable and soil-tight as such relevant properties are the aperture size and shape, and the permittivity. Yet, as very often the material has to fulfil a main and a minor function, is possible that a geotextile with a filter function has to absorb tensile stresses. Soil reinforcement requests strong, relatively stiff and preferably water-permeable materials, thus governing properties are strength and stiffness although deformations and puncture may have a great impact on the admissible stresses.

During installation and handling, the geotextile is submitted to significant mechanical stresses; moreover, some filling procedures (*e.g.*, with soil/water mixtures) causes abrasion of the internal side of the fabric which is typically compensated by a higher thickness. When the tube is inflated with mixtures of soil and water, the internal hydraulic pressure applies a very significant tensile force on the geotextile.

From the previous chapter it has been demonstrated that maintenance on a regular basis is anticipated. To expect otherwise may result in failure. It has also become clear that, except may be for very small projects, the installation needs an experienced contractor and/or supervision in order to ensure an optimal quality work. Negligence in materials and site preparation and positioning may lead to tearing of fabric and differential settlements, eventually causing collapse by excessive deflection, slumping and displacements. Seams and overlaps are always weaker than the original, non-connected fabric, and have thus to be kept to a minimum and pre-fabricated as much as possible.

It has become clear along this section that even though the processes involved in the wave-structure interaction for geosystems are fairly well identified, no reliable design formulae is available for the hydraulic stability. The advances and the limitations of current state-of-knowledge about the hydraulic stability of geotextile encapsulated-sand systems under wave-loading may be summarized as follows:

- Friction is presumed to be the most important stabilizing factor and should be incorporated explicitly in stability formulae; to this respect, and within those given here, only the one proposed by van Steeg and Vastenburg (2010), as given by Eq. (3.7), does so;
- The development of friction is influenced by the interface friction characteristics (*i.e.*, the friction coefficient between elements, and the friction coefficient between the elements and the foundation) and depends on the contributing weight of overlaying elements (which may change due to the migration of sand within the element; and filling-material being washed through the geotextile), and the length of contact areas (which may change due to the individual displacements);
- A connection between sand migration causing considerable changes in shape and instability due to sliding and overturning has been confirmed;
- The hydraulic stability of geotextile encapsulated-sand systems cannot be assessed using the know-how and the design formulae available for materials that retain shape (*e.g.*, via the Hudson formula);
- Deformation affects the hydraulic stability, essentially due to the former two mechanisms: *(i)* sand redistribution at the seaward front of the element, increases the surface areas exposed to drag and lift forces which represent the main destabilizing forces/moments; and *(ii)* reduction of the contact areas between neighbouring elements caused by the uplift the containers by wave action, thus decreasing the stabilizing forces/moments;
- So far, only the formulation by Recio (2007) explicitly establishes a dependency of the stability with deformation yet is limited to, *e.g.*, one type of fabric (non-woven geotextile), specific geometrical conditions, and a container filling-ratio equal to 80%; further, it only considers stability against sliding and overturning;
- Since both, the friction, and the deformation, are strongly dependent on the filling-ratio (*e.g.*, a higher filling percentage leads to less deformation, namely by reducing the chance of flapping), it is recommended that further investigative efforts addressing advantages and disadvantages of higher ratios are carried out;

- Besides filling percentage, the aspects that require the most attention are: density (depends on the filling-material); shape of individual elements (depends partly on the elasticity and thickness of the geotextile); dimensions of individual elements (larger elements are likely less sensitive to sand migration, and are therefore possibly more stable); mode of placement (*i.e.*, overlapping, packing, and orientation with respect to the wave direction); geometrical conditions, namely the presence of a slope which influences the hydraulic responses (*e.g.*, wave breaking, wave run-up, and wave run-down), and the loss of height (it can reach up to about 10%) when subject to severe wave attack;
- The experiments carried out at LWI (see, *e.g.*, Oumeraci and Recio, 2009; and Recio, 2007) have shown that the effect of breaking wave impact on sliding and overturning stability of slope elements may be much less than expected, due to the potential of the structure to effectively damp impact pressure propagation inside the gaps; those experiments have also shown up- and downrush of the longer non-breaking waves and partially breaking waves to be more efficient in destabilising the slope containers;
- With respect to permeability, Recio and Oumeraci (2007b) and Recio (2007) have concluded that the size of the gap governs the overall permeability of structures made of geotextile sand-filled containers, indicating that structure permeability essentially depends on mode of placement and shape of individual elements;
- The former authors have also concluded structure permeability to slightly affect hydraulic stability yet no clear correlation was found by the authors between stability and permeability; and
- van Steeg and Breteler (2008) have identified a further limitation which relates to the influence of currents on the migration of sand within the elements.

Based on the review of current state-of knowledge with regard to the hydraulic stability of geotextile encapsulated-sand systems it has been confirmed that the available research examined only the processes affecting crest and slope elements, confirming as well that the instability caused by scour around those systems has not yet been the specific focus of attention of any research programme regarding the application of geosynthetics and geosystems in coastal engineering.

Over the following three sections, the state-of-knowledge with respect to the physical modelling of cross-shore sediment transport, the cross-shore component of sediment transport, and the development of scour around coastal structures is analysed, whereas in section 3.5 the indentified research and guidance needs are summarized.

3.2. Physical modelling of cross-shore sediment transport

Physical modelling of cross-shore sediment transport requires the determination of the appropriate scaling relationships for both the waves and the sediments. The books by Hughes (1993) and Dalrymple (1985) present a complete discussion of scaling laws as applied to predicting cross-shore sediment transport, whereas the guidelines developed within HYDRALAB III: Integrating European Hydraulic Research Infrastructure (HYDRALAB, 2008, 2007a, 2007b), Tirindelli *et al.* (2000), and Oumeraci (1993) cover many aspects of the inevitable scaling effects in both movable and fixed-bed models. The work by Silva (2010) also describes quite extensively aspects that relate to both, the modelling of sediment transport, and the scaling effects.

3.2.1. General requirements of similitude

In a physical model, the flow conditions are said to be similar to those in the prototype if the model displays similarity of form (geometric similarity), similarity of motion (kinematic similarity) and similarity of forces (dynamic similarity), as described by, *e.g.*, Chanson (2004).

The geometric similarity implies that the ratios of prototype characteristic lengths to model lengths are equal, Eq. (3.13).

$$N_L = \frac{L_m}{L_p} \tag{3.13}$$

In which N_L indicates the ratio of prototype-to-model quantity, and L is a representative unit length (*e.g.*, wave-height, water-depth, wavelength, etc.) and the subscripts 'm' and 'p' denote model and prototype accordingly. Length, area and volume are the parameters involved in geometric similitude.

However, a geometrically similarity system is not enough to ensure that the flow patterns are similar in both model and prototype. Such similarity occurs when the paths of moving particles are geometrically similar, and the ratios of the velocities of particles are similar (*i.e.*, kinematic similarity).

Kinematic similarity implies that the ratios of prototype characteristic velocities to model velocities are the same, Eq. (3.14).

$$N_U = \frac{(U_1)_m}{(U_1)_p} = \frac{(U_2)_m}{(U_2)_p} = \frac{(U_j)_m}{(U_j)_p} \tag{3.14}$$

where N_U indicates the ratio of prototype-to-model quantity, and $U_{1,2,j}$ are velocities.

The combined geometric and kinematic similarities give the prototype-to-model ratios of, for example, time, acceleration, discharge, angular velocity.

Finally, dynamic similarity exists between geometrically and kinematically similar systems if the ratios of all forces in the model and prototype are the same, Eq. (3.15).

$$N_F = \frac{(F_1)_m}{(F_1)_p} = \frac{(F_2)_m}{(F_2)_p} = \frac{(F_j)_m}{(F_j)_p} \tag{3.15}$$

in which N_F indicates the ratio of prototype-to-model quantity, and $F_{1,2,j}$ are forces.

Model similitude can be established by a number of different methods, usually the similitude by dimensional analysis is used. The basic relevant parameters in the realm of fluid physics needed for any dimensional analysis may be grouped as follows (see, *e.g.*, Chanson, 2004; and Hughes, 1993):

- Fluid properties and physical constants. These consist of the fluid's density, ρ_w (kg/m^3), the fluid's dynamic viscosity, μ (N s/m^2), the surface tension, σ (N/m), the modulus of bulk elasticity for gas mediums, K (Pa), and the acceleration of gravity, g (m/s^2) which is identical in both the model and the prototype.
- Form. These may consist of the characteristic length(s) L (m).
- Flow properties. These consist of the velocity(ies), U (m/s) and the pressure difference(s) ΔP (Pa).

Taking into account all basic parameters, dimensional analysis yields Eq. (3.16).

$$f_1(\rho_w, \mu, \sigma, K, \omega, g, L, U, \Delta P) \tag{3.16}$$

The dimensions of the basic parameters, as given by Eq. (3.16), can be grouped into three categories: mass (M), length (L), and time (T). The Buckingham's Π-theorem, work of Edgar Buckingham in the year 1915 (see, *e.g.*, Hughes, 1993), implies that the quantities can be grouped into five independent dimensionless parameters, *i.e.*, eight as given by f_1 minus the former three [M L T], Eq. (3.17).

$$f_2\left(\frac{U^2}{gL}, \frac{\rho_w U^2}{\Delta P}, \frac{\rho_w U L}{\mu}, \frac{\rho_w U^2 L}{\sigma}, \frac{\rho_w U^2}{K}\right) \tag{3.17}$$

$$f_2(Fr, Eu, Re, We, Ma) \tag{3.18}$$

The first ratio is the Froude number (*Fr*), characterizing the ratio of the inertial force to gravity force. The quantity *Eu* is the Euler number, proportional to the ratio of inertial force to pressure force. The third dimensionless parameter is the Reynolds number (*Re*) which characterizes the ratio of inertial force to viscous force. The Weber number (*We*) is proportional to the ratio of inertial force to capillary force (*i.e.*, surface tension). The last parameter is the Sarrau-Mach number (*Ma*), characterizing the ratio of inertial force to elasticity force.

In a geometrically similar model, true dynamic similarity is achieved if and only if each dimensionless parameter (or Π-terms) has the same value in both model and prototype, Eq. (3.19).

$$\mathrm{Fr_p} = \mathrm{Fr_m},\ \mathrm{Eu_p} = \mathrm{Eu_m},\ \ \mathrm{Re_p} = \mathrm{Re_m},\ \ \mathrm{We_p} = \mathrm{We_{pm}},\ \ \mathrm{Ma_p} = \mathrm{Ma_m} \tag{3.19}$$

An additional dimensionless parameter having dynamical significance enters the analysis and provides criteria for dynamic similarity when the specification of the boundary and initial conditions involves three dimensional factors. Such additional parameter is the Strouhal number (*St*) which represents a measure of the ratio of inertial forces due to the unsteadiness of the flow or local acceleration to the inertial forces due to changes in velocity from one point to another in the flow field. The Strouhal number (*St*) is the product of the characteristic length (*L*), and the angular frequency (ω), divided by the fluid velocity (*U*), as given by Eq. (3.21).

$$\mathrm{Fr_p} = \mathrm{Fr_m},\ \mathrm{Eu_p} = \mathrm{Eu_m},\ \ \mathrm{Re_p} = \mathrm{Re_m},\ \ \mathrm{We_p} = \mathrm{We_{pm}},\ \ \mathrm{Ma_p} = \mathrm{Ma_m},\ \ \mathrm{St_p} = \mathrm{St_m} \tag{3.20}$$

$$\mathrm{St} = \frac{\omega \mathrm{L}}{\mathrm{U}} \tag{3.21}$$

Scale effects exist when one or more Π-terms have different values in the model and prototype. Unfortunately, in physical modelling scale effects are not the exception but the rule, thus the assessment of to what extent these effects may change the relative importance of the various forces and to what extent this will affect the obtained results is the key to a proper scaling. As a general principle, those products thought to be the most important must be kept constant.

According to several authors, the relevant forces for most coastal hydrodynamics problems are the gravitational forces, friction, and surface tension (see, *e.g.*, Dalrymple, 1985). Thus, the dimensionless products are combinations of the Froude, Reynolds, and Weber numbers. Neglected are compressibility and elasticity effects.

Complete similarity of Froude, Reynolds and Weber would require scaling of not only physical dimensions, but scaling of fluid properties (*i.e.*, viscosity, fluid density), which can almost never be achieved. Not only is economically unjustifiable the use of other fluids than water for most of the hydraulic. But also for most scales, it is impossible to find an appropriate model fluid. Thus, in practical applications, complete similarity is not possible because the use of the same fluid on both prototype and model prohibits simultaneously satisfying the Froude, Reynolds and Weber number scaling criteria, as the velocity scale (N_U) would have to be equal to the square root of the length scale, *i.e.* $N_L^{½}$, for Froude, to the inverse of the length scale, *i.e.* N_L^{-1}, for Reynolds, and to the inverse square root of the length scale, *i.e.* $N_L^{-½}$, for Weber.

Because of that impossibility scale measurements for coastal models prediction are typically conducted respecting Froude's similarity only and disregarding Reynolds and Weber similarities. That is to say, gravity effects are the most significant; yet, to assume that the viscosity and surface tension of water do not play significant roles the modeller has to insure that the Reynolds number and the Weber number are in the same range as the prototype, sometimes by adding scale-up corrections (*e.g.*, to enhance turbulence).

Although individual scale effects are generally small, they are not always negligible in sum; consequently their careful analysis is imperative to results be reliable. If model scale effects become significant, a smaller prototype-to-model scale ratio should be considered to reduce or eliminate them. At the limit, no scale effects is observed at full-scale (*i.e.*, N_L=1) as all the Π-terms [Eq. (3.17)] are the same in the prototype and model.

3.2.2. Similitude criteria for movable-bed models

A number of studies using dimensional analysis have led to the definition of criteria for dynamic similarity of sedimentary processes based on the parameters grain size Reynolds number, as given by Eq. (3.22), mobility number, as given by Eq. (3.23), relative sediment density, as given by Eq. (3.24), and relative fall speed, as given by Eq. (3.25), for geometrically undistorted movable-bed models. More detail on scale requirements in movable-bed-models may be found in the books by Hughes (1993) and Dalrymple (1985).

- Grain size Reynolds number criteria, *Re**;

$$\mathrm{N_{Re*}} = \frac{\sqrt{\mathrm{N_g N_L}}\mathrm{N_D}}{\mathrm{N_\upsilon}} = 1 \tag{3.22}$$

- Mobility number criteria, *F** (also called Densimetric Froude number or Shields parameter);

$$\mathrm{N_{F*}} = \frac{\mathrm{N_\rho N_g N_L}}{\mathrm{N_{\gamma_i} N_D}} = 1 \tag{3.23}$$

- Relative sediment density criteria, $\frac{\rho_s}{\rho_w}$;

$$\frac{\mathrm{N_{\rho_s}}}{\mathrm{N_{\rho_w}}} = 1 \tag{3.24}$$

- Relative length criteria, $\frac{\lambda}{D}$ (also called geometric particle similitude); and

$$\frac{\mathrm{N_L}}{\mathrm{N_D}} = 1 \tag{3.25}$$

- Relative fall speed criteria, $\frac{W_s}{\sqrt{gH_b}}$.

$$\frac{N_{W_s}}{\sqrt{N_g N_L}} = 1 \tag{3.26}$$

The quantity $\sqrt{gH_b}$ is a characteristic velocity, in which H_b is the breaking wave-height. The quantity w_s is the sediment fall speed or settling velocity (refer to section 3.3 for further detail).

Any dissimilarity on the former prototype-to-model scale relationships may introduce scale effects that will affect the initiation of sediment motion, the sediment transport mode, and the sediment transport rate. As it is impossible to simultaneously satisfy all of the five criterions introduced above, except at full scale, dissimilarities will be reproduced into the model set-up which effects must be considered while interpreting results.

Cross-shore sediment transport and morphological changes normally entails sediment being transported as both, suspended and bed-load material. It also involves portions of the coastal model being eroded and others being accreted. Each of these features has a diverse character which may be more or less well-reproduced in model depending on how well the grain size in the model correctly reproduces the dimensional relationships as given by Eq. (3.22) to (3.26).

Assuming that the perfect model exists only in the prototype itself, the implications of improper scaling of the grain size have to be assessed in the light of the problem in equation. Kamphuis (2009), Oumeraci (1993) and references cited therein discuss in detail the consequences of ignoring the criterions introduced above, from which a summary will now be given.

To simulate erosion, initiation of motion, transport mode, and transport rate, should be modelled correctly; consequently, there will be major scale effects with respect to sediment transport in general, and to erosion in particular, due to improper scaling of those conditions.

The ratios given by Eq. (3.22) and (3.23) form the axes of the Shields diagram (refer to section 3.3 for further detail) indicating that they should be related to initiation of motion. Transport mode is believed to be in close relation to the mobility number, while the transport rate is governed by the criterions relative length, as given by Eq. (3.24), and relative density, as given by Eq. (3.25).

Failure to reproduce correctly the grain size Reynolds number affects the flow regime in the bottom boundary layer. Generally it results in small scale effects provided that the viscous effects are negligible (*i.e.*, if Re^* is large enough which is true when is turbulent and the dominant transport mode is suspension load).

Dissimilarities of the mobility number may produce major scale effects with respect to both, sediment motion and sediment transport mode; namely, the waves can take longer to move sediment in the model, resulting in a slower erosion. In regard to sediment transport mode it generally results in less suspension occurring in the model.

As an alternative to satisfy both the Reynolds and mobility criteria, thereby satisfying the Shields criterion (refer to section 3.3 for further detail) lightweight bed material (*e.g.*, bakelite or polystyrene) is often used. Yet, there are significant scale effects in lightweight models, as pointed out by Kamphuis (see, *e.g.*, Kamphuis, 2009; Hughes, 1993; and Dalrymple, 1985); namely, the incorrect scaling of relative density resulting in inaccurate particle accelerations which may lead to an underestimation of sediment transport rates and to the possibility that particles may go into suspension earlier than in prototype thus altering the mode of sand transport.

A lightweight model is further relatively heavier when not submerged, and this results in a pilling up of material at the shoreline (*i.e.*, particles lifted onto to the beach are much more difficult to move). Moreover, the relative length is not correctly scaled because the lightweight material is quite a bite larger than it should which results in the forces being required to move sediment to be exaggerated in model (*i.e.*, larger transport rate in the model than in the prototype); in addition to the incorrect bedform (modifying the roughness and turbulence and consequently sediment transport), the incorrect bed friction, and the incorrect percolation.

Lightweight sediment is as well relatively more porous because the particles are larger than they should be which increases porosity enabling relatively more wave energy to be absorbed. Furthermore, liquefaction of the movable bed model will occur sooner than it occurs in prototype. What is more, in a lightweight model there is non-similitude of the relative fall speed criteria which implies that the sediment transport will not be properly modelled by the model.

Summing it up, it is possible to conclude that there severe limitations to lightweight coastal sediment models which discourage their use due to both, the difficulty in finding a suitable lightweight material, and the inherent scale effects that accompany their use. According to Oumeraci (1993), a lightweight model should only be used when the required sediment particles in the model are smaller than 80μm because then the sediment would cohesive properties.

At last, there is great evidence that, in the nearshore region, turbulent water motions play a greater role in mobilizing and transporting sediment; and in this region there is increasing evidence that the dimensionless fall speed parameter (refer to section 3.3 further detail), as given by Eq. (3.26), should be similar in both prototype and model (see, *e.g.*, Hughes, 1993). The length scale N_L can be then calculated from N_{ws} assuming a Froude similarity which yields velocities scaled with the square root of the length scale.

3.2.3. Concluding remarks

The coastal mobile bed sediment transport and morphology model is perhaps the most difficult of all physical hydraulic models (Kamphuis, 2009); yet despite the shortcomings it is, in many cases, the most important available instrument to bring about improvements with respect to sediment transport, and erosion.

As has been explained above, setting up a geometrically undistorted wave models with sediment transport involves the correct simulation of the initiation of motion, the transport mode, and the transport rate; consequently, Eqs. (3.22) to (3.26) are to be considered simultaneously; yet as it is not possible to satisfy all criterions in model, the dominant processes must be well understood for determining how to build the model and interpret the results. The scale effects produced by non-satisfied scale requirements must be understood as well.

Detailed discussions of the strengths and weaknesses of coastal models (*e.g.*, the various inherent scale effects) may be found in the books by Hughes (1993) and Dalrymple (1985) from which a brief review has been given here. All in all it is possible to conclude that it is usual in coastal models to satisfy the Froude criterion for all velocities, that is all velocity scales are kept the same and equal to $(N_L)^{\frac{1}{2}}$, valid also for the fall speed velocity (w_s), sought to be the must important parameter in wave models with sediment transport to maintain similarity between the prototype and the model (see, *e.g.*, Hughes, 1993).

3.3. Cross-shore sediment transport mechanisms

The most important consideration and ultimate criterion in a design for the coastal zone is often the movement of sediment (Kamphuis, 2000). A link to this perspective has already been established in the previous chapter, while explaining how the anticipated impact of structures on coastal processes, particularly in what concerns the entrapment of sediment, is becoming more and more decisive in coastal engineering and management. It is therefore not surprising that considerable effort has been spent within coastal science and engineering in studying transport processes, and the ensuing morphological response. Yet, as it will be argued along this section, improvements of the accuracy of sediment transport prediction are still needed.

Sediment transport prediction is contingent upon an understanding of two components, namely the longshore sediment transport also known as the littoral drift current, which causes sediment to be moved from one coastal stretch to the adjacent ones, and the cross-shore sediment transport, which causes sediment to move within the beach-profile.

Both components, longshore and cross-shore, occur simultaneously in nature; however, the need for simplicity and convenience in research and practice has led to the separate modelling of the components. Longshore sediment transport models have been used for about 50 years, whereas cross-shore sediment transport models have been of interest for less than two decades. That separation arise from the recognition that under a number of coastal engineering scenarios of interest, transport is dominated by either the longshore or the cross-shore component (see, *e.g.*, USACE, 2008) but has led to an uneven development in understanding each component and to limitations on prediction accuracy of both components. This same general idea has been expressed by Aagard and Bryan (2003) when stating that relatively robust models exist for the prediction of longshore sediment transport, this is not the case for the cross-shore component.

In the present contribution, a focus is given only on the cross-shore component of sediment transport for its relevance in predicting, for instance, beach and dune response to storms, beach nourishment project evolution, seasonal changes of shoreline positions, and scour around coastal structures. More detail on the longshore component may be found in, *e.g.*, Nielsen (2009), USACE (2008), van Rijn (2006), and Dronkers (2005).

The cross-shore component of the sediment transport encompasses two directions of net transport offshore-directed, such as occurs during storms, and onshore-directed, which dominates during mild wave action. The two components, offshore and onshore, appear to occur in significantly distinct modes and with markedly disparate time scales, and result in an adjustment toward an equilibrium profile by erosion or accretion that is respectively the removal or deposition of volumes of sand.

A complete understanding of the processes and conditions affecting changes in the cross-section of a beach is complex. Not only the spatial and temporal scales range significantly from instantaneous motion of individual particles on a time-scale comparable to that of the local turbulence to seasonal and longer term movement of large sediment bodies, but also the natural variability of the beach-profile affects singularly the forcing mechanisms. A complete understanding of cross-shore sediment transport is further complicated by the contributions of both bed and suspended load modes of sediment transport. According to USACE (2008), the partitioning between those two, depends in an unknown way on grain size, local wave energy, and other variables.

From the available knowledge, it appears that the cross-shore transport processes, and the ensuing morphological response, vary with the sediment properties, and the hydrodynamic conditions. According to Dalrymple (1985), the former is adequately characterized by the parameters and the properties size, density, fall speed, and bottom shear stress; while the later may be characterized by the wave characteristics, general space and time parameters, local water depth, acceleration of gravity, sea bottom roughness, fluid density, and fluid kinematic viscosity.

The contributions of each, sediment properties, and hydrodynamic conditions, and the interplay between both are discussed later along this section.

3.3.1. Considerations on sediment properties

It has been suggested above that transport processes depends very much on the sediment properties size, density, fall speed, and bottom shear stress.

The sediment size is often evaluated in regard to the quantity diameter (*D*). The diameter within natural samples of soil is determined by grain size distribution; as it consists of a heterogeneous mixture of particles, from coarser to finer, cobble, gravel, sand, silt or clay. The size distribution of such soil is generally analysed by sieving methods yielding sieve diameters. Graphing the cumulative weight percent retained/passing by a given sieve diameter will result in the sediment grain-size distribution curve. Based upon the grain size distribution it is classified as well-graded when having large range of grain sizes, or poorly (or uniformly) graded when otherwise.

The grain-size distribution curve is used further to read off particular sizes which can be used to determine other quantities, for instance, the median particle size (D_{50}), which is the size at which 50% by weight is finer. As further examples are the grain sizes at which 10% of the sample passed (D_{10}), 30% of the sample passed (D_{30}), and 60% of the sample passed (D_{60}), which may be used to calculate several useful coefficients, namely:

- Coefficient of permeability of the soil, *k*, given by the empirical correlation developed by Hazen (1911) – also cited in Massel (2005), as given by Eq. (3.27) in which *k* is in m/s and D_{10} in cm;

$$k \sim C\, D_{10}^2 \quad 0.4 \leq C \geq 1.2 \text{ (typically } C = 0.5) \tag{3.27}$$

- Uniformity coefficient, C_u, as given by Eq. (3.28); and

$$C_u = \frac{D_{60}}{D_{10}} \tag{3.28}$$

- Curvature coefficient, C_c, as given by Eq. (3.29);

$$C_c = \frac{D_{30}^2}{D_{60} D_{10}} \tag{3.29}$$

The density of sediment, termed as ρ_s, is dependent on mineral constituents. For quartz and clay minerals the density is approximately equal to 2650kg/m^3, while the density of carbonate material may be somewhat smaller, 2500 to 2650kg/m^3. Other relevant sediment properties related to the density of sediment are, the relative density, and the immersed relative density.

The relative density also known as specific gravity, S_s, is defined as the ratio of the sediment density and the fluid density, *i.e.*

$$S_s = \frac{\rho_s}{\rho_w} \tag{3.30}$$

and the sediment immersed relative density also known as immersed sediment buoyancy, ρ', is given by Eq. (3.31).

$$\rho' = \frac{\rho_s - \rho_w}{\rho_w} = S_s - 1 \tag{3.31}$$

The sediment fall speed also known as the fall velocity or the settling velocity, w_s, is a behavioural property that is sought to be a function of the sediment's grain size, density, and shape, and the fluid's density, and viscosity. It is one of the key variables in the study of sediment transport, especially when suspension is the dominant process, since it serves to characterize the restoring forces opposing turbulent entraining forces acting on the particle (Jiménez and Madsen, 2003).

In most cases, the estimation of sediment fall speed of natural sediments is predicted by empirical relationships derived from experimental results, as it difficult (even impossible) to measure actual in situ values. The practical implications imposed by this empirical approach are discussed later in this chapter, whereas several of those empirically derived formulas are herein described.

The sediment fall speed has not infrequently been estimated based upon the terminal fall velocity of a sphere in a fluid at rest by equating the balance between the effective weight forces to the Newtonian expression of drag resistance, as given by Eq. (3.32). The rationale for Eq. (3.32) is discussed extensively by Graf (1984).

$$(S_s - 1)\rho_w g\frac{\pi}{6}D^3 = \frac{1}{2}\rho_w C_D \frac{\pi}{4}D^2 w_s^2 \tag{3.32}$$

where the drag coefficient, C_D, is a dimensionless quantity known to be a function of the Reynolds number (*Re*), as given by Eq. (3.33). Figures 3.12 and 3.13 display the variation of the C_D with *Re* for experimental and calculated data.

$$Re = \frac{w_s D}{\upsilon} \tag{3.33}$$

with υ being the kinematic viscosity.

Rearranging Eq. (3.34) in terms of the settling velocity:

$$w_S = \left[\frac{4(S_s - 1)gD}{3C_D}\right]^{0.5} \tag{3.34}$$

In the Stokes region (*Re*<1, this occurs if either the viscosity is very large or the particle is very small) the drag coefficient is given by $24Re^{-1}$ (see, *e.g.*, van Rijn, 2006), yielding Eq. (3.35). The former relation was obtained by Stokes (1851) assuming a very slow and steady moving sphere in an infinite liquid (see, *e.g.*, Cheng, 1997).

$$w_S = \frac{(S_s - 1)gD^2}{18\upsilon} \tag{3.35}$$

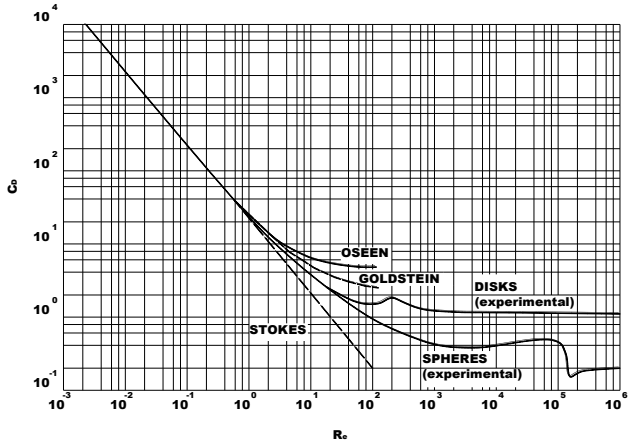

Figure 3.12: Drag coefficient *vs.* Reynolds number for spheres and disks, experimental data (after Rouse, 1938 in Graf, 1984).

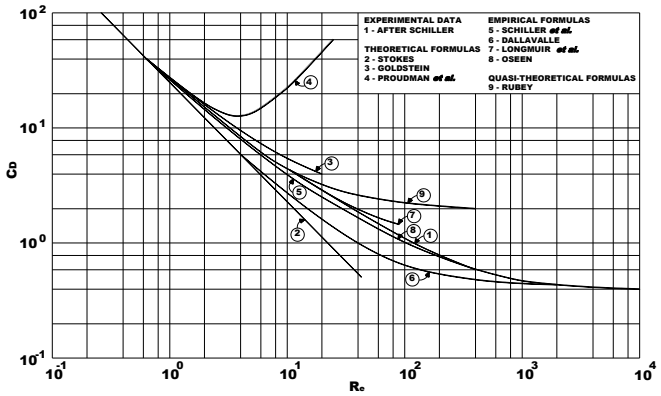

Figure 3.13: Drag coefficient *vs.* Reynolds number, experimental data compared with formulas (after Graf *et al.* (1966) adapted from Graf, 1984).

Outside the Stokes region there is no simple expression for the drag coefficient (van Rijn, 2006). As seen from Figures 3.12 and 3.13 the C_D-value decreases rapidly outsides the Stokes region and becomes nearly constant for 10^3~10^5, yielding w_s proportional to $D^{0.5}$. More detail on the references in Figures 3.12 and 3.13 may be found in Graf (1984).

When dealing with natural sediments another variable, the shape factor (*SF*), must be included while relating the drag coefficient with the Reynolds number. Graf (1984) reports that Albertson (1953), studying the shape effect of gravel particles on settling velocity, finds it suitable to use a shape factor suggested by McNown *et. al.* (1950), as given by Eq. (3.36).

$$\mathrm{SF} = \frac{\mathrm{c}}{\sqrt{\mathrm{ab}}} \tag{3.36}$$

where *SF* is the shape factor, *a* is the largest length scale associated with the particle, *b* is an intermediate length and *c* is the minimum length. The *SF*-factor for natural sand is approximately 0.7 (see, *e.g.*, van Rijn, 2006). Further details on different shape factor can be found in Graf (1984). Figure 3.14 plots the drag coefficient as a function of Reynolds number for different shape factors, as obtained by Albertson (1953). As expected the drag coefficient increases to decreasing shape factor (higher deviation of the natural shape from a sphere). Moreover, the drag coefficients at various shape factors approach constant values at high Reynolds numbers, as for spheres. This indicates fully developed turbulent boundary layers around the grains and has been showed also by the studies of Komar and Reimers (1978) and Swamee and Ojha (1991), cited by, *e.g.*, Smith and Cheung (2003).

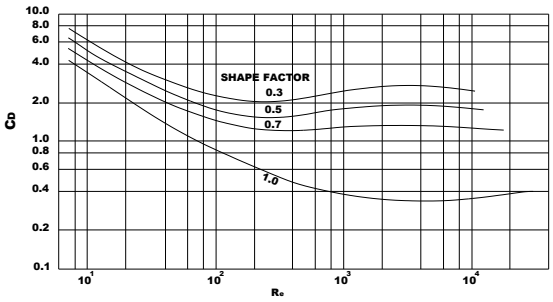

Figure 3.14: Drag coefficient as a function of Reynolds number for different shape factors (Albertson (1953), adapted from Graf, 1984).

van Rijn (2006), Jiménez and Madsen (2003), Cheng (1997) and further references cited therein include several of the most important formulas to compute the settling velocity of natural sediments, for example, Zanke (1977), Hallermeier (1981), Dietrich (1982), van Rijn (1984), Julien (1995), Soulsby (1997), Cheng (1997), Sistermans (2000), Ahrens (2000, 2003), and Jiménez and Madsen (2003), for quartz particles, and for calcareous particles the ones from van der Meulen (1988), and Smith and Cheung (2003).

Zanke (1977) has proposed the expression as given by Eq. (3.37) for the particle fall velocity in the turbulent regime.

$$w_s = \frac{10\upsilon}{D}\left[\left(1 + \frac{0.01(S_s - 1)gD^3}{\upsilon^2}\right)^{0.5} - 1\right] \tag{3.37}$$

Hallermeier (1981) presented a particularly useful set of empirical relationships to calculate the sediment fall speed, which is often use in movable-bed modelling (see, *e.g.*, Hughes, 1993). Hallermeier assembled a large data set of previously determined experimental values of sediment terminal fall speed and associated properties of the sediment and fluid. Hallermeier related the sediment fall speed Reynolds number to the immersed sediment buoyancy, *A*, by the empirical expression Eq. (3.38).

$$\frac{w_s\, D_{50}}{\upsilon} = c_1(A)^{c_2} \tag{3.38}$$

where c_1 and c_2 are empirical constants and A is given by Eq. (3.39).

$$A = \frac{\rho' g\,(D_{50})^3}{\upsilon^2} \tag{3.39}$$

Then Hallermeier found that the experimental data were best represented by three different expressions, valid over different ranges of the immersed sediment buoyancy parameter, *A*. The explicit equations for sediment fall speed are given by Eq. (3.40) to (3.42).

$$w_s = \frac{\rho' g\,(D_{50})^2}{18\upsilon} \quad \text{for } A < 39 \tag{3.40}$$

$$w_s = \frac{(\rho' g)^{7/10}\,(D_{50})^{11/10}}{6(\upsilon)^{2/5}} \quad \text{for } 39 < A < 1x10^4 \tag{3.41}$$

$$w_s = \frac{(\rho' g)^{1/2}\,(D_{50})^{1/2}}{0.91} \quad \text{for } 1x10^4 < A < 3x10^6 \tag{3.42}$$

van Rijn (1984) used Eq. (3.37) in his formulation as given by Eq. (3.43) to (3.45).

$$w_S = \frac{(S_s - 1)gD^2}{18\upsilon} \text{ for } 1 < D \leq 100\mu m \tag{3.43}$$

$$w_s = \frac{10\upsilon}{D}\left[\left(1 + \frac{0.01(S_s - 1)gD^3}{\upsilon^2}\right)^{0.5} - 1\right] \text{ for } 100 < D < 1000\mu m \tag{3.44}$$

$$w_s = 1.1[(S_s - 1)gD]^{0.5} \text{ for } D \geq 1000\mu m \tag{3.45}$$

Cheng (1997) developed a new formula for predicting the settling velocity of natural sediment particles, as given by Eq. (3.46). The formula is based on analysis of 56 data sets with particle sizes between about 10 and 10000μm, and proposes an explicit relationship between the particle Reynolds number and a dimensionless particle parameter, *D**. It is applicable to a wide range of Reynolds numbers from the Stokes flow to the turbulent regime. Cheng (1997) compared his formula against the widely used diagrams proposed by the U.S. Inter-Agency Committee (1957) to find a good agreement between both (see Figure 3.15).

$$w_s = \frac{\upsilon}{D_n}[(25 + 1.2(D^*)^2)^{0.5} - 5]^{1.5} \tag{3.46}$$

in which D_n is the nominal diameter and D^* is given by Eq. (3.47).

$$D^* = D\left[\frac{(S_s - 1)g}{\upsilon^2}\right]^{1/3} \tag{3.47}$$

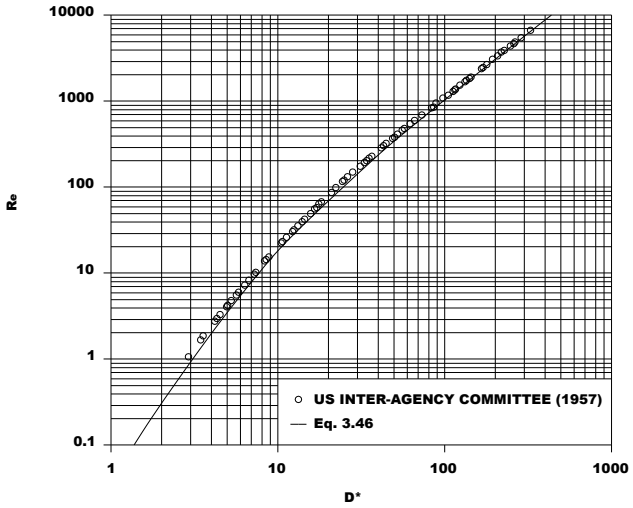

Figure 3.15: Comparison between Cheng (1997) and the U. S. Inter-Agency Committee Data (1957).

Sistermans (2000) has proposed the expression as given by Eq. (3.48) to compute the fall velocity of particles in the size range of 62 to 500μm (see, *e.g.*, van Rijn, 2006).

$$w_s = 10^{-Y} \tag{3.48}$$

where the quantity *Y* is given by Eq. (3.49).

$$Y = \alpha(\log D)^3 + \beta(\log D)^2 + \gamma(\log D) + \varepsilon \tag{3.49}$$

in which *D* is the particle size (in m) and the quantities α, β, γ, and ε may related to the water temperature, *Te* (in ºC), by Eq. (3.50) to (3.53).

$$\alpha = 0.9608(Te)^{-0.1675} \tag{3.50}$$

$$\beta = 10.869(Te)^{-0.1577} \tag{3.51}$$

$$\gamma = 38.994(Te)^{-0.1491} \tag{3.52}$$

$$\varepsilon = 46.125(Te)^{-0.1373} \tag{3.53}$$

In 2002 the expression by Zanke was modified into Eq. (3.54).

$$w_s = \frac{14.7\upsilon}{D}\left[\left(1 + \frac{0.0057(S_s - 1)gD^3}{\upsilon^2}\right)^{0.5} - 1\right] \tag{3.54}$$

Based on data fitting of 52 measured fall velocities of natural quartz particles, Ahrens (2000, 2003) presented a new formula as given by Eq. (3.55), valid in the range $1<A<10^8$ including particle sizes from about 62 to 25000μm.

$$w_s = \frac{\upsilon}{D_s}[c_L A + c_T A^{0.5}] \tag{3.55}$$

in which D_s is the sieve diameter and A, c_L, and c_T are given by Eq. (3.56) to (3.58), respectively.

$$A = \frac{(S_s - 1)gD_s^3}{\upsilon^2} \tag{3.56}$$

$$c_L = 0.055 \tanh(12A^{-0.59}e^{-0.00004A}) \tag{3.57}$$

$$c_T = 1.01 \tanh\left(0.016A^{0.5}e^{-\frac{115}{A}}\right) \tag{3.58}$$

Jiménez and Madsen (2003) derived a new formula from the previous work of Dietrich (1982). This new formula predicts the settling velocity, as a function of a dimensionless fluid-sediment parameter S^*, provided the sediment shape factor and roundness are known. In case no information on shape and roundness factors is available, Jiménez and Madsen (2003) recommend using the formula with a shape factor of 0.7 and a roundless of 3.5 for naturally worn particles. The general expression by Jiménez and Madsen (2003) reads as Eq. (3.59).

$$w_s = [(S_s - 1)gD_n]^{0.5}\left[A + \frac{B}{S^*}\right]^{-1} \tag{3.59}$$

in which D_n is the nominal diameter ($D_n \sim 1.1D_s$ with D_s being the sieve diameter) and S^* is given by Eq. (3.60). A and B are coefficients respectively, 0.79 and 4.61 for perfect spheres, and 0.95 and 5.12 for naturally worn sand (shape factor equal to 0.7 and roundless equal to 3.5).

$$S^* = \frac{D}{4\upsilon}[(S_s - 1)gD]^{0.5} \tag{3.60}$$

Eq. (3.59) was fitted to Dietrich's empirical expression for the non-dimensional fall velocity of spheres with S^* in the range 0.5-30, corresponding to natural quartz spheres of 62 to 1000μm in water, resulting in A equal to 0.79 and B equal to 4.61. The coefficients A and B may change to incorporate the effects of shape and roundness. These coefficients decrease with increasing roundness, resulting in an increase in particle fall velocity. The original paper by Jiménez and Madsen (2003) provides some more values of A and B for different roundnesses. To validate their formula, different published data sets with particle sizes between 60 to 4500μm have been used. The formulas established by Zanke (1997) – also used by van Rijn (1984), Julien (1995), Soulsby (1997), Cheng (1997) and Ahrens (2000) were also applied to those data sets. The former three expressions based on the sieve diameter, D_s, can be expressed by Eq. (3.61), respectively.

$$w_s = [(S_s - 1)gD_s]^{0.5}[(1 + \beta(S^*)^2)^{0.5} - 1]\left[\frac{\alpha}{S^*}\right] \tag{3.61}$$

with α and β equal to respectively, 2.5 and 0.16 for Zanke (1977), 2.0 and 0.22 for Julien (1995), and 2.59 and 0.166 in Soulsby (1997). The comparison results show that most expressions yield values (in 90% of the cases) within 20% of the measured values (sediments between 60 to 4500μm). The scores within 10% of the measured values are in the range of 46% to 77% for the formulas applied. Eq. (3.59) yields marginally better results than the other formulas.

Zhiyao *et. al* (2008) developed a new relationship between the Reynolds number and the dimensionless particle parameter (D^*), based on the general relationship between the drag coefficient and the Reynolds number of a particle described by Cheng (1997). Then by using a trial-and-error procedure to minimize errors, Zhiyao *et. al* (2008) derived a new expression for predicting the settling velocity of natural sediment particles (valid for $Re<2x10^5$), which reads as Eq. (3.62).

$$w_s = \frac{\upsilon}{D} D^{*3} \left[38.1 + 0.93 D^{*\frac{12}{7}} \right]^{-\frac{7}{8}} \tag{3.62}$$

in which the quantity D^* is given by Eq. (3.47).

Figure 3.16 shows the measured and regressed fall velocities of calcareous sediment samples (with densities in the range of 2600 to 2800kg/m^3) as obtained by Smith and Cheung (2003). The results of the latter authors are in good agreement with those of van der Meulen (1998) – also cited in van Rijn (2006) – with coral sand particles (with densities in the range of 2500 to 2650 kg/m^3), see Figure 3.17.

The computed sediment fall speed for each of the previously referred empirical relationships should provide similar results. The dependency on the sediment's grain size, density, and shape, and on the fluid's density, and viscosity has been demonstrated. Particularly relevant is the sediment shape factor as has been demonstrated by contrasting drag coefficients for spheres and natural sediments. Under the condition of high Reynolds numbers, say, 10^3~10^5, the drag coefficient of spheres has an average value of about 0.4 while for natural sediment particles, C_D lies between 1.0~1.2 (Cheng, 1997), which corresponds to an error in the estimate of the settling velocity magnified by a factor close to three if grains are assumed to be spheres. This error will be ultimately reflected in the prediction of suspended load transport.

To the preceding considerations is necessary to add another one which is related to the effect of sediment concentration. In high-concentration flows the suspended particles cannot settle freely due to the presence of the surrounding particles. This process is known as hindered settling and consists of various effects, such as the return flow and wake formation around the particles and the increase of density and viscosity of the suspension.

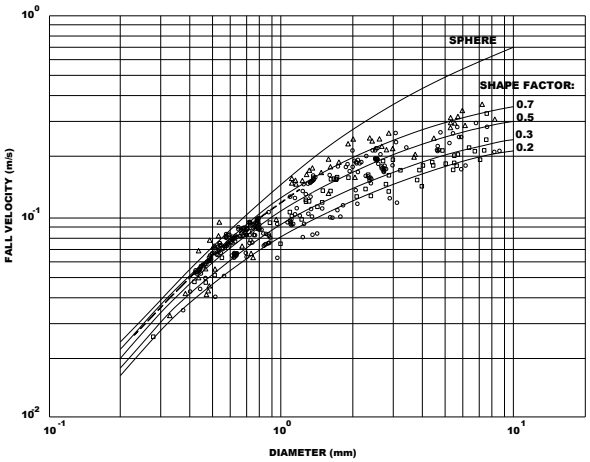

Figure 3.16: Fall velocity of calcareous sand as function of nominal diameter and shape factor (adapted from Smith and Cheung, 2003).

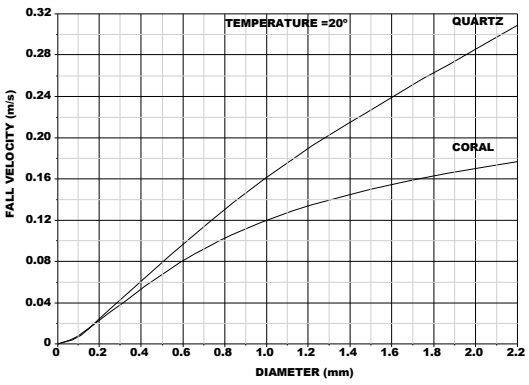

Figure 3.17: Fall velocity of coral sand (after van der Meulen (1998), adapted from van Rijn, 2006).

The hindered settling effect was studied experimentally by, *e.g.*, McNown-Lin (1952), Richardson and Zaki (1954), Richardson and Meikle (1961), Oliver (1961), Li and Mehta (1998), Winterwerp (1999), Baldock *et. al* (2004) – for discussion see, *e.g.*, van Rijn (2006).

There is yet another sediment property relevant to sediment transport, which is the bottom shear stress. It characterizes the linkage between fluid and sediment, and is a fundamental parameter for sediment entrainment by the flow and initiation of suspension, as will be later discussed.

3.3.2. Initiation of motion

The knowledge on initiation of motion is very much related to the pioneering experimental work of Shields (1936), which demonstrated that the dimensionless critical shear stress [Eq. (3.63)] at which near-uniform grains start moving varies with the grain-size Reynolds number, Re^* [Eq. (3.64)] that is used to describe the flow regime in the bottom boundary layer (see, *e.g.*, van Rijn, 2006).

$$\tau_{c,n}^{*} = \frac{\tau_{c,n}}{(S_s - 1)gD_n} \tag{3.63}$$

$$Re^{*} = \frac{U^{*}D_n}{\upsilon} \tag{3.64}$$

in which $\tau_{c,n}^{*}$ is the critical shear stress at incipient motion for a grain size of interest D_n, and U^* is the critical shear velocity for incipient motion of the sediment. Of particular importance is the determination of the dimensionless critical shear stress values of the median grain size, $\tau_{c,50}^{*}$. The general form of Shields' data is the Shields diagram (Figure 3.18).

Shields diagram remains the most widely used criterion for incipient motion (Cao *et al.*, 2006) and is reasonably well-supported by many subsequent studies with rounded, uniform particles, as reported by Buffington and Montgomery (1997) in their systematic analysis of eight decades of incipient motion studies; nevertheless, the experimental work by many researchers has shown that measurable quantities of bed load-transport are obtained at shear stresses much smaller than based on such curve (see, *e.g.*, van Rijn, 2006).

The numerous additions, revisions, and modifications of the Shields curve since its original publication, evidence the stochastic nature of acting fluid forces and stabilizing forces (for discussion, see, *e.g.*, Smith and Cheung, 2004, Buffington, 1999, and Buffington and Montgomery, 1997 *inter alia*) and have led to the recognition that incipient motion of a particular grain size is inherently a statistical problem, depending on probability functions of both turbulent shear stress (see, *e.g.*, Zanke, 2003; Lopez and Garcia, 2001; Keshavarzy and Ball, 1999 – cited in van Rijn, 2006; and Papanicolaou, 1997), and inter-granular geometry (*i.e.*, friction angles) of the bed material, the latter being controlled by sediment shape (see, *e.g.*, Göğüş and Defne, 2005, and Smith and Cheung, 2004), density (see, *e.g.*, Nielsen, 2009), sorting (see, *e.g.*, Mitchener and Torfs, 1996), and packing (see, *e.g.*, Patel and Ranga Raju, 1999 – cited in van Rijn (2006), and Komar, 1998). The effect of bed slope on the initiation of motion has been studied by, *e.g.*, Dey (2003), while the effect of seepage flows by, *e.g.* Nielsen (2009), Cheng and Chiew (1999), and Xie *et al.* (2009). For coastal application, recent work by Terrile *et al.* (2006) indicates that wave shape has strong and as yet not fully understood influence on the initiation of sediment motion.

Zanke (2003) made an attempt to include the turbulence characteristics into the initiation of motion, based on the presuppose that the critical shear stress responsible for inducing motion in non-turbulent flow is solely defined by the angle of internal friction or the angle of repose of single grains [Eq. (3.65)]. In turbulent flow, fluctuations in the shear stress as well as lift forces produced by these fluctuations also occur. Owing to this, the effective shear stress acting on a grain (Eq. (3.66), Figure 3.19) is increased above the time-averaged shear stress due to turbulent stress peaks on the one hand, and on the other hand, the grains exposed to the flow become effectively lighter due to lift forces.

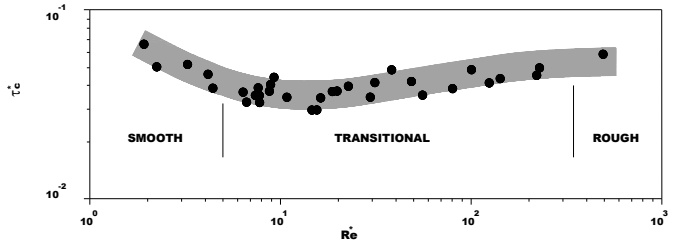

Figure 3.18: Shields-curve
(redrafted from Rouse (1939), adapted from Buffington and Montgomery, 1997).

$$\tau^*_{c,\mathrm{eff}} = (1 - n)\tan\phi \tag{3.65}$$

in which $\tau^*_{c,eff}$ is the effective instantaneous dimensionless bed shear stress at incipient motion, n is the sediment porosity, and ϕ is the angle of internal friction or the angle of repose of single grains.

$$\tau^*_{c,\mathrm{eff}} = \tau^*_c + \tau^{*\prime}_c \tag{3.66}$$

where τ^*_c is the time-average dimensionless (Shields) bed shear stress, and $\tau^{*\prime}_c$ is dimensionless bed shear stress fluctuation.

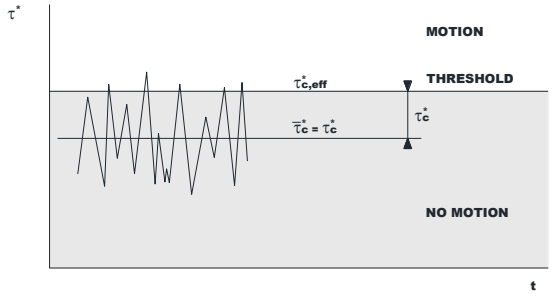

Figure 3.19: The effective shear stress $\tau^*_{c,eff}$ and the shear stress τ^*_c averaged over time t responsible for the initiation of motion
(adapted from Zanke, 2003).

From the basic Eq. (3.65), under consideration of the turbulence-induced shear stress peaks and the lift forces (reducing submerged weight of particle), Zanke (2003) arrived at Eq. (3.67) for the time-averaged critical shear stress in turbulent flow (for derivation, see Zanke, 2003).

$$\tau^*_c = \frac{(1 - n)\tan\phi}{\left(1 + \frac{u'_{c,b}}{u'_b}\right)^2 \left(1 + \frac{\sigma_L}{\tau_b}\tan\phi\right)} \tag{3.67}$$

where $u'_{c,b}$ is the near-bed velocity fluctuation at initiation of motion that may be related to the quantity u'_{rms} which is the standard deviation of $u'(t)$ as given by Eq. (3.68), u'_b is the time-averaged near-bed velocity at initiation of motion, σ_L is the lift stress acting on the particle, and τ_b is the bed shear stress acting on particle.

$$u'_{c,b} = n\, u'_{rms} \tag{3.68}$$

in which n is the level of turbulence.

Figures 3.20 to 3.24 illustrate some results of the critical non-dimensional shear stress, , as function of the non-dimensional roughness height, k_s^+ [Eq. (3.69)], based on Zanke (2003) approach and using empirical data of near-bed velocity profile and corresponding turbulence characteristics reported in the literature (for discussion, see Zanke, 2003).

$$k_s^+ = \frac{U^* k_s}{\upsilon} \tag{3.69}$$

in which k_s^+ is the grain size Reynolds number to equivalent sand roughness height k_s.

The effects of shear stress fluctuations (Figure 3.19) as well as fluctuations in the lift forces are shown in Figure 3.20. The effect of shear stress peaks is illustrated in the figure by (A), whereas (B) shows the reduction in the shear stresses required to initiate motion as a result of lift forces. As noted by Zanke (2003) the reference curve "without turbulence" is not possible in reality as only turbulent flows can provide the forces necessary to initiate motion.

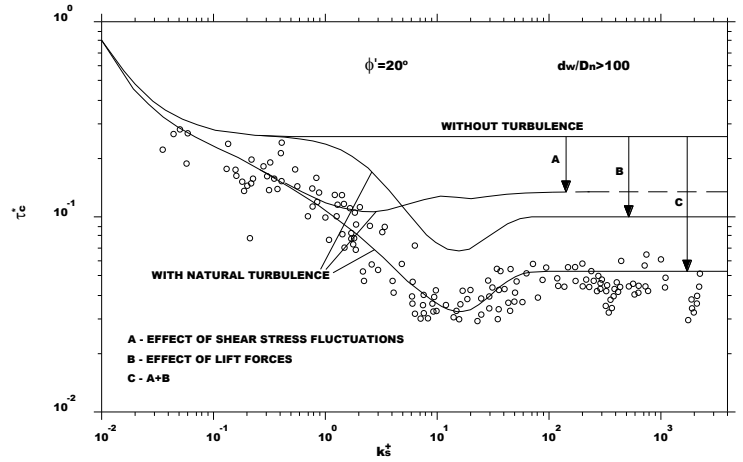

Figure 3.20: Critical shear stresses for non-turbulent flow (u'=0) and a flow with "normal" turbulence (adapted from Zanke, 2003).

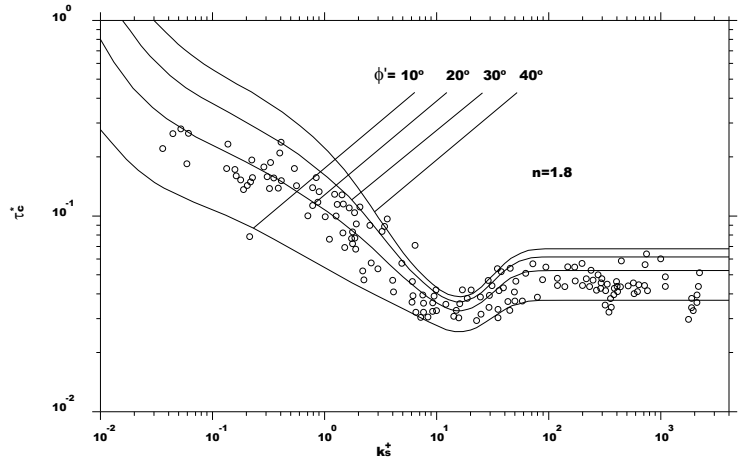

Figure 3.21: Effect of different angles of repose ϕ, or correspondingly different angles of grain contact ϕ' (adapted from Zanke, 2003).

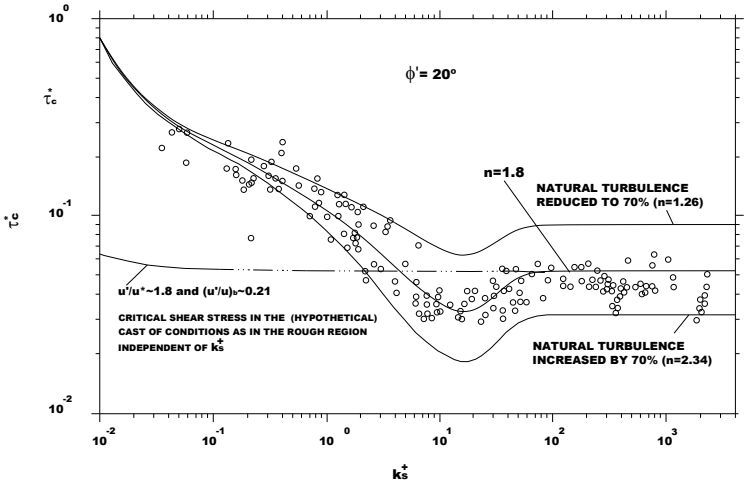

Figure 3.22: Effect of damped and enhanced turbulence (adapted from Zanke, 2003).

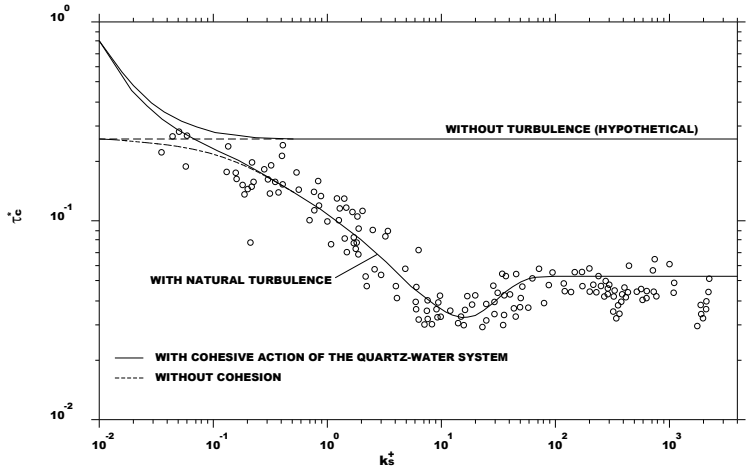

Figure 3.23: Effect of cohesive action
(adapted from Zanke, 2003).

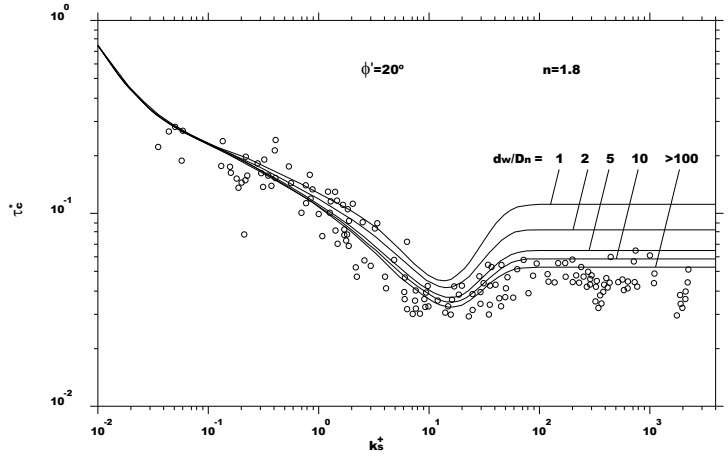

Figure 3.24: Effect of relative water depth, d_w/D_n
(adapted from Zanke, 2003).

The previous figures show the influence of the individual effects of the angle of internal friction (or the angle of contact between grains), the level of turbulence, cohesive forces and the relative water depth (=d_w/D_n, where d_w is the water depth and D_n is the grain diameter of interest).

Figure 3.21 shows the influence of ϕ. Larger angles of friction or grain contact angles lead to higher critical shear stresses, whereby the effect for small k_s^+ is greater than in the hydraulically rough region (k_s^+>~7x10^1). Figure 3.22 indicates the way in which the initiation of motion is promoted by turbulence-enhancing effects (*e.g.*, structures) at low flow rates. Due to the viscous sub-layer of the boundary layer these effects are damped on moving towards the fine-grain region. The dashed line indicates the initiation of motion in the absence of the viscous sub-layer. Figure 3.23 illustrates the action of cohesion in the quartz-water system, which becomes effective at k_s^+<~5x10^{-1} and increases the resistance of sediment to movement. The influence of low relative water depths d_w/D_n is seen in Figure 3.24. With decreasing relative water depth the required shear stress increases (*i.e.* the load on the bed reduces for otherwise constant conditions), whereby this effect decreases significantly on moving towards the hydraulically smooth region and practically disappears at k_s^+=10^{-1}. This effect also disappears for values of d_w/D_n >~100.

Analysis of the potential of using probability tools in the characterization of the turbulent processes involved in the mechanics of sediment transport have been studied also by Lopez and Garcia (2001), Keshavarzy and Ball (1999) – cited in van Rijn (2006), and Papanicolaou (1997).

The influence of sediment shape, density, sorting and packing in the dimensionless critical shear stress have been established by Nielsen (2009), Göğüş and Defne (2005), Smith and Cheung (2004), Mitchener and Torfs (1996), Patel and Ranga Raju (1999), and Komar (1998).

Göğüş and Defne (2005) have studied the threshold of motion of single particles having different shapes and sizes under subcritical, uniform flow conditions. The effect of particles' shape and size is expressed by two dimensionless parameters function of the particle's defining lengths, *a*, *b*, and *c*, and volume, $\forall$ (see Eq. (3.70), Figure 3.25). The types of particles considered were: cubes, spheres, rectangular prisms, and irregular particles with diameters between 10 and 100mm.

The results of Göğüş and Defne (2005) plotted in terms of the Shields-parameter and the grain-size Reynolds number shows a marked influence of shape, as seen in Figure 3.26. Relative roughness (ratio of depth and particle diameter) and channel slope were also found by Göğüş and Defne (2005) to have a marked influence.

Similar conclusion of marked influence of shape was drawn in the study by Smith and Cheung (2004) on the initiation of motion of four natural and five sieved calcareous sand samples in unidirectional flow. Figure 3.27 shows the critical shear stress data in terms of the median equivalent diameter (top panel), median nominal diameter (middle panel), and median sieve diameter (bottom panel), reported in Smith and Cheung (2004) and various studies reference therein. The data follow the general shape of the Shields-curve, but the critical shear stresses are significantly larger (factor 1 to 1.5) in the hydraulic smooth flow regime and significantly smaller (factor 1 to 1.5) in the rough turbulent regime (see Figure 3.18).

$$SF = f(a, b, c, \forall) = f\left(\frac{a+b}{2c}, \frac{\forall}{abc}\right) \tag{3.70}$$

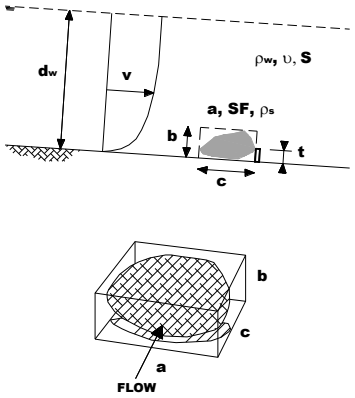

Figure 3.25: Parameters related to condition of incipient motion (top panel) and imaginary rectangular prism enfolding particle (bottom panel) (adapted from Göğüş and Defne, 2005).

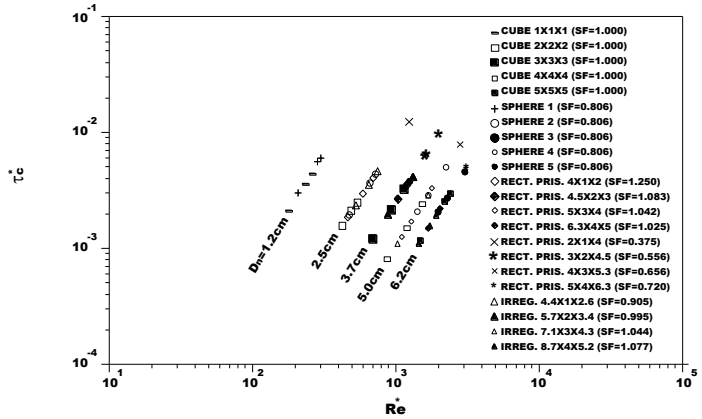

Figure 3.26: τ_c^* *vs.* Re* for solitary particles, SF in the range 0.375–1.250 (adapted from Göğüş and Defne, 2005).

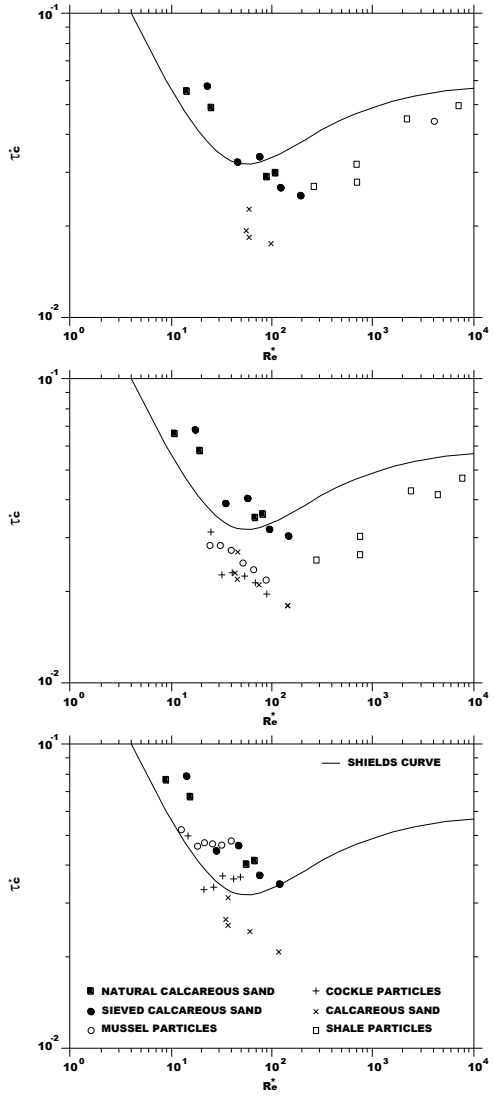

Figure 3.27: Initiation of motion in terms of median nominal diameter (top panel), median sieve diameter (middle panel), and median equivalent diameter (bottom panel) (adapted from Smith and Cheung, 2004).

Wang and Dittrich (1999) cited in van Rijn (2006) have also studied the effect of shape using round elliptical and flat grains to find out that the critical Shields-value was largest for flat grains when they were manually arranged as a well-organized armour layer, while for randomly lying flat and elliptical grains was only marginally larger (only 5 to 10%) than that of round grains.

Within a given, reasonably narrow, range of specific gravity, the critical Shields-parameter is a function of the grain Reynolds number only; however, if vastly S_s-values are considered the dependence of τ_c^* upon S_s is quite strong, as seen in Figure 3.28 (Nielsen, 2009).

The critical Shields parameter is also affected by cohesive particle-particle interaction effects, by sorting, and by packing (or bulk density) effects. Cohesive sediments are much more resilient to erosion than indicated by the Shields diagram (Nielsen, 2009), whereas the presence of sand may enhance the erosion process very significantly as described by Mitchener and Torfs (1996). The process of sorting (or grain selection) by which grains of different diameter move to a certain position in the morphological system for given hydrodynamic conditions, is expected to affect the initial movement of a particular soil fraction and the behaviour of the fractions when all particles of the bed surface are fully mobilized; whilst the process of packing defined as the effective utilization of space by mutual arrangement of the constituent soil grains, is expected to affect the exposure or hiding factor.

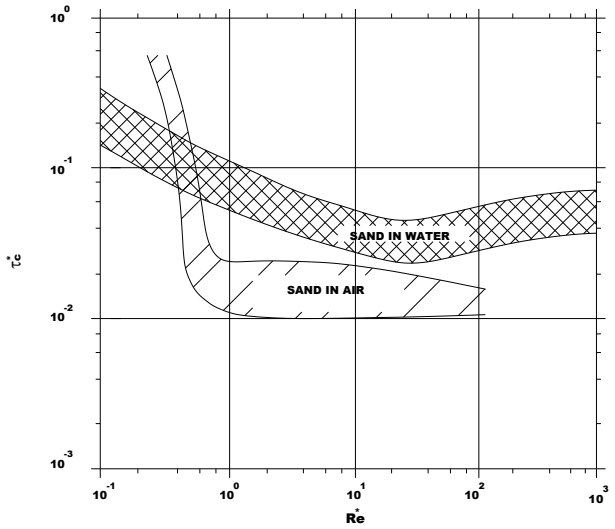

Figure 3.28: Shields-parameter in terms of the grain size Reynolds number for quartz in water and in air, S_s respectively equal to 2.65 and 2200 (adapted from Nielsen, 2009).

Figure 3.29 shows the critical bed-shear stress as a function of particle diameter based on the results of several authors (van Rijn, 2006). The Shields-curve for uniform sediment is also shown. The available data of Figure 3.29 can be used to derive the hiding-exposure factors as presented in the top and middle panels in Figure 3.30. The bottom panel in Figure 3.30 refers to the pivoting angle of the grain about one of its contact points with underlying grains, which is related, according to Komar (1998), to the initiation of motion of a grain by the flowing fluid.

Most of the existing empirical hiding factors are presented in the extensive review of Buffington and Montgomery (1997) yet, as concluded by the former authors and also by van Rijn (2006) no universal relation can be found.

The dimensionless critical shear stress can also be influenced by bed slope however, as most of the data are derived from nearly horizontal bed (see, *e.g.*, Buffington and Montgomery, 1997) its effect on the compiled $\tau^*_{c,50}$ values is minimal.

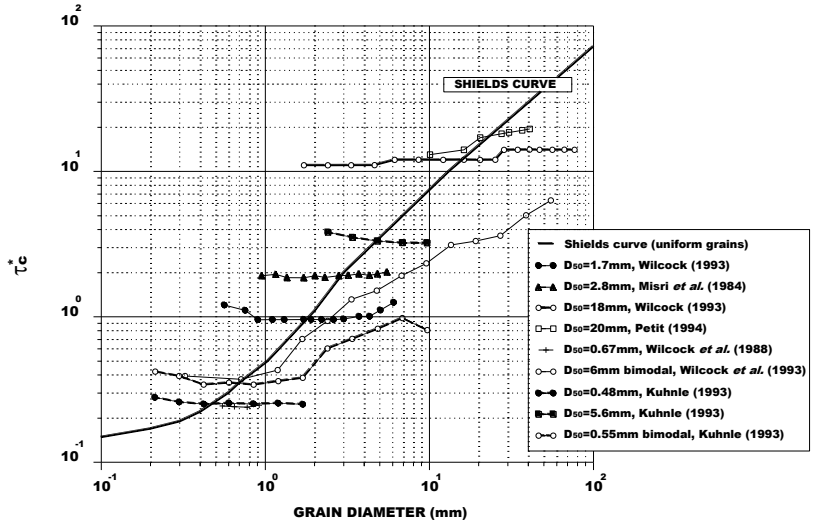

Figure 3.29: Critical bed shear stress (in N/m^2) of individual size fractions in a mixture, as a function of grain diameter (after Wilcock (1993), adapted from van Rijn, 2006).

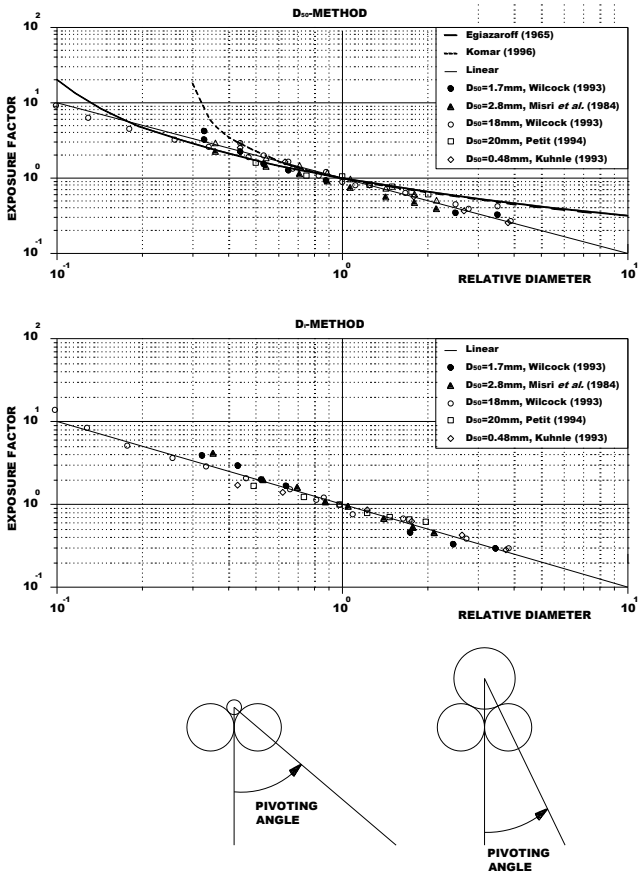

Figure 3.30: Hiding factors according to several authors;
hiding-exposure factor based on D_{50}-method (top panel); hiding-exposure factor based on D_i-method (middle panel); and pivoting angles (bottom panel)
(adapted from van Rijn, 2006).

Figure 3.31 show the forces on a sediment particle resting on a longitudinal sloping bed, and a transverse sloping bed. In the former, the particle will be set to motion when the sum of the critical fluid force and the gravity force component force is just equal to the stabilizing force; while in the latter, a sediment particle resting on a transverse sloping bed will be set in motion when the resulting driving fluid force is equal to the stabilizing fluid force, yielding Eq. (3.71) for a combination of a longitudinal and transverse bed slope where $\tau_{c,0}^{*}$ is the critical Shields parameter for horizontal bed.

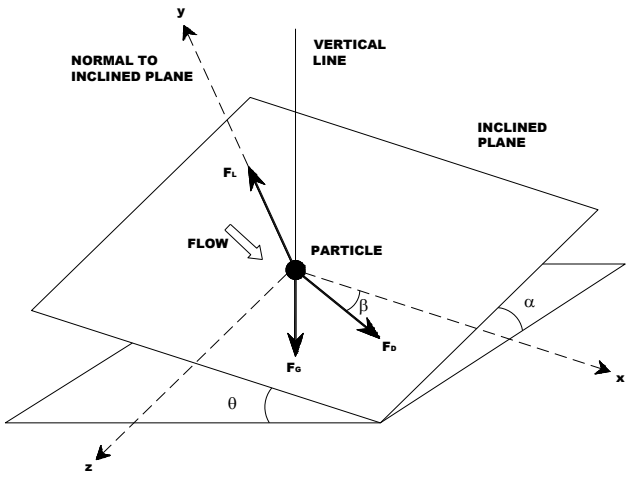

Figure 3.31: Forces on a sediment particle (a) longitudinal bed slope and (b) transverse bed slope
(adapted from Dey, 2003).

$$\tau^*_{c,b} = k_\beta k_\alpha \tau^*_{c,0} \tag{3.71}$$

in which the quantities k_β and k_α are factors that take into account the effect of the longitudinal bed slope (β) and the lateral bed slope (α).

Schoklitsch (1914) and Leitner (1912), both cited in van Rijn (2006) presented factors k_β and k_α as given by respectively Eq. (3.72) and (3.73).

$$k_\beta = \frac{\sin(\phi - \beta)}{\sin(\phi)} \tag{3.72}$$

where positive value of β refers to down-sloping bed, and negative one to up-sloping bed.

$$k_\alpha = \cos\alpha \left[1 - \frac{\tan^2(\alpha)}{\tan^2(\phi)}\right]^{0.5} \tag{3.73}$$

Chiew and Parker (1984) and Lau and Engel (1999) both cited in van Rijn (2006) studied the threshold condition for the initiation of motion of cohesionless sediments on a longitudinal slopping bottom to conclude that the critical bed shear stresses of sediments lying on slopes ranging from steep positive to negative can be reasonably well described by the Schoklitsch-factor, whereas it is slightly underestimated for negative values ϕ/β. Yet, Whitehouse *et al.* (2000) convincingly show that the Schoklitsch-factor works well over a large range of conditions (van Rijn, 2006).

In a more recent work on the threshold of sediment motion on combined transverse and longitudinal sloping beds, Dey (2003) has derived a rather complicated expression to describe the critical bed shear stress along combined longitudinal and transverse bed slopes (or banks), which reads as Eq. (3.74).

$$k_\beta k_\alpha = a[-b + (b^2 + c)^{0.5}] \tag{3.74}$$

in which a, b, and c are given by Eq. (3.75) to (3.77), and η is the ratio of lift (F_L), and drag forces (F_D) on particle as given by Eq. (3.78). The angles α, β and θ are defined as represented in Figure 3.31.

$$a = \frac{1}{[(1 - \eta \tan\phi)\tan\phi]} \tag{3.75}$$

$$b = \sin\beta + \eta\,(\tan\phi)^2 \sqrt{(\cos\beta)^2 - (\sin\alpha)^2} \tag{3.76}$$

$$c = [1 - \eta^2(\tan\phi)^2][(\cos\beta)^2 - (\sin\alpha)^2(\tan\phi)^2 - (\sin\beta)^2 - (\sin\alpha)^2] \tag{3.77}$$

$$\eta = \frac{F_L}{F_D} \tag{3.78}$$

Nielsen (2009) suggests, after a study by Nielsen *et al.* (2001), incorporating the influence of a vertical seepage velocity w (positive upwards) on sediment stability through a modified Shields parameter, as given by Eq. (3.79).

$$\tau^*_c = \frac{U_0^{*2}\left(1 - \alpha\frac{w}{U_0^*}\right)}{\left[S_s - 1 - \beta\frac{w}{K_w}\right] g D_n} \tag{3.79}$$

where U_0^* is the shear velocity with no seepage, α and β are dimensionless coefficients (recommended values of respectively, 16 and 0.4), and K_w is the hydraulic conductivity of water.

The influence of seepage flows have also been studied experimentally by Cheng and Chiew (1999), showing that for a particular size of sediment, the critical shear velocity decreases with increasing seepage velocity; and by Xie *et al.* (2009), showing that under the action of outflow seepage through a bank slope, sediments are more prone to incipient motion.

Nielsen (2009) note that, particularly in the swash zone, but possibly in the nearshore area in general, the seepage forces associated with in- or out-flow of water from the bed may influence the sediment mobility. The effects of a positive seepage velocity are to firstly thicken the boundary layer thus reducing the critical Shields parameter, and secondly to destabilize the particles through the upward seepage F_s. For infiltration both effects are reversed.

Martin (1970) cited by Nielsen (2009) found experimentally that either of the two effects may be dominant, depending on the sediment size and density. For large or very dense particles, the mobilizing effect of the increased shear stress dominates; whereas for finer and/or lighter sediments the stabilizing effect of the downward drag dominates.

Incipient sediment motion in waves has been studied recently by Terrile *et al.* (2006) to confirm that the acceleration plays a role for the initiation of motion, since combinations of similar orbital velocity and varying acceleration magnitude resulted in no motion, some motion and motion as acceleration increased.

The experiments carried out by Terrile *et al.* (2006) were supported by the findings of Bagnold (1963) which recognized the potential importance of wave-induced accelerations in general; Madsen (1974) which showed that horizontal pressure gradients associated with steep fronts of waves or bores might induce bulk instability and hence vastly enhanced shoreward sediment transport; Nielsen (1979) that discussed the likely Keulegan-Carpenter number effects associated with accelerations in wave sediment transport; Hallermeier (1981) which experimentally investigated initiation of motion by regular, symmetric waves for relatively coarse sand and show that a Shields-like parameter could describe the discrimination between motion and no motion; Nielsen (1992) which discussed the importance of the saw-tooth asymmetry of surf zone waves in the acceleration process; Sleath (1994) and subsequent works which quantified the acceleration effects in wave-induced sediment transport in terms of an acceleration parameter; Ribberink *et al.* (2000) which showed that real waves in a flume, as opposed to Stokes-wave-like velocities in U-tubes generated at least two times more sediment transport for the same orbital velocity magnitude, a difference which could be due to either saw-tooth asymmetry or boundary layer streaming being present in the flume waves but not in the U-tube experiments; Drake and Calantoni (2001) which made a quantitative process-based model to incorporate the effect of pressure gradients on particle motions; and finally, Hoefel and Elgar (2003) which used their sediment transport skewness formulation to show that flow acceleration may play a role in predicting onshore bar movement under moderate wave conditions.

Terrile *et al.* (2006) experiments with regular shoaling waves also lead to conclude that qualitatively initiation of motion occurs at or is very close to the maximum shear stress due to the combined effects of drag/lift and acceleration as introduced by Nielsen and Callaghan (2003).

Based on the above analysis to publications on the initiation of sediment motion is possible to conclude that the response to the flow, for any given grain, depends on a wide range of possible (and complicated) combinations of sediment characteristics (possibly containing a mixture of densities, sizes and shapes), hiding-exposure factors, and nature of flow.

Particle movement will occur when the instantaneous fluid force on the particle is just larger than the instantaneous resisting force related to the submerged particle weight and the friction coefficient, which may be affected by the degree of exposure of the particle with respect to the neighbouring ones, as well as by cohesive forces and in-bed pressure gradients.

The hydrodynamic conditions within the nearshore region (focus of attention in the experiments carried out within the present research programme), and the combined influence of sediment properties (as seen along this paragraph) and hydrodynamic processes (some of which were already described along section 3.1 of the current chapter) in cross-shore sediment transport, are described in the following paragraph; whereas the concept of equilibrium beach-profile shape and its temporal variability are introduced later.

3.3.3. Sediment transport processes

In a coastal environment sediment transport generally occurs under the combined influence of a variety of hydrodynamic processes such as winds, waves and currents. Mostly the forcing due to waves is discussed in further detail bellow. A fuller understanding can be gained from standard texts on coastal processes and morphodynamics such as Nielsen (2009), van Rijn (2006), Dronkers (2005), and Short (1999).

Figure 3.32 gives a schematic representation of sediment transport mechanisms along a cross-shore beach-profile of a straight sandy coast. The type and magnitude of forcing within the nearshore active zone (*i.e.*, where sediment motion and beach-profile change occurs) is markedly different inside and outside the surf zone. The surf zone is the border area between the sea and the land within which waves dissipate at least part of their energy through breaking (Nielsen, 2009). Depending on the deep-water wave characteristics and the beach slope, the surf zone may be many wavelengths wide or very narrower.

The sand transport processes induced by non-breaking waves along a straight cost are explained by van Rijn (2006) as follows: *(i)* net onshore-directed wave related transport due to asymmetry of the near-bed orbital velocities with relatively large onshore peak velocities under the wave crests and relatively small offshore peak velocities under the wave troughs; *(ii)* net onshore-directed current related transport due to the generation of a quasi-steady onshore-directed weak mean current (streaming) in the wave boundary layer; net offshore-directed mean current may be generated in strongly asymmetric wave motion over a steep slope; bed ripples may also have a directional effect on the mean current; *(iii)* net offshore-directed wave-related transport due to the generation of bound waves associated with variations of the radiation stresses under irregular wave groups (peak velocities and concentrations are out of phase).

Whereas van Rijn (2006) explains the sand transport processes induced by breaking waves (surf zone) as follows: *(i)* net forward (onshore) transport by asymmetric wave; *(ii)* net backward (offshore) transport due to the generation of a net return flow (wave-generated undertow) in the near-bed region balancing the onshore mass flux between the wave crest and trough; *(iii)* wave-related transport rates due to the generation of low-frequency wave motion (bound long waves and free waves may be generated) longshore- and offshore-directed transport due to the generation of large-scale circulation cells with longshore currents and offshore rip currents; *(iv)* gravity-induced transport (bed-load) in down-sloping direction.

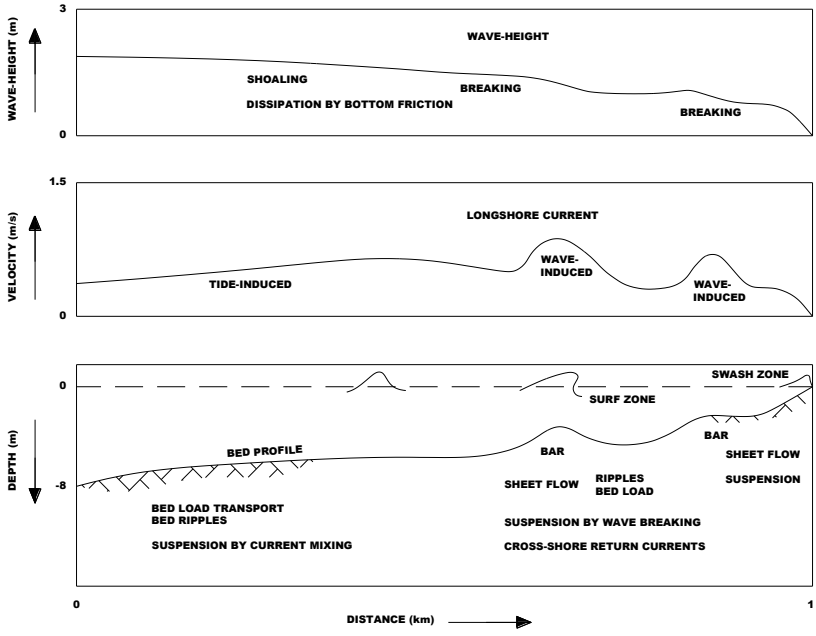

Figure 3.32: Sediment transport mechanisms along cross-shore profile; cross-shore distribution of wave-heights (top panel); cross-shore distribution of longshore current (middle panel); and sediment transport processes along cross-shore profile (bottom panel) (adapted from van Rijn, 2006).

In deeper waters, most of the sediment is transported due to tidal or other ocean currents near the bed profile; whereas in somewhat shallower waters, but still outside the surf zone, the transport process is generally concentrated near the bed profile and the sediment is moved either as bed- (*i.e.*, that part of the sediment load, which is supported by intergranular forces) or suspended-load (*i.e.*, sediment load is supported by upward fluid drag). The first type dominates in areas where the mean currents are relatively weak in comparison with the wave motion (small ratio of depth-averaged velocity and peak orbital velocity) while the suspension of sediments seems to be linked to ripple-related vortices (van Rijn, 2006). As an indication of this, the bed will often be covered by sharp crested, shore-parallel ripples (vortex ripples), over which most of the sediment is transported in suspension (Nielsen, 2009).

Sediment entrainment over rippled beds has been described by Inman and Bowen (1963) – cited by Short (1999), as follows: *(i)* under the wave crest a vortex is formed in the trough between ripple crests (Figure 3.33a); *(ii)* sediment from the trough becomes entrained in this vortex (Figure 3.33b); *(iii)* the vortex is ejected when the velocity reverses, and is transported backwards across the ripple crest under the wave trough; simultaneously a new one is formed under the wave trough (Figure 3.33c); and *(iv)* the new vortex is ejected during the next velocity reversal (Figure 3.33d).

The quantities A, λ, and η in Figure 3.33 are the wave amplitude, and the ripples length (which is estimated to be in the order of 1.3A) and height (estimated to be about 0.2A), respectively. Nielsen (2009) refer to a study by Löfquist (1978) on the modelling of vortex ripple formation and their adjustment to varying flow conditions to say that it is still a challenge.

A more recent study by Marieu *et al.* (2008) also deals with the modelling of vortex ripple morphodynamics to conclude, *inter alia*, that ripple migration is a significant mode of cross-shore sediment transport in coastal areas.

In the surf zone sediment transport is generally dominated by waves through wave breaking and the associated wave-induced currents in the longshore (which originates the littoral drift current) and cross-shore (*e.g.*, rip currents, and wave-generated undertow) directions. Both the processes, breaking and wave-induced oscillatory water motion, involve large sediment entrainment and transport. Around the breakpoint, the sediment transport occurs throughout the depth, as breaking waves typically generate strong vertical flows, which bring large amounts of sediment towards the surface that can hold suspended (stirring) for many wave periods to be then transported as suspended load by net (wave-cycle averaged) currents. The sediment concentrations are typically larger near the plunging breakpoint decreasing sharply on both sides of that location. Within the surf zone, the bed may be covered with megaripples or be almost perfectly flat.

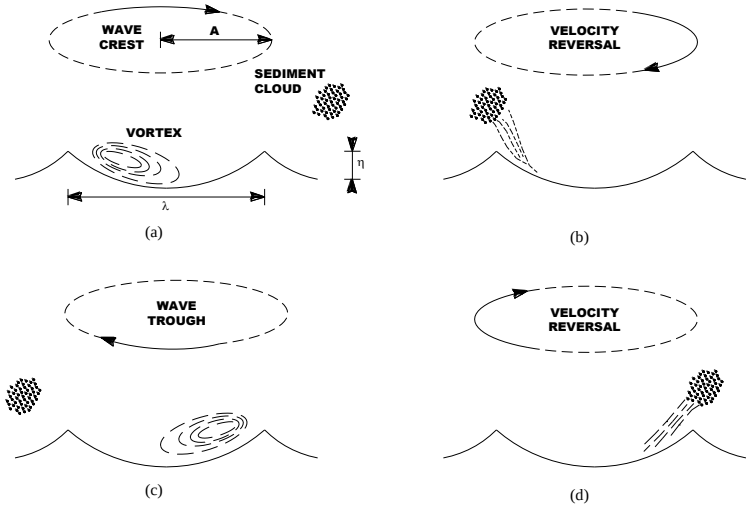

Figure 3.33: Sediment resuspension under symmetric waves on a rippled bed (arrow describes orbital motion) (modified from Short, 1999).

Sediment transport in the swash zone is an area of great challenge for present and future research (Nielsen, 2009). Understand is lacking for both the components of sediment transport, the cross-shore, and the longshore, sediment transport. Nielsen (2009) raises several points of concern in regard to sediment motion namely the influence of in- or outflow of water through the sand surface, the horizontal pressure gradients in the bed under swash bore fronts which may be strong enough to cause fluidization, thus enhancing sediment transport rates, and the surfbeat and the associated, occasionally very violent, backwash, which may undoubtedly be significant contributors to erosion during storms. At the highest levels of the swash-zone, conditions may be quantitatively different depending on whether the slope continues as a beach, or end as a foot of a structure, or as a dune scarp.

The transport mode which is designated as sheet flow may be present inside the surf- and swash-zones (Figure 3.32). It involves a mixture of bed-load and suspended-load, which is concentrated in a very thin layer.

As has been seen here sediment transport processes and bathymetry, are changed by and have an influence on how waves approach the coast, from incipient wave breaking to the transformation of wave-height through the surf zone, and associated hydrodynamic processes (*e.g.*, wave setup and setdown, wave run-up, and nearshore currents).

There is yet another phenomenon – specific to wave reflection from beaches – which develops between the incident surface waves of certain periods and erodible beds with sinusoidal bathymetric variations (ripples), causing a reflection of a part of the incident wave energy. This phenomenon, dubbed Bragg reflection after a similar resonant phenomenon in optics, has been studied by Mei (1985), Davies and Heathershaw (1983), and Kirby (1986). Later contributions have been made by, *e.g.*, Elgar *et al.* (2003), Dulou *et al.* (2000), Komarova and Newell (2000), Yu and Mei (2000a, 2000b), and Bailard *et al.* (1992).

Essentially, the following main findings arose from the studies on the Bragg resonance mechanism: sufficient reflection must be present so that the waves are partially standing (Mei, 1985); resonant interactions, associated with wave reflection, may occur between surface waves and bottom undulations provided that their respective wavelengths are in the approximate (Bragg scattering) ratio of two to one (Bailard *et al.*, 1992), also shown in the experiments by Dulou *et al.* (2000); there is an approximately linear increase in the reflection coefficient with the increase in the number of bottom undulations (USACE, 2008); reflection increases if the amplitude of the bottom undulations increases o the water depth over the undulations decreases (USACE, 2008); waves transmitted through the bars may undergo partial reflection at the shoreline (Elgar *et al.*, 2003), followed by re-reflections from the bars, complicating the wave transformation (Yu and Mei, 2000a).

Davies and Heathershaw (1983) also observed from their experiments that new ripples may develop on a region of flat bed, as a result of wave reflection from the existing megaripples.

Additionally, it has been suggested by Mei (1985), that the Bragg resonance mechanism which develops on a nearshore bar system will set-up a standing wave pattern seaward of the bar system that, in turn, causes the bar system to extend in the seaward direction.

The subject of net transport-rates in the several flow regimes is extensively treated in the book by van Rijn (2006) with over 100 references. Those references include, *e.g.*, the works by, Watanabe and Sato (2004) , O'Donoghue and Wright (2004), Wright and O'Donoghue (2002) , Hassan (2003), Dohmen-Janssen (1999), Dibajnia and Watanabe (1992), King (1991), Sawamoto and Yamashita (1986) and Horkawa and co-workers (1982) on net transport rates in the sheet flow regime; and van der Werf and co-worker (2006, 2005), van Rijn (2000, 1993), and FredsØe and Deidgaard (1992) on suspension (sand concentrations) and sand transport in oscillatory flow above rippled beds. van Rijn (2006) also gives a review on available sand transport models to be used in morphodynamic models for practical applications.

Other recent reviews on nearshore hydrodynamics, sediment transport, and morphological evolution may be found in, *e.g.*, Bakhtyar (2009), Cacchione, *et al.* (2008), and Myrhaug and Holmedal (2005), Myrhaug, *et al.* (2004), and Myrhaug, *et al.* (2001).

3.3.4. Aspects of beach-profiles

A beach exposed to changing hydrodynamic conditions respond with readjustments in beach- and nearshore-profiles. The shapes of profiles across the nearshore active zone result from the interplay of hydrodynamic forcing and local geological conditions. Typically the coastlines are divided by dominant material (*i.e.*, as rocky, sandy, or muddy coasts) but may as well be categorised as either eroding or accreting.

Some effects of coastal structures in causing disequilibrium in longshore and cross-shore sediment transport and the associated profile changes have been introduced in Chapter 2, the growing of importance of the anticipated impact of structures on coastal processes have likewise been discussed. Those changes (*i.e.*, to which degree significant profile readjustments occur) and those impacts (*i.e.*, to which degree the systems are knocked out of equilibrium) are therefore fundamental to a number of coastal engineering problems, on which are included beach-dune-system's response to storms, evolution of artificial sand-nourishments, scour and more widespread beach lowering, 3D-flows of sand around coastal structures, and seasonal changes of shoreline position.

This paragraph presents the most important concepts of coastal morphodynamics (*e.g.*, the equilibrium profile shape, and the depth of closure), the anticipated changes in cross-shore profile during erosion/accretion cycles under normal and storm conditions, and the available models to predict cross-shore profile change. The reader is referred to the books by Nielsen (2009), USACE (2008), Schwartz (2005), Dronkers (2005), and Short (1999), and to the reports by Pape (2010), Zheng (1996), and Dean and Zheng (1994), which also includes summaries to previous works.

Figure 3.34 shows a typical shore-normal cross-section (or beach-profile) of the coastal zone; it also shows the typical divisions by subzones (*i.e.*, backshore, foreshore, inshore, and offshore) and typical summer (*i.e.*, swell) and winter profiles (*i.e.*, storm). The general beach-profile characteristics are expected to be a function of a certain given set of wave, tide and sediment parameters, as given by Eq. (3.80).

$$\mathrm{f}\left(\frac{\mathrm{H_b}}{w_s \mathrm{T}}, \frac{\text{Tide Range}}{\mathrm{H_b}}\right) \tag{3.80}$$

where H_b/w_sT is typically designated as the Gourlay parameter (Ω) after the study Gourlay (1968), see, *e.g.*, Nielsen (2009) and depends on wave parameters (*i.e.*, breaking-height, H_b, and wave-period, T) and sediment properties (*i.e.*, sediment fall-speed).

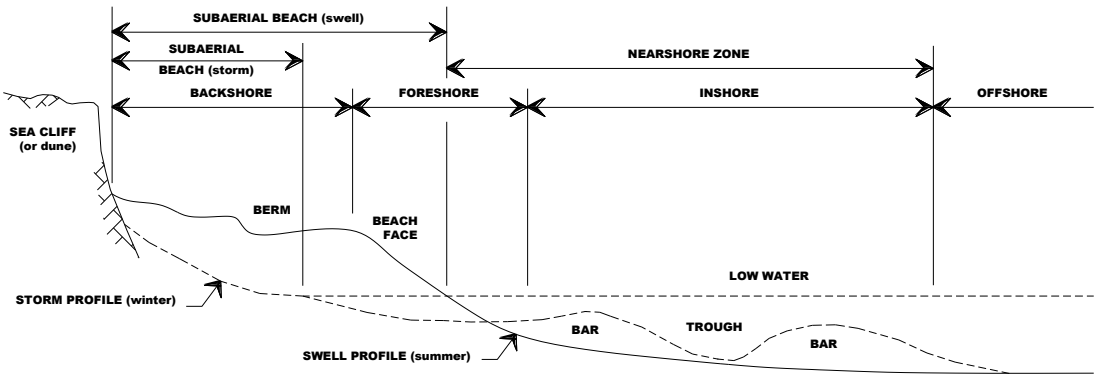

Figure 3.34: Terminology for the coastal zone along a shore-normal profile (modified from Schwartz, 2005).

According to the balance of destructive and constructive forces and assuming that the dominant destructive force was either the wave energy per unit water volume, the wave energy dissipation per unit surface area, or the uniform average longshore shear stresses across the surf zone, Dean (1977) – cited in, *e.g.*, USACE (2008) – has proposed an equilibrium condition for beach-profiles, as given by Eq. (3.81).

$$\mathrm{d}(x) = \mathrm{A}\, x^{\mathrm{n}} \tag{3.81}$$

in which *d* is the profile depth to MSL at distance *x* from the MSL shoreline and *A*, representing a sediment scale parameter depends the grain size *D* (for a summary of recommended *A* values refer to USACE, 2008). The exponent *n* taken to be equal to 2/3 provided the best overall fit to Dean (1977) data. Nielsen (2009) also notes that the 2/3 power can also be arrived at theoretically by seeking constant bed shear stress magnitude.

Kriebal *et al.* (1991) – cited in, *e.g.*, USACE (2008) – developed a similar correlation valid over a range of typical grain sizes (0.1 to 0.4mm) to found that the sediment scale parameter may be related to the sediment fall-speed as given by Eq. (3.82). The same dependence of *A* on fall velocity to 2/3 has also been suggested by Hughes (1993) based on dimensional analysis.

$$\mathrm{A} = 2.25 \left(\frac{{w_{\mathrm{s}}}^2}{\mathrm{g}}\right)^{\frac{1}{3}} \tag{3.82}$$

The shape given by Eq. (3.81) is a useful practical approximation although the slope of the beach profile at the water line (x=0) is infinite and it cannot represent bars (as the beach-profile form is monotonic). To overcome such limitation in regard to beach face slope (β) the relationship as given by Eq. (3.83), can be used instead.

$$x = \frac{\mathrm{d}}{\beta} + \left(\frac{\mathrm{d}}{\mathrm{A}}\right)^{\frac{3}{2}} \tag{3.83}$$

Bodge (1992) and Komar and McDougal (1994) – both cited by USACE (2008) – have each proposed slightly different forms of an exponential beach-profile, as given by Eq. (3.84) and Eq. (3.85), accordingly.

$$\mathrm{d}(x) = \mathrm{d}_0(1 - \mathrm{e}^{-\mathrm{k}x}) \tag{3.84}$$

$$\mathrm{d}(x) = \frac{\beta}{\mathrm{k}}(1 - \mathrm{e}^{-\mathrm{k}x}) \tag{3.85}$$

where d_0 is the asymptotic depth at a great offshore distance, and *k* is a decay constant.

It is expectable the beach-profiles to fit the exponential forms better as compare to the former because Eqs. (3.84) and (3.85) have two free parameters from the individual profile being represented (*i.e.*, d_0 and *k*); yet, for that same reason those exponential forms can be applied only as diagnosis but not as prognosis.

To overcome the inability of Eq. (3.81) to represent bars, a few authors have introduced a two-section equilibrium profile shape (see, *e.g.*, Inman *et al.*, 1993), and even a three-section one (see, *e.g.*, Wang and Davis, 1998).

Inman *et al.* (1993) developed an equilibrium beach-profile that treats a profile as two segments, the inner (bar-berm) and the outer (shorerise) portions, which are matched at the breakpoint-bar and fit by power function similar to that of Dean (1977), as given by Eq. (3.86).

$$\mathrm{d}(x) = \mathrm{B}\, x^{\mathrm{m}} \tag{3.86}$$

Figure 3.35 shows the coordinates of Inman *et al.* (1993) curve fitting in which the subscripts 1 to 3 correspond to bar-berm and shorerise curves. In addition to parameter *B* and exponent *m* in Eq. (3.86), the origins of the two curves must be determined from the profile data, which means that this method is mostly useful for a beach with measured data available.

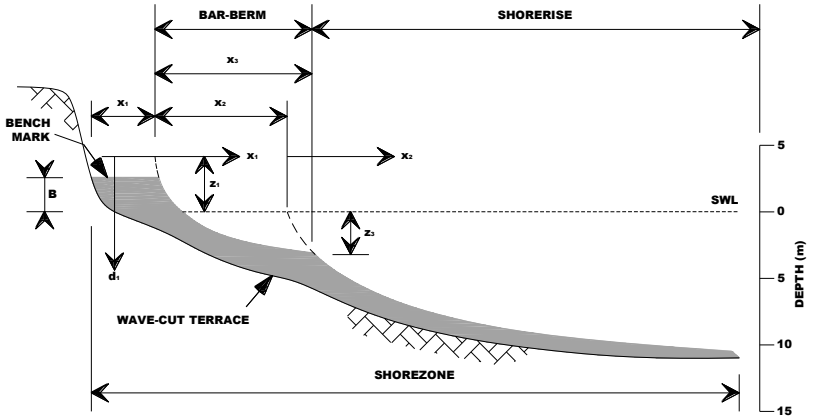

Figure 3.35: Definition sketch for Inman *et al.* (1993) curve fitting.

Wang and Davis (1998) proposed a three-segment beach profile model capable of reproducing commonly observed bar and trough features, which was developed and calibrated with profiles from Sand Key, Florida. The beach profile was divided into three independent segments: *(i)* a inner surf zone described by the equilibrium conditions as given by Eq. (3.81); *(ii)* a landward slope of breakpoint-bar described by a plane slope; and *(iii)* a nearshore zone (seaward from the bar top) describe by another power function, as given by .

$$\mathrm{d}(x) = \mathrm{A}_2\,(x - x_2)^{\mathrm{m}} \tag{3.87}$$

in which A_2 is a scale parameter, just as A in Eq. (3.81), which is related to sediment grain size and its distribution, and the parameter, x_2, is related to the distance from the shoreline to the bar top, which is introduced to link the inner surf and nearshore portions.

Kamphuis *et al.* (1986) – cited by Kamphuis (2000) – showed beach slopes through the breaker zone to be a function of the ratio of disturbing wave forces to restoring particle forces, as given by Eq. (3.88), as steep beach slopes result in a large dissipation rate (breaker type tend toward plunging and collapsing, as explained in section 3.1), thereby resulting in more concentrated disturbing forces. Thus smaller grain sizes are readily removed from steeper beaches and the larger sizes remain.

$$\beta = 1.8\left(\frac{\mathrm{H_b}}{\mathrm{D_{50}}}\right)^{-\frac{1}{2}} \tag{3.88}$$

A more recent study by Bernabeu *et al.* (2003) has included reflection to develop a new equilibrium profile model. Such model is based on a two-section profile scheme, largely corresponding to the surf and shoaling-dominated zones of the beach profile.

A further comment to the equilibrium condition as given by Eq. (3.81) is that wave (and/or tidal) conditions are not included. This is a shortcoming as although grain size diameter appears to be the prime factor defining profile shape, it is anticipated that wave (and/or tidal) characteristics do have some effect.

The profile depth according to Eq. (3.81) increases infinitely with distance to shoreline, which is clearly unrealistic as the beach-profile is limited seawards to where the wave conditions can no longer change it (sediment will continue moving back and forth without producing any noticeable depth readjustment). Such limit is normally designated as the closure depth (d_c) and has been first discussed by Hallermeier (1981) – cited by, *e.g.*, Kamphuis (2000) – which formulates it as a function of the annual average ($\overline{H_s}$) and standard deviation (σ_{H_s}) of the significant wave-height and the corresponding period (T_p) as given by Eq. (3.89). Eq. (3.90) is an approximation to Eq. (3.89) suggested by CUR (1990) – also cited by Kamphuis (2000).

$$\mathrm{d_c} = \left[\overline{H_s} - 0.3\,\sigma_{H_s}\right]\mathrm{T_p}\sqrt{\frac{\mathrm{g}}{5000\,\mathrm{D_{50}}}} \tag{3.89}$$

$$d_c = 1.6\, H_{s,12} \tag{3.90}$$

in which $H_{s,12}$ is the significant wave-height that occurs 12 hours per year on average.

The above-mentioned Gourlay parameter (Ω) has been used in a number studies to classify wave-dominated beaches (see, *e.g.*, Short, 1999; and Pais-Barbosa, 2007). In his study, Gourlay (1968) – also cited by Short (1999) – found that when Ω<1 laboratory beaches tended to be steep and stable; whereas when Ω>1-2 they eroded with the sediment forming a terrace at the base of the beach.

Short (1999) refers to a study by Wright and Short (1994) that has adapted the Gourlay parameter for use on natural beaches. Based on both, beach experiments from representative types and numerous observations of natural wave-dominated, micro-tidal beaches around the south-east Australian coast, Wright and Short (1994) have found that when Ω<1 beaches tended to be reflective (*i.e.*, steep and barless), when Ω>6 they tended to be dissipative (*i.e.*, flat and multi-barred), and in-between (Ω=2-5) they were what they called intermediate.

Short (1999) provide a graph sediment grain-size *vs.* breaker wave-height on occurrence for each classification type, from which is possible to conclude that dissipative beaches will typically occur in fine sandy beaches with high waves and shorter periods; whereas reflective beaches are typically composed of coarse sand and submitted to lower waves with longer periods.

Based also on the classification by Wright and Short (1994), Short (1999) gives an impression on rates of change stressing that dissipative beaches tend to have relatively stable morphologies exhibiting minimal shoreline change. A number of factors can explain it, namely *(i)* a fine low gradient profile is less susceptible to change as compared to a steeper and coarser profiles; *(ii)* the beach is suited to high storms, and consequently experiences little erosion during storm events; *(iii)* coupled with this is the fact that the beach accommodates higher waves by causing them to break further seaward on the gentle nearshore slope thereby dissipating their energy over a wider surf zone; *(iv)* the greater dissipation in turn increases the elevation of wave set-up which accommodates the greater inshore volume of water.

Beach-profiles may undergo short- or long-term changes. When, over the long-term, volumes of beach material that are moved offshore do not all come back onshore, the beach will undergo erosion (*i.e.*, shoreline position is moved landwards). It is easily perceived that beach-profile changes, due either to daily (between tides) or seasonal natural variability (summer and winter) or anthropogenic factors with impact on sediment dynamics (*e.g.*, coastal structures as seen in Chapter 2), and sediment budgets assessment are very important tools for coastal engineering and management practice, especially in areas with massive urban development standing close to the shore.

Yet, the state-of-the-art of hydrodynamics and sediment transport modelling is still not progressed to the level where the development of complex topography can be predicted (Nielsen, 2009); which implicates that change in beach morphodynamics can only be predicted by the use of models involving too many simplifications as compare to nature, by the extrapolation of historical data, or by physical modelling which also involves some simplifications as compare to nature.

3.3.5. Concluding remarks

In the introduction to this section it was noted that the movement of sediment is very often the most important consideration and ultimate criterion in a design for the coastal zone; yet, as has been argued herein, it still poses some of the greatest challenges in coastal research.

From the available knowledge, it appears that sediment transport processes and the ensuing morphological response vary with the sediment properties (*e.g.*, grain size, density, and fall-speed), the antecedent morphology, the hydrodynamic conditions (*e.g.*, wave-height, and wave-period), and the interplay between both.

Sediment transport is accurately described by the critical value for initiation of motion (which depends on, *e.g.*, grain size, shape, density, sorting, and wave shape), subsequent transport (which depends on, *e.g.*, the structure of the flow, and bedform geometry), and the path back to the bottom (which depends on, *e.g.*, sediment fall-speed).

Typically, the particle moves by rolling and/or sliding particle motion, saltating, or hopping particle motion, and suspended particle motion. The transport of particles by rolling, sliding and saltating is called bed load transport, while the transport of suspended particles is called suspended load transport. Bed-load and suspended-load modes often occur simultaneously, and appear to be governed in an unknown way by grain size, local wave energy, and several other variables.

Based on the above analysis on the initiation of sediment motion it was possible to conclude that the response to the flow, for any given grain, depends on a wide range of possible (and complicated) combinations of sediment characteristics (possibly containing a mixture of densities, sizes and shapes), hiding-exposure factors, and nature of flow.

Particle movement will occur when the instantaneous fluid force on the particle is just larger than the instantaneous resisting force related to the submerged particle weight and the friction coefficient, which may be affected by the degree of exposure of the particle with respect to the neighbouring ones, as well as by cohesive forces and in-bed pressure gradients.

The transport processes and the bathymetry are changed by and have an influence on how waves approach the coast, from incipient wave breaking to the transformation of wave-height through the surf zone, and associated hydrodynamic processes (*e.g.*, wave setup and setdown, wave run-up, and nearshore currents). The type and magnitude of forcing within the nearshore active zone (*i.e.*, where sediment motion and beach-profile change occurs) is markedly different inside and outside the surf zone. Net transport reflects the relative strengths and durations of seaward *vs.* landward flow patterns.

A beach exposed to changing hydrodynamic conditions respond with readjustments (in *e.g.*, the steepness of the slope, and the migration of bars) in beach- and nearshore-profiles.

The processes and conditions affecting those readjustments are complicated. Not only the spatial and temporal scales range significantly from instantaneous motion of individual particles on a time-scale comparable to that of the local turbulence to seasonal and longer term movement of large sediment bodies; but also the natural variability of the beach-profile affects singularly the forcing mechanisms.

It will be seen hereafter that such processes and conditions are further complicated by the presence of a structure which will induce a change of the flow pattern around it.

3.4. Scour around coastal structures

The term scour generally refers to the localized erosion of the base of a structure. It is the result of an increase in the local sediment transport capacity due to change of the flow pattern, resulting in one or more of the following phenomena (see, *e.g.*, Sumer and FredsØe, 2002): *(i)* the contraction of flow; *(ii)* the formation of a horseshoe vortex in front of the structure; *(iii)* the formation of lee-wake vortices (with or without vortex shedding) behind the structure; *(iv)* the generation of turbulence; *(v)* the occurrence of wave breaking; and *(v)* the pressure differentials in the soil that may produce “quick” conditions/liquefaction allowing the material to be carried off by currents.

Depending on the spatial extent, scour may lead to an overall degradation of the bed or to local scour holes (CIRIA *et al.*, 2007). While the latter may lead to the gradual dislocation of the foundation and decrease the geotechnical stability of the structure Oumeraci (1993), increased water depths due to scour may increase the hydraulic loading in front of the structure (CIRIA *et al.*, 2007).

The present section aims at briefly describing the state-of-the-art knowledge on the hydrodynamic processes causing scour around coastal structures, highlighting its potential impact on the stability of the structure, and on the dominant response mechanisms of the bed sediments. The books of Sumer and FredsØe (2002), Whitehouse (1998), Hoffmans and Verheij (1997), and Breusers & Raudkivi (1991) cover many of the background information on the process of scour and the prediction methods that are currently in use and are valuable references for the understanding of the mechanics of scour in the marine environment. Lillycrop and Hughes (1993), CIRIA (1986) and Markle (1986) report scour related problems in the UK and in the USA based on field surveys. Oumeraci (1993) makes an attempt to identify the problems associated with the development of prediction methods of bottom scour caused by waves in front of vertical structures by using bed scale models, while Wallis *et al.* (2009) and Sutherland *et al.* (2008) provide a synthesis of existing information and approaches to predicting general beach lowering, and derive a new scour prediction method. The European Union Marine Science and Technology (EU MAST) III project, designated as ‘‘Scour Around Coastal Structures’’ (SCARCOST), which run from September, 1997 through August, 2000 has also given a valuable contribution to the study of the potential risk for scour in the vicinity of coastal structures, and to prepare and disseminate practical guidelines, to be developed from the research programme and also taking into account all state-of-the-art knowledge. The results of SCARCOST are included in Sumer and FredsØe (2002) but are as well summarized in the paper by Sumer *et al.* (2001). All these references compile a very high percentage of existing studies on the scour development near coastal structures for which key aspects and general discussion are summarized below. Greater detail can be found in the original reference.

3.4.1. General principles of scour

The presence of a structure will induce a change of the flow pattern around it. This disturbance is associated with an increase in the bed shear stress and in the turbulence level. Where it is located determines which hydrodynamic actions may dominate and which modes of sediment transport may result at a given site, wave climate, and water depth.

Figure 3.36 schematically shows the dominant actions, modes of sediment transport and different types of scour as a function of the location of the structure.

For an off-shore structure (location 1) scour is due to standing wave conditions. Typically, suspended-load transport dominates for common bed sediment sizes and moderate water depths. When a structure is located inside the surf zone (location 2), the waves may break just before or on the structure itself. The dominant mode of transport is suspended-load transport. For structures installed at the swash zone (locations 3a and 3), sheet flow conditions resulting from wave up- and downrush dominate.

Time development scour depth is a relevant consideration in practice, as it is the rate at which the scour occurs. While scour depth, for a given structure and wave climate, indicates the degree of potential scour, the latter is a measure on whether substantial scour is produced during a given storm or consecutive storms. Experimental data and observations show that a scour hole produced after a storm may be backfilled (Sumer and FredsØe, 2002) and that scour may develop rapidly and be then refilled for a given storm (see, *e.g.*, Fowler, 1993). In areas of varying tidal range and wave climate, the development of a scour hole will be an episodic process with periods of erosion followed by infilling, and perhaps even general accretion of the bed (Powell and Lowe, 1994). Storm and persistence is thus relevant to account for in scour development, as the time required for the scour process to reach equilibrium can be much longer than the duration of many storm events.

Scour is most commonly classified as follows (Whitehouse, 1998): *(i) l*ocal scour: *e.g.* steep-sided scour pits around single piles; *(ii)* global or dishpan scour: shallow wide depressions under and around individual installations; and *(iii)* overall sea bed movement: erosion, deposition, bedform.

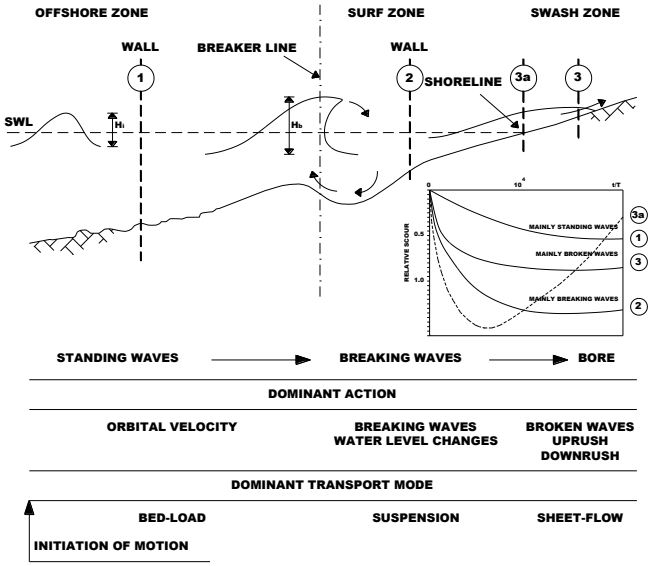

Figure 3.36: 2D-scour scenarios as a function of the location of the structure (modified from Oumeraci, 1993).

The distinction between two categories of scour, the clear-water, and the live-bed, is also generally accepted (see. *e.g.*, Sumer and FredsØe, 2002; Whitehouse, 1998). In the case of the clear-water scour, no sediment motion takes place far from the structure, while, in the case of the live-bed scour, the sediment transport prevails over the entire bed.

Researchers have typically developed non-dimensional relationships for predicting scour, usually expressing relative scour in terms of the scour depth to incident wave-height ratio (S_d/H).

The authors Sumer and FredsØe (2002) propose three additional non-dimensional parameters that may be responsible for the scour process regarding the presence of a structure: distance of the structure to deep-water wavelength ratio (x/L_0); water-depth at the structure to deep-water wave-height ratio (d_w/H_0); and penetration of the breaker down to the bed ($T\sqrt{gH_b}/d_w$). Definitions are as proposed in Figures 3.36 and 3.37.

Finally, the sediment properties characterized in terms of the conventional Shields parameter (τ_c), and the ratio of the fall-velocity to friction-velocity (w_s/U_{fm}), and the wave boundary layer over the seabed characterized in terms of the deep-water wave-height to grain-size ratio (H_0/D_n), and the grain-size Reynolds number (Re), as described in section 3.3 of the current chapter, may also influence the scour process.

Studies by Carpenter and Keulegan (1958) – also cited by Sumer and FredsØe (2002), showed that for oscillatory flows, scour at the bed was not strongly related to the grain-size Reynolds number (Re), so that it may be omitted. For live-bed scour the conventional Shields parameter (τ_c) influence on the scour characteristics is weak, and may therefore be omitted as well. The Shields parameter influence is also reduced in the presence of wave breaking due to the turbulent nature of the entraining flow.

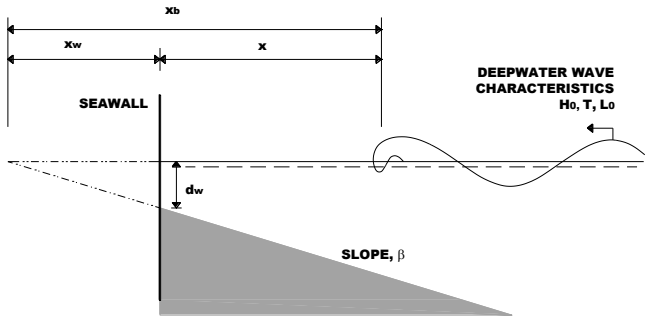

Figure 3.37: Definition sketch.

Thus, the revised governing non-dimensional variables that may be responsible for the scour process comes down to the following:

$$\frac{H_0}{L_0};\ \beta;\ \frac{d_w}{H_0}\left(\text{or alternatively } \frac{d_w}{L_0}\right);\ \frac{x}{L_0};\ \frac{T\sqrt{gH_b}}{d_w};\ \frac{w_s}{U_{fm}};\ \frac{H_0}{D_n}\left(\text{or alternatively } \frac{L_0}{D_n}\right) \tag{3.91}$$

The time scale of scour is expected to depend on the same parameters responsible for the scour itself but no detailed study is yet available. Sumer and FredsØe (2002) propose the formulation, as given by Eq. (3.92).

$$T^* = T^*\left[\frac{H_0}{L_0};\ \beta;\ \frac{d_w}{H_0};\ \frac{x}{L_0};\ \frac{T\sqrt{gH_b}}{d_w};\ \tau_c;\ \frac{w_s}{U_{fm}};\ \frac{H_0}{D_n};\ \mathrm{Re}\right] \tag{3.92}$$

in which T^* is the normalized time scale defined by Eq. (3.93).

$$T^* = \frac{\sqrt{g(S_s-1){D_n}^3}}{H_0^2}T \tag{3.93}$$

in which T is the time scale of scour (*i.e.*, the time during which a substantial amount of scour occurs).

3.4.2. Predicting scour depth

Findings of comprehensive survey to seawalls in the UK (see, *e.g.*, Wallis *et al.*, 2009; Whitehouse, 1998; and CIRIA, 1986) and rubble-mounds in the USA (see, *e.g.*, Lillycrop and Hughes, 1993; and Markle, 1986) confirm that scour represent the most serious form of damage. Similar conclusions were drawn in Silvester and Hsu (1997) that cite evidence of scour from Europe, Japan, United States and Africa; also Veloso-Gomes *et al.* (2009b) report and analyse scour at different coastal defence structures along the Portuguese west coast. Thus predicting scour depth and more widespread beach lowering is a central issue for coastal defence design.

This paragraph draws together key research on methods developed to predict scour depth around coastal structures for the case of 2D-scour scenarios (*i.e.*, where the waves approach the coast at a right angle). Special attention is given to studies that were able to isolate which parameters may have a greater impact on scour development and rate, as well as to those that may have a follow on in the present contribution. Where appropriate design formulations and shortcomings in the available knowledge are given.

Most of the relevant and detailed physical movable-bed wave-model scour tests have been performed for the cases of 2D-scour at vertical-wall and rubble-mound breakwaters with non-breaking regular period waves. Of particular interest are the scour depth design formulations by Xie (1981), Sumer and FredsØe (2000), O'Donoghue (2001), and Hughes and Fowler (1991).

One of the fundamental findings of these studies is that there are basically two distinct sand transport mechanisms leading to two distinct types of scour patterns, depending on the sand grain size and the wave conditions Oumeraci (1993).

Figure 3.38 illustrates the two scour patterns identified as N-type, scour location at the nodes (N), and L-type, scour location at the anti-nodes or loops (L), the criteria for the occurrence of N or L-type scour is also shown. The dominant mode of sand transport, suspension and no-suspension, is what determines which scour pattern will occur in the movable-bed model.

As seen in Figure 3.39, the N-type scour pattern is when the scour holes are located beneath the nodes while the ridges occur at the anti-nodes indicating that the majority of sand is transported by the suspension-mode. When the ridges are beneath the nodes while the scour holes are located at about halfway between the nodes and anti-nodes it corresponds to an L-type scour pattern indicative of sand being transported by the no-suspension-mode.

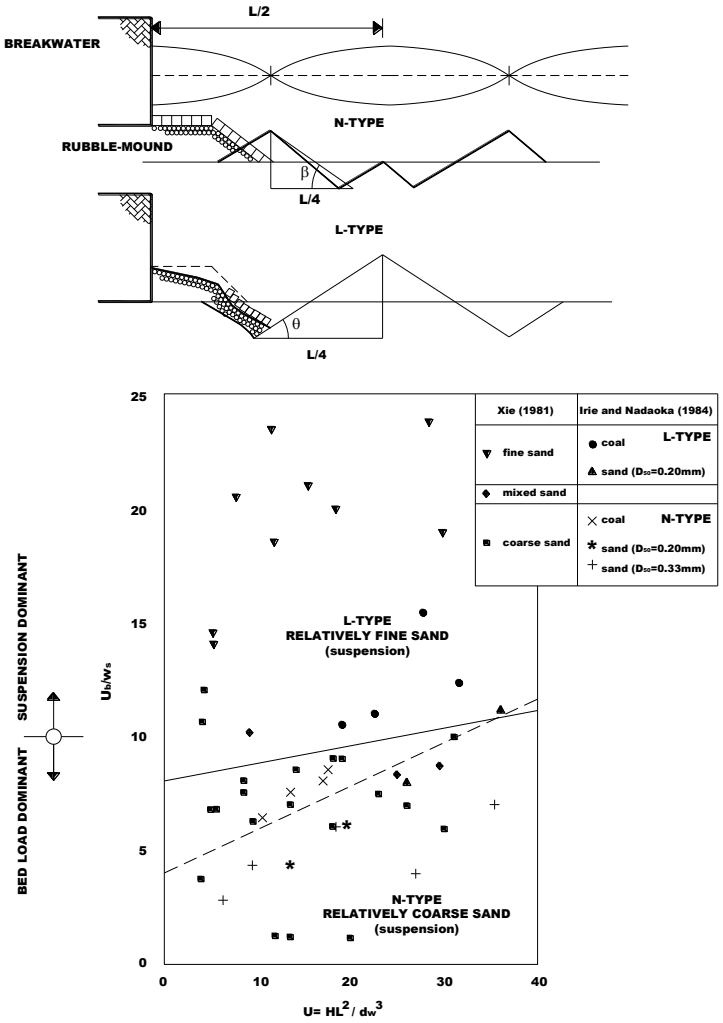

Figure 3.38: Critical appearance of N, L-type scour in the movable-bed
(modified from Oumeraci, 1993).

$\frac{U_{bmax}-U^*}{w_s} \geq 16.5$ Xie (1981)

$\frac{U_{bmax}}{w_s} \geq 10$ Irie and Nadaoka (1984)

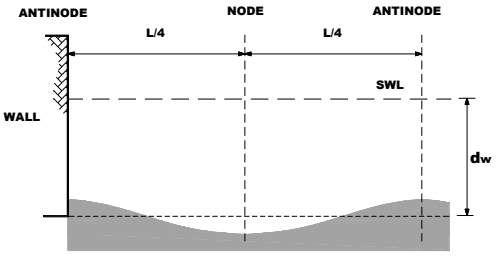

$\frac{U_{bmax}-U^*}{w_s} < 16.5$ Xie (1981)

$\frac{U_{bmax}}{w_s} < 10$ Irie and Nadaoka (1984)

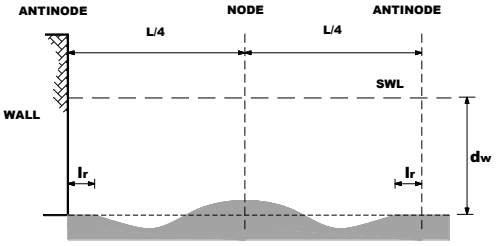

Figure 3.39: Scour/deposition pattern: suspension-mode of sand transport (top),
no-suspension-mode of sand transported (bottom)
(adapted from Xie, 1981).

The described scour-and-deposition patterns in front of a structure is the response of the sediment bed to a system of re-circulating cells (consisting of bottom and top cells) to a standing wave, as illustrated in Figure 3.40. Those patterns are heavily dependent on the mode of transport (thus on the movable-bed model scale) and may be explained as follows (see, *e.g.* Oumeraci, 1993):

- If the sand size is relatively small, the fine sand particles on the sea bed are mobilized by the first-order oscillatory bed velocity U_x which is about an order of magnitude larger than the mean drift (mass transport) velocity $\bar{u}_m$ (Figure 3.40). Due to the large orbital bed velocity U_x at the nodes, the fine sand particles near the nodes are lifted into suspension within the boundary layer where the flow pattern is such that the outer flow (at upper edge of boundary layer) is towards anti-nodes and away from the nodes (Figure 3.40). This outer flow (with the mean velocity $\bar{u}_m$) then drifts the suspended fine particles from nodes to anti-nodes which finally deposits where the local oscillatory velocity U_x diminishes, *i.e.* at the anti-nodes (U_x=0). This means that the sand particles are moved according to the circulation pattern in a standing wave. As a result of this first mechanism, scour holes develop beneath nodes and ridges beneath anti-nodes, *i.e.* with spacing of one half wavelength of the incident waves (Figure 3.39a).
- If the sand size is relatively coarse, the coarse sand grains are also mobilized by the orbital bed velocity U_x however, because of their larger mass they cannot so easily be brought into suspension as for the finer particles. The former will thus likely remain moved by shear stress and rolled on the sea bed. Since the near flow within the bottom boundary layer is towards nodes and away from anti-nodes (Figure 3.40) the coarse particles are drifted as bed load from anti-nodes to nodes where they finally deposit. As a result of this second mechanism, ridges develop beneath nodes and scour holes at half way between nodes and anti-nodes, *i.e.* with spacing of ¼ wavelength of the incident waves (Figure 3.39b).

Xie (1981) experimentally investigated the scour (for both modes of transport) in front of a vertical concrete wall, and has found remarkable correlation between the scour depth S_d/H and the parameter d_w/L; the larger the value d_w/L, the smaller the scour depth.

Figure 3.41 displays Xie's (1981) results, while Eq. (3.94) and Eq. (3.95) are the empirical expressions for the maximum scour depth inferred by the author for respectively, the suspension-mode of sand transport, and the no-suspension-mode of sand transport.

$$\frac{S_d}{H} = \frac{0.4}{\left[\sinh\left(\frac{2\pi d_w}{L}\right)\right]^{1.35}} \tag{3.94}$$

$$\frac{S_d}{H} = \frac{0.3}{\left[\sinh\left(\frac{2\pi d_w}{L}\right)\right]^{1.35}} \tag{3.95}$$

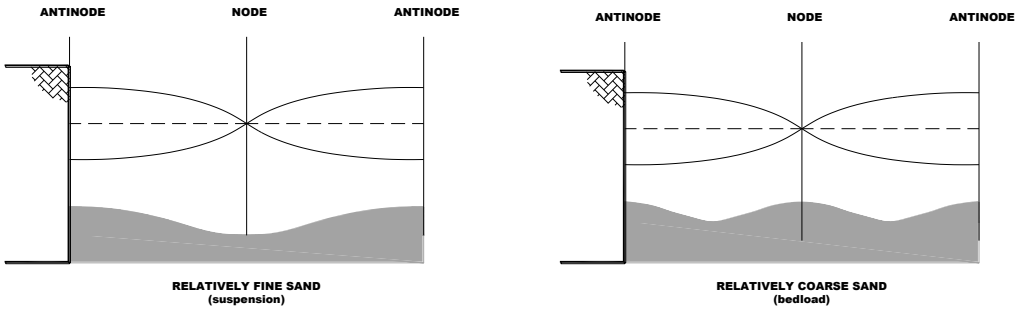

Figure 3.40: Steady streaming in the vertical plane in front of a vertical-wall breakwater (adapted from Oumeraci, 1993).

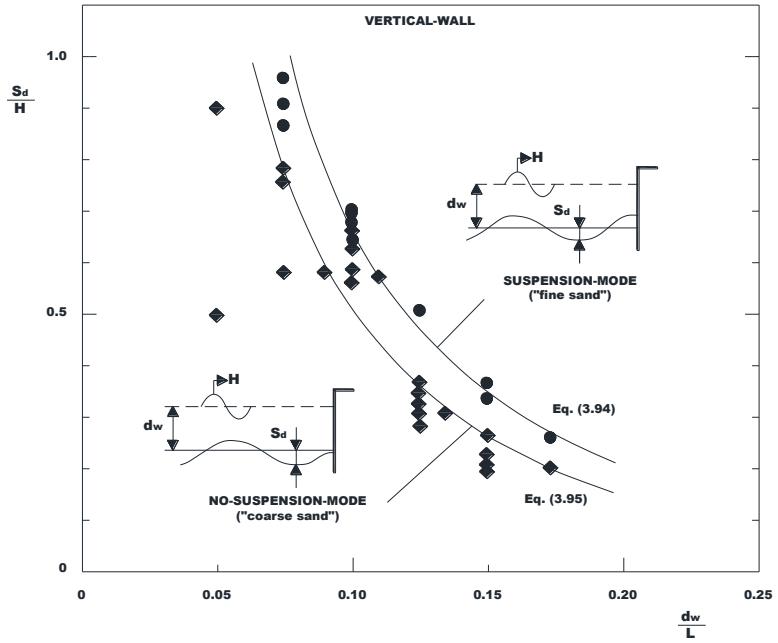

Figure 3.41: Maximum scour depth at vertical-wall breakwater, live-bed
(adapted from Xie, 1981).

Sumer and FredsØe (2000) have developed a study of 2D-scour at a rubble-mound breakwater very much in line with the work of Xie (1981) for vertical-wall breakwaters to find out that the 2D scour-and-deposition pattern in front of a rubble-mound breakwater emerges in the form of alternating and deposition areas lying parallel to the breakwater, similar to the case of the vertical-wall breakwater (Figure 3.42).

The latter authors also found that the scour depth at the rubble-mound breakwater is smaller than that at the vertical-wall breakwater, and that it decreases with decreasing slope (Figure 3.43). The reason for this lies in the reflection coefficient. As first revealed by Sawaragi (1966) – cited in Fowler (1993), the scour development is dependent on the permeability of the structure, and on the coefficient of wave reflection. This author also noted that, for breaking waves, the depth of scour is the result of a process interspersed with episodic accretion and erosional events. The scour dependency on the coefficient of wave reflection was also demonstrated in the numerical study of Arneborg *et al.* (1995) – cited in Gislason *et al.* (2009), evidencing that the scour depth decreases with decreasing values of the reflection coefficient.

Sumer and FredsØe (2000) give the following empirical expression for the maximum scour depth at a rubble-mound breakwater in the case of no-suspension-mode of sand transport (plotted curve in Figure 3.43):

$$\frac{S_d}{H} = \frac{f(\alpha)}{\left[\sinh\left(\frac{2\pi d_w}{L}\right)\right]^{1.35}} \tag{3.96}$$

in which $f(\alpha)$ is given by Eq. (3.97).

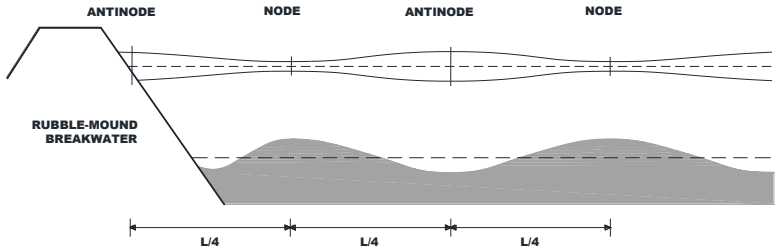

Figure 3.42: Schematic illustration of the scour/deposition pattern in the case of a rubble-mound breakwater, no-suspension-mode of sand transport, regular waves
(adapted from Sumer and FredsØe, 2000).

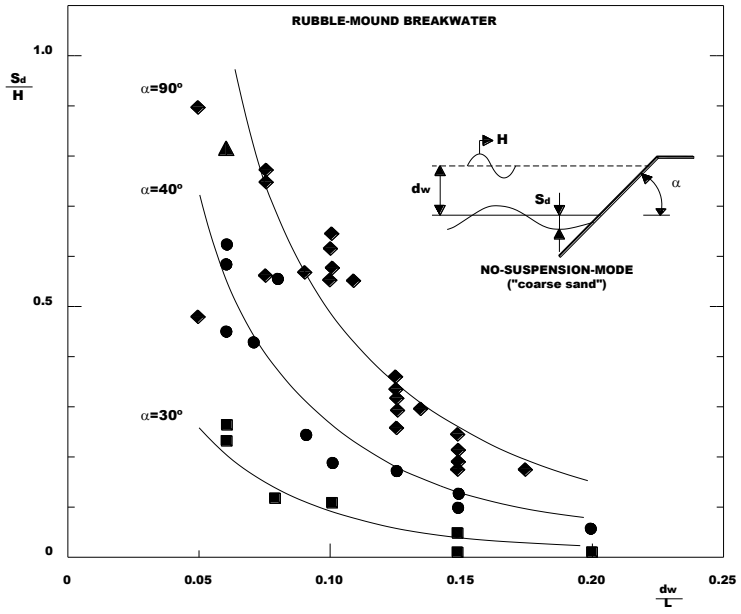

Figure 3.43: Maximum scour depth at a rubble-mound breakwater (regular waves), live-bed (adapted from Sumer and FredsØe, 2000).

$$f(\alpha) = 0.3 - 1.77e^{-\frac{\alpha}{15}} \tag{3.97}$$

in which α is the breakwater slope in degrees (Figure 3.43) in the range $30^o \leq \alpha \leq 90^o$.

O'Donoghue (2001) made an analysis of the N-type bed response based on a general characterization of the N-type profile geometry and on physical reasoning applied to available experimental data, namely Xie (1981). O'Donoghue (2001) derived a new method for predicting the N-type equilibrium scour profile given by Eq. (3.98), which revealed a non-linear dependence of scour on wave-height and a direct dependence of scour on wave period. Predictions of scour using this new method are much greater than scour predictions based on the existing interpretation of experimental wave-tests.

$$\frac{S_{max}}{H} = 1 - \frac{\left(\frac{d_w}{L}\right)}{0.002 + \left(\frac{d_w}{L}\right)^{2.9}} \tag{3.98}$$

Eq. (3.98) is valid for ratios of water-depth to wavelength in the range 0.05-0.2.

As previously mentioned many of the most important scour tests have been performed with regular period waves, rather than irregular waves with a natural spectral shape. Only very few studies with a limited number of tests were conducted with irregular waves (*e.g.*, Sumer and FredsØe, 2000; Kraus and Smith, 1994; Hughes and Fowler, 1991; and Xie, 1981).

Xie (1981) was among the earliest researchers to perform scour tests using both regular and irregular waves yet with a limited number of irregular waves. As depicted in Figure 3.44, Xie compared scour development for regular and irregular standing waves to find that for regular waves the sea bed develops rhythmic features while for the irregular ones the sea bed form decreases in amplitude with increasing distance from seawall. Similar conclusion was drawn by Sumer and FredsØe (2000) which can be explained by the fact that, in the case of irregular waves, the wave-height only emerges as a standing wave pattern close to the structure. The latter authors also found that the maximum scour depth in the case of irregular waves is generally smaller than that of the corresponding regular-wave cases.

Figure 3.45 displays Sumer and FredsØe (2000) results, where H is taken as H_{RMS}, while L is the wavelength associated with the peak period.

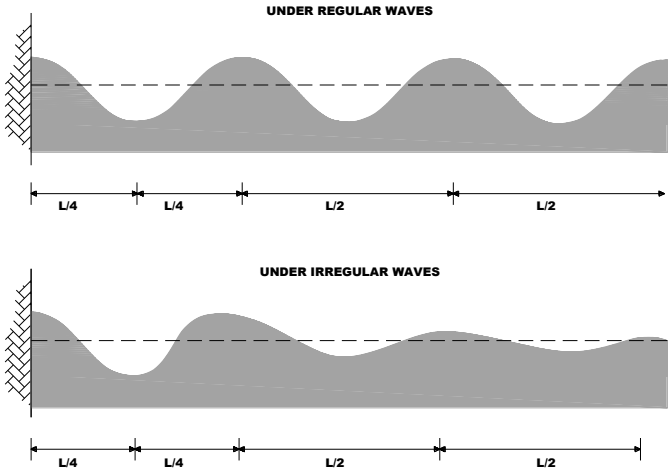

Figure 3.44: Suspension-mode of sand transport with regular waves (top panel), and irregular waves (bottom panel, in which *L* is the wavelength associated with the peak period) (adapted from Xie, 1981).

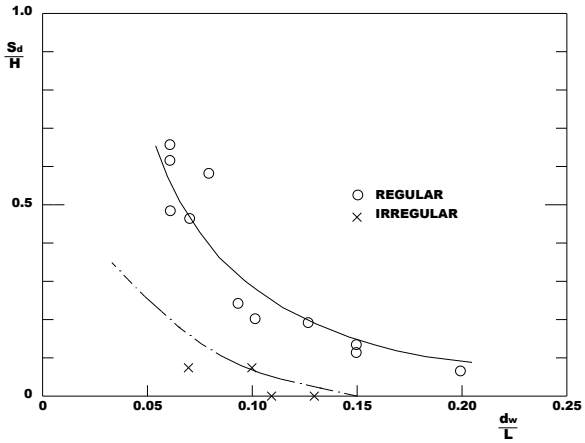

Figure 3.45: Comparison of the maximum scour depth at a rubble-mound breakwater, α=40°, no-suspension-mode of sand transport, live-bed (adapted from Sumer and FredsØe, 2000).

These results show good, quantitative agreement with the results of Hughes and Fowler (1991) for the case of a vertical-wall breakwater. The empirical expression, as given by (3.99), has been proposed by Hughes and Fowler (1991) for the case of normally incident, non-breaking irregular waves.

$$\frac{S_{max}}{(U_{RMS})_m T_p} = \frac{0.05}{\left[\sinh\left(\frac{2\pi d_w}{L}\right)\right]^{0.35}} \tag{3.99}$$

where T_p is the wave period of the spectral peak. $(U_{RMS})_m$ is the root-mean-square of horizontal velocity and may be calculated applying Eq. (3.100), which is valid for $2\pi d_w/L$ in the range of 0.05-3.0.

$$\frac{(U_{RMS})_m}{g\frac{2\pi}{L}T_p H_{m0}} = \frac{\sqrt{2}}{4\pi\cosh\left(\frac{2\pi d_w}{L}\right)}\left[0.54\cosh\left(\frac{1.5-\frac{2\pi d_w}{L}}{2.8}\right)\right] \tag{3.100}$$

in which H_{m0} is the zeroth-moment wave-height defined as 4 times the standard deviation of sea surface elevation (refer to Chapter V for more complete definition).

Figure 3.46 compares the preceding relation with that of Xie (1981) regular wave result. The scour depth in the case of irregular waves is reduced by half of that caused by regular wave trains with the same height (H_s is selected as the equivalent wave-height).

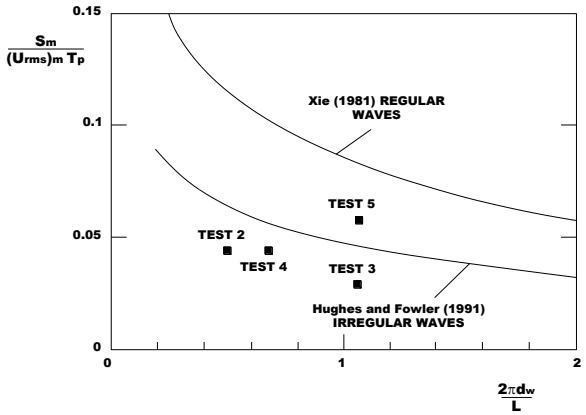

Figure 3.46: Comparison of the maximum scour depth at a vertical-wall breakwater for normally incident regular and irregular wave, (modified from Sumer and FredsØe, 2002).

The comparison between scour development tests caused by regular wave trains and irregular ones also suggests that the use of random wave may simplify to some extent the scaling problem, because the natural variations within the random wave field may assure correct redistribution over the entire extent of the modelled sea bed cross-shore profile Oumeraci (1993).

All the previously mentioned studies but Sawaragi (1966) – cited in Fowler (1993) – have been performed under non-breaking waves. However, the wave breaking not only affects the scour but also exacerbates it. Indeed, the available results indicate the importance of breaking waves in exacerbating scour (Whitehouse, 1998); yet the knowledge of scour due to breaking waves is very limited, and the mechanisms responsible for this kind of scour are not well understood (see, *e.g.*, Sumer and FredsØe, 2002), which suggests the need for further research.

The governing parameters presumably leading to scour due to normally incident breaking waves are the breaker type – that may be correlated to the surf similarity parameter, Eq. (3.1); and, as aforementioned, the location of the structure; the sediment properties; and the wave boundary layer over the seabed.

As seen before, the breaker type refers to the form of the wave at breaking. A natural beach profile and the presence of a structure may change the breaker type and its characteristics, modifying as well the forcing mechanisms of the scour process. The naturally occurring morphologic perturbations of longshore bars and troughs exert strong control over shallow-water wave transformation; likewise, breaking waves modify the beach profile (Smith and Kraus, 1991). Similarly the presence of a structure modifies the profile and incident waves, with obvious impact on scour development.

The flow processes may result from the waves breaking before they reach the structure (top left panel in Figure 3.47), the waves breaking on the structure itself (top right panel in Figure 3.47), or the waves overtopping the structure (bottom left panel in Figure 3.47). The scour mechanism for each of these cases is different. According to Oumeraci (1993), the most dramatic failures due to bottom scour in the field occurred for wave breaking just in front of the structure.

In the early nineties the U.S. Army Corps of Engineers, Waterways Experiment Station, Coastal Engineering Research Centre run a research and development programme on Laboratory Studies on Scour. The reports Fowler (1992, 1993), produced within this programme, include the results from 22 movable-bed wave-model tests, of which 18 were run using irregular wave trains (H_0 is taken as the significant wave-height, H_s), and the other 4 with regular ones. Three locations of the seawall, x_w – simulated by a vertical wall – were tested, to know at approximately ±0.90m, and at the shoreline (x_w=0), in front of a plane beach (slope 1:15). For all the test conditions reported in Fowler (1992), waves broke well seaward or immediately in front of the seawall.

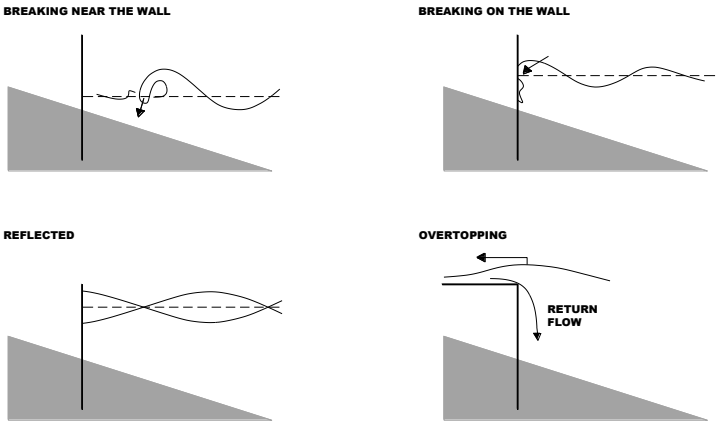

Figure 3.47: Flow processes leading to 2D-scour by normally incident breaking waves (adapted from Sumer and FredsØe, 2002).

Figure 3.48 displays a typical sequence of cross-shore profiles surveyed during the tests, while Figure 3.49 is the plot of the results of scour depth *vs.* incident deep-water wave-height by Fowler (1992) for regular and irregular waves pooled with data from other experimental tests. Figure 3.50 displays Fowler's (1992) data, as normalized scour depth *vs.* the relative depth at vertical seawall, with plot of derived equation for prediction maximum scour depth, Eq. (3.101); valid for situations where $-0.011 \leq d_w/L_0 \leq 0.025$, and $0.015 \leq H_0/L_0 \leq 0.04$.

$$\frac{S_{max}}{H_0} = \left(22.72\frac{d_w}{L_0} + 0.25\right)^{\frac{1}{2}} \tag{3.101}$$

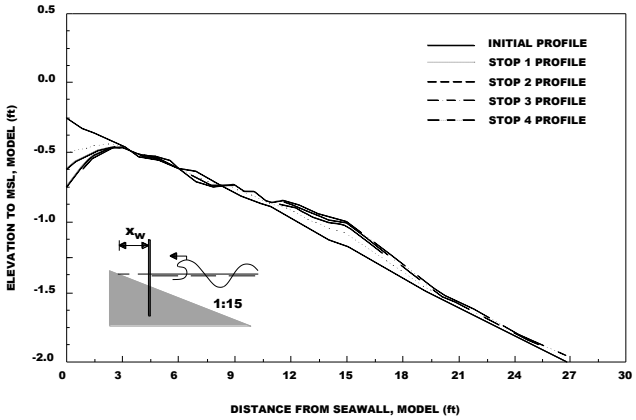

Figure 3.48: Typical cross-shore profile sequence, H_s~0.21m, T_p=1.97s, d~1.16m, and d_w~0.06m (adapted from Fowler, 1992).

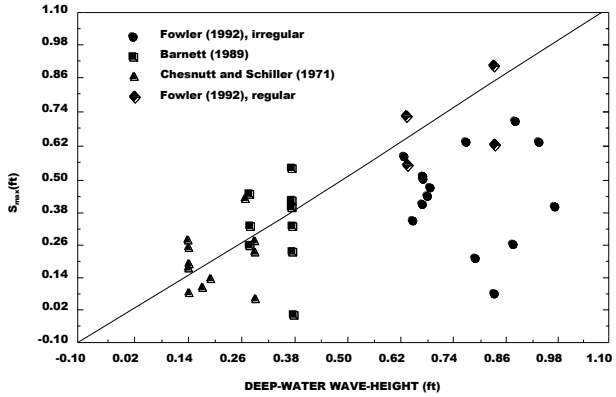

Figure 3.49: Pooled data set of maximum scour depth *vs.* deep-water wave-height (adapted from Fowler, 1992).

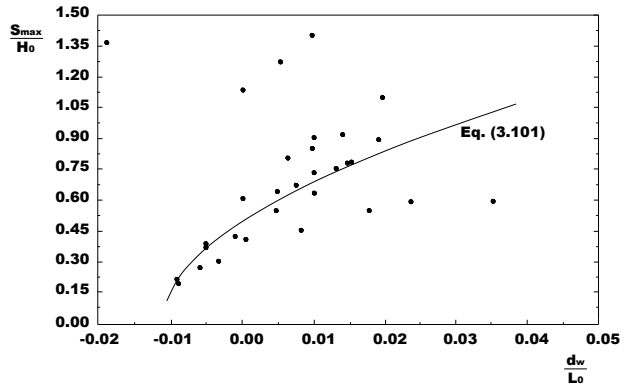

Figure 3.50: Pooled data set of relative maximum scour depth *vs.* relative depth of Fowler (1992), Barnett (1989), and Chesnutt and Schiller (1971) with plot of Eq. (3.101) (adapted from Fowler, 1992).

Fowler's predicative Eq. (3.101) does not include any parameters relating to sediment properties, which are expected to have some influence in the scouring process (USACE, 2008). Also, scour estimation method proposed by Fowler (1992) does not account for current flow along the vertical wall.

Other conclusions drawn by Fowler (1992) are as follows: *(i)* significant wave-height is the best irregular wave design parameter for matching results based on regular wave tests; *(ii)* in the case of the regular wave tests, the scour depth increases by approximately 15%; *(iii)* the data from Fowlers' study and numerous field studies tend to support the most widely used rule-of-thumb, that is to say the maximum scour depth will be less than or equal to the incident unbroken wave-height.

Scour of coarse sediment beaches (5mm<D_{50}<30mm) fronting vertical walls is discussed by Powell and Lowe (1994) experimental study, and Carpenter and Powell (1998) numerical simulations with COSMO-2D; see also Powell and Whitehouse (1998) and Whitehouse (1998). The COSMO-2D is a cross-shore based numerical model developed by HR Wallingford, which according to Whitehouse (1998) has limited capability for predicting accretion.

Figure 3.51 is the contour plot of experimentally obtained scour depth by Powell and Lowe (1994) for the case of a plane shingle (mean grain size of 12mm) beach with slope 1:17 in front of a vertical seawall, after 3000 irregular waves. It has become clear from this study that the wave steepness is an important parameter.

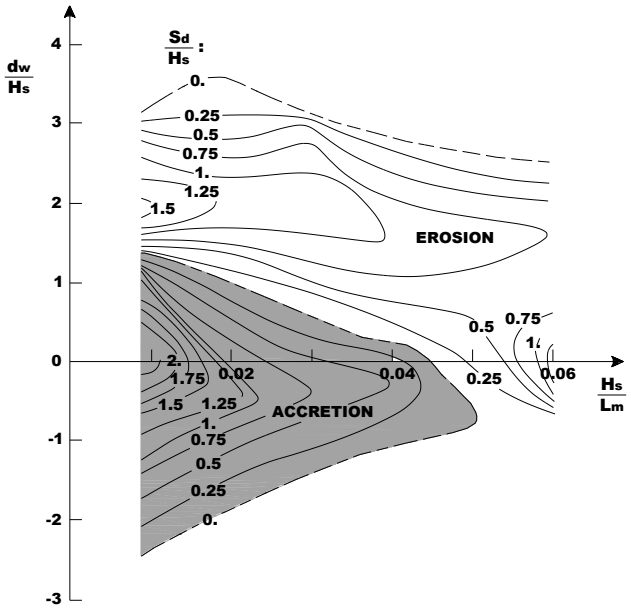

Figure 3.51: Contour plot of experimentally obtained scour depth (adapted from Powell and Lowe, 1994).

The numerical simulation by Carpenter and Powell (1998) has resulted in a similar diagram (Figure 3.52) for the case of a plane sandy (mean grain size of 0.2mm) beach with slope 1:75 in front of a vertical seawall, after 3000 irregular waves. Both graphs provide dimensionless graphs to predict maximum scour depth as a function of significant wave-height, wave steepness, and local water depth.

McDougal *et al.* (1996) carried out a numerical study of scour in front of a vertical seawall. The latter authors used the widely known model SBEACH, which is comprised of a wave transformation model, to predict the refraction, shoaling, breaking, and reflection from the seawall, and a cross-shore sediment transport algorithm, to predict the beach profile. The numerical model results have been compared with the SUPERTANK Laboratory Data Collection Project, as described by McDougal *et al.* (1996), and the empirical expression, as given by Eq. (3.101). Eq. (3.102) has been determined from the obtained numerical scour depth data.

$$\frac{S}{H_0} = 0.41\beta^{0.85}\left(\frac{L_0}{H_0}\right)^{1/5}\left(\frac{d_w}{H_0}\right)^{1/4}\left(\frac{H_0}{d}\right)^{1/3} \tag{3.102}$$

McDougal *et al.* (1996) stressed that the objective is not to develop a design equation, but rather identify those variables which are important in the scour process.

Sutherland *et al.* (2008) recommends the use Eq. (3.103) for predicting scour depth at vertical seawalls, which limits of applicability are water-depth at the toe of the seawall (d_w) to mean wavelength (L_m) ratio in the range of -0.013 to 0.18.

$$\frac{S_{max}}{H_s} = 4.5\ e^{-8\pi\left(\frac{d_w}{L_m}+0.01\right)}\left(1 - e^{-6\pi\left(\frac{d_w}{L_m}+0.01\right)}\right) \tag{3.103}$$

As previously mentioned, there is a third flow process that may induce scour which is wave overtopping. Although it seems to be a relevant process – for instance, Kraus and McDougal (1996), noted new results regarding the effect of seawalls on the beach being that *(i)* wave reflection at walls may not be a significant contributor to profile change, and *(ii)* scour at seawalls in the field may be more a product of longshore transport and return of overtopping water than a result of direct cross-shore wave action – there is not much information on scour caused by overtopping and consequent return flow. A sketch of wave deformation and scouring process is given in Figure 3.53.

No prediction method exist (see, *e.g.*, Sumer and FredsØe, 2002), yet as the key mechanisms of the overtopping scour process seem to be identified as being the rate of return flow, which enters into the main water-body as a jet flow, and the depth of water receiving the return flow (Figure 3.54).

3D scour mechanisms have been investigated by *e.g.* TØrum *et. al.* (2003), and Sumer and FredsØe (1997); see also Sumer and FredsØe (2002) for additional information and studies on scour generated by obliquely incident breaking waves and other 3D effects.

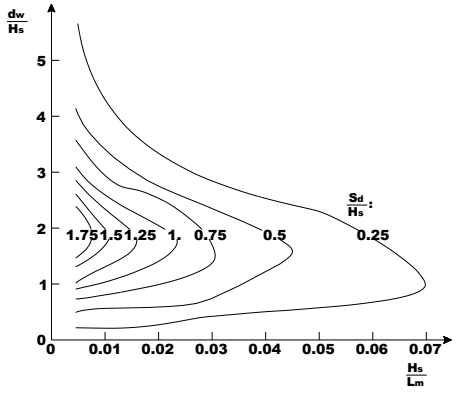

Figure 3.52: Contour plot of numerically obtained scour depth
(adapted from Carpenter and Powell, 1998).

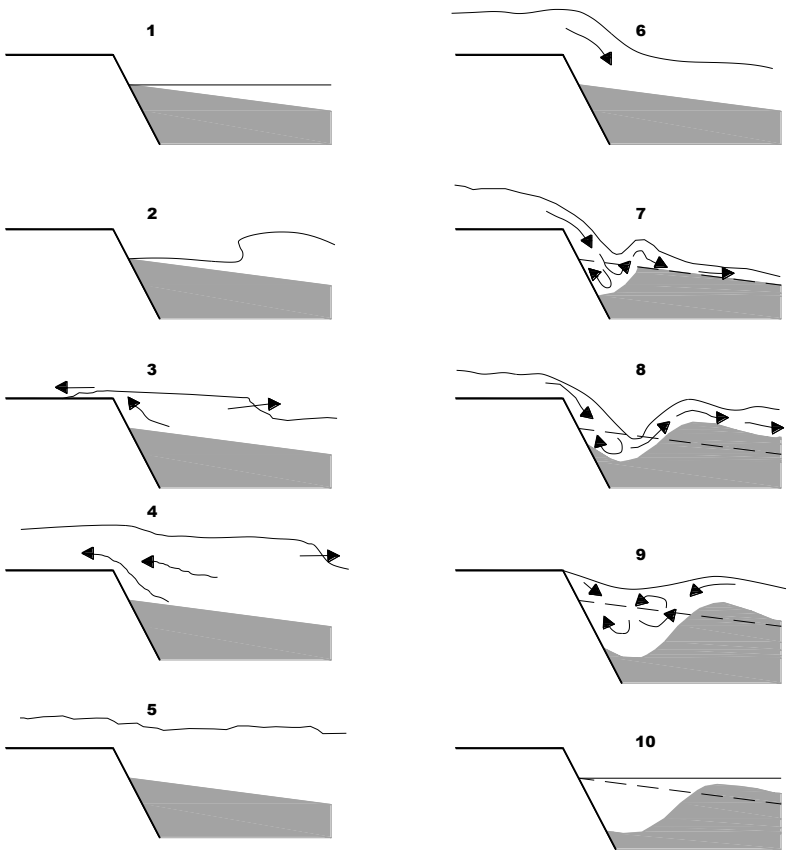

Figure 3.53: Sketch of wave deformation and scouring process.

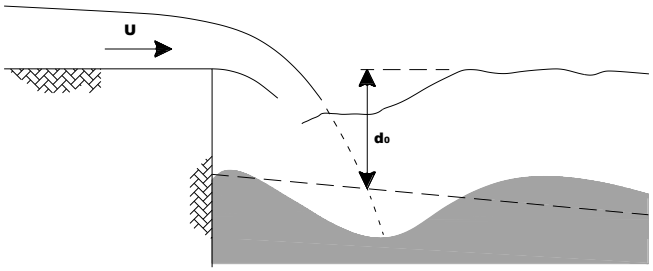

Figure 3.54: Water jet of the return flow.

3.4.3. Liquefaction

Liquefaction refers to the loss of shear resistance in saturated, cohesionless soils during dynamic loading, typically earthquakes, but may also be observed in loose, fine marine soils under wave-loading. Under the liquefaction condition the soil fails, eventually precipitating, *e.g.*, failure of the supported structure, or sink of large individual elements (like large sand-containers or tubes) into the seabed. An indirect effect of local wave-induced liquefaction around coastal structures is that it may enhance scour, thus leading to instability of the structures.

Wave-induced liquefaction is generated mainly by either the build-up of pore-pressure known as residual liquefaction or the upward vertical pressure gradient in the soil during the passage of a wave-trough known as momentary liquefaction.

Sumer *et al.* (1999) displays recorded time-series of pore-pressure and water surface elevation from laboratory experiments under regular wave-loading, 10cm wave-height and 1.6sec wave-period, showing the build-up of pore-pressure at depth of 16.5cm in the soil (D_{50}=45μm), and 42cm water depth (Figure 3.55). Such generation of excess pore-water pressure is similar to that occurring during an earthquake.

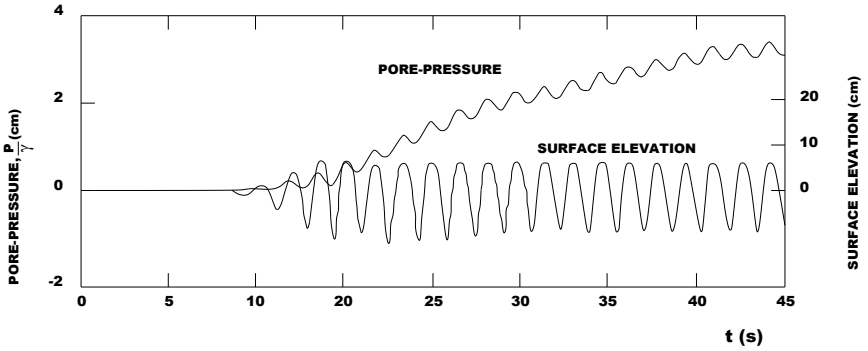

Figure 3.55: Build-up of pore-pressure
(adapted from Sumer *et al.*, 1999).

Sumer & FredsØe (2002) give a review on the many studies devoted to the theoretical and experimental investigation of the build-up of pore-water pressure and the resulting liquefaction of sediments under waves, namely Seed and Rahman (1978); Clukey *et al.* (1983); Barends and Calle (1985); Spierenburg (1987); McDougal *et al.* (1989); de Groot *et al.*(1991); de Groot and Meijers (1992); Tzang *et al.* (1992); Foda and Tzang (1994); Foda (1995); Sekiguchi *et al.* (1995); Tzang (1998); Sassa and Sekiguchi (1999); and Sumer *et al.* (1999).

More recent studies by Sumer *et al.* (2006) and Miyamoto *et al.* (2004) describe the progressive solidification of a liquefied sand layer during continued wave-loading from theoretical and experimental investigation.

The complete sequence of events of sediment behaviour under a progressive wave may be described by reference to Figure 3.56. The first of these events is the build-up of pore-water pressure, when the excess pore-pressure reaches its maximum value (p_{max}) the liquefaction first emerges at the mudline and subsequently spreads downwards. This sequence of processes is followed by dissipation of the accumulated excess pore-water pressure and compaction of the sediment which is followed by the formation of bed ripples.

With the introduction of waves, pore-pressure begins to build-up as the seabed grains experience shear strains/deformations. This shear strains tend to rearrange the soil grains into a more dense packing that is with less space in the voids, at the expense of the pore-volume. If drainage of pore-water is impeded, which happens in fine sediment soils as the accumulated pore pressures will not dissipate as rapidly as they develop, pore-pressures increase progressively with the shear load. This leads to the transfer of stress from the soil skeleton to the pore-water inducing a decrease in effective stress and shear resistance of the soil. If the accumulated pressure reaches the overburden-pressure value (that is the submerged weight), the soil will be liquefied. As mentioned, this process is called the residual liquefaction.

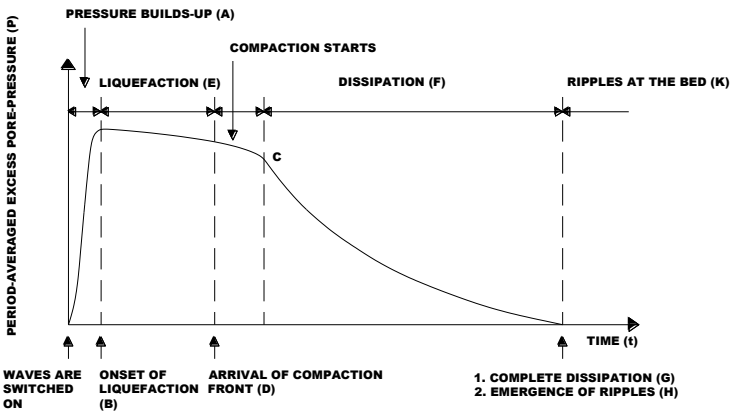

Figure 3.56: Schematic description of time series of period-averaged excess pore pressure at depth z
(adapted from Sumer *et al.*, 2006).

The second mechanism generating soil liquefaction is related to the phase-resolved component of the waves. As explained in the book by Sumer & FredsØe (2002) this kind of liquefaction occurs during the passage of the wave-trough. As seen from figure Figure 3.57, the pore-pressure (in excess of the hydrostatic pressure) under the wave-trough has a negative sign. Figure 3.58 displays a sketch of the pressure distributions in soil across depth under wave trough, for a saturated soil (there is no gas/air in soil), and an unsaturated soil (there is gas/air in soil). In the latter case, the pore-pressure is dissipated at a very fast rate with the depth and thus there is an awful amount of pressure gradient generated, while in the case of a completely saturated soil, the pressure gradient is not tremendously large. This upward-directed pressure gradient induces a lift force on the soil, which exceeding the submerged weight of soil causes momentary liquefaction.

As seen from the preceding description, the essential components of the liquefaction mechanisms are the quantities wave-induced shear stresses in the soil, the pore-water pressure (phase-resolving component) and the ground-water flow, which are governed by the Biot's consolidation equations. This approach was first discuss by Biot (1941, 1956), latter modified by Yamamoto *et. al.* (1978), Madsen (1978), and Mei and Foda (1981) – also described by, *e.g.*, Sumer and FredsØe (2002) and Mei (1989). Sumer and FredsØe (2002) provide a thorough derivation of the Biot's equations, which may be summarized in the following six steps:

- Equilibrium conditions for a stress field;
- The stress-strain relationships;
- The stress-strain relationships in the case of a poro-elastic soil, that is a soil where voids are filled with water, thus the normal stresses are apportioned by soil and by water,
- The equations of equilibrium for a pore-elastic soil,
- Darcy's law;
- Continuity equation for the pore-water.

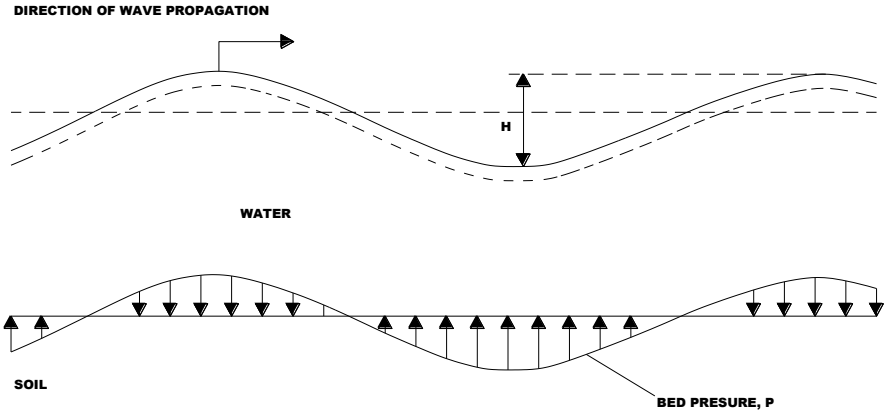

Figure 3.57: Pressure variation due to a progressive wave over a horizontal seabed (adapted Sumer and FredsØe, 2002).

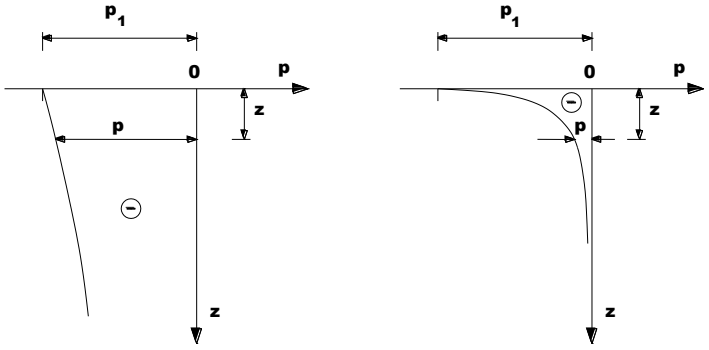

Figure 3.58: Pressure distributions in soil across depth, saturated soil (left panel), and unsaturated soil (right panel) (adapted from Sumer and FredsØe, 2002).

To obtain the following four equations, corresponding to three equations of equilibrium [Eqs (3.104) to (3.106)] and one storage equation [Eq. (3.107)], known as the Biot's consolidation equations, the entire set of equations are Sumer and FredsØe (2002) and cross-references, should be consulted for the full derivation steps.

$$G\nabla^2 u + \frac{G}{1-2\upsilon}\frac{\partial \epsilon}{\partial x} = \frac{\partial p}{\partial x} \tag{3.104}$$

$$G\nabla^2 v + \frac{G}{1-2\upsilon}\frac{\partial \epsilon}{\partial y} = \frac{\partial p}{\partial y} \tag{3.105}$$

$$G\nabla^2 w + \frac{G}{1-2\upsilon}\frac{\partial \epsilon}{\partial z} = \frac{\partial p}{\partial z} \tag{3.106}$$

$$\frac{k}{\gamma_w}\nabla^2 p = \frac{n}{K_w}\frac{\partial p}{\partial t} + \frac{\partial \epsilon}{\partial t} \tag{3.107}$$

in which G is the shear modulus, which may be linked to the Young's modulus E and the Poison's ratio υ by:

$$G = \frac{E}{2(1+\upsilon)} \tag{3.108}$$

The quantity ϵ is termed the volume expansion, Eq. (3.109). k is the coefficient of permeability of the soil (may be estimated by the Hazen formula as given in section 3.3.1), n is the porosity, and γ_w is the specific weight of water. The apparent bulk modulus of the pore-water, K_w, is related to the true bulk modulus of pore-water without air/gas, K_{0w}, as given by Eq. (3.110).

$$\epsilon = \frac{\partial u}{\partial x} + \frac{\partial v}{\partial y} + \frac{\partial w}{\partial z} \tag{3.109}$$

$$\frac{1}{K_w} = \frac{S_r}{K_{0w}} + \frac{1-S_r}{p_0} \tag{3.110}$$

in which S_r is the degree of saturation (=1 for saturated soils), and p_0 is the absolute pressure.

The Biot's consolidation equations are to be solved to get the four unknown quantities, namely u, v, w, and p. Once the solution is obtained, then the stresses in the soil can be found from Eqs. (3.111) to (3.113):

$$\sigma_x = 2G\left(e_x + \frac{\upsilon\,\epsilon}{1-2\upsilon}\right) - p \tag{3.111}$$

$$\sigma_y = 2G\left(e_y + \frac{\upsilon\,\epsilon}{1-2\upsilon}\right) - p \tag{3.112}$$

$$\sigma_z = 2G\left(e_z + \frac{\upsilon\,\epsilon}{1-2\upsilon}\right) - p \tag{3.113}$$

The quantities e_x, e_y,and e_z, represent the strains, namely the linear deformation per unit length, as given by Eq. (3.114).

$$e_x = \frac{\partial u}{\partial x}, \qquad e_y = \frac{\partial v}{\partial y}, \qquad e_z = \frac{\partial w}{\partial z} \tag{3.114}$$

In order to solve the *Biot* equations the following boundary conditions should be specified: *(i)* pressure at the bed surface; *(ii)* stresses at the bed surface, and *(iii)* the boundary conditions at large depths.

To the purposes of the present contribution is above all pertinent to focus on the wave-induced pore-water pressures, as it was one of the quantities measured during the experimental work. Reference is made to Sumer and FredsØe (2002) regarding the details of the stresses in soil under a progressive wave.

The pressure generated by a progressive wave, at a given place in the water column is given by the static and the dynamic components of pressure. Definition sketch is provided in Figure 3.59.

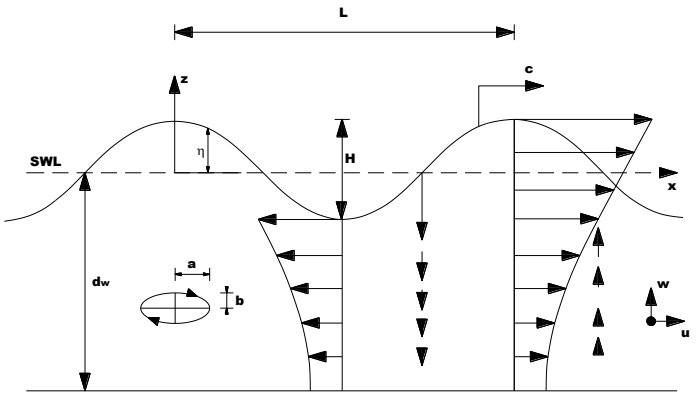

Figure 3.59: Definition sketch.

From the two-dimensional small-amplitude or linear wave theory, the fluctuating component in the water column ($-d_w \leq z \leq 0$) is given by Eq. (3.115). More detail on the small-amplitude wave theory can be found in, *e.g.*, USACE (2008), and Kamphuis (2000).

$$p(x,z,t) = -\rho\, g\, z + \rho\, g\, \frac{\cosh\left[\frac{2\pi}{L}(d_w + z)\right]}{\cos\left(\frac{2\pi d_w}{L}\right)} \frac{H}{2} \cos\left(\frac{2\pi\, x}{L} - \frac{2\pi\, t}{T}\right) \tag{3.115}$$

It is also important to calculate the wave-induced pore-water pressures in the soil with depth, as they have an influence on the geotechnical stability of structures, and may have an effect on the sediment transport.

Many theoretical and experimental results indicate that wave-induced pore-pressures in the soil suffer attenuation with depth (see, *e.g.*, TØrum, 2007; Massel, *et al.*, 2004 and 2005; de Rouck and Troch, 2002; Mei, 1989).

At the mudline the dynamic pressures in the water column and sand surface should be the same, thus there is no attenuation. At sufficiently large depths into the seabed ($z \to \infty$), no pore-water pressure will develop ($p \to 0$).

A recently published technical note by TØrum (2007) is a good reference to the most recent, and relevant, publications on this topic. Of particular interest to the present investigation, is the author's comparison of the wave-induced pore-pressures in sand bottoms measured by de Rouck (1991) – a summary of which may be found in the papers by de Rouck and Troch (2002), Troch (2001), and Troch *et al.* (1998), and calculated pressures by the method developed by Mei and Foda (1981) – also described by Mei (1989).

Mei and Foda (1981) expression for the wave induced pore pressure ratio from waves traveling over a horizontal bottom with an infinite thick homogeneous and isotropic soil layer should be first introduced before discussing the conclusions drawn by TØrum (2007). That expression, as given by Eq. (3.116), follows to some extent previous work on the mechanics of porous media, which have amplified the Biot theory.

$$\frac{p(z)}{p(0)} = \left[\frac{1}{1+m} e^{-\lambda z} + \frac{m}{1+m} e^{(i-1)\frac{z}{\sqrt{2}\delta}}\right] e^{i(\lambda x - wt)} \tag{3.116}$$

where *p(z)* is the wave-induced pore-pressure at depth *z* below the bed surface and *p(0)* is the wave-induced pressure at the bed surface, and *i* the imaginary unit, $i = \sqrt{-1}$. The quantities *m*, and δ are given by Eqs. (3.117) and (3.118).

$$m = \frac{n}{1-2\upsilon} \frac{G}{K_w} \tag{3.117}$$

$$\delta = \left(\frac{k}{\gamma} \frac{G}{w}\right)^{1/2} \left[\frac{nG}{K_w} + \frac{1-2\upsilon}{2(1-\upsilon)}\right]^{-1/2} \tag{3.118}$$

Figure 3.60 shows a comparison of the calculated and the measured pressure amplitudes in sand for storm waves with 6.25s wave period. TØrum (2007) concluded from his analysis that the air/gas content during the prototype pore-pressure measurements at Zeebrugge breakwater, in Belgium, was on average 3%. The author presented some inconclusive reasons for that, namely the deterioration of organic material or air trapped in pores during a lower water level several thousand years ago.

Similar conclusions were drawn by Massel, *et. al.* (2005, 2004). The authors discuss attenuation of wave-induced pore-water pressure in shallow water based on the comparison of theoretical results with experimental data collected in the Large Wave Channel in Hannover. The former authors have estimated apparent bulk modulus of the pore-water, K_w, from the best fit of the experimental pore-pressures to the theoretical ones, concluding that it is very probable that during the sand layering in the wave channel, some pores within the beach body will be saturated by air/gas micro-bubbles.

TØrum (2007) study does not address the topic of liquefaction due to wave-induced gradients; yet, the author points to the fact that the extent to what wave-induced pore-pressures induce liquefaction at the sea bottom and the extent to what this will affect sand transport is still under debate.

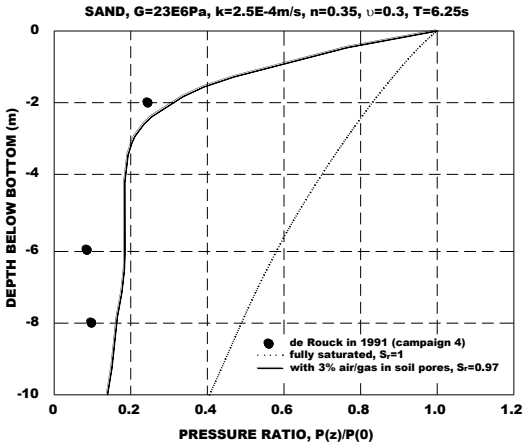

Figure 3.60: Wave-induced pore-pressure amplitude ratios in sand
(adapted from TØrum, 2007).

3.4.4. Concluding remarks

Scour may reduce the level of the beach in front of a structure and increase the risk of undermining. Moreover, wave induced liquefaction may reduce the bearing capacity of the seabed around a structure.

It has become clear that scour is a complex processes, for which there are no specific (generally accepted) guidance for estimating maximum scour depth and other characteristics of scour development. The preceding analysis shows that the scour characteristics may be a function of the nine non-dimensional parameters indicated in Eq. (3.91) and the time scale is expected to depend on those parameters as well.

Several field, experimental and numerical studies have developed non-dimensional relationships for predicting scour, typically expressing relative scour in terms of the scour depth to incident wave-height ratio (S_d/H). Table 3.VI is an attempt to combine and compare existing methods of predicting scour depth, shortcomings are given as well.

Overall, two main shortcomings may be identified in the available results. The first is that the great majority of the studies were performed for regular standing wave conditions, rather than irregular waves with a natural spectral shape. The second main shortcoming concerns the dominant mode of sand transport, as for the majority of the movable-bed model wave-tests performed the no-suspension-mode has been the dominant mode of sand transport which does not correspond to what occurs in the natural scale.

Table 3.VII: Comparative of predicting scour depth formulations.

Ref.	Formulation	Applicability	Other Remarks
Xie (1981)	$\frac{S_d}{H} = \frac{C}{\left[\sinh\left(\frac{2\pi d_w}{L}\right)\right]^{1.35}}$ C :: *0.4 for fine sand (suspension)* *0.3 for coarse sand (no-suspension)*	Valid for :: *Normally incident, non-breaking regular waves* *Flat sandy bed in front of a vertical-walled structure* Limits :: $\frac{U_{bmax}-U^*}{w_s} \geq 16.5$ (suspension) $\frac{U_{bmax}-U^*}{w_s} < 16.5$ (no-suspension)	*Similitude is achieved when* $\frac{U_{bmax}-U^*}{w_s}$ *remains the same for both, model and prototype.*
Sumer and FredsØe (2000)	$\frac{S_d}{H} = \frac{f(\alpha)}{\left[\sinh\left(\frac{2\pi d_w}{L}\right)\right]^{1.35}}$ f(α) :: $f(\alpha) = 0.3 - 1.77e^{-\frac{\alpha}{15}}$	Valid for :: *Normally incident, non-breaking regular waves* *Flat sandy bed in front of a sloped structure* Limits :: $\frac{U_{bmax}-U^*}{w_s} \geq 16.5$ (suspension) $\frac{U_{bmax}-U^*}{w_s} < 16.5$ (no-suspension	*Replication of* Xie (1981) *for a sloped structure.*
O'Donoghue (2001)	$\frac{S_{max}}{H} = 1 - \frac{\left(\frac{d_w}{L}\right)}{0.002 + \left(\frac{d_w}{L}\right)^{2.9}}$	Valid for :: *Normally incident, non-breaking regular waves* *Coarse sand (no-suspension)* *Vertical-walled structure* Limits :: $0.5 \leq \frac{d_w}{L} \leq 0.2$	*Best-fit from* Xie (1981).
Hughes and Fowler (1991)	$\frac{S_{max}}{(U_{RMS})_m T_p} = \frac{0.05}{\left[\sinh\left(\frac{2\pi d_w}{L}\right)\right]^{0.35}}$	Valid for :: *Normally incident, non-breaking irregular waves* *Fine sand (suspension)* *Flat sandy bed in front of a vertical-walled structure* Limits :: $0.05 \leq \frac{2\pi d_w}{L} \leq 3.0$	*Modification of* Xie (1981) *for irregular waves.*
Fowler (1992)	$\frac{S_{max}}{H_0} = \left(22.72\frac{d_w}{L_0} + 0.25\right)^{\frac{1}{2}}$	Valid for :: *Normally incident, breaking, regular or irregular waves* *Beach in front of a vertical-walled structure* Limits :: $-0.011 \leq \frac{d_w}{L_0} \leq 0.025$ $0.015 \leq \frac{H_0}{L_0} \leq 0.04$	Fowler (1992) *pooled data set of a number of experiments.* McDougal *et al.* (1996) *found an inverse dependency between scour-depth and the deep-water wavelength, or wave period.*
McDougal *et al.* (1996)	$\frac{S}{H_0} = 0.41\beta^{0.85}\left(\frac{L_0}{H_0}\right)^{1/5}\left(\frac{d_w}{H_0}\right)^{1/4}\left(\frac{H_0}{d_w}\right)^{1/3}$	Valid for :: *Normally incident, breaking waves* *Beach in front of a vertical-walled structure*	*Numerical model results, which have been compare with* SUPERTANK *and* Fowler (1992) *experimental results.*
Sutherland *et al.* (2008)	$\frac{S_{max}}{H_s} = 4.5\, e^{-8\pi\left(\frac{d_w}{L_m}+0.01\right)}\left(1 - e^{-6\pi\left(\frac{d_w}{L_m}+0.01\right)}\right)$	Valid for :: *Normally incident, breaking waves* *Beach in front of a vertical seawall* Limits :: $-0.013 \leq \frac{d_w}{L_m} \leq 0.18$	*It is an envelope for a number of existing scour predictors.* *Conservative formulation which may be used in the absence of site-specific information on beach slope.*

In regard to the referred shortcoming, some researchers have suggested the usefulness of defining an equivalent wave-height with certain statistical significance (*i.e.*, a wave-height with the same effects on scour as those of a regular wave train with the same height). However, as noted by Hughes and Fowler (1991) it is not clear how to apply a scour predictor developed from regular wave laboratory experiments to a natural situation with irregular waves where wave reflections can be expected to become increasingly out of phase with distance from the wall.

It may be noted as well that all experimental studies were performed with plane beaches (several with flat beaches). This is a necessity, as experiments have to be made from controllable laboratory conditions, yet it would be important to try to investigate the scour process on a developed profile, as the naturally occurring morphologic perturbations exert strong control over shallow-water wave transformation, and vice-versa. Within these interactions, the mode of transport may also change, which may lead to the replacement of the deposition areas with the scour areas, and vice-versa. The latter effect will cause scouring in the previous deposition areas, and will eventually result in an overall scouring in front of the structure.

A more general remark that can be drawn from what has been briefly described is that the available datasets tend to support the most widely used rules-of-thumb, being that (see, *e.g.*, USACE, 2008): *(i)* maximum scour at the toe of a sloping structure is expected to be somewhat smaller than that calculated for a vertical wall at the same location and under the same wave conditions; hence, a conservative scour estimate is provided by the vertical-wall scour prediction equations; *(ii)* structures with larger porosity will experience smaller wave-induced scour; *(iii)* scour depths are significantly increased when along-structure currents act concurrently with wave; *(iv)* obliquely incident waves may cause larger scour than normally incident waves because the short-crested waves increase in size along the structure. Also, oblique waves generate flows parallel to the structure; *(v)* the loss of shear resistance in saturated, cohesionless soils during dynamic loading may have catastrophic consequences.

The study of wave-induce pore-pressure, namely the build-up of pore-water pressure as the seabed grains experience shear strains/deformations, and the attenuation of wave-induced pressure in shallow water with depth, is a key topic to assess the liquefaction potential. Wave-induced pore-water pressures may be relevant as well in understanding the surf zone hydrodynamics and the sediment transport mechanisms.

3.5. Summary and conclusions drawn from current state-of-the-art

Geotextile encapsulated sand-systems are experiencing since few decades a growth in interest for their wide utilization in coastal engineering and management, particularly for their use as permanent coastal structures. Recent years have witnessed a great development of the manufacturing sector of plastics and related products in both, new uses, and new products.

The herein presented literature survey to the state-of-knowledge with respect to the application of geotextile as containment systems in coastal engineering, the understanding of cross-shore sediment transport, and the scour development around coastal structures due to normally incident waves has identified the following research and guidance needs:

- Wave tests on the stability of geotextile encapsulated sand-systems against scour and more widespread beach lowering;
- Detailed processes research to improve the understanding of cross-shore sediment transport; the dependence of sediment processes and the ensuing morphological response on the sediment properties, the hydrodynamic conditions, and the interplay between both has been established but needs to be further clarified and quantified;
- Forcing mechanisms for instantaneous motion of individual particles and of large sediment bodies, which is relevant for both cross-shore transport, and the stability of geotextile sand-filled elements;

- Long-term effect on stability of sediment movement inside the elements; continuing work to incorporate the effects of deformation on stability; this could include the following three items;
- Contribution of friction to stability addressing the aspects where there is still considerable uncertainty, *e.g.*, the influence of the interface friction characteristics (*i.e.*, the friction coefficient between elements, and the friction coefficient between the elements and the foundation), and the quantification of the contributing weight of overlaying elements (which may change due to the migration of sand within the element; and filling-material being washed through the geotextile), and the length of contact areas (which may change due to the individual displacements), to the development of friction;
- Friction to be explicitly incorporated into stability formulae, as it presumably the most important stabilizing factor;
- Effect of geotextile permeability on sediment movement inside the elements, including the assessment of the potential for liquefaction of sand inside the containers;
- Consideration should be given to attempt to quantify the relevancy of the aspects that require the most attention in regard to are: *(i)* filling percentage; *(ii)* density (depends on the filling-material); *(iii)* shape of individual elements (depends partly on the elasticity and thickness of the geotextile); *(iv)* dimensions of individual elements (larger elements are likely less sensitive to sand migration, and are therefore possibly more stable); *(v)* mode of placement (*i.e.*, overlapping, packing, and orientation with respect to the wave direction); *(vi)* geometrical conditions, namely the presence of a slope which influences the hydraulic responses (*e.g.*, wave breaking, wave run-up, and wave run-down), and the loss of height (it can reach up to about 10%) when subject to severe wave attack;
- Consideration should be given to sketch the background against which the decision for one type of scheme/material by comparing, within the same experimental procedure, different protection schemes incorporating different geotextile encapsulated sand-systems;

The research and application of geotextiles and geosystems in coastal engineering is still in its infancy, making its first stuttering steps towards its potential.

4. PROBLEM STATEMENT AND EXPERIMENTAL SET-UP

The present chapter describes the set-up used for the experimental analysis of geotextile sand-filled systems under wave loading and implementation. It is divided in four sections referring to description and problem statement, experimental set-up, instrumentation and data processing, and test conditions.

In section 4.1 the motivation and challenges of the present research programme are explained with respect to the summary and conclusions drawn from current state-of-the-art, as seen in the previous chapter, and to the application of the results in coastal engineering practice.

The experiments were conducted in a section of the Hydraulics Laboratory wave basin, Department of Civil Engineer (DEC) of the Faculty of Engineering of the University of Porto (FEUP) that is described in section 4.2. The overall summary of test conditions is given as well in section 4.2. Next in section 4.3 the instrumentation used in the experiments and calibration are introduced. Post-processing of the data measured by those devices is discussed in section 4.4.

4.1. Description and problem statement

The application of geosynthetics and geosystems in coastal engineering and management still has a very incidental character, and it is usually not treated as a serious alternative to the conventional solutions. The explanation for this lays on uncertainty, partly related to the lack of suitable design methods, and partly related to durability and life-time performance issues.

The initial interest on the incorporation of synthetic fabrics in coastal engineering was rather focused on temporary and emergence works but in recent years attention has turned to the use of these materials in permanent structures and as alternative to more traditional materials and systems. The reasons for this shift in attention have been explained over Chapter 2 of the present contribution, while it has become clear from Chapter 3 that considerable research still needs to be performed.

Efforts in this research concentrated on *(i)* the stability of geotextile encapsulated sand-systems against scour and more widespread beach lowering; *(ii)* the cross-shore component of sediment transport to study the response of a dune-beach system under conditions of erosion, accretion, persistent erosion and conditions alternating between periods of erosion and accretion; and *(iii)* the comparison of four different coastal protection schemes against each other, and against a reference case.

In total five models, corresponding to three erosion control systems with two configurations, one nearshore detached submerged breakwater with four configurations, and one non-protected dune-beach system as reference, were taken for the investigation. Model characteristics were derived from the prototype dune-beach system of Estela, as described in section 2.3 of the present contribution and further explained in this chapter.

The overall performance of each coastal protection scheme was evaluated against its hydraulic stability under wave loading and on its efficiency in maintaining a beach and in protecting the shoreline, based on the measurement of wave-induced morphodynamic changes over shorter and longer time-scales. As detailed bellow, five perspectives were considered in this assessment.

- Stability of geotextile encapsulated sand-systems under wave-loading;
- Scour-depth development: scour holes development and scour-and-deposition patterns over the cross-shore length of the model; observations of erosion and backfilling during a test duration; dependency between scour-depth and the non-dimensional variables given by Eq. (3.91);
- Storm response: changes in cross-shore beach-profile when exposed to storm conditions lasting for a test duration of 30minutes; beach levels drawdown at the structure and more widespread beach lowering;
- Recovery between storms: response to the changing forcing conditions; build up during swell conditions, followed by beach levels drawdown during storm conditions; volumetric changes due to seasonal variability; and
- Coastal evolution: beach-profile change under persistent erosional conditions.

The application of the research results to coastal engineering practice is illustrated in Chapter 5, and further summarized over Chapter 6.

4.2. Experimental set-up

The experiments were carried out in a partition of the wave basin of DEC-FEUP Hydraulics Laboratory. The basin is 28m long, 12m wide but was partitioned to a wave channel of 2.25m wide, comprising 3 wave-paddles (Figure 4.1a). The movable-bed model nearshore hydrodynamics and relevant sediment parameters were scaled to Froude similarity (see further details in paragraph 4.2.3). At one end irregular waves of varying significant wave-height and period but with a constant spectral shape (JONSWAP spectrum) were generated in working water-depth of 0.58m, which corresponds to the mean water level in prototype.

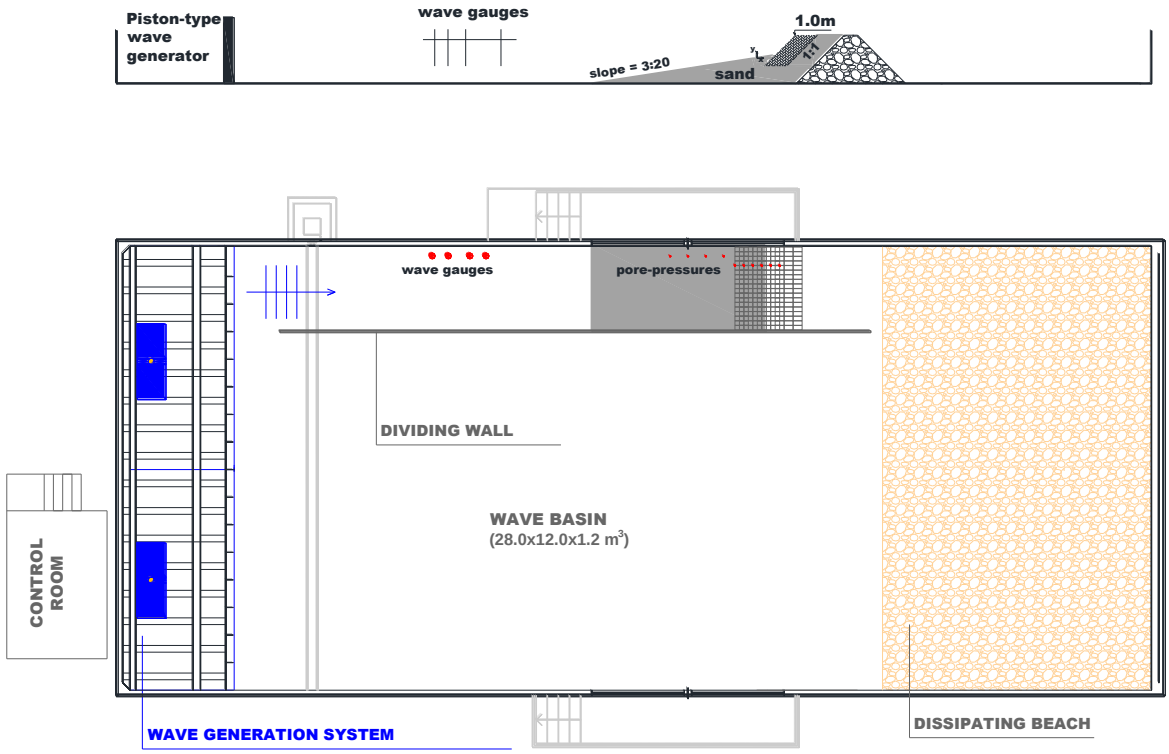

Figure 4.1: Experimental set-up in the wave basin of DEC-FEUP Hydraulics Laboratory:
(a) cross-section (top panel); (b) plan view (bottom panel).

A plane beach (gradient β=0.15) started 9.7m from the wave paddles (Figure 4.1b) followed by a dune (or erosion control system). Surface elevations were recorded in front of the beach slope (Figure 4.1b) from an array of four wave probes, which are described in section 4.3.3. Miniature pore-pressure sensors (described in paragraph 4.3.2) were installed to study wave-induced pore-pressure variations. The beach-profile was surveyed at the end of each wave-run segment using a 2D-bed profiler (described in paragraph 4.3.4) that drives along a support beam. The origin of the horizontal co-ordinate, x, and the origin of the vertical co-ordinate, z, is taken as the intersection of the still water line with the beach face, positive onshore (Figure 4.1b). A 10cm square grid was installed on the glass wall of the basin allowing the visual inspection of profile changing during experiments and providing a reference in viewing the visual recording of the tests.

Time-series data and profiles were collected from over 150 movable-bed tests, with different models and wave conditions. The following paragraphs provide insight into the planning and design of the scale model tests and justify how they were derived from prototype.

4.2.1. Considerations on choice of model scale

The fundamental condition to be satisfied in a model test is that the model must behave in a manner similar to the prototype (Goda, 2000) which usually implies similarity in the geometric shape, in the kinematics of the various motions, and in the dynamic forces acting in the model and in the prototype. Failure to reflect geometric, kinematic and dynamic quantities and properties of the prototype in the model introduces uncertainty in the interpretation of the results measured from the physical model. However, as seen in the previous chapter, complete similarity is, to say the least, seldom possible and thus, several model laws of similitude have been derived based on the predominant forces for which dynamic similarity is to be maintained.

In hydraulic model tests concerning sea waves, the viscosity and surface tension of water usually do not play significant roles, leaving inertia and gravitational forces as the governing forces (see, *e.g.*, Dalrymple, 1985; Hughes, 1993; and Goda, 2000). Therefore, scale measurements for coastal models prediction must always be performed with respect to Froude similarity, which dictates that the scales for the time and velocity must be equal to the square root of the length scales.

Typically a model test on sea waves is undistorted because the horizontal and vertical motions of water particles by wave action should be reproduced with the same scale. A model is called undistorted when it is made with the same geometric scale in the horizontal and vertical direction, when otherwise the model is called distorted. By using an undistorted model the length scale, which is the ratio between a representative unit length in the model and in the prototype, as given by Eq. (3.13), must be the same for all parts of the model. The geometric scale, N_L, is usually selected as the largest model possible to obtain results of highest possible accuracy.

For the 2D-experiments described in this thesis the selected model scale was based on considerations of the size of the prototype dune-beach system, the size of the available facility, grain size diameters, and controlling factors with respect to the limiting values of the period and height of the model waves.

As a rule of thumb, Goda (2000) suggests that for irregular waves the significant wave-height is best set above 0.10m and that the significant wave-period of model waves is preferably longer than 1.0s and never shorter than 0.8s.

4.2.2. Wave conditions

The incident waves were chosen from the statistical analysis by Coelho (2005) of the data recorded by the oceanographic buoy at *Leixões* from 1981 to 2003.

The author observed that the month of December is the one with the higher number of storm occurrences in a month (about 20% of month records), while the months of June, July, August never experience storm events. The years 1993, 1998, and 1999 where the ones with the higher number of storm occurrences in a year, slightly outpacing 15%. Globally, 8.6% of records are in a situation of storm.

50 cases of persistent storm were observed in the data in analysis. A storm is when records are collected at intervals of less than the usual 3 hours and the significant wave-height is over 3m. A persistent storm is when there are at least ten storm records over a period exceeding 8 hours.

The storm with greater duration (about 164h) was held from December 26, 1998, and January 1, 1999, during which 230 values of significant wave-height and the respective periods and wave direction have been recorded. During that period, the maximum significant wave-height was 8.89m and the average wave-height was 5.31m. Twelve records had duration of over 48h. The average length of persistent storm event is about 34h.

Table 4.I summarizes the statistical analysis by Coelho (2005).

From this study is possible to find that the significantly more frequent wave-heights range from 0.5 to 2.5m, with ~72% of cases, the maximum wave-height being recorded was 9m, which does not mean that there were no upper ceilings. Wave-heights higher than 2.5m correspond to ~27%, from which no more than 11% above 5.5m. Only 1% of the records are from waves lower than 0.5m. The more frequent values of wave period vary between 7 and 11s, with less than 4s and higher than 17s as minimum and maximum observed respectively.

Table 4.I: Number of records by class of significant wave-height, H_s (m), and respective wave periods, T_p (s), with basis on the records by the oceanographic buoy at *Leixões* from 1981 to 2003 (modified from Coelho, 2005).

	≤ 0.5	**0.5-1.5**	**1.5-2.5**	**2.5-3.5**	**3.5-4.5**	**4.5-5.5**	**5.5-6.5**	**6.5-7.5**	**7.5-8.5**	**8.5-9.5**	**Σ**
≤ 4	9	6									**15**
4-5	18	219									**237**
5-6	63	1008	198								**1269**
6-7	69	2006	761	17							**2853**
7-8	70	2246	1094	158	3						**3571**
8-9	19	1952	1472	368	42						**3853**
9-10	5	1454	1549	627	150	45					**3830**
10-11		897	1374	727	253	112	23				**3386**
11-12	1	423	1047	711	333	262	63	8			**2848**
12-13		134	476	471	320	322	135	22	2		**1882**
13-14		21	140	240	202	242	148	74	10	2	**1079**
14-15		4	24	71	98	199	80	50	23	8	**557**
15-16		2	12	20	20	96	44	17	12	5	**228**
16-17			5	4	5	17	36	5	6	3	**81**
> 17			2	3	1	4	8	1			**19**
Σ	**254**	**10372**	**8154**	**3417**	**1427**	**1299**	**537**	**177**	**53**	**18**	**25708**

The controlling factors with respect to the limiting values of the period and height of the model waves were determined in correspondence with the statistical analysis provided in Coelho (2005) along with the threshold of maximum wave-height that can be achieved at a particular frequency which is limited by either the performance of the wave generation system (maximum stroke, velocity and force achievable) or the wave breaking.

The experiments were conducted only for irregular waves. It has been demonstrated many times by several authors (see, *e.g.*, Goda, 2000) that the use of regular waves with height and period equal to those of significant wave can give inconsistent or erroneous results in the analysis of wave transformation and action of waves. Therefore, in this research, the irregularity of wave form as an important feature of waves in the sea has been taken.

4.2.3. Movable-bed model

The general principles of sediment transport in coastal regimes have already been considered in the previous chapter. So have been the major requirements for proper design of the movable-bed model and possible shortcomings. In the present research the following procedures are taken forward while selecting the scaling criteria and scale ratios of the models employed:

- Geometrically undistorted model;
- The nearshore hydrodynamics and relevant sediment parameters are modeled to Froude similarity;
- The movable-bed model is composed of sand material;
- The dominant mode of transport is suspended load transport; and
- The movable-bed model should be made as large as possible so that the character of the wave breaking process is properly simulated, *i.e.*, so that viscous and surface tension effects are negligible.

The first approximations to the beach slope and sand material in the model have been derived from prototype. As far as the beach slope is concerned, it was kept as a plane slope for most of the experiments, to facilitate the direct comparison of the measurements. With respect to the sand material, sediment transport scaling rules, as described in *e.g.* Hughes (1993), Oumeraci (1993), and Dalrymple (1985), were calculated based on samples collected from the prototype in two beaches along the NW Portuguese coast at different positions along- and across-shore. Sieving curves of both the sands, prototype and model, are given in Appendix A.

Such scaling rules define the criteria for dynamic similarity of sediment processes based on prototype-to-model scale criterion. Those scaling rules have already been identified in paragraph 3.2.2 of the previous chapter and are as follows:

- Grain size Reynolds number, which describes the flow regime in the bottom layer, as given by Eq. (3.22);
- Mobility number, which describes both the initiation of motion and the transport mode, as given by Eq. (3.23);
- Relative sediment density, which describes the density of the sediment related to that of the surrounding fluid, as given by Eq. (3.24);
- Relative length, which describes the bed topography, as given by Eq. (3.25); and
- Relative fall speed criterion, which describes the restoring forces opposing turbulent entraining forces acting on the particle, as given by Eq. (3.26).

As expected, satisfying all of the above scaling criteria is impossible; thus it is necessary to identify the key dimensionless parameters or physical features related to the hydrodynamic and sedimentary processes that must be held constant between prototype and model. In this respect, the prevailing processes to be preserved in prototype-to-model were the characteristics of sediment transport dynamics in the nearshore.

According to Hughes (1993), in the nearshore region, turbulent water motions play a greater role in mobilizing and transporting sediment; and in this region there is increasing evidence that the dimensionless fall speed parameter, as given by Eq. (3.26), should be similar in both prototype and model.

van Rijn (2006), Jiménez and Madsen (2003) and further references cited therein include several of the most important formulas to compute the fall speed of natural sediments, for example, Zanke (1977), Hallermeier (1981), Dietrich (1982), van Rijn (1984), Julien (1995), Soulsby (1997), Cheng (1997), Sistermans (2000), Ahrens (2000, 2003), and Jiménez and Madsen (2003), for quartz particles, and for calcareous particles the ones from van der Meulen (1988), and Smith and Cheung (2003).

In the current investigation, the sediment fall speed of both the sands, prototype and model, were calculated using Hallermeier's relationships, Eqs. (3.40) to (3.42).

The median grain size diameter of the prototype sand, as presented in Table 4.II, corresponds to median grain size diameter of the sand referenced as intermediate 2 (see Appendix A). The choice was based on the gradations of the grain size distribution which is similar to the sand referenced as SP55 that is used in the model. SP55 has been chosen within the commercially available sand, also considering the controlling factors with respect to the limiting values of the period and height of the model waves, as described earlier. The specific gravity of the model sediment, as given in Table 4.II, is calculated from the average value of a range of specific weights for SP55 as given by, *e.g.*, Caldeira and Gonçalves da Silva (2000).

Table 4.II provides sediment properties for both sands prototype and model. The length scale model N_L was set equal to approximately 12.

Table 4.II: Sediment properties.

Parameter	Prototype	Model
Median grain size diameter (D_{50})	453μm	273μm
Specific gravity (Ss)	2.65	2.55
Immersed sediment buoyancy (ρ')	1.65	1.55
Immersed sediment grain buoyancy (A)	1017	310
Sediment fall speed (w_s)	5.578cm/s	3.383cm/s

4.2.4. Geotextile encapsulated-sand systems

Three types of geosystems were used in the model tests; sand-filled containers, and sand wrapped around geotextile sheets made both from commercially available non-woven geotextile filters, and geotextile tubes of different sizes made from commercially available woven geotextile filters.

Although the geosystems used in the model tests were made from commercially available geotextile materials, they are not obviously suitable for use in the prototype. Taken into account what have already been considered over the previous chapters, about the materials, and about scaling relationships, the following scaling aspects would require some consideration while scaling down the material properties: stiffness and tensile strength of the geotextile during wave experiments; stiffness and tensile strength of the geotextile during filling; and sand tightness.

The proper scaling of several of the former aspects is not possible to fulfill, so a compromise is deemed necessary. Here it is assumed that the geotextiles in the model are relatively too strong (about 1:1 to 1:3 of the prototype geotextiles); yet, since they are not loaded to rupture it can be neglected. In regard to filling, the strength had only to ensure no damage to the geotextile during handling. Flexibility is warrant by a thinner geotextile. The hydraulic permeability of a GSC-structure depends mainly on the size between neighbouring containers (Recio, 2007), thus so long the geometry is properly scaled the model represents adequately the permeability in the prototype. This means that aspects such as dimensions, placement and shape, also related to filling percentage and geotextile stiffness, have to be taken forward into the model. Both aspects, filling percentage and stiffness, may not be neglected in model, as failure to address them properly may result in a too large permeability in model compared to prototype by lower adaptation curvatures of the containers to the adjacent ones.

The requirements regarding geotextile sand tightness are, as given in Eq. (4.1) and (4.2), see, *e.g.*, CUR (2006), and van Steeg *et al.* (2010). The quantity C_u is the uniformity coefficient, as given by Eq. (3.28).

$$O_{90} \leq D_{90} \tag{4.1}$$

$$O_{90} \leq 1.5\, D_{10} \sqrt{C_u} \tag{4.2}$$

According to the grain distribution (see appendix A), D_{90} is equal to 345μm, D_{10} to 186μm, and D_{60} to 291μm, yielding C_u equal to 1.565, as given by Eq. (3.28). The opening sizes of the chosen geotextiles are in agreement with these requirements (see Tables 4.III and 4.IV).

Eleven configurations, divided by the following four categories, have been tested:

- Test Series B: GSC-structure (2 configurations);
- Test Series C: Sand wrapped around geotextile sheets (2 configurations, plus a preliminary one);
- Test Series D: Geotextile tubes (2 configurations); and
- Test Series E: Nearshore breakwater (4 configurations).

A description of each category is given in the following paragraphs while here it is portrayed the set-up of the geosystems employed in each test series.

Approximately 720 geotextile sand-filled containers were pre-fabricated for the experiments. The containers were made by cutting the fabric into suitable rectangular pieces, and then folding and sewing leaving just a 2cm opening at the top for filling. Each bag was then filled with the same (dry) sand as the one used in the model, and the 2cm opening was shut using glue and galvanized steel staples to minimise rusting. A balance was used to ensure each bag was consistently filled to approximately the same weight.

The dimension width of the commonly used geotextile sand-filled container can be related to its length, L, as generally it is about twice as large as its width. The height depends on the filling percentage. The dimensions of an empty container selected as prototype representative has a length of approximately 3.09m by 1.57m wide, which corresponds to an estimate of $1.5m^3$ volume fill at 80% rate (see, *e.g.*, Recio, 2007).

To build the embankment with geotextile sand cushions 5 identical wraps and a final wrap at the slope and base were necessary. The geotextile sand-wraps were made by cutting the geofabric into suitable pieces. During the first experiments with this structure it was found that a significant amount of sand was leaving the cushions through the lateral edges so it was necessary to provide an additional restraint with sand-filled containers.

The technical data of the needle-punched non-woven geotextile selected to the experiments, Secutext® 301GRK C, is presented in Table 4.III; whereas Table 4.IV provides the technical data of the woven geotextile used to fabricate the geotextile tubes, Geolon® PE 300. The technical data of the prototype materials respectively, Terrafix® Soft Rock type R 1006 and Geotube® GT1000, are given as well.

Table 4.III: Needle-punched non-woven geotextile, Terrafix® Soft Rock type R 1006 and Secutext® 301GRK C (after NAUE).

Property	Test Method	Unit	Prototype	Model
Raw material	-	-	Polyester PES, white	Polypropylene PP, white
Mass per unit area	ISO 9864:2005	g/m^2	1000	300
Thickness	ISO 9863-1:2005	mm	5.3	1.6
Tensile strength **MD: machine direction** **CD: cross direction**	ISO 10319: 2008	kN/m	 30 50	 13 22
Elongation at nominal strength **MD: machine direction** **CD: cross direction**	ISO 10319: 2008	%	 50 40	 50 30
Puncture force	ISO 12236:2006	kN	-	3.89
Static puncture (CBR test)	ISO 12236:2006	mm	-	30
Characteristic opening size	ISO 12956: 1999	µm	70	70
Water permeability **VI_{H50}-index** **low-$rate_{H50}$-index**	ISO 11058: 2010	m/s $l/m^2 s$	$1.0x10^{-2}$ 10	$4.0x10^{-2}$ 40

Table 4.IV: Woven geotextile, Geotube® GT1000 and Geolon® PE 300 (after TENCATE).

Property	Test Method	Unit	Prototype	Model
Raw material	-	-	Polypropylene PP, white	Polyethylene PE, black
Mass per unit area	ISO 9864:2005	g/m^2	1000	300
Tensile strength **MD: machine direction** **CD: cross direction**	ISO 10319: 2008	kN/m	 198 189	 40 20
Elongation at nominal strength **MD: machine direction** **CD: cross direction**	ISO 10319: 2008	%	 15 11	 20 20
Puncture force	ISO 12236:2006	kN	20	4
Dynamic perforation (cone drop)	ISO 13433: 2006	mm	6	12
Characteristic opening size	ISO 12956: 1999	µm	416	230
Water permeability	ISO 11058: 2010	$l/m^2 s$	20	65

Three dimensions of tubes were used. In prototype, the diameters of the tubes are Ø1.60m, Ø3.25m, and Ø5.00m, accordingly small, medium and large tube. The theoretical parameters that relate the diameter of the tube with the dimensions of the tube when filled are given in Figure 4.2.

Three large, three medium, and six small sized tubes were pre-fabricated with an edge open. Each geotextile tube was then filled with the same sand as the one used in the movable-bed model, and then the top opening was sewed with a nylon yarn. To ensure all geotextile tubes were consistently filled to approximately the same weight of sand unopened dry-sand bags were used. The larger tubes were filled with 7 bags of 50kg each; the medium with 4 ½; and the smaller with only 2 ¼.

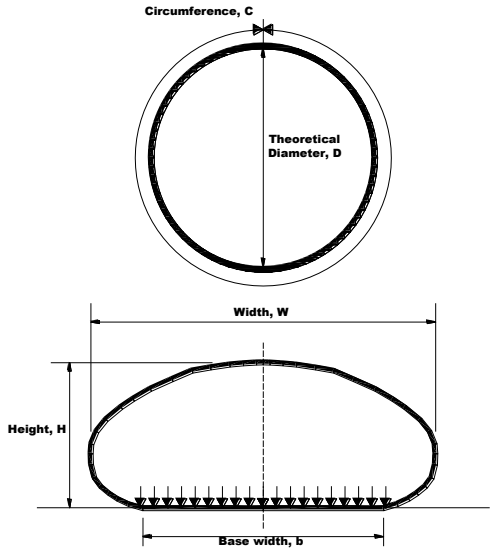

Parameters	With respect to Diameter	With respect to Circumference
Maximum Filling Height	H ~ 0.6 D	H ~ 0.19 C
Filling Width	W ~ 1.4 D	W ≈ 0.45 C
Contact Base Width	b ~ 0.9 D	b ≈ 0.29 C
Transversal Section Area	A ~ 0.65 D^2	A ≈ 0.07 C^2
Average Vertical Tension on Base	σ'_v ~ 0.72 γ D	σ'_v ~ 0.24 γ C

Note: γ is the specific weight of the filling material

Figure 4.2: Geotube® important parameters (after TENCATE).

In Appendix C, several views during the several stages of model construction (filling, sewing, handling, etc.) are given for reference.

4.2.5. Test conditions

Different model layouts are sketched in Figure 4.3, while the test conditions are summarized in Table 4.V.

The water depth in the experiments was maintained constant at 0.58m. The origin coordinates was taken as the intersection of the still-water-level (SWL) with the beach face, positive onshore.

The preparation of the input signal to the wavemaker consisted in the creation of log files with the required parameters for each of the 10 sea states (*i.e.*, name to be used, a description, the directional spreading function, the modal period in s, the significant wave-height in m, and the spectral shape, γ). For these tests a sharply peaked spectrum of the type JONSWAP, with a peak enhancement factor γ=3.3, was used. Refer to Chapter 5 for more detail on such wave spectrum.

Three different models of dune reinforcement made from geotextile sand-filled systems with slope 1:1 were employed in these experiments: several individual geotextile sand-filled containers, designated as Model B (Figure 4.3); a wrapped-around system, designated as Model C (Figure 4.3); and geotextile tubes, designated as Model D (Figure 4.3).

The two variants for each model, configurations 1 and 2, differ from each other by the position of the structure toe, placed at level +0.00m (HZ) that is (x,z)~(0.16,-0.16), and +2.00m (HZ) that is (x,z)~(0.31,0), respectively. All models have the crest height at 0.42m and were built with a 1:1 slope.

Model B was built from several sand-filled containers placed in a double layer with about 60% overlap. 720 containers were used to build B1, and only 576 were necessary to build B2, as the four deepest rows of B1 are removed in B2.

The wrapped around model was designated by Model C. The first layout to be built, experienced significant loss of sand through the lateral edges, and thus it was necessary to provide an additional restraint with sand-filled containers. This restraint was incorporated within the sand cushion, and it was rather slim in comparison to the development of the model in length, and thus its influence on the model results is negligible. In any case, a comparison between both of the layouts is given for reference along with the analysis in the forthcoming chapter.

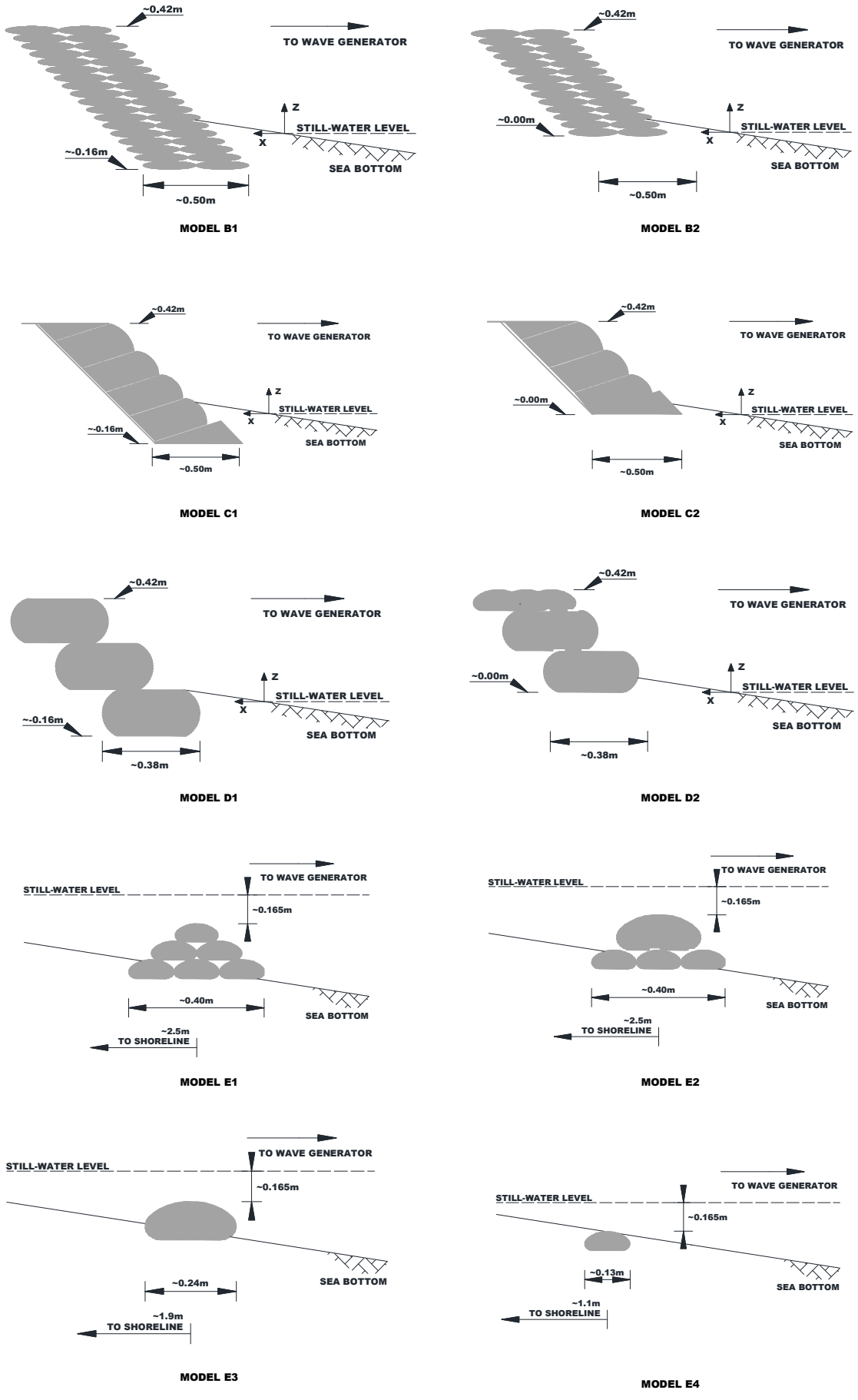

Figure 4.3: Definition sketch of tested models (not to scale).

Table 4.V: Test conditions: sea-states.

Initial Condition	Balance	Sea-State	Prototype		Model	
			H_s [m]	T_p [s]	H_s [m]	T_p [s]
Plane beach-profile slope	Accretion	Sea-State 1	0.5	6	0.04	1.73
		Sea-State 2	0.5	8	0.04	2.31
		Sea-State 3	0.5	10	0.04	2.89
		Sea-State 4	1.0	6	0.08	1.73
		Sea-State 5	1.0	8	0.08	2.31
		Sea-State 6	1.0	10	0.08	2.89
	Erosion	Sea-State 7	2.0	8	0.17	2.31
		Sea-State 8	2.0	10	0.17	2.89
		Sea-State 9	2.0	12	0.17	3.46
		Sea-State 10	1.5	10	0.125	2.89
Wave-changed cross-shore beach-profile	Infilling and again Erosion	Sea-State 8	2.0	10	0.17	2.89
		Sea-State 3	0.5	10	0.04	2.89
	Persistent Erosional Conditions	Sea-State 10	1.5	10	0.125	2.89

Again the two variants of the model (*i.e.*, C1 and C2) differ from each other by the position of the structure toe. From C1 to C2 the model was raised by 16cm, and instead the 5 identical wraps and the final wrap at the slope and base used in C1, only 4 wraps and the final one was necessary to built C2. The slope was built at 1:1 with steps.

Model D was constructed from geotextile tubes. Due to constraints related with the height of the tubes there is an additional difference in configurations 1 and 2, other than the position of the base of foundation, which is the top row. Model D1 consists of three stacked large tubes, while D2 consists of two stacked large tubes and a top row of three small ones. With this change the crest height is approximately on the same level as the other models. The slope was built at approximately 1:1.

A submerged nearshore breakwater model made from geotextile tubes with 0.165m submergence with four different configurations and placed at given distances from the shoreline was employed (Figure 4.3). The first three models are considered passive structures, as they protect what is behind the structure but do not arrest the ongoing erosion in the coastal profile, while the fourth model is considered an active structure. Model E configurations were deduced from the definition parameters, the position to the shoreline, and the submergence. The latter was kept constant at 0.165m. With respect to the former, the locations of the submerged nearshore breakwater were off-shore zone, surf zone and an in-between locations having Model A as reference. This model was constructed from geotextile tubes, either as stacked tubes, E1 and E2, or single tubes, E3 and E4 (Figure 4.3). The four configurations were as follows:

- Test Series E1: six small stacked tubes (3-2-1 stack); the baseline is z~-0.38m placed at and the model axis is at x~-2.5m;
- Test Series E2: three small tubes placed behind each other and a fourth medium tube on (3-1 stack); the baseline is z~-0.38m placed at and the model axis is at x~-2.5m;
- Test Series E3: one single medium tube; the baseline is z~-0.3m placed at and the model axis is at x~-1.9m; and
- Test Series E4: one single small tube; the baseline is z~-0.24m placed at and the model axis is at x~-1.1m.

A model test with a non-reinforced dune was also employed as a reference case. The non-reinforced dune was designated by Model A. The dune toe starts at (x,z)~(0.37,0.06) from the shoreline. The seaward slope of the dune has an angle of 45º. The crest height of the dune is at 0.42m, while its width is of *ca.* 0.50m.

As seen from Table 4.V, two kinds of tests were carried out: wave-run segments with plane beach-profile slopes; and wave-run segments with wave-changed cross-shore beach-profiles.

For each wave run-segment with plane beach, the bed conditions were thoroughly checked before the experiment and the bed was carefully leveled to the desired gradient. To minimize the error caused by the initial bed profile, the sand bed was repeatedly leveled until the measured beach-profile was within a minimum tolerance range based on the ideal conditions. To prevent disturbances and to assure that the level of sand saturation was roughly the same for each wave-run segment with plane beach, the water during leveling was kept to SWL. Above it, the beach-profile was slowly wet so as to reduce air entrainment.

Although a plane-beach is a reasonable first approximation of the profile, the naturally occurring morphologic perturbations of bars and troughs exert strong control over shallow-water wave transformation; likewise breaking waves modify the beach-profile. Engineered changes in the profile, such as reef (submerged) breakwaters and protective sandbars constructed in dredging and beach nourishment operations, similarly modify the profile and incident waves (Smith and Kraus, 1991). To investigate to which extent the profile and the waves respond to morphologic perturbations, selected wave-run segments with wave-changed cross-shore beach-profiles were performed.

4.3. Instrumentation

The following instrumentation has been used in the present contribution: twelve miniature pore-pressure sensors of the type PDCR-81 from GE Druck; four HR Wallingford wave probes of 600mm length; and a HR Wallingford 2D bed profiler. The key features of the former instruments and data output are summarized below. Some aspects of data post-processing are given in section 4.4. Special attention is given to the miniature pore-pressure sensors and respective DAQ-system, which have never been used at FEUP hydraulics laboratory outside the present research. Further details on such system and other instrumentation may be found in Rosa-Santos (2010), Silva (2010), Neves (2007), and Taveira-Pinto *et al.* (2007).

4.3.1. Wave generation system

The wave basin of FEUP hydraulics laboratory is equipped with a HR Wallingford wave generation system that comprises **(**HR Wallingford, 2007**)**: a wave machine of two identical modules each having eight paddles of 0.74m width that can move independently to one another; a control unit that interconnects the signal generation computer and the wave machine; and the signal generation computer that runs the HR WaveMaker signal generation program and is fitted with the necessary output cards to interface with the control unit. The control system is fitted with the HR Wallingford Dynamic Wave Absorption (DWA) module. Due to limited space behind the wavemaker, a beach made from reticulated plastic foam material has been incorporated into the framework of each module.

The maximum wave-height that can be achieved at a particular frequency is limited by either the performance of the wave generation system (maximum stroke, velocity and force achievable) or depth induced wave breaking. FEUP hydraulics laboratory wavemaker specifications are: paddle stroke 1.08m; paddle velocity 0.87m/s; paddle force 1.5kN; and nominal motor power 1.38kW. The theoretical performance of the wavemaker for several water depths (WD), with and without the DWA in use, is shown in Figure 4.4. As one can see, the maximum wave-height is reduced when absorption is being used, as the wavemaker must be able to absorb waves at the same time that it is generating them.

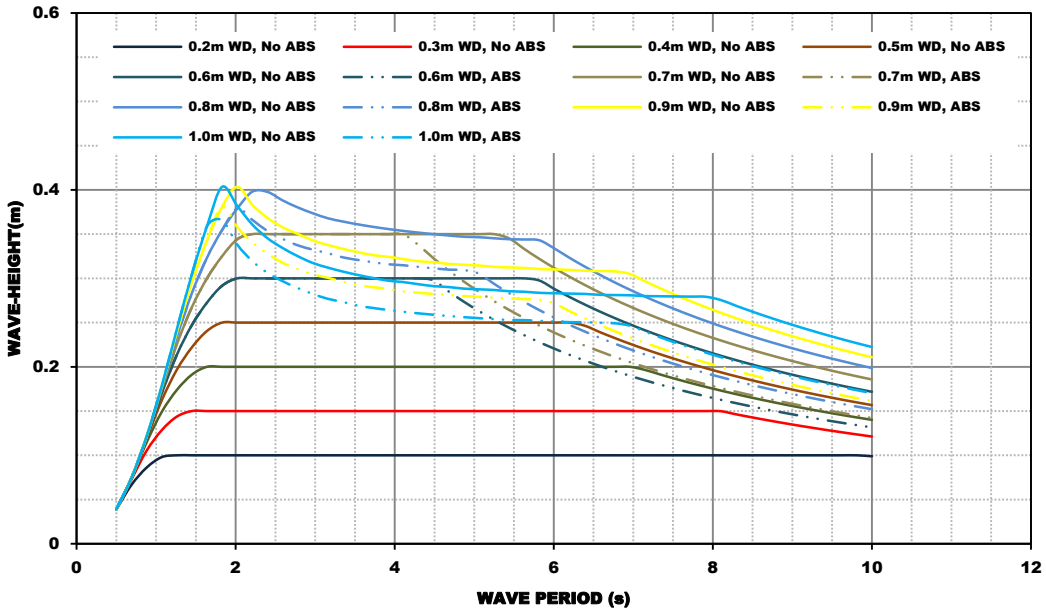

Figure 4.4: Theoretical performance of HR Wallingford multi-element wave generation system (after HR Wallingford).

The dynamic wave absorption is achieved by measuring the wave-height at each paddle and manipulating this signal to produce an Equivalent Paddle Position Signal (EPP). The EPP can be considered to be the position the paddle would have to be in to produce the measured water level position without any reflection. The difference between the EPP signal and the Demand Input Position (DIP) signal is due to the wave reflected back to the paddle, which either increases or decreases the water level. By modifying the DIP signal to take into account this difference wave can be absorbed (HR Wallingford, 2007).

The wave generation control program in use at FEUP hydraulics laboratory is the HR WaveMaker, which is a wave synthesizer package written and developed by HR Wallingford, Ltd.

The program generates regular (sinusoidal) waves and random waves using two methods, those of digitally filtered white noise and summation of sine waves, and incorporates the facility of generating user defined spectral shapes **(**HR Wallingford, 2007**)**. Long and short-crested waveforms are possible. The random waves conform to one of two standard spectral shapes, JONSWAP and Pierson-Moskowitz, although less used spectral definitions can be input using the user-defined option. The potentiality of the wavemaker to generate waves at an angle instead of only in a direction normal to it has not been used in the present contribution.

The transfer function between wave amplitude and paddle displacement at given water depth and frequency may be entered manually from experimental data, or be set-up using theoretical values. In general, is adequate to use a standard paddle transfer function.

4.3.2. Pressure sensors

Miniature pore-pressure sensors of the type PDCR-81 (Figure 4.5) from GE Druck have been installed for the study of wave penetration and wave propagation. The main eligibility criteria for selecting this transducer device were: minimal size; operating pressure ranges; fast response and infinite resolution. According to its manufacturer, the main features of PDCR-81 are: ceramic filter; rugged construction; and long-term survivability. The transduction principle of this sensor is a silicon integrated strain gauge bridge. A gauge pressure type indicates that the pressure being measured is referenced to a known pressure level; in the present case, it is referenced to the ambient atmospheric pressure.

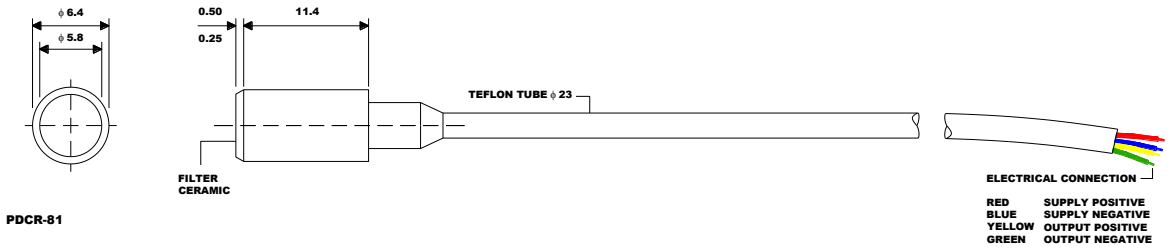

Figure 4.5: Definition sketch of pore-pressure sensor PDCR-81.

The data acquisition system (DAQ-system) comprise (Figure 4.6): a modular multi-channel measuring and I/O-system type e.bloxx; and a programmable automation controller type e.pac; both powered by Gantner instruments Test & Measurement GmBH.

From the whole product line of different e.bloxx the choice for e.bloxx A1-1 concern firstly the sensor principle and then its higher versatility in placement when compared to similar e.bloxx A1-4 and A1-8 modules. The decentralized structure of A1-1 permits it to be put more close to the sensor even if it means being physically separated from the other modules.

The e.bloxx A1-1 is a 1-channel module that samples at 19-bits of resolution and up to 1kHz depending on the module and signal type used. With the addition of e.pac test controller to the DAQ-system measuring rates close to those limits were possible. A universal interface converter of the type ISK 200 (powered by Gantner instruments Test & Measurement GMBH) was primarily used instead of e.pac but later abandoned, because of limited sampling rate (~10Hz).

Module parts are as seen in Figure 4.7 while Tables 4.VI to 4.VIII present respectively the characteristics, the terminal strip for RS 485 bus and power supply, the terminal strip for sensor connection, and the functional diagram of the e.bloxx A1-1.

Figure 4.6: System set-up for measuring pressure.

1 **Pluggable screw-type terminal strip for connection of RS-385 BUS and power supply**

2 **Power error LED (red/green)**

3 **Pluggable screw-type terminal strip for sensor connection**

4 **Rapid BUS link plugs**

Figure 4.7: Parts of the e.bloxx A1-1, single channel universal analog input (modified from Gantner, 2006).

Table 4.VI: Characteristics of e.bloxx A1-1 module.

	e.bloxx A1-1
Voltage Supply	10-30 VDC
Power Consumption	1.5 W
Variable/Channels	8
Analog Inputs	1
Analog Outputs	-
Relay Outputs	1
Digital Inputs	1
Digital Outputs	-
Fieldbus Interface	RS 485
Protocols	ASCII - Modbus-RTU - Profibus-DP - LocalBus
Quantity to measure Sensor Principle	
Voltage	x
Current	x
Resistance	x
Pt100/Pt1000	x
Cryo Sensor	-
Thermocouple	x
Strain Gauge Full Bridge	x
Strain Gauge Half Bridge	-
Strain Gauge Quarter Bridge	-
Inductive Full Bridge	-
Inductive Half Bridge	-
LVDT	-
Potentiometer. Transducer	x
Piezoresistance Transducer	-
Status	x
Frequency	-
Counter	-

Table 4.VII: Description of terminal strip for RS 485 bus and power supply
(reproduced from Gantner, 2006).

Terminal		Description
	**A**	RS 485 Bus Interface A
	B	RS 485 Bus Interface B
	+V	Power Supply +
	0V	Power Supply -

Table 4.VIII: Description of terminal strip for sensor connection
(reproduced from Gantner, 2006).

Terminal		Description
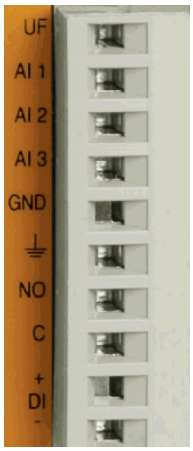	**UF**	Force Output to Supply Measurements Voltage
	AI 1	Analog Input 1
	AI 2	Analog Input 2
	AI 3	Analog Input 3
	GND	Analog Ground
	⏚	Grounding
	NO	Solid State Relay Output - Normally Open
	C	Solid State Relay Output - Common
	DI +	Digital Input +
	DI -	Digital Input -

The e.pac test controller handles all of the synchronized data acquisition with connected e.bloxx. It comprises: 4 slave interfaces to connect up to 30 additional e.bloxx modules per slave interface; a Profibus-DP interface; and an Ethernet interface. An e.pac module can be connected either to a local network or directly to a PC/laptop via RS 232 and Ethernet. The e.pac module, as seen in Figure 4.6 (right on top panel), was connected to a PC/laptop via Ethernet.

Module parts are as seen in Figure 4.8 while Tables 4.IX to 4.XII present respectively the characteristics, the terminal strip for RS 485 bus and power supply, the terminal strip for digital signals, the terminal strip for RS 485, and the terminal script for RS 232 of the e.pac.

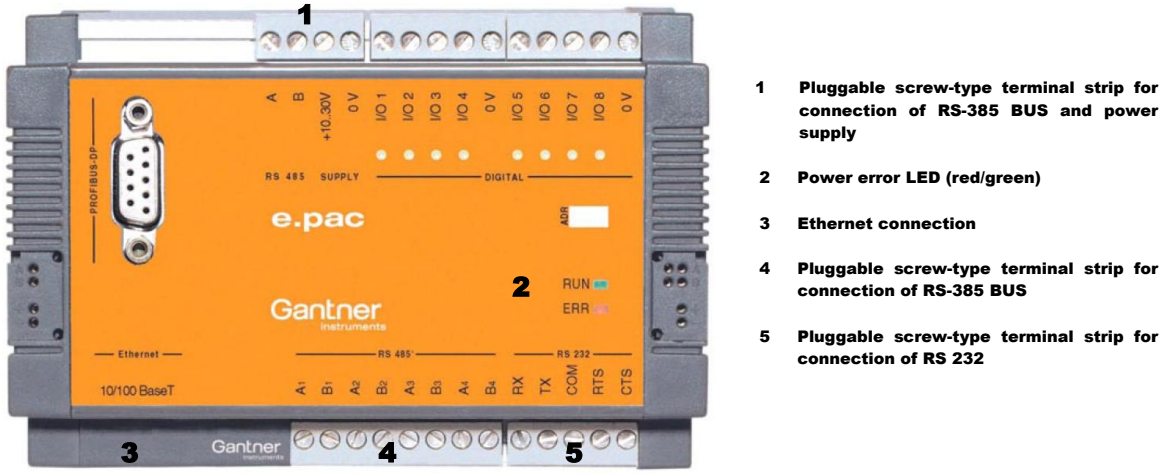

Figure 4.8: Parts of the programmable automation controller type e.pac.

Table 4.IX: Description of terminal strip for RS 485 bus and power supply
(reproduced from Gantner, 2006).

Terminal	Description
A	RS 485 Bus Interface A (Only Used for Service)
B	RS 485 Bus Interface B (Only Used for Service)
+10..30VDC	Power Supply +
0V	Power Supply -

Table 4.X: Description of terminal strip for digital signals
(reproduced from Gantner, 2006).

Terminal	Description	
I/O 1	Digital Input/Output 1	Output "System running"
I/O 2	Digital Input/Output 2	Output "LifeSignal"
I/O 3	Digital Input/Output 3	Input "Trigger arm"
I/O 4	Digital Input/Output 4	Input "Trigger event"
0V	Digital Ground	
I/O 5	Digital Input/Output 5	Output "Trigger arm state"
I/O 6	Digital Input/Output 6	Output "Trigger event state"
I/O 7	Digital Input/Output 7	I/O "Sync. Reset"
I/O 8	Digital Input/Output 8	I/O "Sync. Signal"
0V	Digital Ground	

Table 4.XI: Description of terminal strip for RS 485
(reproduced from Gantner, 2006).

Terminal	Description
A1	RS 485 Bus Interface A - UART 0
B1	RS 485 Bus Interface B - UART 0
A2	RS 485 Bus Interface A - UART 1
B2	RS 485 Bus Interface B - UART 1
A3	RS 485 Bus Interface A - UART 2
B3	RS 485 Bus Interface B - UART 2
A4	RS 485 Bus Interface A - UART 3
B4	RS 485 Bus Interface B - UART 3

Table 4.XII: Description of terminal strip for RS 232
(reproduced from Gantner, 2006).

Terminal	Description
RX	Receive Data
TX	Transmit Data
COM	Common/Ground
RTS	Request to Send
CTS	Clear to Send

The e.commander software is used to define all settings of e.pac, like the interface settings and internal settings for the memory (circle buffer), synchronization and life time. This software also includes the Configuration Software ICP 100 for configuration of e.bloxx measurement modules and the visualization tool Green Eye Writer to evaluate measurement data.

Having connected all supply and communication cables, connected the e.pac to the PC via Ethernet and setting the IP address of the network, e.commander is able to communicate with e.pac and check the system to see if the configuration correlates with hardware. The configuration of the DAQ-system is saved in a project (*e.g.*, PhD_Luciana.epj) and can be read, saved, changed and loaded from/into the e.pac at any time.

At the first start-up is necessary to configure e.bloxx modules with ICP 100. This software includes all functions to set the module parameters and to define the I/O functions (*e.g.*, type of measurement). Configuration of modules with ICP 100 by using the configuration software e.commander is as seen in Figure 4.9. Each row in the Variable Settings table corresponds to one variable which details can be set via the corresponding column: Channel-Type; Variable Name; Sensor; Type of Measurement; Connection; Terminals; Format/Adjustments; Range/Error; Additionals; and Profibus-DP Configuration. These settings define how the signal at the in- and output of the e.bloxx will be processed.

Clicking in the Channel-Type field one can choose from several proposals (Figure 4.10): Alarm; Analog Input; Arithmetic; Digital Input; Digital Output; and Setpoint. Any user defined name of up to 20 characters can be entered for each Variable Name.

In the column Sensor appears the designation of the connected sensor for the analog and digital sensor variables. The sensor can be selected from a list or customized according to the measurement quantity or the principle of measurement. For the current measurements a custom sensor, PDCR-81, was defined with the following characteristics: Bridge Full 4 Wire as the principle of measurement and mbar as the unit.

Type of Measurement, Connection and Terminals are automatically set and displayed once a type of sensor is selected to a channel. Connection and Terminals columns display how the selected sensor must be connected to the module; the wiring diagram is as seen in Figure 4.11.

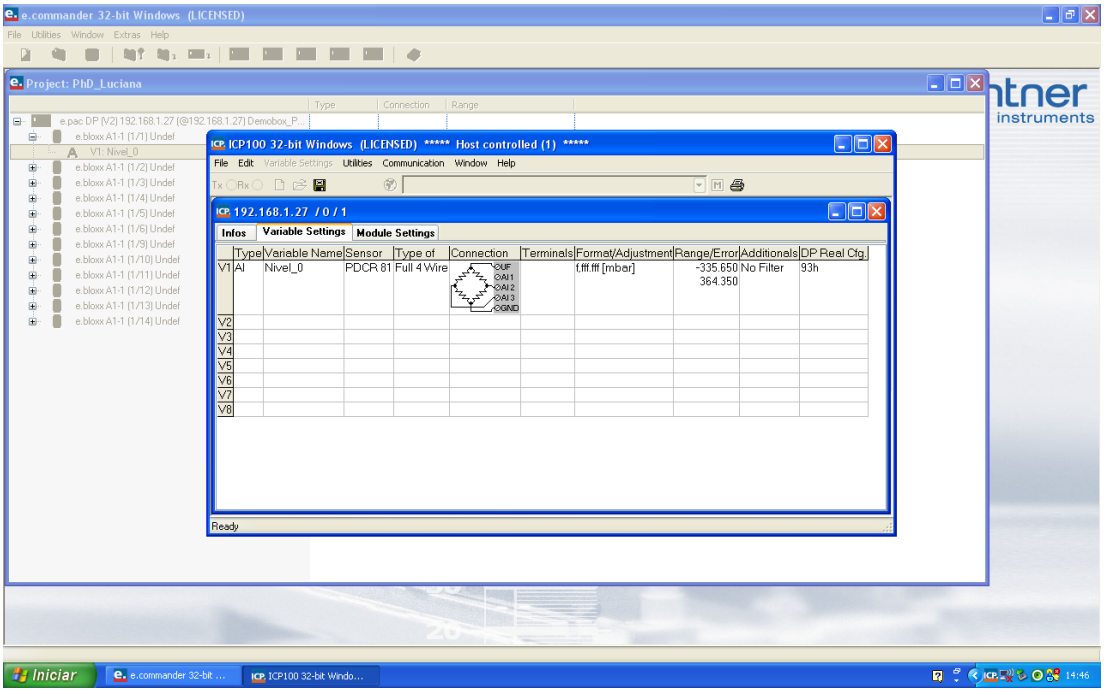

Figure 4.9: ICP 100 modules configuration table.

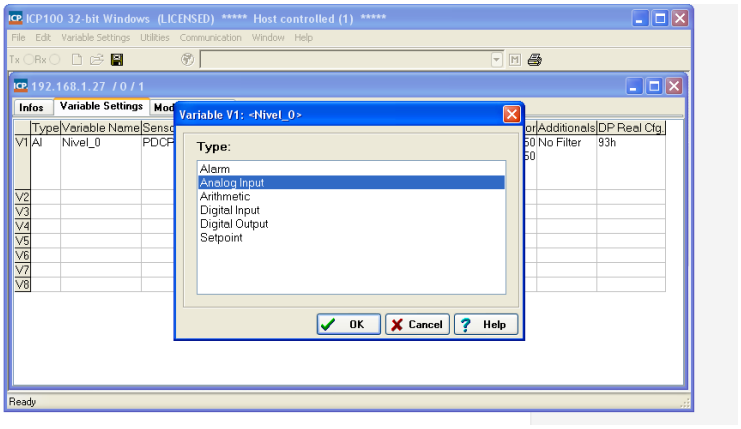

Figure 4.10: Channel-type selected: Analog Input.

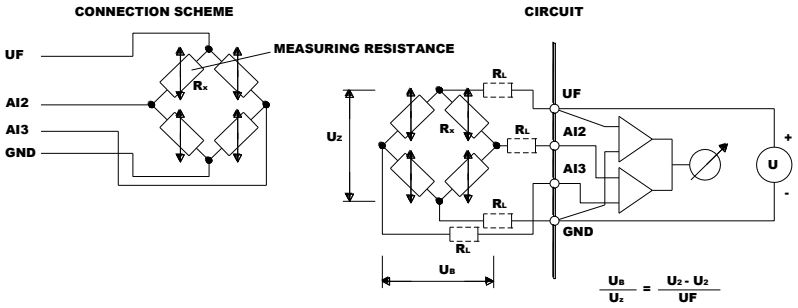

Figure 4.11: Analog Input, measurement with a Resistance Bridge.

Once the sensor is connected to the DAQ-system, signal-conditioning (*i.e.*, sensor linearization and calibration) is required. Sensor linearization is basically providing correlative relations between the measured values, in mV/V, and the displayed value, in mbar. For PDCR-81, the conversion formula provided by the manufacturer is a function of the excitation voltage, the full scale capacity of the sensor (±350mbar), and the sensitivity of the sensors (which ranged from 0.018 to 0.020mV/V/mbar). After scaling the signal it is necessary to obtain a proper rest position (*i.e.*, adjust the offset so that the measured pressure at this position is close to null). Such operation is done in the Format/Adjustment column, an example of signal conditioning is given in Figures (Figure 4.12) and (Figure 4.13). After configuration and correct sensor connection and resting the actual values of each variable can be displayed and monitored on screen in real time.

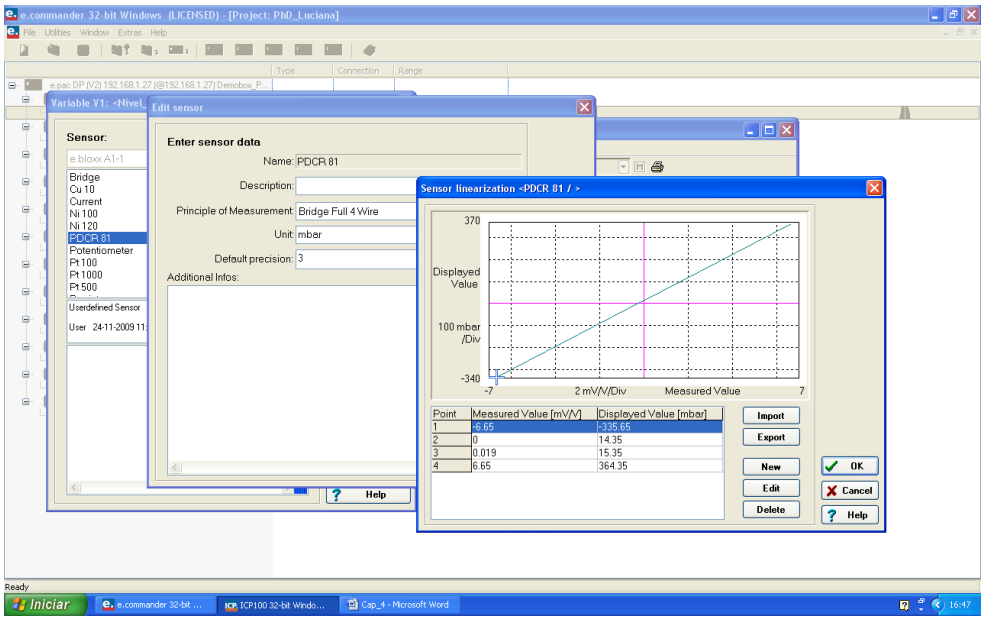

Figure 4.12: Linearization of PDCR 81 sensors.

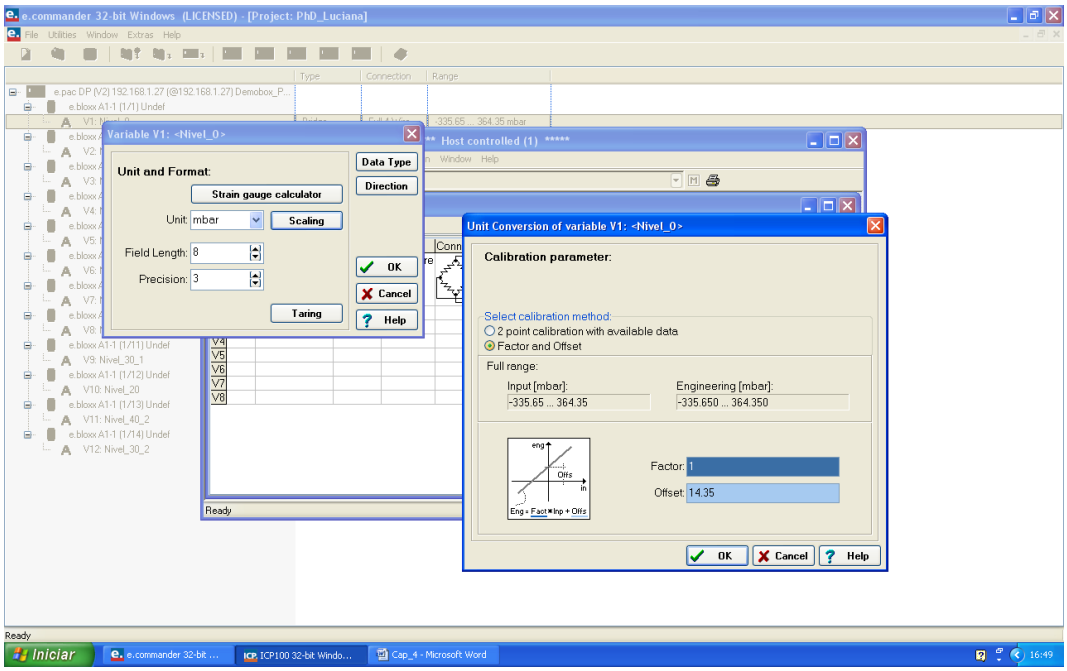

Figure 4.13: Setting the rest position of PDCR 81 sensors.

4.3.3. Wave probes

For measuring water level change, an array of four HR Wallingford wave probes of 600mm length was used. Each wave probe comprise two parallel stainless steel rods with plastic head and foot (Figure 4.14). The wave probes are connected by cable to a wave probe monitor that permits measuring the current flowing between the wires immersed in water. This current is converted to an output voltage that is directly proportional to the immersed depth.

During measurements, the wave probes are fixed to a certain level that enables the head to be above the highest wave peak and the foot to be low enough to detect the trough of the lowest. Daily, and every time the probes have been displaced within the array, calibration of all wave probes is needed. Several factors may influence the accuracy of the measurements (*e.g.*, changes in water level, water temperature, accumulations of material around the rods, low and raise of the probe, etc.), and thus their regular calibration assures the reliability of the measurements.

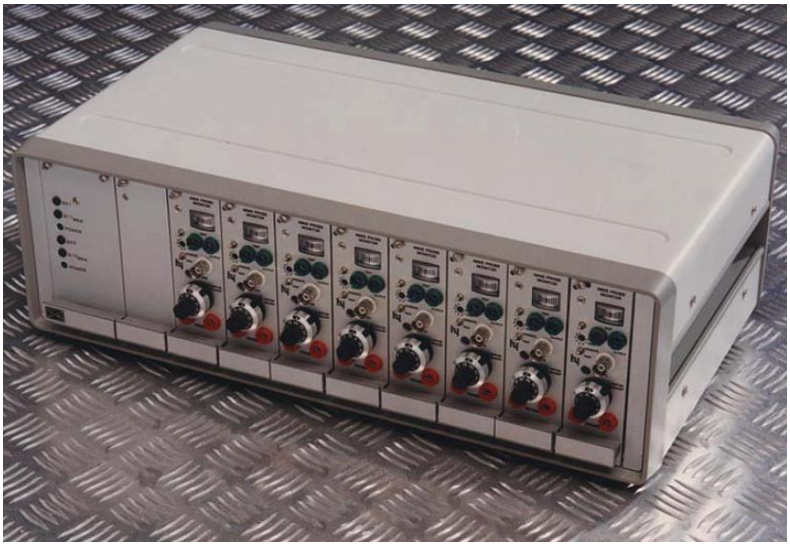

Figure 4.14: Wave probe and wave monitor.

The calibration from wave-height to output voltage is achieved by measuring the change in voltage when the probe is raised or lowered by a know amount in still water. Three calibration points over the working range were used. The calibration factor was accepted for goodness of fit over 0.999, otherwise the calibration was repeated.

The sampling rate was 30Hz.

The software used for data acquisition and analysis was HR DAQ, it comprises (HR Wallingford, 2006): a calibration routine; a data acquisition routine with real time display of acquire data; and a suite of analysis packages (including routines for spectral and statistical analysis and for reflection analysis).

4.3.4. 2D-bed profiler

A HR Wallingford bed profiler has been used to measure the changes in beach-profile (Figure 4.15). It comprises: a support beam, Figure 4.15; a profiler carriage (containing the motors for both the horizontal and vertical drives together with all associated electronic circuitry), Figure 4.15; a probe (four types of probe are available), Figure 4.15; and a control program. The profiler carriage is a rigid die-cast enclosure to which is fitted the guide bearings and probe support.

The 2D-bed profiler specifications are (HR Wallingford, 2009): horizontal travel extensive by multiples of 4.6m (beam length); horizontal velocity 100mm/s (nominal); vertical travel 340-940mm (underside of beam to bed); vertical velocity 50mm/s (nominal); vertical resolution ±1mm; power supply 210-250V 47-63Hz at 100mA; cable length 25m (profiler to power supply).

Beach-profile change along-shore was found negligible; therefore, the profile was measured using a touch sensitive probe at one horizontal direction, at approximately half model width where influences of lateral boundaries were minimal. Switches were placed limiting cross-shore travel to 3m. The choice for a touch sensitive probe regards mainly to its versatility to work both in air and in water and with almost any bed material, disregarding the fact that it cannot be used to make continuous profile while the carriage is moving.

The profiler control program is a dedicated version of Keithley Asyst VIEWDAC (HR Wallingford, 2009). that uses MS DOS operating system. It comprises two main panels: a strip chart of what is being profiled; and a control panel containing all of the features required to set-up a profile, to move the profiler and to set a datum point on the model.

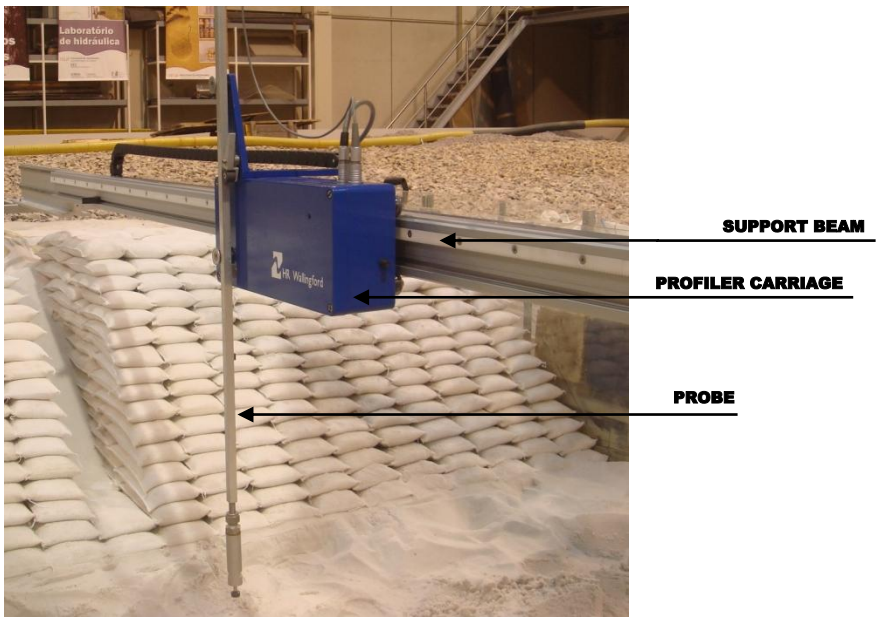

Figure 4.15: 2D-bed profiler.

The program for the incremental profiling with the touch sensitive probe is STEP.BAT (the data is saved in ASCII format). Main parameters to be entered are the horizontal and vertical positions of the carriage, the start and end positions (relative to the horizontal zero), and the steps in profile.

The 2D-bed profiler is installed in a fixed position.

4.4. Data post-processing

In all tests, wave-data records, pressure-data records and cross-shore beach-profiles were collected. All tests were recorded on video. A 10cm square grid was installed on the glass wall of the basin allowing the visual inspection of profile changing during experiments and providing a reference in viewing the visual recording of the tests.

The wave characteristics were estimated based on the surface elevations recorded at deep-water, backshore the 3:20 sloped plane beach, by means of the four wave gauges as described in paragraph 4.3.3. The first probe (labeled as S1) was at ~5.5m from the wavemaker (~8.8m from the shoreline). The distances between the other wave-gauges positions (labeled as S2, S3, and S4 shoreward) were fixed using the Probe Spacings utility under the Reflection Analysis in the HR DAQ software, which calculates a valid frequency range for a given geometry and water depth. For each of the test conditions, the distances between the probes were defined so that the valid range would contain the frequency limits $0.5f_p$ and $2f_p$, where f_p is the peak frequency in each sea-state as given in Table 4.V.

The Reflection Analysis in the HR DAQ software calculates as well the incident and reflected wave spectral energy and the reflection coefficients at frequencies spread over the valid frequency range. Furthermore it computes the bulk reflection coefficient as the average of the reflection coefficients/the ratio of the total reflected and incident energies. To separate the incident and reflected waves a least squares method is used. This method is a development of the technique described by Mansard and Funke in 1980, cited in HR Wallingford (2005). The signals from the four wave gauges were processed to yield the following wave characteristics of the incoming waves:

- H_s: the significant wave-height (m), based on the wave spectrum;
- H_{mean}: the mean measured wave-height in the wave record (m);
- H_{max}: the maximum measured wave-height in the wave record (m);
- H_{min}: the minimum measured wave-height in the wave record (m);
- H_{RMS}: the root-mean-square wave (m);
- $H_{1/10}$: the highest one-tenth wave (m);
- N: number of waves during a test (-);
- T_p: the peak period, the wave period corresponding to the peak of the variance spectral density (s).
- $S_{0,p}$: deep water wave steepness based on the wave peak period (-). The wave steepness has been determined with the use of Eq. (3.3);
- $S(f)$: the variance spectral density (m^2/Hz); and
- $\xi_{0,p}$: deep water breaker parameter (-).The breaker parameter has been determined with the use of Eq. (3.1).

The analysis and discussion of the generated wave spectrum against the target spectrum, and of the reflection analysis is given in the following chapter.

In hydraulic model studies wave reflection is typically determined from the spatial variation of wave conditions. Wave gauge arrays are used for this analysis. Wave reflection cannot be directly measured; the uncertainties of the reflection coefficient are thus significantly larger than the uncertainties of directly measurable wave parameters like local wave-height or wave pressure.

The wave-induced pore-pressure variations data is similar to any other type of surface elevation data due to random seas, and thus it can be analysed with resource to techniques for the analysis of random wave data, that is the time domain analysis, and the frequency domain analysis.

Matlab® 2009 routines which allowed the processing of the dynamic pressure component signal with respect to energy spectral balance, spectral moments, cross-shore gradients in wave-induced pressure energy, and envelope pressures around the structures were used. Some of those routines make use of the Matlab toolbox for analysis of random waves and loads, WAFO (see, *e.g.*, Brodtkorb *et al.*, 2000; and WAFO-group, 2000).

The beach-profile was surveyed at the end of each wave-run segment and prior to. The profiles were sampled at approximately 0.5cm cross-shore. The transformation of the origin coordinates, so that it is taken as the intersection of the still water line with the beach face, positive onshore (Figure 4.1), was achieved by post-processing of the output data file.

The readings of the profile after post-processing were then introduced into AutoCAD® 2010 and Microsoft Office Excel® 2007 for visualization, comparison and analysis.

5. DISCUSSION OF RESULTS

In this chapter the experimental research carried out on the stability analysis of geotextile encapsulated-sand systems under wave-loading is evaluated. In section 5.1 the methodology for evaluation is described and used terms are explained. The results of the measurements are presented in sections 5.2, 5.3, 5.4, and 5.5, referring to spectral and statistical wave analysis, reflection analysis, wave-induced pore-pressures, and beach-profile evolution, respectively. A discussion is given in section 5.6; while in section 5.7 the extrapolation of experimental results on the prototype is essayed.

5.1. Methodology

To achieve the aim of this thesis, a systematic study on the stability analysis of geotextile encapsulated-sand systems under wave-loading was conducted based on the measurement of wave-induced morphodynamic changes. At first the characteristics for various erosion control system layouts were studied aiming to provide insights into the efficiency of each system in maintaining a beach and in protecting the shoreline. For this purpose different models of active and passive coastal defence structures were set-up to run on similar hydrodynamic and morphodynamic conditions. The intercomparison carried out on the hydrodynamic and morphodynamic outputs produced by each scheme focused on the scour and deposition patterns over the test period evaluated on the parameters deepwater wave characteristics (H_0, L_0), reflection coefficient (K_r), and wave-induced pore-pressures. The next step was to increase understanding of the response of the beach under persistent erosional conditions and under periods of erosion followed by infilling and again erosion.

Five models, corresponding to three erosion control systems with two configurations, one nearshore detached breakwater with four configurations and one non-protected beach and dune system as reference were taken for the investigation (see Figure 4.3). The models were submitted to a total of ten different sea-states, combinations of four values of significant wave-height, H_s and four values of peak period, T_p.

For each of the selected models the hydrodynamic characteristics were measured by the method described in section 4.3.3. Further to these measurements, wave-induced pore-pressure variations were recorded at four locations along the plane-beach and at various locations within the structure. The beach-profile was surveyed at the end of, and prior to, each wave-run. A 10cm square grid was installed on the glass wall of the basin allowing the visual inspection of profile changing during experiments and providing a reference in viewing the visual recording of the tests. In total over 150 random-wave tests were conducted, of which the foremost are ranked in order for evaluation in Table 5.I. This rank is not the same in which the tests were carried out. The ID of each experiment indicates the date and key characteristics so that, Test_B2_10_3h_20100210 corresponds to Model B, variant 2, sea-state 10, after a total duration of 3h, conducted in February 10, 2010. Table 5.I also gives an overview on which tests are clustered for evaluation on the following test properties:

- Generated wave spectrum against targeted spectrum is the first evaluation (read as GWC in Table 5.I); it includes the analysis of individual wave characteristics of the incoming waves, and wave spectra. The intercomparison between models entail that each comparable experiment have been set-up to run on similar hydrodynamic conditions;

Table 5.I: Overview of experiments.

Test ID	System	Targeted Sea-state		Balance	GWC	K_r	PPVar	BPEv
		H_s [m]	T_p [s]					
Test_A_7_20100409	Reference	0.17	2.31	Erosion	√	√	√	√
Test_B1_7_20091031	Passive				√	√	-	-
Test_B2_7_20100323					√	√	√	√
Test_C1_7_20100427					√	√	√	√
Test_C2_7_20100503					√	√	-	√
Test_D1_7_20100512					√	√	-	√
Test_D2_7_20100518	Passive				√	√	√	√
Test_E2_7_20100524	Active				√	√	√	√
Test_A_8_20100405	Reference	0.17	2.89	Erosion	√	√	√	√
Test_B1_8_20100105	Passive				√	√	-	√
Test_B2_8_20100325					√	√	√	√
Test_C1_8_20100428					√	√	√	√
Test_C2_8_20100504					√	√	√	√
Test_D1_8_20100510					√	√	√	√
Test_D2_8_20100517					√	√	√	√
Test_E2_8_20100522	Active				√	√	√	√
Test_E3_8_20100526					√	√	-	√
Test_E4_8_20100525					√	√	√	√
Test_A_9_20100413	Reference	0.17	3.46	Erosion	√	√	√	√
Test_B1_9_20100106	Passive				√	√	-	√
Test_B2_9_20100329					√	√	√	√
Test_C1_9_20100426					√	√	√	√
Test_C2_9_20100505					√	√	-	√
Test_D1_9_20100511					√	√	-	√
Test_D2_9_20100518					√	√	√	√
Test_E2_9_20100524	Active				√	√	√	√
Test_E3_9_20100526					√	√	√	√
Test_E4_9_20100525					√	√	√	-
Test_A_10_20100331	Reference	0.125	2.89	Erosion	√	√	-	√
Test_B1_10_20100112	Passive				√	√	-	√
Test_B2_10_20100210					√	-	√	-
Test_C1_10_20100420					√	√	√	√
Test_C2_10_20100429					√	√	√	√
Test_D1_10_20100511					√	√	√	√
Test_D2_10_20100515					√	√	√	√
Test_E1_10_20100520	Active				√	√	√	√
Test_E2_10_20100521					√	√	√	√
Test_E3_10_20100526					√	√	√	√
Test_E4_10_20100525					√	√	√	√

Table 5.I: Overview of experiments (cont.).

Test ID	System	Targeted Sea-state		Balance	GWC	K_r	PPVar	BPEv
		H_s [m]	T_p [s]					
Test_A_1_20100407	Reference	0.04	1.73	Accretion	√	√	√	√
Test_B1_1_20091030	Passive				√	√	-	-
Test_B2_1_20100223					√	√	√	-
Test_C1_1_20100419					√	√	√	√
Test_C2_1_20100502					√	√	√	√
Test_D1_1_20100512					√	√	√	√
Test_D2_1_20100518					√	√	√	√
Test_A_2_20100407	Reference	0.04	2.31	Accretion	√	√	√	√
Test_B1_2_20091030	Passive				√	√	-	-
Test_B2_2_20100223					√	√	√	√
Test_C1_2_20100419					√	√	√	√
Test_C2_2_20100502					√	√	√	√
Test_D1_2_20100512					√	√	√	√
Test_D2_2_20100518					√	√	√	√
Test_A_4_20100408	Reference	0.08	1.73	Accretion	√	√	-	√
Test_B1_4_20091030	Passive				√	√	-	-
Test_B2_4_20100223					√	√	√	√
Test_C1_4_20100419					√	√		√
Test_C2_4_20100503					√	√	√	√
Test_D1_4_20100512					√	√	√	√
Test_D2_4_20100518					√	√	-	√
Test_A_5_20100408	Reference	0.08	2.31	Accretion	√	√	-	√
Test_B1_5_20091030	Passive				√	√	-	-
Test_B2_5_20100223					√	√	-	√
Test_C1_5_20100419					√	√	√	√
Test_C2_5_20100503					√	√	√	√
Test_D1_5_20100512					√	√	√	√
Test_D2_5_20100518					√	√	√	√
Test_A_6_20100413	Reference	0.08	2.89	Accretion	√	√	√	√
Test_B1_6_20100104	Passive				√	√	-	√
Test_B2_6_20100324					√	√	√	√
Test_C1_6_20100419					√	√	-	√
Test_C2_6_20100504					√	√	√	√
Test_D1_6_20100510					√	√	√	√
Test_D2_6_20100517					√	√	√	√

Table 5.I: Overview of experiments (cont.).

Test ID	System	Targeted Sea-state		Balance	GWC	K_r	PPVar	BPEv
		H_s [m]	T_p [s]					
Test_A_10_1h_20100331	Reference	0.125	2.89	Persistent Erosional Conditions	√	√	-	-
Test_A_10_2h_20100331					√	√	-	√
Test_A_10_3h_20100331					√	√	-	√
Test_A_10_4h_20100401					√	√	-	√
Test_A_10_6h_20100401					√	√	-	√
Test_B1_10_1h_20100112	Passive	0.125	2.89	Persistent Erosional Conditions	√	√	-	√
Test_B1_10_1.5h_20100112					√	√	-	√
Test_B1_10_2h_20100112					√	√	-	√
Test_B1_10_3h_20100114					√	√	-	√
Test_B1_10_4h_20100115					√	√	-	√
Test_B1_10_5h_20100115					√	√	-	√
Test_B1_10_6h_20100120					√	√	-	√
Test_B1_10_8h_20100120					√	√	-	√
Test_B1_10_10h_20100120					√	√	-	√
Test_B1_10_12h_20100125					√	√	-	-
Test_B1_10_14h_20100125					√	√	-	-
Test_B2_10_1h_20100210	Passive	0.125	2.89	Persistent Erosional Conditions	√	√	√	-
Test_B2_10_2h_20100210					√	√	-	-
Test_B2_10_3h_20100212					√	√	√	-
Test_B2_10_4h_20100212					√	√	-	-
Test_B2_10_4h_8_20100212					√	√	-	-
Test_C1_10_1h_20100420	Passive	0.125	2.89	Persistent Erosional Conditions	√	√	√	√
Test_C1_10_2h_20100420					√	√	-	√
Test_C1_10_3h_20100420					√	√	-	√
Test_C1_10_4h_20100420					√	√	-	√
Test_C1_10_6h_20100421					√	√	-	√
Test_C1_10_8h_20100421					√	√	√	√
Test_C1_10_9h_20100421					√	√	-	√
Test_C2_10_1h_20100429	Passive	0.125	2.89	Persistent Erosional Conditions	√	√	-	√
Test_C2_10_2h_20100429					√	√	-	√
Test_C2_10_3h_20100430					√	√	-	√
Test_C2_10_4h_20100430					√	√	-	√
Test_C2_10_6h_20100430					√	√	√	√
Test_C2_10_8h_20100430					√	√	√	√
Test_D1_10_1h_20100511	Passive	0.125	2.89	Persistent Erosional Conditions	√	√	√	√
Test_D1_10_2h_20100511					√	√	-	√
Test_D1_10_3h_20100511					√	√	√	√
Test_D1_10_4h_20100511					√	√	-	√
Test_D1_10_6h_20100511					√	√	√	√

Table 5.I: Overview of experiments (cont.).

Test ID	**System**	**Targeted Sea-state**		**Balance**	**GWC**	K_r	**PPVar**	**BPEv**
		H_s **[m]**	T_p **[s]**					
Test_D2_10_1h_20100515	Passive	0.125	2.89	Persistent Erosional Conditions	√	√	√	√
Test_D2_10_2h_20100515					√	√	√	√
Test_D2_10_3h_20100516					√	√	√	√
Test_D2_10_4h_20100516					√	√	√	√
Test_D2_10_6h_20100516					√	√	√	√
Test_E2_10_1h_20100521	Active	0.125	2.89	Persistent Erosional Conditions	√	√	√	√
Test_E2_10_2h_20100521					√	√	√	√
Test_E2_10_3h_20100522					√	√	√	√
Test_E2_10_4h_20100522					√	√	√	√
Test_E3_10_1h_20100526	Active	0.125	2.89	Persistent Erosional Conditions	√	√	√	√
Test_E3_10_2h_20100526					√	√	-	√
Test_E4_10_1h_20100525	Active	0.125	2.89	Persistent Erosional Conditions	√	√	√	√
Test_E4_10_2h_20100525					√	√	√	√
Test_A_8_3a_20100405	Passive	0.04	2.89	Infilling and again Erosion	√	√	√	√
Test_A_8_3b_20100406					√	√	√	√
Test_A_8_2x_20100406		0.17	2.89		√	√	√	√
Test_B2_8_6_20100326	Passive	0.08	2.89	Infilling and again Erosion	√	√	√	√
Test_B2_8_10_20100326		0.125	2.89		√	√	√	√
Test_C1_8_3a_20100428	Passive	0.04	2.89	Infilling and again Erosion	√	√	√	√
Test_C1_8_3b_20100428					√	√	√	√
Test_C1_8_2x_20100428		0.17	2.89		√	√	√	√
Test_C2_8_3a_20100504	Passive	0.04	2.89	Infilling and again Erosion	√	√	√	√
Test_C2_8_3b_20100504					√	√	√	√
Test_C2_8_2x_20100504		0.17	2.89		√	√	√	√
Test_D1_8_3a_20100510	Passive	0.04	2.89	Infilling and again Erosion	√	√	√	√
Test_D1_8_3b_20100510					√	√	√	√
Test_D1_8_2x_20100510		0.17	2.89		√	√	√	√
Test_D2_8_3a_20100517	Passive	0.04	2.89	Infilling and again Erosion	√	√	√	√
Test_D2_8_3b_20100517					√	√	-	√
Test_D2_8_2x_20100517		0.17	2.89		√	√	√	√
Test_E2_8_3a_20100524	Active	0.04	2.89	Infilling and again Erosion	√	√	√	√
Test_E2_8_3b_20100524					√	√	√	√
Test_E2_8_2x_20100524		0.17	2.89		√	√	√	√

- Reflection coefficient (K_r), which follows from a computation on the wave-data from all the four wave gauges. The computation separates the incident and reflected significant wave-height and determines the reflection coefficient, as described in section 4.4;
- Wave-induced pore-pressure variations, including time-domain and frequency-domain analysis (read as PPVar in Table 5.I), are evaluated to study wave propagation along the beach slope (including attenuation of wave-induced pore-pressures in the soil with depth, see section 3.3), wave-induced pressures over the reinforced dune, and over the submerged breakwater; and
- Beach-profile evolution under erosional and accretionary breaking random-wave conditions (read as BPEv in Table 5.I). Both localized scour and more widespread beach lowering are assessed. The scour development with regard to the scour and deposition patterns over the test period, that is to say the bar/trough formation and maintenance, is evaluated with regard to the reflection coefficient and to the wavelength. The scour is expressed as the maximum difference in meters between the wave-changed seabed and the initial bed and is given as the dimensionless scour depth (S_d/H_0). The results are compared to previous studies.

A number of other tests, which are not included within the considered clusters for evaluation, were carried out within this research programme comprising tests that had to be repeated for varied reasons (*e.g.*, the parameter beach-profile evolution was not recorded), sequences of erosion, infilling and again erosion that were not reproduced in further models (*e.g.*, infilling after sea-state 9 while experimenting with Model B1), tests in working water depths other than that of 0.58m, and the experimenting with the first Model C layout. Although not representative these additional tests may still bring about a contribution, namely on the assessment of test reproducibility, and on constructability; thus they will be referred to when appropriate.

5.2. Irregular wave generation

The wave generation system, as described in section 4.3, is able to produce regular (sinusoidal) and random waves, however, only the former feature with a standard spectral shape has been used in the current experimental work. As such the target wave spectrum is the standard JONSWAP wave spectrum that may be defined by the parameters peak frequency (f_p), significant wave-height (H_s), and shape parameter (γ) as described by Eq. (5.1).

$$S(f) = \frac{\alpha H_s^2 f_p^4}{f^5} e^{-\left[1.25\left(\frac{f_p}{f}\right)^4\right]} \gamma^{e^{-\left[\frac{(f-f_p)^2}{2\sigma^2 f_p^2}\right]}} \tag{5.1}$$

where the quantities σ and α are given by Eqs. (5.2) and (5.3) respectively.

$$\sigma = \begin{cases} 0.07, \text{for } f \leq f_p \\ 0.09, \text{for } f > f_p \end{cases} \tag{5.2}$$

$$\alpha = \frac{0.0624}{0.230 + 0.0336\gamma - \frac{0.185}{1.9 + \gamma}} \tag{5.3}$$

in which the quantity γ is the shape parameter, typically ranging from 1 to 7, with default 3.3.

As a check of correctness of the wave motion generated, the measured spectral densities of the incoming wave spectra, as mentioned earlier in section 4.4, should conform to the theoretical JONSWAP spectrum used in the wave generation control program input and defined by the aforesaid parameters f_p, H_s, and γ.

Yet, it is very likely the obtained spectra and the theoretical one to differ significantly outside the frequency limits $0.5f_p$ and $2f_p$. Indeed, unwanted generation in the upper and lower frequency tails of the spectrum is a known model effect which has been recognized for many years and in many publications.

The available data suggest that those discrepancies are due to the spurious superharmonic and subharmonic higher-order waves generated by, *e.g.*, reflections from boundaries and wave absorbers, linear and non-linear distortions caused by a rigid paddle, wave-wave interactions transferring wave energy into adjacent frequencies during propagation, resonance of water behind the paddle or loss of water through gaps (*e.g.*, between the paddles, the side walls and the bottom), and recirculation currents within the wave facility. For discussion see, *e.g.*, Frigaard and Lykke Andersen (2010), Zhang and Schäffer (2007), Baldock (2006), Batjes *et al.* (2004), Schäffer and Steenberg (2003), Schäffer (1996), Hughes (1993), Batjes *et al.* (1987), Suh and Dalrymple (1987) cited in Hughes (1993), Dalrymple (1985), and references cited therein.

Whether this is considered an important deficiency may depend on the problem studied (Dalrymple, 1985), when the goal pursued with a physical modelling is to seek qualitative insight into a phenomenon not yet described or understood it might not be as important as when it comes to verifying (or disproving) theoretical results.

For the following, some of such effects and model results are raised concurrently. Yet, it is convenient to provide an explanation as to why:

- The gain parameter was set to 1.0 (*i.e.*, the value by default in the HR WaveMaker signal generation program) in the current experimental work;
- The set down compensation was switched out; and
- The HR Wallingford Dynamic Wave Absorption module (HR Wallingford, 2007), described in section 4.3, was switched in.

The gain parameter is used to fine tune the wave-height measured in the basin by uniformly correcting the energy in the sea-state. Note that it does not change the spectral shape of the measured spectrum, which depends on the input sea-state, or on the transfer function, but only calibrates the wave-height if it is slightly high or low compared with the demand. Setting the gain so that the generated irregular wave trains fit the target spectrum involves an iterative approach, which requires several test realizations with long enough duration to give stable wave statistics. By not adjusting the gain, it is assumed that a variation in incident to input wave-height may occur, however, so long that it has negligible variation across the different models for the same input parameters it does not significantly impact the accuracy of the measurement results (also because some of the measurement results are given as dimensionless ratios of the wave-height, *e.g.*, the dimensionless scour depth, S_d/H_0).

The set down compensation is a second-order driving signal that is added to the primary signal in real time (HR Wallingford, 2003). The purpose of this compensation is to ensure that the set down is modelled realistically, and spurious subharmonic wave energy minimised.

The correction for second-order effects is important because systems using first-order wavemaker theory for generating laboratory waves (as used in the HR Wallingford wave generation system) fail to generate correctly second-order subharmonics and superharmonics that exist in naturally occurring irregular waves (see, *e.g.*, Goda, 2000; and Kamphuis, 2000, for discussion on wave generation and random seas).

Although generating laboratory waves using first-order irregular wave theory is satisfactory for many physical model studies (Hughes, 1993), numerous authors have contributed to the derivation of nonlinear wavemaker theory for unidirectional waves (Zhang and Schäffer, 2007) while recognizing that waves at frequencies outside the usual primary-wave spectrum are important for several phenomenon along the coast and in the ocean (see, *e.g.*, Schäffer and Steenberg, 2003).

The recognition that in some instances second-order effects may have an important role in the context of model response has lead to the development of techniques that would ensure correct reproduction of the second-order effects. Yet, misleading results are given, not only by the non-consideration of those effects, but also by their unrealistic modelling. If, for instance, the bound long wave – set down – is reflected as a free

long wave back to the paddles, and again re-reflected shoreward to once more reach the testing section, at this point unwanted wave energy is present and no longer is the test reproducing natural bound wave energy. The uncertainty on whether the set down would introduce disturbances affecting the measurements has motivated the non-use of set down compensation in the experiments described in this thesis. A further argument against using the set down compensation facility is linked to the fact that there is experimental evidence that commonly used irregular wave-height parameters are not influenced significantly by whether or not unwanted spurious waves are suppressed (Hughes, 1993).

Has already been mentioned above, one of the main problems associated with the modelling of waves in laboratory is the presence of re-reflected waves altering the characteristics of the wave train incident to the testing section repeatedly. In consequence, an effective absorption of the waves propagating towards the wave generator is necessary.

The impact of such absorption system increases with model reflection coefficient increase, *i.e.* it has a higher impact for installations where large reflections from the model are expected. Although this was not the case of the model under study in the current experimental work, for which relatively low reflection was expected, the HR Wallingford Dynamic Wave Absorption module (HR Wallingford, 2007) has been switched in, based on concerns over the fact that the testing section was relatively short in length, and that recirculation and reflections from boundaries were likely to occur.

A further concern has been the susceptibility of the basin where the experiments were carried out, to resonant oscillations forced across the boundaries. Those oscillations are long-period standing waves which characteristics are generally controlled by basin size, shape, and water depth (USACE, 2008).

In Appendix C, the calculations made to determine the natural free oscillating periods are provided for reference. Considering that the natural free oscillating periods of the basin are apparently about the same order of magnitude as the periodic disturbing force (*i.e.*, the peak wave period of the incident waves), it is expected the HR Wallingford Dynamic Wave Absorption module to be able to absorb the energy from those oscillating waves.

5.2.1. Generated wave conditions

The evaluation of the generated wave conditions provides confidence that the different models have been set-up to run on similar hydrodynamic conditions, and thus that the comparison applied to the wave-induced morphodynamic change is possible and reliable.

The wave-data recorded during the experimental work was processed using the analysis routine of the software HR WaveData (see, *e.g.*, HR Wallingford, 2005), as introduced in section 4.4. That routine includes both a spectral analysis using Fast Fourier Transform (see, *e.g.*, Frigaard and Lykke Andersen, 2010; Dalrymple, 1985; and Burcharth and Borsen, 1978) and a statistical analysis. The former enabled the calculation of some relevant wave parameters (*e.g.*, the number of waves, the highest one-third wave, and the highest wave-height of the signal), while the latter transforms the measured calibrated time-series into the frequency domain to obtain the response spectrum, from which many of the commonly used design parameters can be calculated (*e.g.*, the peak wave period, and the significant wave-height).

In Figures 5.1 to 5.11 the frequency spectral density functions of the wave spectra computed for each surface elevation probe, S1 to S4, as described in section 4.3, and of the frequency spectral density functions of the incident wave spectra, is plotted against the theoretical JONSWAP spectrum. The given examples were chosen to illustrate measures of fit to JONSWAP for each model with different experimental conditions.

The black line in Figures 5.1 to 5.11 is the result of fitting Eq. (5.1) with corresponding values of significant wave-height and period.

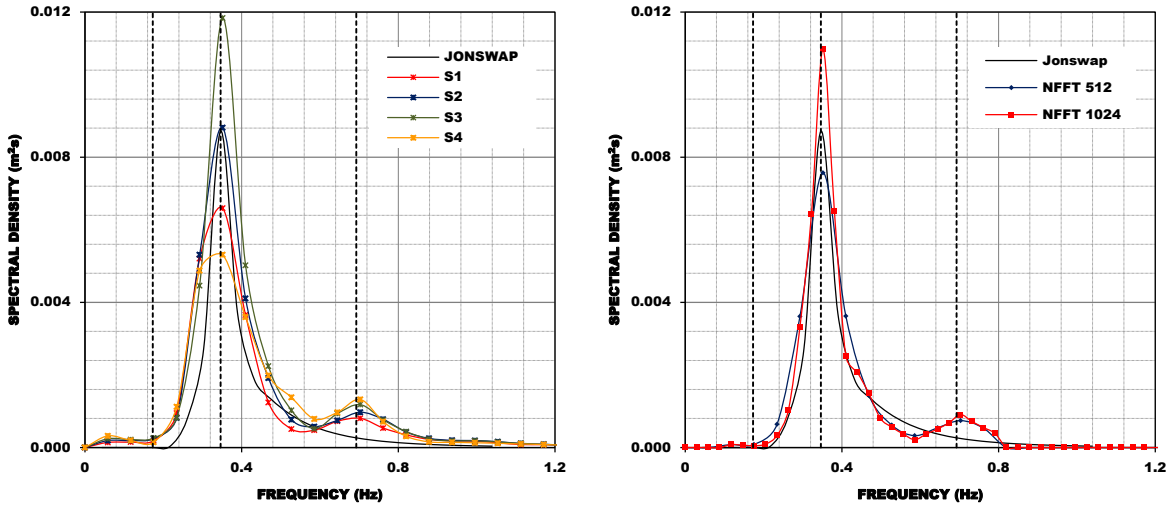

Figure 5.1: Model A, sea-state 10 (H_s=0.125m, f_p=0.346Hz) – spectral densities of the wave spectra as measured by probes S1 to S4 (left), spectral densities of the computed incident wave spectra (right).

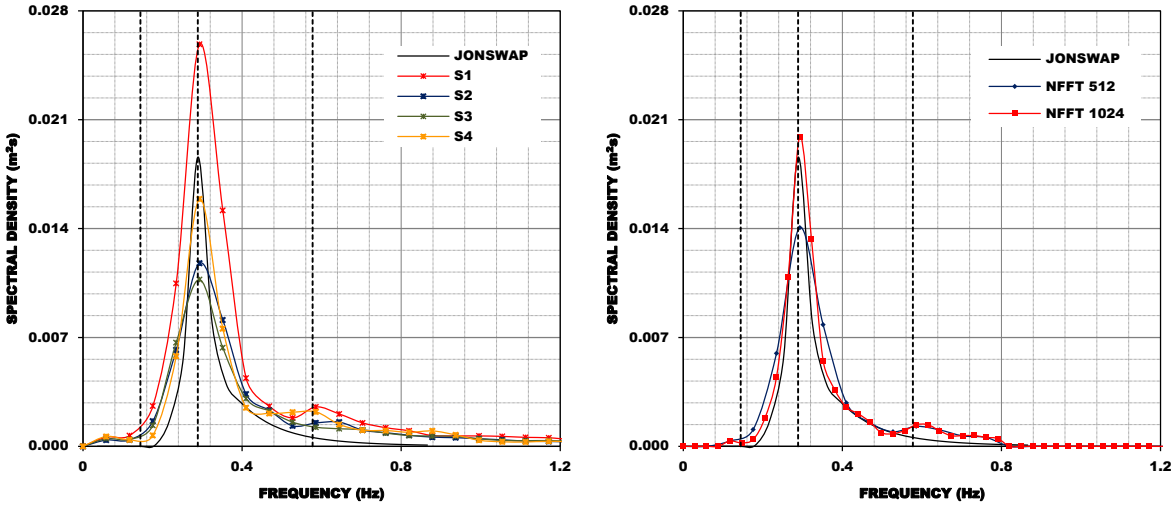

Figure 5.2: Model B1, sea-state 9 (H_s=0.17m, f_p=0.289Hz) – spectral densities of the wave spectra as measured by probes S1 to S4 (left), spectral densities of the computed incident wave spectra (right).

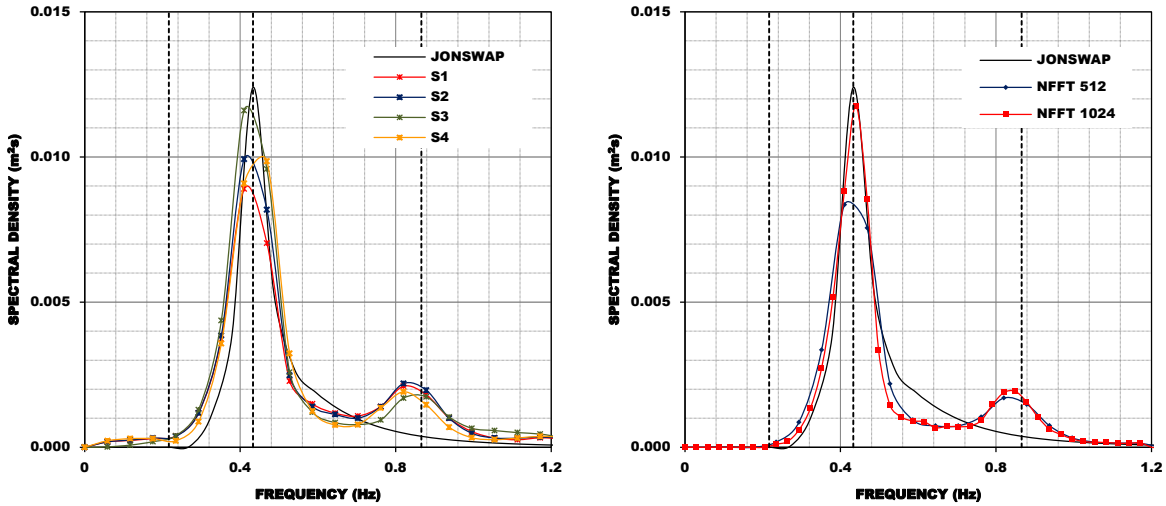

Figure 5.3: Model B2, sea-state 7 (H_s=0.17m, f_p=0.433Hz) – spectral densities of the wave spectra as measured by probes S1 to S4 (left), spectral densities of the computed incident wave spectra (right).

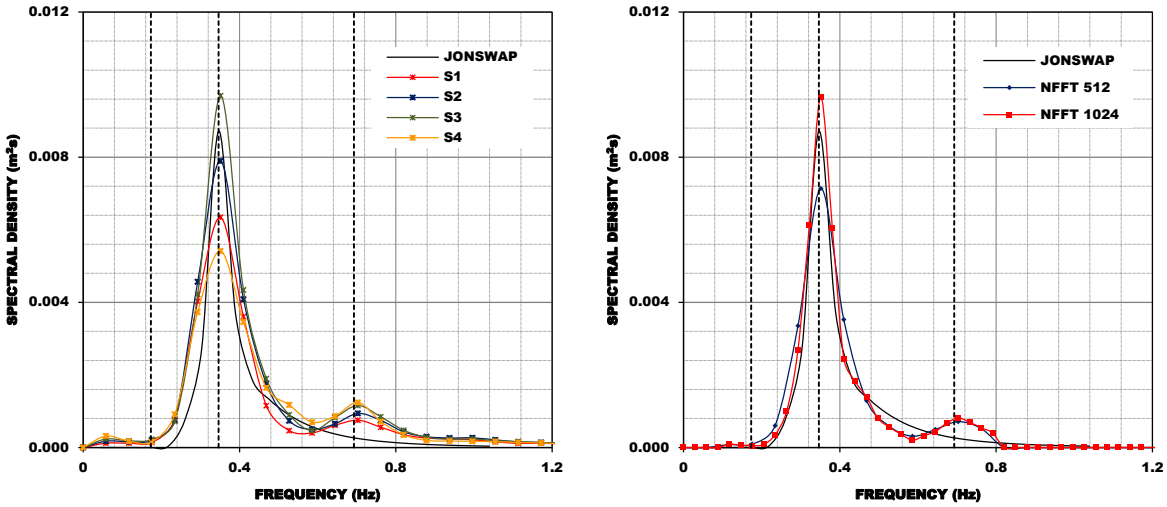

Figure 5.4: Model C1, sea-state 10 (H_s=0.125m, f_p=0.346Hz) – spectral densities of the wave spectra as measured by probes S1 to S4 (left), spectral densities of the computed incident wave spectra (right).

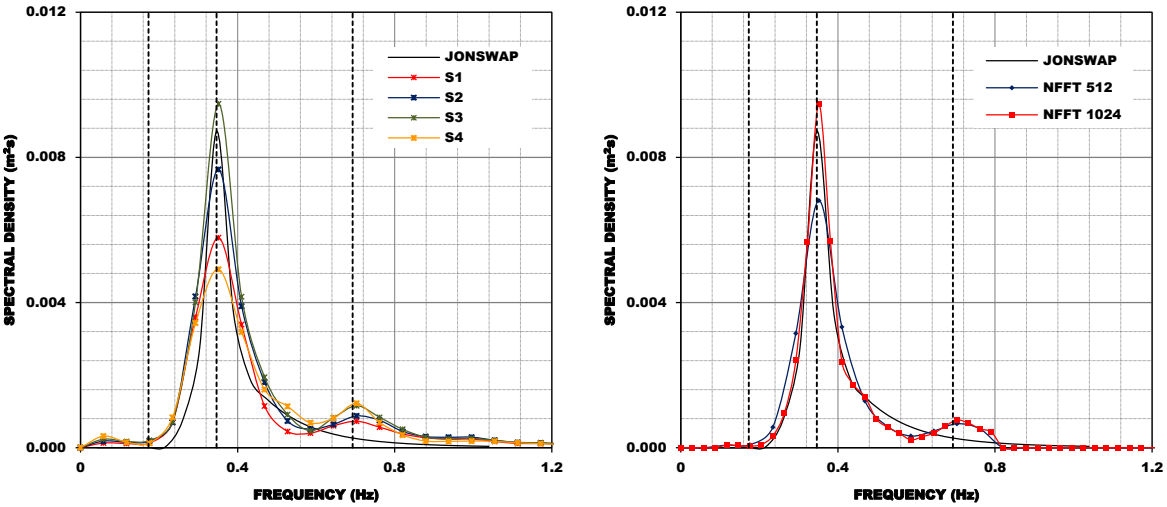

Figure 5.5: Model C2, sea-state 10 (H_s=0.125m, f_p=0.346Hz) – spectral densities of the wave spectra as measured by probes S1 to S4 (left), spectral densities of the computed incident wave spectra (right).

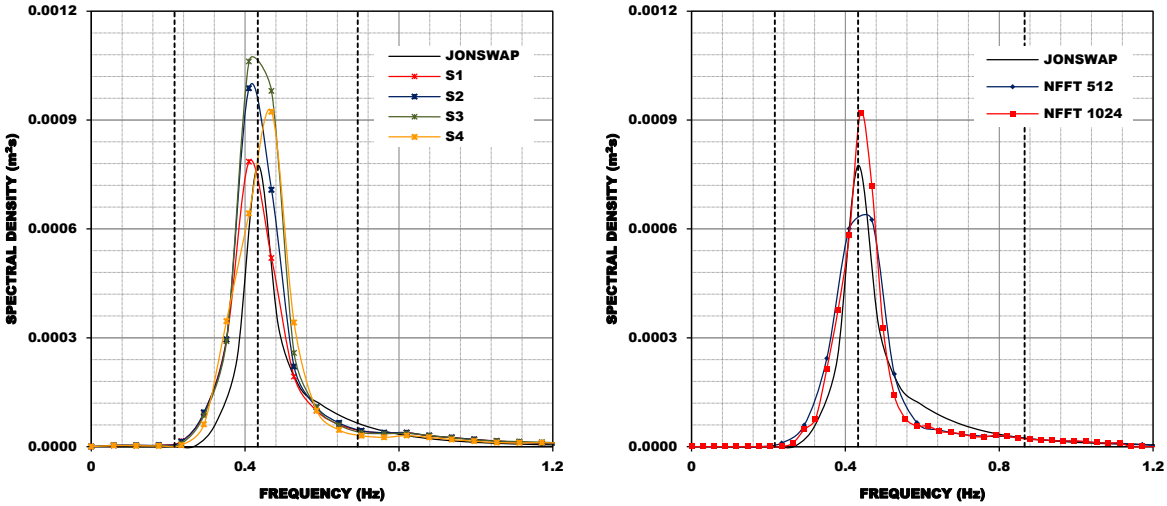

Figure 5.6: Model D1, sea-state 2 (H_s=0.04m, f_p=0.433Hz) – spectral densities of the wave spectra as measured by probes S1 to S4 (left), spectral densities of the computed incident wave spectra (right).

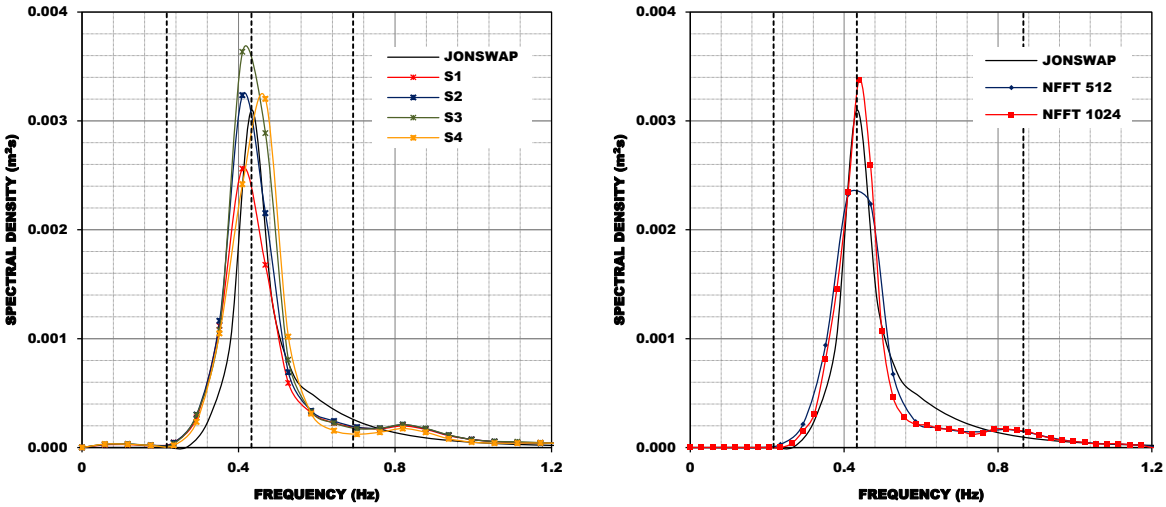

Figure 5.7: Model D2, sea-state 5 (H_s=0.08m, f_p=0.433Hz) – spectral densities of the wave spectra as measured by probes S1 to S4 (left), spectral densities of the computed incident wave spectra (right).

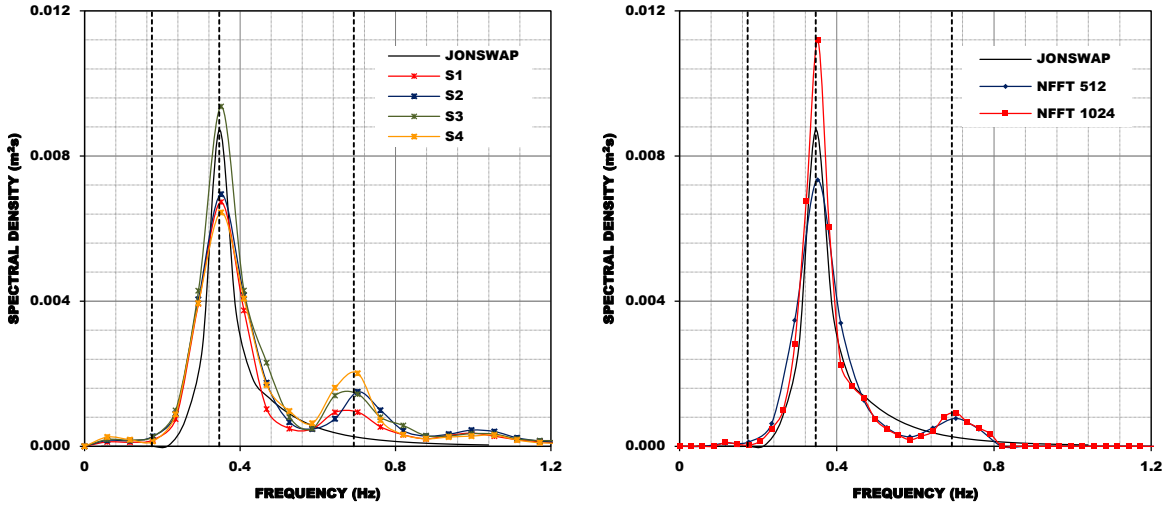

Figure 5.8: Model E1, sea-state 10 (H_s=0.125m, f_p=0.346Hz) – spectral densities of the wave spectra as measured by probes S1 to S4 (left), spectral densities of the computed incident wave spectra (right).

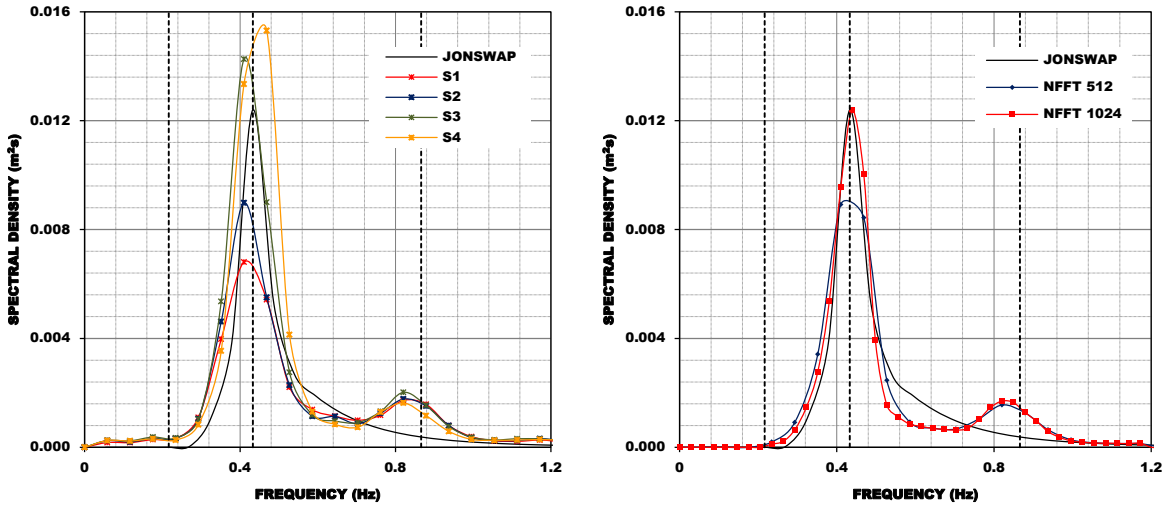

Figure 5.9: Model E2, sea-state 7 (H_s=0.17m, f_p=0.433Hz) – spectral densities of the wave spectra as measured by probes S1 to S4 (left), spectral densities of the computed incident wave spectra (right).

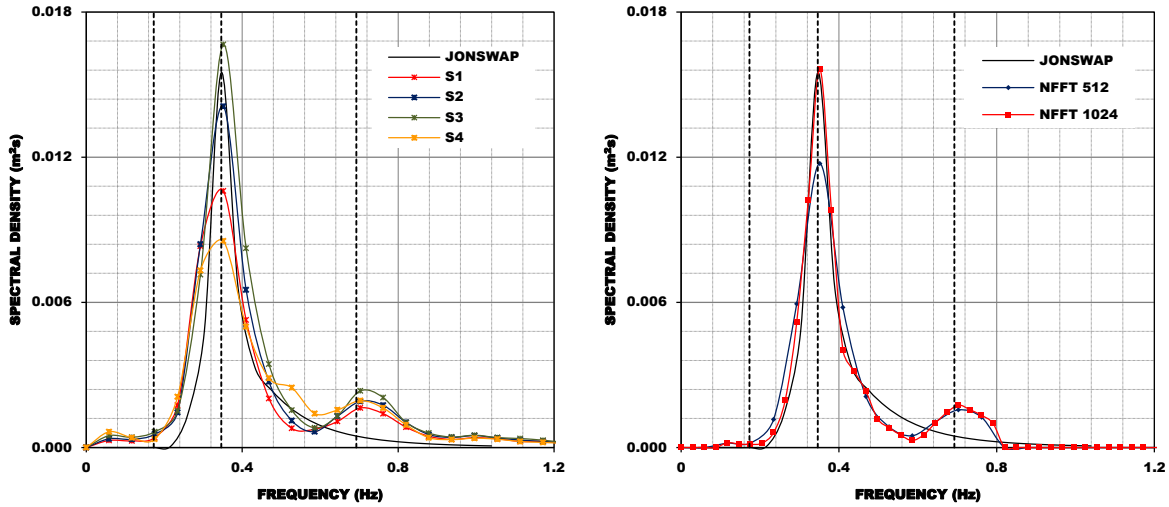

Figure 5.10: Model E3, sea-state 8 (H_s=0.17m, f_p=0.346Hz) – spectral densities of the wave spectra as measured by probes S1 to S4 (left), spectral densities of the computed incident wave spectra (right).

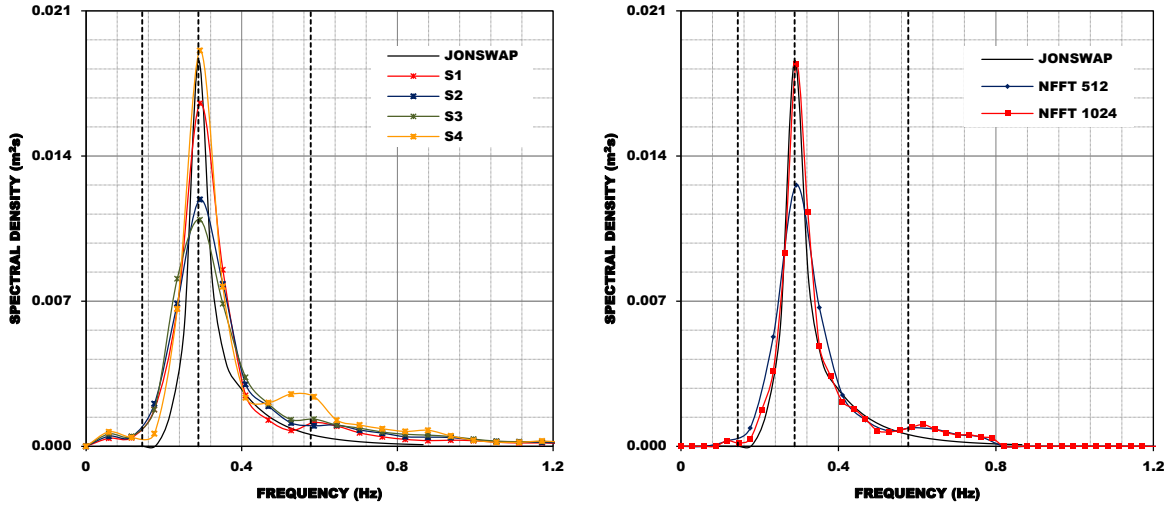

Figure 5.11: Model E4, sea-state 9 (H_s=0.17m, f_p=0.289Hz) – spectral densities of the wave spectra as measured by probes S1 to S4 (left), spectral densities of the computed incident wave spectra (right).

The vertical dashed black lines are representative of the peak wave frequency (f_p) and the frequency limits, which correspond to halve and two times that peak wave frequency, $0.5f_p$ and $2f_p$ respectively.

The wave spectra of the probes S1 to S4 were estimated for a window size of spectrum smoothing of 512, *i.e.* the window length (NFFT) is 512 data points; while the sizes of the windowing function to compute the spectral densities of the incident wave spectra were 512 and 1024. The size of the windowing function choice is based on the degree of variance and bias in the result. It is a trade-off as the larger the window, the higher is the variance and the lower is the bias. How the window size affects the spectral estimate computed is show in Figure 5.12 for two different experimental conditions.

After thorough analysis of the different calculated response spectra with four different sizes of the windowing function, *i.e.* values of 2^N equal to 512, 1024, 2048, and 4096, for all experimental conditions with Model A, it was decided that the number of spectral bands over which the spectrum will be smoothed would correspond to window sizes of 512, and 1024; as neither using a block size of 2^9, nor a block size of 2^{10}, provide significant benefits in regard to better fit of JONSWAP spectrum over the other. So as for the spectral analysis using Fast Fourier Transform of the other experimental conditions, window lengths of 512 and 1024 were used.

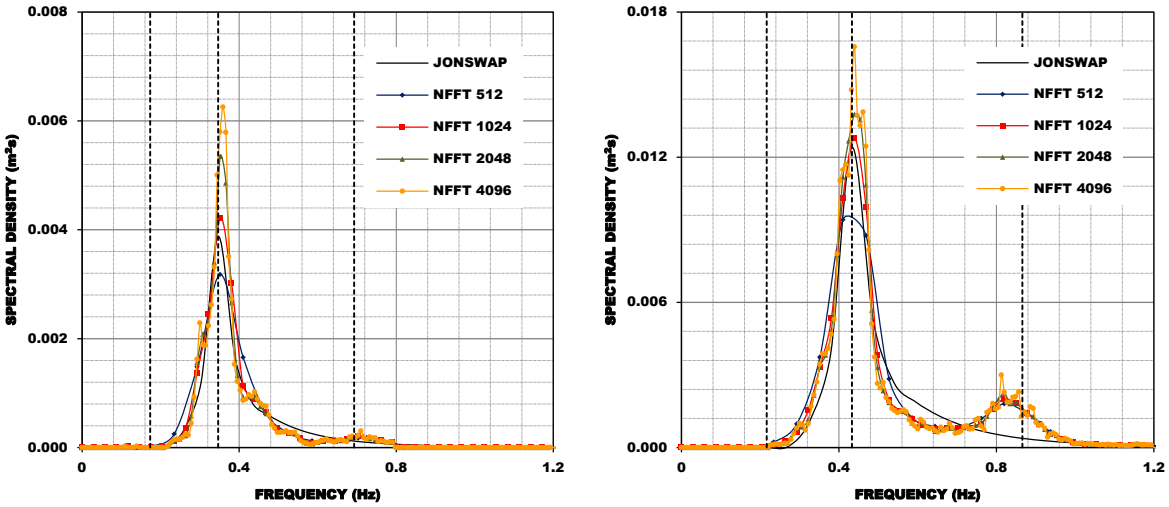

(a) sea-state 6 (H_s=0.08m, f_p=0.346Hz) (b) sea-state 7 (H_s=0.17m, f_p=0.433Hz)

Figure 5.12: Effect of different window sizes on spectrum smoothing, Model A.

As shown in Figures 5.1 to 5.11 the frequency spectrum of the response incident wave spectra reproduces with a reasonable approximation the spectral shapes specified in the wave generation system, within a frequency region near the peak wave frequency (f_p). Yet, it indicates that approximation becomes weaker near the frequency limit $2f_p$ where singularities are present, especially at the most energetic sea-states and peak frequencies of 0.346 and 0.433 Hz. Those singularities, which correspond to a wave energy density transfer from low to higher frequencies, may be ascribed to nonlinear effects when the waves interact with the beach, most especially by the presence of a barred profile.

To this respect, it should be interesting to note some observations made during the experiments. Notably, under more rough conditions, waves would typically break on the nearshore-bar (or submerged breakwater) dissipating a part of the wave energy. The remaining energy would be, part reflected seaward, and part transmitted leeward side. The transmitted energy, would again be dissipated on the structure (or dune), and the remaining energy reflected seaward. These wave-wave and wave energy dissipation, transmission and reflection interactions are the most probable cause of the second peak appearing.

Similar spectral shapes have been observed in the wave transmission spectrum by a number of experimental studies on submerged and low-crested structures (see, *e.g.*, Neves, 2007; Bleck, 2003, and Yoshida *et al.*, 2002). Typically, the transmitted wave has much of its energy at the same frequency as the incident wave, but a portion of the transmitted energy has shifted to the higher harmonic frequencies of the incident wave (USACE, 2008). Typically it is transmitted to frequencies around two times the peak frequency.

Still about the impact of those singularities, it should be noted that the corresponding waves account for a very small portion of the total available energy.

With regard to the spectral densities of the surface elevation probes wave spectra, left panels in Figures 5.1 to 5.11 indicate that the wave energy is spread. The figures also indicate that the wave energy is concentrated around the frequency peak, f_p, for most of the experimenting conditions. In Figures 5.3, 5.6, 5.7, and 5.9, the position of the peak is slightly shifted.

Conclusively, although some difference is observed between the actual and standard spectra, possibly due to shallow water effects and to nonlinear effects when the waves interact with the beach, the response spectrum describes the features of the standard spectrum quite well.

For the purpose of evaluating whether the tests within a same cluster were set-up to run on similar hydrodynamic conditions, a similar approach has been used. Figures 5.13 to 5.15 present some selected results of such comparison applied to experimental conditions under the same input sea-state.

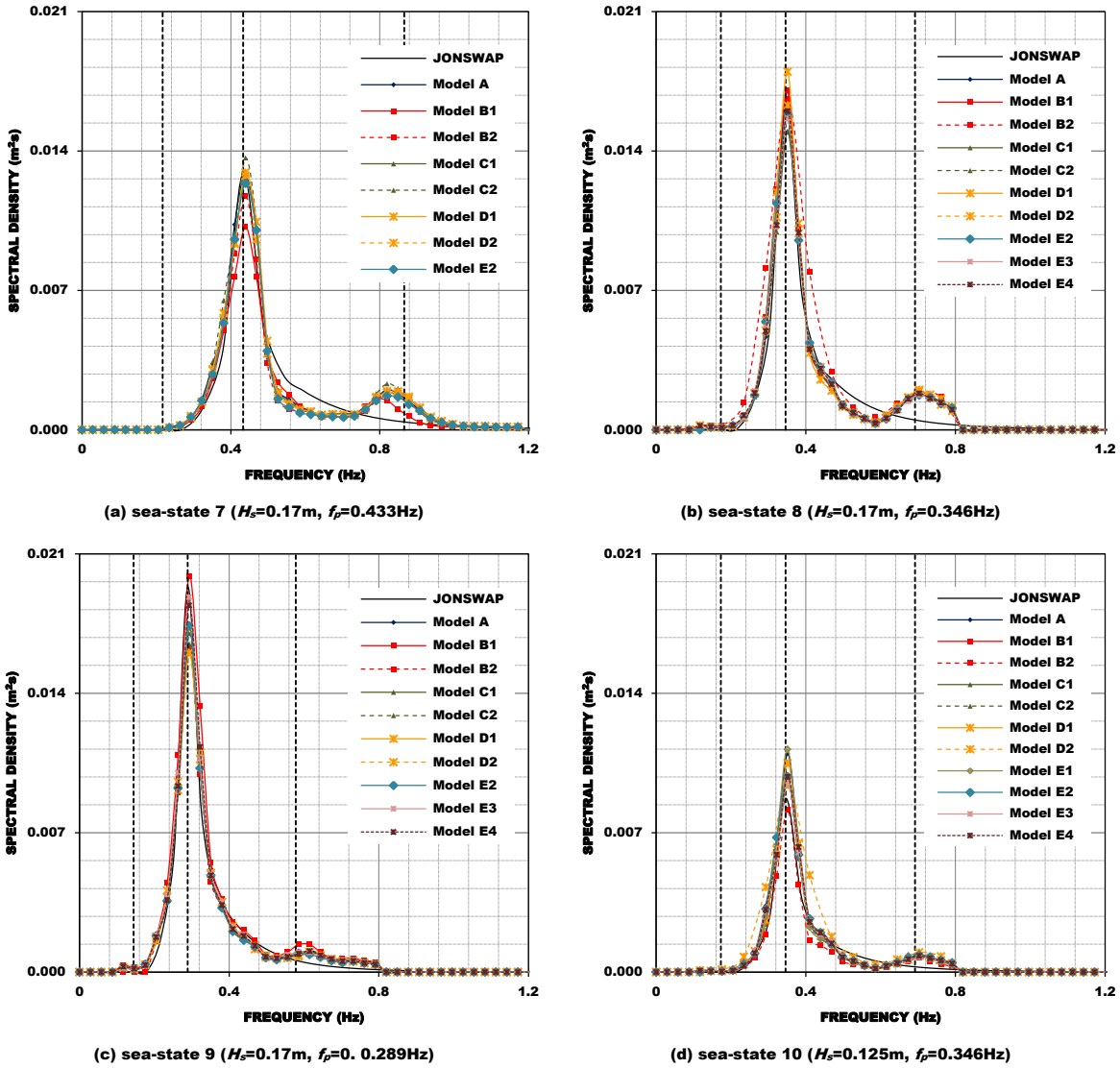

Figure 5.13: Spectral densities of the incident wave spectra, erosion.

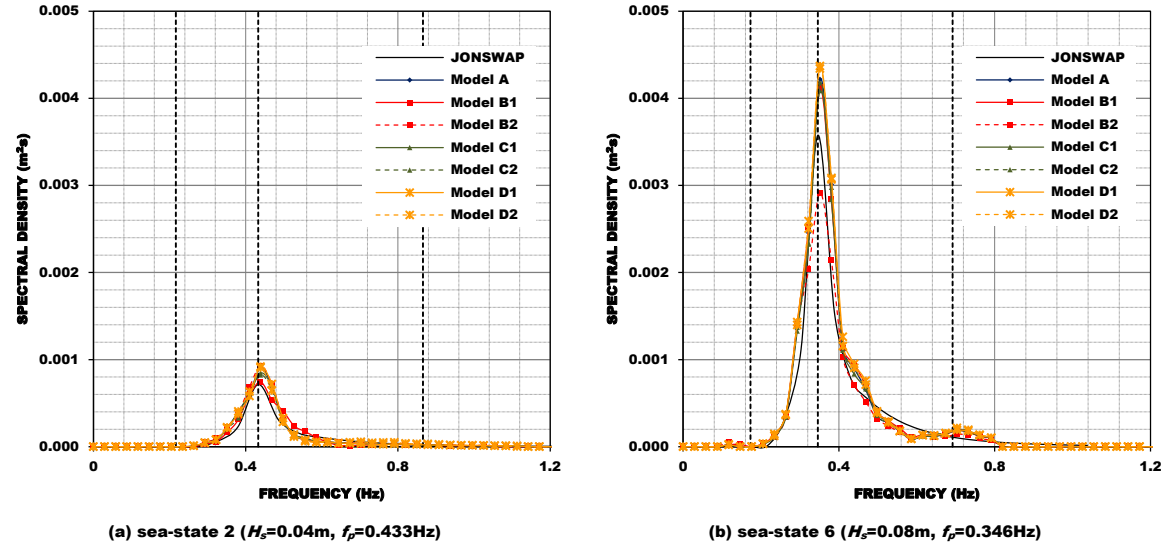

Figure 5.14: Spectral densities of the incident wave spectra, accretion.

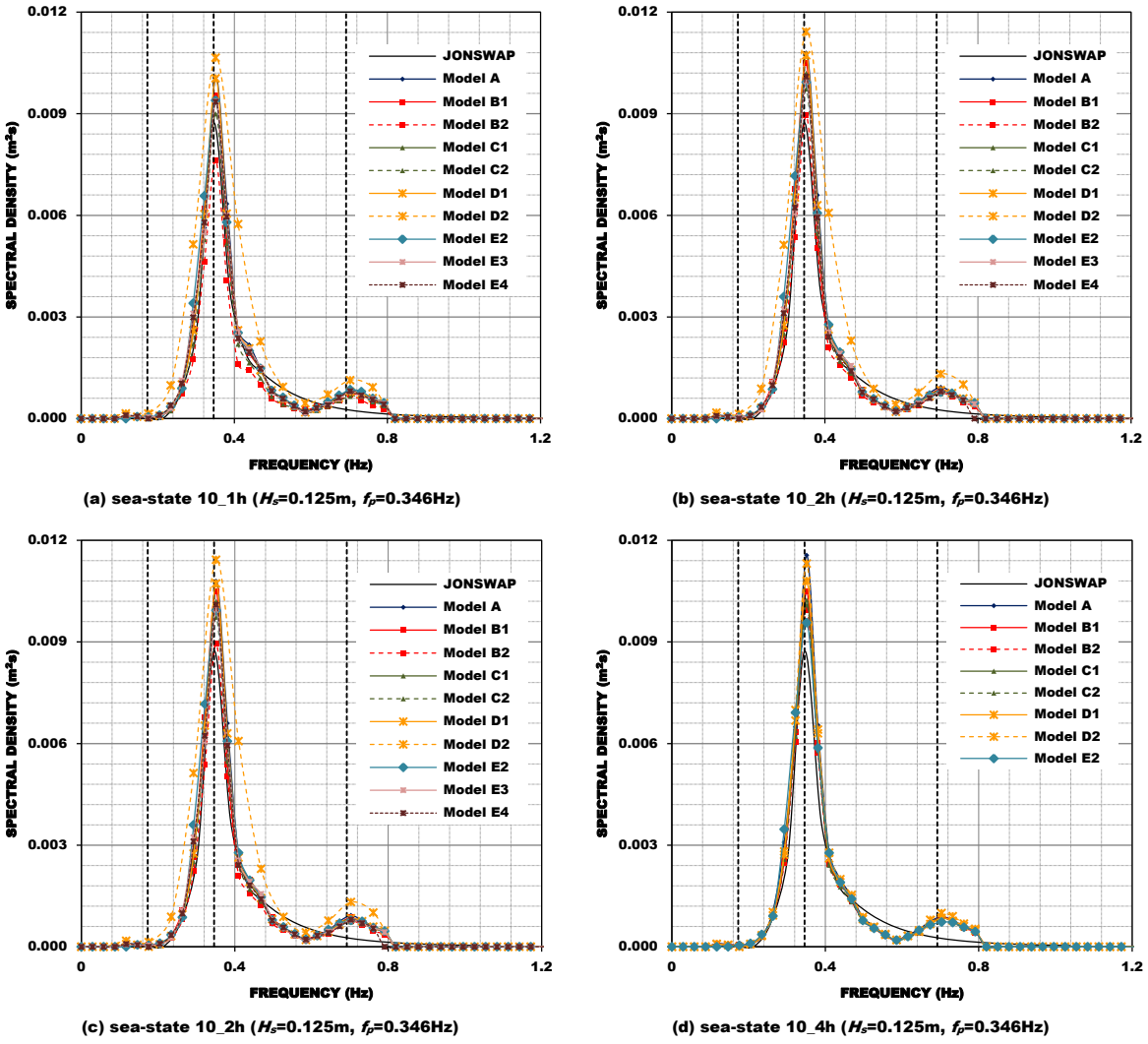

Figure 5.15: Spectral densities of the incident wave spectra, persistent erosional conditions.

Qualitatively speaking, the selected results indicate that there is only very slight deviation between the response incident wave spectra across the various models, and from these to the standard form. A higher deviation is observed for models D2, sea-state 10 (Figures 5.13d, 5.15a, 5.15b, and 5.15c), and B2, sea-state 8 (Figure 5.13b). It is intriguing to notice that in Figure 5.15d there is no longer a deviation. The origin of the observed deviations is not clear, thus the results within those experimenting conditions, need to be treated with care.

Figures 5.13 to 5.15 also indicate that the wave energy is concentrated around the frequency peak, f_p, or equivalently its inverse the peak period, T_p, and that the values are within the input parameter significant wave period, as described in section 4.2. Further, scattering is noticeable in the peak spectral densities, which influence is analysed later.

Although the representation of a sea-state with characteristic wave-heights and period parameters and its spectral description are two perspectives of the same physical phenomenon (*i.e.*, it is possible to relate one perspective to the other), a variance spectrum such as the ones illustrated in the previous figures say nothing about how high the individual waves are.

To convert spectral analysis into meaningful and commonly used design parameters (*e.g.*, the significant wave-height) is necessary to define the moments of the wave spectrum as given by Eq. (5.4).

$$m_h = \int_0^{\infty} f^h \, S(f) \, df \tag{5.4}$$

where m_h is the moment of h order of the wave spectrum, from which is possible to estimate the heights of representative waves. For example, it is possible to estimate the significant wave-height, H_s, from the representative value of the total wave energy, the zero moment, m_0, when the wave follows the Rayleigh distribution (see, *e.g.*, Goda, 2000). Needless to say that m_0 is actually the area under the variance spectrum curve.

Table 5.II lists the mostly used relationship of the moments of the wave spectrum to the heights and periods of representative waves, assuming that the wave-height follows the Rayleigh distribution. So, the estimation of significant wave-height based on the incident wave spectra is always possible by evaluating the integral m_0 with Eq. (5.12). The heights other than the significant wave-height can be derived by means of Eqs. (5.13) to (5.15). In the case of the peak period, T_p, the mean period of the zero-downcrossing waves, T_z, the period between crests, T_c, and the mean period, T_m, they can be yielded from the moments of the wave spectrum using Eqs. (5.16) to (5.19).

Other expressions in Table 5.II concern the spectral width parameters, ε_1 and ε_2, which denote the broadness factor, and the narrowness parameter, respectively.

Table 5.III summarize the computed representative wave-heights and periods derived from spectral analysis. The results are ranked in accordance to Table 5.I, the targeted sea-state is given as a reference.

Table 5.II: Important relationships in spectral analysis.

Zero moment, m_0	$m_0 = \int_0^\infty S(f)\, df$	(5.5)
First-order moment, m_1	$m_1 = \int_0^\infty f\, S(f)\, df$	(5.6)
Second-order moment, m_2	$m_2 = \int_0^\infty f^2\, S(f)\, df$	(5.7)
Third-order moment, m_3	$m_3 = \int_0^\infty f^3\, S(f)\, df$	(5.8)
Fourth-order moment, m_4	$m_4 = \int_0^\infty f^4\, S(f)\, df$	(5.9)
Spectral width parameters, ε_1	$\varepsilon_1 = \sqrt{1 - \frac{m_2^2}{m_0 m_4}}$	(5.10)
Spectral width parameters, ε_2	$\varepsilon_2 = \sqrt{\frac{m_0 m_2}{m_1^2} - 1}$	(5.11)
Significant wave-height, H_s	$H_s = 4\sqrt{m_0}$	(5.12)
Mean wave-height, H_m	$H_m = \sqrt{2\pi}\sqrt{m_0}$	(5.13)
Maximum wave-height, H_{max}	$H_{max} = 1.83 * 4\sqrt{m_0}$	(5.14)
Root-mean-square wave-height, H_{rms}	$H_{rms} = 2 * \sqrt{2\pi}\sqrt{m_0}$	(5.15)
Peak period, T_p	$T_p = \frac{1}{f_p}$	(5.16)
Mean period of the zero-downcrossing waves, T_z	$T_z = \sqrt{\frac{m_0}{m_2}}$	(5.17)
Period between crests, T_c	$T_c = \sqrt{\frac{m_2}{m_4}}$	(5.18)
Mean period, T_m	$T_m = \frac{m_0}{m_1}$	(5.19)

Table 5.III: Representative wave-heights and periods derived from spectral analysis.

Test ID	Targeted Sea-state		Generated Sea-state		H_{max} [m]	H_{rms} [m]	Mean Sea-state	
	H_s [m]	T_p [s]	H_s [m]	T_p [s]			H_m [m]	T_m [s]
Test_A_7_20100409	0.17	2.31	0.196	2.28	0.358	0.245	0.123	1.67
Test_B1_7_20091031			*0.177*		*0.323*	*0.222*	*0.111*	*1.68*
Test_B2_7_20100323			*0.186*		*0.341*	*0.233*	*0.117*	*1.64*
Test_C1_7_20100427			0.193		0.354	0.242	0.121	1.66
Test_C2_7_20100503			0.202		0.369	0.253	0.126	1.65
Test_D1_7_20100512			0.196		0.359	0.246	0.123	1.66
Test_D2_7_20100518			0.194		0.355	0.243	0.121	1.64
Test_E2_7_20100524			0.190		0.348	0.238	0.119	1.66
Test_A_8_20100405	0.17	2.89	0.201	2.84	0.368	0.252	0.126	1.86
Test_B1_8_20100105			0.204		0.373	0.255	0.128	1.88
Test_B2_8_20100325			*0.228*		*0.418*	*0.286*	*0.143*	*1.89*
Test_C1_8_20100428			0.193		0.353	0.242	0.121	1.87
Test_C2_8_20100504			0.195		0.356	0.244	0.122	1.88
Test_D1_8_20100510			0.204		0.373	0.255	0.128	1.86
Test_D2_8_20100517			0.201		0.367	0.251	0.126	1.87
Test_E2_8_20100522			0.198		0.363	0.249	0.124	1.89
Test_E3_8_20100526			0.196		0.359	0.246	0.123	1.88
Test_E4_8_20100525			0.197		0.361	0.248	0.124	1.87
Test_A_9_20100413	0.17	3.46	0.202	3.41	0.369	0.253	0.126	2.04
Test_B1_9_20100106			0.213		0.390	0.267	0.134	2.05
Test_B2_9_20100329			*0.185*		*0.339*	*0.232*	*0.116*	*2.07*
Test_C1_9_20100426			0.193		0.353	0.242	0.121	2.06
Test_C2_9_20100505			0.196		0.358	0.245	0.123	2.05
Test_D1_9_20100511			0.192		0.352	0.241	0.121	2.08
Test_D2_9_20100518			0.198		0.362	0.248	0.124	2.07
Test_E2_9_20100524			0.195		0.356	0.244	0.122	2.05
Test_E3_9_20100526			0.202		0.369	0.253	0.126	2.04
Test_E4_9_20100525			0.200		0.366	0.251	0.125	2.04
Test_A_10_20100331	0.125	2.89	0.157	2.84	0.288	0.197	0.099	1.88
Test_B1_10_20100112			0.150		0.274	0.188	0.094	1.88
Test_B2_10_20100210			*0.133*		*0.243*	*0.167*	*0.083*	*1.85*
Test_C1_10_20100420			0.150		0.274	0.188	0.094	1.89
Test_C2_10_20100429			0.147		0.269	0.184	0.092	1.88
Test_D1_10_20100511			0.154		0.282	0.193	0.096	1.88
Test_D2_10_20100515			*0.174*		*0.318*	*0.218*	*0.109*	*1.87*
Test_E1_10_20100520			0.155		0.284	0.195	0.097	1.86
Test_E2_10_20100521			0.153		0.279	0.191	0.096	1.90
Test_E3_10_20100526			0.150		0.274	0.188	0.094	1.90
Test_E4_10_20100525			0.151		0.277	0.189	0.095	1.89

Table 5.III: Representative wave-heights and periods derived from spectral analysis (cont.).

Test ID	Targeted Sea-state		Generated Sea-state		H_{max} [m]	H_{rms} [m]	Mean Sea-state	
	H_s [m]	T_p [s]	H_s [m]	T_p [s]			H_m [m]	T_m [s]
Test_A_1_20100407	0.04	1.73	0.070	1.63	0.128	0.087	0.044	1.44
Test_B1_1_20091030			0.039		0.071	0.049	0.024	1.45
Test_B2_1_20100223			0.037		0.068	0.046	0.023	1.42
Test_C1_1_20100419			0.036		0.066	0.045	0.022	1.47
Test_C2_1_20100502			0.033		0.060	0.041	0.021	1.41
Test_D1_1_20100512			0.036		0.065	0.045	0.022	1.41
Test_D2_1_20100518			0.036		0.066	0.045	0.023	1.39
Test_A_2_20100407	0.04	2.31	0.048	2.28	0.087	0.060	0.030	1.75
Test_B1_2_20091030			0.045		0.083	0.057	0.028	1.77
Test_B2_2_20100223			0.049		0.090	0.061	0.031	1.75
Test_C1_2_20100419			0.047		0.086	0.059	0.030	1.76
Test_C2_2_20100502			0.046		0.085	0.058	0.029	1.75
Test_D1_2_20100512			0.048		0.088	0.060	0.030	1.74
Test_D2_2_20100518			0.048		0.088	0.060	0.030	1.73
Test_A_4_20100408	0.08	1.73	0.064	1.63	0.117	0.080	0.040	1.51
Test_B1_4_20091030			0.078		0.142	0.097	0.049	1.47
Test_B2_4_20100223			0.072		0.132	0.090	0.045	1.41
Test_C1_4_20100419			0.071		0.131	0.090	0.045	1.46
Test_C2_4_20100503			0.069		0.127	0.087	0.043	1.41
Test_D1_4_20100512			0.073		0.133	0.091	0.046	1.42
Test_D2_4_20100518			0.071		0.129	0.089	0.044	1.41
Test_A_5_20100408	0.08	2.31	0.089	2.28	0.163	0.112	0.056	1.74
Test_B1_5_20091030			0.091		0.166	0.114	0.057	1.78
Test_B2_5_20100223			0.086		0.158	0.108	0.054	1.72
Test_C1_5_20100419			0.092		0.168	0.115	0.058	1.75
Test_C2_5_20100503			0.056		0.102	0.070	0.035	1.88
Test_D1_5_20100512			0.094		0.172	0.118	0.059	1.72
Test_D2_5_20100518			0.093		0.171	0.117	0.059	1.72
Test_A_6_20100413	0.08	2.89	0.098	2.84	0.179	0.123	0.061	1.93
Test_B1_6_20100104			0.098		0.179	0.123	0.061	1.94
Test_B2_6_20100324			0.086		0.158	0.108	0.054	1.98
Test_C1_6_20100419			0.097		0.177	0.121	0.061	1.92
Test_C2_6_20100504			0.097		0.178	0.122	0.061	1.93
Test_D1_6_20100510			0.100		0.183	0.125	0.063	1.93
Test_D2_6_20100517			0.100		0.183	0.125	0.063	1.93

Table 5.III: Representative wave-heights and periods derived from spectral analysis (cont.).

Test ID	Targeted Sea-state		Generated Sea-state		H_{max} [m]	H_{rms} [m]	Mean Sea-state	
	H_s [m]	T_p [s]	H_s [m]	T_p [s]			H_m [m]	T_m [s]
Test_A_10_1h_20100331	0.125	2.89	0.153	2.84	0.280	0.192	0.096	1.88
Test_A_10_2h_20100331			0.156		0.286	0.196	0.098	1.87
Test_A_10_3h_20100331			0.158		0.290	0.198	0.099	1.86
Test_A_10_4h_20100401			0.160		0.292	0.200	0.100	1.87
Test_A_10_6h_20100401			0.161		0.295	0.202	0.101	1.86
Test_B1_10_1h_20100112	0.125	2.89	0.149	2.84	0.272	0.186	0.093	1.89
Test_B1_10_1.5h_20100112			0.153		0.279	0.191	0.096	1.88
Test_B1_10_2h_20100112			0.153		0.280	0.192	0.096	1.87
Test_B1_10_3h_20100114			0.148		0.271	0.186	0.093	1.87
Test_B1_10_4h_20100115			0.153		0.280	0.191	0.096	1.86
Test_B1_10_5h_20100115			0.149		0.273	0.187	0.093	1.87
Test_B1_10_6h_20100120			0.150		0.274	0.188	0.094	1.87
Test_B1_10_8h_20100120			0.151		0.276	0.189	0.095	1.87
Test_B1_10_10h_20100120			0.152		0.278	0.190	0.095	1.85
Test_B1_10_12h_20100125			0.143		0.262	0.179	0.090	1.86
Test_B1_10_14h_20100125			0.148		0.272	0.186	0.093	1.87
Test_B2_10_1h_20100210	0.125	2.89	0.130	2.84	0.238	0.163	0.081	1.86
Test_B2_10_2h_20100210			0.141		0.258	0.177	0.088	1.86
Test_B2_10_3h_20100212			0.153		0.279	0.191	0.096	1.87
Test_B2_10_4h_20100212			0.150		0.274	0.188	0.094	1.87
Test_B2_10_4h_8_20100212	0.17		0.196		0.359	0.246	0.123	1.86
Test_C1_10_1h_20100420	0.125	2.89	0.148	2.84	0.271	0.186	0.093	1.89
Test_C1_10_2h_20100420			0.152		0.278	0.190	0.095	1.88
Test_C1_10_3h_20100420			0.152		0.279	0.191	0.095	1.88
Test_C1_10_4h_20100420			0.152		0.279	0.191	0.095	1.87
Test_C1_10_6h_20100421			0.153		0.281	0.192	0.096	1.87
Test_C1_10_8h_20100421			0.155		0.283	0.194	0.097	1.87
Test_C1_10_9h_20100421			0.151		0.277	0.189	0.095	1.85
Test_C2_10_1h_20100429	0.125	2.89	0.141	2.84	0.258	0.177	0.088	1.87
Test_C2_10_2h_20100429			0.148		0.271	0.185	0.093	1.88
Test_C2_10_3h_20100430			0.150		0.275	0.188	0.094	1.87
Test_C2_10_4h_20100430			0.150		0.275	0.188	0.094	1.87
Test_C2_10_6h_20100430			0.148		0.270	0.185	0.093	1.88
Test_C2_10_8h_20100430			0.151		0.275	0.189	0.094	1.87
Test_D1_10_1h_20100511	0.125	2.89	0.152	2.84	0.277	0.190	0.095	1.88
Test_D1_10_2h_20100511			0.155		0.283	0.194	0.097	1.87
Test_D1_10_3h_20100511			0.156		0.285	0.195	0.097	1.87
Test_D1_10_4h_20100511			0.156		0.285	0.195	0.097	1.87
Test_D1_10_6h_20100511			0.155		0.284	0.194	0.097	1.86

Table 5.III: Representative wave-heights and periods derived from spectral analysis (cont.).

Test ID	Targeted Sea-state		Generated Sea-state		H_{max} [m]	H_{rms} [m]	Mean Sea-state	
	H_s [m]	T_p [s]	H_s [m]	T_p [s]			H_m [m]	T_m [s]
Test_D2_10_1h_20100515	0.125	2.89	0.187	2.84	0.342	0.234	0.117	1.89
Test_D2_10_2h_20100515			0.193		0.352	0.241	0.121	1.87
Test_D2_10_3h_20100516			0.156		0.285	0.195	0.098	1.86
Test_D2_10_4h_20100516			0.159		0.292	0.200	0.100	1.86
Test_D2_10_6h_20100516			0.160		0.293	0.200	0.100	1.86
Test_E2_10_1h_20100521	0.125	2.89	0.151	2.84	0.277	0.190	0.095	1.90
Test_E2_10_2h_20100521			0.154		0.283	0.194	0.097	1.91
Test_E2_10_3h_20100522			0.141		0.258	0.177	0.088	1.91
Test_E2_10_4h_20100522			0.152		0.278	0.190	0.095	1.92
Test_E3_10_1h_20100526	0.125	2.89	0.149	2.84	0.273	0.187	0.093	1.90
Test_E3_10_2h_20100526			0.152		0.278	0.190	0.095	1.89
Test_E4_10_1h_20100525	0.125	2.89	0.149	2.84	0.273	0.187	0.093	1.90
Test_E4_10_2h_20100525			0.151		0.276	0.189	0.095	1.89
Test_A_8_3a_20100405	0.04	2.89	0.052	2.84	0.095	0.0652	0.033	1.887
Test_A_8_3b_20100406			0.052		0.095	0.0652	0.033	1.887
Test_A_8_2x_20100406	0.17	2.89	0.202		0.370	0.2533	0.127	1.867
Test_B2_8_6_20100326	0.08	2.89	0.096	2.84	0.176	0.1204	0.060	1.909
Test_B2_8_10_20100326	0.125	2.89	0.149		0.272	0.1864	0.093	1.880
Test_C1_8_3a_20100428	0.04	2.89	0.050	2.84	0.092	0.0629	0.031	1.916
Test_C1_8_3b_20100428			0.051		0.092	0.0633	0.032	1.904
Test_C1_8_2x_20100428	0.17	2.89	0.196		0.358	0.2454	0.123	1.880
Test_C2_8_3a_20100504	0.04	2.89	0.049	2.84	0.090	0.0617	0.031	1.913
Test_C2_8_3b_20100504			0.050		0.092	0.0629	0.031	1.896
Test_C2_8_2x_20100504	0.17	2.89	0.193		0.353	0.2415	0.121	1.881
Test_D1_8_3a_20100510	0.04	2.89	0.051	2.84	0.093	0.0640	0.032	1.890
Test_D1_8_3b_20100510			0.052		0.094	0.0646	0.032	1.887
Test_D1_8_2x_20100510	0.17	2.89	0.196		0.359	0.2458	0.123	1.885
Test_D2_8_3a_20100517	0.04	2.89	0.052	2.84	0.096	0.0658	0.033	1.887
Test_D2_8_3b_20100517			0.052		0.096	0.0658	0.033	1.887
Test_D2_8_2x_20100517	0.17	2.89	0.198		0.363	0.2488	0.124	1.869
Test_E2_8_3a_20100524	0.04	2.89	0.052	2.84	0.096	0.0656	0.033	1.877
Test_E2_8_3b_20100524			0.050		0.091	0.0624	0.031	1.888
Test_E2_8_2x_20100524	0.17	2.89	0.191		0.350	0.2395	0.120	1.879

Comparing the targeted sea-state with the generated one, using the parameters significant wave-height and peak period – input *vs.* incident – given in Table 5.III, is possible to conclude that the incident wave-height is generally higher than the input wave-height, and that the incident and input peak periods are approximately the same. Using scaled prototype values, it means that the chosen wave-height range from 0.5 to 2.0m is actually ranging from about 0.5 to 2.5m, which is still, according to the study by Coelho (2005), referred in section 4.2, within the significantly more frequent wave-heights range.

The incident wave characteristics across the different models for the same input sea reproduce with a reasonable approximation similar hydrodynamic conditions; thus, a comparison between the morphodynamic outputs produced by each scheme is feasible. Table 5.IV contains the mean ($\overline{H_s}$) and the standard deviation (σ) of the previous sets of data results. The higher standard deviations noticeable for sea-states 8, and 10 confirm what has already been observed previously in Figure 5.13b Model B2, sea-state 8, and Figure 5.13d Model D2, sea-state 10. The influence of Model A, sea-state 1, and Model C2, sea-state 5 has also repercussions in the standard deviations of the corresponding sea-states. Excluding those experimenting conditions from the calculation of the mean significant wave-height and the standard deviation would result in a significant decrease of the former; indeed the standard deviation would fall to values around the lowest in Table 5.IV. Taking, for example, Model A, sea-state 1, would result in a σ equal to 0.0019m. So for this reason the referred experimenting conditions will be treated with care in the comparison with the other tests.

The statistical analysis of the surface elevation signals in the time domain was used to yield information on the number of waves. On average each wave-run was submitted, in a 30mn duration test, to *ca.* of 1200 waves. Also based on such an analysis, several types of representative waves could be defined (*e.g.*, the heights and periods of the highest wave, the highest one-third, the highest one-tenth, and the mean wave) by the zero-downcrossing (or zero-upcrossing) method as briefly explained in section 4.3. However, it was decided the individual wave characteristics to be estimated from the analysis of the measured calibrated time-series in the frequency domain, instead of the alternative analysis in the time domain.

Table 5.IV: Mean significant wave-height and standard deviation for each test cluster.

Balance	**Sea-state**	**Targeted H_s [m]**	**Targeted T_p [s]**	**$\overline{H_s}$ [m]**	**σ [m]**
Erosion	7	0.17	2.31	0.192	0.0075
	8		2.89	0.202	0.0096
	9		3.46	0.198	0.0075
	10		2.89	0.152	0.0096
Accretion	1	0.04	1.73	0.041	0.0129
	2		2.31	0.047	0.0014
	4	0.08	1.73	0.071	0.0042
	5		2.31	0.086	0.0134
	6		2.89	0.097	0.0048
Persistent Erosional Conditions	10_1h	0.125	2.89	0.151	0.0144
	10_2h			0.156	0.0139
	10_4h			0.154	0.0039
	10_6h			0.155	0.0052
Infilling and again Erosion	8_3a	0.04	2.89	0.051	0.0013
	8_3b			0.051	0.0010
	8_2x	0.17		0.196	0.0038

5.2.2. Evaluation of incident wave conditions

Global qualitative evaluation of the various response incident wave conditions derived from the analysis, spectral and statistical, is given in Table 5.V. The plus [+], minus [–], and plus-minus [±] signs in the evaluation column indicate, respectively, a good, a poor, or a fair fitting, on the following aspects:

(i) The general fitting to the standard JONSWAP spectrum, as given by Eq. (5.1) with the input values of the significant wave-height and period;
(ii) The comparison between the incoming wave spectra within the various experimental conditions under the same input sea-state; and
(iii) The wave characteristics of the incoming waves.

The remarks are a summary of the results of fitting.

Table 5.V: Qualitative overall evaluation of the various response incident wave spectra.

Balance	**Sea-state**	**Targeted**		**Evaluation**	**Remarks**
		H_s [m]	**T_p [s]**		
Erosion	7	0.17	2.31	+ + ±	Models B1 and B2 with lower H_s
	8		2.89	+ ± ±	Model B2 with slightly different shape of incoming wave spectra and higher H_s
	9		3.46	+ + ±	Model B1 with higher H_s Model B2 with lower H_s
	10		2.89	+ ± ±	Model B2 with lower H_s Model D2 with slightly different shape of incoming wave spectra and significantly higher H_s
Accretion	1	0.04	1.73	+ + ±	Model A with higher H_s
	2		2.31	+ + +	-
	4	0.08	1.73	+ + ±	Model A with slightly lower H_s
	5		2.31	+ + ±	Model C2 with lower H_s
	6		2.89	+ + ±	Model B2 with lower H_s
Persistent Erosional Conditions	10_1h	0.125	2.89	+ ± ±	Model B2 with slightly lower H_s Model D2 with slightly different shape of incoming wave spectra and significantly higher H_s
	10_2h			+ ± ±	Model B2 with slightly lower H_s Model D2 with slightly different shape of incoming wave spectra and significantly higher H_s
Infilling and again Erosion	8_3a	0.04	2.89	+ + +	-
	8_3b			+ + +	-
	8_2x	0.17		+ + +	-

5.3. Reflection analysis

Has been already described in the previous chapter the reflection analysis carried out on the data collected during the tests on the stability analysis of geotextile encapsulated-sand systems under wave-loading, follows from a computation using the reflection analysis routines in the HR DAQ software. Such routines provide results for the spectral densities of the incident and reflected wave spectra, and the reflection coefficients at frequencies spread over the valid frequency range. Furthermore, it computes the bulk reflection coefficient as the average of the reflection coefficients divided by the ratio of the total reflected and incident energies, as given by Eq. (3.4).

For purposes of comparison the following outputs are under consideration:

- Incident wave spectra *vs.* reflected wave spectra; and
- Bulk reflection coefficient variation with
  - *(i)* Significant wave-height;
  - *(ii)* Dimensionless wave-height; and
  - *(iii)* Surf similarity parameter Eq. (3.1).

The main objective of this section is to investigate the governing hydraulic parameters for wave reflection from the dual system beach-structure. It is anticipated that the effect of wave breaking on the beach slope (Models A to D), or over the submerged breakwater (Model E), will cause an increase in energy dissipation and commensurate decrease in the reflection coefficient. As so, decreasing reflection coefficient with increasing wave-height is a likely result. The effect of structure porosity (*i.e.* wave penetration into the structure) is introduced here but discussed in greater detail in section 5.4, on wave-induced pore-pressure variation.

Later along this chapter some insights on the coupled feedback between beach-profile geometry change and incident wave conditions change are essayed.

5.3.1. Incident wave spectra *vs.* reflected wave spectra

The reflected wave conditions were determined from the spatial variation of wave conditions, using a least squares method (see section 4.4) for separating incident and reflected waves from synoptic surface elevation time-series recorded from an array of four wave-gauges with known spacing (see section 4.3).

The previous section already showed spectral analysis results with respect to incident wave spectra. Such analysis was used to evaluate the general fitting of the response spectrum to the standard JONSWAP, and to compute the characteristics of the incident waves from the moments of the wave spectra.

Examples of the spectral densities of the reflected wave spectra in various experimenting conditions defined in Table 5.I are illustrated in Figures 5.16 to 5.26. These represent each model and variant in study. All diagrams are grouped in sets of four [(a) to (d)], according to tested incident wave conditions of (a) erosion, (b) accretion, (c) persistent erosional conditions, and (d) erosion followed by infilling and again erosion, but for Model B1, which was not tested under the latter condition, and for Model E which was not tested under accretionary conditions. Each figure contains the spectral densities of the incident and reflected wave spectra, and the reflection coefficients at frequencies spread over the valid frequency range. The vertical dashed black lines are representative of the peak wave frequency and the frequency limits, which correspond to halve and two times that peak wave frequency, $0.5f_p$ and $2f_p$ respectively. The theoretical JONSWAP spectrum, as given by Eq. (5.1) with the input values of the significant wave-height and period is plotted as reference. The limits for the x- and the y-axis were set to the same values within all diagrams, which facilitate the comparison of the total available energy in each one of the illustrated examples.

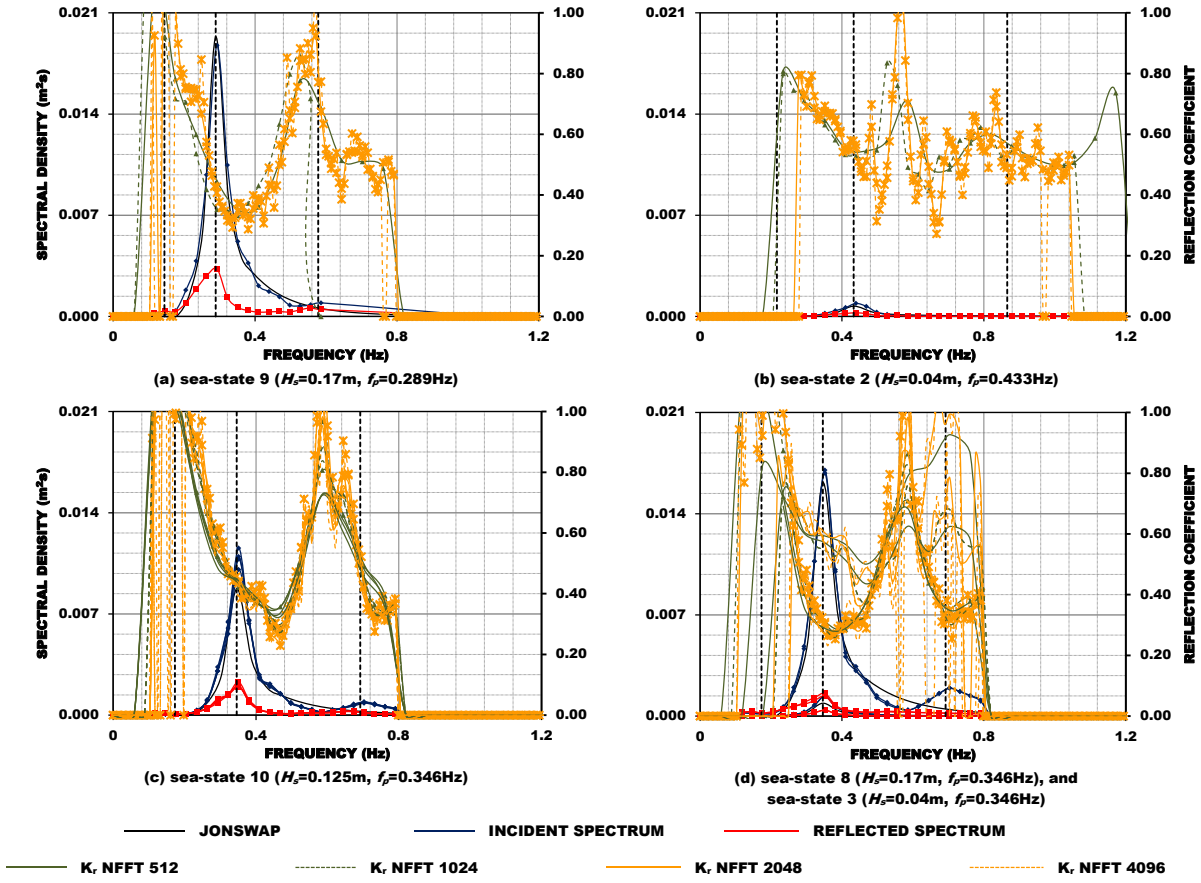

Figure 5.16: Spectral densities of the reflected wave spectra: Model A (a) erosion, (b) accretion, (c) persistent erosional conditions, and (d) erosion followed by infilling and again erosion.

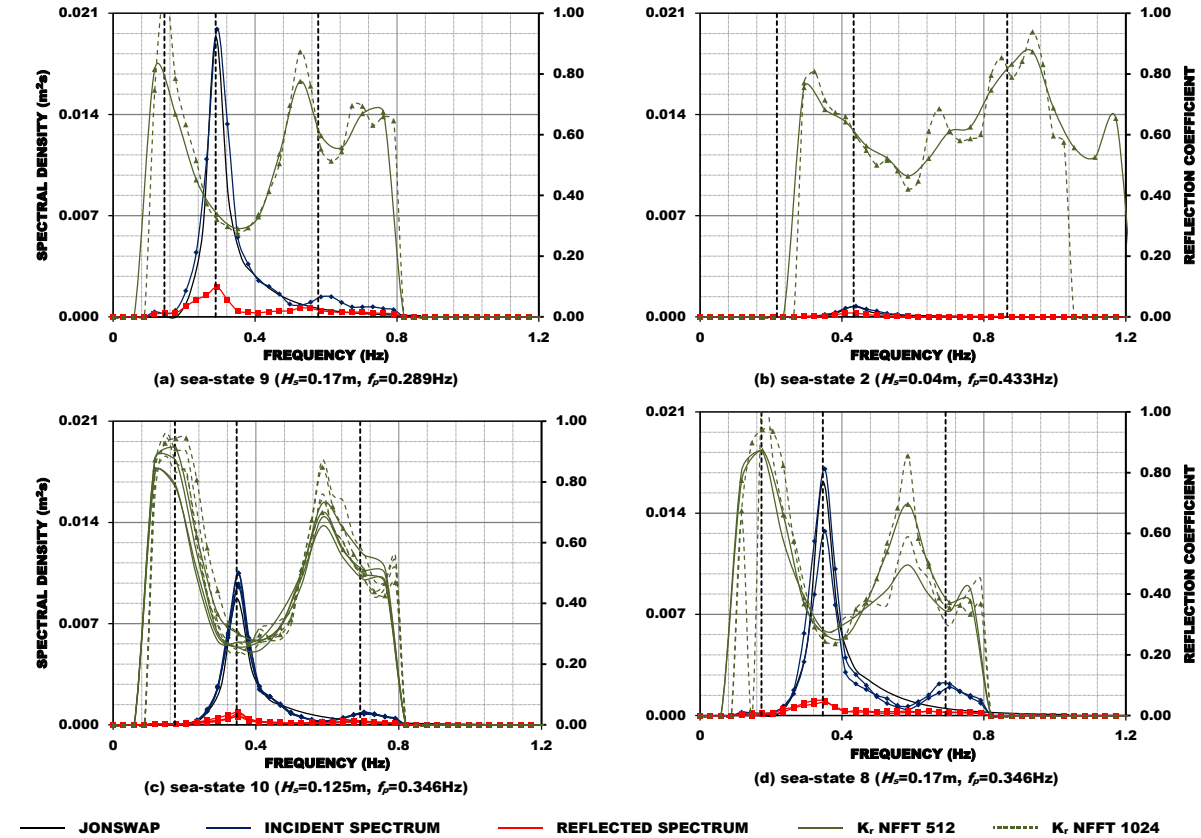

Figure 5.17: Spectral densities of the reflected wave spectra: Model B1 (a) erosion, (b) accretion, (c) persistent erosional conditions, and (d) erosion.

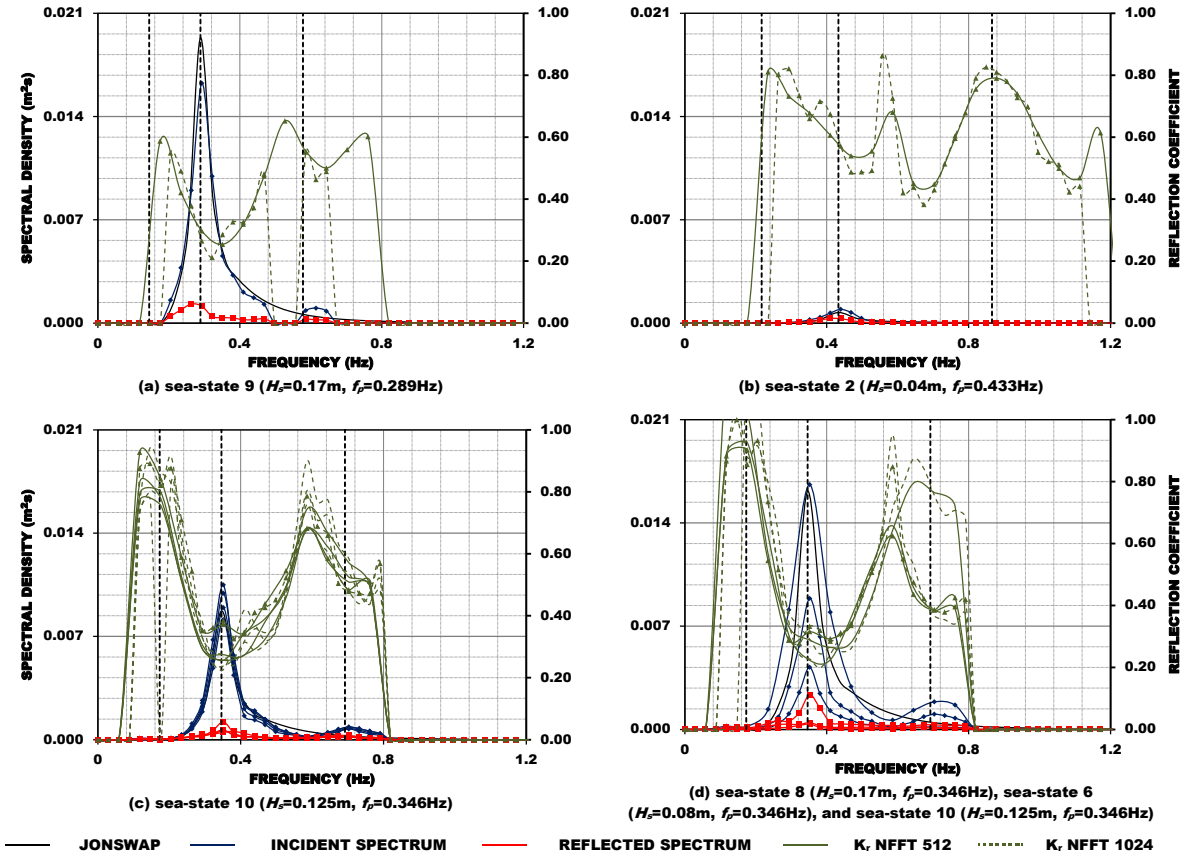

Figure 5.18: Spectral densities of the reflected wave spectra: Model B2 (a) erosion, (b) accretion, (c) persistent erosional conditions, and (d) erosion followed by infilling and again erosion.

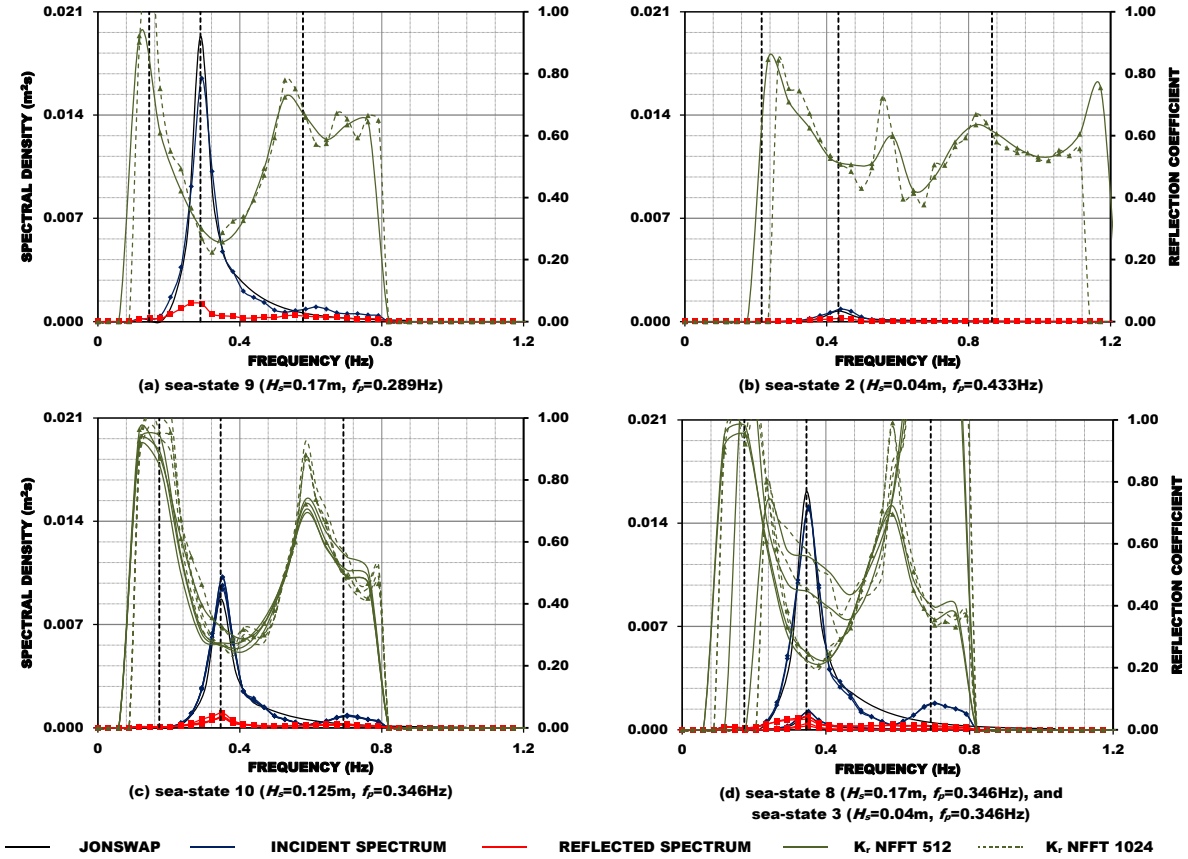

Figure 5.19: Spectral densities of the reflected wave spectra: Model C1 (a) erosion, (b) accretion, (c) persistent erosional conditions, and (d) erosion followed by infilling and again erosion.

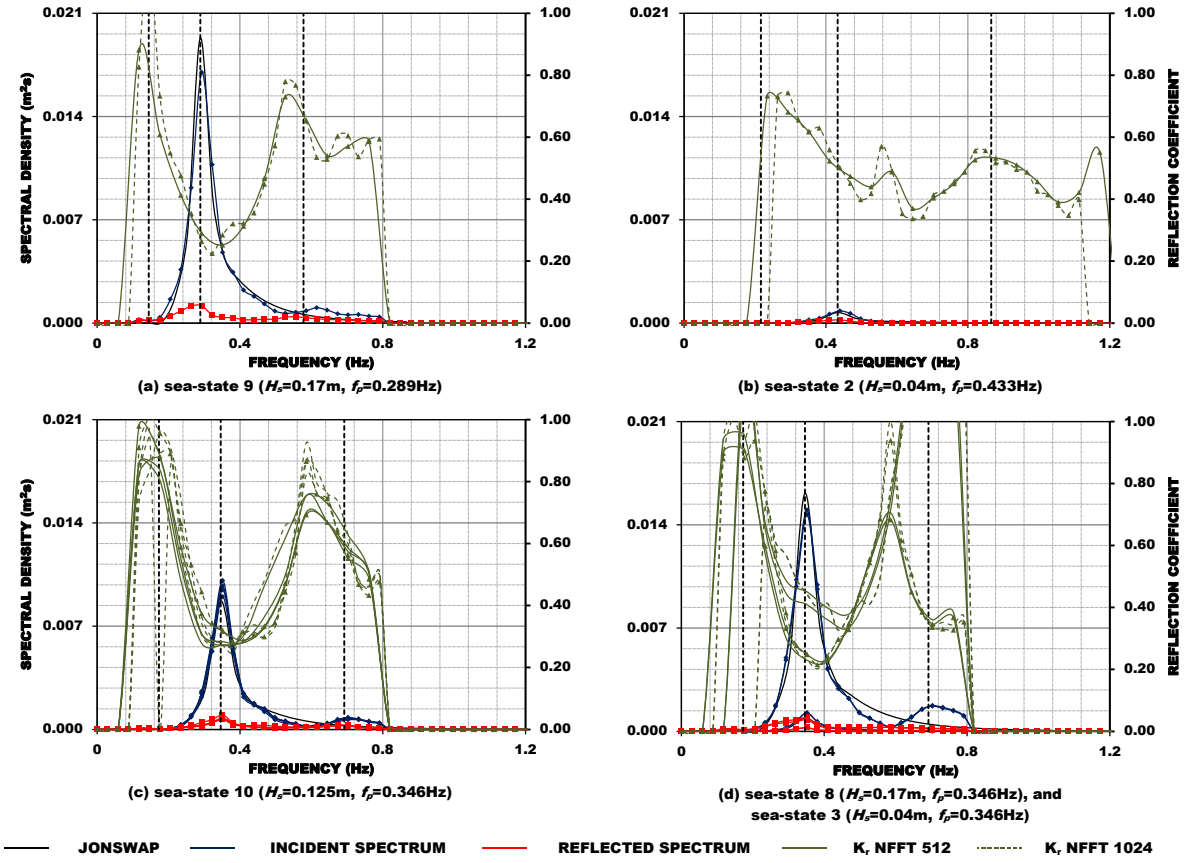

Figure 5.20: Spectral densities of the reflected wave spectra: Model C2 (a) erosion, (b) accretion, (c) persistent erosional conditions, and (d) erosion followed by infilling and again erosion.

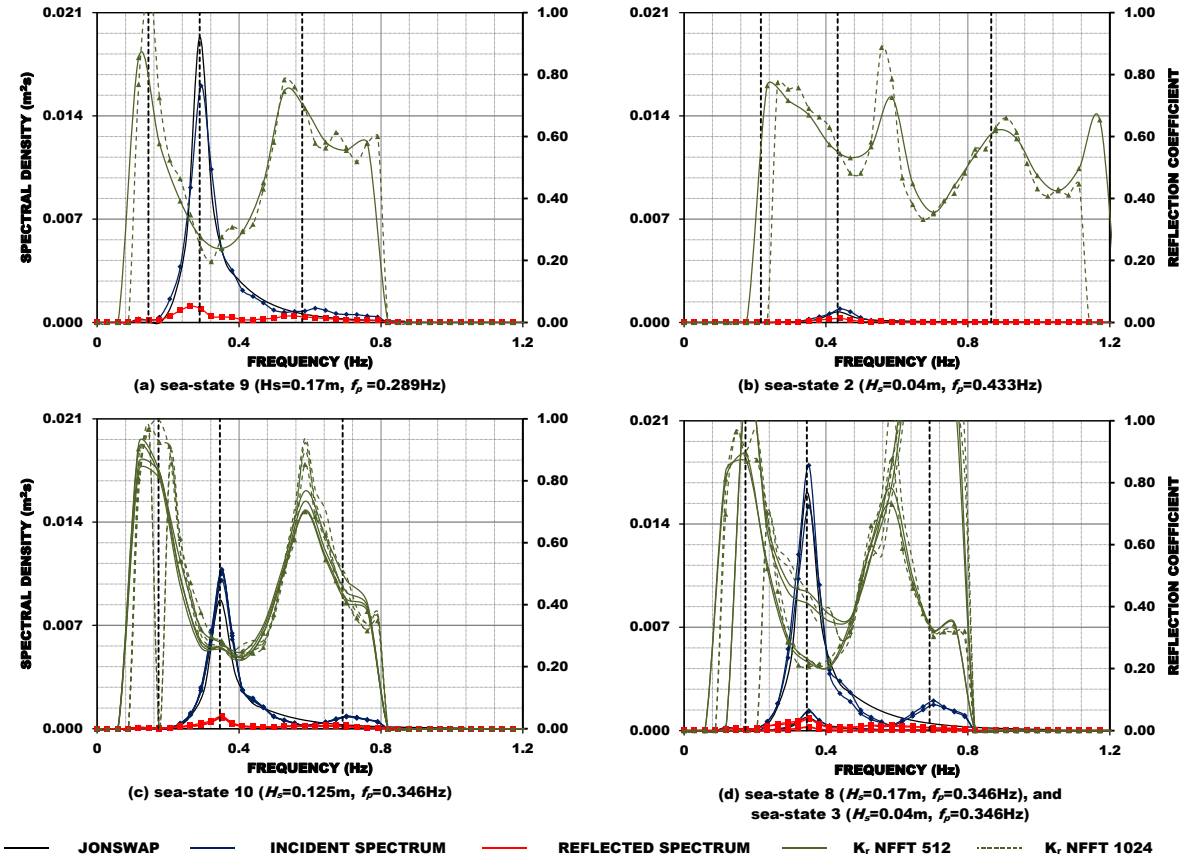

Figure 5.21: Spectral densities of the reflected wave spectra: Model D1 (a) erosion, (b) accretion, (c) persistent erosional conditions, and (d) erosion followed by infilling and again erosion.

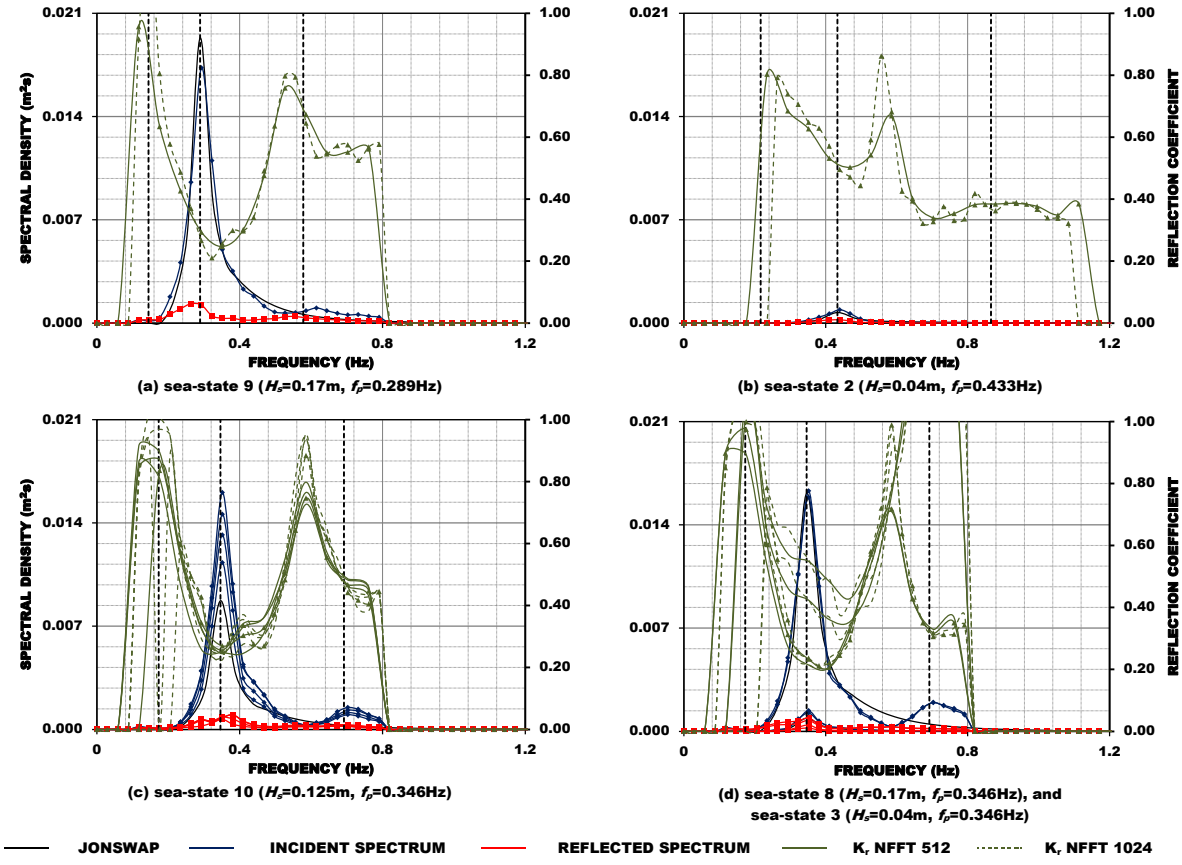

Figure 5.22: Spectral densities of the reflected wave spectra: Model D2 (a) erosion, (b) accretion, (c) persistent erosional conditions, and (d) erosion followed by infilling and again erosion.

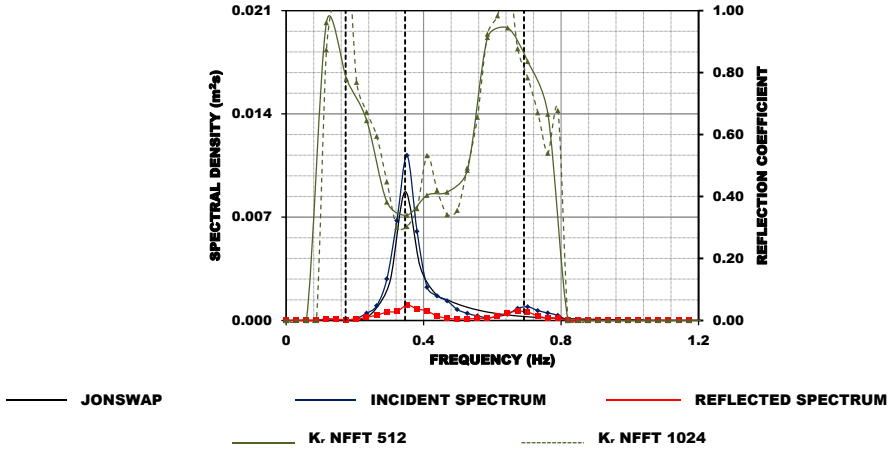

Figure 5.23: Spectral densities of the reflected wave spectra: Model E1, sea-state 10 (H_s=0.125m, f_p=0.346Hz).

Figure 5.16 further depicts how the window size affects the reflection analysis results. In the same manner as in the case of the incident wave spectra, the size of the windowing function choice is based on the degree of variance and bias in the result. After thorough analysis it was decided that the number of spectral bands over which the spectrum will be smoothed would correspond to window sizes of 512, and 1024. The plotted incident and reflected wave spectra corresponds to the one computed with blocks of 1024 (2^{10}) data points.

It should be noted that the results of wave reflection are bound to large uncertainty because it is a parameter that cannot be directly measured. Typically that uncertainty is even larger outside a frequency region near the peak wave frequency (f_p). Yet, the very high reflection coefficients observed in the lower frequencies (as seen in Figures 5.16 to 5.26) are consistent with results on the reflection of ocean surface gravity waves from beaches (see, *e.g.*, Raubenheimer *et al.*, 1995; and Elgar *et al.*, 1994).

Elgar *et al.* (1994) investigated the energy of seaward and shoreward propagating ocean surface gravity waves on a natural beach to find out that most of the incident wave energy is dissipated by wave breaking in the surf zone, but under some conditions reflection back toward deep water is significant. The ratio of seaward to shoreward propagating infragravity energy was often greater than 1, and as high as 3 when swell-sea energy was maximum. The field observations presented in Elgar *et al.* (1994) support the hypothesis that infragravity energy is predominantly generated in very shallow water and radiated seaward.

Such high reflection coefficients visible in frequency regions outer the peak are, however, not likely to account for a significant portion of the bulk reflection coefficient as the total available energy in those frequency regions is very low.

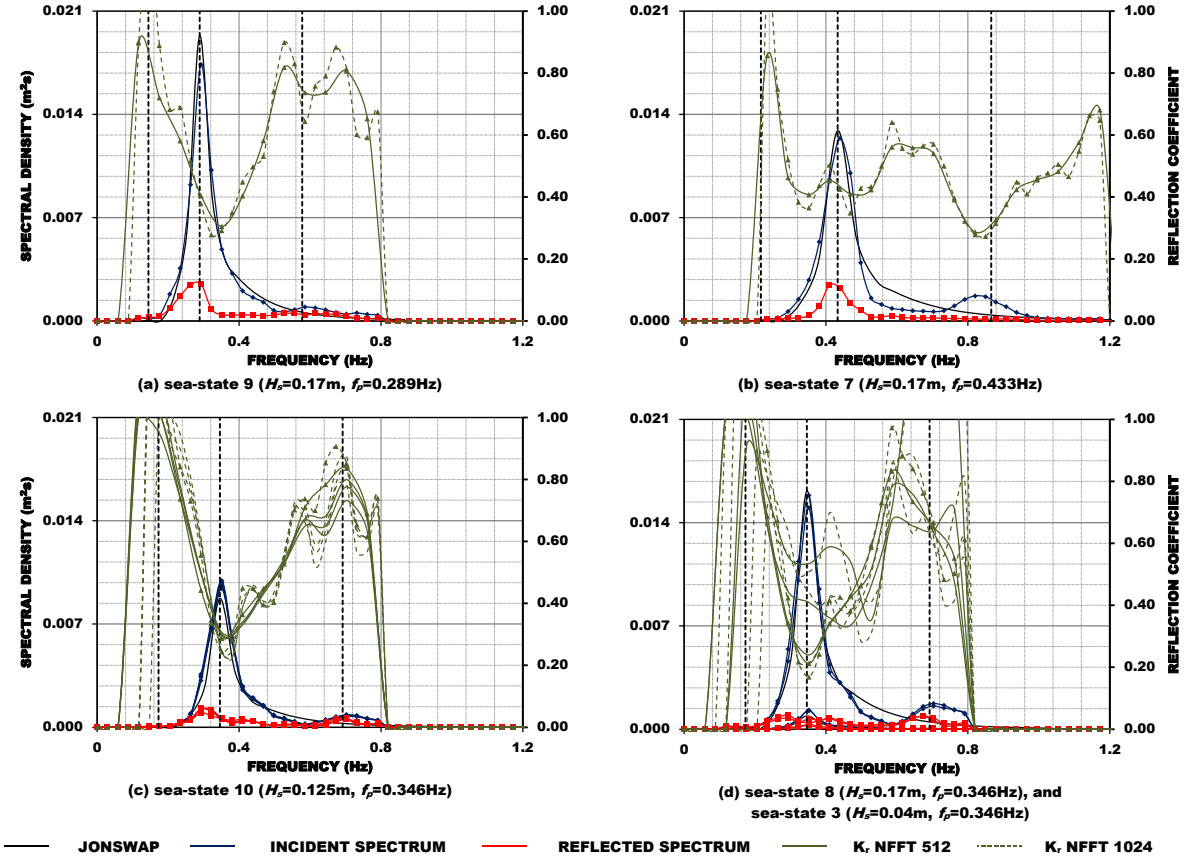

Figure 5.24: Spectral densities of the reflected wave spectra: Model E2 (a) erosion, (b) erosion, (c) persistent erosional conditions, and (d) erosion followed by infilling and again erosion.

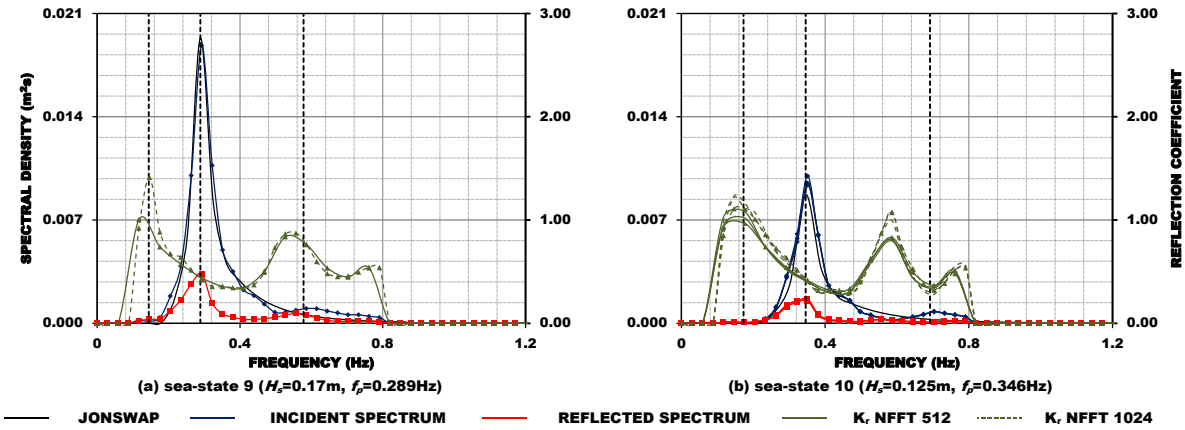

Figure 5.25: Spectral densities of the reflected wave spectra: Model E3 (a) erosion, (b) persistent erosional conditions.

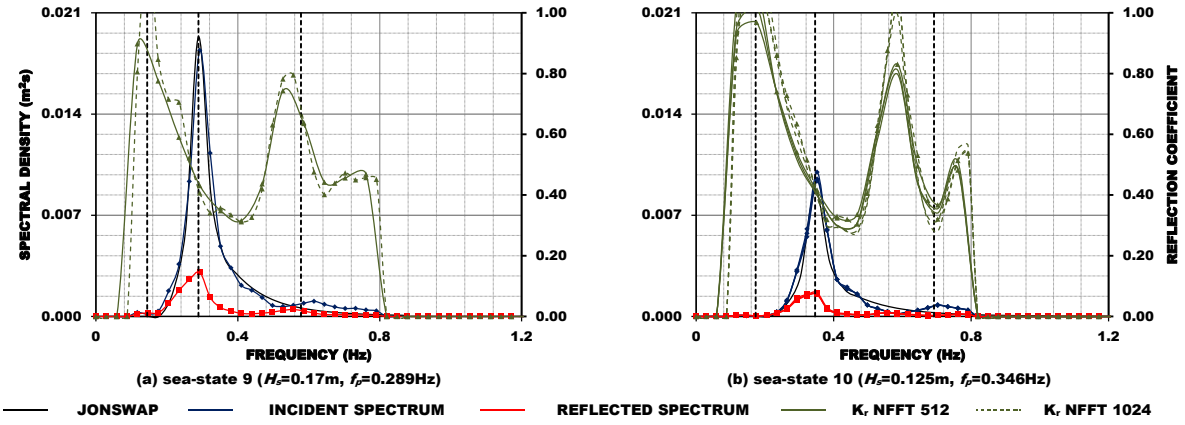

Figure 5.26: Spectral densities of the reflected wave spectra: Model E4 (a) erosion, (b) persistent erosional conditions.

The observed ratios of seaward to shoreward propagating energy, as depicted in Figures 5.16 to 5.26, indicate that most of the incident wave energy within a frequency region near the peak wave frequency, f_p, is dissipated. As expected, energy dissipation increases as the total available wave energy increases. This is evidenced, for example, by Figure 5.16d, which shows spectral densities of the incident and reflected wave spectra for the most (*i.e.*, significant wave-height of 0.17m) and the least (*i.e.*, significant wave-height of 0.04m) energetic sea-states within the current research programme.

While analysing the spectral densities of the incident and reflected wave spectra under persistent erosional conditions (*i.e.*, sea-state 10 after 30mn, 1h, 2h, and 4h) is interesting to notice that there is no considerable evidence of modification, neither on the spectral densities of the reflected wave spectra, nor on the reflection coefficients spread over the valid frequency range.

In regard to the reflection coefficients spread over the valid frequency range is possible to conclude that the incident lower-frequency subharmonics appear to be fully reflected at the shoreline, while the higher-frequency components appear to be subject to a significant dissipation near the frequency limit $2f_p$ for incident wave spectra exhibiting a wave energy density transfer from low to higher frequencies (see, *e.g.*, Figures 5.24b, and 5.26b).

5.3.2. Reflection coefficient

At the beginning of this section, three main parameters (*i.e.*, significant wave-height, dimensionless wave-height, and surf similarity parameter) were specified for the analysis of the reflection coefficients. They are now used to analyse how the wave reflection from the dual system beach-structure is affected by each one of those three parameters.

The analysis aims at providing insights on the processes: *(i)* wave energy dissipation on the beach slope (or over the submerged breakwater), which is mostly wave breaking; and *(ii)* wave penetration into the structure, which is discussed in greater detail in the following section. The impact of such processes on the morphological behaviour of the beach-profile under the influence of wave action, namely as to how the reflection modifies the beach-profile (*e.g.*, through the formation and maintenance of a nearshore-bar) is introduced in a later section.

The computed values of the reflection coefficient, K_r, for each experiment defined in Table 5.I are presented in Tables 5.VI to 5.XIII, along with the deepwater condition (H_0, L_0) – where H_0 is taken after H_s; the dimensionless wave-height, with the input values (H_0, T_p); and the surf similarity parameter, which is influenced by deepwater wave characteristics and beach slope (or structure slope) as given by Eq. (3.1). Prototype scale is used for all values in Tables 5.VI to 5.XIII.

The tables are organized by model and within each model by balance condition. The reflection coefficients, obtained from the analysis of the tests with each of the selected models (*i.e.*, test series B: GSC-structure with two variants; test series C: sand wrapped around geotextile sheets with two variants; test series D: geotextile tubes with two variants; and test series E: nearshore submerged detached breakwater or sill with four variants) and the reference case (*i.e.*, test series A: non-reinforced dune) are plotted against the parameters significant wave-height, dimensionless wave-height, and surf similarity parameter.

From the analysis of Table 5.VI is possible to conclude that, on the whole, for test series A, the reflection coefficient increases with decreasing wave-height (Figure 5.27), and also that it increase with increasing wave period thereby increasing with increasing wavelength. In general, the reflection coefficient decreases with increasing dimensionless wave-height (Figure 5.28), the opposite tendency is observed for the variation of K_r with the surf-similarity parameter, ξ (Figure 5.29).

It is also interesting to note that under persistent erosional conditions there is only a slight variation in the calculated reflection coefficient within the 6h duration of the test, indicative of a developed beach-profile on which changes become less prevalent. A similar observation may be given in regard to the tests with balance conditions of erosion, followed by infilling, and again erosion where only slight variation in the calculated reflection coefficient occurs from the first wave run-segment with erosional conditions and the final wave run-segment with again the same conditions.

A more in-depth analysis of the morphodynamic output produced by each wave run-segment against the reflection coefficient is given later along this chapter.

Table 5.VI: Model A: reflection coefficient; deepwater wave characteristics; dimensionless wave-height, and surf similarity parameter (prototype scaled).

Test ID	**Balance**	**H_s [m]**	**T_p [s]**	**K_r**	**L_0 [m]**	**$\frac{H_0}{gT_p^2}$**	**ξ**	**Hydraulic Stability**
Test_A_7_20100409	Erosion	2.35	7.90	0.342	97.4	0.00384	0.965	-
Test_A_8_20100405		2.41	9.84	0.390	151.1	0.00254	1.187	-
Test_A_9_20100413		2.42	11.81	0.490	217.9	0.00177	1.422	-
Test_A_10_20100331		1.88	9.84	0.471	151.1	0.00198	1.343	-
Test_A_1_20100407	Accretion	0.84	5.65	0.366	49.8	0.00269	1.155	-
Test_A_2_20100407		0.58	7.90	0.577	97.4	0.00094	1.951	-
Test_A_4_20100408		0.77	5.65	0.559	49.8	0.00246	1.208	-
Test_A_5_20100408		1.07	7.90	0.537	97.4	0.00175	1.432	-
Test_A_6_20100413		1.18	9.84	0.584	151.1	0.00124	1.700	-
Test_A_10_1h_20100331	Persistent Erosional Conditions	1.84	9.84	0.477	151.1	0.00193	1.361	-
Test_A_10_2h_20100331		1.87		0.471		0.00197	1.348	-
Test_A_10_3h_20100331		1.90		0.462		0.00200	1.339	-
Test_A_10_4h_20100401		1.92		0.464		0.00202	1.331	-
Test_A_10_6h_20100401		1.93		0.462		0.00203	1.327	-
Test_A_8_3a_20100405	Infilling and again Erosion	0.62	9.84	0.599	151.1	0.00066	2.334	-
Test_A_8_3b_20100406		0.62		0.549		0.00066	2.338	-
Test_A_8_2x_20100406		2.42		0.382		0.00255	1.186	-

Figure 5.27 shows the variation of the reflection coefficient with the significant wave-height. One interesting feature shown in the figure are the clusters that appear around some values of wave-height demonstrating what have already been said with respect to the reflection coefficient not varying so much for the same input sea regardless of the initial bed condition (*i.e.*, beach-profile evolving from a plane bottom slope or from a modified one). A scattered value in the plot, corresponding to Test_A_1_20100407, may be due to a measurement inaccuracy.

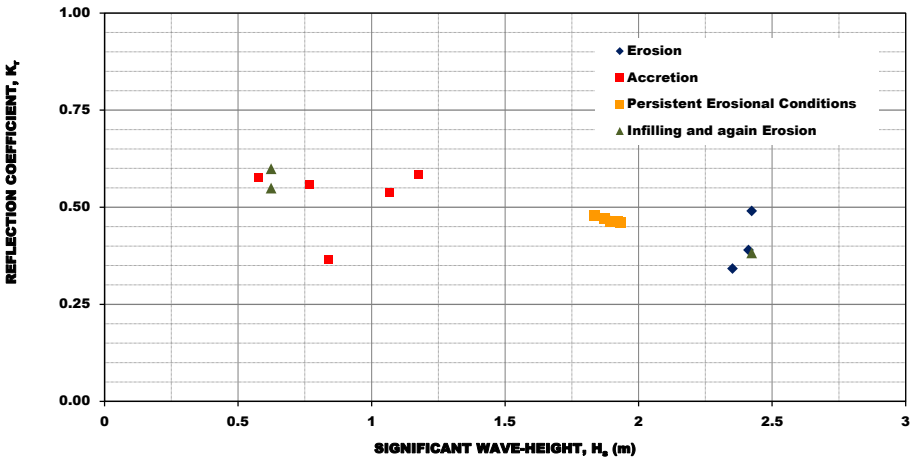

Figure 5.27: Model A: reflection coefficient *vs.* significant wave-height.

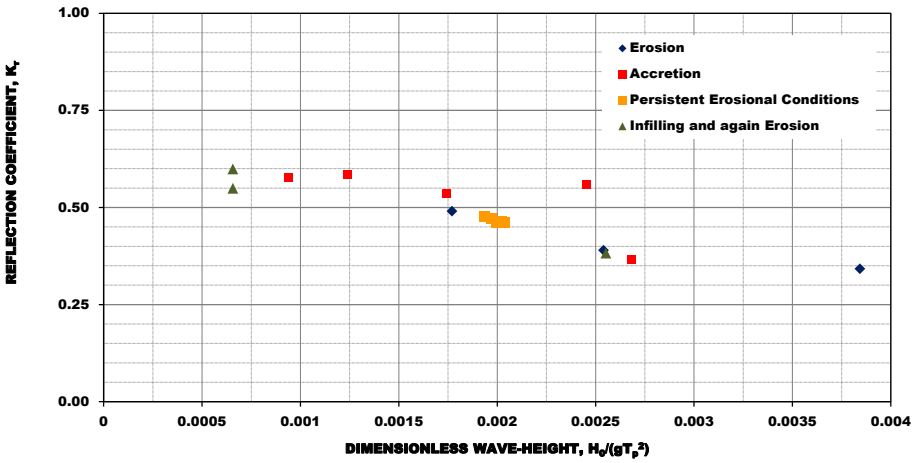

Figure 5.28: Model A: reflection coefficient *vs.* dimensionless wave-height.

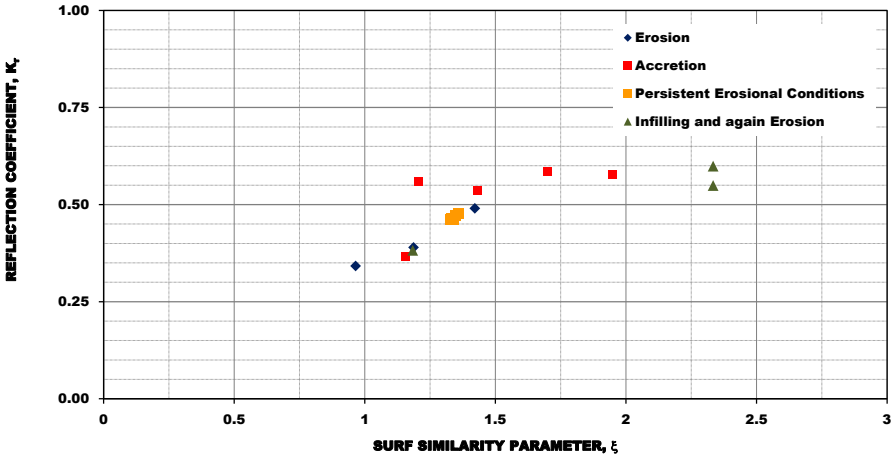

Figure 5.29: Model A: reflection coefficient *vs.* surf similarity parameter.

The data on Table 5.VII illustrate that, for Model B1, the reflection coefficients for the most energetic sea-states are lower than those calculated for Model A, indicating that a greater part of the incident wave energy is dissipated. It also demonstrates that for the same input wave-height, the reflection coefficient increases with wave-period. Figures 5.30 to 5.32 depict the variation of the reflection coefficient with the parameters in analysis. Although overall a much greater scatter is observed in the data as compared to Model A, the trend with parameters in analysis has a similar development (*i.e.*, decrease with wave-height and dimensionless wave-height, and increase with surf similarity parameter).

Table 5.VII: Model B1: reflection coefficient; deepwater wave characteristics; dimensionless wave-height, and surf similarity parameter (prototype scaled).

Test ID	**Balance**	**H_s [m]**	**T_p [s]**	**K_r**	**L_0 [m]**	**$\frac{H_0}{gT_p^2}$**	**ξ**	**Hydraulic Stability**
Test_B1_7_20091031	Erosion	2.12	7.90	0.297	97.4	0.00347	1.016	Unstable
Test_B1_8_20100105		2.45	9.84	0.353	151.1	0.00258	1.179	Unstable
Test_B1_9_20100106		2.56	11.81	0.417	217.9	0.00187	1.385	Unstable
Test_B1_10_20100112		1.80	9.84	0.380	151.1	0.00190	1.374	Unstable
Test_B1_1_20091030	Accretion	0.47	5.65	0.450	49.8	0.00150	1.547	Stable
Test_B1_2_20091030		0.54	7.90	0.601	97.4	0.00088	2.014	Stable
Test_B1_4_20091030		0.94	5.65	0.323	49.8	0.00299	1.094	Stable
Test_B1_5_20091030		1.09	7.90	0.480	97.4	0.00178	1.417	Stable
Test_B1_6_20100104		1.18	9.84	0.621	151.1	0.00124	1.700	Stable
Test_B1_10_1h_20100112	Persistent Erosional Conditions	1.79	9.84	0.337	151.1	0.00188	1.379	Unstable
Test_B1_10_1.5h_20100112		1.84		0.336		0.00193	1.361	Unstable
Test_B1_10_2h_20100112		1.84		0.334		0.00193	1.361	Unstable
Test_B1_10_3h_20100114		1.78		0.351		0.00187	1.384	Unstable
Test_B1_10_4h_20100115		1.84		0.367		0.00193	1.361	Unstable
Test_B1_10_5h_20100115		1.79		0.363		0.00188	1.379	Unstable
Test_B1_10_6h_20100120		1.80		0.361		0.00190	1.374	Unstable
Test_B1_10_8h_20100120		1.81		0.360		0.00191	1.370	Unstable
Test_B1_10_10h_20100120		1.82		0.379		0.00192	1.365	Unstable
Test_B1_10_12h_20100125		1.72		0.352		0.00181	1.408	Unstable
Test_B1_10_14h_20100125		1.78		0.420		0.00187	1.384	Unstable

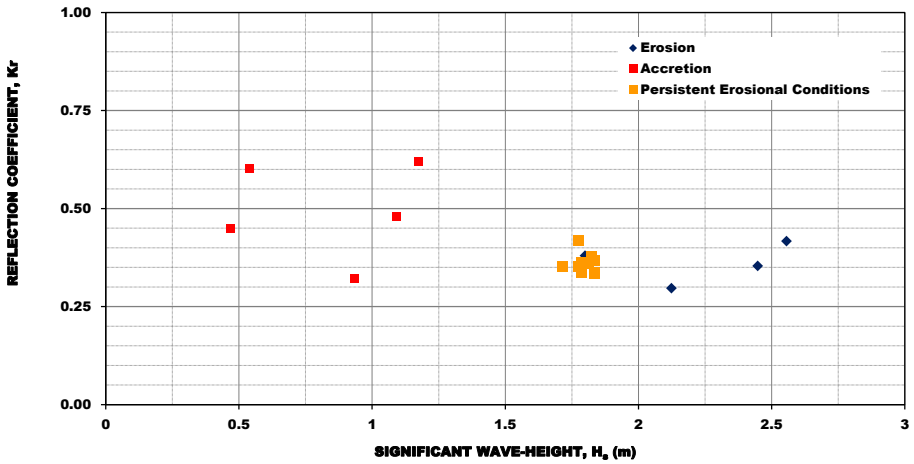

Figure 5.30: Model B1: reflection coefficient vs. significant wave-height.

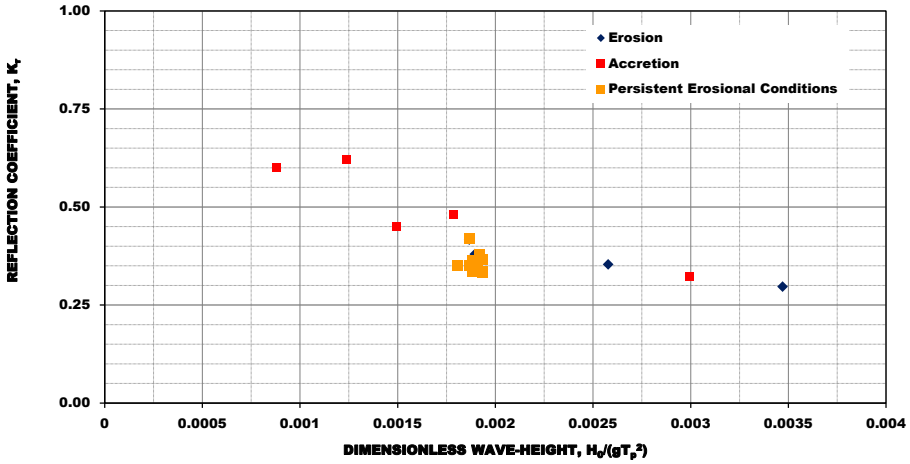

Figure 5.31: Model B1: reflection coefficient *vs.* dimensionless wave-height.

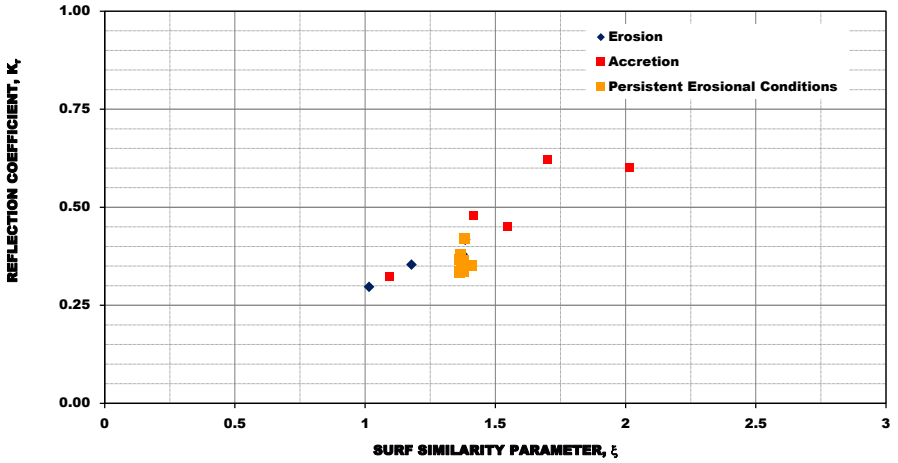

Figure 5.32: Model B1: reflection coefficient *vs.* surf similarity parameter.

Figures 5.33 to 5.35 plot the data included in Table 5.VIII with respect to variant 2 of Model B.

In general, despite some scattered values, the data evidence the same variation trend in respect to significant wave-height, dimensionless wave-height, and surf similarity parameter as has been observed in the computed reflection coefficient of test series A, and B1; that is the reflection coefficient decreases with increasing significant wave-height (Figure 5.33), increasing wave-period, increasing dimensionless wave-height (Figure 5.34), and decreasing surf similarity parameter (Figure 5.35).

In comparison to the reflection coefficients obtained from the analysis of the tests with no protective structure (*i.e.*, Model A), the ones obtained for Model B2 under balance conditions of erosion, persistent erosion and infilling followed by erosion indicate that a greater part of the incident wave energy is dissipated, as those coefficients tend to be lower in Model B2 than in Model A, similarly to what has been drawn up already for Model B1. The reason models B1 and B2 ensue a greater dissipation of wave energy, however, is only to a certain extent related to the effect of the structures, as it is also related to the beach-profile morphodynamics, namely by the presence of a barred profile.

The data included in Table 5.VIII and plotted in Figures 5.33 to 5.34 is not as evident as to the moderate variation of the compute reflection coefficient for the same input sea, which may be due to the slightly lower values of significant wave-height in the tests, Test_B2_10_1h_20100210 and Test_B2_10_2h_20100210, as has been commented earlier in the evaluation of the response incident wave conditions. Test_B2_10_4h_8_20100212 was setup to run under sea-state 8 thus the observed difference was expected.

Table 5.VIII: Model B2: reflection coefficient; deepwater wave characteristics; dimensionless wave-height, and surf similarity parameter (prototype scaled).

Test ID	Balance	H_s [m]	T_p [s]	K_r	L_0 [m]	$\frac{H_0}{gT_p^2}$	ξ	Hydraulic Stability
Test_B2_7_20100323	Erosion	2.23	7.90	0.326	97.4	0.00365	0.991	Unstable
Test_B2_8_20100325		2.74	9.84	0.360	151.1	0.00288	1.115	Unstable
Test_B2_9_20100329		2.22	11.81	0.338	217.9	0.00162	1.486	Unstable
Test_B2_10_20100210		1.60	9.84	0.416	151.1	0.00168	1.460	Stable
Test_B2_1_20100223	Accretion	0.44	5.64	0.477	49.8	0.00142	1.588	Stable
Test_B2_2_20100223		0.59	7.90	0.608	97.4	0.00096	1.931	Stable
Test_B2_4_20100223		0.86	5.64	0.389	49.8	0.00276	1.139	Stable
Test_B2_5_20100223		1.03	7.90	0.555	97.4	0.00169	1.457	Stable
Test_B2_6_20100324		1.03	9.84	0.603	151.1	0.00109	1.815	Stable
Test_B2_10_1h_20100210	Persistent Erosional Conditions	1.56	9.84	0.386	151.1	0.00164	1.476	Stable
Test_B2_10_2h_20100210		1.69		0.356		0.00178	1.418	Unstable
Test_B2_10_3h_20100212		1.84		0.350		0.00193	1.361	Unstable
Test_B2_10_4h_20100212		1.80		0.367		0.00190	1.374	Unstable
Test_B2_10_4h_8_20100212		2.35		0.336		0.00248	1.202	Unstable
Test_B2_8_6_20100326	Infilling and again Erosion	1.15	9.84	0.360	151.1	0.00121	1.718	Unstable
Test_B2_8_10_20100326		1.79		0.332		0.00188	1.379	Unstable

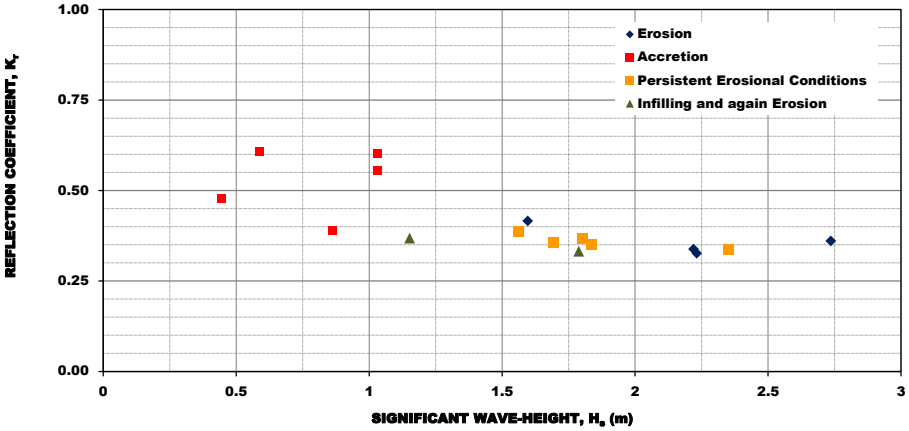

Figure 5.33: Model B2: reflection coefficient *vs.* significant wave-height.

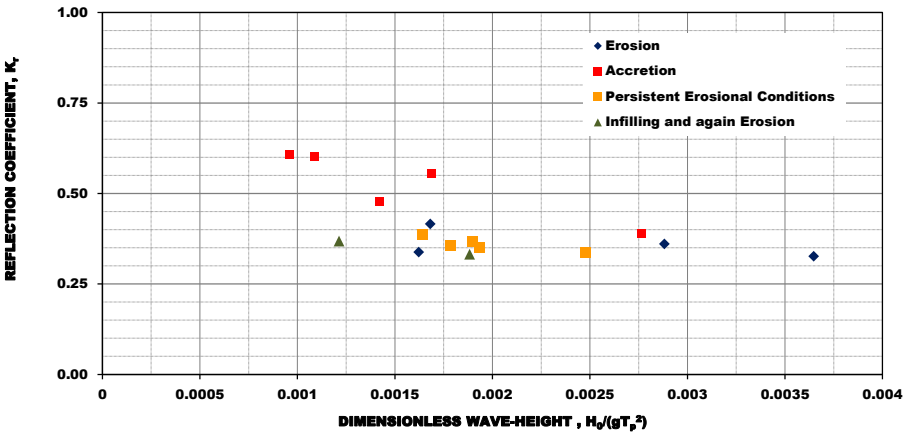

Figure 5.34: Model B2: reflection coefficient *vs.* dimensionless wave-height.

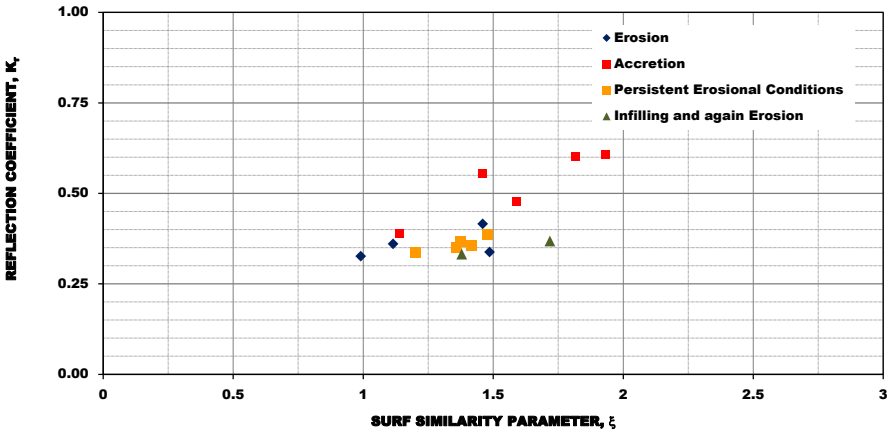

Figure 5.35: Model B2: reflection coefficient *vs.* surf similarity parameter.

The data included in Table 5.IX refers to Model C1 and is plotted in Figures 5.36 to 5.38.

Table 5.IX: Model C1: reflection coefficient; deepwater wave characteristics; dimensionless wave-height, and surf similarity parameter (prototype scaled).

Test ID	**Balance**	H_s **[m]**	T_p **[s]**	K_r	L_0 **[m]**	$\frac{H_0}{gT_p^2}$	ξ	**Hydraulic Stability**
Test_C1_7_20100427	Erosion	2.32	7.90	0.287	97.4	0.00378	0.973	Deformations
Test_C1_8_20100428		2.32	9.84	0.345	151.5	0.00244	1.212	Deformations
Test_C1_9_20100426		2.32	11.81	0.391	217.9	0.00169	1.455	Deformations
Test_C1_10_20100420		1.80	9.84	0.391	151.1	0.00190	1.374	Deformations
Test_C1_1_20100419	Accretion	0.43	5.64	0.504	49.8	0.00154	1.523	Stable
Test_C1_2_20100419		0.56	7.90	0.539	97.4	0.00092	1.971	Stable
Test_C1_4_20100419		0.85	5.64	0.382	49.8	0.00272	1.147	Stable
Test_C1_5_20100419		1.10	7.90	0.477	97.4	0.00180	1.409	Stable
Test_C1_6_20100419		1.16	9.84	0.605	151.1	0.00123	1.709	Stable
Test_C1_10_1h_20100420	Persistent Erosional Conditions	1.78	9.84	0.347	151.1	0.00187	1.384	Deformations
Test_C1_10_2h_20100420		1.82		0.348		0.00192	1.365	Deformations
Test_C1_10_3h_20100420		1.82		0.350		0.00192	1.365	Deformations
Test_C1_10_4h_20100420		1.82		0.356		0.00192	1.365	Deformations
Test_C1_10_6h_20100421		1.84		0.353		0.00193	1.361	Deformations
Test_C1_10_8h_20100421		1.86		0.357		0.00196	1.352	Deformations
Test_C1_10_9h_20100421		1.81		0.384		0.00191	1.370	Deformations
Test_C1_8_3a_20100428	Infilling and again Erosion	0.60	9.84	0.514	151.1	0.00063	2.381	Deformations
Test_C1_8_3b_20100428		0.61		0.604		0.00064	2.357	Deformations
Test_C1_8_2x_20100428		2.35		0.344		0.00248	1.202	Deformations

The data on Table 5.IX illustrate that, for Model C1, the reflection coefficients for the most energetic sea-states are lower than those calculated for Model A, indicating that a greater part of the incident wave energy is dissipated. It also demonstrates that for the same input wave-height, the reflection coefficient increases with wave-period. Figures 5.36 to 5.38 depict the variation of the reflection coefficient with the parameters in analysis. On the whole, the trend with parameters has a similar development as in the other models (*i.e.*, decrease with wave-height and dimensionless wave-height, and increase with surf similarity parameter).

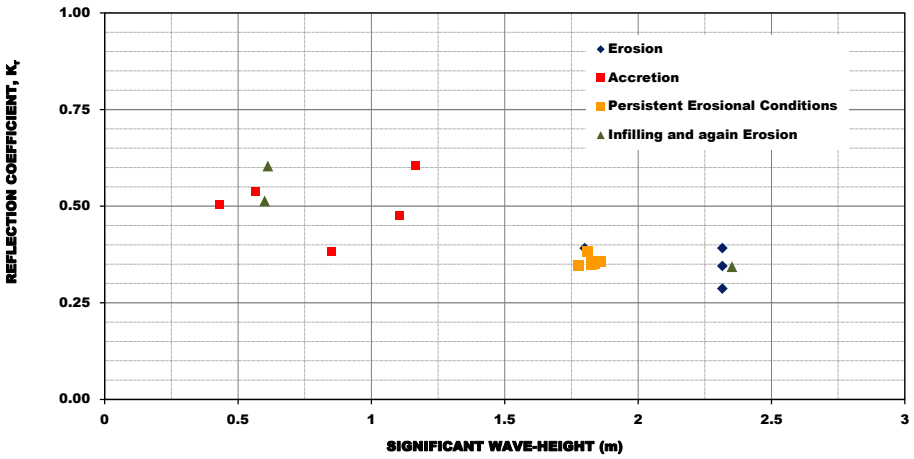

Figure 5.36: Model C1: reflection coefficient *vs.* significant wave-height.

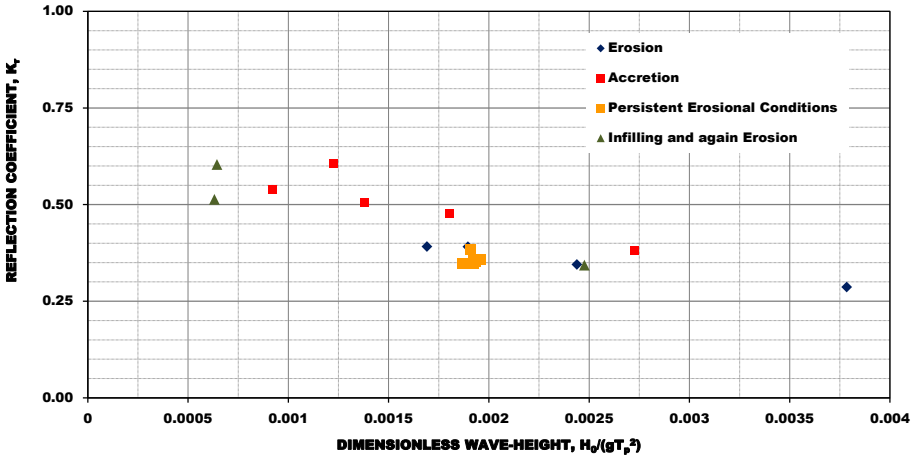

Figure 5.37: Model C1: reflection coefficient *vs.* dimensionless wave-height.

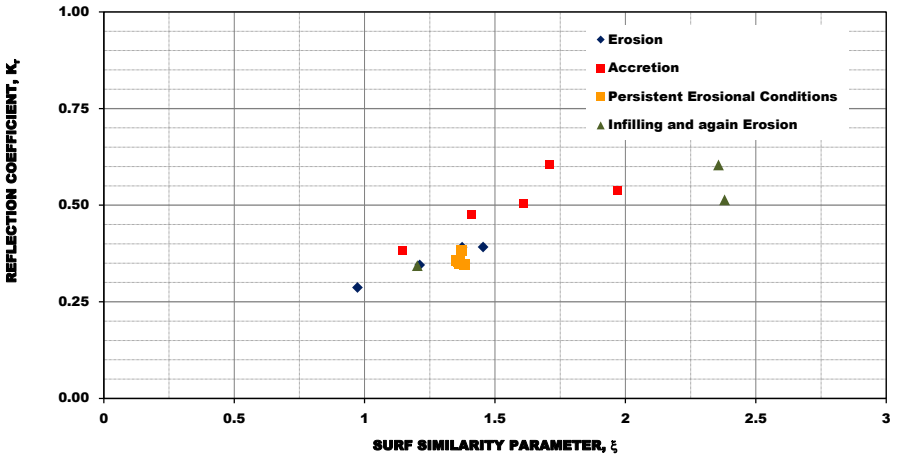

Figure 5.38: Model C1: reflection coefficient *vs.* surf similarity parameter.

The previous figures show that under persistent erosional conditions there is only a slight variation in the calculated reflection coefficient within the 9h duration of the test, indicative of a developed beach-profile on which changes become less prevalent. A similar observation may be given in regard to the tests with balance conditions of erosion, followed by infilling, and again erosion where only slight variation in the calculated reflection coefficient occurs from the first wave run-segment with erosional conditions and the final wave run-segment with again the same conditions.

Table 5.X summarizes the computed values of the coefficients of wave reflection for Model C, variant 2, and the respective parameters of significant wave-height, peak wave-period, deepwater wavelength, dimensionless wave-height, and surf similarity. The same variation trend with parameters is observed in Model C2 measurement results, that is decrease with wave-height (Figure 5.39) and dimensionless wave-height (Figure 5.40), and increase with surf similarity parameter (Figure 5.41). Overall, and for the same input sea, the reflection coefficient increases with peak wave-period increase.

Moderate variation of the reflection coefficient is observed within the different wave run-segments with sea-state 10, persistent erosional conditions; the same observation may be applied to the tests under balance conditions of infilling and again erosion.

Table 5.X: Model C2: reflection coefficient; deepwater wave characteristics; dimensionless wave-height, and surf similarity parameter (prototype scaled).

Test ID	**Balance**	**H_s [m]**	**T_p [s]**	**K_r**	**L_0 [m]**	**$\frac{H_0}{gT_p^2}$**	**ξ**	**Hydraulic Stability**
Test_C2_7_20100503	Erosion	2.42	7.90	0.295	97.4	0.00396	0.951	Deformations
Test_C2_8_20100504		2.34	9.84	0.342	151.1	0.00246	1.205	Deformations
Test_C2_9_20100505		2.35	11.81	0.378	217.9	0.00172	1.444	Deformations
Test_C2_10_20100429		1.76	9.84	0.391	151.1	0.00186	1.388	Deformations
Test_C2_1_20100502	Accretion	0.40	5.65	0.481	49.8	0.00127	1.682	Stable
Test_C2_2_20100502		0.55	7.90	0.517	97.4	0.00090	1.992	Stable
Test_C2_4_20100503		0.83	5.65	0.335	49.8	0.00265	1.163	Stable
Test_C2_5_20100503		0.67	7.90	0.678	97.4	0.00110	1.806	Stable
Test_C2_6_20100504		1.16	9.84	0.598	151.1	0.00123	1.709	Stable
Test_C2_10_1h_20100429	Persistent Erosional Conditions	1.69	9.84	0.390	151.1	0.00178	1.418	Deformations
Test_C2_10_2h_20100429		1.78		0.361		0.00187	1.384	Deformations
Test_C2_10_3h_20100430		1.80		0.354		0.00190	1.374	Deformations
Test_C2_10_4h_20100430		1.80		0.356		0.00190	1.374	Deformations
Test_C2_10_6h_20100430		1.78		0.375		0.00187	1.384	Deformations
Test_C2_10_8h_20100430		1.81		0.359		0.00191	1.370	Deformations
Test_C2_8_3a_20100504	Infilling and again Erosion	0.59	9.84	0.480	151.1	0.00062	2.405	Deformations
Test_C2_8_3b_20100504		0.60		0.516		0.00063	2.381	Deformations
Test_C2_8_2x_20100504		2.32		0.336		0.00244	1.212	Deformations

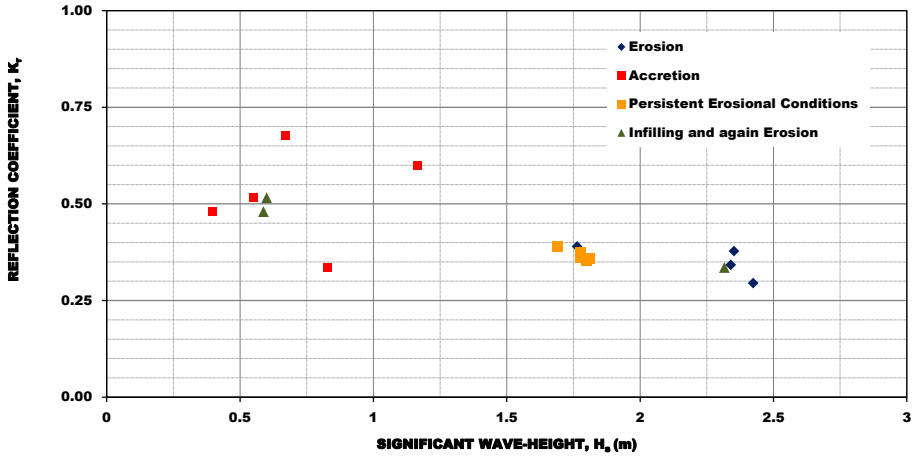

Figure 5.39: Model C2: reflection coefficient *vs.* significant wave-height.

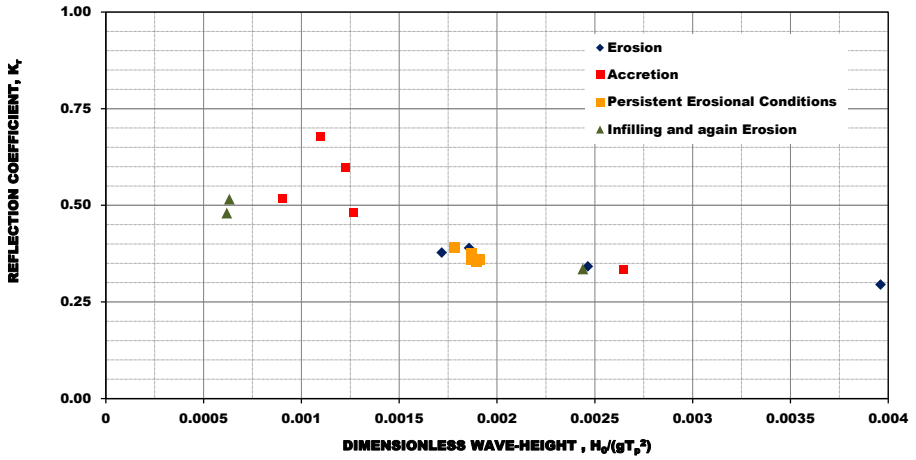

Figure 5.40: Model C2: reflection coefficient *vs.* dimensionless wave-height.

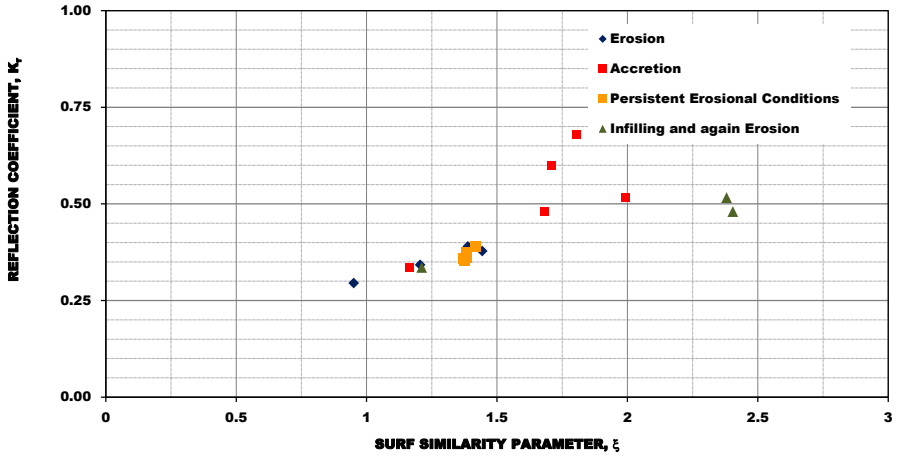

Figure 5.41: Model C2: reflection coefficient *vs.* surf similarity parameter.

Figures 5.42 to 5.44 plot the data included in Table 5.XI. Again the same variation trend with respect to significant wave-height, dimensionless wave-height, and surf similarity parameter, as has been observed over the analysis of the coefficients of wave reflection for models A, B, and C, that is the reflection coefficient decreases with increasing significant wave-height (Figure 5.42), increasing wave-period, increasing dimensionless wave-height (Figure 5.43), and decreasing surf similarity parameter (Figure 5.44), is observed for Model D, variant 1. Such coefficient also increases with wave-period increase.

In comparison to the reflection coefficients obtained from the analysis of the tests with no protective structure (*i.e.*, Model A), the ones obtained for Model D1 under balance conditions of erosion, persistent erosion and infilling followed by erosion indicate that a greater part of the incident wave energy is dissipated, as those coefficients tend to be lower in Model D1 than in Model A, similarly to what has been drawn up already for models B and C.

Likewise, there is only a slight variation of the coefficients of wave reflection for the same input sea-state regardless of the initial bed condition.

Table 5.XI: Model D1: reflection coefficient; deepwater wave characteristics; dimensionless wave-height, and surf similarity parameter (prototype scaled).

Test ID	Balance	H_s [m]	T_p [s]	K_r	L_0 [m]	$\frac{H_0}{gT_p^2}$	ξ	Hydraulic Stability
Test_D1_7_20100512	Erosion	2.35	7.90	0.284	97.4	0.00384	0.965	Stable
Test_D1_8_20100510		2.45	9.84	0.305	151.1	0.00258	1.179	Stable
Test_D1_9_20100511		2.30	11.81	0.366	217.9	0.00168	1.459	Stable
Test_D1_10_20100511		1.85	9.84	0.336	151.1	0.00195	1.356	Stable
Test_D1_1_20100512	Accretion	0.43	5.65	0.528	49.8	0.00138	1.610	Stable
Test_D1_2_20100512		0.58	7.90	0.578	97.4	0.00094	1.951	Stable
Test_D1_4_20100512		0.88	5.65	0.365	49.8	0.00280	1.131	Stable
Test_D1_5_20100512		1.13	7.90	0.454	97.4	0.00184	1.394	Stable
Test_D1_6_20100510		1.20	9.84	0.560	151.1	0.00126	1.683	Stable
Test_D1_10_1h_20100511	Persistent Erosional Conditions	1.82	9.84	0.324	151.1	0.00192	1.365	Stable
Test_D1_10_2h_20100511		1.86		0.323		0.00196	1.352	Stable
Test_D1_10_3h_20100511		1.87		0.327		0.00197	1.348	Stable
Test_D1_10_4h_20100511		1.87		0.333		0.00197	1.348	Stable
Test_D1_10_6h_20100511		1.86		0.353		0.00196	1.352	Stable
Test_D1_8_3a_20100510	Infilling and again Erosion	0.61	9.84	0.486	151.1	0.00064	2.357	Stable
Test_D1_8_3b_20100510		0.62		0.513		0.00066	2.334	Stable
Test_D1_8_2x_20100510		2.35		0.330		0.00248	1.202	Stable

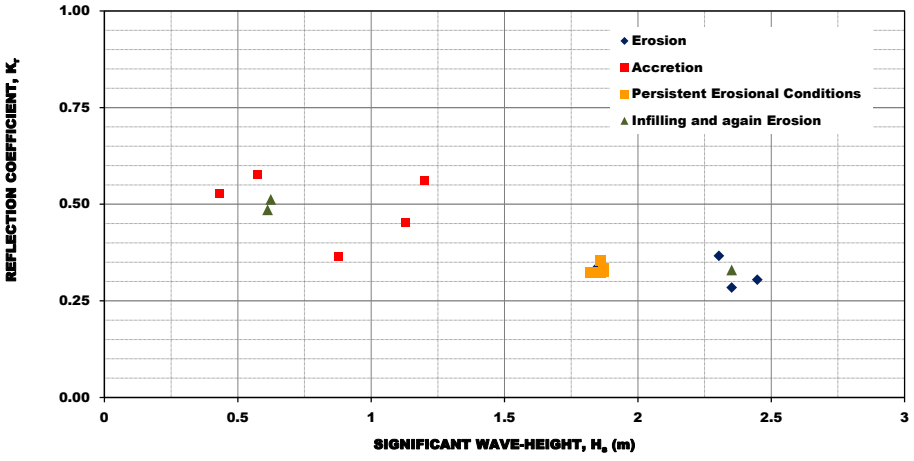

Figure 5.42: Model D1: reflection coefficient *vs.* significant wave-height.

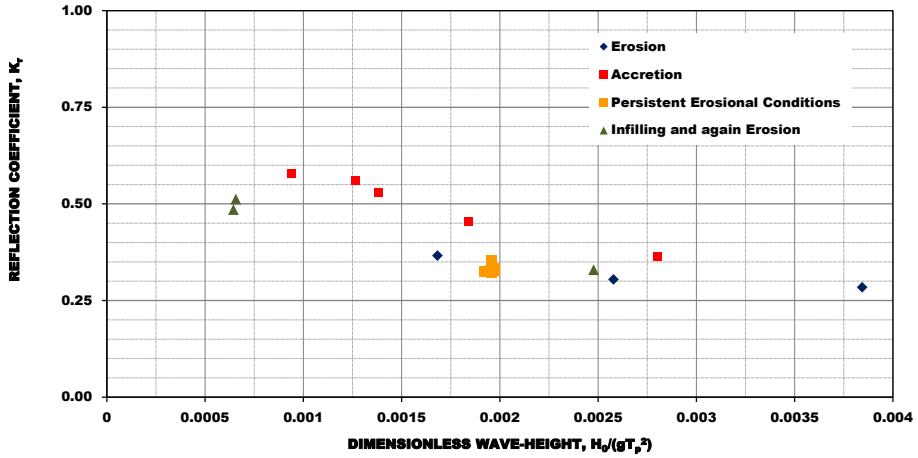

Figure 5.43: Model D1: reflection coefficient *vs.* dimensionless wave-height.

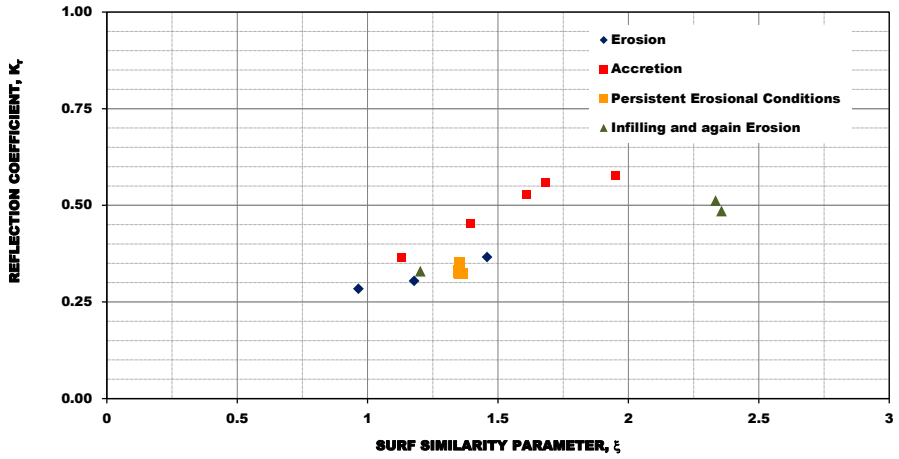

Figure 5.44: Model D1: reflection coefficient *vs.* surf similarity parameter.

Table 5.XII summarizes the computed coefficients of wave reflection for Model D2, whereas in Figures 5.45 to 5.47 those results are plotted against each of the parameters in analysis. The same findings apply to the analysis of the data included Table 5.XII, that is the reflection coefficient decreases with increasing significant wave-height (Figure 5.45), increasing wave-period, increasing dimensionless wave-height (Figure 5.46), and decreasing surf similarity parameter (Figure 5.47), is observed for Model D, variant 2. Such coefficient also increases with wave-period increase.

More scatter around results with balance conditions of persistent erosion may be due to the slightly different shape of incoming wave spectra and significantly higher H_s, as has been remarked earlier in Table 5.V.

Table 5.XIII summarizes the computed values of the coefficients of wave reflection for Model E, and the respective parameters of significant wave-height, peak wave-period, deepwater wavelength, dimensionless wave-height, and surf similarity. Figures 5.48 to 5.56 plot the results of variants 2 to 4 of Model E; Model E1 was excluded because only one incomplete test has been performed with it.

Overall results for Model E show that the reflection coefficient increases with increasing peak wave-period, decreasing significant wave-height, decreasing dimensionless wave-height, and increasing surf similarity parameter; in addition, the results seem to indicate that the parameters distance to shoreline, and surf zone width (which depends on the significant wave-height) have both some effect on the reflection coefficient, thereby on the wave energy dissipation over the submerged detached breakwaters.

A comparative analysis between the various models is given in the following paragraph.

Table 5.XII: Model D2: reflection coefficient; deepwater wave characteristics; dimensionless wave-height, and surf similarity parameter (prototype scaled).

Test ID	Balance	H_s [m]	T_p [s]	K_r	L_0 [m]	$\frac{H_0}{gT_p^2}$	ξ	Hydraulic Stability
Test_D2_7_20100518	Erosion	2.33	7.90	0.276	97.4	0.00380	0.970	Stable
Test_D2_8_20100517		2.41	9.84	0.330	151.1	0.00254	1.187	Stable
Test_D2_9_20100518		2.38	11.81	0.380	217.9	0.00174	1.436	Stable
Test_D2_10_20100515		2.09	9.84	0.344	151.1	0.00220	1.276	Stable
Test_D2_1_20100518	Accretion	0.43	5.65	0.469	49.8	0.00138	1.610	Stable
Test_D2_2_20100518		0.58	7.90	0.533	97.4	0.00094	1.951	Stable
Test_D2_4_20100518		0.85	5.65	0.340	49.8	0.00272	1.147	Stable
Test_D2_5_20100518		1.12	7.90	0.443	97.4	0.00182	1.401	Stable
Test_D2_6_20100517		1.20	9.84	0.586	151.1	0.00126	1.683	Stable
Test_D2_10_1h_20100515	Persistent Erosional Conditions	2.24	9.84	0.359	151.1	0.00236	1.231	Stable
Test_D2_10_2h_20100515		2.32		0.355		0.00244	1.212	Stable
Test_D2_10_3h_20100516		1.87		0.325		0.00197	1.348	Stable
Test_D2_10_4h_20100516		1.91		0.323		0.00201	1.335	Stable
Test_D2_10_6h_20100516		1.92		0.323		0.00202	1.331	Stable
Test_D2_8_3a_20100517	Infilling and again Erosion	0.62	9.84	0.491	151.1	0.00066	2.334	Stable
Test_D2_8_3b_20100517		0.62		0.583		0.00066	2.334	Stable
Test_D2_8_2x_20100517		2.38		0.316		0.00250	1.196	Stable

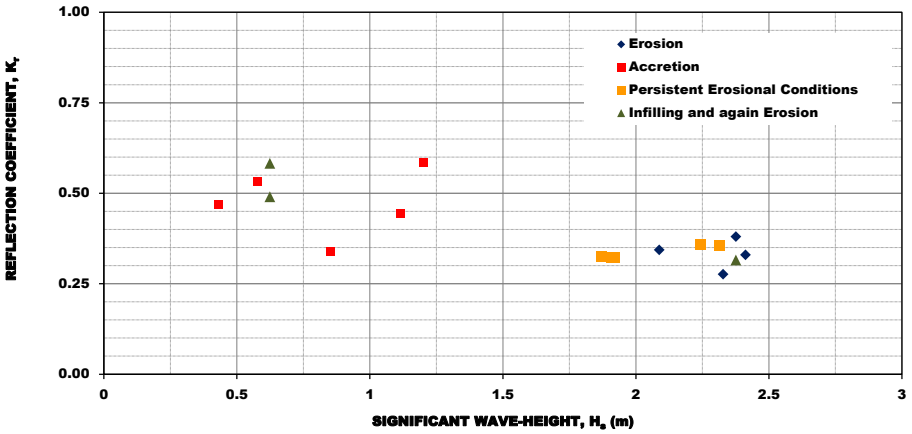

Figure 5.45: Model D2: reflection coefficient *vs.* significant wave-height.

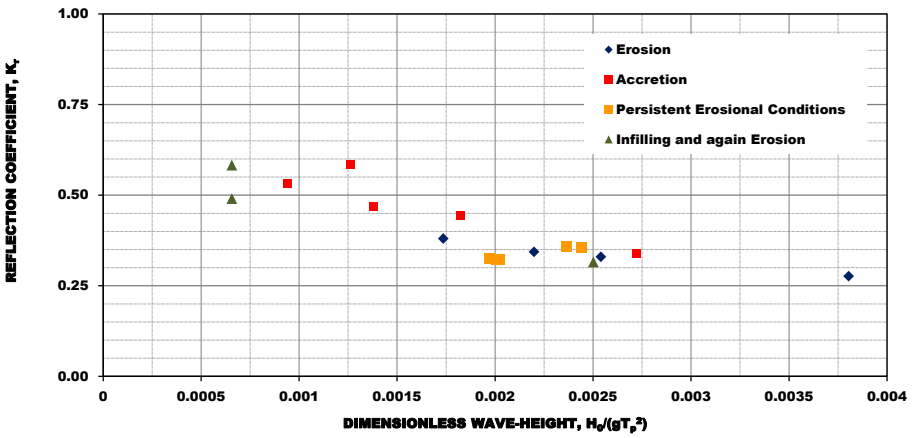

Figure 5.46: Model D2: reflection coefficient *vs.* dimensionless wave-height.

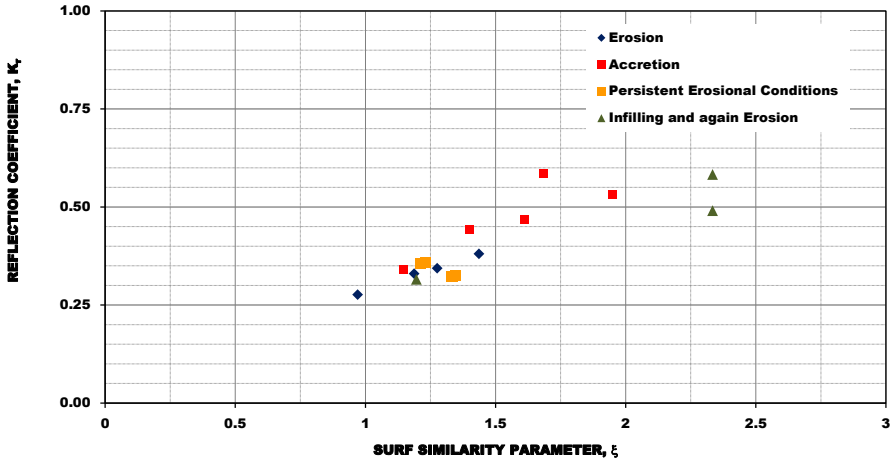

Figure 5.47: Model D2: reflection coefficient *vs.* surf similarity parameter.

Table 5.XIII: Model E: reflection coefficient; deepwater wave characteristics; dimensionless wave-height, and surf similarity parameter (prototype scaled).

Test ID	**Balance**	H_s [m]	T_p [s]	K_r	L_0 [m]	$\frac{H_0}{gT_p^2}$	ξ	**Hydraulic Stability**
Test_E1_10_20100520	Erosion	1.86	9.84	0.451	151.1	0.00196	1.352	Unstable
Test_E2_7_20100524	Erosion	2.28	7.90	0.433	97.4	0.00373	0.980	Stable
Test_E2_8_20100522		2.38	9.84	0.410	151.1	0.00250	1.196	Stable
Test_E2_9_20100524		2.34	11.81	0.489	217.9	0.00171	1.447	Stable
Test_E2_10_20100521		1.84	9.84	0.452	151.1	0.00193	1.361	Stable
Test_E2_10_1h_20100521	Persistent Erosional Conditions	1.81	9.84	0.452	151.1	0.00191	1.370	Stable
Test_E2_10_2h_20100521		1.85		0.445		0.00195	1.356	Stable
Test_E2_10_3h_20100522		1.69		0.460		0.00178	1.418	Stable
Test_E2_10_4h_20100522		1.82		0.447		0.00192	1.365	Stable
Test_E2_8_3a_20100524	Infilling and again Erosion	0.62	9.84	0.660	151.1	0.00066	2.334	Stable
Test_E2_8_3b_20100524		0.60		0.552		0.00063	2.381	Stable
Test_E2_8_2x_20100524		2.29		0.404		0.00241	1.218	Stable
Test_E3_8_20100526	Erosion	2.35	9.84	0.415	151.1	0.00248	1.202	Stable
Test_E3_9_20100526		2.42	11.81	0.484	217.9	0.00177	1.422	Stable
Test_E3_10_20100526		1.80	9.84	0.472	151.1	0.00190	1.374	Stable
Test_E3_10_1h_20100526	Persistent Erosional Conditions	1.79	9.84	0.456	151.1	0.00188	1.379	Stable
Test_E3_10_2h_20100526		1.82		0.446		0.00192	1.365	Stable
Test_E4_8_20100525	Erosion	2.36	9.84	0.404	151.1	0.00249	1.199	Stable
Test_E4_9_20100525		2.40	11.81	0.466	217.9	0.00175	1.429	Stable
Test_E4_10_20100525		1.81	9.84	0.459	151.1	0.00191	1.370	Stable
Test_E4_10_1h_20100525	Persistent Erosional Conditions	1.79	9.84	0.430	151.1	0.00188	1.379	Stable
Test_E4_10_2h_20100525		1.81		0.424		0.00191	1.370	Stable

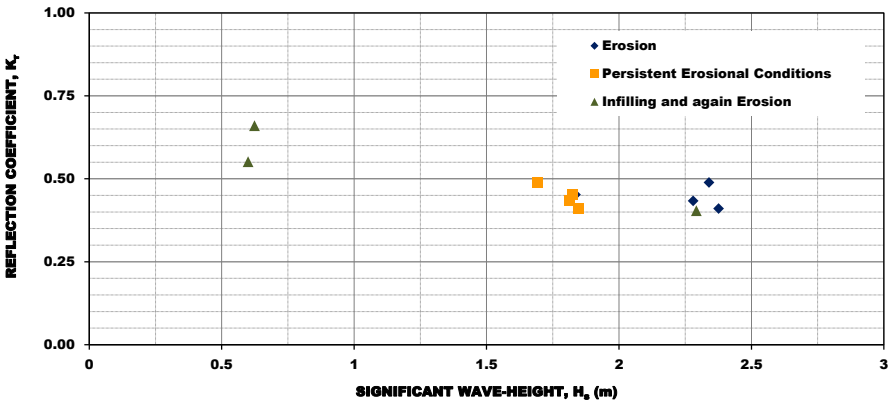

Figure 5.48: Model E2: reflection coefficient *vs.* significant wave-height.

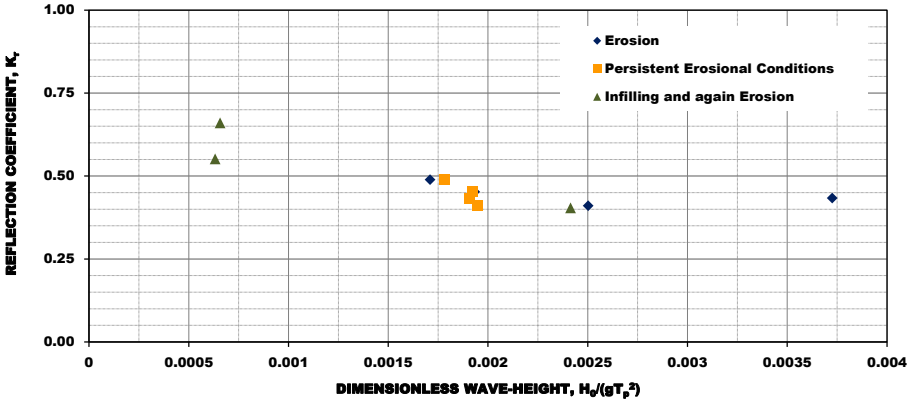

Figure 5.49: Model E2: reflection coefficient *vs.* dimensionless wave-height.

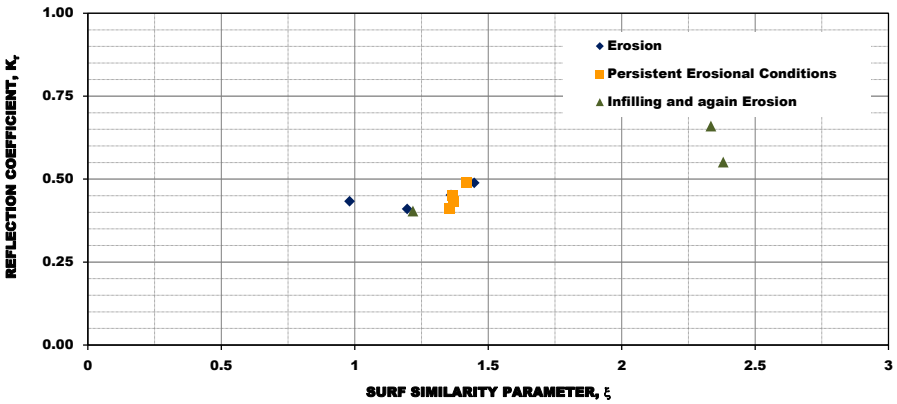

Figure 5.50: Model E2: reflection coefficient *vs.* surf similarity parameter.

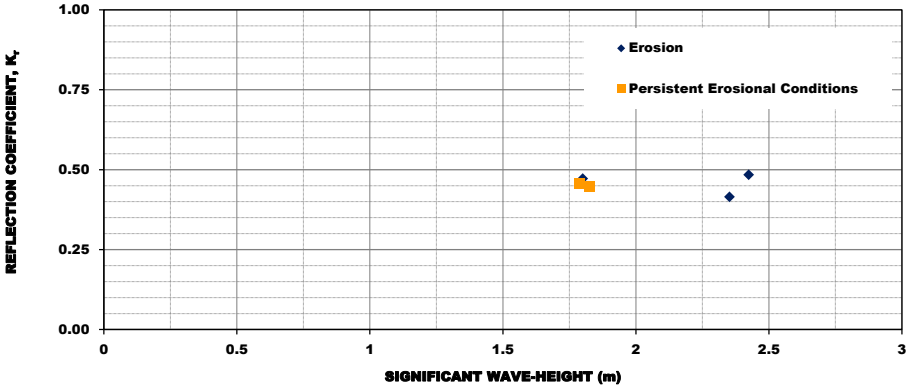

Figure 5.51: Model E3: reflection coefficient *vs.* significant wave-height.

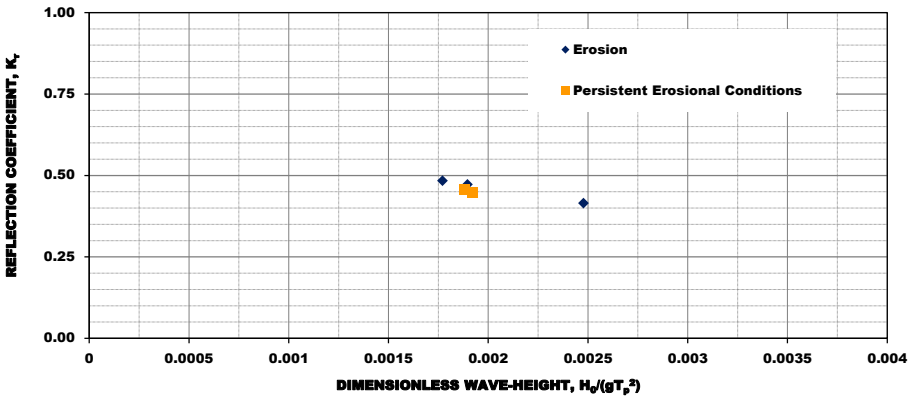

Figure 5.52: Model E3: reflection coefficient *vs.* dimensionless wave-height.

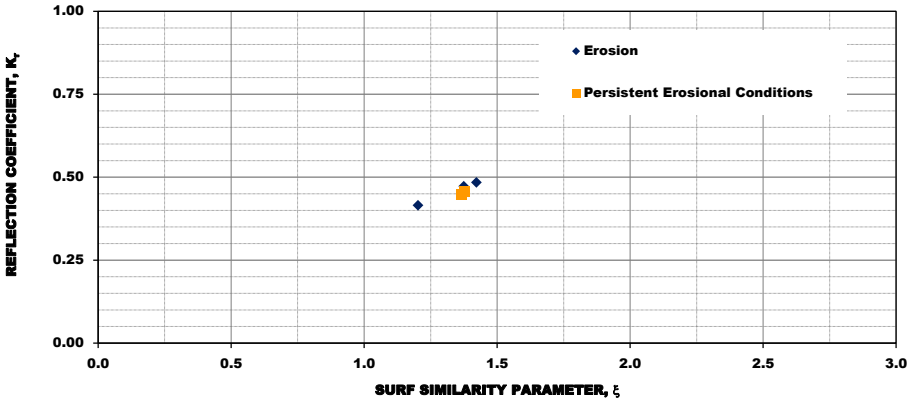

Figure 5.53: Model E3: reflection coefficient *vs.* surf similarity parameter.

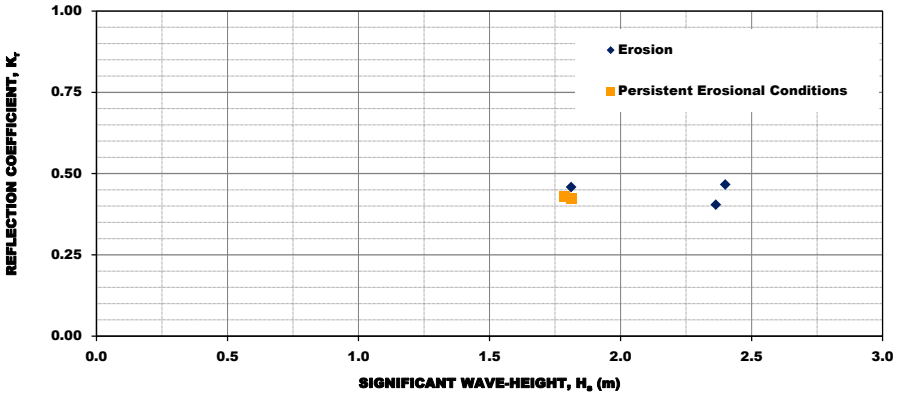

Figure 5.54: Model E4: reflection coefficient *vs.* significant wave-height.

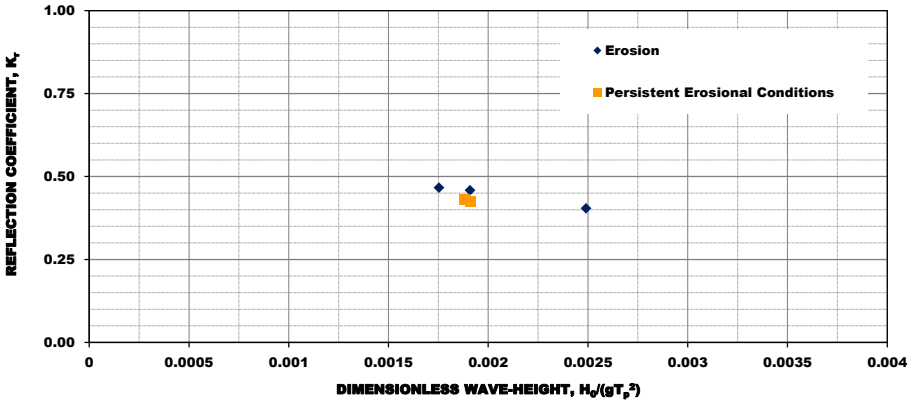

Figure 5.55: Model E4: reflection coefficient *vs.* dimensionless wave-height.

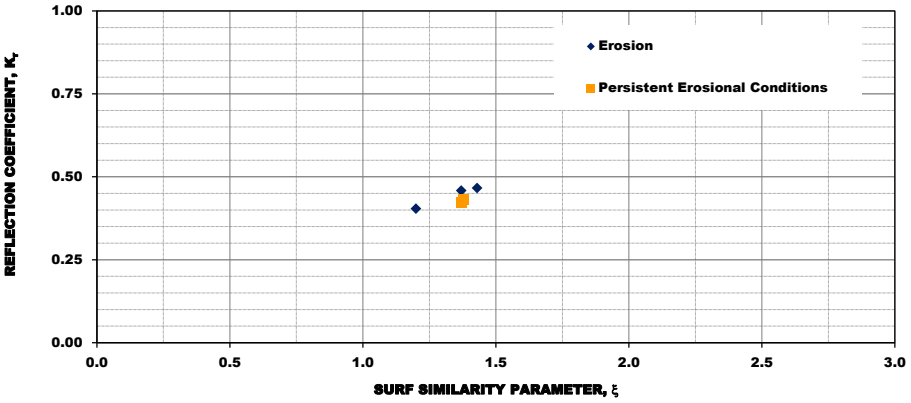

Figure 5.56: Model E4: reflection coefficient *vs.* surf similarity parameter.

5.3.3. Evaluation of reflected wave conditions

A comparative analysis with respect to the reflected wave conditions between the various models is now given. The following aspects were taken into consideration:

(i) Visual observations during the tests showed that under the lowest wave energy conditions (*i.e.*, wave run-segments with sea-states 1 to 6) run-up hardly ever reached the dune face, thereby it is anticipated that the spectral densities of the reflected wave spectra, and the coefficients of wave reflection to be approximately the same within the various models, as presumably only the beach-profile slope will interact with incoming waves;

(ii) Comparison of energy dissipation and commensurate decrease in the reflection coefficient among the various models; and

(iii) Effect of the specific geometrical conditions of each model to reflected wave conditions.

Examples of the spectral densities of the reflected wave spectra in two experiments under accretionary balance conditions are illustrated in Figure 5.57. The selected results indicate that there is only very slight deviation between the reflected wave spectra across the various models, confirming the hypothesis rose in which the incoming wave would only interact with beach-profile slope under the lowest wave energy conditions. The higher deviation is noticed for Model C2, sea-state 5, and may be related to a lower significant wave-height as compared to the other models (refer to Table 5.III, and remarks on Table 5.V). There are also no substantive differences in the spread of the coefficients of wave reflection over the valid frequency range (*i.e.*, within the range of $0.5f_p$ to $2f_p$).

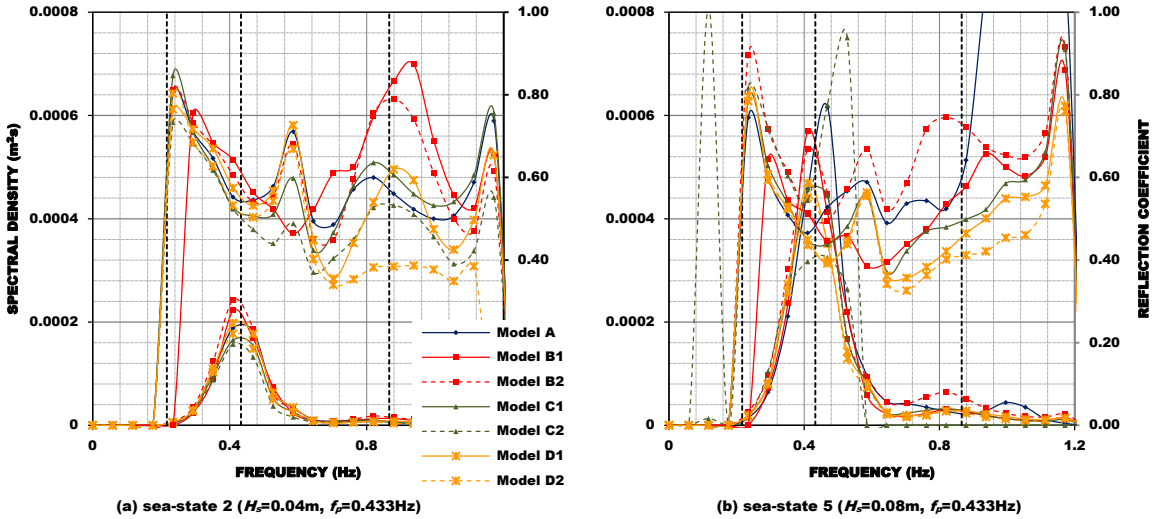

Figure 5.57: Spectral densities of the reflected wave spectra, accretion.

The following figures are the plot of the coefficients of wave reflection *vs.* significant wave-height (Figure 5.58), dimensionless wave-height (Figure 5.59), and surf similarity parameter (Figure 5.60). Except for some scattered values (*e.g.*, Test_A_4_20100408 and Test_C2_5_20100503) there is only a small variation in the coefficients of wave reflection across the various models for the same input sea.

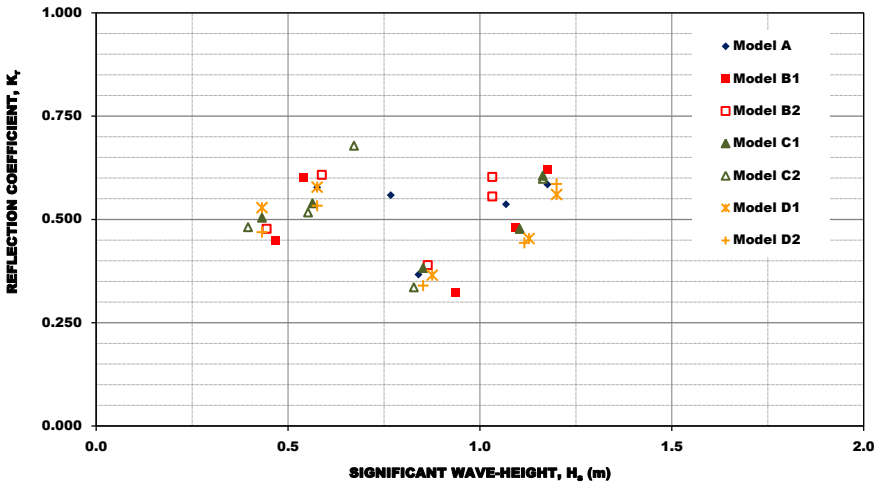

Figure 5.58: Pooled data set of the reflection coefficient *vs.* significant wave-height.

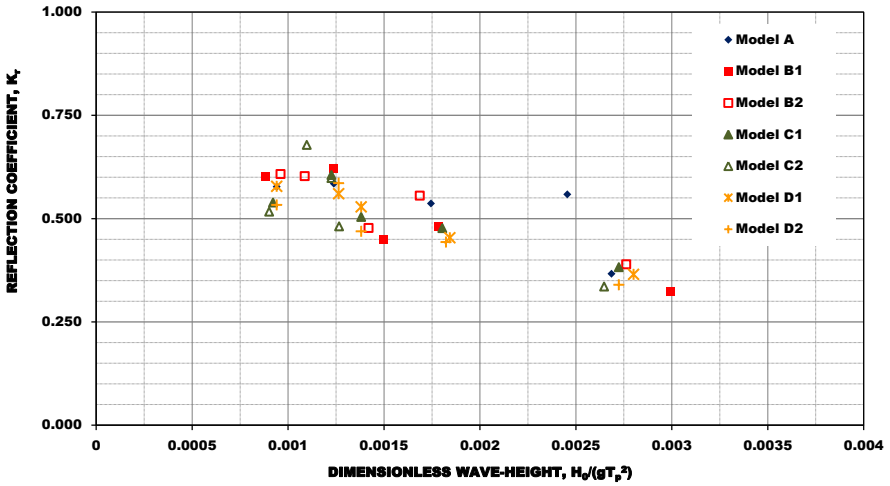

Figure 5.59: Pooled data set of the reflection coefficient *vs.* dimensionless wave-height.

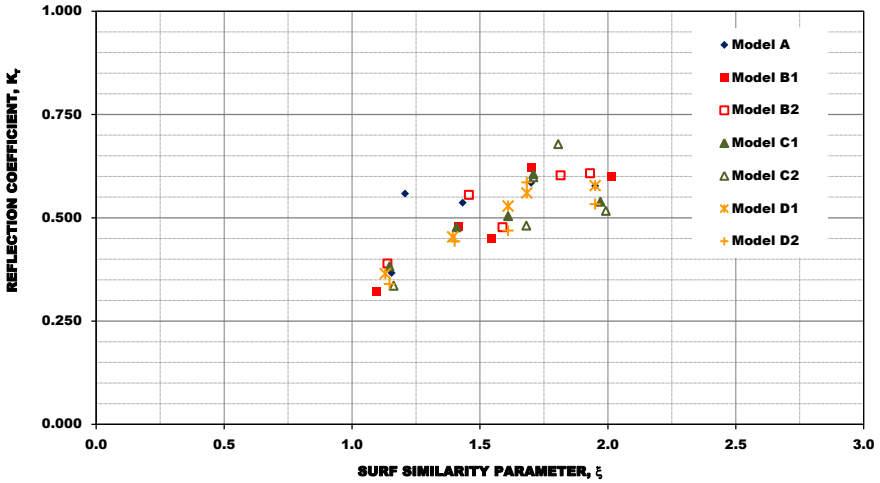

Figure 5.60: Pooled data set of the reflection coefficient *vs.* surf similarity parameter.

The preceding analysis on the reflected wave spectra and the reflection coefficients for the lowest wave energy test conditions, has served to learn to what extend the tests could be replicated. Overall, it provides some confidence on the test's repeatability and reproducibility, which is relevant to compare the experimental results across the various models.

In the next figures the coefficients of wave reflection for balance conditions of erosion are plotted against the significant wave-height (Figure 5.61), the dimensionless wave-height (Figure 5.62), and the surf similarity parameter (Figure 5.63).

The computed reflection coefficients obtained with both 1 and 2 variants of Model D are generally lower than those obtained with the other models. On the contrary, the ones obtained with Model A and Model E, variants 1 to 4, are higher than those obtained with the dune erosion control systems.

While the former may be explained by the specific geometrical conditions of each model, as presumably, the rounded shape of the elements with which is build Model D, and the steps in Model C facilitate the dissipation of some additional wave energy during downrush; the latter may be due to a steeper beach-profile in Model A, as sand is moved by waves from the dune onto the beach, and to the partial attenuation of the incident waves in Model E, of which a substantive part is reflected from the structure seawards.

As has already been seen in Chapter 2, such partial attenuation of the wave action, partly by wave breaking over the structure, and partly by wave reflection seaward, is what determines the efficiency of a detached breakwater (submerged or not) in reducing erosion at the shore. It very much depends on the design crest freeboard, the wave conditions, water level variations, surf zone width (which depends on the significant wave-height), and distance to shoreline. The effect some of these parameters have in reducing the wave action on the beach will be discussed farther along this chapter while evaluating the efficiency of the studied systems in maintaining a beach and in protecting the shoreline.

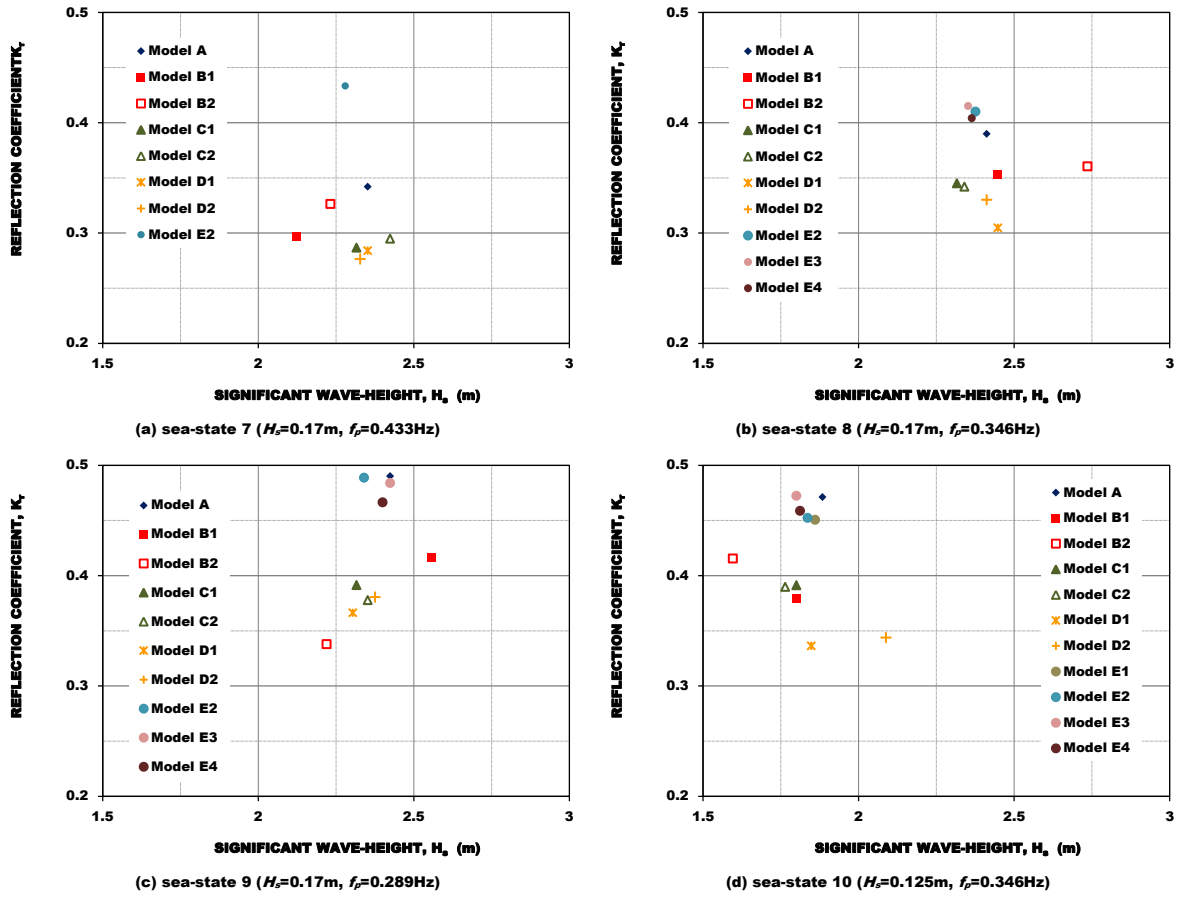

Figure 5.61: Pooled data set of the reflection coefficient *vs.* significant wave-height, erosional conditions.

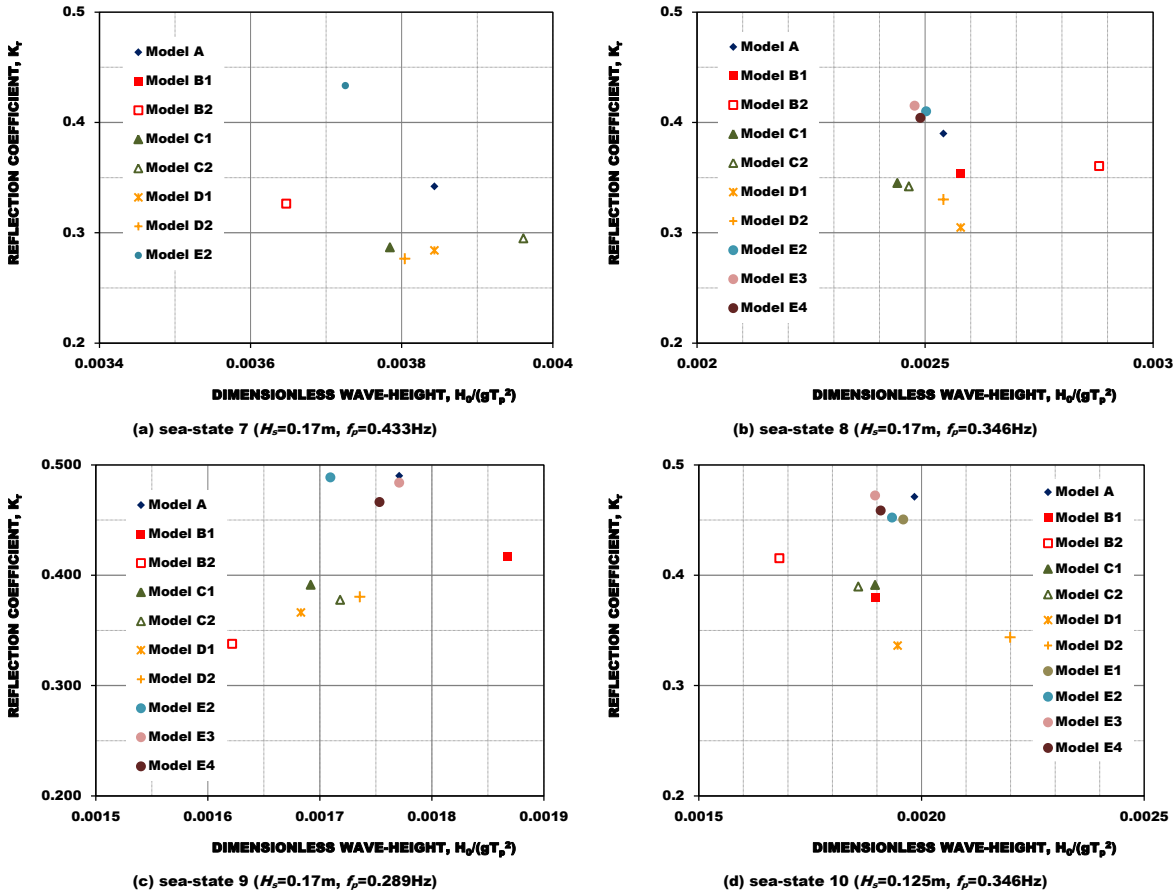

Figure 5.62: Pooled data set of the reflection coefficient *vs.* dimensionless wave-height, erosional conditions.

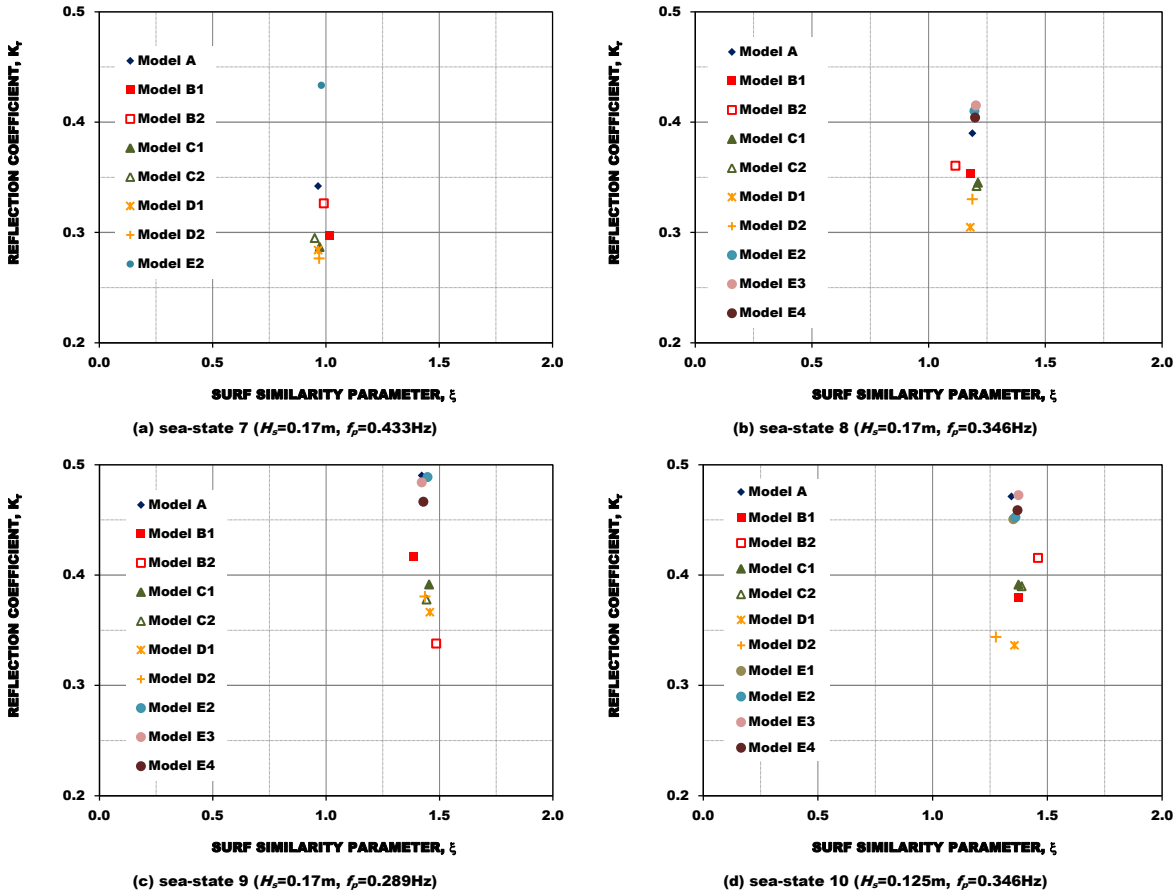

Figure 5.63: Pooled data set of the reflection coefficient *vs.* surf similarity parameter, erosional conditions.

5.4. Wave-induced pore-pressure variations

In this section wave-induced pore-pressure variations, including time-domain and frequency-domain analysis, are evaluated to study wave propagation over the beach slope and wave-induced pressures on the dune (or over the submerged nearshore breakwater). Pressures were measured by the method described in section 4.3.2.

In the study of the wave propagation over the beach slope, the dynamic pressure component is examined with respect to energy spectral balance and cross-shore gradients in wave-induced pressure energy flux. Representative pressures are estimated from spectral moments.

The definition sketch, including the location and submergence of the PDCR-81 sensors (P5 to P8), is as shown in Figure 5.64. Figure 5.65 are views during model construction.

Later in section 5.6 the estimated significant-pressure to incident wave-height ratio is revised with regard to existing theories on the attenuation of pore-pressure induced by waves travelling over a porous soil.

In the study of the wave-induced pressures on the dune (models B to D) and over the submerged nearshore breakwater (Model E), pressure distributions into the structure at different peak pressure instants were computed, by using as input the experimental results. The pressure was recorded at several locations along the structure slope and to the interior, as given in Figure 5.66 and summarized in Table 5.XIV.

Both the variants 1 and 2 of Model B, were instrumented with 8 sensors; 4 along the slope face (P1F to P4F), and 4 others in the interior at the second bag layer face (P1I to P4I), left panel in Figure 5.66. P2, P3, and P4 were approximately 0.16m apart, while P1 was approximately 0.08m apart from P2. Figure 5.67 are views during model construction.

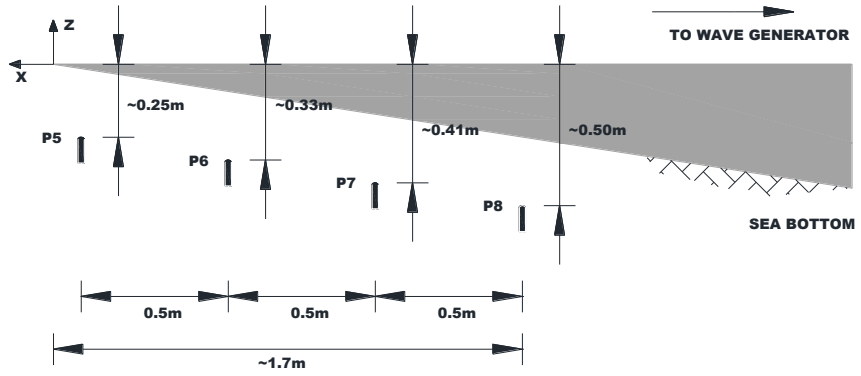

Figure 5.64: Definition sketch of pore-pressure sensors location and submergence in the beach sand (not to scale).

Figure 5.65: Aspects of pore-pressures buried in the sand, during model construction.

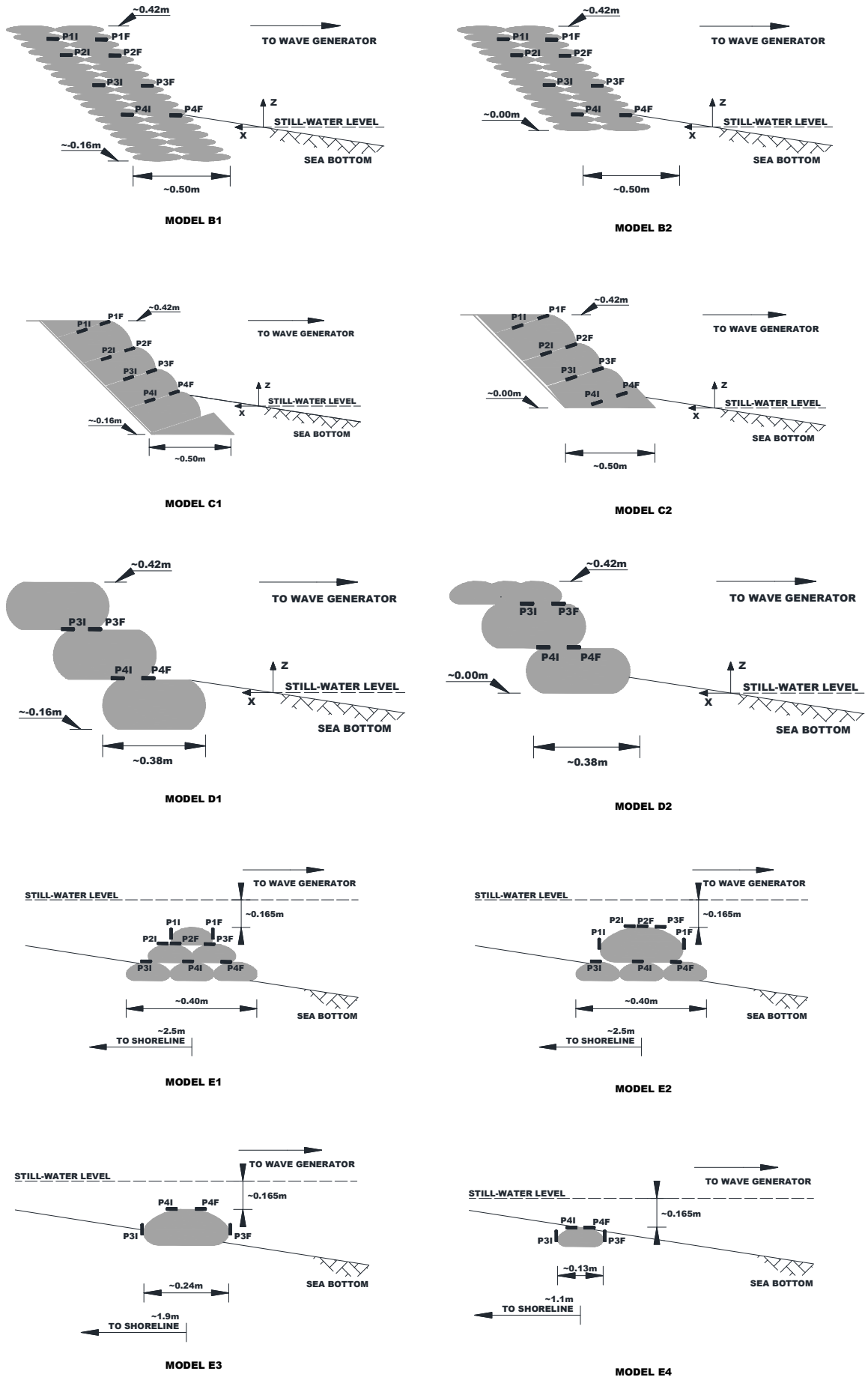

Figure 5.66: Definition sketch of pore-pressure sensors' (P1 to P4) location for the different test series (not to scale).

Table 5.XIV: Location pore-pressure sensors (P1 to P4) to still-water level.

Sensor ID	Model B	Model C	Model D1	Model D2
P1	0.33	0.38	-	-
P2	0.25	0.28	-	-
P3	0.17	0.18	0.22	0.38
P4	0.08	0.08	0.03	0.19

Model C, variants 1 and 2, were instrumented with the same 8-sensor configuration, 4 at the face (P1F to P4F), and another 4 to the interior at approximately half-wrap-length (P1I to P4I). Sensors were approximately 0.1m apart from each other.

Model D was instrumented with only 4 sensors (P3 and P4). As there were only two layers between the tubes, so have the number of sensors and the spacing to be decreased and increased accordingly. Sensors were approximately 0.19m (*i.e.*, approximately the height of a large tube) apart from each other; interior sensors were placed at approximately half-tube-width (P3I and P4I).

Finally, Model E variants 1 and 2 were instrumented with 8 sensors each, while variants 3 and 4 were instrumented with only four sensors each. In the former, P3I, P4I, and P4F were placed at the top of the lower tube layer facing the flow, P1F and P1I were at the top layer facing up, P3F and P2F were at the top of the middle layer (E1) or top layer (E2) facing the wave, and P2I was facing the shore. In the later, sensors P3 (face and interior) were facing up, sensor P4F was facing the wave, and sensor P4I was facing the backwash.

Figure 5.68 shows an aspect of the placement of P3I, P4I, and P4F at the bottom layer, as seen the crystal tube on which the sensors were introduced into was sewed to the tubes as a way to ensure minimum displacement.

Figure 5.67: Aspects of pore-pressures along the structure slope face (test series B), during model construction.

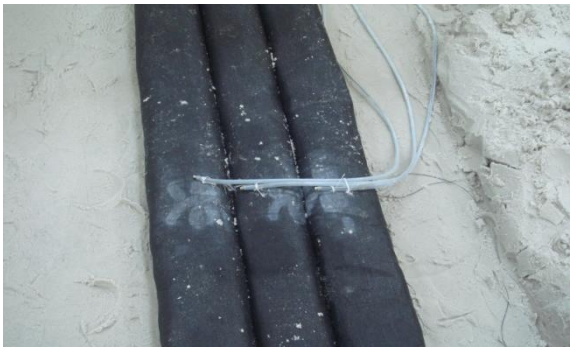

Figure 5.68: Aspect of pore-pressures placement (Model E1), during construction.

5.4.1. Wave propagation across the beach-profile

In the study of the wave propagation over the beach slope, the data recorded by the pore-pressure sensors buried into the sand (see Figure 5.64) was analysed in both time- and frequency-domains. WAFO (see, *e.g.*, Brodtkorb *et al.*, 2000; and WAFO-group, 2000), which is a Matlab toolbox for analysis of random waves and loads developed at the Lund University in Sweden, has been used to process the signals recorded by the four consecutive pore-pressure sensors.

The main objective of this analysis is to study the wave propagation over the beach slope, namely how the incident waves respond to morphologic perturbations, by examining the energy spectral balance computed from the recorded pressure time-series, the cross-shore gradients in wave-induced pressure energy flux and the corresponding spectral moments. For the reason that it makes use of an equipment which has never been employed before at FEUP hydraulics laboratory outside this experimental work, the present analysis aims also at bringing insight on the potentiality of the use of the PDCR-81 miniature pore-pressure sensors. Such type of sensors has advantages (*e.g.*, the minimum encroachment/influence on other measurements, and high frequency of response) and disadvantages (*e.g.*, the requirement of a rigid structure to be mounted to may complicate the set-up, and the measurement diaphragm is fragile and may be easily damaged) when compared to other measuring systems that may verify or disprove its use.

An example of elevation and pressure time-series recorded during a test with erosional waves is presented in Figure 5.69. As earlier described, the surface elevation change was detected by an array of four probes, S1 to S4, installed seawards the beach slope; while the pore-pressure sensors, P5 to P8, installed along the beach, measured the oscillations of wave-induced pressures. From the example is clearly perceptible the attenuation of pore-pressures (and consequently the attenuation of the pore-pressure heights).

Similarly to what has been done for estimating the spectral densities of the incident and reflected wave spectra, the wave-induced pressure spectra estimated with four different sizes of the windowing function, *i.e.*, values of 2^N equal to 8192, 16384, 32768, and 65536, were examined for various experimental conditions with Model A. Figure 5.70 shows examples of how the window size affects the computed spectral estimate for each one of the pressure sensors, P5 to P8, and for two different experimental conditions, sea-state 6 (left panel) and sea-state 7 (right panel). Following that examination, it was concluded that the number of periodgrams to be used in smoothing would be equal to 2^{15} (*i.e.*, 32768) for all experimenting conditions.

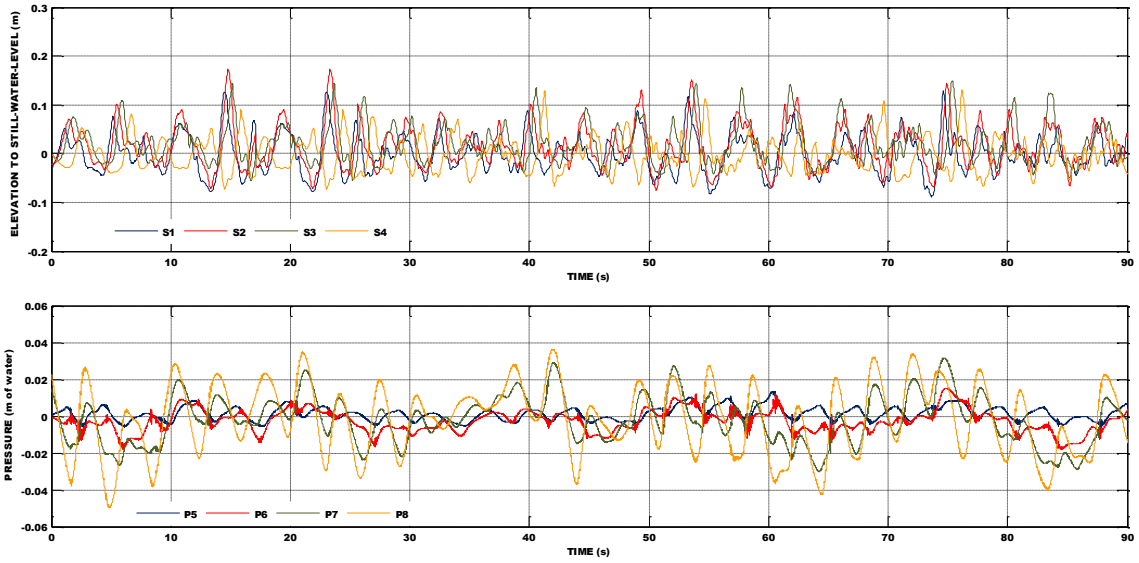

Figure 5.69: Example of elevation (top panel) and pressure (bottom panel) time-series recorded during experimental tests, sea-state 9 (H_s=0.17m, f_p=0.289Hz).

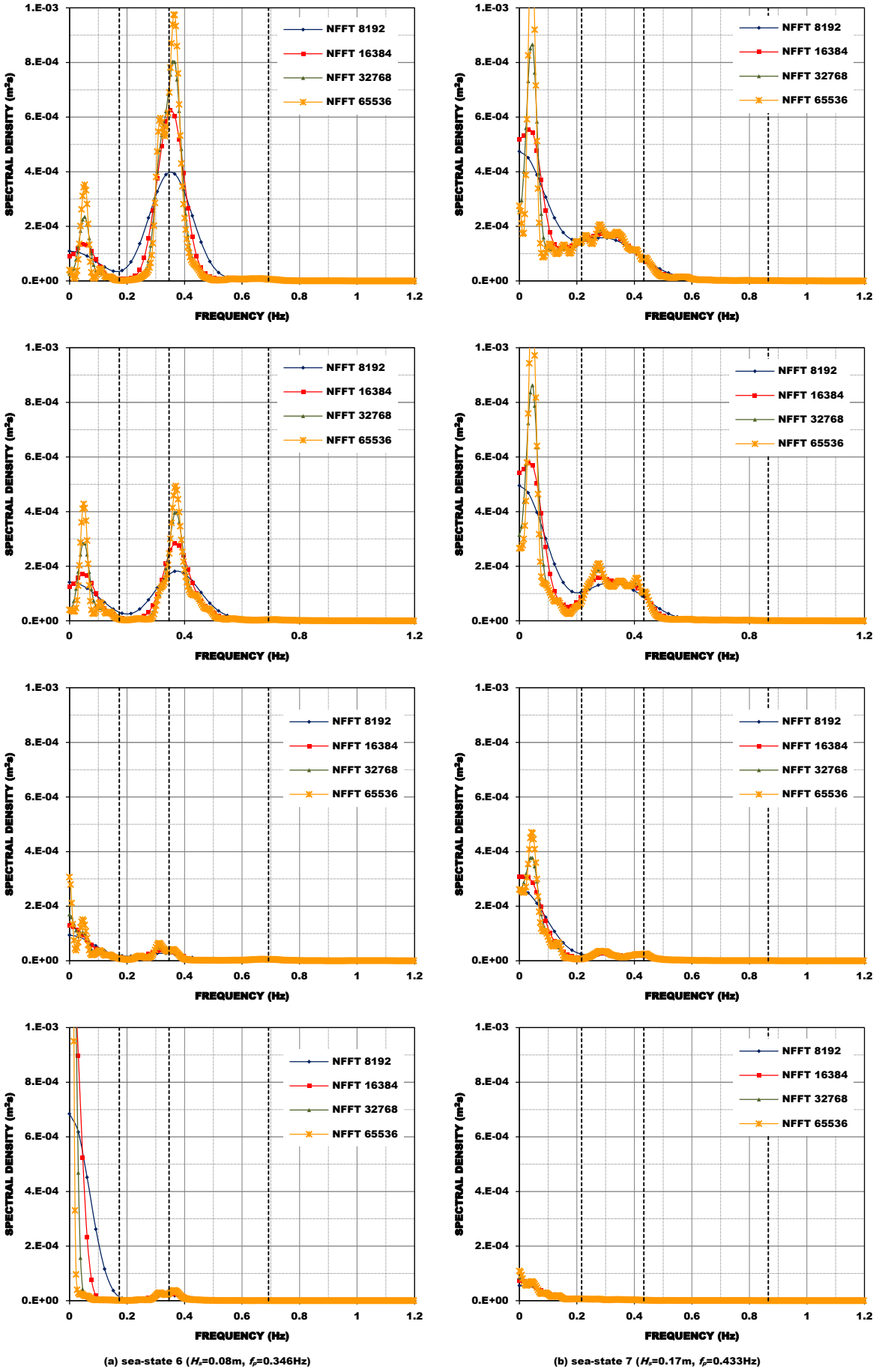

Figure 5.70: Model A, effect of different window sizes on spectrum smoothing.

In Figure 5.71 the frequency spectral density functions of the wave spectra computed for each surface elevation probe, S1 to S4, and of the pore-pressure spectra for each pressure sensor, P5 to P8, are shown for the given example. The pressure spectra of the sensors P5 to P8 were estimated for a window size spectrum smoothing of 32768, *i.e.*, window length (NFFT) of 32768 data points; while the size of the windowing function to compute the wave spectra was 512. The frequency spectral density functions of the wave spectra are plotted against the theoretical JONSWAP spectrum. The vertical dashed black lines are representative of the peak wave frequency (f_p) of the input sea and the frequency limits, which correspond to halve and two times that peak wave frequency, 0.5 f_p and 2.0f_p respectively.

It can be noticed in the right panel of Figure 5.71 that some of the incident wave energy was transferred to components with both higher (less perceptible) and lower frequencies. Such energy transferring occurs at harmonic frequencies ($2f_p$, $3f_p$, ...) and at the infragravity band (see, *e.g.*, Norheim *et al.*, 1998) and results from near-resonant nonlinear triad interactions in shallow water (see, *e.g.*, Henderson *et al.*, 2006; Battjes *et al.*, 2004; Herbers *et al.*, 2000; Masselink, 1998; Norheim *et al.*, 1998; Herbers and Burton, 1997; and references cited therein for discussion on the nonlinear transformation of a wave over a bottom with a bar-tough profile based on field and laboratory investigations and numerical simulations).

Similar energy transferring is observed for the various test conditions. The spectral energy balance in shoaling and breaking waves propagating over the beach slope is illustrated with the sea-state cases that span the range of balance conditions of accretion (sea-state 6), erosion (sea-state 8), persistent erosion (sea-state 10) and accretion followed by erosion (sea-states 3 and 8). For each sea-state case, and model, the evolution of the density spectrum across the beach is shown. Later over this paragraph that evolution with wave-period is examined as well.

Figure 5.72 depicts the evolution of the spectral density of wave-induced pore-pressure across the beach as measured by sensors P5 to P8 under sea-state 6. As can be observed, the general shape of the wave spectrum and location of peak periods are reasonably well described from the pressure measurements. The characteristics of the observed evolution of the spectra are somewhat similar across the various models with the amplification of lower-frequency components and the decay around the incident wave peak period. A difference is observed though in Model C1 where the peak of the pressure spectra is shifted to near the frequency limit 0.5f_p.

The energy losses associated to wave-breaking are noticeable across all measurements, but more pronounced at P7 and P6. Close to the shoreline infragravity motions dominate, whereas the energy at higher frequencies is mostly featureless and lacks a structure (*i.e.*, has no significant peaks and the energy is uniformly distributed within the primary and second-harmonic).

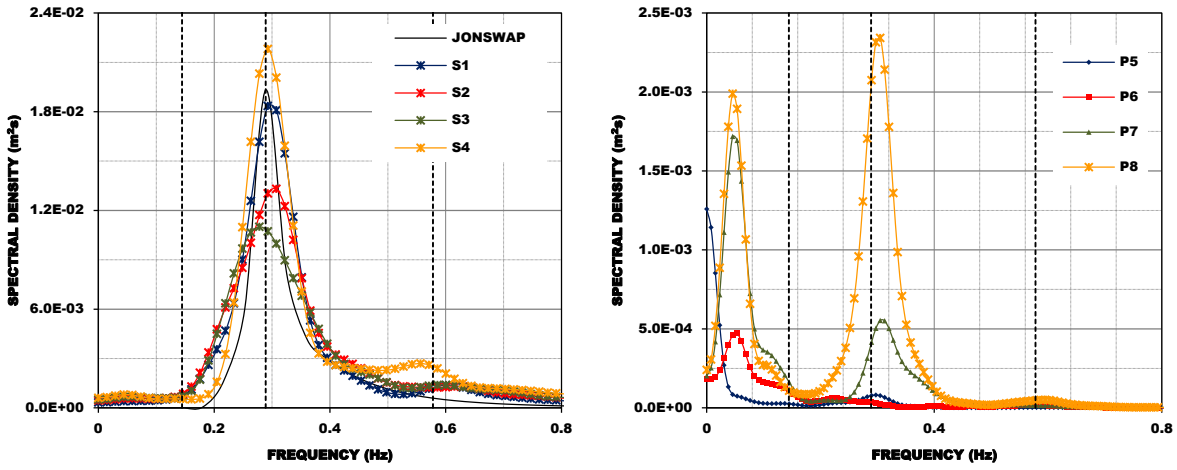

Figure 5.71: Example of spectral densities of the wave spectra as measured by probes S1 to S4 (left panel), and by the pore-pressure sensors P5 to P8 (right panel), sea-state 9 (H_s=0.17m, f_p=0.289Hz).

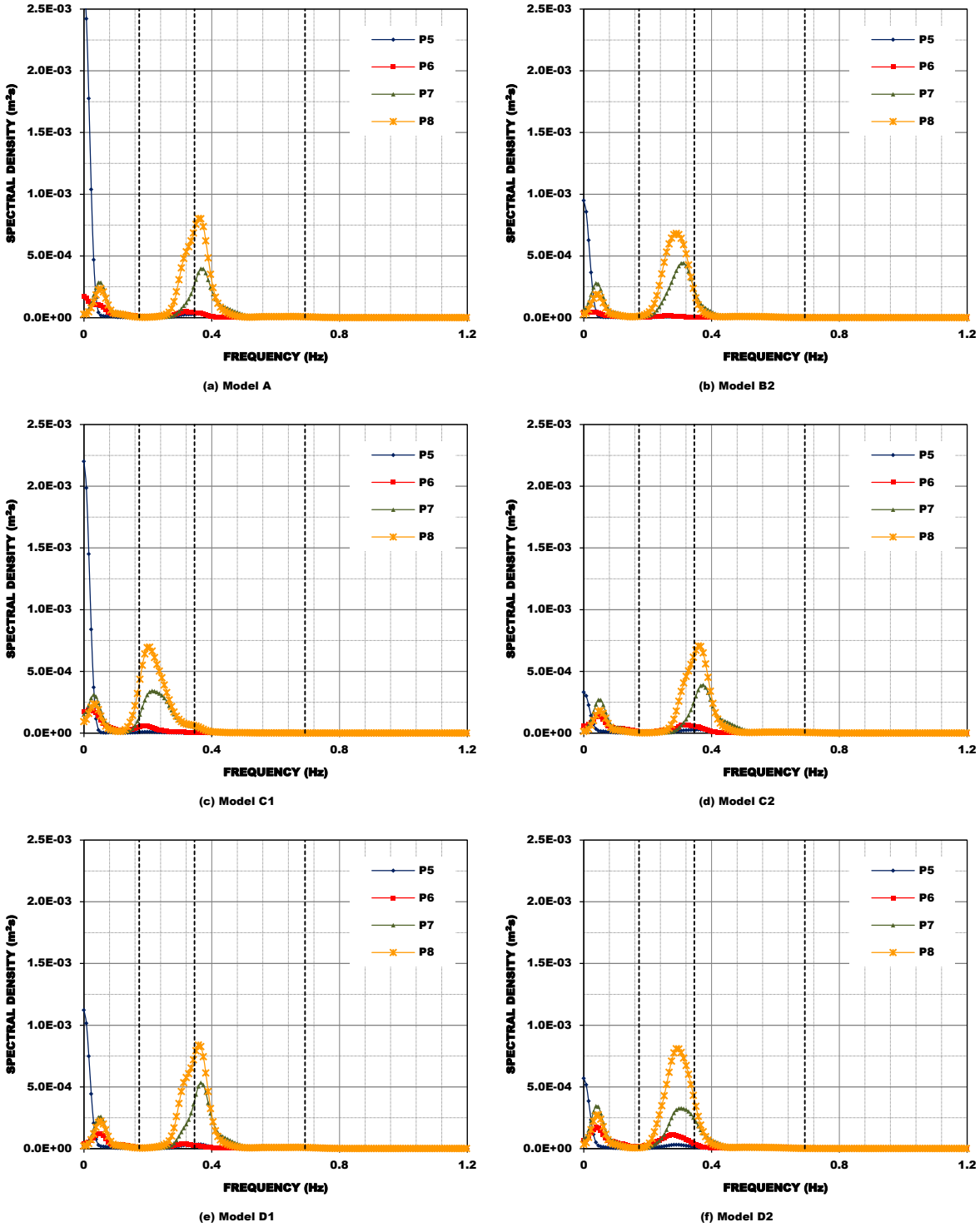

Figure 5.72: Evolution of spectral density across the surf zone under accretionary sequences, sea-state 6 (H_s=0.08m, f_p=0.346Hz).

Figure 5.73 shows segments of the wave-induced pressure time-series recorded under sea-state 8 for the various models, in which is apparent the decrease in wave-height across the surf zone; whereas Figure 5.74 plots the corresponding evolution of the spectral density across the beach as measured by sensors P5 to P8 as the waves propagate over the beach-profile slope.

The spectra evolution observed in the erosional sequences shows a strong decay of spectral levels around the primary-harmonic of the incident wave spectra across the surf zone, whereas at the shoreline infragravity motions dominate. Again the general shape and location of peak periods are reasonably well described.

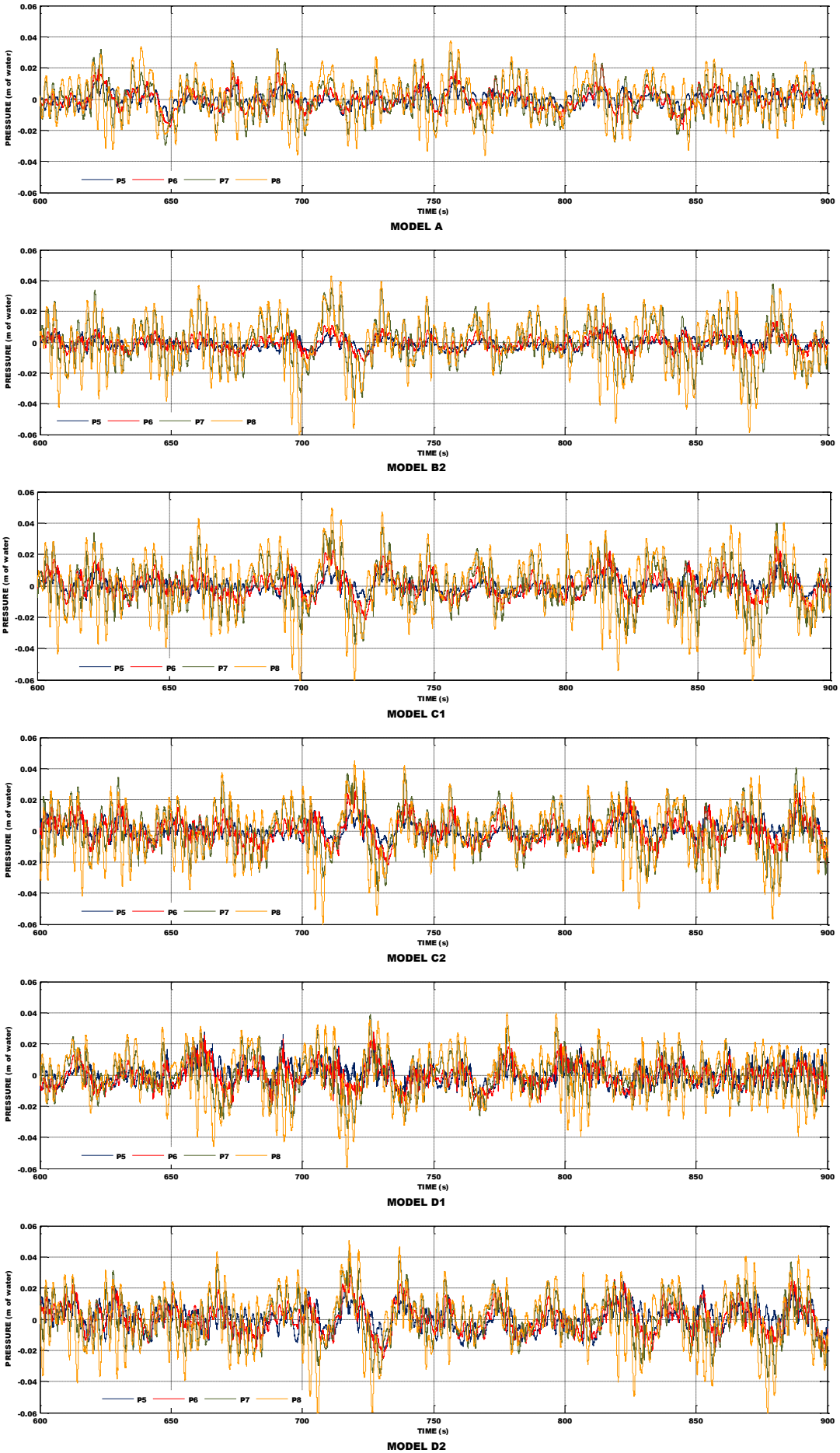

Figure 5.73: Segments of pressure time-series, sea-state 8 (H_s=0.17m, f_p=0.346Hz).

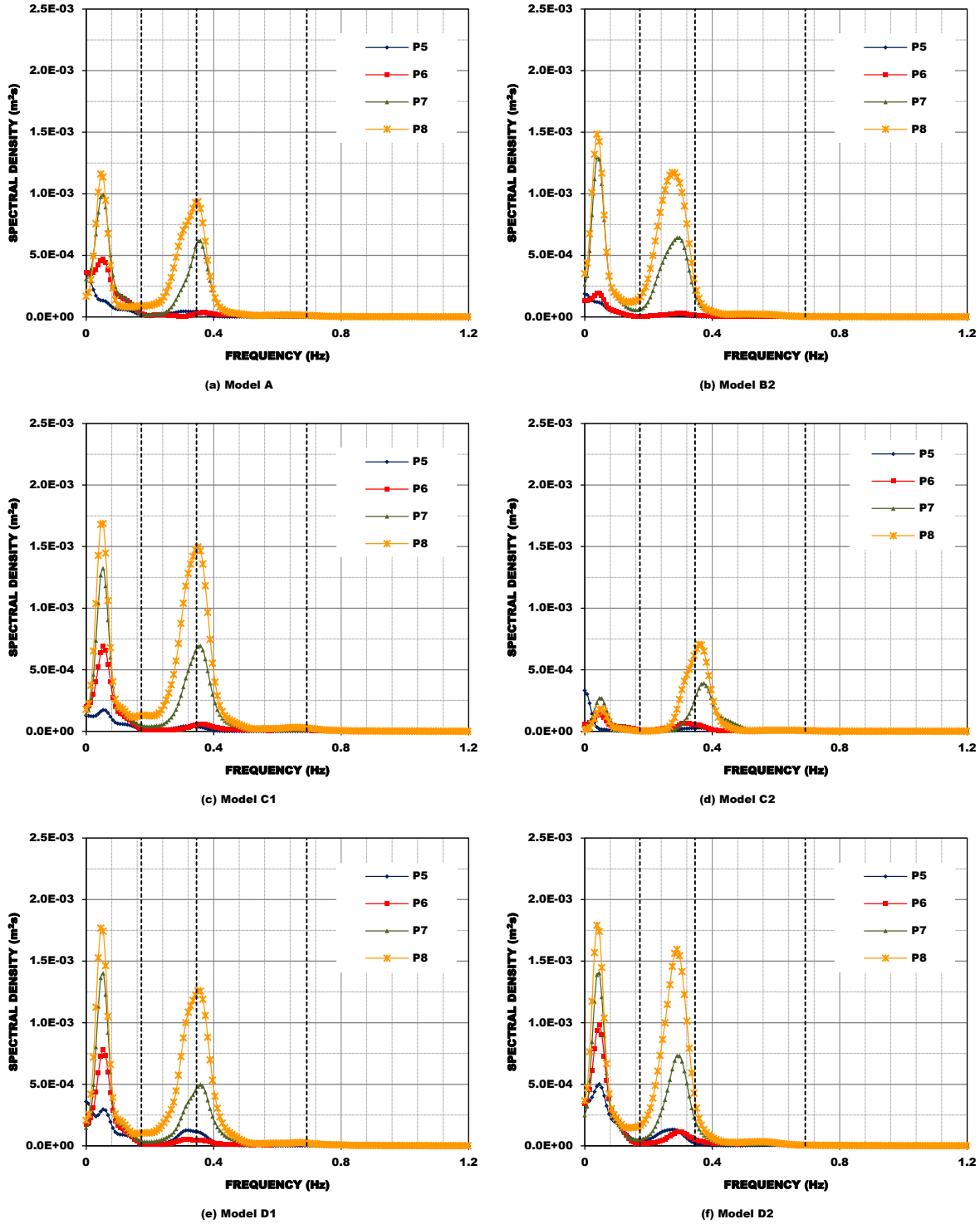

Figure 5.74: Evolution of spectral density across the surf zone under erosional sequences, sea-state 8 (H_s=0.17m, f_p=0.346Hz).

In Figure 5.75 the evolution of the spectral density across the surf zone for tests under persistent erosional conditions at different states is presented. The time window does not correspond in all models because some of the files were corrupted (likely due to communication loss during the experiments) and could not be used. The estimated spectra evidence a growth evolution of both the subharmonics and superharmonics components in all models except A and D2. In variants 1 and 2 of Model C, an even more interesting feature is noticeable in the pressure spectra, which is a growth in the third-harmonic. The energy transfer to a third-harmonic has been observed previously in investigations by, *e.g.*, Herbers *et al.* (2000) and Norheim *et al.* (1998).

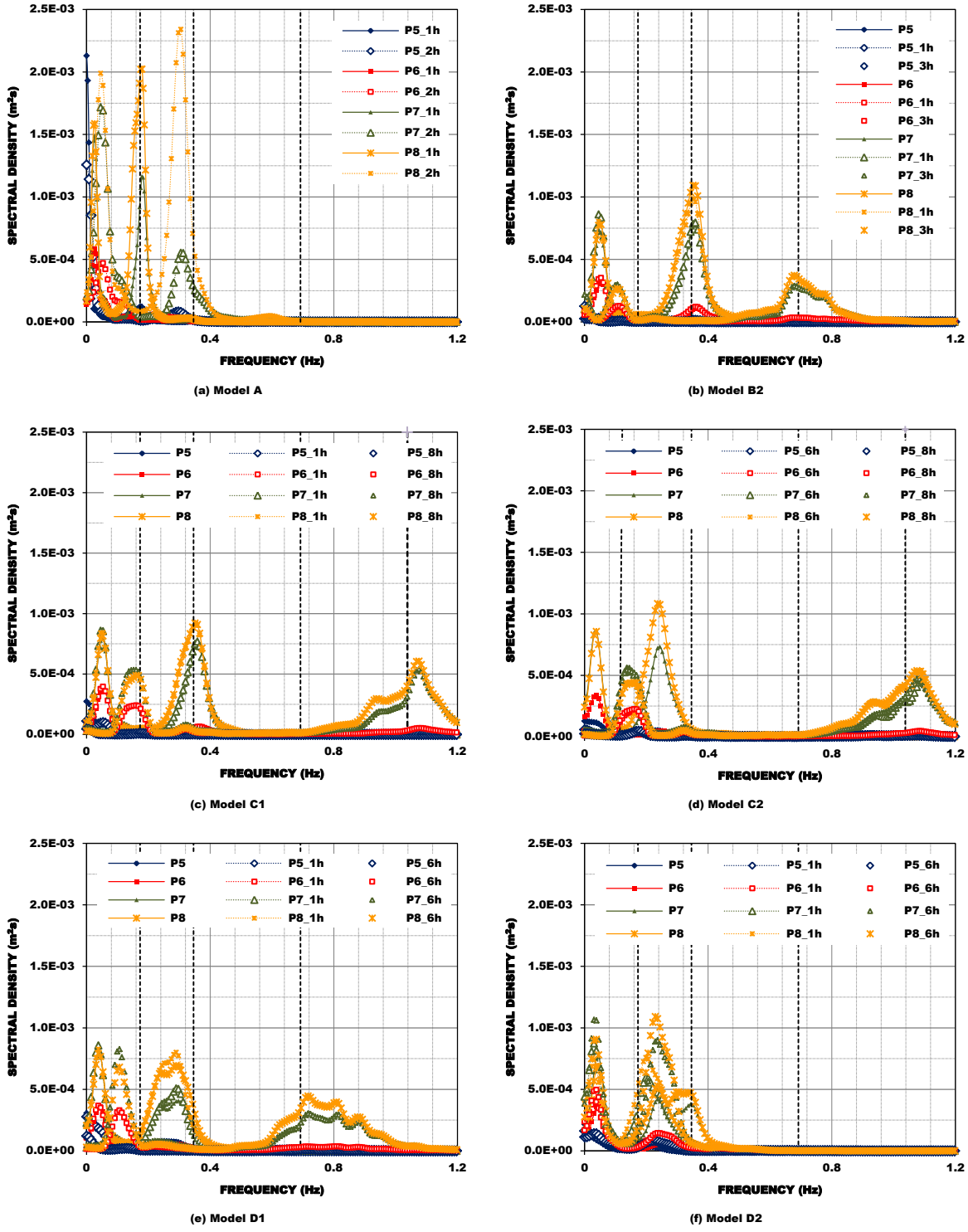

Figure 5.75: Evolution of spectral density across the surf zone under persistent erosional conditions, sea-state 10 (H_s=0.125m, f_p=0.346Hz).

Under balance conditions of infilling and again erosion the density spectra experience similar growth in the lower frequencies (Figure 5.76). It is also apparent from Figure 5.75 that such an evolution is observed under both storm and milder conditions; this has already shown up in Figure 5.72. Moreover, except for models A and D1 under sea-state 8_2x, the evolution of the spectra is only slightly different across the various models. One possible reason for the differences observed, is the associated effect of wave transformation, beach-profile change, and geometrical characteristics of the model. These reasons will be discussed later on in paragraph 5.4.4 and in section 5.6.

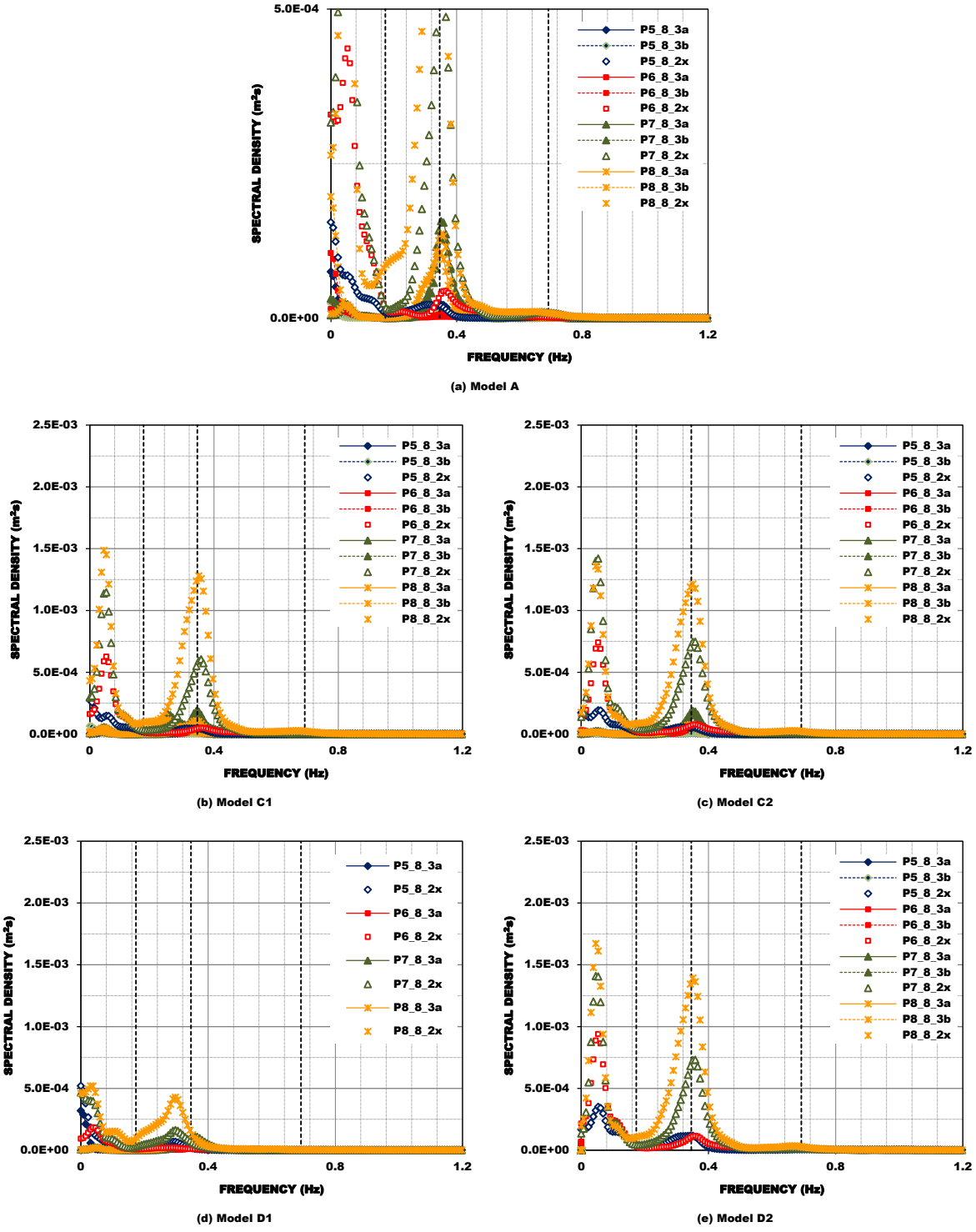

Figure 5.76: Evolution of spectral density across the surf zone under balance conditions of accretion followed by erosion, sea-state 3 (H_s=0.04m, f_p=0.346Hz) and sea-state 8 (H_s=0.17m, f_p=0.346Hz).

Figures 5.77 to 5.80 plot the evolution of spectral density of wave-induced pressures across the surf zone with incident peak wave-period and constant incident wave-height. As can be observed, a strong decay of the wave-induced pressure spectra occurs when waves propagate over the beach slope. The yellow line in Figure 5.77 serves to put in evidence that in Model A the location of the peak pressure spectra coincides with the incident wave spectra, which is not always the case in the other models (*e.g.*, under wave run-segments with sea-state 9). An overall agreement in the expected energy increase around the primary-harmonic with increase period is apparent. With respect to energy dissipation across the various models it will be deduced from the estimated cross-shore gradients in wave-induced pressure energy flux.

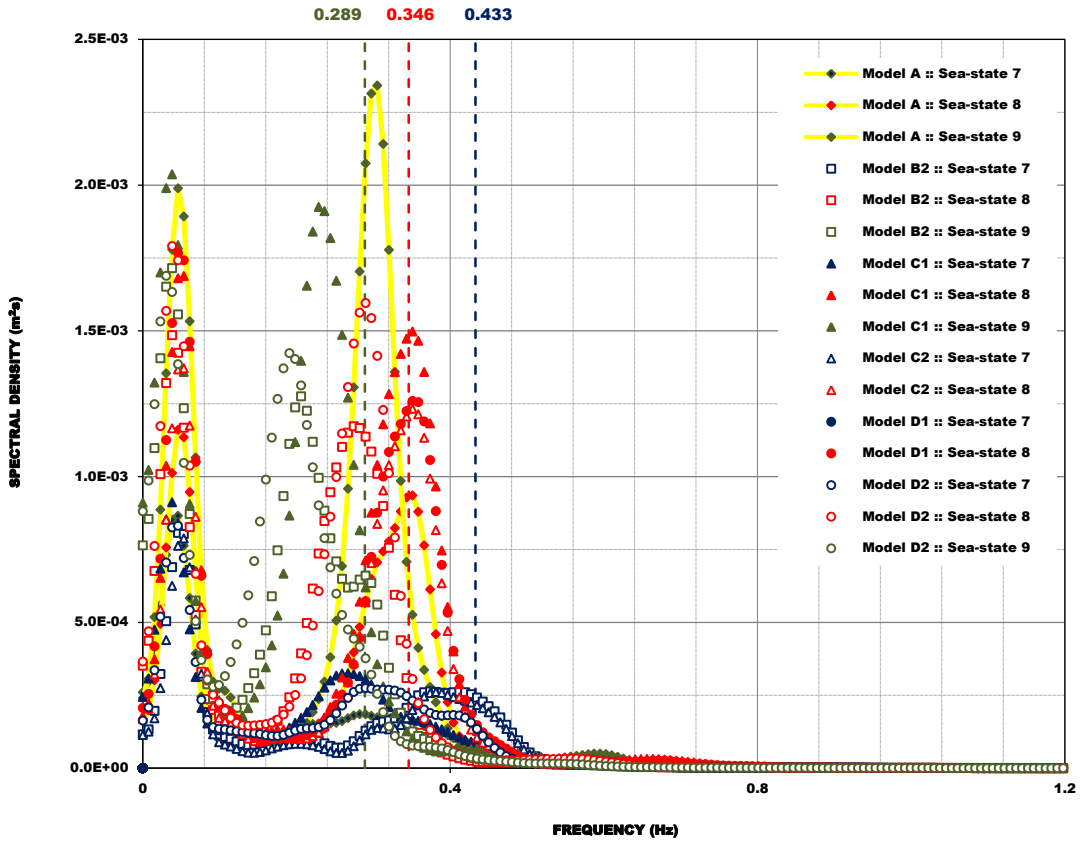

Figure 5.77: Evolution of spectral density at sensor P8 with incident peak wave-period.

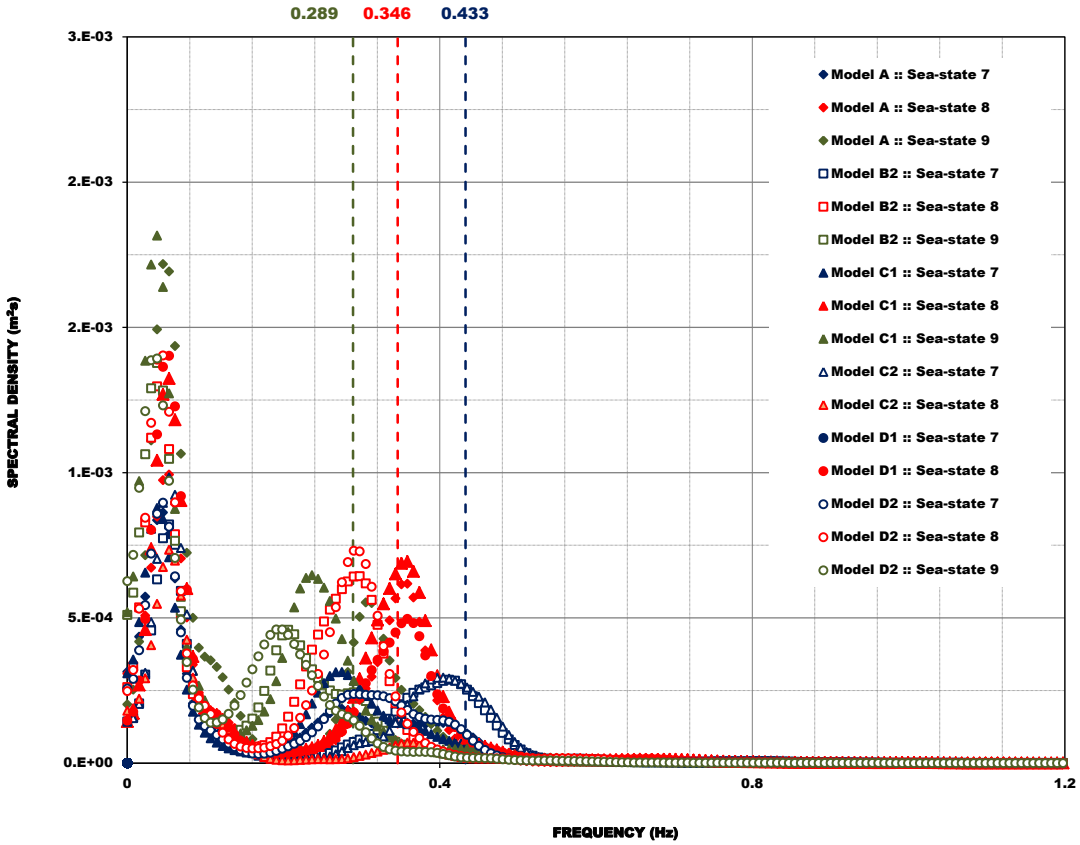

Figure 5.78: Evolution of spectral density at sensor P7 with incident peak wave-period.

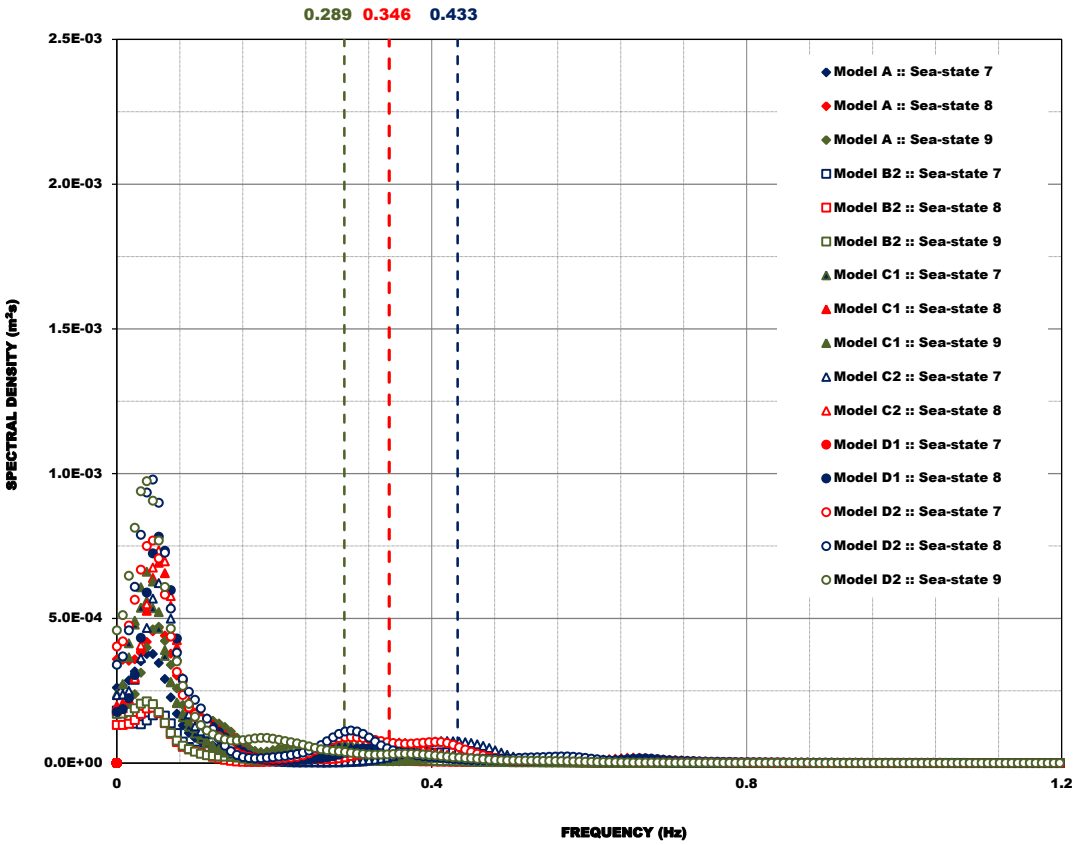

Figure 5.79: Evolution of spectral density at sensor P6 with incident peak wave-period.

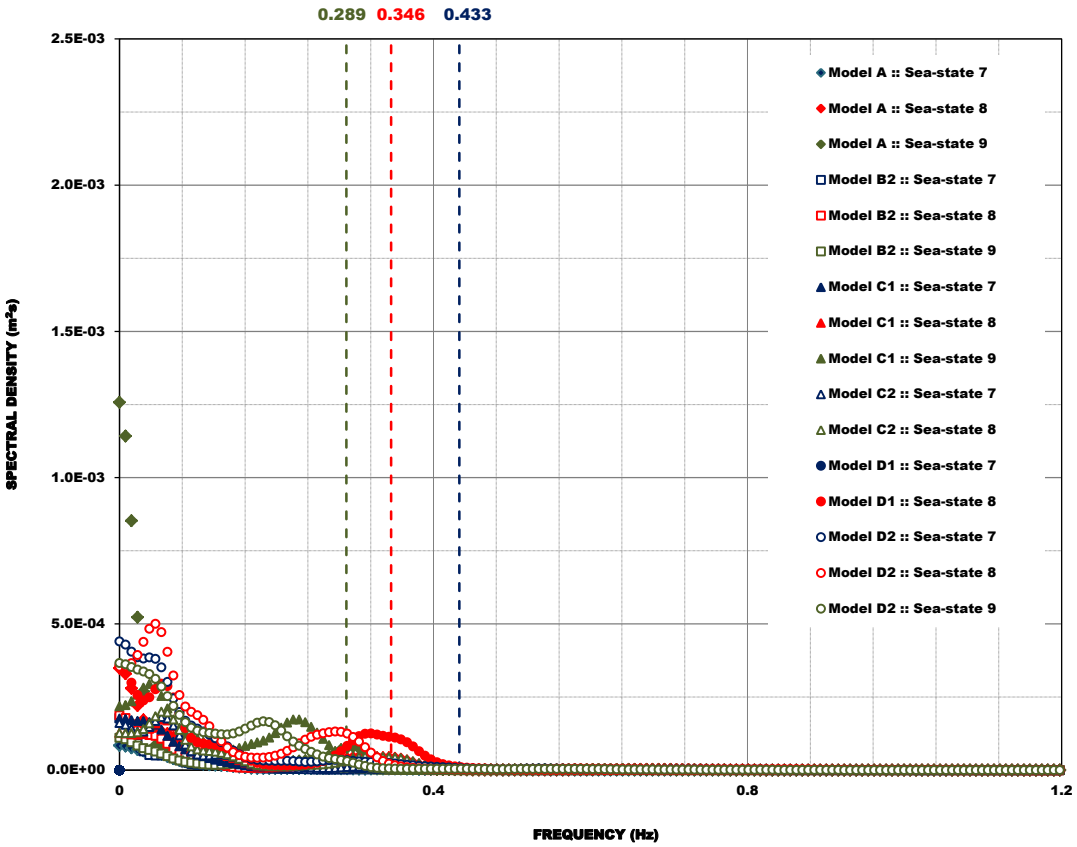

Figure 5.80: Evolution of spectral density at sensor P5 with incident peak wave-period.

The energy balance was evaluated at each midway point between adjacent sensors (*i.e.*, from P8 to P7, P7 to P6, and P6 to P5, see Figure 5.66). The energy flux gradient was estimated based on a finite difference approximation, as given by Eq. (5.20).

$$F_s(f) = \frac{S_2(f)\sqrt{gd_{w_2}} - S_1(f)\sqrt{gd_{w_1}}}{x_2 - x_1} \tag{5.20}$$

where x is the cross-shore position of a pair of adjacent sensors (see, *e.g.*, Figure 5.64) to which correspond a water depth (d_w) as summarized in Table 5.XV, and a spectra [S(f)]. The subscripts denote relative positioning, being '1' the deepest and '2' the shallowest.

Figures 5.81 to 5.83 plot energy flux gradients for each model and variant (except variant 1 of Model B) and for three selected tests in this study. Those selected tests are similar in input wave-period, T_p equal to 2.31s (corresponding to 8s on the prototype), and dissimilar in input significant wave-height, to know input H_s equal to 0.04m (Figure 5.81), 0.08m (Figure 5.82), and 0.17m (Figure 5.83). Again the vertical dashed black lines are representative of the peak wave frequency (f_p) of the input sea and the frequency limits, which correspond to halve and two times that peak wave frequency, 0.5 f_p and 2.0f_p respectively.

The incident wave energy for run-segments with sea-state 2 is very little and the small waves propagate almost across the whole beach-profile without breaking. As seen in Figure 5.81, the negative energy flux values around the peak frequency of the input wave spectrum (models A, B2, C2 and D1) and in the band between the frequency limit (0.5f_p) and that peak (models C1 and D2) are barely balanced by the positive fluxes to higher frequencies than those. When waves propagate through P7 to P6 the energy flux gradient is practically null or negative indicating a strong decay in the energy of the spectrum. From P6 to the shallowest sensor P5 a strong gain is observed at lower frequencies in all models but Model C1. The intercomparison between the models reveals only slight differences in shape (these are higher in Model D2); yet relatively higher negative and positive energy fluxes are noticeable in Model D1, at the peak frequency of the input wave spectrum and at the infragravity band.

Looking still at mild wave conditions but higher incident wave height (H_s=0.08m, input sea) the estimated energy flux gradients at the deepest sensors are similar in shape to those estimated for sea-state 2, that is a gain of energy close to the spectral peak frequency. The largest negative energy transfer occurs between sensors P7 and P6 at both higher and lower frequencies; yet losses of energy are perceptible at lower frequencies within the deepest sensors, and around the peak and at slightly higher frequencies between the shallowest. The energy transfer at low frequencies is excited predominantly at the beach face. Again no markedly differences exist between the models with respect to the positive energy flux gradients within sensors P8 and P7, the decay in the energy of the spectrum between sensors P7 and P6, and the excitation at the low frequencies occurring between sensors P6 and P5. Again, the energy flux gradients in Model D2 are similar in shape to that occurring in the other models but differ in magnitude level.

Table 5.XV: Distance to shoreline, water depth and depth of burial of sensors P5 to P8.

Sensor ID	Distance to Shoreline [m]	Water Depth [m]	Depth of Burial [m]
P8	1.7	0.255	0.245
P7	1.2	0.180	0.230
P6	0.7	0.105	0.225
P5	0.2	0.030	0.220

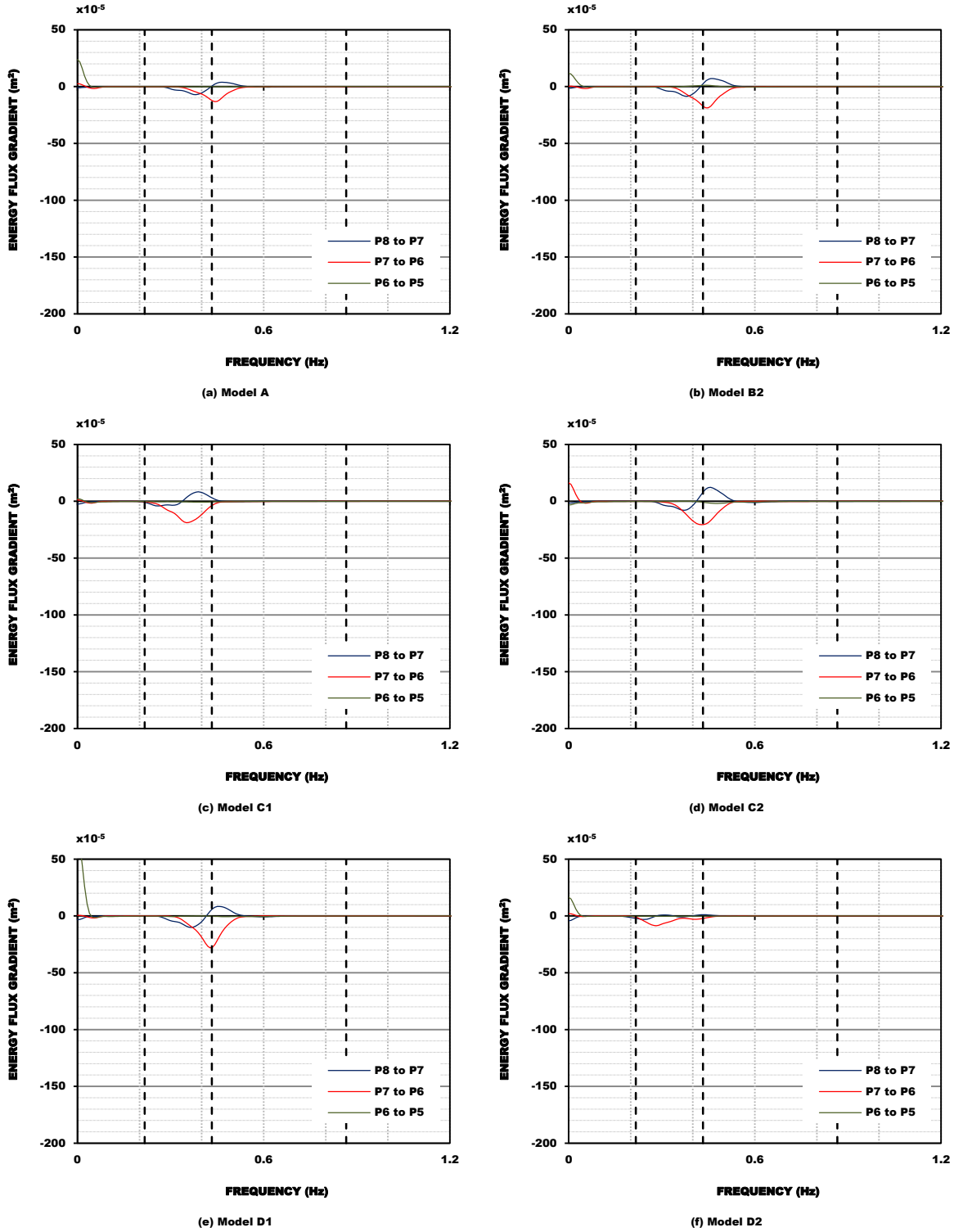

Figure 5.81: Energy flux gradients, sea-state 2 (H_s=0.04m, f_p=0.433Hz).

In the most energetic sea-state being examined in regard to energy fluxes, the entire transect of the beach-profile is well within the surf zone. The spread and large energy losses perceptible in the tests with sea-state 7 (Figure 5.83) are an indication of wave breaking and dissipation. From the deepest sensor (P8) to the shallowest a continued decline in the estimated cross-shore energy flux gradient is observed. Overall, very large flux gradients are observed around the peak incident wave spectrum and at lower frequencies. With respect to the former there is a substantive loss of energy at those frequencies from P7 to P6 and a moderate one from P8 to P7 (except in Model C2), which is partly compensated in models A and B2 when waves propagate from P6 to P5 and fairly continued in the remaining models.

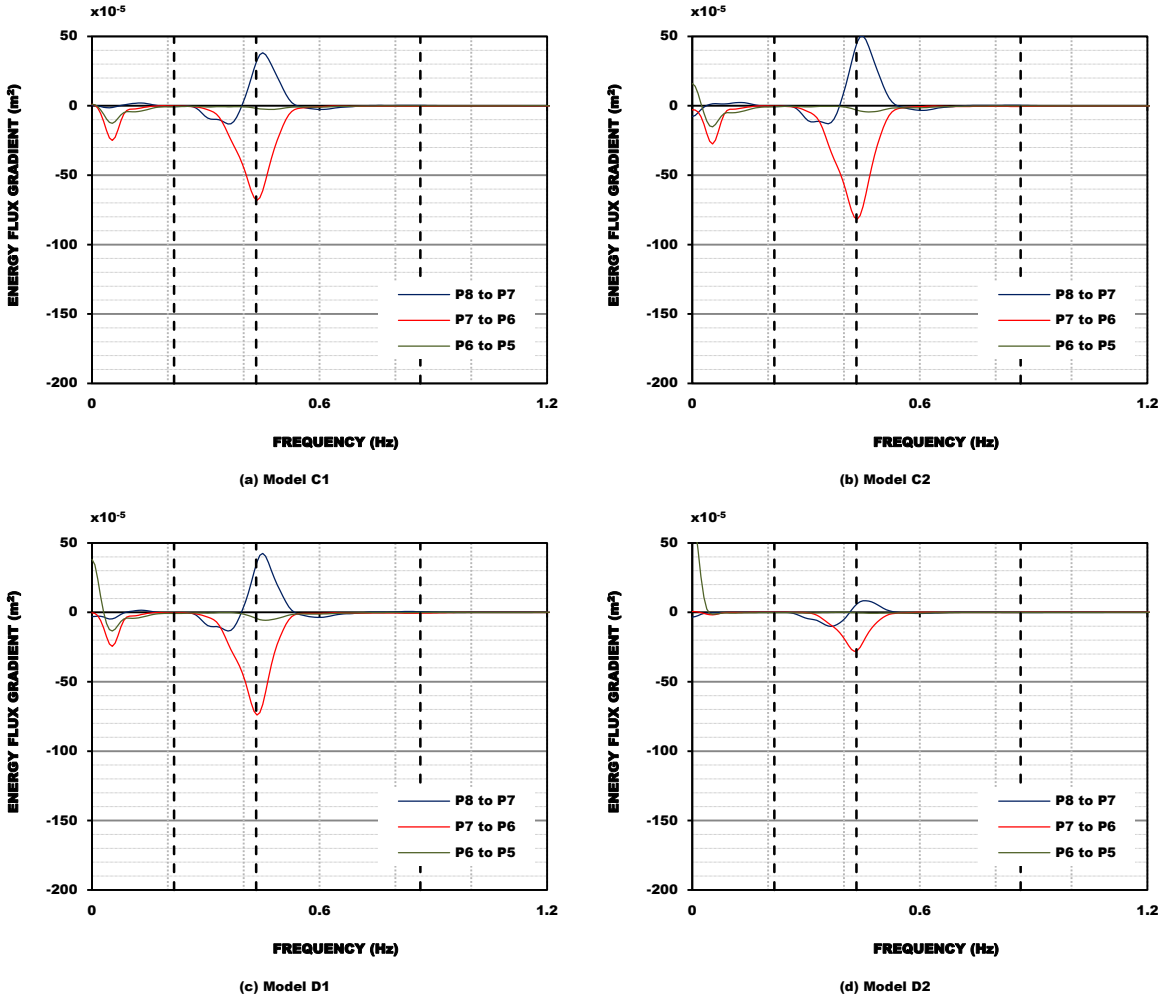

Figure 5.82: Energy flux gradients, sea-state 5 (H_s=0.08m, f_p=0.433Hz).

Even though the just presented estimated spectral energy balances did not include the examination of nonlinear interaction from which would benefit from, it still provides some useful information on how waves have propagated through the beach-profile onto the beach face. The energy growth in higher and lower harmonics occurs beyond the outer edge of the surf zone.

Around the peak of the input wave spectrum the energy flux is primarily balanced to become unbalanced into the surf zone, where a continued decay in the energy of the spectrum indicates wave dissipation. In the most energetic sea-states such a continued decline in the estimated cross-shore energy flux gradient is observed across all sensors. With respect to the energy that is transferred to the lower and infragravity frequencies it may be trapped close to the shore (see, *e.g.*, Thomson, 2006; and Herbers *et al.*, 2000) or can propagate to deep water.

In regard to energy dissipation across the various models it is possible to conclude that no major differences can be inferred from the estimated cross-shore gradients in wave-induced pressure energy flux, as only relatively minor differences are observed, even when compared to the reference case (*i.e.*, the non-protected dune-beach-system, Model A). There are only small differences occurring in *(i)* Model D2 for sea-state 2 with a general low energy flux (Figure 5.81) and for sea-state 5 (Figure 5.82); and in *(ii)* Model C2 for sea-state 7 (Figure 5.83) with more energy being transferred to near the frequency limit (0.5f_p), although a similar transfer is apparent across the various models it is comparably higher in Model C2 than in the other models. The data presented so far is insufficient to provide a definitive explanation for the observed differences, as a hypothesis they may result from wave-wave interactions due to particular circumstances associated with wave reflection from structure and being transmitted and reflected from the bottom undulations.

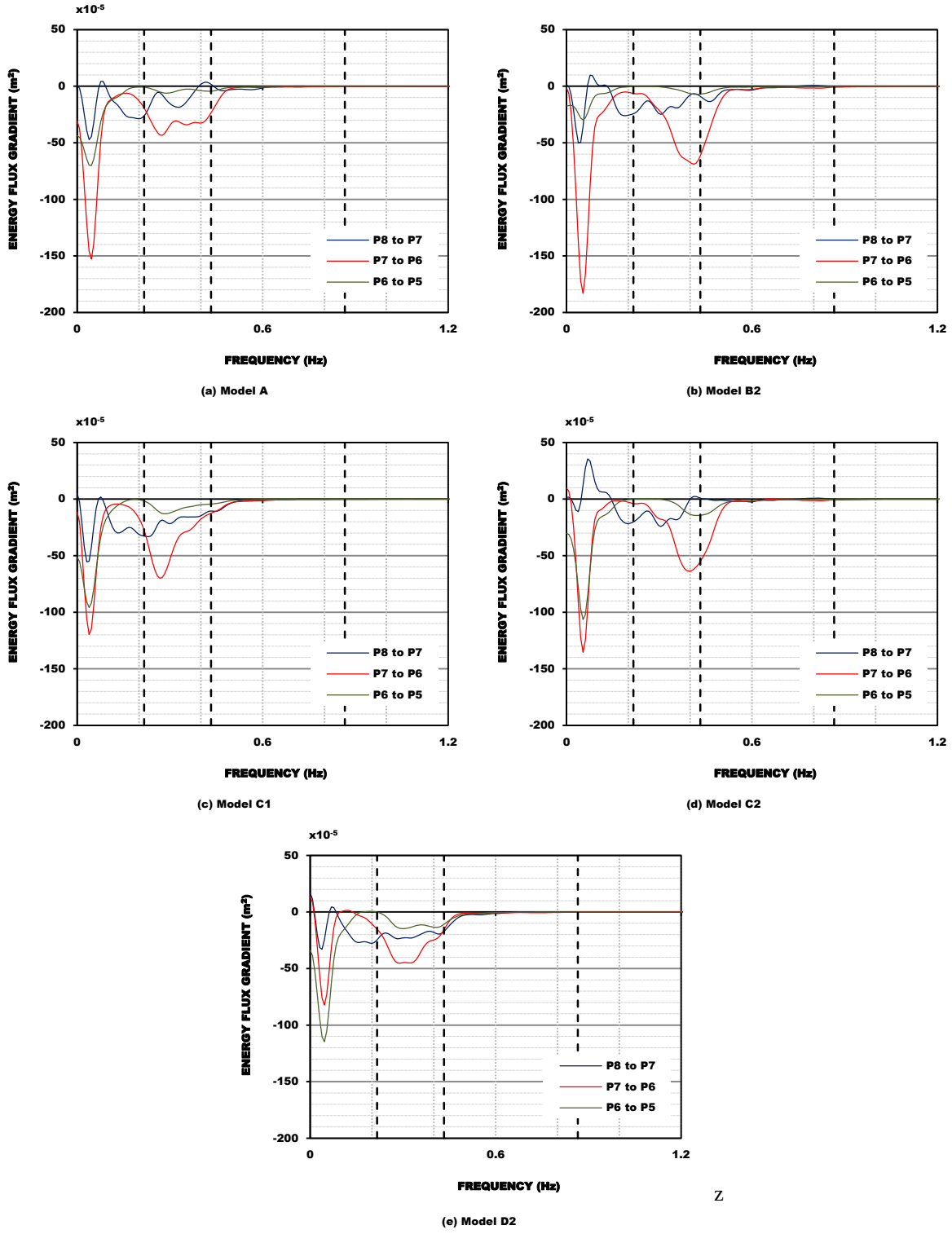

Figure 5.83: Energy flux gradients, sea-state 7 (H_s=0.17m, f_p=0.433Hz).

In Tables 5.XVI to 5.XXI the significant and maximum pressures estimated from the zeroth-moment [Eqs. (5.12) and (5.14), accordingly], as has been done to calculate the representative wave-heights and in assuming it follows a Rayleigh distribution, are given. The significant pressure to significant wave-height ratio is given also in Tables 5.XVI to 5.XXI. Later over section 5.6 that ratio is discussed by comparison with the attenuation of wave-induced pore-pressures in the soil with water depth, sensor depth of burial, significant wave-period and degree of saturation, as calculated by the theory developed by Mei and Foda (1981) – cited in Mei (1989), as given by Eq. (3.116).

Table 5.XVI: Model A: significant and maximum pressures derived from spectral moments.

Test ID	Incident		Sensor ID	m_o	P_s [m of water]	P_{max} [m of water]	$\frac{P_s}{H_s}$
	H_s [m]	T_p [s]					
Test_A_7_20100409	0.196	2.28	P5	7.76E-06	0.011	0.020	0.06
			P6	3.58E-05	0.024	0.044	0.12
			P7	9.23E-05	0.038	0.070	0.19
			P8	9.91E-05	0.040	0.073	0.20
Test_A_8_20100405	0.201	2.84	P5	2.64E-05	0.021	0.038	0.10
			P6	4.94E-05	0.028	0.051	0.14
			P7	1.24E-04	0.045	0.082	0.22
			P8	1.72E-04	0.053	0.097	0.26
Test_A_9_20100413	0.202	3.41	P5	4.00E-05	0.025	0.046	0.12
			P6	4.73E-05	0.028	0.051	0.14
			P7	1.61E-04	0.051	0.093	0.25
			P8	2.94E-04	0.069	0.126	0.34
Test_A_1_20100407	0.070	1.63	P5	9.93E-07	0.004	0.007	0.06
			P6	2.68E-06	0.007	0.013	0.10
			P7	8.99E-06	0.012	0.022	0.17
			P8	1.10E-05	0.013	0.024	0.19
Test_A_2_20100407	0.048	2.28	P5	5.59E-06	0.009	0.016	0.19
			P6	1.03E-06	0.004	0.007	0.08
			P7	5.66E-06	0.010	0.018	0.21
			P8	6.06E-06	0.010	0.018	0.21
Test_A_6_20100413	0.098	2.84	P5	5.95E-05	0.031	0.057	0.32
			P6	1.70E-05	0.016	0.029	0.16
			P7	5.36E-05	0.029	0.053	0.30
			P8	8.76E-05	0.037	0.068	0.38
Test_A_10_1h_20100331	0.153	2.84	P5	3.38E-05	0.023	0.042	0.15
			P6	2.60E-05	0.020	0.037	0.13
			P7	9.47E-05	0.039	0.071	0.25
			P8	1.49E-04	0.049	0.090	0.32
Test_A_8_3a_20100405	0.052	2.84	P5	3.58E-06	0.008	0.015	0.15
			P6	2.30E-06	0.006	0.011	0.12
			P7	1.27E-05	0.014	0.026	0.27
			P8	1.02E-05	0.013	0.024	0.25
Test_A_8_3b_20100406	0.052		P5	1.33E-06	0.005	0.009	0.10
			P6	3.55E-06	0.008	0.015	0.15
			P7	1.17E-05	0.014	0.026	0.27
			P8	1.57E-05	0.016	0.029	0.31
Test_A_8_2x_20100406	0.202		P5	1.31E-05	0.014	0.026	0.07
			P6	4.42E-05	0.027	0.049	0.13
			P7	1.16E-04	0.043	0.079	0.21
			P8	1.41E-04	0.047	0.086	0.23

Table 5.XVII: Model B2: significant and maximum pressures derived from spectral moments.

Test ID	Incident		Sensor ID	m_o	P_s [m of water]	P_{max} [m of water]	$\frac{P_s}{H_s}$
	H_s [m]	T_p [s]					
Test_B2_7_20100323	0.186	2.28	P5	3.38E-05	0.023	0.042	0.12
			P6	2.60E-05	0.020	0.037	0.11
			P7	9.47E-05	0.039	0.071	0.21
			P8	1.49E-04	0.049	0.090	0.26
Test_B2_8_20100325	0.228	2.84	P5	1.42E-05	0.015	0.027	0.07
			P6	1.81E-05	0.017	0.031	0.07
			P7	1.49E-04	0.049	0.090	0.21
			P8	2.24E-04	0.060	0.110	0.26
Test_B2_9_20100329	0.185	3.41	P5	9.95E-06	0.013	0.024	0.07
			P6	1.98E-05	0.018	0.033	0.10
			P7	1.39E-04	0.047	0.086	0.25
			P8	2.57E-04	0.064	0.117	0.35
Test_B2_10_20100210	0.133	3.41	P5	6.62E-06	0.010	0.018	0.08
			P6	3.55E-05	0.024	0.044	0.18
			P7	1.16E-04	0.043	0.079	0.32
			P8	1.60E-04	0.051	0.093	0.38
Test_B2_1_20100223	0.037	1.63	P5	2.09E-06	0.006	0.011	0.16
			P6	2.20E-06	0.006	0.011	0.16
			P7	2.21E-06	0.006	0.011	0.16
			P8	2.63E-06	0.006	0.011	0.16
Test_B2_2_20100223	0.049	2.28	P5	5.41E-06	0.009	0.016	0.18
			P6	1.69E-06	0.005	0.009	0.10
			P7	8.42E-06	0.012	0.022	0.24
			P8	7.85E-06	0.011	0.02	0.22
Test_B2_4_20100223	0.072	1.63	P5	5.62E-06	0.009	0.016	0.13
			P6	4.87E-06	0.009	0.016	0.13
			P7	9.25E-06	0.012	0.022	0.17
			P8	1.03E-05	0.013	0.024	0.18
Test_B2_6_20100324	0.086	2.84	P5	2.13E-05	0.018	0.033	0.21
			P6	5.23E-06	0.009	0.016	0.10
			P7	5.95E-05	0.031	0.057	0.36
			P8	7.73E-05	0.035	0.064	0.41
Test_B2_10_1h_20100210	0.130	2.84	P5	5.00E-06	0.009	0.016	0.07
			P6	3.72E-05	0.024	0.044	0.18
			P7	1.24E-04	0.045	0.082	0.35
			P8	1.47E-04	0.049	0.090	0.38
Test_B2_10_3h_20100212	0.153		P5	5.07E-06	0.009	0.016	0.06
			P6	2.30E-05	0.019	0.035	0.12
			P7	8.75E-05	0.037	0.068	0.24
			P8	9.19E-05	0.038	0.070	0.25

Table 5.XVIII: Model C1: significant and maximum pressures derived from spectral moments.

Test ID	Incident		Sensor ID	m_o	P_s [m of water]	P_{max} [m of water]	$\frac{P_s}{H_s}$
	H_s [m]	T_p [s]					
Test_C1_7_20100427	0.193	2.28	P5	1.77E-05	0.017	0.031	0.09
			P6	5.05E-05	0.028	0.051	0.15
			P7	9.89E-05	0.040	0.073	0.21
			P8	1.15E-04	0.043	0.079	0.22
Test_C1_8_20100428	0.202	2.84	P5	2.23E-05	0.019	0.035	0.10
			P6	5.69E-05	0.030	0.055	0.16
			P7	1.53E-04	0.049	0.090	0.25
			P8	2.72E-04	0.066	0.121	0.34
Test_C1_9_20100426	0.193	3.41	P5	4.31E-05	0.026	0.048	0.13
			P6	5.10E-05	0.029	0.053	0.15
			P7	1.75E-04	0.053	0.097	0.27
			P8	3.11E-04	0.071	0.130	0.37
Test_C1_10_20100420	0.150	2.84	P5	1.58E-05	0.016	0.029	0.11
			P6	3.13E-05	0.022	0.040	0.15
			P7	1.16E-04	0.043	0.079	0.29
			P8	1.46E-04	0.048	0.088	0.32
Test_C1_1_20100419	0.036	1.63	P5	1.13E-05	0.013	0.024	0.36
			P6	1.70E-06	0.005	0.009	0.14
			P7	2.32E-06	0.006	0.011	0.17
			P8	2.67E-06	0.007	0.013	0.19
Test_C1_2_20100419	0.047	2.28	P5	1.19E-06	0.004	0.007	0.09
			P6	1.67E-06	0.005	0.009	0.11
			P7	9.60E-06	0.012	0.022	0.26
			P8	7.64E-06	0.011	0.020	0.23
Test_C1_4_20100419	0.071	1.63	P5	1.16E-06	0.004	0.007	0.06
			P6	5.11E-06	0.009	0.016	0.13
			P7	9.65E-06	0.012	0.022	0.17
			P8	1.01E-05	0.013	0.024	0.18
Test_C1_5_20100419	0.092	2.28	P5	2.20E-06	0.006	0.011	0.07
			P6	7.99E-06	0.011	0.020	0.12
			P7	3.79E-05	0.025	0.046	0.27
			P8	2.68E-05	0.021	0.038	0.23
Test_C1_10_1h_20100420	0.148	2.84	P5	1.38E-05	0.015	0.027	0.10
			P6	3.21E-05	0.023	0.042	0.16
			P7	1.21E-04	0.044	0.081	0.30
			P8	1.44E-04	0.048	0.088	0.32
Test_C1_10_8h_20100421	0.155		P5	3.22E-06	0.007	0.013	0.05
			P6	4.02E-05	0.025	0.046	0.16
			P7	1.67E-04	0.052	0.095	0.34
			P8	1.76E-04	0.053	0.097	0.34
Test_C1_8_3a_20100428	0.050	2.84	P5	1.70E-06	0.005	0.009	0.10
			P6	6.95E-06	0.011	0.020	0.22
			P7	1.70E-05	0.016	0.029	0.32
			P8	1.28E-05	0.014	0.026	0.28
Test_C1_8_3b_20100428	0.051		P5	3.17E-06	0.007	0.013	0.14
			P6	5.51E-06	0.009	0.016	0.18
			P7	1.62E-05	0.016	0.029	0.31
			P8	1.25E-05	0.014	0.026	0.27
Test_C1_8_2x_20100428	0.196		P5	2.46E-05	0.020	0.037	0.10
			P6	5.19E-05	0.029	0.053	0.15
			P7	1.34E-04	0.046	0.084	0.23
			P8	2.34E-04	0.061	0.112	0.31

Table 5.XIX: Model C2: significant and maximum pressures derived from spectral moments.

Test ID	Incident		Sensor ID	m_o	P_s [m of water]	P_{max} [m of water]	$\frac{P_s}{H_s}$
	H_s [m]	T_p [s]					
Test_C2_7_20100503	0.193	2.28	P5	2.06E-05	0.018	0.033	0.09
			P6	5.53E-05	0.030	0.055	0.16
			P7	1.02E-04	0.040	0.073	0.21
			P8	9.49E-05	0.039	0.071	0.20
Test_C2_8_20100504	0.195	2.84	P5	2.52E-05	0.020	0.037	0.10
			P6	6.19E-05	0.031	0.057	0.16
			P7	1.57E-04	0.050	0.092	0.26
			P8	2.23E-04	0.060	0.110	0.31
Test_C2_10_20100429	0.147	2.84	P5	1.55E-05	0.016	0.029	0.11
			P6	2.68E-05	0.021	0.038	0.14
			P7	1.16E-04	0.043	0.079	0.29
			P8	1.53E-04	0.049	0.090	0.33
Test_C2_1_20100502	0.033	1.63	P5	5.10E-07	0.003	0.005	0.09
			P6	2.41E-06	0.006	0.011	0.18
			P7	2.49E-06	0.006	0.011	0.18
			P8	3.05E-06	0.007	0.013	0.21
Test_C2_2_20100502	0.046	2.28	P5	3.36E-06	0.007	0.013	0.15
			P6	3.94E-06	0.008	0.015	0.17
			P7	1.08E-05	0.013	0.024	0.28
			P8	8.77E-06	0.012	0.022	0.26
Test_C2_4_20100503	0.069	1.63	P5	1.20E-06	0.004	0.007	0.06
			P6	6.71E-06	0.010	0.018	0.14
			P7	1.11E-05	0.013	0.024	0.19
			P8	1.19E-05	0.014	0.026	0.20
Test_C2_5_20100503	0.056	2.28	P5	5.90E-06	0.010	0.018	0.18
			P6	1.04E-05	0.013	0.024	0.23
			P7	4.67E-05	0.027	0.049	0.48
			P8	3.13E-05	0.022	0.040	0.39
Test_C2_6_20100504	0.097	2.84	P5	1.12E-05	0.013	0.024	0.13
			P6	1.98E-05	0.018	0.033	0.19
			P7	5.38E-05	0.029	0.053	0.30
			P8	7.66E-05	0.035	0.064	0.36
Test_C2_10_6h_20100430	0.148	2.84	P5	1.19E-05	0.014	0.026	0.09
			P6	3.41E-05	0.023	0.042	0.16
			P7	1.59E-04	0.050	0.092	0.34
			P8	1.74E-04	0.053	0.097	0.36
Test_C2_10_8h_20100430	0.151		P5	1.10E-05	0.013	0.024	0.09
			P6	3.71E-05	0.024	0.044	0.16
			P7	1.67E-04	0.052	0.095	0.34
			P8	1.76E-04	0.053	0.097	0.35
Test_C2_8_3a_20100504	0.049	2.84	P5	1.76E-06	0.005	0.009	0.10
			P6	7.05E-06	0.011	0.020	0.22
			P7	1.42E-05	0.015	0.027	0.31
			P8	8.24E-06	0.011	0.020	0.22
Test_C2_8_3b_20100504	0.050		P5	2.14E-06	0.006	0.011	0.12
			P6	7.11E-06	0.011	0.020	0.22
			P7	1.53E-05	0.016	0.029	0.32
			P8	9.05E-06	0.012	0.022	0.24
Test_C2_8_2x_20100504	0.193		P5	2.73E-05	0.021	0.038	0.11
			P6	6.31E-05	0.032	0.059	0.17
			P7	1.64E-04	0.051	0.093	0.26
			P8	2.16E-04	0.059	0.108	0.31

Table 5.XX: Model D1: significant and maximum pressures derived from spectral moments.

Test ID	Incident		Sensor ID	m_o	P_s [m of water]	P_{max} [m of water]	$\frac{P_s}{H_s}$
	H_s [m]	T_p [s]					
Test_D1_8_20100510	0.204	2.84	P5	4.53E-05	0.027	0.049	0.13
			P6	6.07E-05	0.031	0.057	0.15
			P7	1.38E-04	0.047	0.086	0.23
			P8	2.52E-04	0.064	0.117	0.31
Test_D1_10_20100511	0.154		P5	2.68E-05	0.021	0.038	0.14
			P6	3.00E-05	0.022	0.040	0.14
			P7	1.07E-04	0.041	0.075	0.27
			P8	1.51E-04	0.049	0.090	0.32
Test_D1_1_20100512	0.036	1.63	P5	3.50E-06	0.007	0.013	0.19
			P6	2.07E-06	0.006	0.011	0.17
			P7	2.31E-06	0.006	0.011	0.17
			P8	3.09E-06	0.007	0.013	0.19
Test_D1_2_20100512	0.048	2.28	P5	1.40E-05	0.015	0.027	0.31
			P6	1.93E-06	0.006	0.011	0.13
			P7	1.15E-05	0.014	0.026	0.29
			P8	1.10E-05	0.013	0.024	0.27
Test_D1_4_20100512	0.073	1.63	P5	1.71E-06	0.005	0.009	0.07
			P6	6.08E-06	0.010	0.018	0.14
			P7	1.06E-05	0.013	0.024	0.18
			P8	1.34E-05	0.015	0.027	0.21
Test_D1_5_20100512	0.094	2.28	P5	1.06E-05	0.013	0.024	0.14
			P6	1.01E-05	0.013	0.024	0.14
			P7	4.10E-05	0.026	0.048	0.28
			P8	3.03E-05	0.022	0.040	0.23
Test_D1_6_20100512	0.10	2.84	P5	2.81E-05	0.021	0.038	0.21
			P6	1.43E-05	0.015	0.027	0.15
			P7	6.25E-05	0.032	0.059	0.32
			P8	9.06E-05	0.038	0.070	0.38
Test_D1_10_1h_20100511	0.152	2.84	P5	2.54E-05	0.020	0.037	0.13
			P6	2.96E-05	0.022	0.040	0.14
			P7	1.09E-04	0.042	0.077	0.28
			P8	1.47E-04	0.049	0.090	0.32
Test_D1_10_3h_20100511	0.156		P5	2.03E-05	0.018	0.033	0.12
			P6	3.20E-05	0.023	0.042	0.15
			P7	1.34E-04	0.046	0.084	0.29
			P8	1.58E-04	0.050	0.092	0.32
Test_D1_10_6h_20100511	0.155		P5	9.47E-06	0.012	0.022	0.08
			P6	4.13E-05	0.026	0.048	0.17
			P7	1.61E-04	0.051	0.093	0.33
			P8	1.75E-04	0.053	0.097	0.34
Test_D1_8_3a_20100510	0.051	2.84	P5	9.21E-06	0.012	0.022	0.24
			P6	3.74E-06	0.008	0.015	0.16
			P7	1.11E-05	0.013	0.024	0.25
			P8	9.81E-06	0.013	0.024	0.25
Test_D1_8_3b_20100510	0.052		P5	2.99E-06	0.007	0.013	0.13
			P6	4.15E-06	0.008	0.015	0.15
			P7	1.14E-05	0.014	0.026	0.27
			P8	9.87E-06	0.013	0.024	0.25
Test_D1_8_2x_20100510	0.196		P5	2.82E-05	0.021	0.038	0.11
			P6	1.74E-05	0.017	0.031	0.09
			P7	5.15E-05	0.029	0.053	0.15
			P8	9.14E-05	0.038	0.070	0.19

Table 5.XXI: Model D2: significant and maximum pressures derived from spectral moments.

Test ID	Incident		Sensor ID	m_o	P_s [m of water]	P_{max} [m of water]	$\frac{P_s}{H_s}$
	H_s [m]	T_p [s]					
Test_D2_7_20100518	0.194	2.28	P5	4.58E-05	0.027	0.049	0.14
			P6	7.37E-05	0.034	0.062	0.18
			P7	9.93E-05	0.040	0.073	0.21
			P8	1.11E-04	0.042	0.077	0.22
Test_D2_8_20100517	0.201	2.84	P5	5.99E-05	0.031	0.057	0.15
			P6	8.03E-05	0.036	0.066	0.18
			P7	1.52E-04	0.049	0.090	0.24
			P8	2.66E-04	0.065	0.119	0.32
Test_D2_9_20100518	0.198	3.41	P5	5.02E-05	0.028	0.051	0.14
			P6	8.03E-05	0.036	0.066	0.18
			P7	1.42E-04	0.048	0.088	0.24
			P8	2.66E-04	0.065	0.119	0.33
Test_D2_10_20100515	*0.174*	*2.84*	P5	1.92E-05	0.018	0.033	0.10
			P6	3.65E-05	0.024	0.044	0.14
			P7	1.16E-04	0.043	0.079	0.25
			P8	1.34E-04	0.046	0.084	0.26
Test_D2_1_20100518	0.036	1.63	P5	1.35E-06	0.005	0.009	0.14
			P6	2.66E-06	0.007	0.013	0.19
			P7	2.21E-06	0.006	0.011	0.17
			P8	2.97E-06	0.007	0.013	0.19
Test_D2_2_20100518	0.048	2.28	P5	4.31E-06	0.008	0.015	0.17
			P6	1.33E-06	0.005	0.009	0.10
			P7	4.75E-06	0.009	0.016	0.19
			P8	4.74E-06	0.009	0.016	0.19
Test_D2_4_20100518	0.071	1.63	P5	4.67E-06	0.009	0.016	0.13
			P6	2.22E-06	0.006	0.011	0.08
			P7	2.70E-06	0.007	0.013	0.10
			P8	3.40E-06	0.007	0.013	0.10
Test_D2_5_20100518	0.093	2.28	P5	7.45E-06	0.011	0.020	0.12
			P6	1.13E-05	0.013	0.024	0.14
			P7	4.20E-05	0.026	0.048	0.28
			P8	3.24E-05	0.023	0.042	0.25
Test_D2_6_20100518	0.100	2.84	P5	1.63E-05	0.016	0.029	0.16
			P6	2.71E-05	0.021	0.038	0.21
			P7	5.97E-05	0.031	0.057	0.31
			P8	9.88E-05	0.040	0.073	0.40
Test_D2_10_1h_20100515	*0.187*	2.84	P5	1.76E-05	0.017	0.031	0.09
			P6	3.74E-05	0.024	0.044	0.13
			P7	1.19E-04	0.044	0.081	0.24
			P8	1.32E-04	0.046	0.084	0.25
Test_D2_10_6h_20100516	0.160		P5	2.09E-05	0.018	0.033	0.11
			P6	4.79E-05	0.028	0.051	0.18
			P7	1.57E-04	0.050	0.092	0.31
			P8	1.62E-04	0.051	0.093	0.32
Test_D2_8_3a_20100517	0.052	2.84	P5	4.50E-06	0.008	0.015	0.15
			P6	9.68E-06	0.012	0.022	0.23
			P7	1.38E-05	0.015	0.027	0.29
			P8	9.48E-06	0.012	0.022	0.23
Test_D2_8_2x_20100517	0.198		P5	5.01E-05	0.028	0.051	0.14
			P6	8.24E-05	0.036	0.066	0.18
			P7	1.61E-04	0.051	0.093	0.26
			P8	2.53E-04	0.064	0.117	0.32

5.4.2. Wave-induced pressures over the dune

As has already been described earlier in Chapter 4 the miniature pore-pressure sensors and DAQ-system choice was based on frequency response, so that it ensured the instrument could respond at the required sampling rate. The frequency response is of particular importance in the likeliness of impulsive wave loading (*i.e.*, an abnormally high breaking wave pressure) as its duration will be very short. Such impulsive pressure is exerted when an incident wave begins to break in front of a structure and collides with it having an almost vertical wave front. According to Goda (2000), in a vertical wall it may rise up to more than ten times the hydrostatic pressure corresponding to the wave-height.

In Figure 5.84 pressure-time curves recorded at the surface slope in Model B2 (top panel) and Model C2 (bottom panel) about P3 and P4 levels (refer to Figure 5.66) are shown to illustrate impulse pressure patterns due to impinging waves. The main feature of an impulse is that it is split into two peaks, a very intense one of short duration followed by a second of much less intensity but longer duration. Upon analysis of the pressure-time curves, it is found (for those particular cases and within the time span presented here) that the maximum value of impulse pressure along the slope occurs around P4 (*i.e.*, at the lowest level); it is also found that the wave-induced impulse pressure has reached up to about two times the input significant wave-height.

A comparison of recorded pressure-time curves, at face and to the interior, about P3 and P4 (see Figure 5.66) in Model B1 is given in Figure 5.85. The measurement results for this particular case suggest that there is some significant damping from surface to the interior; it also shows that the wave-induced pressure have reached up to about one and a half times the input significant wave-height within the time span presented here. It should be noted that the pressure time-curves presented in Figure 5.85 will be the only result on wave-induced pressure for Model B1 due to the fact that the data sets for this model are too short (very few minutes only).

The analysis of wave-induced pressures over the reinforced dune aims at providing qualitative information on *(i)* impulsive wave loading along the slope face; and *(ii)* wave penetration from the slope surface to the interior, and includes all measurements but the ones made with accretionary wave run-segments and with models A (no measurements over the slope were made with this model) and B1. Such information can be important to assess which structural elements will have a higher frequency of response than that of the whole structure. It can also be important to compare the pressure profiles between the various models, most particularly to gain more information concerning the damping effect produced by each model.

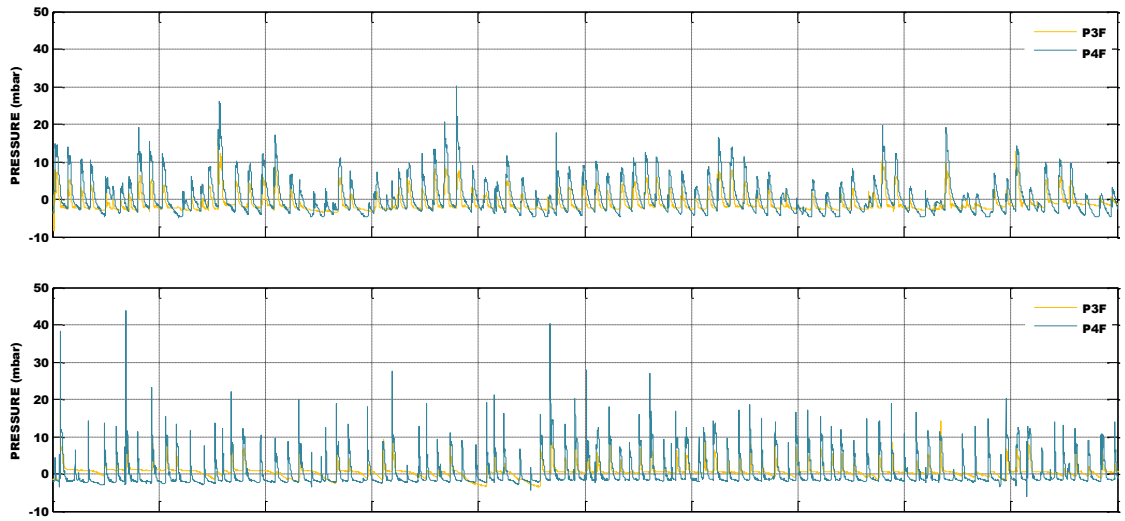

Figure 5.84: Pressure-time curves recorded at the surface slope in Model B2 (top panel) and Model C2 (bottom panel), erosional conditions with sea-state 9 (H_s=0.17m, f_p=0.289Hz).

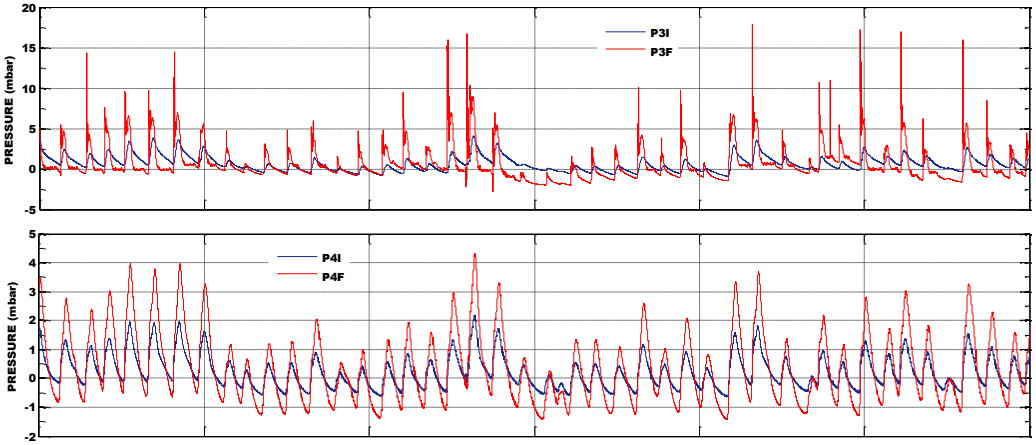

Figure 5.85: Model B1, sea-state 10 (H_s=0.125m, f_p=0.346Hz): pressure-time curves recorded at levels 3 and 4 (respectively, P3F and P3I and P4F and P4I in Figure 5.66).

The magnitude and levels at which the maximum positive and negative pressures occur for each wave condition are presumably linked to the distance to still-water-level and the elevation of the wave when striking the structure. To a certain extent magnitude and levels are expected to be also linked to the internal run-up, which depends on the structure permeability (refer to Figure 3.3).

With respect to pressure distribution it is likely that above the region of maximum impulse, magnitude pressure will decrease to zero (for non-overtopped structures); whereas below that region it should decrease by an order of magnitude and then remain constant to the bottom. Nonetheless, a minor secondary positive pressure may occur about the level of maximum run-up, caused by the motion of the wave during uprush and by the static head of water on the slope. At the time of maximum run-up the velocity field changes because the water reaches zero velocity and there is a high pressure gradient seaward-directed (induced by the maximum static head over the slope). While descending, the flow is nearly parallel to the structure; whilst at the limit of downrush the velocity field changes again when plunging into the next wave. Typically at this point very strong forces perpendicular to the slope are generated.

Pressure distribution is influenced as well by the in- and out-flows respectively caused by the build-up and fall off of the hydrostatic pressure inside the structure. The inflow occurs during the uprush phase, while the outflow may occur later during the uprush (depends on structure porosity and occurs only until another wave reaches the structure) and during the downrush. The maximum seaward directed pressure is generated by the wave downrush and the increase in the water table slope.

In regard to the experimental conditions in the present study it should be noted that the front face of the wave advancing up the beach towards the structure was already a broken one, thereby the relevant hydrodynamic wave actions occurring should be linked to run-up, R_u, and run-down, R_d caused by the wave up- and downrush on the structure slope. What is more the impulse is not anticipated to rise as high as it would if the structure had been placed at the surf zone rather than at the shoreline.

Examples of pressure distribution profiles over the slope face and to the interior in various experimenting conditions are illustrated in Figures 5.86 to 5.91. The given examples represent each model and variant in the study. All diagrams are grouped in sets of two [(a) and (b)] according to model variant, except for Model B. Each set contains a left and a right panel which correspond to envelope pressures (*i.e.*, maximum and minimum impulse pressure) measured at each point level, respectively at the surface slope (left panel) and at approximately half-model-width to the interior (right panel). The measured values of pressure have all been normalized to the incident significant wave-height. The points at which the measurements were taken are referenced to still-water-level (refer to Figure 5.66 and Table 5.XIV) in order to more easily compare the results between the various models.

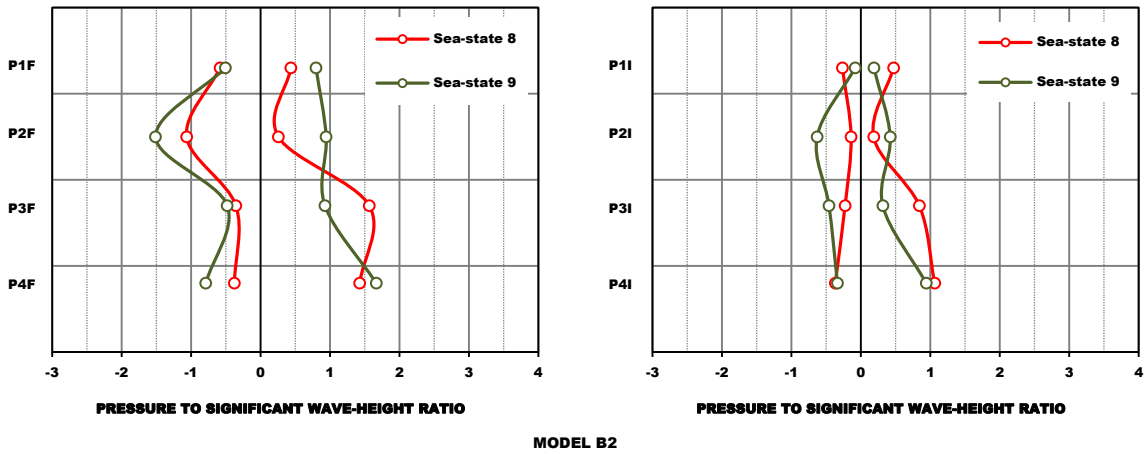

Figure 5.86: Model B: pressure envelope profiles over the beach slope (left panel) and to the interior (right panel), erosional conditions.

The recorded wave-induced pressures over the dune reinforced with geotextile containers, Model B, variant 2, when exposed to erosional sequences are shown in Figure 5.86. Sea-state 7 has not been plotted because only two out of the four levels were measured (levels 2 and 1 had missing values).

It is apparent from Figure 5.86 that, for this model variant, the maximum value of the measured pressure under erosional wave run-segments has reached up to about one and a half times the incident significant wave-height and that it has occurred around level 4 (*i.e.*, approximately at 0.08m, measured vertically from the initial shoreline position) for sea-states 8 and 9. The impulse pressure that occurs about level 3 (*i.e.*, z~0.17m) for sea-state 8 is believed to be caused by the slight variations in the shape of generated sea-state (refer to Table 5.V), which likely determines the higher incident significant wave-height in sea-state 8 (H_S=0.202m) as compared to sea-state 9 (H_S=0.185m). It is also seen from Figure 5.86 that the minimum value occurred around level 2 (*i.e.*, z~0.25m).

For this model variant the pressure measurements inside the structure evidence a somewhat similar pattern to those at the surface (*i.e.*, the higher positive or negative pressures measured at the surface correspond with the higher positive or negative pressures at the interior), having only a lower magnitude.

The results seem to indicate that under sea-states 8 and 9 the structural elements which have had the higher frequency of response were those standing more close to the bottom for both the up- and downrush phases of the wave, whereas the elements at the middle/top layers have had a higher frequency of response during the wave downrush.

The recorded pressures over the wrapped-around system, Model C, when exposed to erosional sequences are shown in Figure 5.87. It is seen that for this model the maximum value of the measured pressure under erosional wave run-segments has reached up to about one and a half times the incident significant wave-height in variant 1 and to about two times that height in variant 2.

The effect of the wave-period and of the wave-height in the maximum pressure is also apparent from Figure 5.87 (*i.e.*, a general increase of pressure with wave-period and with wave-height – refer to Table 5.III to learn the representative wave characteristics on each test condition).

The negative pressures have in this model a slightly lower magnitude when compared to Model B. A possible reason for that may be a decrease in the outflow associated to a decrease in the inflow, as evidenced by the very significant decrease in pressure magnitude from surface to the interior.

Likewise the results seem to indicate that under erosional sequences the structural elements which have had the higher frequency of response were those standing close to the bottom.

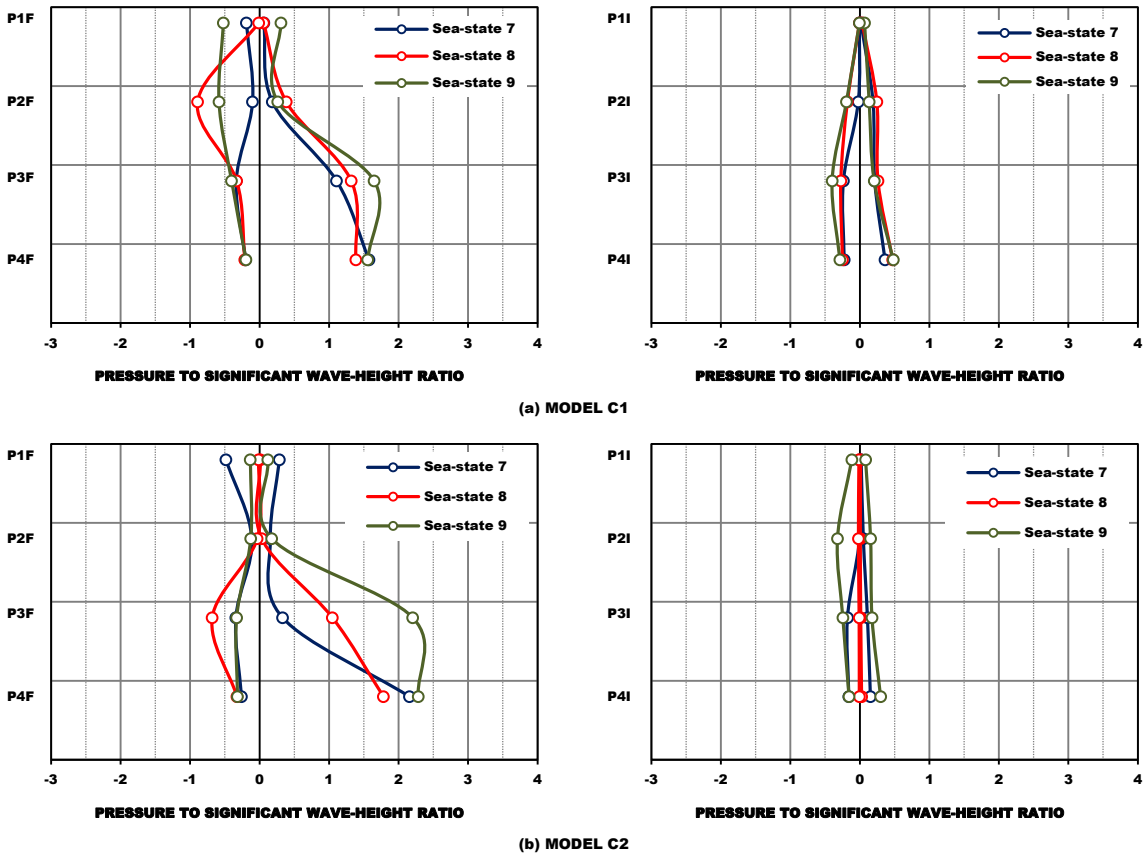

Figure 5.87: Model C: pressure envelope profiles over the beach slope (left panel) and to the interior (right panel), erosional conditions.

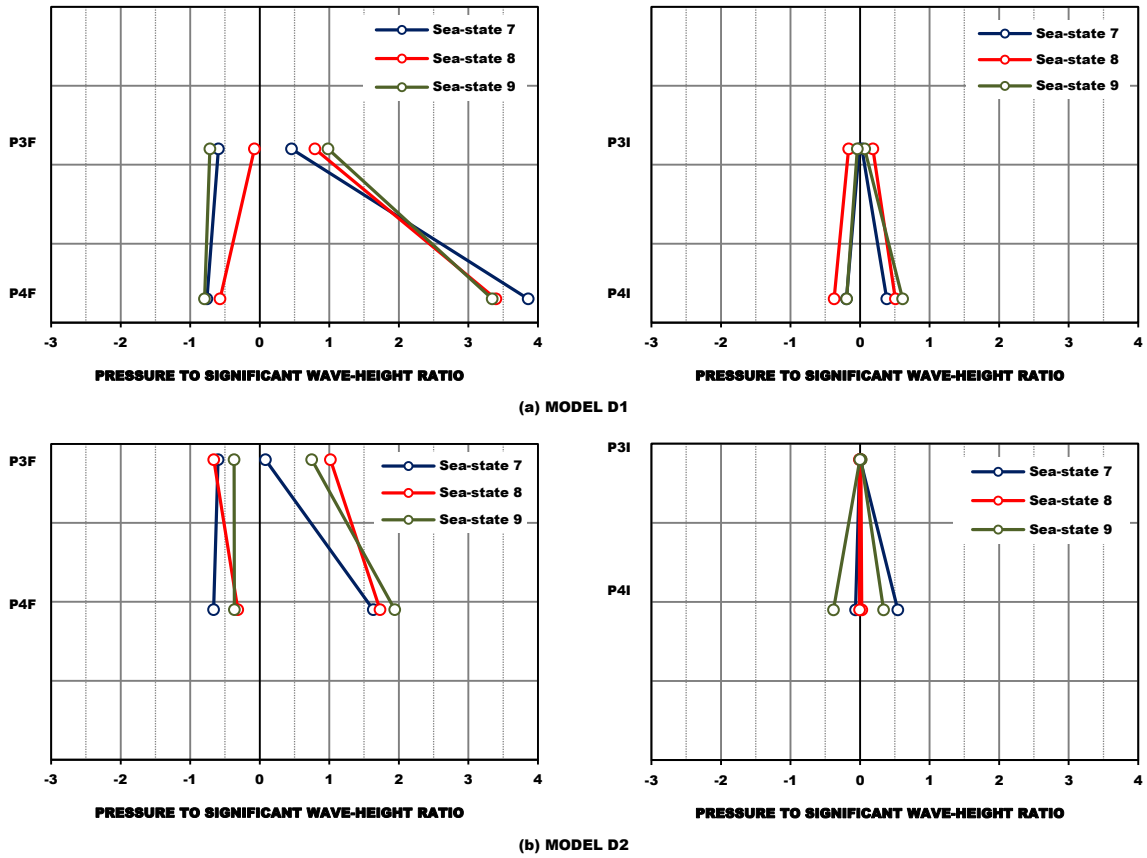

Figure 5.88: Model D: pressure envelope profiles over the beach slope (left panel) and to the interior (right panel), erosional conditions.

The envelopes of recorded pressure distributions for Model D are shown in Figure 5.88. Here the levels at which the pressure was taken are quite different, as the uppermost measurement in Model D1 is approximately the lowest position in Model D2; yet a general increasing trend to the bottom can be seen in Model D2 results, while in Model D1 a general decreasing trend to the top is noticeable. Thus is possible to conclude that the maximum pressure distribution recorded for Model D under erosional conditions follow a pattern similar to those measured for the equivalent tests with the other two models. Yet, as seen in Figure 5.88 the maximum values of the measured pressures under erosional wave run-segments are somewhat higher than those in models B and C reaching up to about four times the incident significant wave-height for variant 1 of this model; and thrice that height for variant 2 in assuming a linear distribution bellow level 4. Like in Model C, the results evidence a very significant decrease in pressure magnitude from surface to the interior.

The results also seem to indicate that, for the tests under erosional waves and for both the up- and downrush phases of the wave, the topmost structural elements have had a lower frequency of response than those standing close to the bottom; yet the maximum pressure measurements made at the uppermost level in variant 1 are about the same order of magnitude as the significant wave-height. The magnitudes of the negative pressures are relatively low and appear to have only slight variation from top to bottom.

From the data already presented it was seen that the highest wave-induced pressures over the slope were recorded at the lowest measurement positions. This is in agreement with the literature in which several references have successfully established a relation between the elevation of the point of maximum impulse pressure and the area between the crest of the wave and the still-water-level (see, *e.g.*, Recio, 2007 and Recio and Oumeraci, 2007c for discussion on wave induced pressure and forces on a structure made of geotextile sand containers; Goda, 2000 on breaking wave pressures on vertical breakwaters; and references cited therein).

Analysing the plots of the pressure envelope profiles over the beach slope is also possible to confirm that substantive damping in pressure occurs from surface to interior. It is also observable that the higher damping occurs in models C and D than in B, which indicates that the higher the void ratio of the structure, the higher is the wave penetration into the structure. Further clarification is required with respect to how the geometrical conditions of the structure (*e.g.*, the shape of the elements) influences the distribution of pressures over the slope. The trend of wave-induced pressure with wave-period and wave-height increase needs further clarification as well.

The pressure distribution for test series with persistent erosional conditions (sea-state 10) is shown in the following figures for Model B variant 2 in Figure 5.89, for Model C variants 1 and 2 in Figure 5.90, and for variants 1 and 2 of Model D in Figure 5.91.

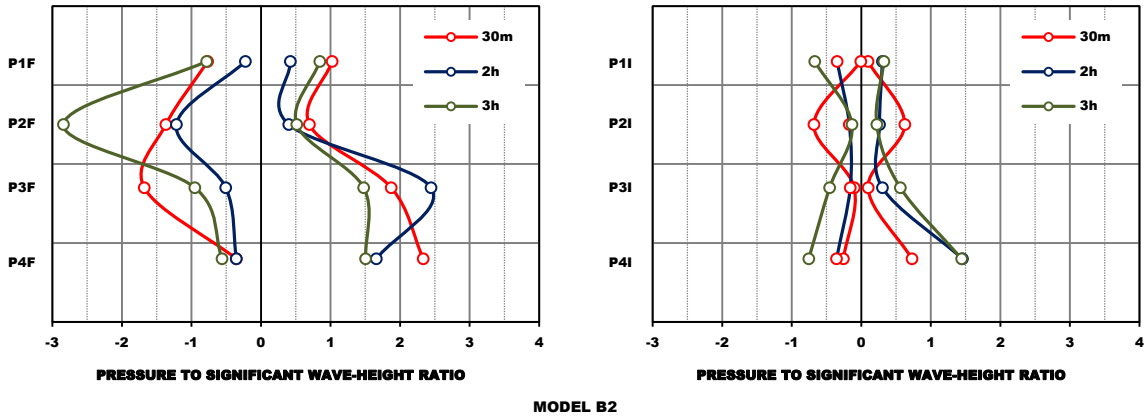

Figure 5.89: Model B: pressure envelope profiles over the beach slope (left panel) and to the interior (right panel), persistent erosional conditions.

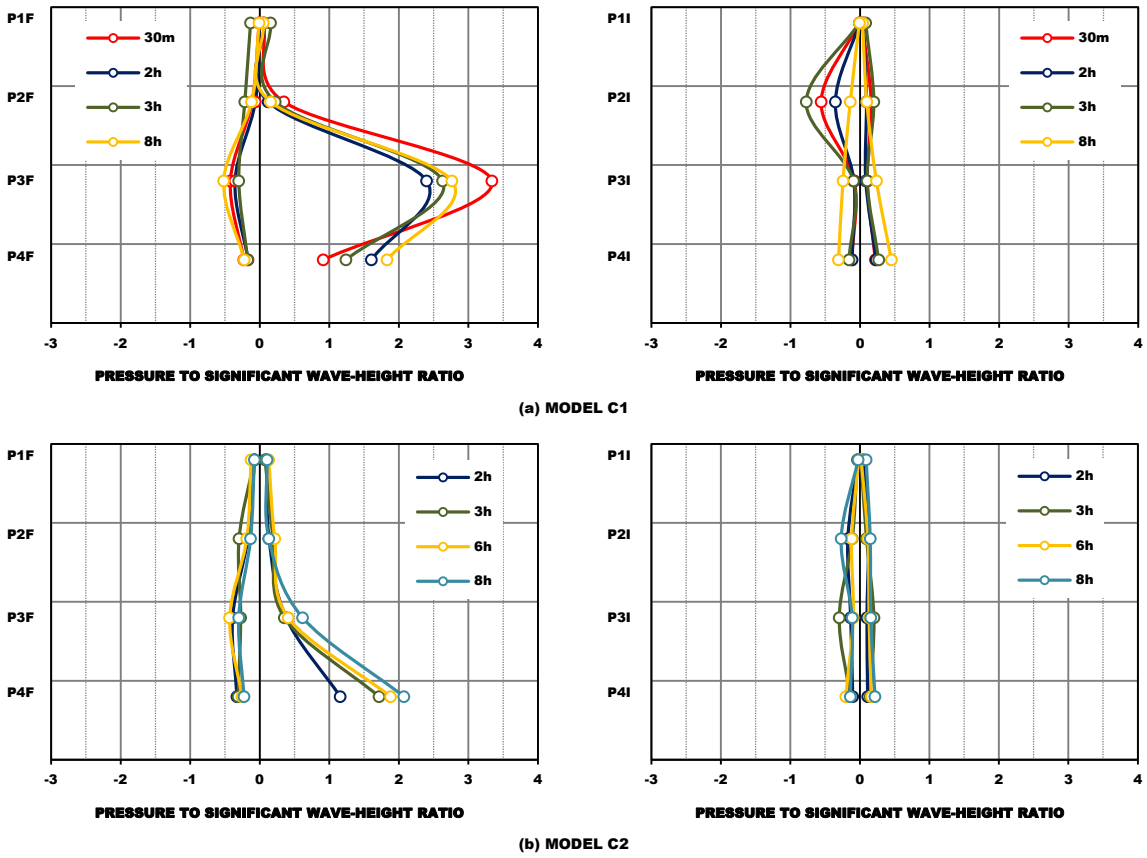

Figure 5.90: Model C: pressure envelope profiles over the beach slope (left panel) and to the interior (right panel), persistent erosional conditions.

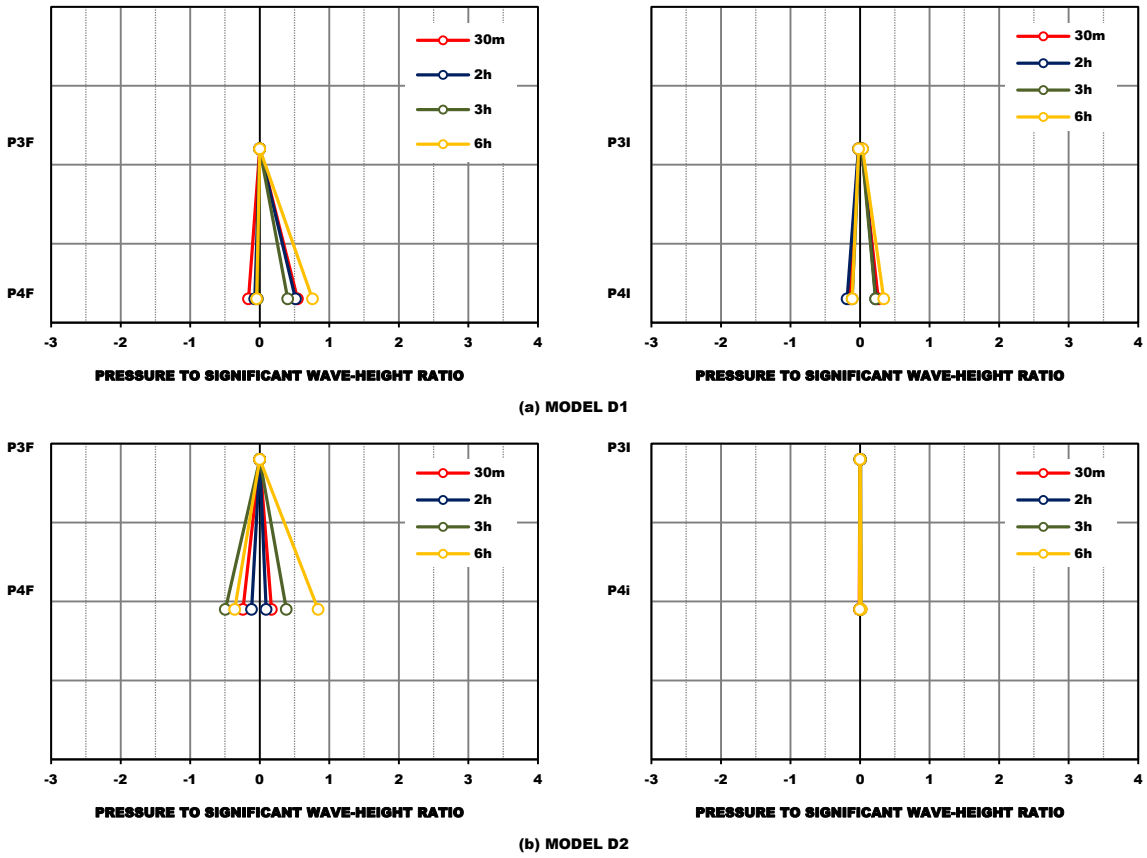

Figure 5.91: Model D: pressure envelope profiles over the beach slope (left panel) and to the interior (right panel), persistent erosional conditions.

Overall models B and C follow similar distribution patterns to those observed under erosional sequences (*i.e.*, the highest wave-induced pressures over the slope were recorded at the lowest measurement positions and substantial damping in pressure from surface to interior). The impulse to wave-height ratio at the surface of the slope is of the same order of magnitude than that recorded under erosional waves.

An interesting feature can be found though in the right panel of Figure 5.89 which is a pressure to significant wave-height ratio inside the structure, at 2 and 3h, equal to that observed at the surface slope. Presumably this was caused by considerable displacement of individual geotextile elements.

In regard to Model D it evidences some odd measurements, namely the extremely low ratio of pressure to incident significant wave-height at the surface around level 3 and the null ratio at level 4 in variant 1 and the null values measured at the interior. Such anomalous measurements were most likely caused by something blocking the sensor area or air build-up between the filter and the sensor membrane.

5.4.3. Wave-induced pressures over the submerged detached breakwater

In this paragraph, results of wave-induced pressures over the submerged nearshore detached breakwaters are presented. As sketched in Figure 5.66, the considered structures were submerged, with a freeboard at z~-0.165m, slope inclined at 45º, and placed at approximately -2.5, -1.9 and -1.1m from the initial shoreline position. Results of free surface elevation and pressure spectra at different locations over the structure and beach-profile are shown.

The following figures show the pressure time-series of free surface displacement from the laboratory measurements with Model E, for variants 2 (Figure 5.92), 3 (Figure 5.93) and 4 (Figure 5.94), corresponding to incident wave spectra with similar significant wave-height (H_s=0.17m) and wave period (T_p=3.46s). Segments of only 100s are plotted, for clarity. The measurements with Model E, variant 1, have not been included in the analysis because the test was interrupted when the structure became unstable after approximately 11mn wave action. Each figure includes five segments of free surface evolution from seaward (top panel) to shoreward (bottom panel) measured at about the structure toe in the seaside (only in Figure 5.92), at both the seaside and leeside crest limits, over the crest (only in Figures 5.93 and 5.94) and over the beach slope at approximately -1.7m of the shoreline.

The selected examples illustrate the displacement of free surface and the propagation over the nearshore submerged breakwaters. As can be observed, the seaside is dominated by steep, pitched-forward crests of near breaking waves, whereas at the leeside crest limit the wave-profile displays a similar but attenuated wave field (a rough estimate of 30 to 40% reduction in height for the maximum waves). Furthermore, is apparent in the third diagram in Figure 5.92 (*i.e.*, P3F) a very strong downrush flow on the exposed face of the structure extending to the toe. Visual observations during the tests with both the types of model, passive and active coastal defence structures, suggest that such a downrush flow produces the maximum loading to the toe responsible for causing scour on the sand seabed close to the structure. A typical sequence illustrating the propagation of breaking waves over the submerged structures during the downrush phase is shown in the snapshots presented in Figure 5.95, to illustrate the phenomenon and to support with evidence the importance of this load as affecting stability. The snapshots also illustrate the intensity of turbulence due to wave breaking over the structure. Apparently, turbulence intensity reaches maximum values during the wave downrush over a trough region and is then spread by the bore in the onshore direction over the crest of the structure. Figures 5.92 to 5.94 plot the surface elevation as measured by sensor P8, buried into the sand (see Figure 5.65), which location relative to surf zone changes with model variant so that it is seaward a second breaker line which develops at the leeside of the breakwater in E2, just at the leeside of E3 and within the surf zone in E4. The peculiar surface elevation measured by P4I (Figures 5.93 and 5.94) is likely due to the build-up of the hydrostatic (visible from the whole series).

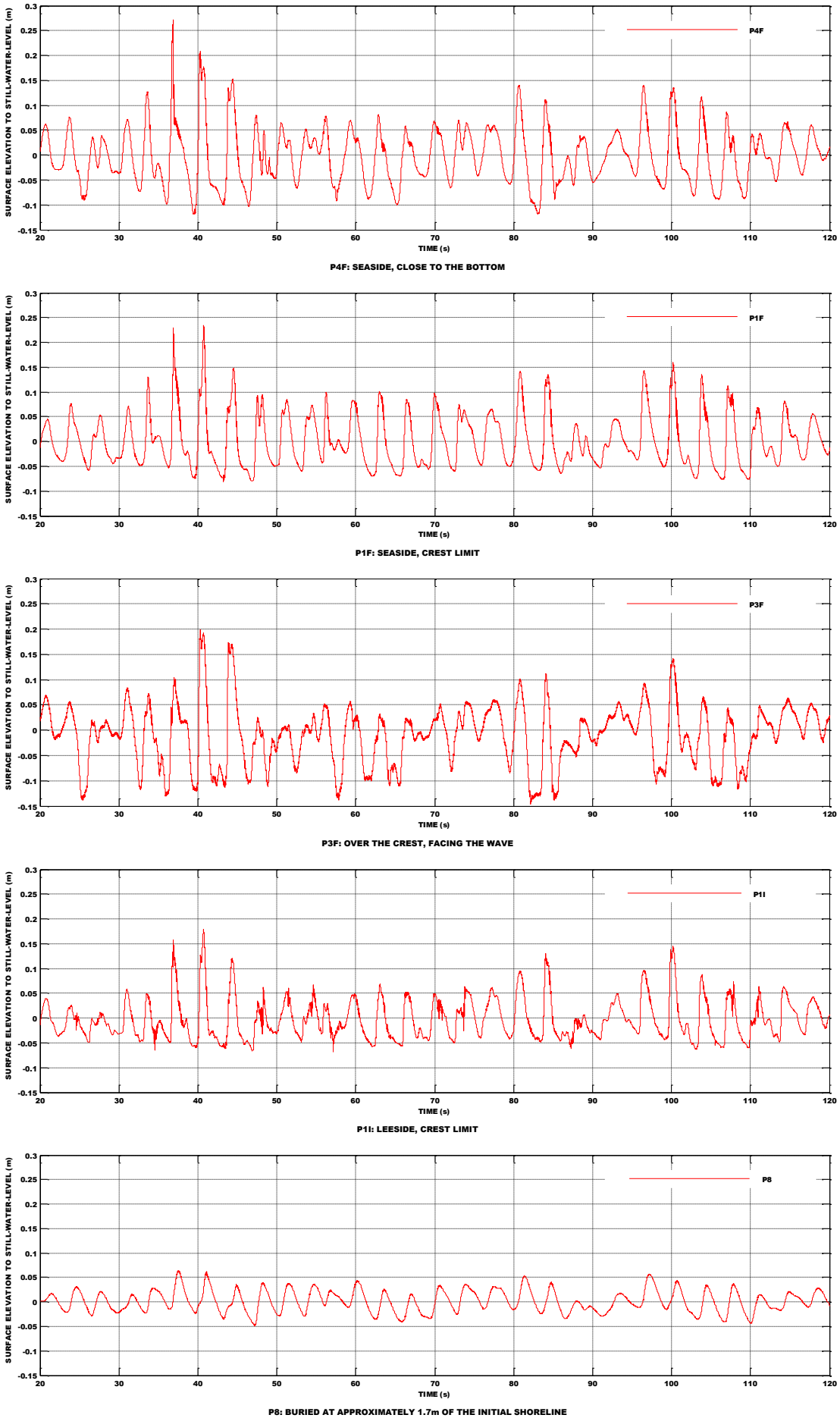

Figure 5.92: Model E2: segments of recorded pressure time-series, sea-state 9 (H_s=0.17m, f_p=0.289Hz).

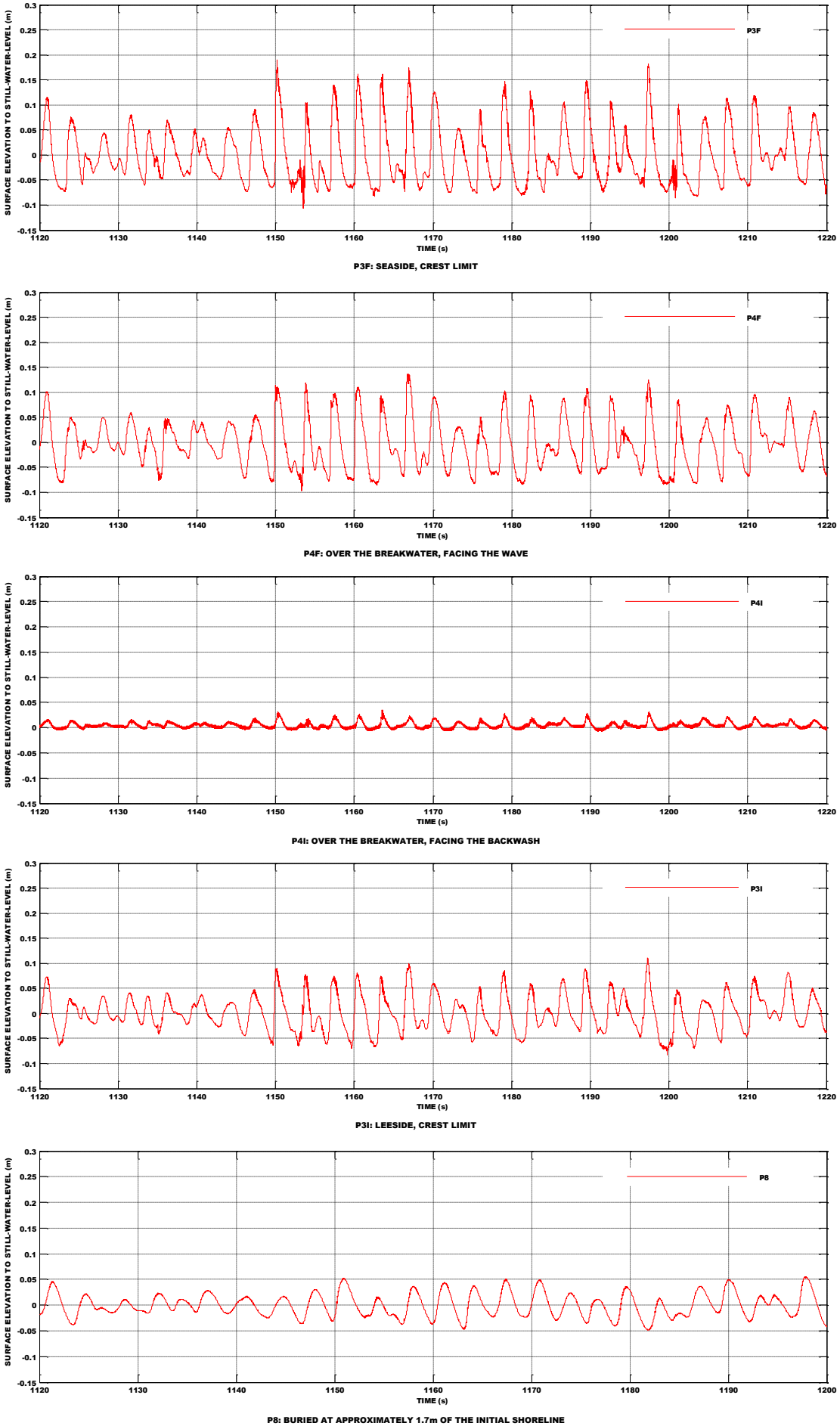

Figure 5.93: Model E3: segments of recorded pressure time-series, sea-state 9 (H_s=0.17m, f_p=0.289Hz).

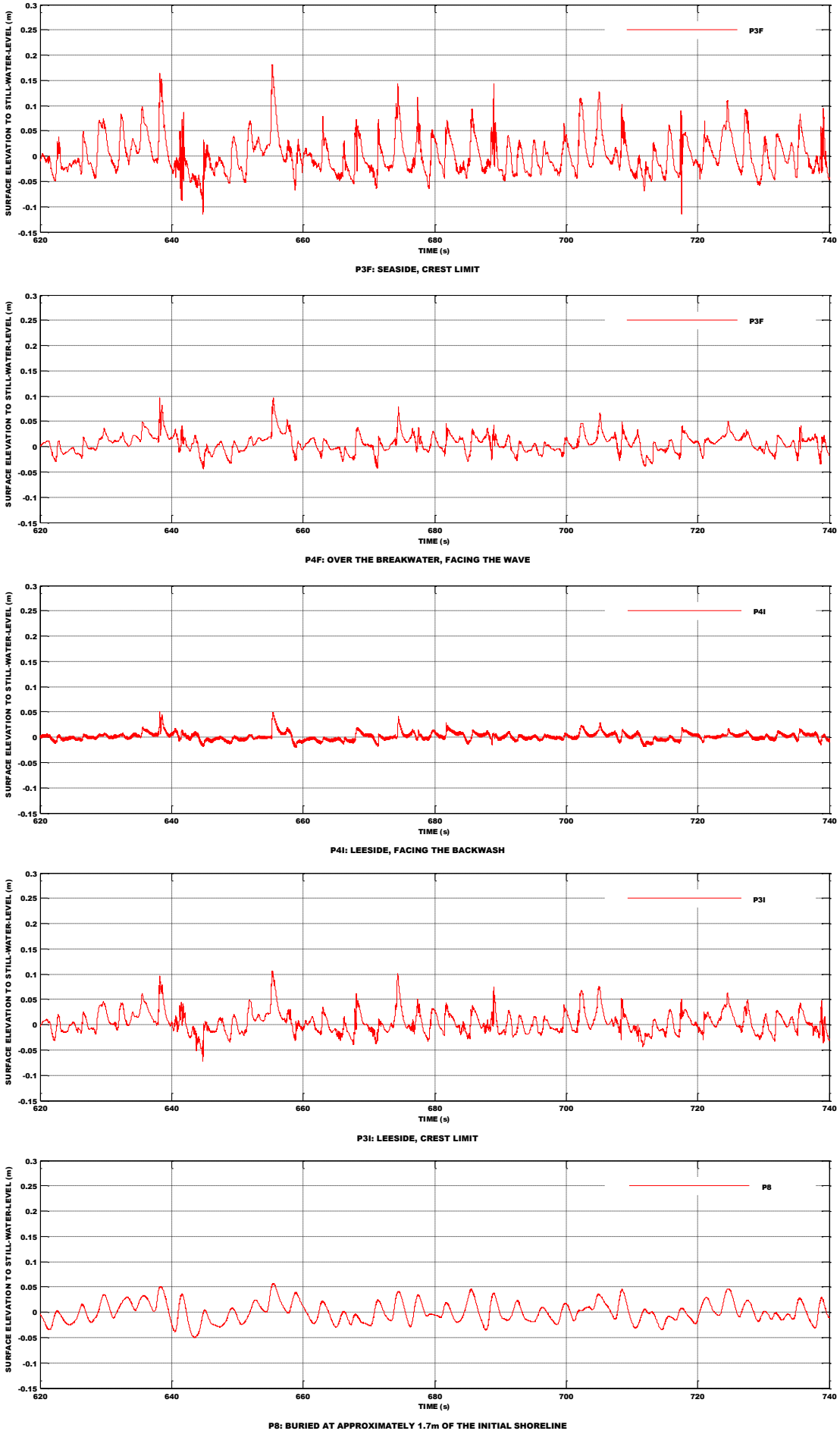

Figure 5.94: Model E4: segments of recorded pressure time-series, sea-state 9 (H_s=0.17m, f_p=0.289Hz).

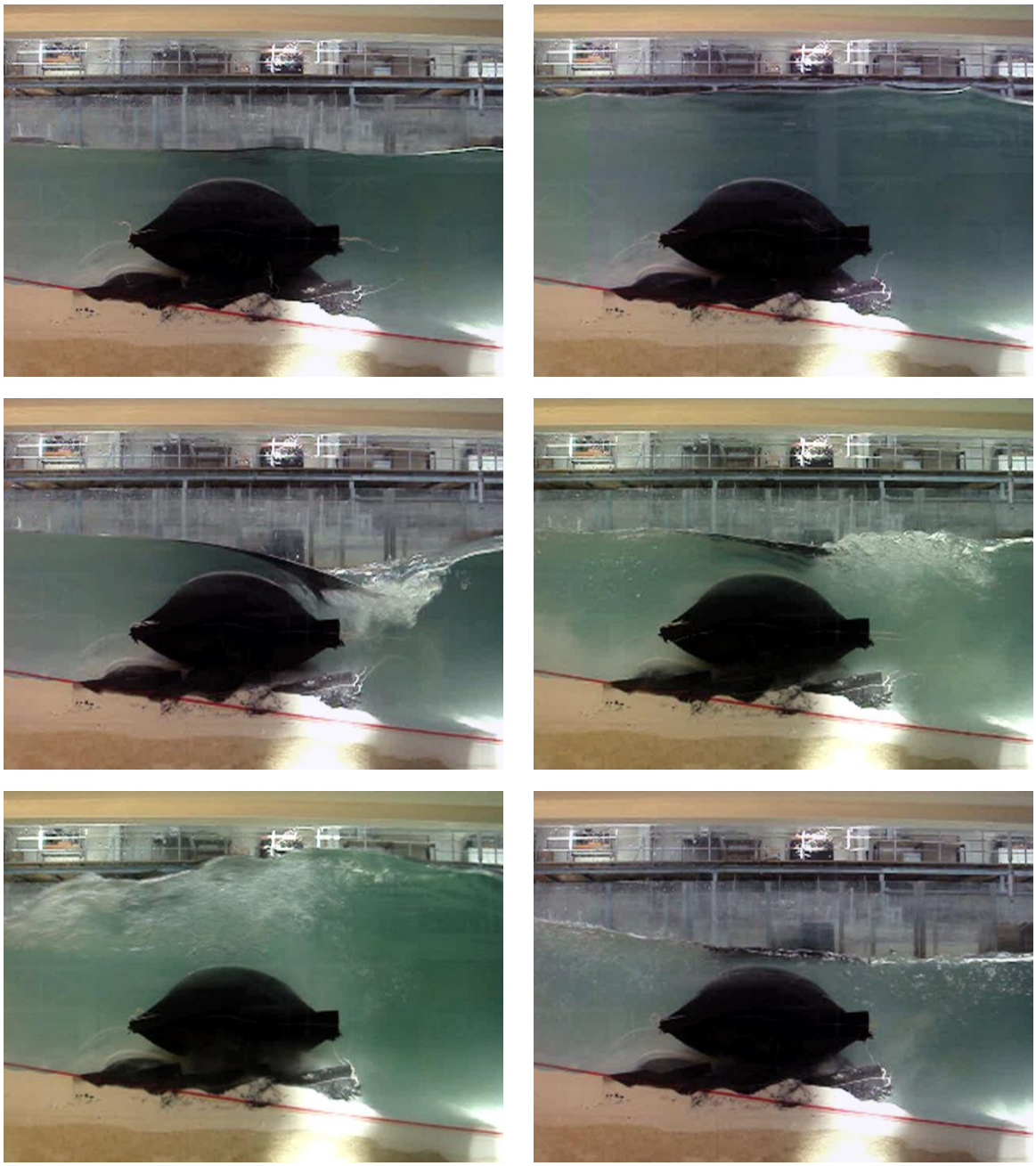

Figure 5.95: Model E2: wave downrush over the submerged structure, sea-state 8 (H_s=0.17m, f_p=0.346Hz).

Figure 5.96 presents the free surface displacement envelopes and still-water-level over the submerged structure when exposed to sea-states 9 and 10, corresponding to respectively wave-heights of 0.125 and 0.17m and wave-periods of 2.89 and 3.46s, computed from pressure measurements. Only two examples per model variant are given whereas for the remainder tests with erosional waves a summary is included in Table 5.XXII. Significant and maximum pressures derived from spectral moments at each measurement point level are also included in the same table. Snapshots taken during the tests are provided in Figures 5.97 and 5.98, as comparison reference for Figure 5.96. As can be observed, the processes of wave shoaling and breaking over the structure seem to be correctly captured by the pressure sensors, with the exception of the upper envelopes in models E3 and E4 sea-state 9 which appear to be underestimated. This may have been caused by turbulent entrainment of air. It is seen that waves shoal as they pass over the submerged structure. It can be noticed as well that the lowest levels below still-water take place just about the seaside crest section for Model E variant 2 and on both sides in variant 3. In regard to Model E4 the upper and lower envelopes were estimated from the measurements at the middle of the crest (sensor P4F) and were taken equal to that elevation at both crest limit sections.

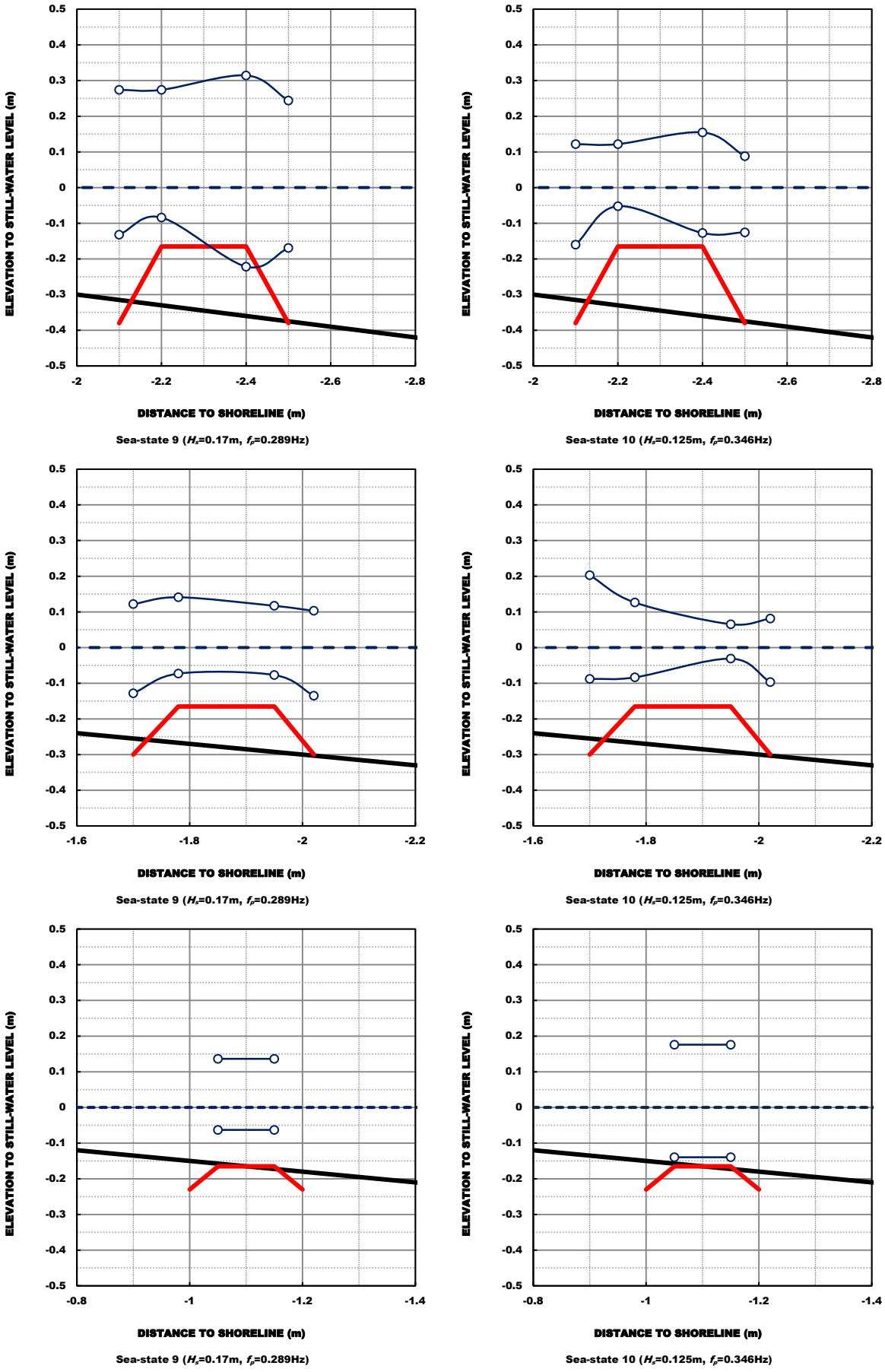

Figure 5.96: Computed envelopes of free surface displacement: Model E2 (top panel), Model E3 (middle panel), and Model E4 (bottom panel).

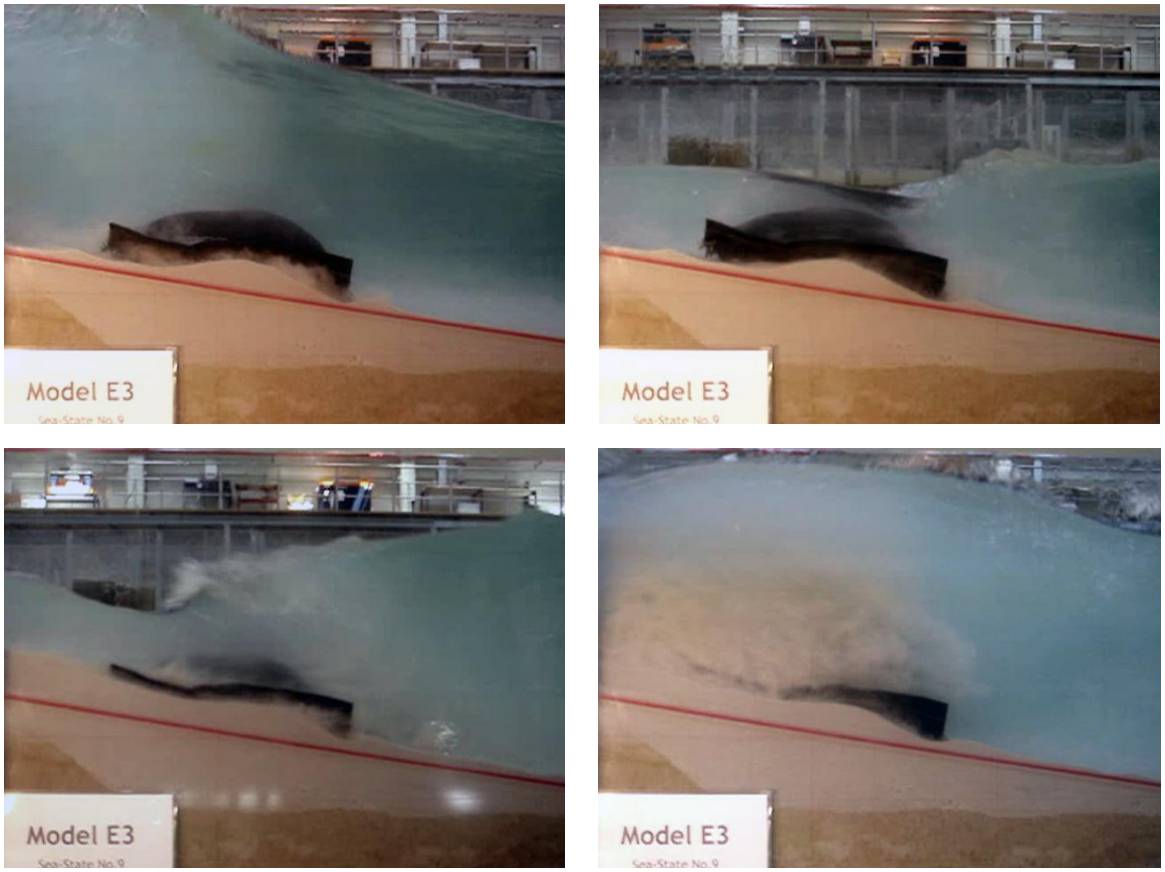

Figure 5.97: Model E3: wave shoaling and breaking over the submerged nearshore breakwater, sea-state 9 (H_s=0.17m, f_p=0.289Hz).

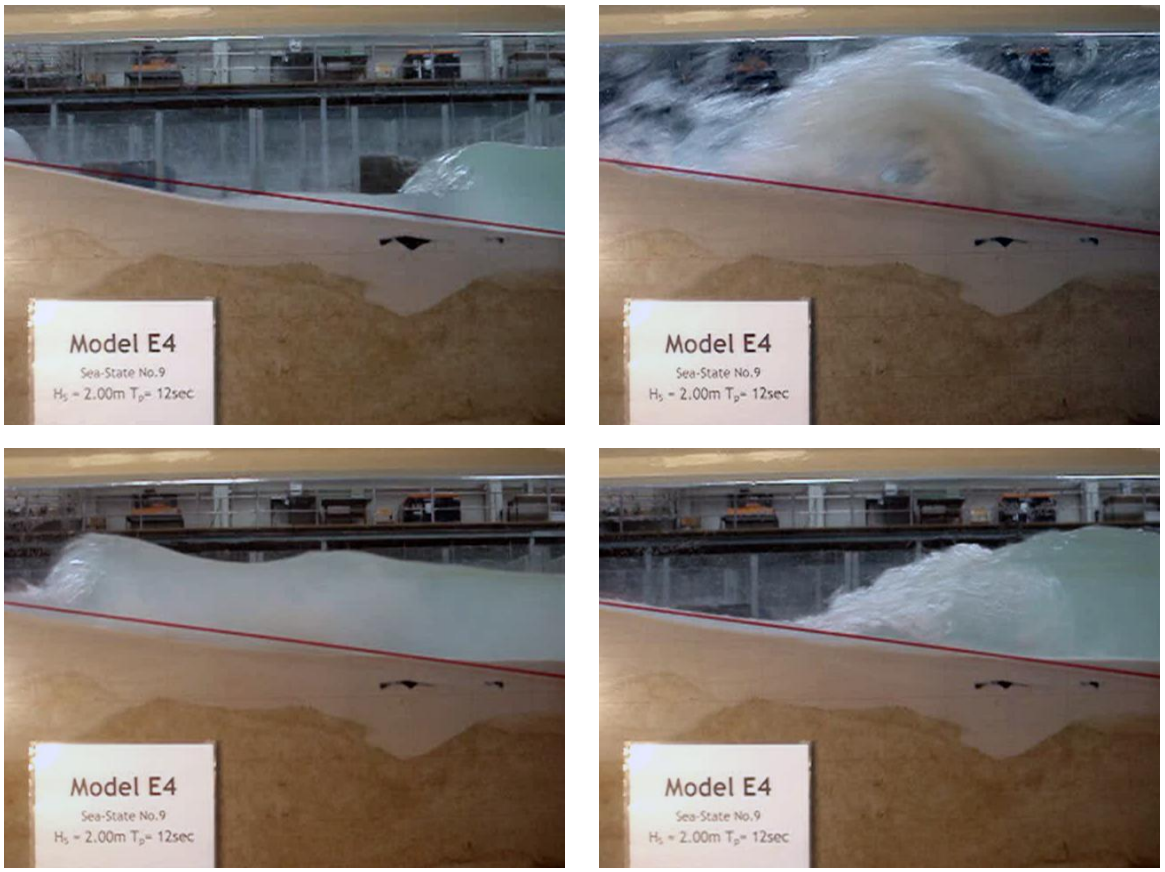

Figure 5.98: Model E4: wave shoaling and breaking over the submerged sill, sea-state 9 (H_s=0.17m, f_p=0.289Hz).

Table 5.XXII: Summary of significant and maximum pressures derived from spectral moments.

Test ID	H_s [m]	T_p [s]	Sensor ID	m_0	P_s [m of water]	P_{max} [m of water]	η_{max} [m]	η_{min} [m]
Test_E2_7_20100524	0.190	2.28	P1F	3.16E-04	0.071	0.130	0.113	-0.132
			P1I	6.98E-04	0.106	0.193	0.109	-0.080
			P2F	6.74E-04	0.104	0.190	0.111	-0.075
			P2I	1.82E-03	0.170	0.312	0.121	-0.257
			P3F	2.10E-03	0.183	0.335	0.150	-0.171
			P3I	6.83E-04	0.105	0.191	0.134	-0.059
			P4F	2.62E-03	0.205	0.375	0.114	-0.254
			P4I	1.33E-03	0.146	0.267	0.129	-0.134
Test_E2_8_20100522	0.198	2.84	P1F	6.31E-04	0.101	0.184	0.150	-0.055
			P1I	3.61E-04	0.076	0.139	0.108	-0.085
			P2F	4.86E-04	0.088	0.161	0.112	-0.059
			P2I	9.07E-04	0.120	0.220	0.099	-0.152
			P3F	1.39E-03	0.149	0.273	0.190	-0.155
			P3I	9.52E-04	0.123	0.226	0.183	-0.073
			P4F	2.30E-03	0.192	0.351	0.119	-0.207
			P4I	1.03E-03	0.129	0.235	0.247	-0.152
Test_E2_9_20100524	0.195	3.46	P1F	2.60E-03	0.204	0.374	0.239	-0.092
			P1I	1.63E-03	0.161	0.295	0.235	-0.124
			P2F	2.14E-03	0.185	0.338	0.254	-0.132
			P2I	2.09E-03	0.183	0.335	0.211	-0.222
			P3F	2.76E-03	0.210	0.385	0.244	-0.169
			P3I	2.29E-03	0.191	0.350	0.274	-0.084
			P4F	2.74E-03	0.209	0.383	0.207	-0.161
			P4I	2.44E-03	0.198	0.362	0.314	-0.142
Test_E2_10_20100521	0.153	2.84	P1F	6.57E-04	0.103	0.188	0.122	-0.052
			P1I	3.22E-04	0.072	0.131	0.092	-0.052
			P2F	4.76E-04	0.087	0.160	0.089	-0.045
			P2I	6.03E-04	0.098	0.180	0.072	-0.160
			P3F	1.19E-03	0.138	0.252	0.148	-0.127
			P3I	1.03E-03	0.129	0.235	0.143	-0.067
			P4F	1.20E-03	0.139	0.254	0.088	-0.125
			P4I	7.76E-04	0.111	0.204	0.155	-0.091
Test_E3_9_20100526	0.202	3.46	P3F	3.13E-03	0.224	0.410	0.103	-0.135
			P3I	1.36E-03	0.148	0.270	0.122	-0.128
			P4F	2.44E-03	0.198	0.361	0.117	-0.077
			P4I	1.97E-03	0.178	0.325	0.141	-0.073
Test_E3_10_20100526	0.150	2.84	P3F	5.59E-04	0.170	0.310	0.203	-0.088
			P3I	1.80E-03	0.095	0.173	0.081	-0.097
			P4F	1.22E-04	0.132	0.242	0.126	-0.084
			P4I	1.10E-03	0.044	0.081	0.065	-0.031
Test_E4_8_20100525	0.197	2.84	P3F	9.62E-05	0.039	0.072	0.076	-0.033
			P4F	5.02E-04	0.090	0.164	0.184	-0.069
Test_E4_9_20100525	0.200	3.46	P3F	4.23E-01	0.060	0.041	0.085	-0.035
			P4F	2.66E-01	0.134	0.092	0.136	-0.063
Test_E4_10_20100525	0.151	2.84	P3F	6.04E-05	0.031	0.057	0.106	-0.038
			P4F	2.84E-04	0.067	0.123	0.176	-0.140

The upper and lower surface elevation envelopes over the submerged structure provide a rough indication of the change in the flow pattern induced by the presence of the structure. The snapshots further illustrate that change and add an indication on the *(i)* generation of turbulence, *(ii)* occurrence of wave breaking, and *(iii)* patterns of sediment transport around the structure. As there is a relation between all these patterns and the development of scour they provide a rough indication on where scour is likely to be expected (*e.g.*, at the seaside in Model E2, at both sides in Model E3, and probably also at both sides in Model E4).

Figure 5.99 is a pooled data set of the obtained leeside to seaside significant pressure ratios for each model variant and sea-state. It includes all tests performed with the nearshore submerged detached breakwater, comprising those included in Table 5.XXII and those performed with balance conditions of persistent erosion and infilling followed by erosion (only for Model E2). As can be observed attenuation decreases with increasing distance to shoreline. With respect to this a remark should be made to the fact that it is only partly related to the structure as a significant portion of that attenuation is caused by wave transformation while propagating over the beach. On average the attenuation in Model E2 is about 30%, while in models E3 and E4 that attenuation is roughly 40% and 60%, accordingly.

The estimated pressure spectra at some selected locations are now analysed with the objective of comparing the spectral densities of *(i)* the incident wave spectra to those of the pressure spectra (Figure 5.100); *(ii)* the pressure spectra at the sea- and lee-sides crest limits of the structure (Figure 5.100); and *(iii)* the wave-induced pressure spectra over the beach profile (Figure 5.101).

As can be observed in Figure 5.100, a good description of the incident wave train spectral is obtained in terms of energy peaks location and spectral shape for sea-state 10 in models E2 and E4, and for sea-state 9 in Model E3 around the peak of the incident wave spectrum. For sea-state 9 in Model E2 the spectral shape is fairly well described but the peak location is shifted to lower frequencies; moreover in higher frequencies the spectrum is much more broaden. For sea-state 10 in Model E3 the shape matches in lower tail around the peaks but departs in the higher tail. For sea-state 9 in Model E4 the shape is much more broaden. Energy growth is observed in the lower harmonics. Overall is possible to conclude that the incident wave spectra are well captured by the pressure sensors and the differences (in energy, shape, and location of the peak) are linked to processes of wave transformation over the submerged structure.

By comparing the spectral densities at sea- and lee-side limit sections of the submerged structure is possible to confirm that it dissipates a significant part of the incident wave energy. It is also possible to confirm that more energy is dissipated by Model E4 and less in Model E2. On the whole the spectra at the leeside experienced a broadening.

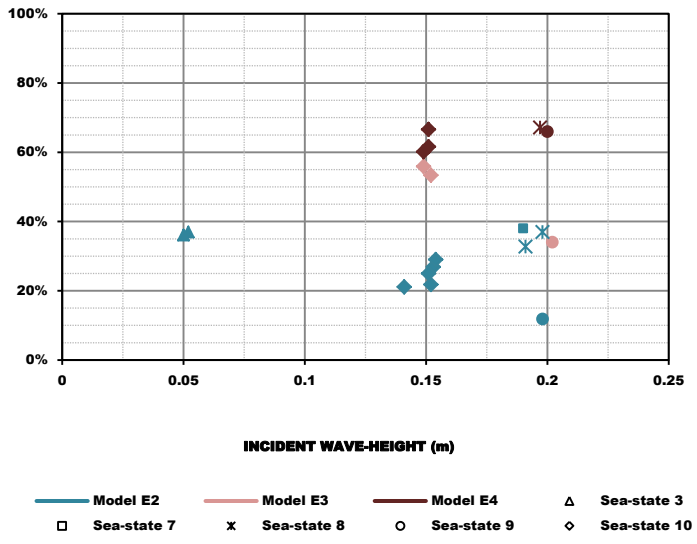

Figure 5.99: Pooled data set of the lee- to seaside significant pressure ratio, at crest.

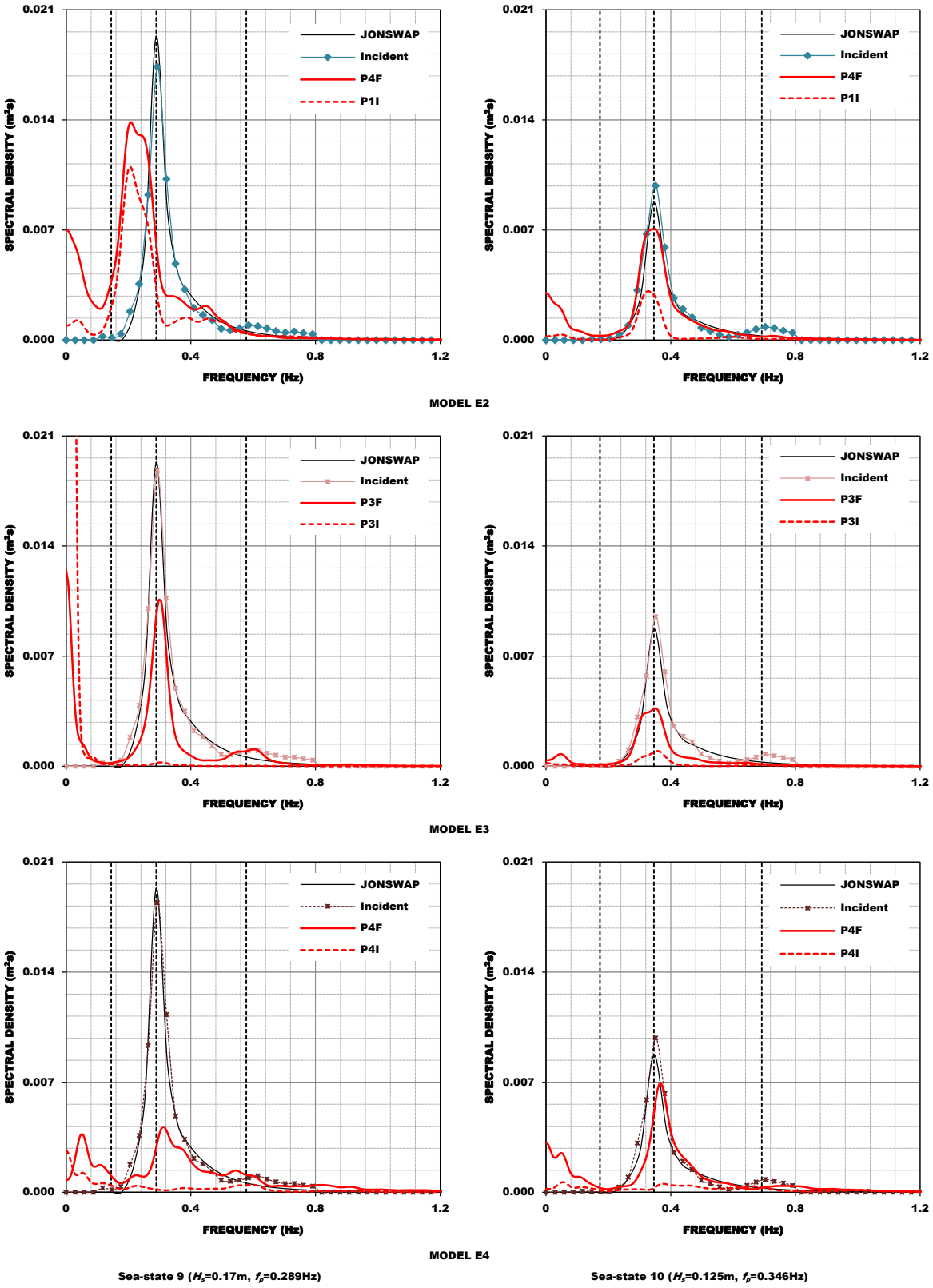

Figure 5.100: Spectral densities of the pressure spectra over the submerged structure against incident wave spectra and the theoretical JONSWAP spectrum.

The main differences observed in the wave propagation spectra with respect to shape and location of the peak occur for Model E2 (Figure 5.101); yet both are similar to that estimated for the leeside crest limit section. For models E3 and E4 the differences to the reference case are observed in the energy at the peak, which are higher than in Model A. A slight growth at second-harmonic is also observed for these models.

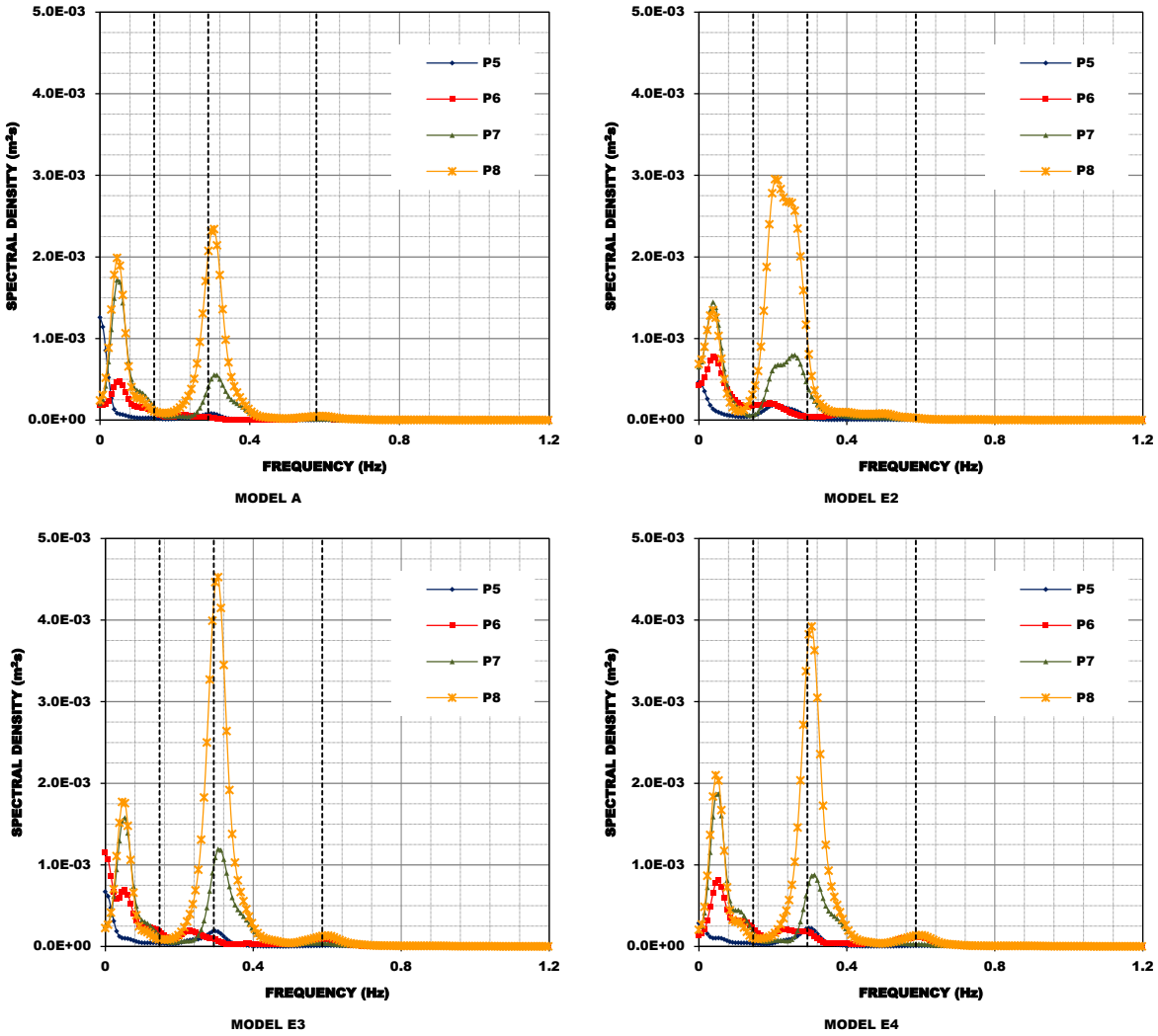

Figure 5.101: Wave propagation over the beach in Model E as compared to the reference case Model A, sea-state 9 (H_s=0.17m, f_p=0.289Hz).

5.4.4. Evaluation of wave-induced pressure variations

This section had two main objectives *(i)* to study the wave propagation over the beach slope, namely how the incident waves respond to morphologic perturbations, and *(ii)* to study the wave-induced pressures on the dune (Models B to D) and over the submerged nearshore breakwater (Model E). In the study of the wave propagation over the beach, the dynamic pressure component was examined with respect to energy spectral balance and cross-shore energy flux gradients. The differences on the energy transfer to higher and lower frequencies were small across models (B to D) even when compared to the reference case. With respect to wave-induced pressures on the dune reinforcement results indicate that the structural elements which have had a higher frequency of response than that of the whole structure were those more close to the bottom. They also indicate that significant damping occurs from surface to interior and that the damping effect is lower for the structure with the highest porosity (Model B). The results for the submerged breakwaters indicate a significant attenuation of incident wave-energy; about 40% on average (see Figure 5.99). Wave shoaling and breaking over the structure seemed to be correctly captured but underestimated in some cases possibly due to turbulent entrainment of air.

Complementarily the miniature pore-pressure sensors of the PDCR-81 type have proven to be adequate and capable of producing meaningful information. Data handling and manipulation has not been always easy due to the large data sets on each test.

5.5. Beach-profile evolution

The results on the morphological behaviour of the beach-profile when subjected to the action of normally-incident irregular breaking waves, obtained from the experimental work, are evaluated as separate test series with respect to reference case, and *per* test cluster. The objectives of such evaluation are to *(i)* understand the lowering of the beach in front of coastal defence structures built with geotextile encapsulated-sand systems; *(ii)* examine mechanisms that produce scour; and *(iii)* examine the equilibrium bar/trough features. A global analysis in terms of the interaction of the tested structures with the cross-shore sediment transport, and equilibrium profiles, namely in what concerns the bar/trough formation and maintenance, is given in paragraph 5.5.4. In section 5.6 the laboratory results on beach-profile evolution are compared with cross-shore sediment transport models; while in section 5.7 the extrapolation of results on the prototype is essayed.

5.5.1. Results for separate test series with respect to reference case

In this paragraph, the morphological development under the various experimenting conditions is set against the reference case (*i.e.*, Model A, test with a non-reinforced dune). For each model the loss and recover of supporting beach material from in front of the structure, the erosion development and sedimentation, the subsidence and structure deformation under storm conditions, is discussed with regard to the measurements.

It is important to note beforehand that the survey length to Model B, variant 1, cross-shore profile is approximately 0.5m shorter than that of the other models. The reason why it occurred had to do with set-up limitations, which could be surpassed later. The profiles missing from the analysis (refer to Table 5.I) had data inconsistencies which relate to an equipment failure (2D-profiler had to be sent to repair) and to a change in the position of the profiler from initial tests to final ones.

5.5.1.1. Model B

As listed in Table 5.I, Model B was submitted to balance conditions of accretion, erosion, and persistent erosion. The variant 2 of Model B also run for the infilling and again erosion balance condition, yet this condition is not directly comparable with that of Model A, once the input seas are different.

Figure 5.102 displays the resulted end beach-profiles from a run-segment with accretionary waves with a significant wave-height of 0.08m and peak period of 2.89s (input sea-state 6) in Model B, variants 1 and 2. The initial profile (black solid line) was a plane beach (gradient β=0.15). The end beach-profiles resemble each other. Moderate sand accumulation is observed at the shoreline, the source of which is the erosion in the inner surf zone; the outer surf zone remained stable. The slightly milder wave conditions in Model B2 (see Table 5.III) may be responsible for the slightly lower erosion in the inner surf zone. For the remainders run-segments with accretionary waves, the beach-profile experienced similar evolution. Yet, the higher accumulation at the shoreline in Model A, apparently the result of some dune reshaping, was not recognised in the milder wave conditions (*i.e.*, significant wave-height of 0.04m), presumably for the reason that under low energy conditions wave run-up hardly ever reached the dune face and thus the profile.

The results for run-segments with erosional waves of 0.17m significant wave-height and 3.46s peak period (input sea-state 9) are presented in Figure 5.103. As shown, the beach-profile changes have a similar evolution across the two model variants. The shoreline has retreated as far as the established structure and a nearshore-bar has developed. The erosion in the vicinity of the shoreline roughly equalled the accumulation in the bar area, indicating that the sand was transported from the beach and deposited near the main breaker line. The somehow surprising lower seabed level along-shore in variant 2 of Model B as compare to variant 1 is apparently a consequence of higher sediment fluxes towards offshore (*i.e.*, outside the 2D-bed profiler range), as observed but not quantified during the experimental work.

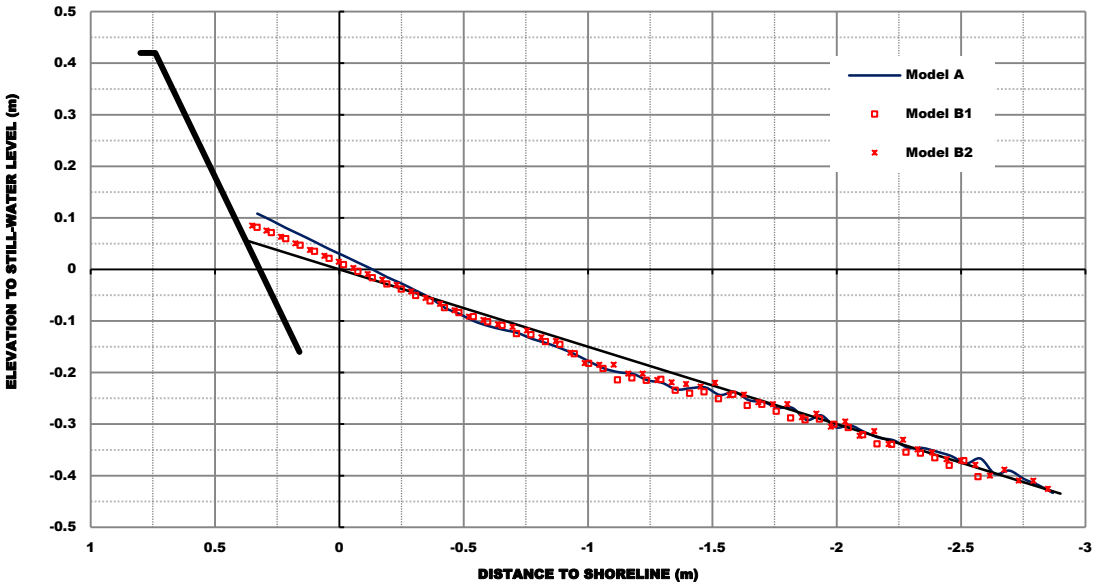

Figure 5.102: Initial and end beach-profiles for Model B, variants 1 and 2, sea-state 6 (H_s=0.08m, T_p=2.89s).

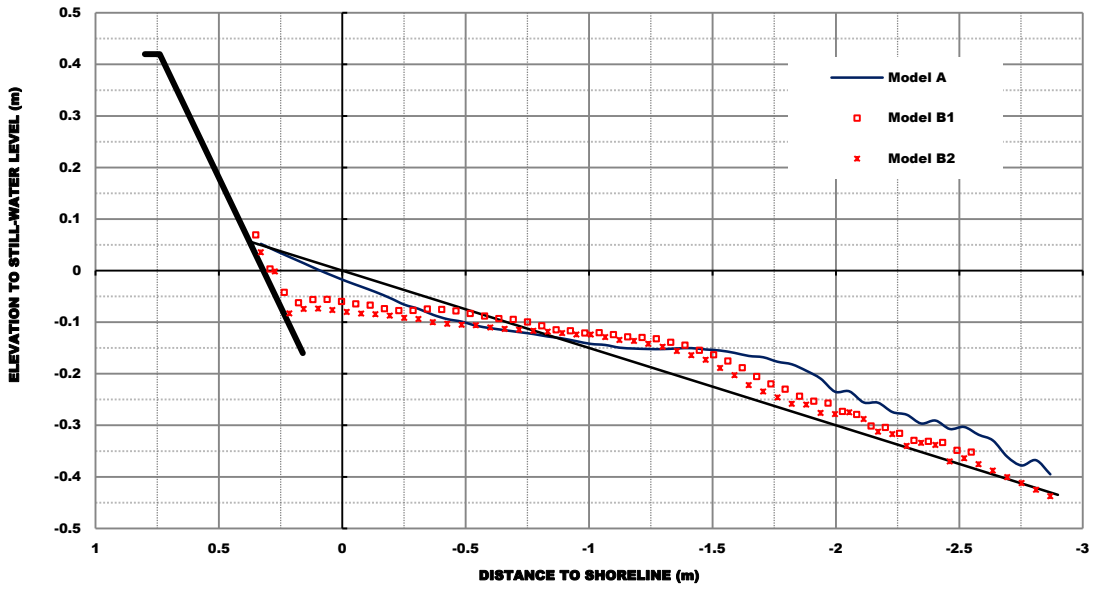

Figure 5.103: Initial and end beach-profiles for Model B, variants 1 and 2, sea-state 9 (H_s=0.17m, T_p=3.46s).

The bar accumulation in the case of Model A is greater as compared to Model B; while the shoreline recession is much smaller. These are expected morphologic changes as the profile is fed with the sands from the eroding dune. The end profile had a much gentler overall slope than the initial one because of erosion in the vicinity of the original shoreline and development of the break-point bar.

For the remainders run-segments with the larger waves, the beach-profile experienced similar erosional sequence from reflective to dissipative beach. Such erosional sequence as has been characterized by Short (1999) consists of two complementary mechanisms designed to accommodate the higher waves and greater volume of water moving in and across the surf zone. First, beach erosion lowers and widens the beach surf zone by moving sand from beach inner surf zone and depositing it in the outer surf zone. Second, this process causes waves to break further seaward and across a wider surf zone thereby lowering incident wave-height and energy at the shore, and providing a wider surf zone for both energy dissipation and surf zone circulation.

To investigate the response of the dune-beach system to antecedent morphology, the end beach-profile with sea-state 10 was exposed to further wave run-segments with identical input sea-state. Figure 5.104 displays a sequence of profiles surveyed during the tests with Model B1, again Model A is given for reference.

The analysis of Figure 5.104 reveals that initially the sand is removed from the beach face to be deposited near the main breaker line; with time the morphology near the structure (close to the initial shoreline) become arrested (*i.e.*, change is very insignificant) and a double bar along the beach-profile starts to develop, as sediments are moved further seaward and a moderately deep trough starts to build-up. The observed behaviour seems to indicate that when a beach-profile is exposed to persistent erosional sequences (even under constant wave conditions) it will experience a cross-shore profile migration as the sediments initially deposited at the lower beach face move further seaward, thereby extending the bar. Figure 5.104 also reveals that the scour hole which develops close to the structure has experienced periods of erosion and infilling.

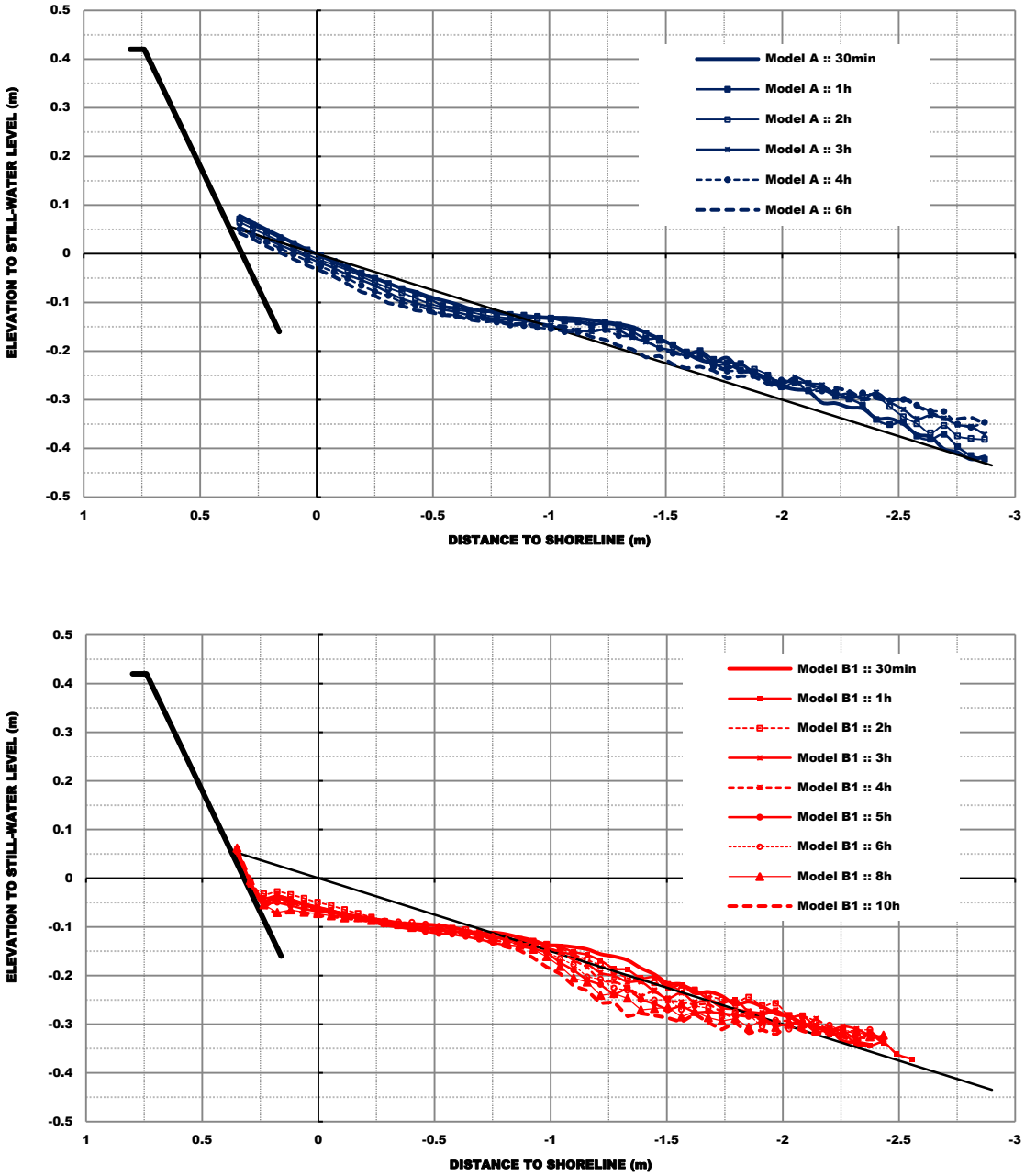

Figure 5.104: Beach-profile sequences for Model A (top panel), Model B, variant 1 (bottom panel), sea-state 10 (H_s=0.125m, T_p=2.89s).

On the basis of what has been analysed so far, it appears that overall morphodynamic changes for both Model B variants are much alike with respect to beach-profile evolution. To some extent this is an expected result given that similar geometrical conditions yield similar wave-structure interaction thereby similar wave-induced morphodynamic change; likewise, given the differences in the position of the structure toe it was expected that around the structure distinctions between the two variants would come into view.

Figure 5.105 shows cross-sectional views of Model B during test series with sea-state 10. The photos present different moments during the tests, yet evidence of a much greater subsidence in variant 2 stands out when comparing one to another. A rough measurement made during the experiment has demonstrated that after 4h the lowest front row had rotated by approximately 7 degrees.

After Test_B2_10_4h_8_20100212 (*i.e.*, sea-state 8 for 30mn, over a profile exposed to sea-state 10 during 4h) practically all bags at the lowest front rows had been pull-out, the bags at the middle rows had been displaced, and only the highest front rows seemed to be fairly undisturbed (Figure 5.106).

From the analysis of Tables 5.VII and 5.VIII is possible to conclude that the structure built with geotextile sand-filled containers corresponding to an estimate of 1.5m^3 in prototype, has become unstable (*i.e.*, a significant number of bags being pulled-out and displaced) when exposed to waves with a significant wave-height around 1.80m.

Figure 5.105: Cross-sectional views of Model B, variant 1 (left panel) and variant 2 (right panel), during test series with balance conditions of persistent erosion (sea-state 10, H_s=0.125m, T_p=2.89s).

Figure 5.106: Model B2, after Test_B2_10_4h_8_20100212, persistent erosion followed by sea-state 8 (H_s=0.17m, T_p=2.89s).

5.5.1.2. Model C

Model C was submitted to balance conditions of accretion, erosion, persistent erosion, and to conditions of infilling and again erosion.

Figure 5.107 displays the measured end beach-profiles from a run-segment with accretionary waves with a significant wave-height of 0.04m and peak period of 2.31s (input sea-state 2) in Model C, variants 1 and 2. The black solid line represents the initial plane beach-profile. As expected the end beach-profiles resemble each other. The moderate sand accumulation recognized at the shoreline results from the erosion in the inner surf zone; whereas the outer surf zone beach-profile remained stable. For the remainders run-segments with accretionary waves, the beach-profile experienced similar evolution.

The results for run-segments with erosional waves with 0.17m significant wave-height and 2.31s peak period (input sea-state 7), and with waves with significant wave-height of 0.17m and peak period of 3.46s (input sea-state 9) are presented in Figures 5.108 and 5.109. As shown in figures, the beach-profile suffers similar evolution across the two model variants. The shoreline has retreated as far as the established structure and a nearshore-bar has developed. The erosion in the vicinity of the shoreline roughly equalled the accumulation in the bar area, indicating that the sand was transported from the beach and deposited near the main breaker line.

The bar accumulation in the case of Model A is greater as compared to Model C; while the shoreline recession is much smaller. The end beach-profile in Model A had a much gentler overall slope than the initial one. These contrast features had already been observed earlier in Model B and are presumably a consequence of the nourishment with sand from the eroding dune.

To investigate the response of the dune-beach system to antecedent morphology, some selected end beach-profiles were exposed to additional wave run-segments after an erosional sequence. Two perspectives were considered *(i)* response to persistent storm conditions based on the survey of profile changing with wave run-segments with sea-state 10; and *(ii)* response to wave decrease and increase based on the survey of changes in beach profile shape which occur as a result of changing wave conditions.

The erosional sequences with input sea-state 10 for both variants of Model C are depicted in Figure 5.110. Much the same as have been seen previously in Model B the erosion sequences show two moments. On a first moment the sediment is removed from the beach face and is initially deposited in the inner surf zone, with continuous wave action the bar is moved seaward and moderately deep trough starts to develop.

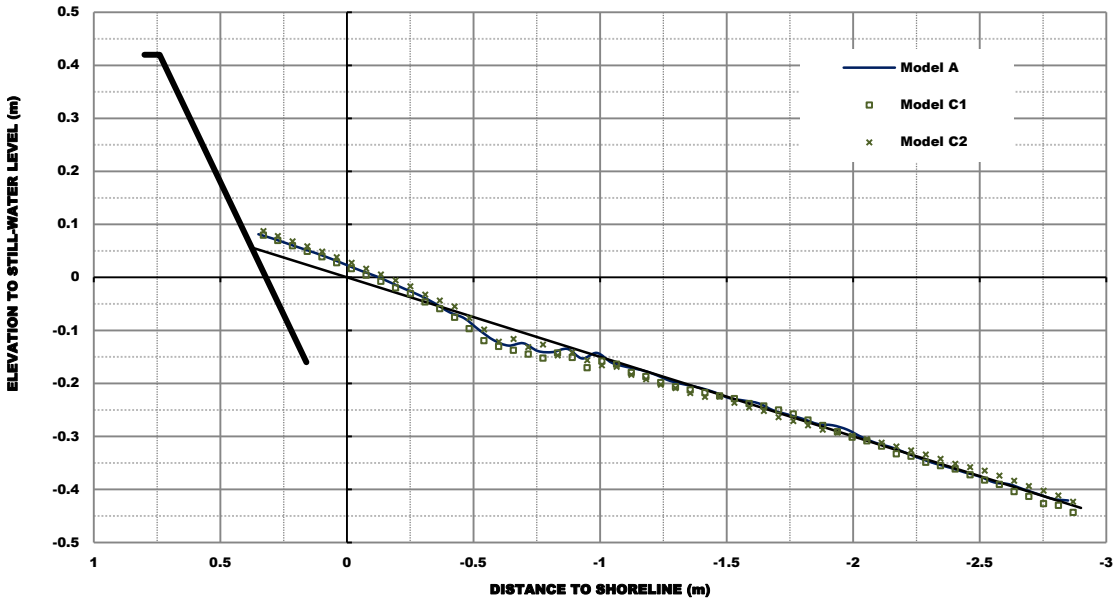

Figure 5.107: Initial and end beach-profiles for Model C, variants 1 and 2, sea-state 2 (H_s=0.04m, T_p=2.31s).

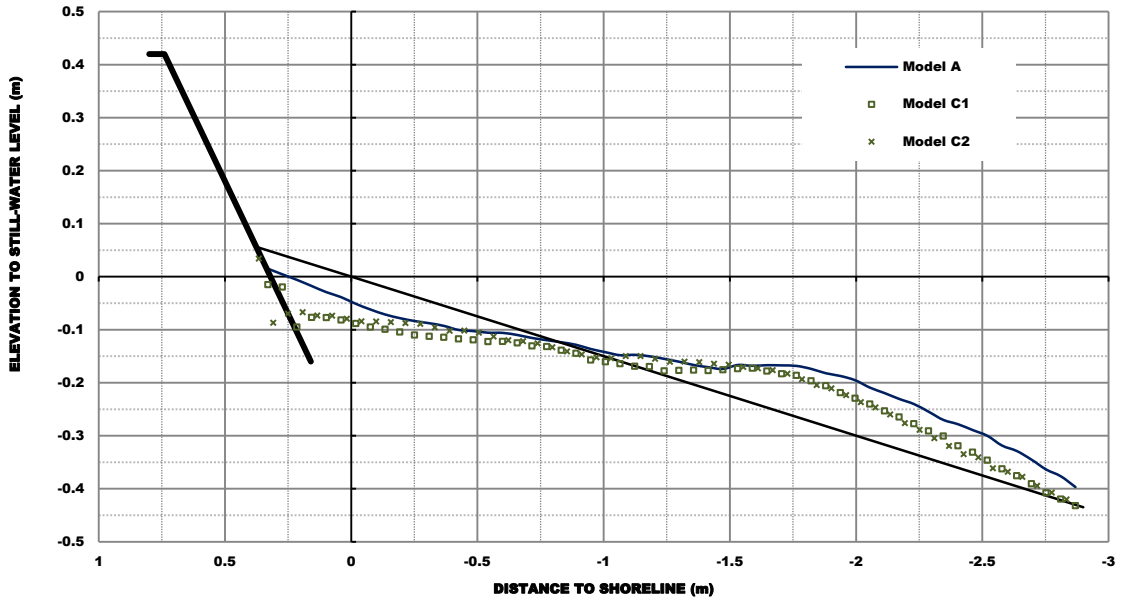

Figure 5.108: Initial and end beach-profiles for Model C, variants 1 and 2, sea-state 7 (H_s=0.17m, T_p=2.31s).

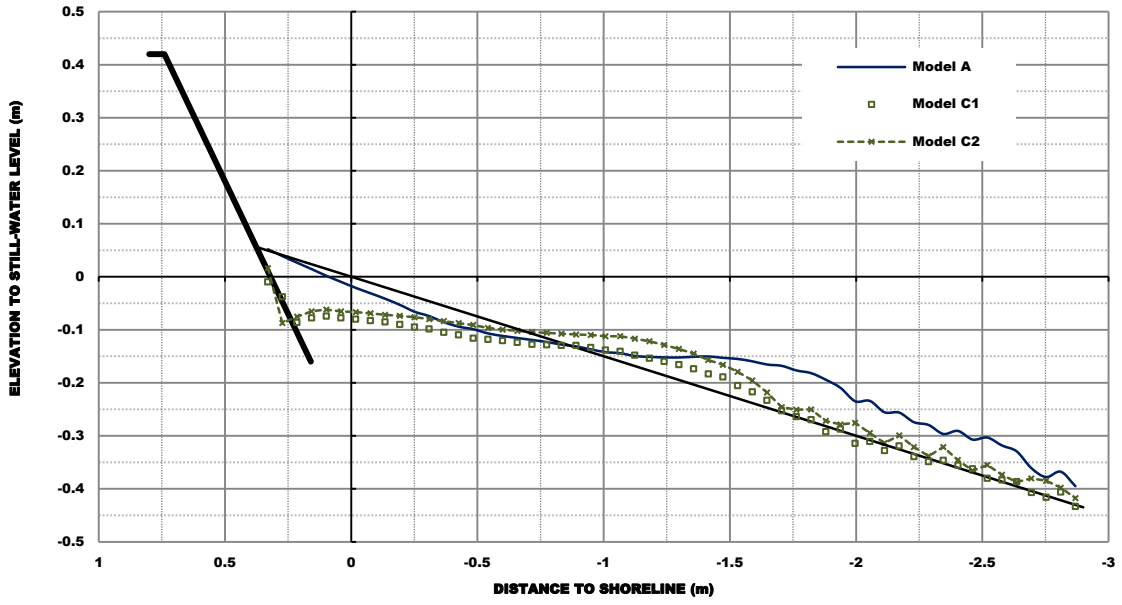

Figure 5.109: Initial and end beach-profiles for Model C, variants 1 and 2, sea-state 9 (H_s=0.17m, T_p=3.46s).

An erosive terrace is form and remains practically unchanged along the erosive sequences in variant 1 of Model C; yet in variant 2 scouring around the structure toe is deeper than in variant 1 and the trough that starts to develop is also deeper in variant 2. The former wave-induced morphological beach-profile change may be linked to the latter as a deeper trough in the inner surf zone will cause waves to break further landward thereby raising incident wave-height and energy at the shore. Also in variant 2, more sand is moved seaward.

The measured end beach-profiles with erosional wave run-segments – sea-state 8 (H_s=0.125m, T_p=2.89s), followed by two accretionary ones – sea-state 3 (H_s=0.04m, T_p=2.89s) – each with 30mn duration, and again an erosional sequence, are plotted in Figure 5.111.

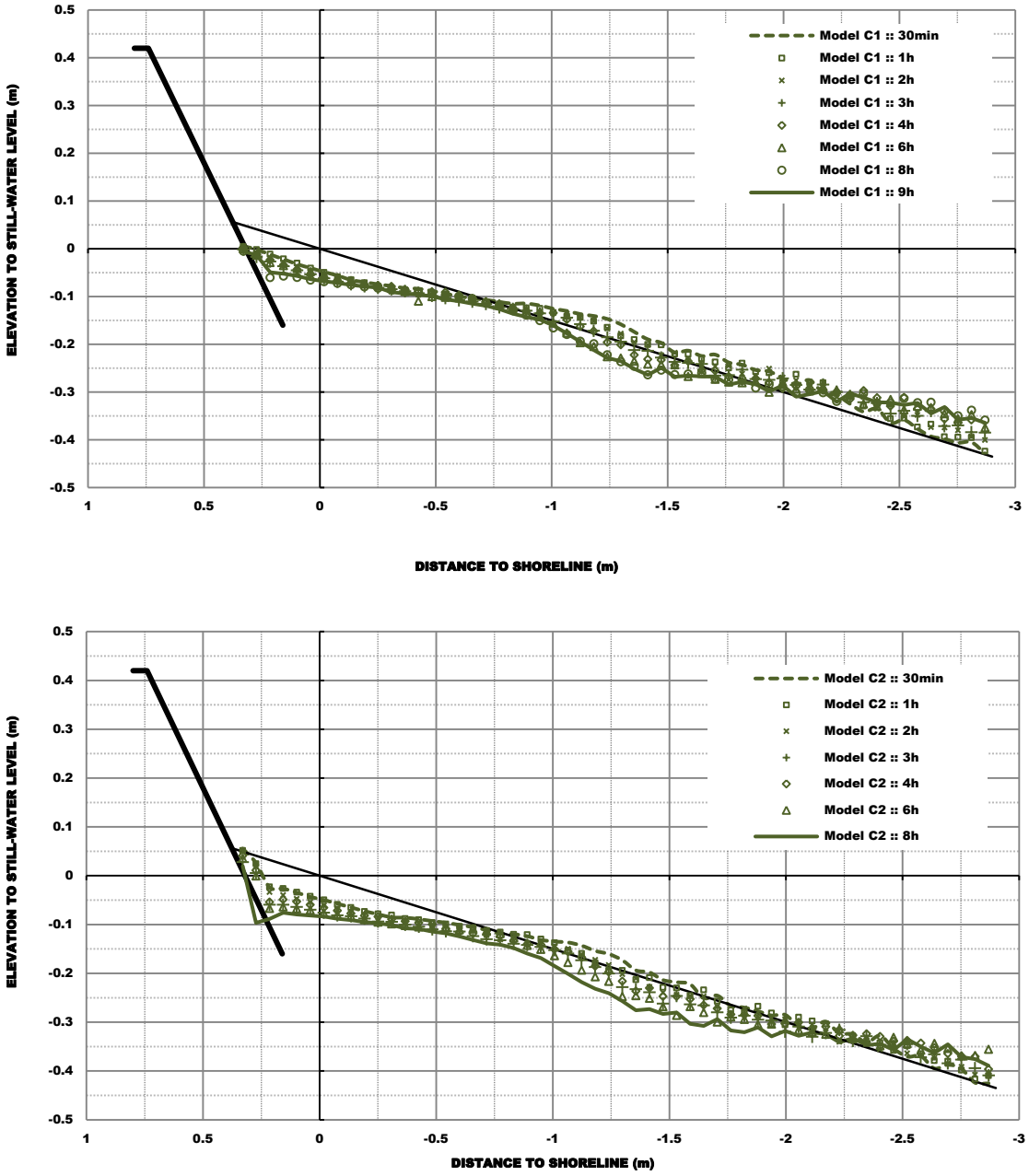

Figure 5.110: Beach-profile sequences for Model C, variants 1 (top panel) and 2 (bottom panel), sea-state 10 (H_s=0.125m, T_p=2.89s).

The complete evolutionary sequence shows that during the first wave run-segment the beach-profile begins to rearrange itself to accommodate the larger waves (reflective to dissipative beach); as the waves decrease to about 0.04m, beach face sediment begins to move shoreward completely back-filling the scour holes which developed during the first wave run-segment; finally, when the waves increase not only the profile is reshaped again to a lower level at the shoreline, but also the scour holes redevelop. No substantive change is produced at the nearshore through the sequence.

Figure 5.111 also shows that the morphology at the shoreline after the accretionary sequences remained arrested during the final erosional one.

Both Model C variants have deformed considerably under the erosional sequences. In regard to subsidence, Model C2 exhibited a rotation of the lowest row of approximately 10 degrees after 40mn of being exposed to sea-state 10, which increase to 11 degrees at 3h.

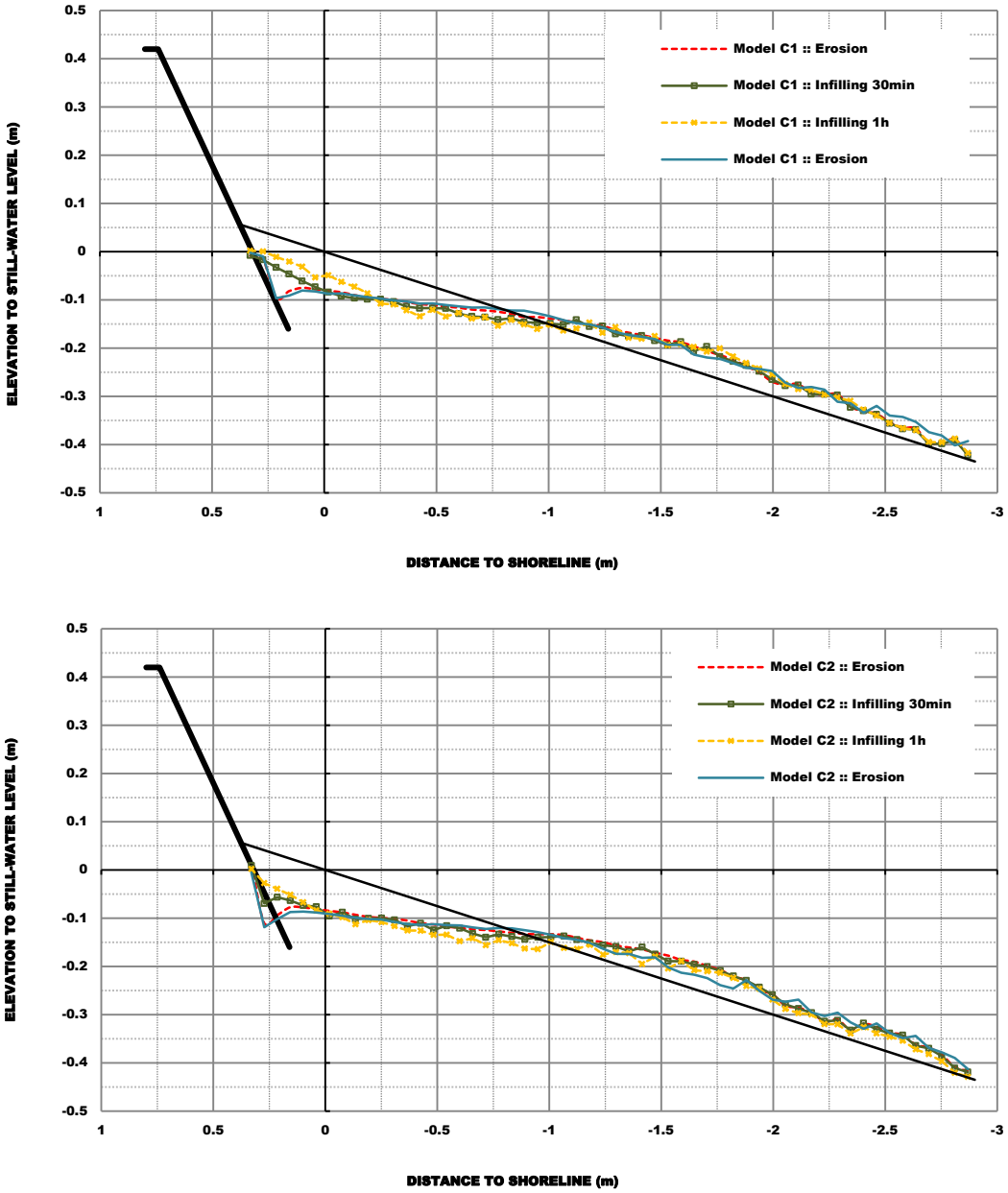

Figure 5.111: Initial and end beach-profiles for Model C, variants 1 (top panel) and 2 (bottom panel). Erosional sea-state 8 (H_s=0.17m, T_p=2.89s), and accretionary sea state 3 (H_s=0.04m, T_p=2.89s).

5.5.1.3. Model D

Model D was exposed to balance conditions of accretion, erosion, persistent erosion, and to conditions of infilling and again erosion.

Figure 5.112 displays the measured end beach-profiles from a run-segment with accretionary waves of 0.08m significant wave-height and 2.31s peak period (input sea-state 5) in Model D, variants 1 and 2. The black solid line represents the initial plane beach-profile.

As has been observed in the preceding analysis for models B and C, the beach-profile change in Model D under accretionary sequences is comparable to the one experienced in the tests with models A, B, and C. The moderate sand accumulation recognized at the shoreline results from the erosion in the inner surf zone; whereas the outer surf zone beach-profile remained stable. For the remainders run-segments with accretionary waves, the beach-profile experienced similar evolution.

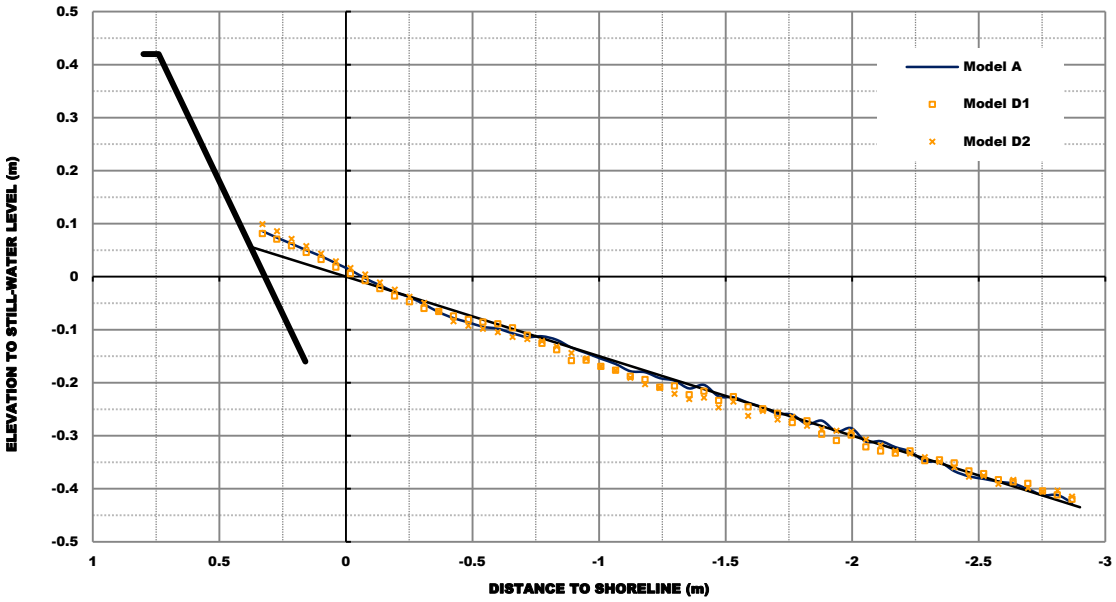

Figure 5.112: Initial and end beach-profiles for Model D, variants 1 and 5, sea-state 2 (H_s=0.08m, T_p=2.31s).

The results for run-segments with erosional waves with significant wave-heights of 0.17m and peak wave-periods of 2.31s (input sea-state 7), and 3.46s (input sea-state 9) are presented in Figures 5.113 and 5.114. Overall the figures show that the beach-profile changes had a similar evolution across the two model variants. The shoreline has retreat as far as the established structure and a nearshore-bar has developed. The erosion in the vicinity of the shoreline roughly equalled the accumulation in the bar area, indicating that the sand was transported from the beach and deposited near the main breaker line.

While comparing the morphodynamic outputs produced by erosional sequences between models D and A the conclusions are very similar to those withdrawn in the preceding analysis. The bar accumulation in the case of Model A is greater as compared to Model D; while the shoreline recession is much smaller. The end profile in Model A exhibits a much gentler overall slope than the initial one.

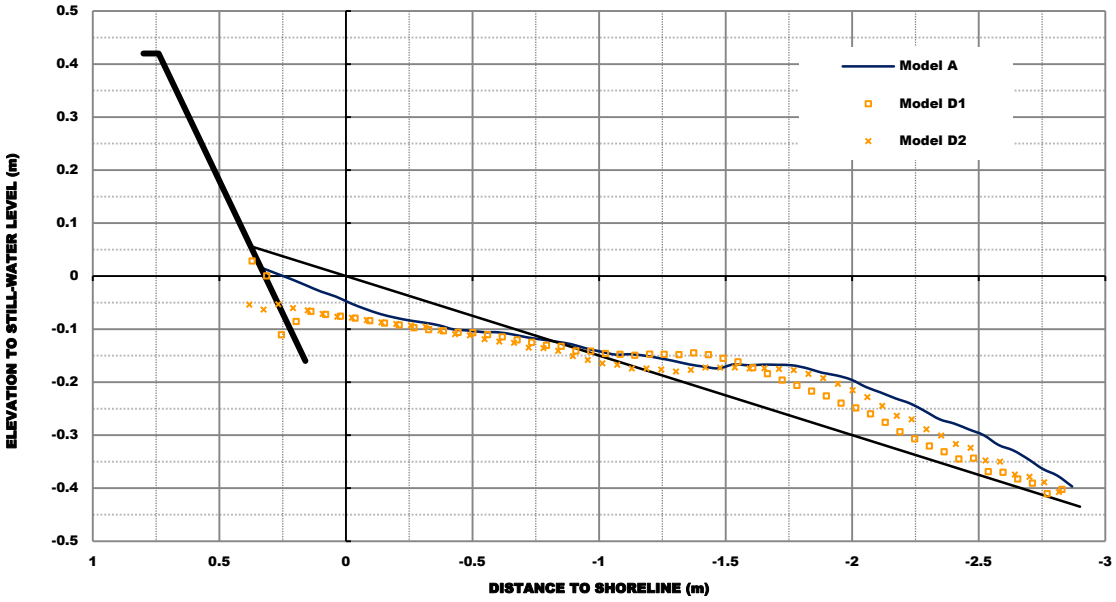

Figure 5.113: Initial and end beach-profiles for Model D, variants 1 and 2, sea-state 7 (H_s=0.17m, T_p=2.31s).

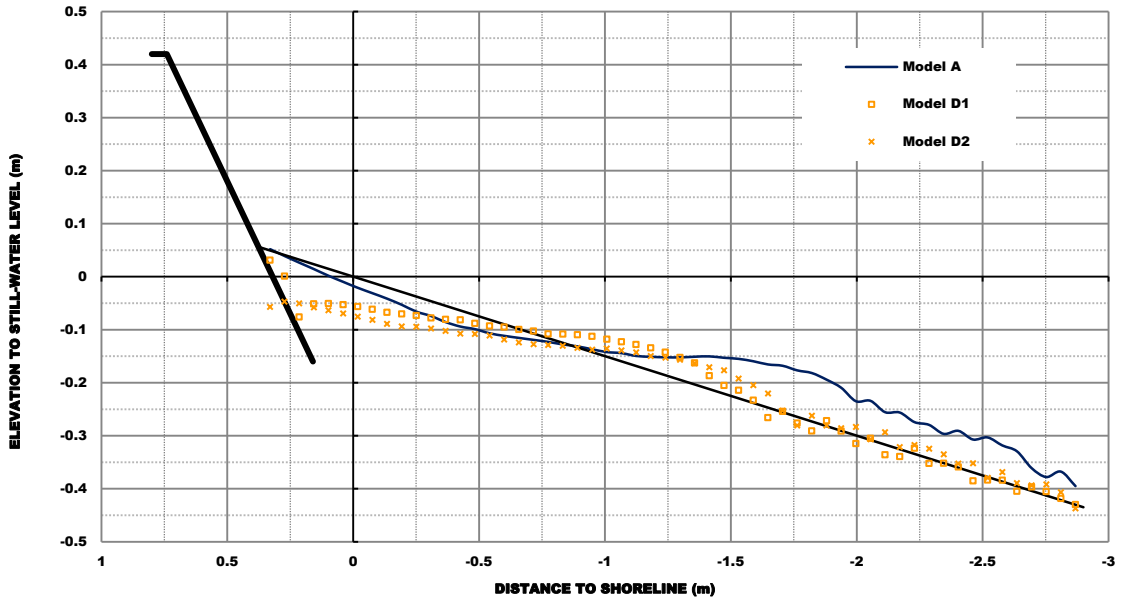

Figure 5.114: Initial and end beach-profiles for Model D, variants 1 and 2, sea-state 9 (H_s=0.17m, T_p=3.46s).

An erosive terrace is form and remains practically unchanged along the erosive sequences in variant 1 of Model D; yet in variant 2 scouring around the structure toe is deeper than in variant 1 and the trough that starts to develop is also deeper in variant 2. The former morphological change may be linked to the latter as a deeper trough in the inner surf zone will cause waves to break further landward thereby raising incident wave-height and energy at the shore. Also in variant 2, more sand is moved seaward.

The erosional sequences with input sea-state 10 for both variants of Model D are depicted in Figures 5.115 and 5.116, accordingly. Essentially the erosion sequences show two moments. On a first moment the sediment is removed from the beach face and is initially deposited in the inner surf zone, then with continuous wave action the bar is moved seaward and a moderately deep trough starts to develop.

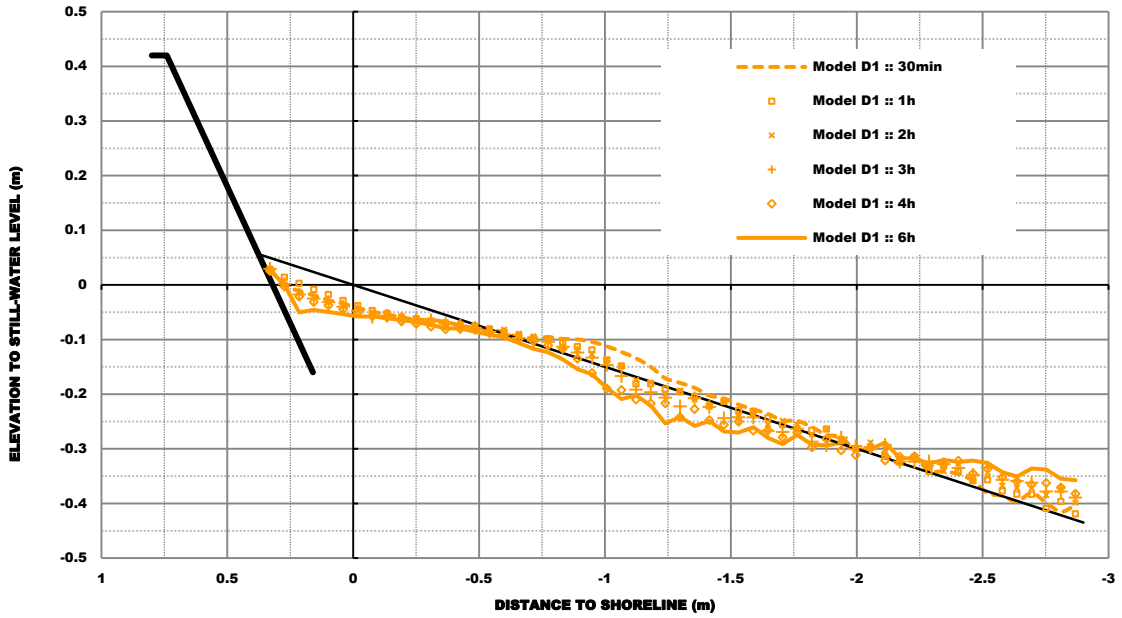

Figure 5.115: Initial and end beach-profiles for Model D1, sea-state 10 (H_s=0.125m, T_p=2.89s).

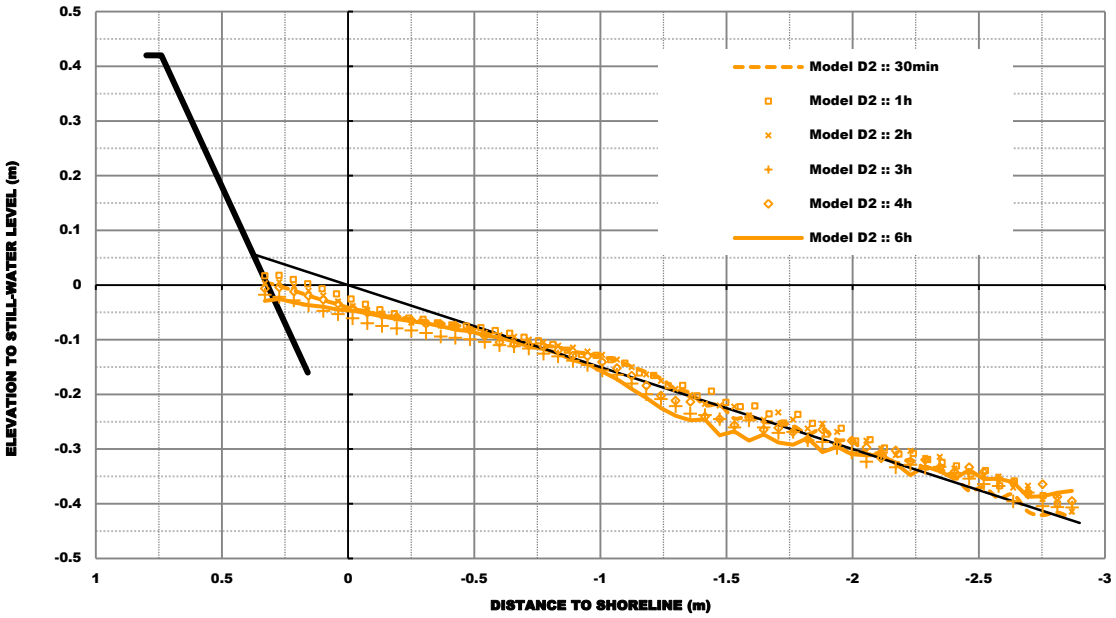

Figure 5.116: Initial and end beach-profiles for Model D2, sea-state 10 (H_s=0.125m, T_p=2.89s).

The measured end beach-profiles with erosional wave run-segments – sea-state 8 (H_s=0.125m, T_p=2.89s), followed by two accretionary ones – sea-state 3 (H_s=0.125m, T_p=2.89s), and again erosional wave run-segments, are plotted in Figures 5.117 and 5.118.

Contrary to what has been observed in the preceding analysis, the accretionary sequences have backfilled the scour holes existing at the end of the first erosive sequence only for Model D2; whereas in Model D, variant 1, the accretionary sequences have just moderately fed the shoreline with sand.

In regard to sediment transport within the erosional sequences, sand is removed from the beach face and is initially deposited in the inner surf zone, with continuous wave action the bar is eroded and the sediment is moved seaward.

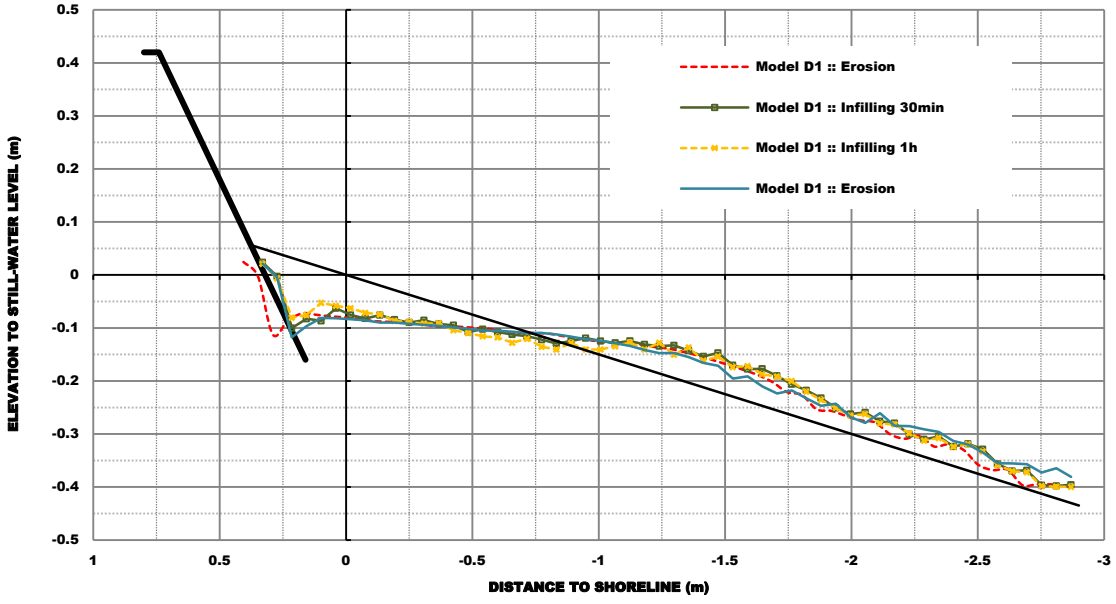

Figure 5.117: Initial and end beach-profiles for Model D1.
Erosional sea-state (Hs=0.17m, Tp=2.89s), and accretionary sea state (Hs=0.04m, Tp=2.89s).

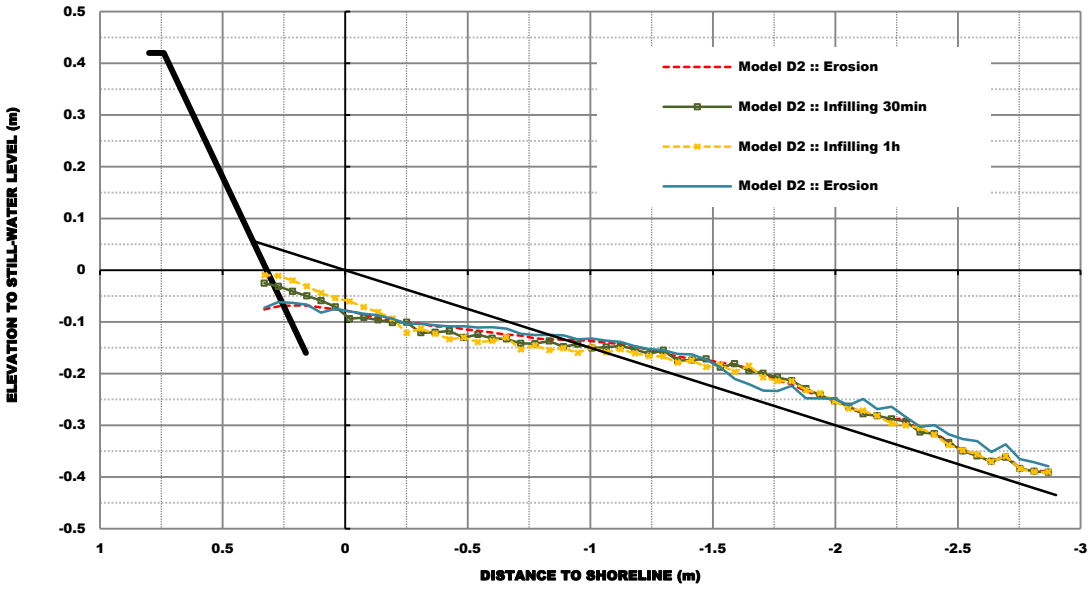

Figure 5.118: Initial and end beach-profiles for Model D2.
Erosional sea-state (Hs=0.17m, Tp=2.89s), and accretionary sea state (Hs=0.04m, Tp=2.89s).

5.5.1.4. Model E

As listed in Table 5.I, the variants 1 to 4 of Model E were submitted to balance conditions of erosion and persistent erosion. Variant 2 also run for the infilling and again erosion balance condition.

The tests are clustered for evaluation based on wave run-segment and the analysis focuses on shoreline retreat/advance, bar/trough formation and maintenance, and scour development. The beach-profile changes for Model E1 have not been included in the analysis because the test was interrupted when the structure become unstable (Figure 5.119), at approximately 11mn wave action.

For each model variant, the morphological development under the various experimenting conditions is set against the reference case (*i.e.*, non-protected dune-beach system). The initial dune-beach system profile and a sketch location of the submerged nearshore detached-breakwaters are given in Figures 5.120 to 5.125 for reference.

Figure 5.120 clearly shows the offshore interruption of sediment transport in Model E2. Indeed, it is traceable in the somewhat substantial shoreline recession and appreciably higher accumulation in the bar area in Model A, while Model E2 exhibits a very interesting bar/trough shaped profile, on which the shoreline remained stable and where the deposition at the leeward side of the structure indicates a second breaker line.

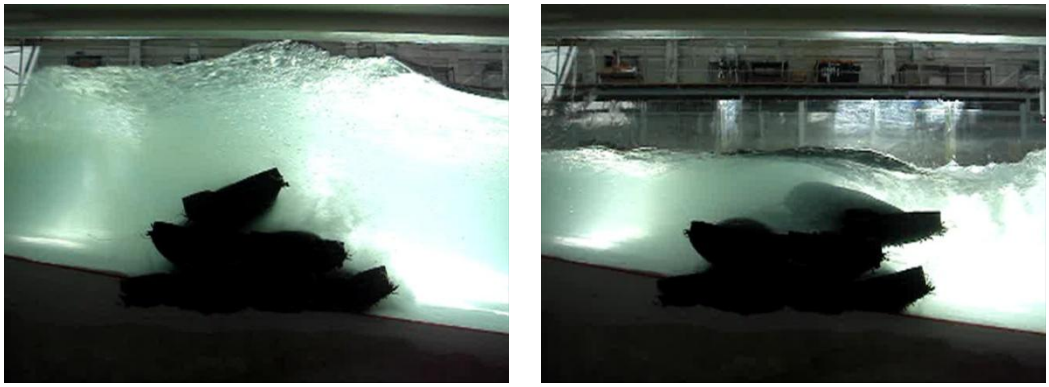

Figure 5.119: Model E1, sea-state 10 (H_s=0.125m, T_p=2.89s): model become unstable, at approximately 11mn wave action.

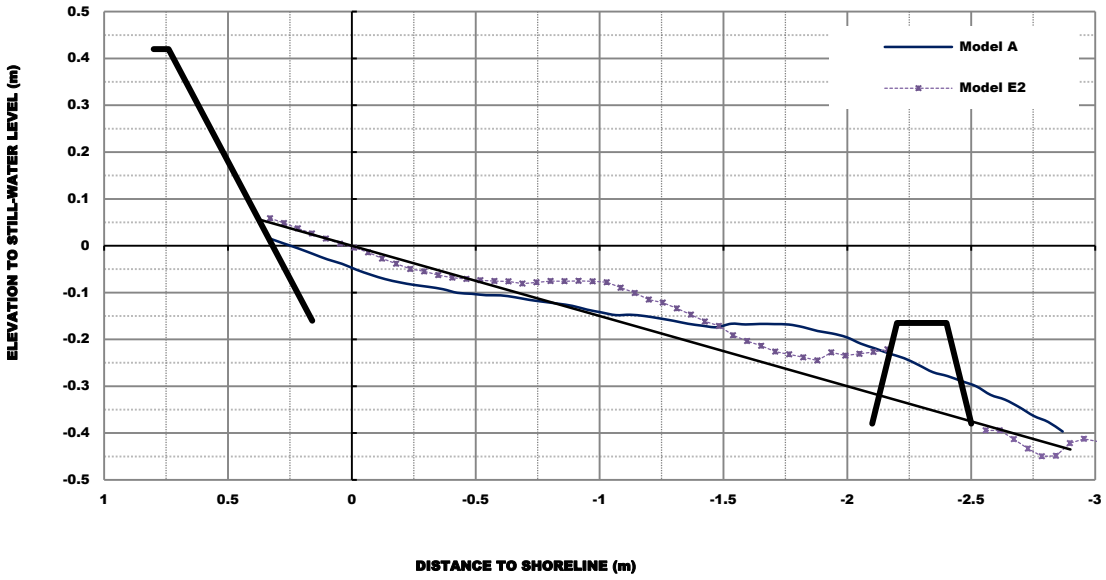

Figure 5.120: Initial and end beach-profiles: sea-state 7 (H_s=0.17m, T_p=2.31s). The initial dune profile is identified and the location of the submerged nearshore detached-breakwaters is sketched.

The comparison between the initial and end beach-profiles (Figures 5.120 to 5.123) show that under erosional sequences the main morphologic changes in Model E2 and E4 occur in the lower beach, whereas at the upper beach the end profile varies slightly from the initial one. Some moderate shoreline accretion is though observed in Model E2 for a few of the wave run-segments.

In Model E2 there is significant deposition in the leeward side of the submerged breakwater, indicating the offshore interruption of sediment transport. For the wave run-segments with higher wave heights a nearshore-bar has developed at approximately 1m from the initial shoreline. This morphologic change indicates a second breaker line.

The end beach-profile of variant 4 of Model E exhibits probably one of the most interesting morphodynamic features with respect to efficiency in maintaining a beach and in protecting the shoreline, when compared to the other models and to the reference case. In Model E4, for the tested significant wave-heights, the nearshore-bar development has similar evolution as compared to Model A. This indicates that for such wave-heights nearshore processes are similar in both the models. However, as the seaward transport from the beach is interrupted by the submerged sill, there is less erosion in the vicinity of the shoreline and less accumulation in the bar area.

In Model E3 there are some markedly differences in the end beach-profiles of this model as compared to models E2 and E4. For instance, significant shoreline erosion is observable during the test with sea-state 8 (Figure 5.121). In fact, under similar wave-run conditions, the beach-profile in Model E3 experienced an evolution at the shoreline similar to Model A (*i.e.*, erosion at the vicinity of the original shoreline and deposition at a nearshore-bar). This is a somehow expected morphologic change as the structure was placed within the main breaker line of Model A, and the structure crest level was placed at approximately the nearshore-bar level. Yet, the end-profiles in Model E3 differ from those in Model A at the seaward side of the structure where the beach-levels are much lower.

In all model variants, some significant scour develops on either sides of the structure. This will be analysed farther over this section.

Figures 5.124 and 5.125 show the end beach-profiles produced by wave run-segments over wave-worked profiles.

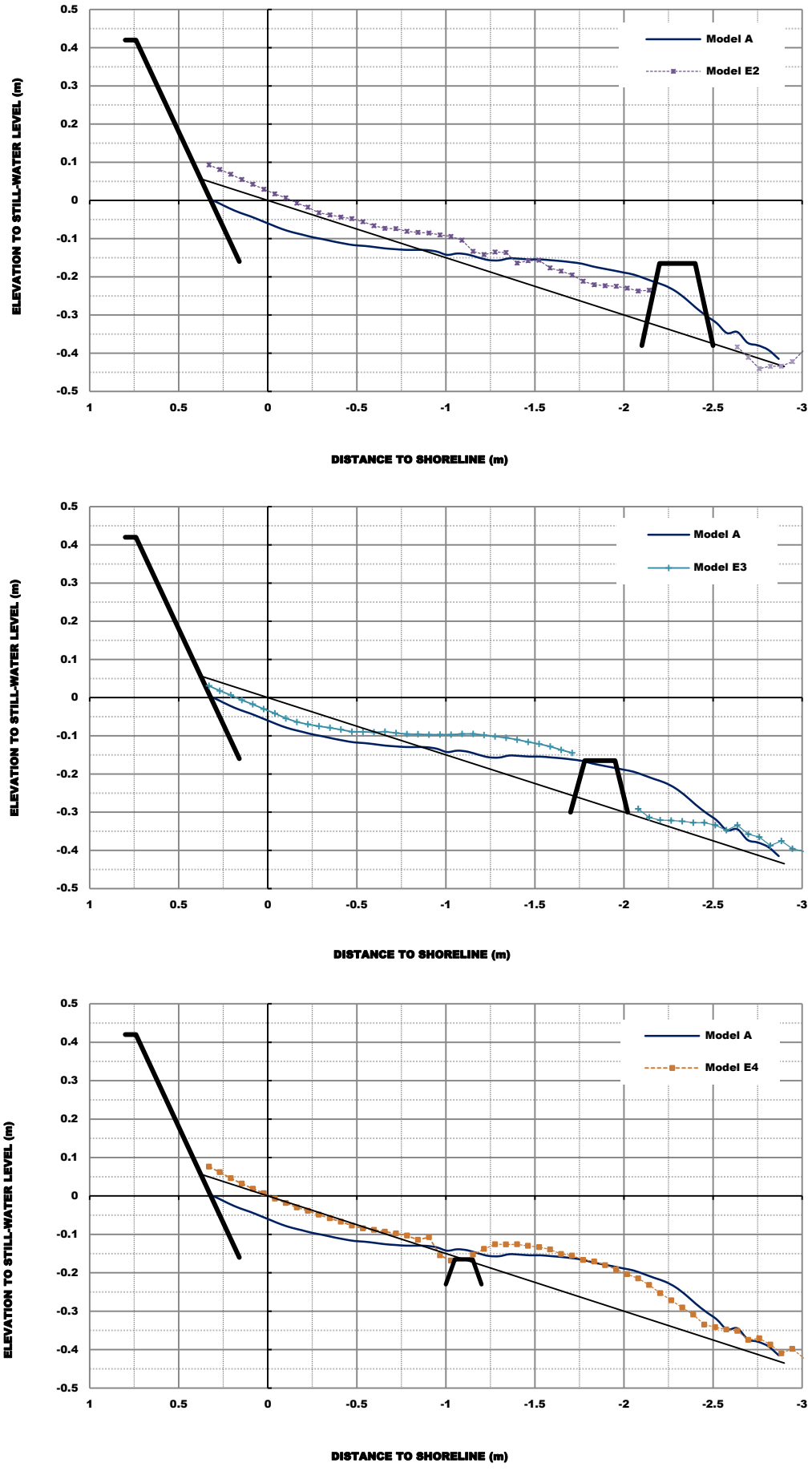

Figure 5.121: Initial and end beach-profiles: sea-state 8 (H_s=0.17m, T_p=2.89s). The initial dune profile is identified and the location of the submerged nearshore detached-breakwaters is sketched.

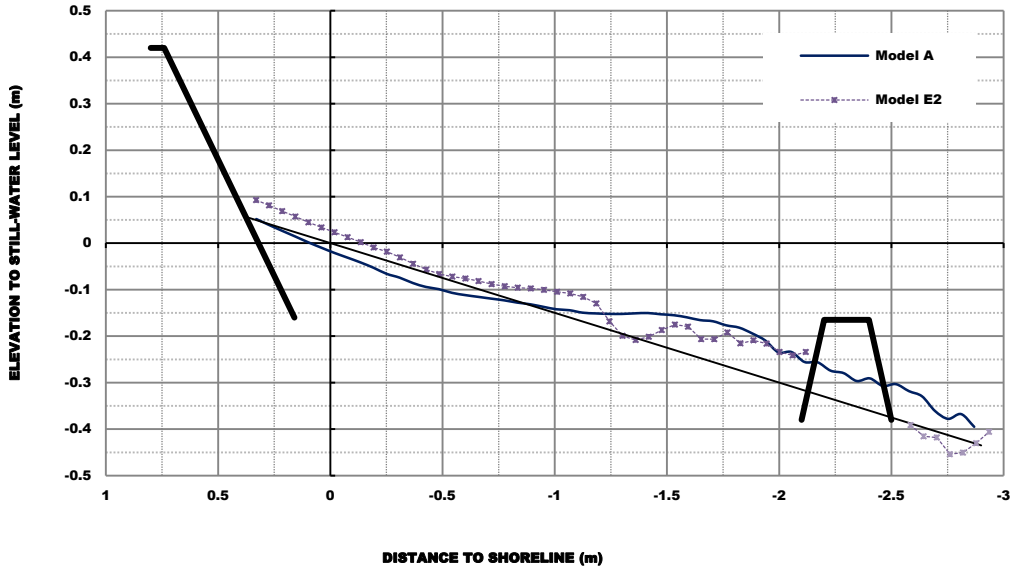

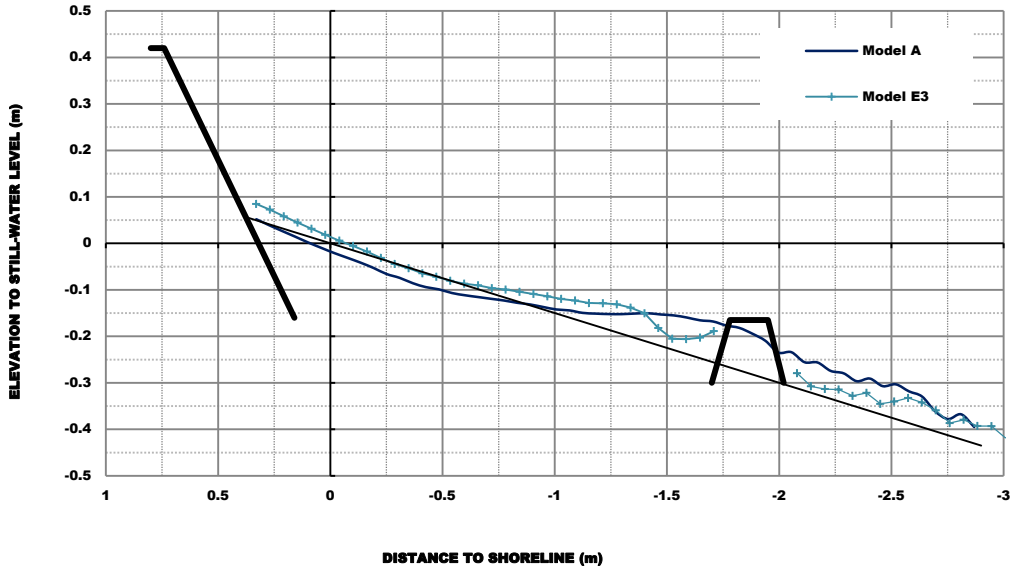

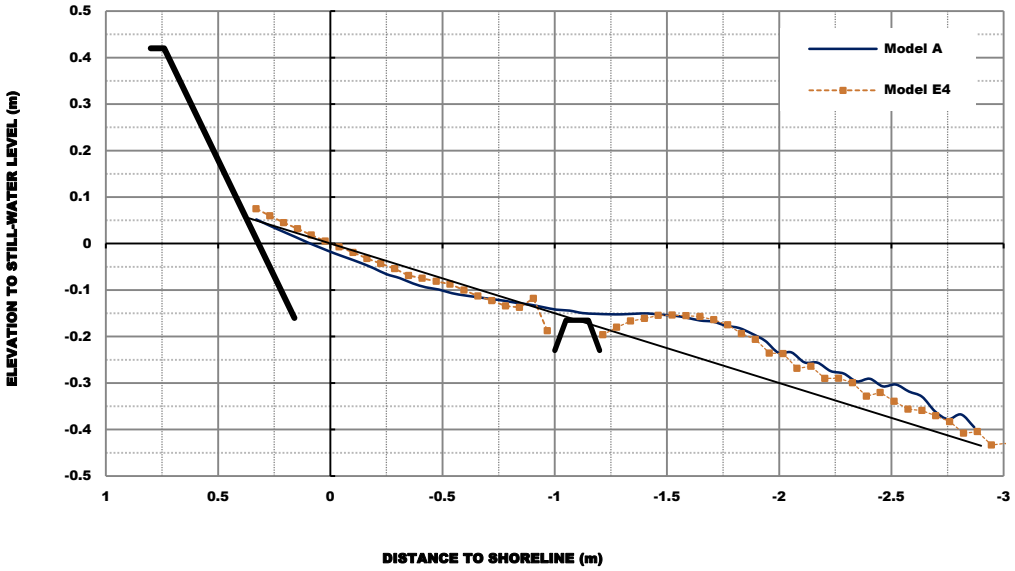

Figure 5.122: Initial and end beach-profiles: sea-state 9 (H_s=0.17m, T_p=3.46s). The initial dune profile is identified and the location of the submerged nearshore detached-breakwaters is sketched.

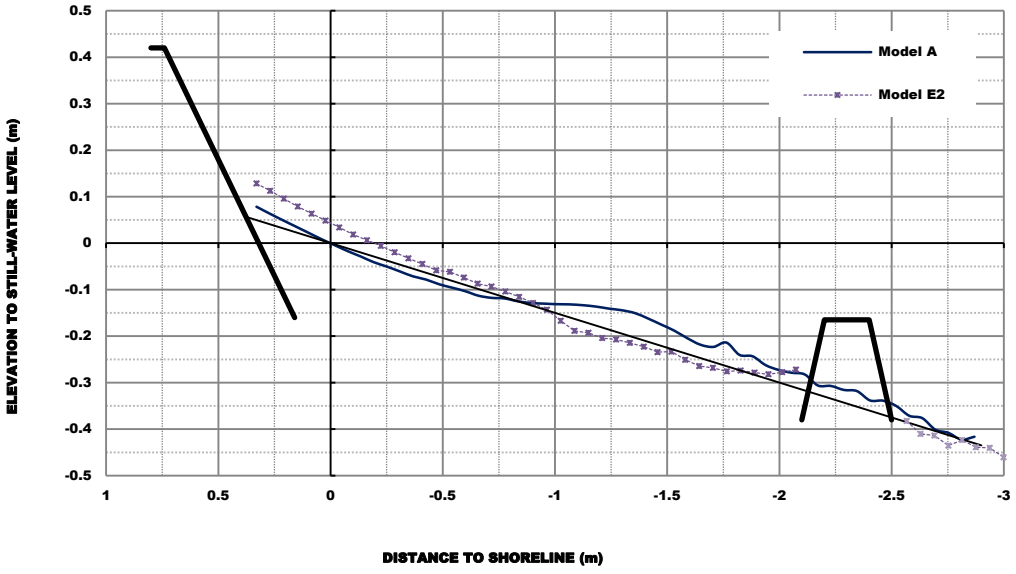

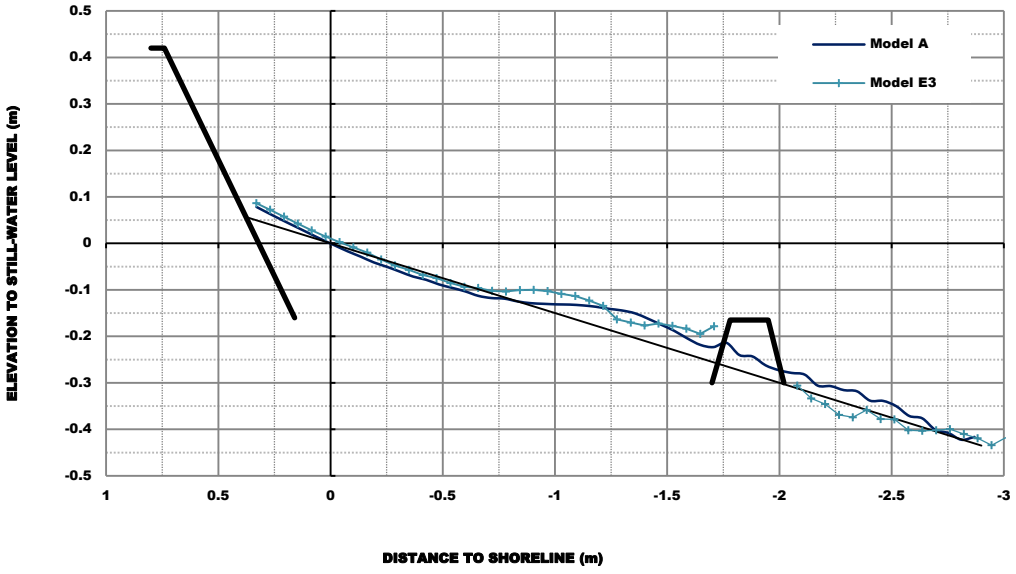

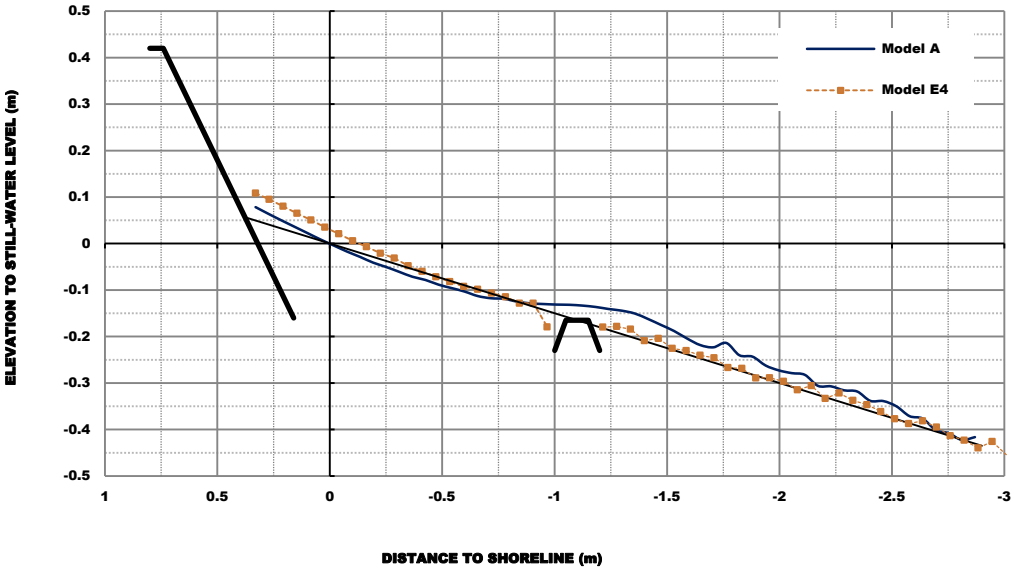

Figure 5.123: Initial and end beach-profiles: sea-state 10 (H_s=0.125m, T_p=2.89s). The initial dune profile is identified and the location of the submerged nearshore detached-breakwaters is sketched.

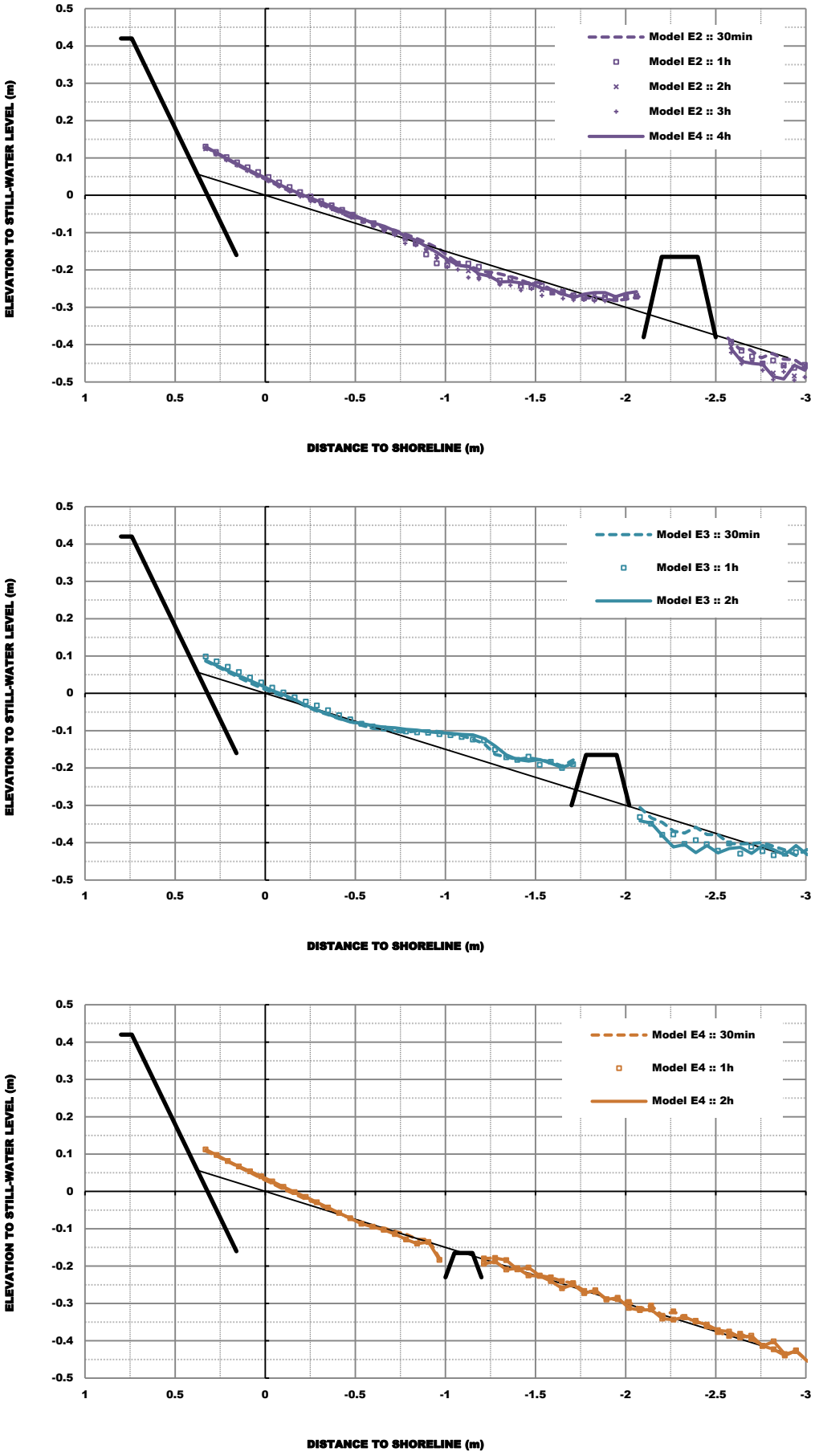

Figure 5.124: Initial and end beach-profiles: persistent erosional conditions. The initial dune profile is identified and the location of the submerged nearshore detached-breakwaters is sketched.

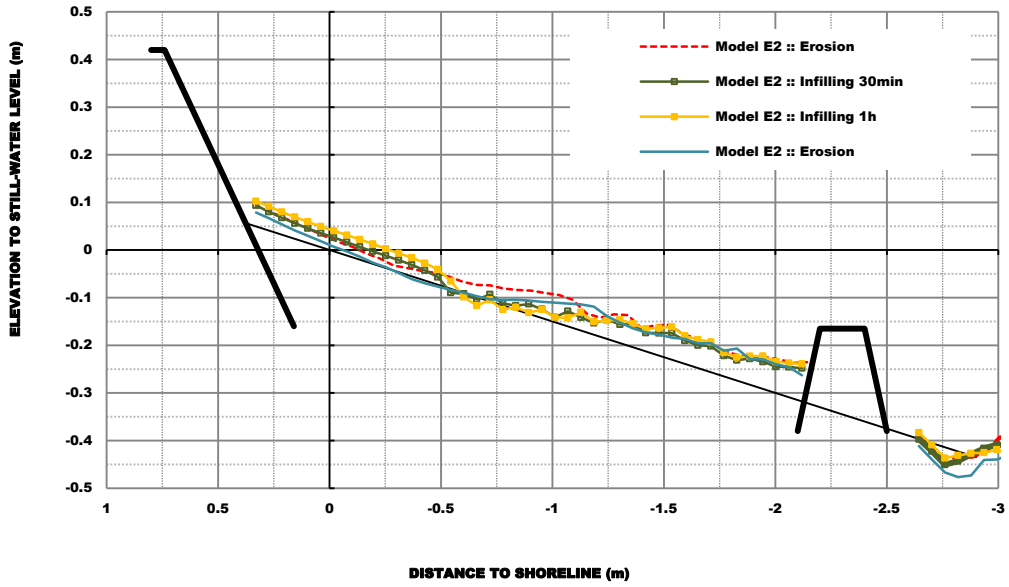

Figure 5.125: Initial and end beach-profiles: accretionary followed by erosional conditions. The initial dune profile is identified and the location of the submerged nearshore detached-breakwaters is sketched.

The results for run-segments with persistent erosional conditions, sea-state 10 (Figure 5.124) and with accretionary waves, sea-state 3, followed by erosional ones, sea-state 8 (Figure 5.125) revealed that the beach morphology at the leeside of the structure has become arrested (*i.e.*, change is very insignificant) under constant wave-height, while at the seaward side the scour hole have deepened from the initial to the end beach-profile.

5.5.2. Volumetric changes

In this paragraph, erosional wave-induced morphodynamic output with respect to sediment displacement between the initial to the end beach-profiles is evaluated *per* test cluster with the following objectives *(i)* understand the lowering of the beach in front of the protection structures; *(ii)* examine the main differences produced by each protection scheme; and *(iii)* examine the equilibrium bar/trough features, which will be discussed more fully in section 5.6. For each test cluster volumetric changes, including *(i)* erosion/accretion volumes, *(ii)* shoreline retreat/advance, and *(iii)* bar/trough formation and maintenance, are briefly discussed in regard to the profile measurements.

Tables 5.XXIII to 5.XXV summarize the computed erosion/accretion volumes, the shoreline retreat/advance, and the offshore distance and elevation of the nearshore bar in post-storm profiles. The results are ranked in accordance to Table 5.I.

The cumulative volumes of material displaced between the initial to the end beach-profiles are refer to as volume lost (erosion) or volume gained (accretion) from the pre-storm to the post-storm profiles. The net volume changes are the differences between the total volumes lost and gained at the baseline (*i.e.*, the initial plane beach-profile is the main reference in all cases) during a storm from zero (initial profile) or from an antecedent morphology. The sign of net volume is positive for a volume gained, otherwise is negative. The shoreline position indicates how much the shoreline retreat or advance during a storm. The sign of shoreline position is positive for a seaward translation.

The offshore distance from the final line-up of the shoreline to the highest vertical elevation of the nearshore-bar at the baseline is the distance to shoreline in Tables 5.XXIII to 5.XXV; such vertical elevation is given in the tables as well.

Table 5.XXIII: Computed volumetric changes under sequences of erosional waves.

Test ID	Volume Change [m^3/m]			Shoreline Position [m]	Nearshore-bar	
	Gain	Loss	Net		Distance to Shoreline [m]	Elevation [m]
Test_A_7_20100409	0.127	0.040	+0.087	-0.25	2.00	0.10
Test_B1_7_20091031	-	-	-	-	-	-
Test_B2_7_20100323	0.084	0.070	+0.014	-0.32	2.10	0.08
Test_C1_7_20100427	0.076	0.078	-0.002	-0.32	1.90	0.07
Test_C2_7_20100503	0.079	0.071	+0.008	-0.32	2.20	0.08
Test_D1_7_20100512	0.074	0.069	+0.005	-0.32	1.90	0.07
Test_D2_7_20100518	0.088	0.078	+0.010	-0.32	2.20	0.10
Test_E2_7_20100524	0.088	0.011	+0.077	-0.02	1.05	0.08
Test_A_8_20100405	0.131	0.055	+0.076	-0.31	2.45	0.11
Test_B1_8_20100105	0.077	0.073	+0.004	-0.32	1.85	0.06
Test_B2_8_20100325	0.078	0.076	+0.002	-0.32	2.05	0.06
Test_C1_8_20100428	0.064	0.066	-0.002	-0.32	1.80	0.05
Test_C2_8_20100504	0.072	0.071	+0.001	-0.32	2.05	0.06
Test_D1_8_20100510	0.070	0.068	+0.002	-0.32	1.90	0.06
Test_D2_8_20100517	0.077	0.074	+0.003	-0.32	2.00	0.06
Test_E2_8_20100522	0.115	0.005	+0.110	+0.13	0.90	0.06
Test_E3_8_20100526	0.119	0.025	+0.094	-0.18	1.95	0.11
Test_E4_8_20100525	0.135	0.003	+0.132	+0.01	1.95	0.10
Test_A_9_20100413	0.114	0.020	+0.094	-0.09	1.90	0.09
Test_B1_9_20100106	0.050	0.052	-0.002	-0.32	1.70	0.05
Test_B2_9_20100329	0.046	0.061	-0.015	-0.32	1.80	0.05
Test_C1_9_20100426	0.015	0.068	-0.053	-0.32	1.80	0.03
Test_C2_9_20100505	0.059	0.051	+0.008	-0.32	1.80	0.06
Test_D1_9_20100511	0.026	0.050	-0.024	-0.32	1.60	0.04
Test_D2_9_20100518	0.035	0.063	-0.028	-0.32	1.80	0.04
Test_E2_9_20100524	0.087	0.006	+0.081	+0.15	0.98	0.05
Test_E3_9_20100526	0.084	-	+0.084	+0.07	1.30	0.06
Test_E4_9_20100525	0.093	0.014	+0.079	-	1.70	0.09
Test_A_10_20100331	0.064	0.009	+0.055	-	1.35	0.05
Test_B1_10_20100112	0.026	0.047	-0.021	-0.32	1.60	0.03
Test_B2_10_20100210	-	-	-	-	-	-
Test_C1_10_20100420	0.041	0.040	+0.001	-0.32	1.60	0.03
Test_C2_10_20100429	0.025	0.034	-0.009	-0.32	1.55	0.03
Test_D1_10_20100511	0.029	0.027	+0.002	-0.32	1.30	0.04
Test_D2_10_20100515	0.017	0.027	-0.010	-0.32	1.40	0.02
Test_E2_10_20100521	0.045	0.023	+0.022	+0.19	-	-
Test_E3_10_20100526	0.050	0.009	+0.041	+0.05	1.10	0.05
Test_E4_10_20100525	0.034	0.004	+0.030	+0.13	-	-

Table 5.XXIV: Computed volumetric changes under persistent erosional conditions.

Test ID	Volume Change [m^3/m]			Shoreline Position [m]	Nearshore-bar	
	Gain	Loss	Net		Distance to Shoreline [m]	Elevation [m]
Test_A_10_1h_20100331	0.070	0.011	+0.059	-	1.30	0.04
Test_A_10_2h_20100331	0.081	0.018	+0.063	-0.05	1.35	0.05
Test_A_10_3h_20100331	0.080	0.025	+0.055	-0.07	1.40	0.04
Test_A_10_4h_20100401	0.080	0.035	+0.045	-0.11	1.50	0.04
Test_A_10_6h_20100401	0.067	0.043	+0.024	-0.15	-	-
Test_B1_10_1h_20100112	0.020	0.051	-0.031	-0.32	-	-
Test_B1_10_1.5h_20100112	0.020	0.055	-0.035	-0.32	-	-
Test_B1_10_2h_20100112	0.020	0.044	-0.024	-0.32	-	-
Test_B1_10_3h_20100114	0.014	0.056	-0.042	-0.32	-	-
Test_B1_10_4h_20100115	0.009	0.070	-0.061	-0.32	-	-
Test_B1_10_5h_20100115	0.008	0.085	-0.077	-0.32	-	-
Test_B1_10_6h_20100120	0.010	0.073	-0.063	-0.32	-	-
Test_B1_10_8h_20100120	0.009	0.095	-0.086	-0.32	-	-
Test_B1_10_10h_20100120	0.005	0.118	-0.113	-0.32	-	-
Test_C1_10_1h_20100420	0.038	0.041	-0.003	-0.32	1.50	0.02
Test_C1_10_2h_20100420	0.046	0.043	+0.003	-0.32	1.50	0.03
Test_C1_10_3h_20100420	0.038	0.048	-0.010	-0.32	-	-
Test_C1_10_4h_20100420	0.041	0.046	-0.005	-0.32	-	-
Test_C1_10_6h_20100421	0.037	0.063	-0.026	-0.32	-	-
Test_C1_10_8h_20100421	0.042	0.072	-0.030	-0.32	-	-
Test_C1_10_9h_20100421	0.037	0.079	-0.042	-0.32	-	-
Test_C2_10_1h_20100429	0.020	0.035	-0.015	-0.32	-	-
Test_C2_10_2h_20100429	0.014	0.045	-0.031	-0.32	-	-
Test_C2_10_3h_20100430	0.015	0.079	-0.064	-0.32	-	-
Test_C2_10_4h_20100430	0.025	0.064	-0.039	-0.32	-	-
Test_C2_10_6h_20100430	0.024	0.089	-0.065	-0.32	-	-
Test_C2_10_8h_20100430	0.019	0.132	-0.113	-0.32	-	-
Test_D1_10_1h_20100511	0.021	0.024	-0.003	-0.32	1.30	0.02
Test_D1_10_2h_20100511	0.029	0.031	-0.002	-0.32	1.30	0.02
Test_D1_10_3h_20100511	0.027	0.042	-0.015	-0.32	-	-
Test_D1_10_4h_20100511	0.025	0.062	-0.037	-0.32	-	-
Test_D1_10_6h_20100511	0.035	0.076	-0.041	-0.32	-	-
Test_D2_10_1h_20100515	0.043	0.021	+0.022	-0.32	1.40	0.02
Test_D2_10_2h_20100515	0.042	0.027	+0.015	-0.32	1.40	0.02
Test_D2_10_3h_20100516	0.010	0.067	-0.057	-0.32	-	-
Test_D2_10_4h_20100516	0.027	0.041	-0.014	-0.32	-	-
Test_D2_10_6h_20100516	0.016	0.068	-0.052	-0.32	-	-

Table 5.XXIV: Computed volumetric changes under persistent erosional conditions (cont.).

Test ID	Volume Change [m^3/m]			Shoreline Position [m]	Nearshore-bar	
	Gain	Loss	Net		Distance to Shoreline [m]	Elevation [m]
Test_E2_10_1h_20100521	0.050	0.032	+0.018	+0.24	-	-
Test_E2_10_2h_20100521	0.046	0.038	+0.012	+0.21	-	-
Test_E2_10_3h_20100522	0.058	0.041	+0.017	+0.18	-	-
Test_E2_10_4h_20100522	0.052	0.035	+0.017	+0.21	-	-
Test_E3_10_1h_20100526	0.092	0.023	+0.069	+0.11	1.10	0.06
Test_E3_10_2h_20100526	0.063	0.029	+0.034	+0.08	1.10	0.06
Test_E4_10_1h_20100525	0.034	0.011	+0.022	+0.15	-	-
Test_E4_10_2h_20100525	0.068	0.025	+0.043	+0.08	-	-

Table 5.XXV: Computed volumetric changes under sequences of accretionary waves followed by erosional ones.

Test ID	Volume Change [m^3/m]			Shoreline Position [m]	Nearshore-bar	
	Gain	Loss	Net		Distance to Shoreline [m]	Elevation [m]
Test_A_8_3a_20100405	0.122	0.058	+0.064	-0.21	2.50	0.12
Test_A_8_3b_20100406	0.130	0.048	+0.082	-0.15	2.45	0.11
Test_A_8_2x_20100406	0.153	0.066	+0.087	-0.32	2.50	0.12
Test_C1_8_3a_20100428	0.060	0.068	-0.008	-0.32	1.80	0.05
Test_C1_8_3b_20100428	0.062	0.061	+0.001	-0.27	1.80	0.05
Test_C1_8_2x_20100428	0.069	0.069	-	-0.32	1.80	0.05
Test_C2_8_3a_20100504	0.068	0.072	-0.004	-0.32	2.05	0.06
Test_C2_8_3b_20100504	0.049	0.082	-0.033	-0.32	2.05	0.05
Test_C2_8_2x_20100504	0.064	0.078	-0.014	-0.32	2.05	0.03
Test_D1_8_3a_20100510	0.089	0.061	+0.028	-0.32	1.90	0.07
Test_D1_8_3b_20100510	0.082	0.060	+0.022	-0.32	1.90	0.06
Test_D1_8_2x_20100510	0.084	0.064	+0.020	-0.32	1.90	0.05
Test_D2_8_3a_20100517	0.074	0.072	+0.002	-0.32	2.00	0.06
Test_D2_8_3b_20100517	0.069	0.070	-0.001	-0.32	2.00	0.05
Test_D2_8_2x_20100517	0.086	0.065	+0.021	-0.32	2.00	0.02
Test_E2_8_3a_20100524	0.095	0.001	+0.094	+0.18	-	-
Test_E2_8_3b_20100524	0.109	-	+0.109	+0.27	-	-
Test_E2_8_2x_20100524	0.082	0.012	+0.070	+0.06	1.10	0.06

Comparisons between the initial plane beach and the end measured profiles are presented in Figures 5.126 to 5.129 for the passive coastal defence structures, models B to D, variants 1 and 2. Figures 5.130 to 5.132 present the results for the active coastal defence structures, Model E, variants 2, 3, and 4.

Model A, the initial dune-beach system profile and a sketch location of the submerged nearshore detached - breakwaters are given as reference.

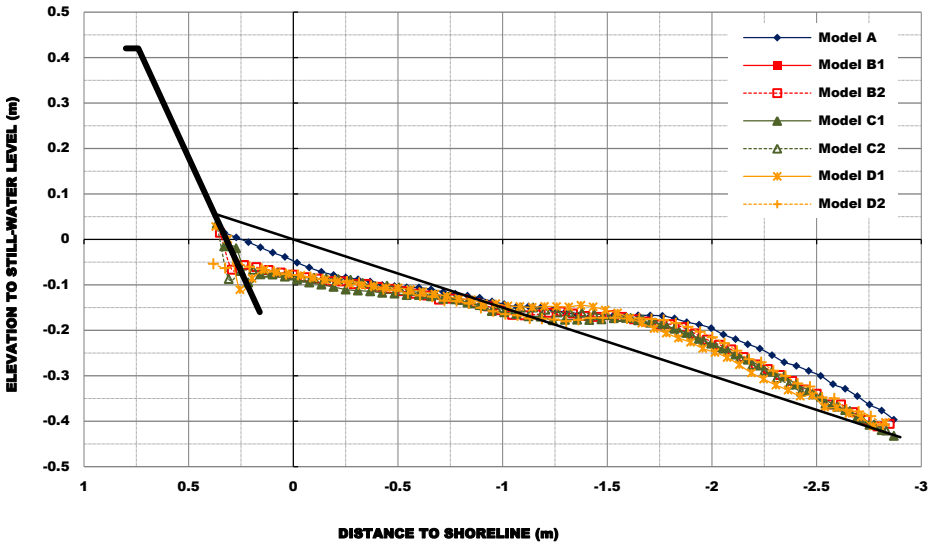

Figure 5.126: Comparison of initial and end beach profiles for sea-state 7 (H_s=2.0m, T_p=8s, in prototype).

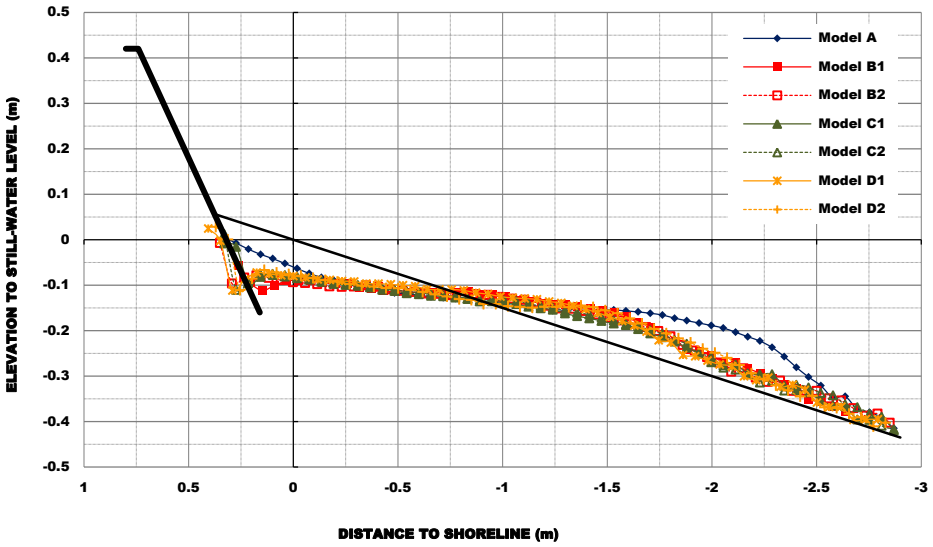

Figure 5.127: Comparison of initial and end beach profiles for sea-state 8 (H_s=2.0m, T_p=10s, in prototype).

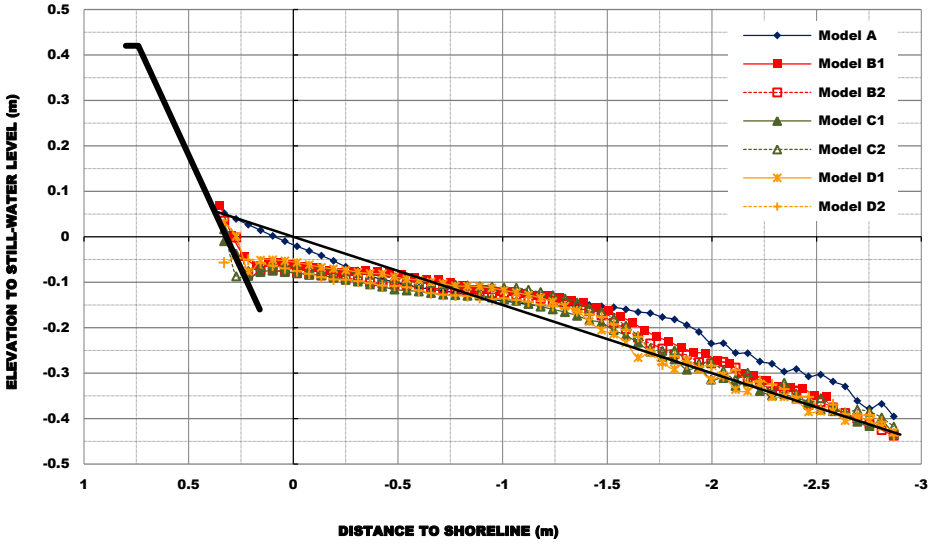

Figure 5.128: Comparison of initial and end beach profiles for sea-state 9 (H_s=2.0m, T_p=12s, in prototype).

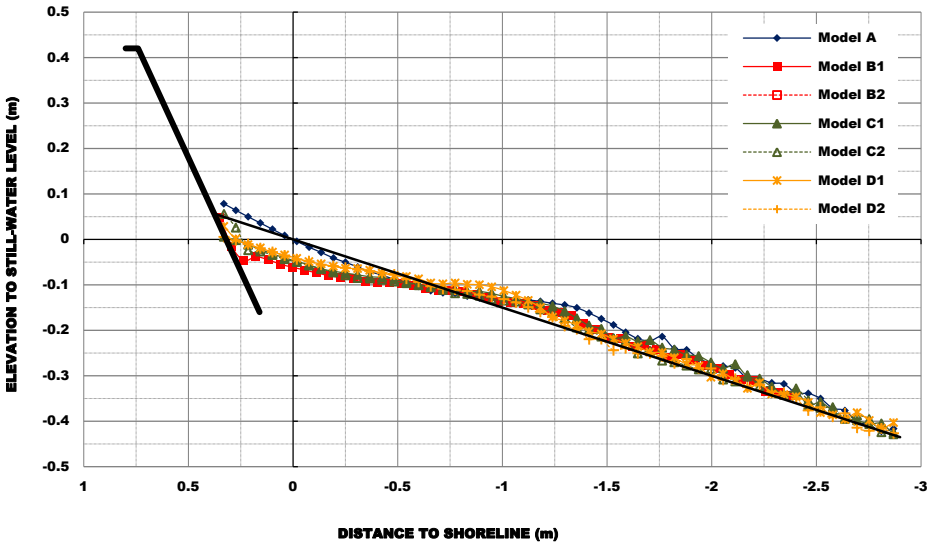

Figure 5.129: Comparison of initial and end beach profiles for sea-state 10 (H_s=1.5m, T_p=10s, in prototype).

Figure 5.126 and the following show that the beach-profile change is similar in the examined cases. The shoreline has retreat as far as the established structure (see also Table 5.XXIII) and a nearshore-bar has developed. The erosion in the vicinity of the shoreline roughly equalled the accumulation in the bar area, indicating that the sand was transported from the beach and deposited near the main breaker line; some of it was carried even farther offshore (*e.g.*, in the cases where the beach-profile was exposed to persistent erosional conditions).

The bar accumulation in the case of Model A is greater as compared to the other cases in analysis, especially during the higher waves; while the shoreline recession is much smaller. Although these may presumably be expected morphologic change given that the sands eroded from the dune would be transported to the beach, it is remarkably striking to realize that the net volume changes in Model A are substantively higher than in the other models which corroborates Dean's approximate principle, *i.e.* eroded volume is less than or equal to volume retained by the structure had it not been in place (see, *e.g.*, USACE, 2008). The distance of the bar to shoreline is similar between models but that distance is generally longer in variants 2.

It is clear from the preceding results and figures that there was a lowering of the beach levels around the various passive coastal protection schemes. Under persistent erosional conditions (even under constant wave-height) the beach level fall as low as the baseline across the entire profile as a result of a cross-shore profile migration; within which the sediments initially deposited at the lower beach face move further seaward, thereby extending the bar, with time a double bar along the beach-profile starts to develop, as sediments are moved offshore and a moderately deep trough starts to build-up.

The analysis of the computed volumetric changes, as given by Tables 5.XXIII to 5.XXV, reveal that the incidence of higher values of cumulative volume lost is in straight connection to the volume of sand deposited in the nearshore-bar. For instance, by comparing the net volume change between Test_C1_10_2h_20100420 and Test_C1_10_3h_20100420 or Test_D2_10_2h_20100515 and Test_D2_10_3h_20100516 is noticeable that those are lower when the bar disappears.

The tests with accretionary waves having a dissipative profile as antecedent morphology show that changing wave conditions (*i.e.*, in this case, wave-height decrease) may not always be capable of moving sand from the bar; moreover the recovery response of sediment flows takes longer. In nature, such lagged response of morphology to changing conditions may often result in sand being lost to the sea, as consequence of the hydrodynamic conditions not being capable of moving sand onshore or as a consequence of sand being driven away by the littoral drift current.

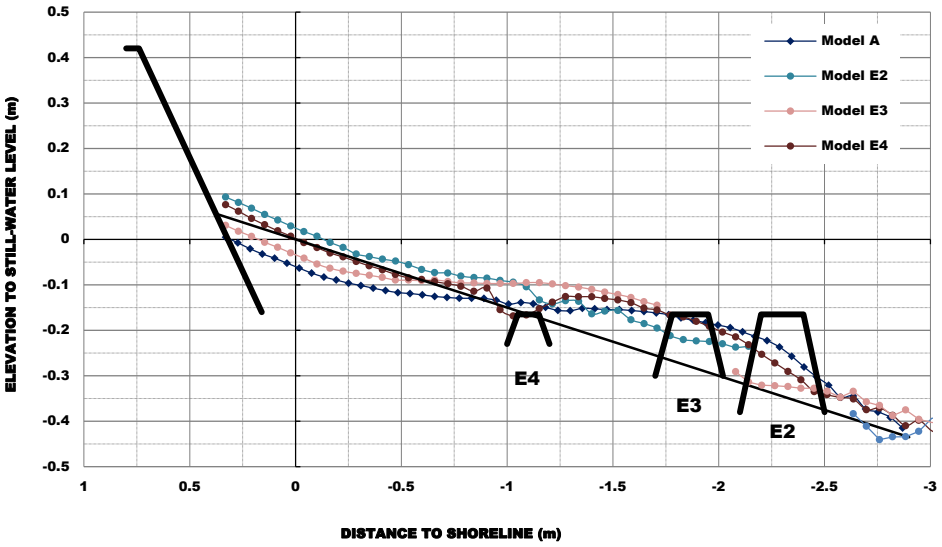

Figure 5.130: Comparison of initial and end beach profiles for sea-state 8 (H_s=2.0m, T_p=10s, in prototype).

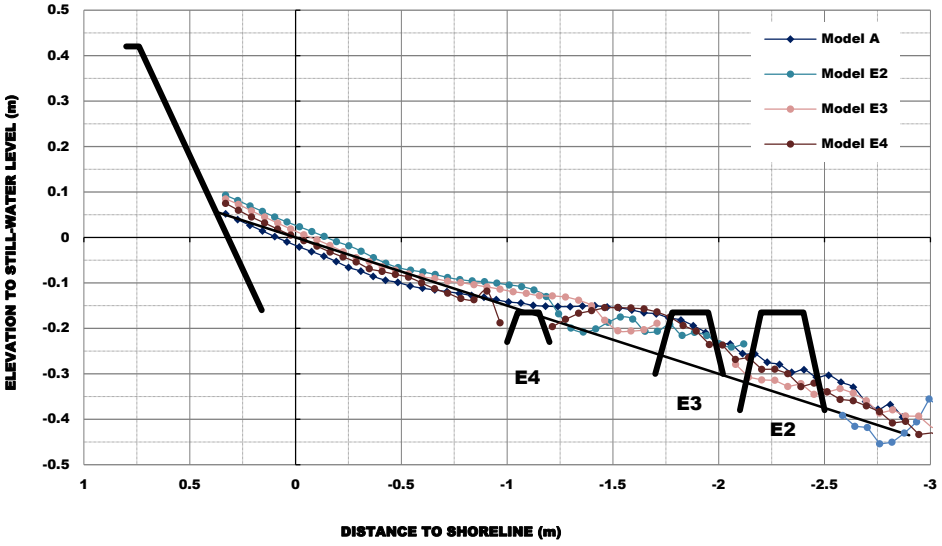

Figure 5.131: Comparison of initial and end beach profiles for sea-state 9 (H_s=2.0m, T_p=12s, in prototype).

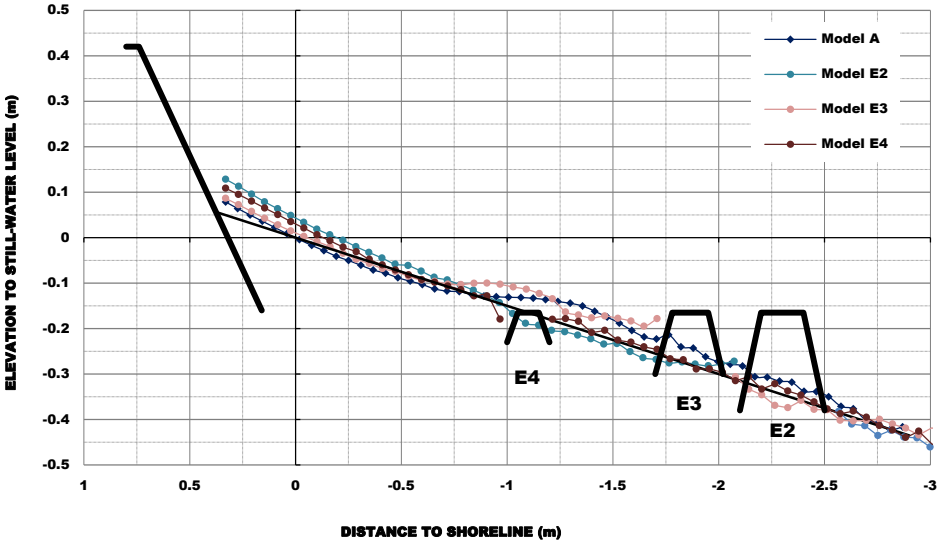

Figure 5.132: Comparison of initial and end beach profiles for sea-state 10 (H_s=1.5m, T_p=10s, in prototype).

Figures 5.130 to 5.132 show that in models E2 and E4 the main morphologic changes occur in the lower beach, whereas at the upper beach the end profile varies slightly from the initial one. Some moderate shoreline accretion is though observable in Model E2 wave run-segments; while in Model E4 the shoreline has progressed only under sea-state 10 (refer to Table 5.XXIII, and Figure 5.132).

In Model E2 there is significant sand deposition in the leeward side of the submerged breakwater, the source of which is the erosion in the dune. For the wave run-segments with higher wave heights a nearshore-bar has developed at approximately 1m from the initial shoreline (refer to the computed results shown in Table 5.XXIII). This morphologic change indicates a second breaker line, which ranges in elevation from 0.07 to 0.05m, and grows with decreasing significant wave-period (refer to Table 5.XXIII). Volume losses are only observed at the seaward side of the structure.

In Model E4 the nearshore-bar development has similar evolution as compare to Model A. Yet as the seaward transport from the beach is interrupted by the submerged sill, there is less erosion in the vicinity of the shoreline and less accumulation in the bar area (refer to Table 5.XXIII). Some localized erosion is observed around the sill, which will be discussed more fully in following paragraph.

There are some markedly differences in Model E3 end profile as compare to models E2 and E4. For instance, significant shoreline erosion is observable during sea-state 8 (Figure 5.130). In fact, under similar wave-run conditions, the beach-profile for Model E3 experienced an evolution similar to Model A. This is an expected morphologic change as the structure was placed within the main breaker line of Model A, and the structure crest level was placed at approximately the nearshore-bar level. Yet, the end-profiles in Model E3 differ from those in Model A at the seaward side of the structure where the beach-level are much lower.

5.5.3. Scour development

In this paragraph, the localized erosions at the base of the geotextile encapsulated sand-systems are evaluated *per* test cluster, with the following main objectives *(i)* examine mechanisms that produce scour; and *(ii)* examine the dependency between scour development and the non-dimensional variables as given by Eq. (3.91), this aspect will be discussed more fully in section 5.6. For each test cluster the ultimate maximum depth of the scouring, through *(i)* S_d (*i.e.* the scour depth at the structure), and *(ii)* S_d/H_s, the normalized scour depth, are discussed with regard to measurements with erosional waves.

Scour development and test conditions with respect to incident wave-conditions (H_s, T_p), reflection coefficient (K_r), deepwater wavelength (L_0), significant wave-height to wavelength ratio (H_0/L_0), and the surf similarity parameter (ξ, refer to Eq. [3.1]) are presented in Tables 5.XXVI to XXVIII. The incident waves used in the tests with erosional sequences had significant wave heights around 0.15 to 0.2m, with peak periods from 2.28 to 3.41s. The deepwater wave-length L_0 ranged from 8.1 to 18.2m. The wave steepnesses H_s/L_0 are from roughly 0.01 to 0.025, and the relative water depths d/L_0 from about 0.03 to 0.07 (not included in the table). Moreover, it has been seen before in Chapter 3 that other than the previous, the governing non-dimensional variables that may be responsible for the scour processes should be (see, *e.g.*, Sumer and FredsØe, 2002), the water depth at the structure to deepwater wave-height ratio (d_w/L_0), distance of the structure to deepwater wavelength (x/d_w), and penetration of the breaker down to the bed ($T\sqrt{gH_b}/h_w$).

For the tests with erosional waves the scour depth at the structure is evaluated against the deepwater wave characteristics (H_0, L_0), while the normalized scour depth is evaluated against each one of the former non-dimensional variables. For the tests with persistent erosional conditions and erosion followed by infilling, the maximum scour depth evolution is evaluated against the time scale. In addition, the scour and deposition patterns are examined to determine which mechanisms are likely to cause localized erosions around the structures and estimate the distance at which the maximum scour-depth is likely to occur.

Table 5.XXVI: Scour development under sequences of erosional waves.

Test ID	Incident		K_r	L_0 [m]	$\frac{H_s}{L_0}$	ξ	S_d [m]	$\frac{S_d}{H_s}$
	H_s [m]	T_p [s]						
Test_B1_7_20091031	0.177	2.28	0.297	8.1	0.0218	1.016	-	-
Test_B2_7_20100323	0.186		0.326		0.0229	0.991	0.111	0.594
Test_C1_7_20100427	0.193		0.287		0.0238	0.973	0.127	0.659
Test_C2_7_20100503	0.202		0.295		0.0249	0.951	0.128	0.634
Test_D1_7_20100512	0.196		0.284		0.0241	0.965	0.143	0.729
Test_D2_7_20100518	0.194		0.276		0.0239	0.970	0.104	0.536
Test_E2_7_20100524	0.190		0.433		0.0234	0.980	0.032	0.168
Test_B1_8_20100105	0.204	2.84	0.353	12.6	0.0162	1.179	0.111	0.544
Test_B2_8_20100325	0.228		0.360		0.0181	1.115	0.140	0.615
Test_C1_8_20100428	0.193		0.345		0.0153	1.212	0.128	0.665
Test_C2_8_20100504	0.195		0.342		0.0155	1.205	0.151	0.776
Test_D1_8_20100510	0.204		0.305		0.0162	1.179	0.144	0.707
Test_D2_8_20100517	0.201		0.330		0.0160	1.187	0.125	0.623
Test_E2_8_20100522	0.198		0.410		0.0157	1.196	0.026	0.134
Test_E3_8_20100526	0.196		0.415		0.0156	1.202	0.039	0.200
Test_E4_8_20100525	0.197		0.404		0.0156	1.199	0.014	0.072
Test_B1_9_20100106	0.213	3.41	0.417	18.2	0.0117	1.385	0.089	0.418
Test_B2_9_20100329	0.185		0.338		0.0102	1.486	0.115	0.623
Test_C1_9_20100426	0.193		0.391		0.0106	1.455	0.118	0.613
Test_C2_9_20100505	0.196		0.378		0.0108	1.444	0.128	0.653
Test_D1_9_20100511	0.192		0.366		0.0106	1.459	0.108	0.564
Test_D2_9_20100518	0.198		0.380		0.0109	1.436	0.106	0.538
Test_E2_9_20100524	0.195		0.489		0.0107	1.447	0.040	0.205
Test_E3_9_20100526	0.202		0.484		0.0111	1.422	-	-
Test_E4_9_20100525	0.200		0.466		0.0110	1.429	0.050	0.251
Test_B1_10_20100112	0.150	2.84	0.380	12.6	0.0119	1.374	0.081	0.540
Test_B2_10_20100210	0.133		0.416		0.0106	1.460	0.095	0.714
Test_C1_10_20100420	0.150		0.391		0.0119	1.374	0.047	0.312
Test_C2_10_20100429	0.147		0.390		0.0117	1.388	0.056	0.381
Test_D1_10_20100511	0.154		0.336		0.0122	1.356	0.044	0.284
Test_D2_10_20100515	0.174		0.344		0.0138	1.276	0.044	0.254
Test_E2_10_20100521	0.153		0.452		0.0121	1.361	0.026	0.167
Test_E3_10_20100526	0.150		0.472		0.0119	1.374	0.029	0.194
Test_E4_10_20100525	0.151		0.459		0.0120	1.370	0.046	0.303

Table 5.XXVII: Scour development under persistent erosional conditions.

Test ID	Incident		K_r	L_0 [m]	$\frac{H_s}{L_0}$	ξ	S_d [m]	$\frac{S_d}{H_s}$
	H_s [m]	T_p [s]						
Test_B1_10_1h_20100112	0.149	2.84	0.337	12.6	0.0118	1.379	0.075	0.506
Test_B1_10_1.5h_20100112	0.153		0.336		0.0121	1.361	0.082	0.533
Test_B1_10_2h_20100112	0.153		0.334		0.0121	1.361	0.067	0.440
Test_B1_10_3h_20100114	0.148		0.351		0.0118	1.384	0.091	0.614
Test_B1_10_4h_20100115	0.153		0.367		0.0121	1.361	0.092	0.603
Test_B1_10_5h_20100115	0.149		0.363		0.0118	1.379	0.088	0.592
Test_B1_10_6h_20100120	0.150		0.361		0.0119	1.374	0.091	0.604
Test_B1_10_8h_20100120	0.151		0.360		0.0120	1.370	0.097	0.644
Test_B1_10_10h_20100120	0.152		0.379		0.0121	1.365	0.102	0.670
Test_B2_10_1h_20100210	0.130	2.84	0.386	12.6	0.0103	1.476	0.083	0.637
Test_B2_10_2h_20100210	0.141		0.356		0.0112	1.418	0.091	0.646
Test_B2_10_3h_20100212	0.153		0.350		0.0121	1.361	0.111	0.727
Test_B2_10_4h_20100212	0.150		0.367		0.0119	1.374	0.107	0.713
Test_B2_10_4h_8_20100212	0.196		0.336		0.0156	1.202	0.182	0.928
Test_C1_10_1h_20100420	0.148	2.84	0.347	12.6	0.0118	1.384	0.047	0.319
Test_C1_10_2h_20100420	0.152		0.348		0.0121	1.365	0.053	0.352
Test_C1_10_3h_20100420	0.152		0.350		0.0121	1.365	0.060	0.395
Test_C1_10_4h_20100420	0.152		0.356		0.0121	1.365	0.059	0.389
Test_C1_10_6h_20100421	0.153		0.353		0.0121	1.361	0.061	0.398
Test_C1_10_8h_20100421	0.155		0.357		0.0123	1.352	0.092	0.597
Test_C1_10_9h_20100421	0.151		0.384		0.0120	1.370	0.081	0.539
Test_C2_10_1h_20100429	0.141	2.84	0.390	12.6	0.0112	1.418	0.055	0.391
Test_C2_10_2h_20100429	0.148		0.361		0.0118	1.384	0.066	0.445
Test_C2_10_3h_20100430	0.150		0.354		0.0119	1.374	0.092	0.611
Test_C2_10_4h_20100430	0.150		0.356		0.0119	1.374	0.086	0.575
Test_C2_10_6h_20100430	0.148		0.375		0.0118	1.384	0.099	0.670
Test_C2_10_8h_20100430	0.151		0.359		0.0120	1.370	0.138	0.911
Test_D1_10_1h_20100511	0.152	2.84	0.324	12.6	0.0148	1.231	0.033	0.175
Test_D1_10_2h_20100511	0.155		0.323		0.0153	1.212	0.046	0.240
Test_D1_10_3h_20100511	0.156		0.327		0.0124	1.348	0.067	0.431
Test_D1_10_4h_20100511	0.156		0.333		0.0126	1.335	0.056	0.352
Test_D1_10_6h_20100511	0.155		0.353		0.0127	1.331	0.078	0.490
Test_D2_10_1h_20100515	0.187	2.84	0.359	12.6	0.0121	1.365	0.036	0.235
Test_D2_10_2h_20100515	0.193		0.355		0.0123	1.352	0.046	0.296
Test_D2_10_3h_20100516	0.156		0.325		0.0124	1.348	0.050	0.319
Test_D2_10_4h_20100516	0.159		0.323		0.0124	1.348	0.055	0.351
Test_D2_10_6h_20100516	0.160		0.323		0.0123	1.352	0.082	0.532

Table 5.XXVII: Scour development under persistent erosional conditions (cont.).

Test ID	Incident		K_r	L_0 [m]	$\frac{H_s}{L_0}$	ξ	S_d [m]	$\frac{S_d}{H_s}$
	H_s [m]	T_p [s]						
Test_E2_10_1h_20100521	0.151	2.84	0.452	12.6	0.0120	1.370	0.040	0.263
Test_E2_10_2h_20100521	0.154		0.445		0.0122	1.356	0.053	0.346
Test_E2_10_3h_20100522	0.141		0.460		0.0112	1.418	0.071	0.503
Test_E2_10_4h_20100522	0.152		0.447		0.0121	1.365	0.063	0.414
Test_E3_10_1h_20100526	0.149	2.84	0.456	12.6	0.0118	1.379	0.054	0.364
Test_E3_10_2h_20100526	0.152		0.446		0.0121	1.365	0.071	0.470
Test_E4_10_1h_20100525	0.149	2.84	0.430	12.6	0.0118	1.379	0.056	0.376
Test_E4_10_2h_20100525	0.151		0.424		0.0120	1.370	0.065	0.431

Table 5.XXVIII: Scour development under sequences of accretionary waves followed by erosional ones.

Test ID	Incident		K_r	L_0 [m]	$\frac{H_s}{L_0}$	ξ	S_d [m]	$\frac{S_d}{H_s}$
	H_s [m]	T_p [s]						
Test_C1_8_3a_20100428	0.050	2.84	0.514	12.6	0.0040	2.381	0.081	1.622
Test_C1_8_3b_20100428	0.051		0.604		0.0040	2.357	0.070	1.377
Test_C1_8_2x_20100428	0.196		0.344		0.0156	1.202	0.129	0.656
Test_C2_8_3a_20100504	0.049	2.84	0.480	12.6	0.0039	2.405	0.110	2.254
Test_C2_8_3b_20100504	0.050		0.516		0.0040	2.381	0.092	1.849
Test_C2_8_2x_20100504	0.193		0.336		0.0153	1.212	0.160	0.828
Test_D1_8_3a_20100510	0.051	2.84	0.486	12.6	0.0040	2.357	0.132	2.595
Test_D1_8_3b_20100510	0.052		0.513		0.0041	2.334	0.132	2.545
Test_D1_8_2x_20100510	0.196		0.330		0.0156	1.202	0.113	0.576
Test_D2_8_3a_20100517	0.052	2.84	0.491	12.6	0.0041	2.334	0.091	1.756
Test_D2_8_3b_20100517	0.052		0.583		0.0041	2.334	0.091	1.756
Test_D2_8_2x_20100517	0.198		0.316		0.0157	1.196	0.084	0.424
Test_E2_8_3a_20100524	0.052	2.84	0.660	12.6	0.0041	2.334	0.036	0.701
Test_E2_8_3b_20100524	0.050		0.552		0.0040	2.381	0.023	0.451
Test_E2_8_2x_20100524	0.191		0.404		0.0152	1.218	0.054	0.281

Figure 5.133 is the plot of the scour depth variation *per* incident significant wave-height and *per* deepwater wavelength, for each model and variant, when exposed to erosional waves. The dashed lines in the left panel of the figure are reference limits of scour to wave-height ratio equal to one, and maximum scour depth in the passive and active coastal protection schemes. In regard to the variation with incident wave-height the results show that the scour depth is less than the incident wave-height, thereby supporting the most widely used rule-of-thumb (*i.e.*, the maximum scour depth will be less than or equal to the incident unbroken wave-height). It is also seen that the maximum scour depth under erosional waves is approximately less than 80% and 30% the incident wave-height for the passive and active erosion control systems, accordingly. Within the active structures Model E4 is the one evidencing the higher scour depths, likely due wave breaking just in front of the structure (refer to Figure 5.98).

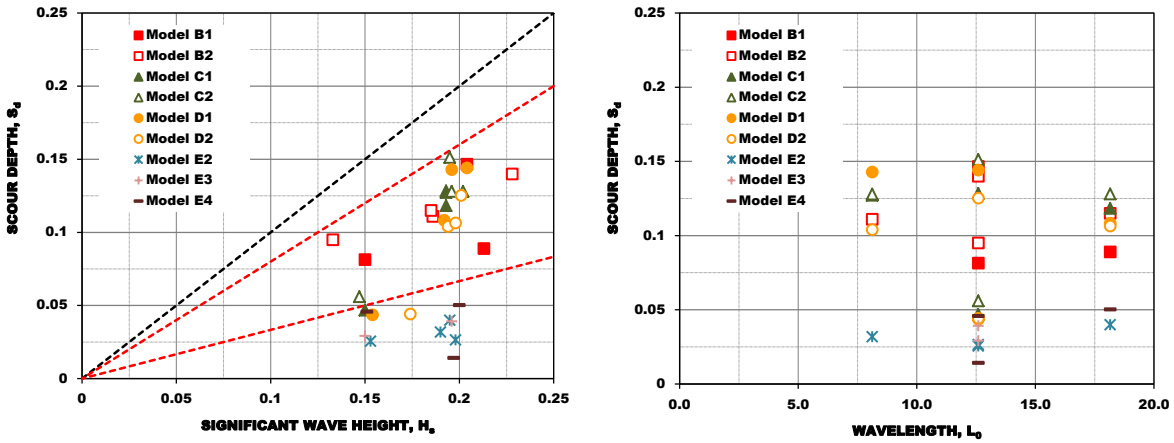

Figure 5.133: Scour depth against deepwater wave characteristics, significant wave-height (left panel) and wavelength (right panel).

Following in Figure 5.134, the normalized scour depth is set against the non-dimensional variables wave steepness (left top panel), surf similarity parameter (right top panel), water depth at the structure to deepwater wavelength ratio (left middle panel), distance of the structure to deepwater wavelength ratio (right middle panel), reflection coefficient (left bottom panel), and penetration of the breaker down to the bed (right bottom panel). The distance x (refer to Figure 3.37) was estimated from the breaking criteria which states that the maximum unbroken wave-height to water depth ratio is less than or equal to 0.78 (see, *e.g.*, Kamphuis, 2000), it should be noted, though, that it is a rough calculation because the experiments were conducted under irregular waves and therefore the breaker line is in fact a wider region. The water depth at the structure, d_w, was taken equal to -0.08m in models B to D and 0.165m in Model E.

The results indicate that under the most energetic sea-states (*i.e.*, 7, 8 and 9) the normalized scour depth at models B to D typically increased as the steepness of the incoming wave increased, but decreased with an increase in the water depth at the structure (*i.e.*, Model E). It is also seen that for models B to D the normalized scour depth generally increased with increase of the surf similarity parameter. In regard to water depth at the structure to deepwater wavelength ratio, the scour depth generally increased with decrease in that ratio, whereas it decreased with distance to deepwater wavelength. Further it decreased with decrease in the reflection coefficient, but increased with an increase in incident wave-height (*i.e.*, is lower for sea-state 10 as compared to sea-states 7, 8, and 9) and decreased with an increase in the water depth at the structure.

Scatter is observed in the variant 1 of Model B for tests with sea-states 9, and 10, and in variant 2 for tests with sea-state 10. The reason for that scatter in Model B1 is unclear but could have resulted from transient backfilled (*i.e.*, the maximum depth may not be apparent at the end of the wave run-segment). In regard to the scatter in Test_B2_10_20100210 it could be an effect of the lower incident wave-height with the corresponding increase in the reflection coefficient.

Overall, the results from the laboratory measurements point out that the maximum scour depth under erosional waves decreased with an increase in the water depth at the structure (*i.e.*, is lower in Model E) but increased with waves breaking near the toe of the structure (Model E4). They also indicate that the scour depth is influenced by the mechanisms of wave reflection off the structure and wave downrush flow on the exposed slope.

For the tests with persistent erosional conditions and erosion followed by infilling, an assumption that the previous mechanisms remain prevalent is made and thus the maximum scour depth evolution is evaluated only against the time scale. Figures 5.135 and 5.136 plot the data measurements on time development of scour depth under persistent erosional conditions, and infilling followed by erosion, accordingly.

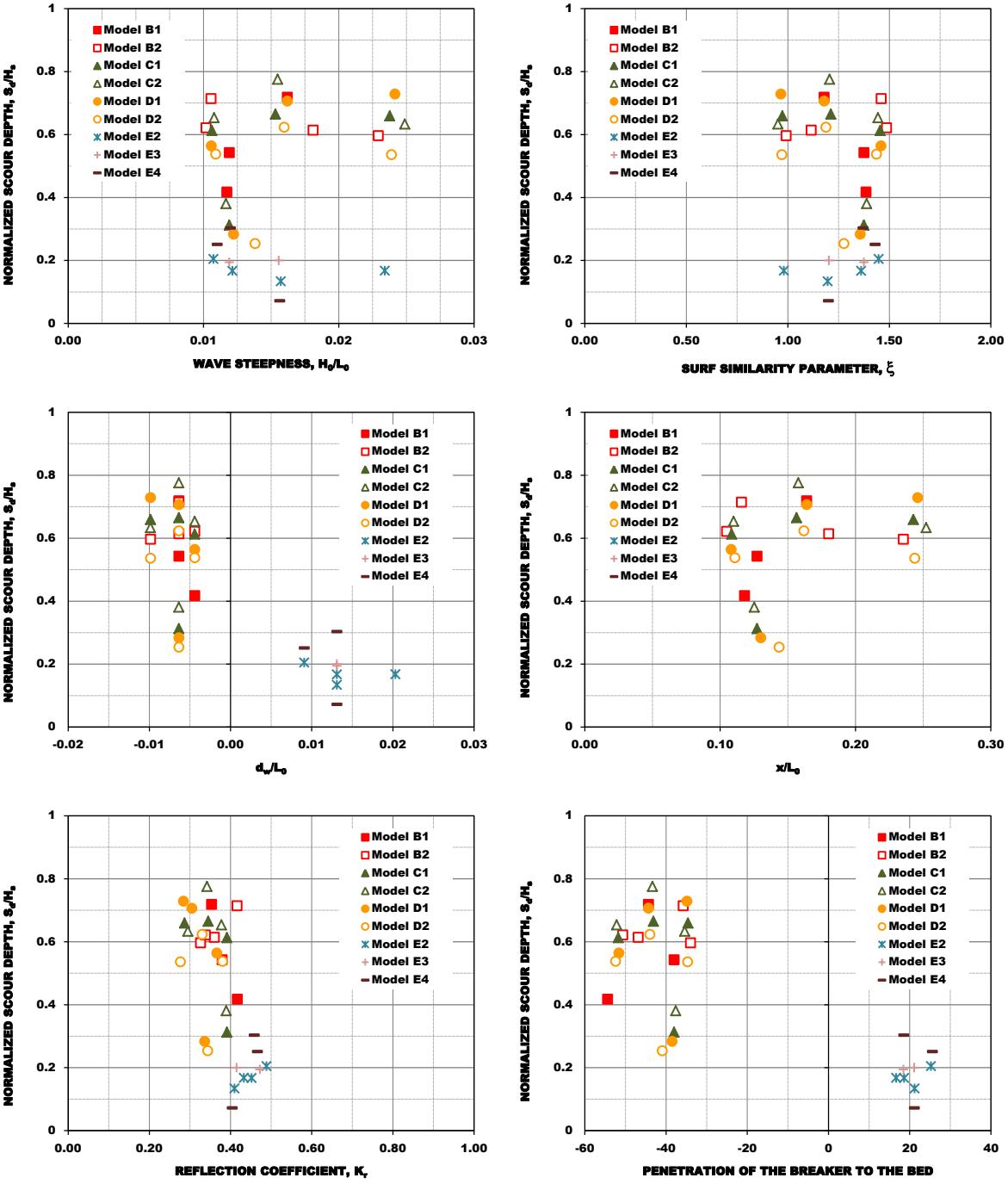

Figure 5.134: Normalized scour depth against non-dimensional variables.

Scour development towards equilibrium is typically described by an initial transitional period, in which there is a substantial amount of scour, followed by an equilibrium stage (see, *e.g.*, Sumer and FredsØe, 2002). Such a description is only seen fairly in the data from the laboratory measurements. As illustrated in Figure 5.135, scour depth increased over the whole duration of the test series (although with episodic decrease, *i.e.*, with backfill); yet it increased rapidly during the first wave run-segment to which followed a moderate (linear trended) increase for models B to D, while for Model E scour depth continued increasing over the whole test series at about the same rate as the first wave run-segment.

Across models, some interesting remarks can be made with respect to scour depth. The first one is that the scour depth experienced by variants 1 are less or equal to that in variants 2. Secondly, Model D experienced less scour when compared to models B and C.

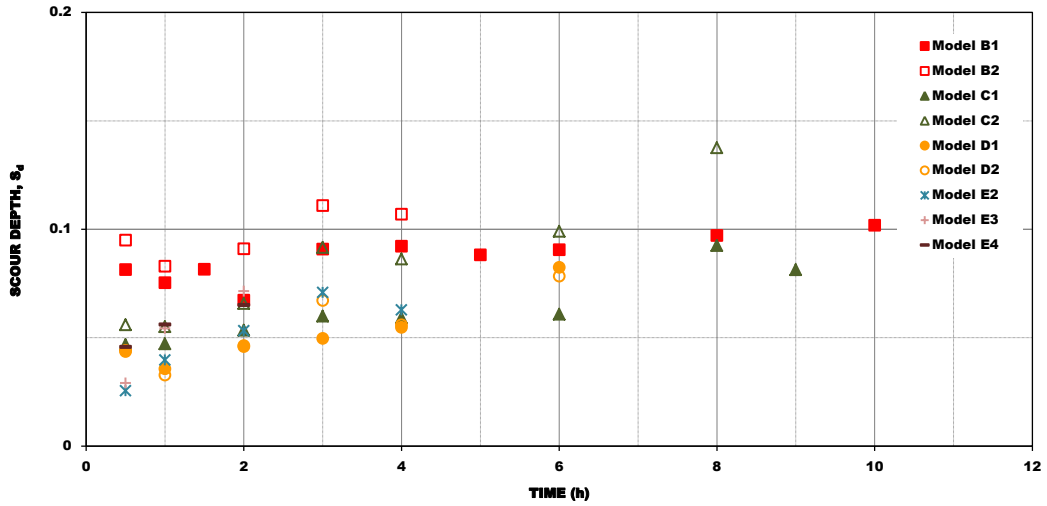

Figure 5.135: Scour depth *vs.* time, persistent erosional conditions.

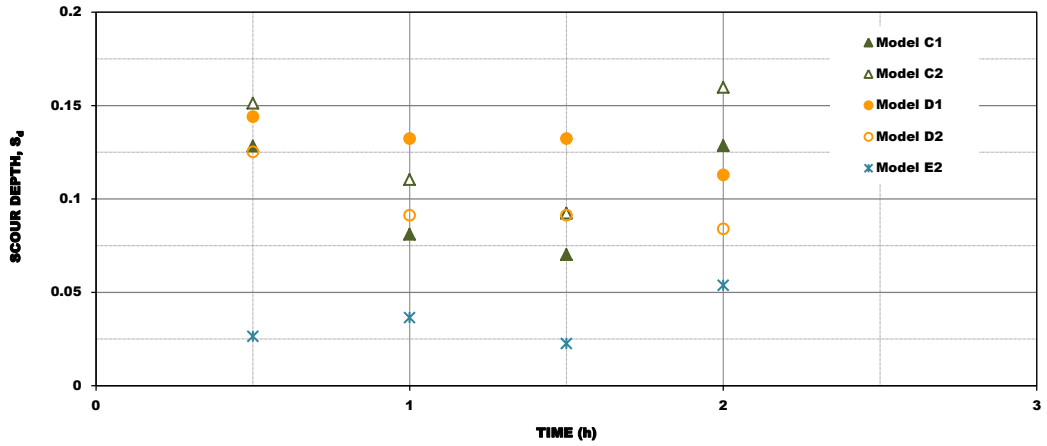

Figure 5.136: Scour depth *vs.* time, infilling followed by erosion.

The tests with erosional waves, followed by accretionary, and again erosional, aim to increase understanding on the changes in beach-profile shape caused by changes in forcing wave conditions. The results indicate that, at the end of the first wave run-segment with erosional waves, the scour depth was larger in models D1 and C2 and identical in models C1 and D2. After the first wave run-segment the scour depth decreased across all models, being more expressive in Model C and in variant 2 of Model D. With continued accretionary waves the scour maintained depth in Model D and backfilled in Model C. When waves rise again the scour depth increased in Model C to approximately the same level as observed at the end of the first run in variant 1 and to a lower level in variant 2, while it decreased in Model D. Again the rise of the beach level at the end of the second wave run-segment with accretionary waves could have resulted from transient backfilled; yet it may also be an indication that scour is controlled not only by forcing wave conditions (provided that these are sufficient to mobilize sediment) but also by the bed and water levels at the structure during the period of higher energy forcing.

Close-ups of the beach levels around the structures are presented in Figures 5.137 to 5.140 for models B to D and Figures 5.141 to 5.143 for Model E, to show where scour is developing. Initial position of the shoreline and a sketch location of the structure are given as reference. As can be observed, the scour hole which develops close to the dune reinforcement is consistent with an erosion caused by a downrush flow (refer to Figures 3.53 and 3.54), while the maximum scour depth around the submerged structures seems to be induced by a downrush flow in Model E2 and by a plunger breaker in models E3 and E4.

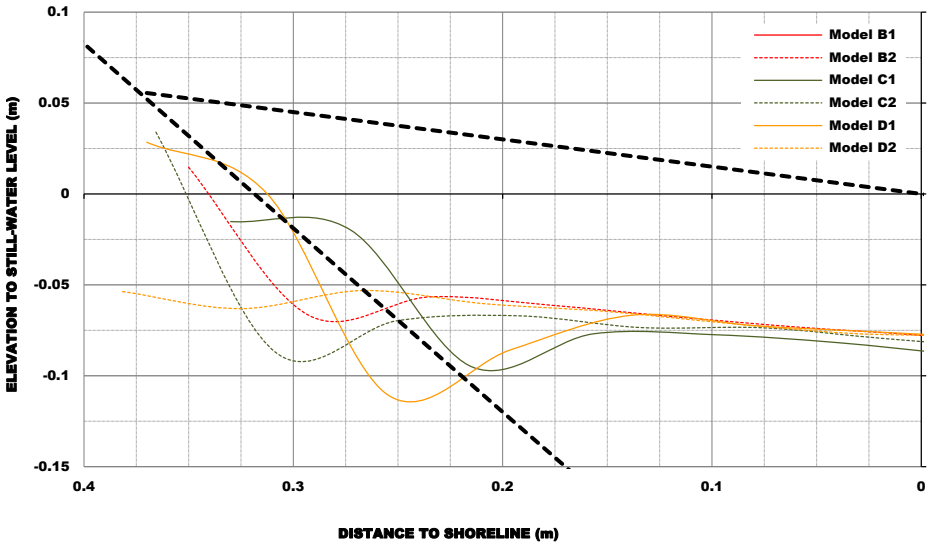

Figure 5.137: Scour patterns around dune reinforcement for sea-state 7 (H_s=2.0m, T_p=8s, in prototype).

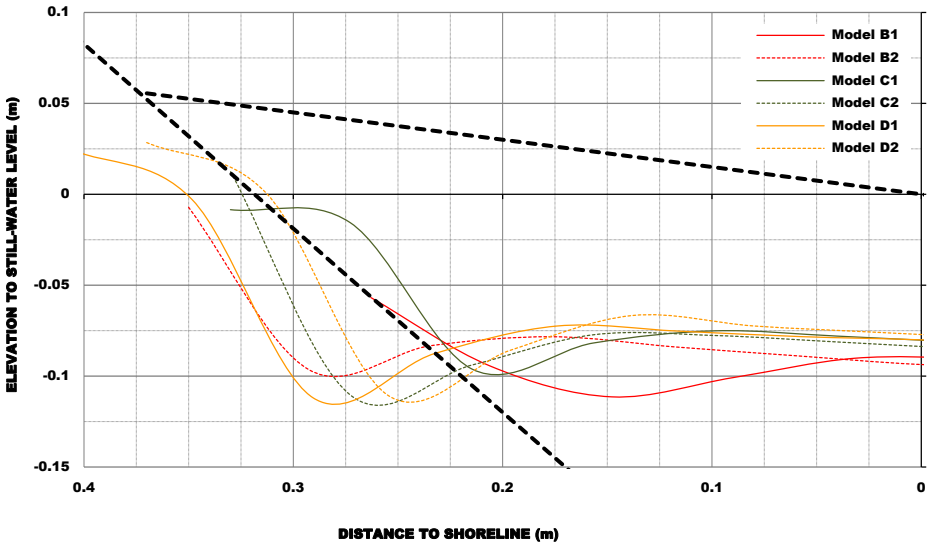

Figure 5.138: Scour patterns around dune reinforcement for sea-state 8 (H_s=2.0m, T_p=10s, in prototype).

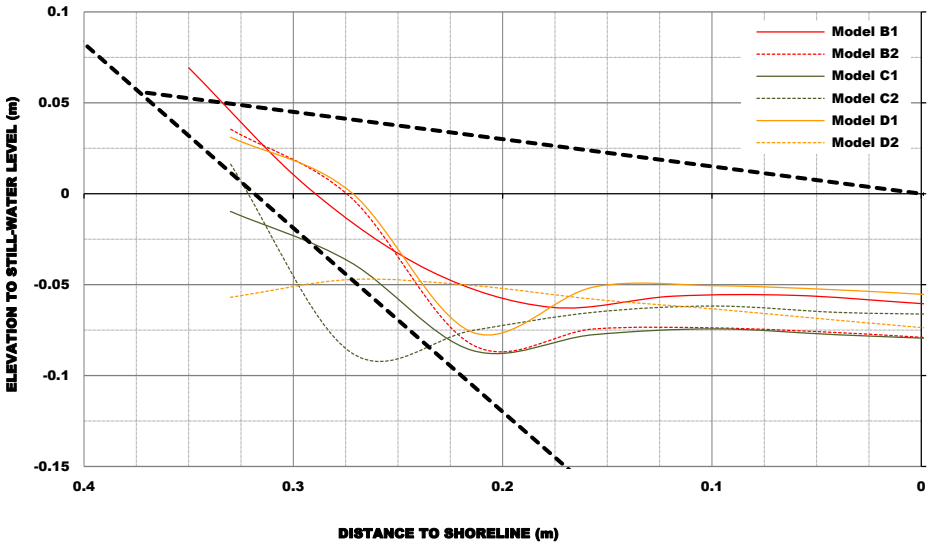

Figure 5.139: Scour patterns around dune reinforcement for sea-state 9 (H_s=2.0m, T_p=12s, in prototype).

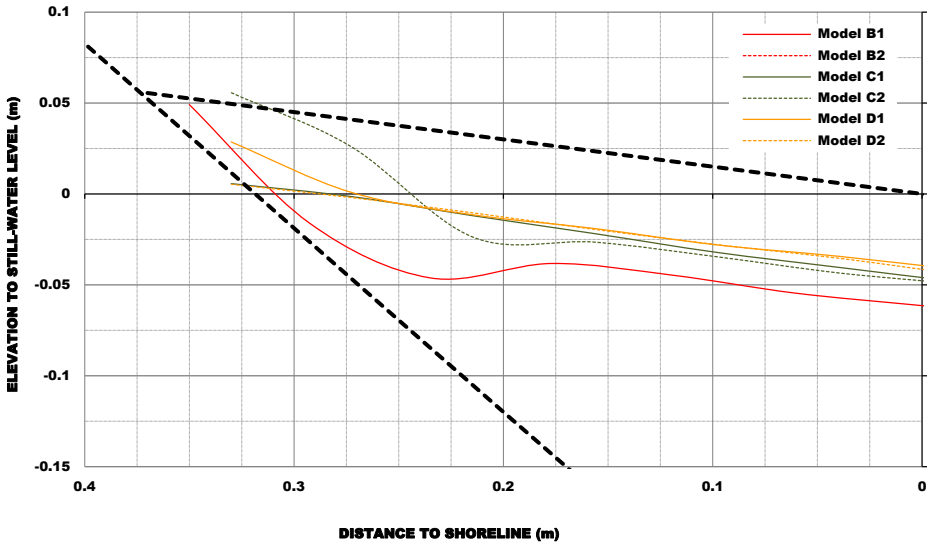

Figure 5.140: Scour patterns around dune reinforcement for sea-state 10 (H_s=1.5m, T_p=10s, in prototype).

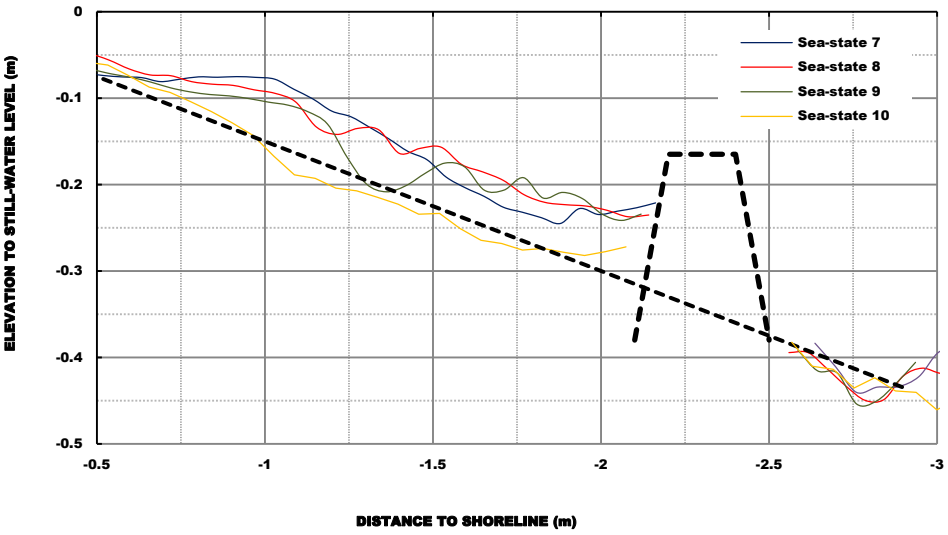

Figure 5.141: Scour patterns around structure E2, all erosional sea-states.

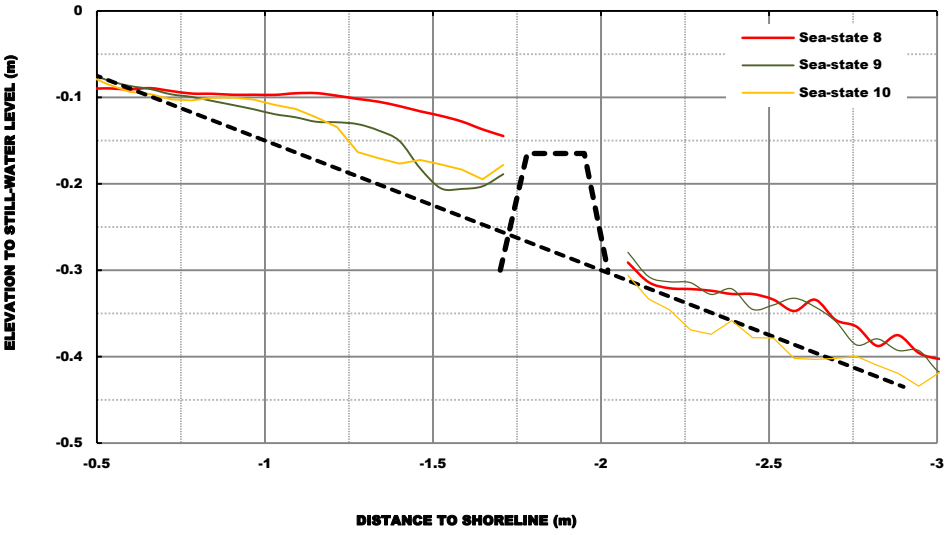

Figure 5.142: Scour patterns around structure E3, all erosional sea-states.

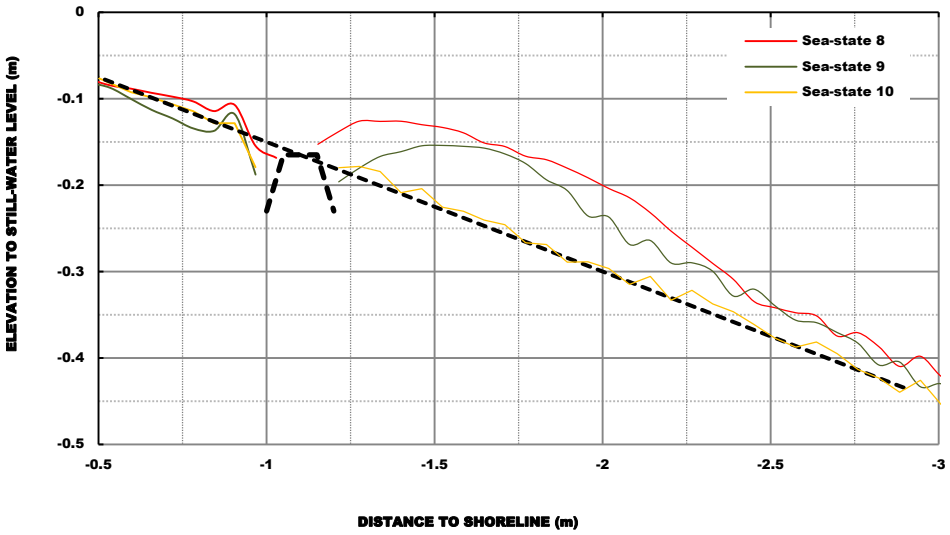

Figure 5.143: Scour patterns around structure E4, all erosional sea-states.

5.5.4. Global evaluation

Beach-profile evolution, volumetric changes, and scour development was analysed based on the laboratory measurements.

Lowering of the beach levels with shoreline retreat as far as the established alignment was observed in front of the passive coastal defence schemes. Identical change in beach-profile shape was observed, that is sediment removal for the beach face and deposition at a nearshore bar. The beach-profile has respond to change in forcing wave conditions, erosional to accretionary, but the recovery occurs at much smaller rate. It was apparent that sediment transport removal from the beach was controlled by the position and elevation of the nearshore bar and thus, to further investigate this mechanism, submerged structures were placed at the main breaker line of Model A, seaward and shorewards. These active coastal defence schemes were capable of retaining more sediment at the upper beach with consequent beach widening.

The results from the laboratory measurements indicate that the maximum scour depth under erosional waves decreased with an increase in the water depth at the structure (*i.e.*, is lower in Model E) but increased with waves breaking near the toe of the structure (Model E4). They also suggest that the scour depth is dominated by the mechanisms of wave reflection off the structure and wave downrush flow on the exposed slope, which may be influenced by the bed and water levels at the structure during the period of higher energy forcing.

5.6. Discussion of experimental results

5.6.1. Evaluation of experimental test procedure

According to several authors, the relevant forces for most coastal hydrodynamics problems are the gravitational forces, friction, and surface tension (see, *e.g.*, Dalrymple, 1985). Thus, the dimensionless products are combinations of the Froude, Reynolds, and Weber numbers. Neglected are compressibility and elasticity effects. Yet the use of the same fluid on both model and prototype prohibits simultaneously satisfying the Froude, Reynolds and Weber number scaling criteria and thus, most coastal models are run respecting Froude's similarity only, which implies assuming that gravitational effects are the most significant and that the viscosity and surface tension of water do not play significant roles.

For coastal sediment models, as the one used in the current investigation, another set of scale relationships governing the initiation of motion, the transport mode, and the transport rate have to be introduced into the model, again with inevitable scale effects. The coastal mobile bed sediment transport and morphology model is perhaps the most difficult of all physical hydraulic models (Kamphuis, 2009); yet despite the shortcomings it is, in many cases, the most important available instrument to bring about improvements with respect to sediment transport, and erosion.

The scale requirements, major scale effects and strengths and weaknesses with respect to sediment transport models were discussed in paragraph 3.2.2., while the considerations taken to select the model scale and set-up the experimental work were explained in section 4.2 and are briefly discussed here.

The characteristics of sediment transport dynamics in the nearshore region were sought to be prevalent and thus, the dimensionless fall speed parameter [Eq. (3.26)] was used to determine the length scale of the geometrically undistorted model, which was scaled to Froude similarity.

In order to minimize scale errors produced by non-satisfied similarity, the model length scale was set to the maximum size that could be accommodated by the facilities at FEUP laboratory of hydraulics having in consideration the prototype characteristics, the sediment scale parameters, and controlling factors with respect to wave conditions. As the influence of surface tension is most significant for periods smaller than 0.35s, and for water-depths less than 2cm (see, *e.g.*, Hughes, 1993) it is anticipated that the scale effects due to non-satisfied Weber are negligible. Moreover, the turbulent characteristics of the nearshore dynamics makes it safe to assume that the spurious effects of viscosity are not underestimated in the model. Sediment transport mechanisms along the cross-shore profile, namely the suspension by wave breaking and the sheet flow conditions in the swash zone, appear to be correctly reproduced in the model.

In regard to the scaling down of the geotextile properties some simplifications were introduced. It was assumed that the geotextiles in the model were relatively too strong but since they were not loaded to rupture it is negligible. In regard to filling, the strength had only to ensure no damage to the geotextile during handling. Flexibility was warrant by a thinner geotextile. The hydraulic permeability of a GSC-structure depends mainly on the size between neighbouring containers (Recio, 2007) and thus, so long the geometry is properly scaled the model should represent adequately the permeability in the prototype (*i.e.*, so long the dimensions, placement and shape, also related to filling percentage, are scaled down correctly). At last, requirements as regard to geotextile sand tightness were considered.

From the above, is possible to conclude that scale errors in the experimental set-up have been mitigated and thus, that their impact on the global analysis of the data from the laboratory experiments is negligible.

In regard to those errors that arise from performing experiments in laboratory facilities – the so-called laboratory effects – the following potential sources of error were examined: *(i)* wave generation; *(ii)* resonant oscillations forced across the boundaries of the test section; *(iii)* absorption of reflected waves; *(iv)* blockage effects; *(v)* compaction of sediments in the bed; and *(vi)* accuracy of the instruments.

In section 5.2 several considerations regarding the irregular wave generation, resonant oscillations across the boundaries of the test section, and absorption of reflected waves have been examined. In addition, the evaluation of generated wave conditions based on the wave-data recorded during the experiments assured that the different models have been set-up to run on similar hydrodynamic conditions and thus, that the comparison applied to the wave-induced morphodynamic change was possible and reliable. Representative sea-states were chosen from the prototype; in addition, the use of irregular wave trains also avoids the model effects of regular wave generation in coastal sediment models.

Blockage effects around the structures were minimal, as only the array of four wave probes were at the flow section during the experiments. The pore-pressure sensors were buried into the sand at sufficient depth so that they would not emerge due to bottom erosion.

For each wave run-segment with plane beach, the bed conditions were thoroughly checked before the experiment and the bed was carefully levelled to the desired gradient. To minimize the error caused by the initial bed profile, the sand bed was repeatedly levelled until the measured beach-profile was within a minimum tolerance range based on the ideal conditions. To prevent disturbances and to assure that the level of sand saturation was roughly the same for each wave-run segment with plane beach, the water during levelling was kept to SWL. Above it, the beach-profile was slowly wet so as to reduce air entrainment.

Respecting the accuracy of the wave probes they were calibrated on daily-basis. The 2D bed-profile was fixed to cross-shore travel in most of the experiments, except in Model B, variant 1, and also after it return from repair. At last the miniature pore-pressure sensors were linear scaled according to the range capacity of the sensor and its sensitivity.

5.6.2. Response of beach-profile to the protection schemes

The results on change in beach-profile shape reported in the section 5.5 have shown that the response of the bottom profile to the presence of a structure installed at the swash zone is identical across the various models. All evidenced sediment removal from the beach face in the vicinity of the original shoreline and development of a break-point bar. The end beach-profiles had a much gentler overall slope and the shoreline position retreated as far as the alignment fixed by the structure.

Under persistent erosional waves, the sediments initially deposited at the lower beach face moved further seaward thereby extending the bar. With time a double bar along the beach-profile developed and a moderately deep trough started to build-up, at this point the beach level fall as low as the baseline across the entire profile.

The tests with accretionary waves having a dissipative profile as antecedent morphology showed that changing wave conditions (*i.e.*, in this case, wave-height decrease) may not always be capable of moving sand from the bar; moreover the recovery response of sediment flows takes longer. In nature, such lagged response of morphology to changing conditions may often result in sand being lost to the sea, as consequence of the hydrodynamic conditions not being capable of moving sand onshore or as a consequence of sand being driven away by the littoral drift current.

As regard to the non-protected model, it experienced identical morphodynamic changes. Yet the bar accumulation was greater and the shoreline recession much smaller. While comparing the end beach-profiles and the computed volumetric changes for models A to D, it was realized that the net volume changes in Model A are substantively higher than in the protected models, which is in full agreement with Dean's approximate principle, *i.e.*, the eroded volume of sand is less than or equal to the volume retained by the structure had it not been in place (see, *e.g.*, USACE, 2008).

The analysis of the computed volumetric changes from the laboratory experiments further indicate that the erosion at the upper beach is in straight connection to the volume of sand deposited in the nearshore-bar, which implies that, under constant forcing, if the bar is at an equilibrium position with the breaking waves, then the entire cross-shore profile should be too.

Based on the observation of the response of the beach-profile to wave forcing in Model A, indication of bar development and near equilibrium position in a non-protected dune-beach system was obtained. Following, the same experimental procedure was repeated, having a nearshore detached submerged breakwater installed at key locations cross-shore. Those key locations were identified from the development of the bar (*i.e.*, location and elevation) in Model A, being those at exactly the same position (Model E3), and seaward (models E1 and E2) and shoreward (Model E4) that position. The submergence was kept constant and equal to 0.165m in all variants of Model E.

The response of beach-profile to the presence of a detached submerged structure installed at the mentioned locations have shown that, as expected, all models have interrupted the offshore sediment transport from the beach. This is apparent from the volumetric changes in Model E as compared to Model A. In practically all tests with Model E the initial shoreline position was maintained or has prograde seaward.

The comparison across models revealed that in models E2 and E4 the main morphologic changes occurred in the lower beach, whereas at the upper beach the end profile varies slightly from the baseline. In Model E2 there was significant sand deposition in the leeward side of the submerged breakwater, likely due to dune erosion. In Model E4 the nearshore-bar development has similar evolution as compare to Model A, although with less erosion in the vicinity of the shoreline and less accumulation in the bar.

The beach-profile in Model E3 experienced an evolution similar to Model A. This was an expected morphologic change as the structure was placed within the main breaker line of Model A, and the structure crest level at approximately the nearshore-bar elevation. Yet, the end-profiles in Model E3 differ from those in Model A at the seaward side of the structure where the beach-level are much lower.

At this point is relevant to compare the beach-profile evolution under erosional waves observed from the laboratory experiments with the equilibrium condition for beach-profiles, as given by Eq. (3.81). The recommended scale parameter A for sediment grain sizes (D_{50}) as the one used in the current investigation is $0.119\text{m}^{1/3}$ (see, *e.g.*, USACE, 2008) and thus, the power-function becomes as presented in Eq. (5.21).

$$\text{d} = 0.119\, x^{\frac{2}{3}} \tag{5.21}$$

Figure 5.144 plots the end beach-profiles for Model A along with the standard equilibrium beach-profile shape, proposed by Dean in 1977 (see, *e.g.*, USACE, 2008) given by Eq. (5.21). The power-function was fit to the initial shoreline position and translated to highest shoreline retreat. As can be observed, the power-function reproduces with reasonable accuracy beach-profiles within the surf zone, whereas farther offshore it under-predicts the water depth. This is an expected result given the monotonic nature of that shape; nonetheless, numerous studies give confidence that Eq. (3.81) both describes nature and has a consistent theoretical basis (see, *e.g.*, USACE, 2008; Wang and Kraus, 2005; Wang *et al.*, 2003).

The comparisons of the power-function with the end beach-profiles for models B to D are not presented, once they are redundant in regard to Model A. In Figures 5.145 to 5.147 comparisons of the power-function with the end beach-profiles for variants 2 to 4 of Model E are shown. The overall match of the power-function to the beach-profile is well.

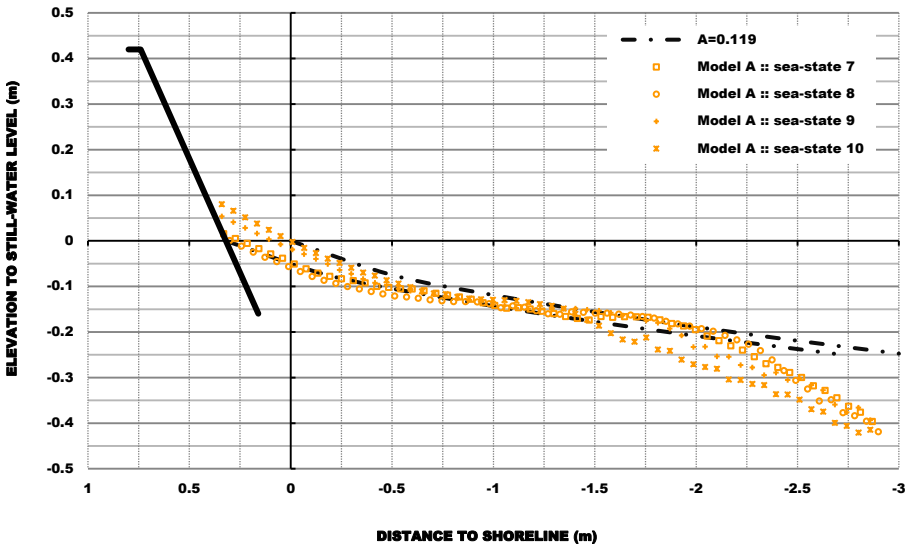

Figure 5.144: End beach-profiles for Model A, and the power-function profile.

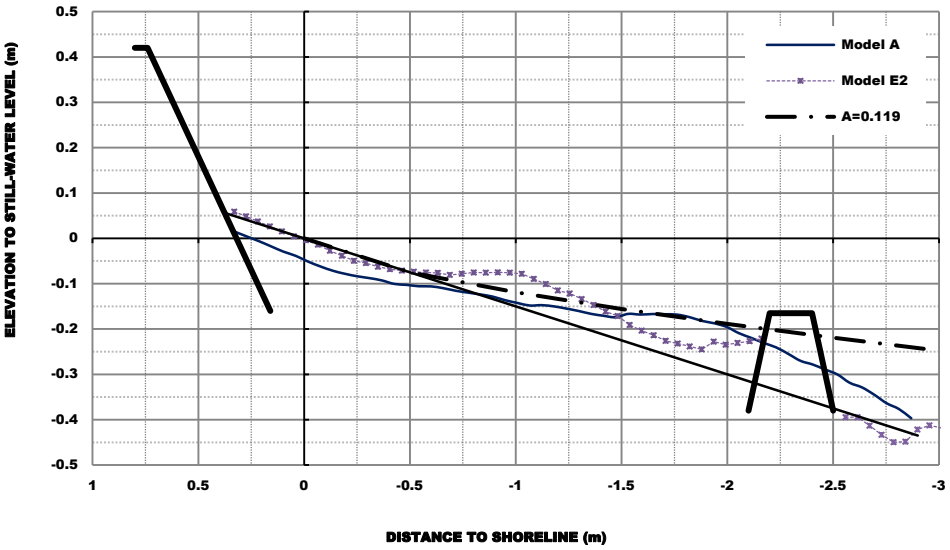

Figure 5.145: End beach-profiles for Model E, and the power-function profile: sea-state 7 (H_s=0.17m, T_p=2.31s).

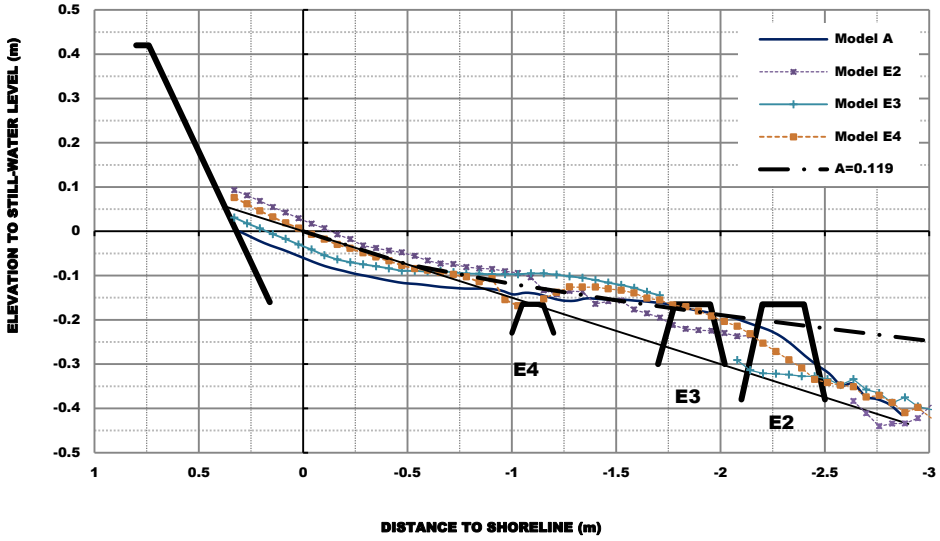

Figure 5.146: End beach-profiles for Model E, and the power-function profile: sea-state 8 (H_s=0.17m, T_p=2.89s).

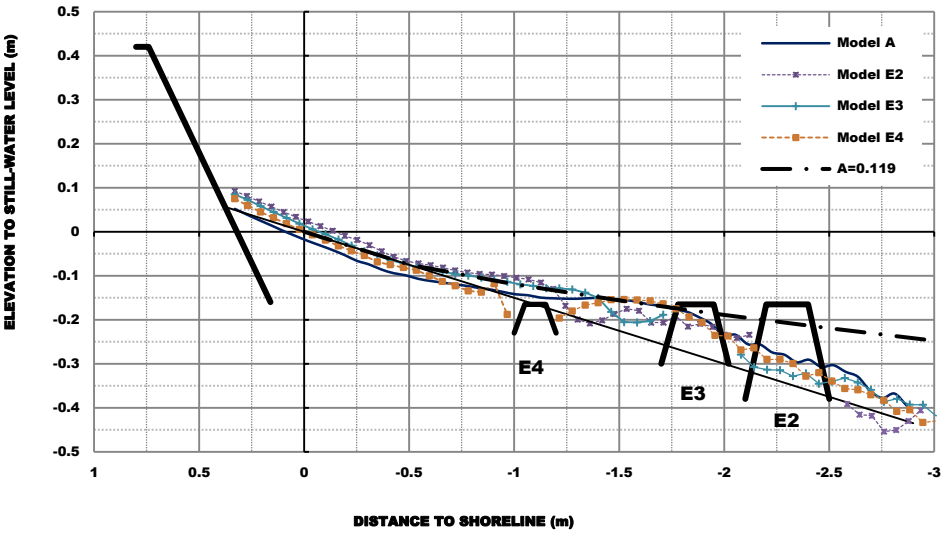

Figure 5.147: End beach-profiles for Model E, and the power-function profile: sea-state 9 (H_s=0.17m, T_p=3.46s).

From the above analysis is possible to conclude that: *(i)* the coastal sediment model was set-up on correct scaling parameters; *(ii)* the differences between models are most significant with respect to scour development around the structures and development of the bar (position and elevation); and *(iii)* the rational from which the position of the nearshore detached submerged breakwaters was defined within the experimental work can be replicated using the power-function as presented in Eq. (5.21).

5.6.3. Scour development

In section 3.4 the general principles of scour and key research on methods to predict scour depth around coastal structures for the case of 2D-scour scenarios were discussed. Overall it has become clear that scour is a complex processes, for which there are no specific (generally accepted) guidance for estimating maximum scour depth and other characteristics of scour development. Field, experimental and numerical studies were able to demonstrate that the scour characteristics may be a function of the non-dimensional parameters indicated in Eq. (3.91) and that the time scale is expected to depend on those parameters as well.

In addition, the following main shortcomings could be identified from the available results: *(i)* the great majority of the studies were performed for regular standing wave conditions; *(ii)* for the majority of the movable-bed model wave-tests performed, the dominant mode of sand transport was the no-suspension-mode which does not correspond to what occurs in the natural scale; and *(iii)* a significant part of the studies have been performed under non-breaking waves.

In the analysis reported in paragraph 5.5.3 the data on scour depth and on relative scour depth (*i.e.*, scour normalized to incident wave-height) obtained from the experimental work was evaluated on the parameters in Eq. (3.91) and also on the reflection coefficient.

The results indicate the scour depth to be less than the incident wave-height, thereby supporting the most widely used rule-of-thumb (*i.e.*, the maximum scour depth will be less than or equal to the incident unbroken wave-height). It is also seen that the maximum scour depth under erosional waves is approximately less than 80% and 30% the incident wave-height for the passive and active erosion control systems, accordingly. Further, scour depth decreased with an increase in the water depth at the structure (*i.e.*, is lower in Model E) but increased with waves breaking near the toe of the structure (Model E4). The results also indicate that it is influenced by the mechanisms of wave reflection off the structure – apparent from the lower depths experienced by Model D as compared to models B and C – and wave downrush flow on the exposed slope.

For the passive coastal protection schemes, the maximum scour depth experienced by variants 1 is less or equal to that in variants 2. If one considers the subsidence observed in variants 2 (refer to paragraph 5.5.1.) is easy to realize that the differences between the variants would be even more noticeable.

For the tests with persistent erosional conditions and erosion followed by infilling, the maximum scour depth evolution was evaluated only against the time scale.

The analysis of the scour development under constant incident wave-height revealed that the depth of scour increased over the whole duration of the test series (although with episodic decrease); yet it increased rapidly during the first wave run-segment to which followed a moderate (linear trended) increase for models B to D, while for Model E scour depth continued increasing over the whole test series at about the same rate as the first wave run-segment.

The delivered time development of maximum scour depth for Model E is comparable to that referred to in previous studies on local scour around low crested structures by Sumer *et al.* (2005); while that observed in the passive structures seems to be the result of the dual effect of beach lowering induced by the response of the profile to changing hydrodynamic conditions (*i.e.*, readjustment towards equilibrium) with localized erosions induced by wave-structure interactions.

The tests with erosional waves, followed by accretionary, and again erosional, aim at increasing understand on the changes in beach-profile shape caused by changes in forcing wave conditions. The data from the laboratory tests evidence the occurrence of transient backfilled when waves decrease (either during the first or the second wave run-segment) followed by a general increase of the depth of scour during the second erosional sequence. That did not occur in Model D, which maybe be due to transient backfilled or an indication that scour is controlled not only by forcing wave conditions (provided that these are sufficient to mobilize sediment) but also by the bed and water levels at the structure during the period of higher wave energy forcing.

Figure 5.148 compares the pooled data set of normalized scour depths *vs.* water depth at the structure to deepwater wavelength ratio delivered from the laboratory measurements with the predictors by Fowler (1992), as given by Eq. (3.101), and by Sutherland *et al.* (2008), as given by (3.102). The latter could be used alone because it is an envelope for a number of existing scour predictors. As can be observed, the measured normalized scour depths in Model E are well within the envelope proposed by Sutherland (2008), while on the contrary the measurements in models B to D are out-of-boundary for most of the experiments. The reason it occurs is related to the underestimation of the normalized scour depths for negative values of water depth at the structure to wavelength ratio (*i.e.*, for structures placed landward the shoreline). As explained by Sumer and FredsØe (2002) in regard to the work by Fowler (1992), the rather small values of relative scour depth for negative values of d_w/L_0 are expected if the structure is well away from the shoreline, however if it is moved further seaward the breaking will take place closer and closer to the structure, therefore the scour depth will consequently increase.

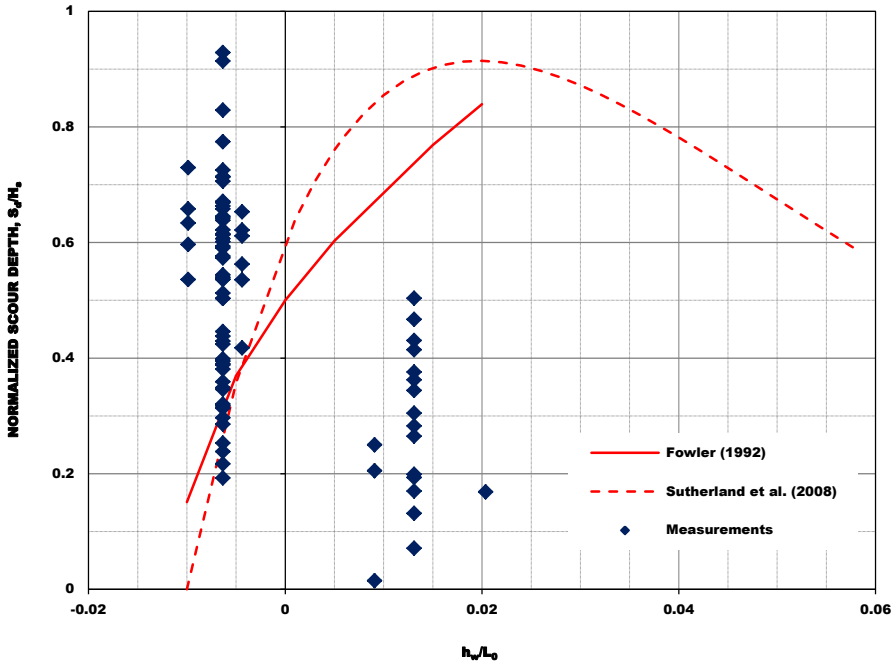

Figure 5.148: Normalized scour depths *vs.* water depth at the structure to deepwater wavelength ratio with plot of Eq. (3.101) and (3.102).

5.6.4. Pressure attenuation in the sand bed

Table 5.XXIX contains the mean significant pressure and the standard deviation of the sets of data results from the laboratory measurements of wave-induced pore pressures. The higher standard deviations (about 0.006-0.007) are noticeable for pressure sensors P5 and P6 for the highest energetic seas and for sensors P7 and P8 for sea-state 8_2x (about 0.006-0.007). The average standard deviation is 0.004, which is only slightly higher than the accuracy of the instrument (±0.2%).

Table 5.XXIX: Mean significant pressure and standard deviation for each test cluster.

Balance	Sea-state	Sensor ID	$\overline{P_s}$	σ [m]	$\overline{H_s}$	$\overline{P_s}/\overline{H_s}$
Erosion	7	P5	0.020	0.007	0.192	0.10
		P6	0.025	0.006	0.192	0.13
		P7	0.037	0.001	0.192	0.19
		P8	0.043	0.005	0.192	0.22
	8	P5	0.022	0.006	0.202	0.11
		P6	0.029	0.006	0.202	0.14
		P7	0.048	0.002	0.202	0.24
		P8	0.061	0.005	0.202	0.30
	9	P5	0.023	0.007	0.198	0.12
		P6	0.028	0.007	0.198	0.14
		P7	0.050	0.003	0.198	0.25
		P8	0.067	0.003	0.198	0.34
	10	P5	0.016	0.004	0.152	0.11
		P6	0.023	0.001	0.152	0.15
		P7	0.043	0.001	0.152	0.28
		P8	0.049	0.002	0.152	0.32
Accretion	1	P5	0.007	0.004	0.041	0.17
		P6	0.006	0.001	0.041	0.15
		P7	0.007	0.003	0.041	0.18
		P8	0.008	0.003	0.041	0.20
	2	P5	0.009	0.004	0.047	0.18
		P6	0.006	0.001	0.047	0.12
		P7	0.012	0.002	0.047	0.25
		P8	0.011	0.006	0.047	0.24
	4	P5	0.006	0.003	0.071	0.09
		P6	0.009	0.002	0.071	0.12
		P7	0.011	0.003	0.071	0.16
		P8	0.012	0.003	0.071	0.17
	5	P5	0.009	0.003	0.086	0.10
		P6	0.011	0.003	0.086	0.13
		P7	0.025	0.003	0.086	0.29
		P8	0.021	0.002	0.086	0.25
	6	P5	0.017	0.005	0.097	0.18
		P6	0.033	0.006	0.097	0.34
		P7	0.039	0.005	0.097	0.40
		P8	0.013	0.005	0.097	0.14
Persistent Erosional Conditions	10_1h	P5	0.017	0.005	0.151	0.11
		P6	0.023	0.002	0.151	0.15
		P7	0.043	0.002	0.151	0.28
		P8	0.048	0.001	0.151	0.32
Infilling and again Erosion	8_3a	P5	0.007	0.002	0.051	0.13
		P6	0.010	0.003	0.051	0.19
		P7	0.015	0.001	0.051	0.29
		P8	0.013	0.001	0.051	0.25
	8_3b	P5	0.008	0.003	0.051	0.15
		P6	0.009	0.001	0.051	0.18
		P7	0.015	0.002	0.051	0.29
		P8	0.014	0.002	0.051	0.27
	8_2x	P5	0.021	0.005	0.196	0.11
		P6	0.028	0.007	0.196	0.14
		P7	0.044	0.009	0.196	0.22
		P8	0.054	0.011	0.196	0.27

The attenuation of wave-induced pore-pressures in the soil with the water depth and the sensor depth of burial, the significant wave-period and the degree of saturation, as calculated by the theory developed by Mei and Foda [Eq. (3.116)], is presented in Table 5.XXX. It is assumed that the sand is isotropic and the flow is 2D. The origin of the Cartesian coordinated (x,z) is fixed on the still-water-level and z is positive upwards. The water depth is *d*, variable with beach slope, and d_b is termed the depth of the impermeable bottom, which is obviously the wave basin bottom. It is assumed that the density of soil is constant, yet the soil skeleton is compressible. In shallow water, the bulk modulus varies with the degree of saturation by water, S_r, [Eq. (3.110), section 3.4.3]. In the absence of a more accurate estimate, the values in TØrum (2007) have been assumed to porosity, *n*, equal to 0.35, coefficient of permeability of sand, *k*, equal to 2.5×10^{-4} m/s, Poisson ratio, ν, equal to 0.3, and Young's modulus, *E*, equal to 45MPa. The degree of saturation is 95%, as estimated by Massel *et al.* (2005) through the comparison of theoretical results with experimental data. Pore-pressures were measured for varying (approximately 0.03-0.26m) and to an average depth of about 0.23m below the sea bottom.

Figure 5.149 compares, for sensors P5 to P8, the wave-induced pore-pressure amplitude ratios, as given in the below table, to the mean significant pore-pressure, $\overline{P_s}$, to incident significant wave-height ratio given in Table 5.XXIX. As can be observed, there are major differences between the amplitude ratios calculated by the method developed by Mei and Foda (1981) and those calculated from measurements of wave-induced pore-pressure and incident wave-height. Mei and Foda (1981) under-predicts the attenuation delivered from measurements.

There are a couple of reasons for that. The first may related to the fact that the expression proposed by Mei and Foda (1981) was developed for waves travelling over a horizontal bottom with an infinite thick homogeneous soil layer, which is not exactly the case; nor only it is not a horizontal bottom, but also the soil layer is not infinite thick. The second is a higher percentage of air/gas content which would have resulted from levelling and justifies as well the noticeable scatter within the same sensor. At last, the even higher differences observed in the shallowest sensors are most probably due to energy dissipation in the surf zone, which may also play a role in the deepest ones especially in the most energetic sea-states.

Table 5.XXX: Attenuation of normalised pressure [Eq. (3.116)] with water depth and sensor depth of burial, significant wave-period and degree of saturation.

Sensor ID	Water Depth [m]	Depth of Burial [m]	T_p	S_r=1	S_r=0.97	S_r=0.95
P8	0.255	-0.242	1.73	0.575	0.415	0.302
			2.31	0.661	0.487	0.377
			2.89	0.718	0.539	0.433
			3.46	0.487	0.577	0.475
P7	0.180	-0.233	1.73	0.531	0.420	0.312
			2.31	0.622	0.493	0.388
			2.89	0.684	0.544	0.443
			3.46	0.728	0.583	0.486
P6	0.105	-0.225	1.73	0.449	0.418	0.316
			2.31	0.549	0.491	0.392
			2.89	0.619	0.543	0.448
			3.46	0.666	0.579	0.488
P5	0.030	-0.217	1.73	0.238	0.391	0.306
			2.31	0.341	0.464	0.381
			2.89	0.422	0.517	0.438
			3.46	0.481	0.555	0.478

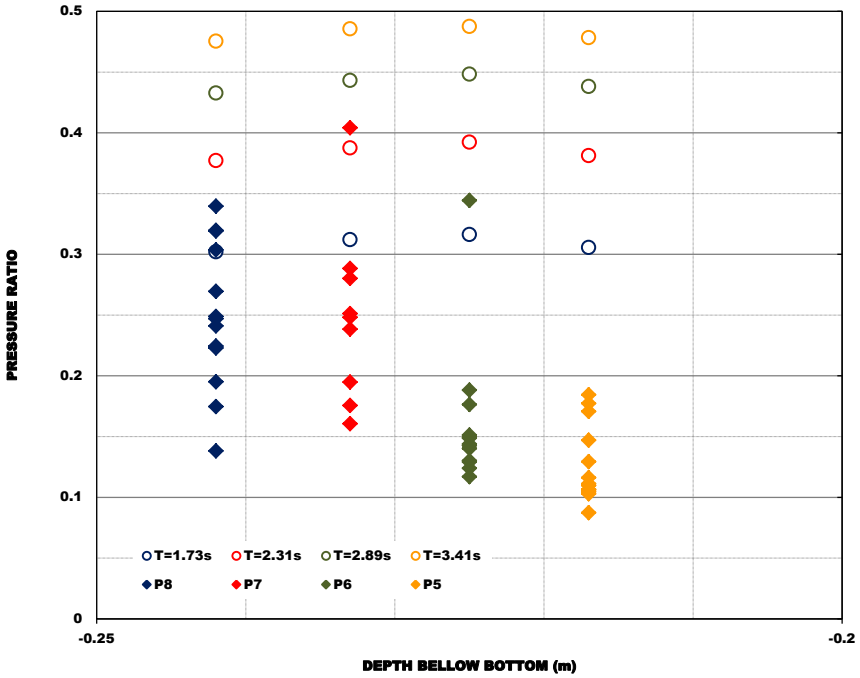

Figure 5.149: Wave-induced pore-pressure amplitude ratios (S_r=0.95).

5.6.5. Global evaluation

At the beginning of this chapter the broad objective of studying the efficiency of various erosion control systems in maintaining a beach and in protecting the shoreline has been established. The study on the stability of geotextile encapsulated sand-systems, with focus on the issue of scour development and more widespread beach lowering, was based on experimental work and compared the hydrodynamic and morphodynamic output produced by each scheme. The analysis shows that the initial plane beach-profile (gradient β=0.15) when exposed to erosional waves moves toward an equilibrium condition which could be described with reasonable accuracy by the equilibrium condition for beach-profiles proposed by Dean (1977) – cited in, *e.g.*, USACE (2008), as given by Eq. (3.81). The advantage of this formulation is that it can be used as a diagnosis (refer to paragraph 3.3.4.) without knowledge of the wave forcing. Eq. (5.21) is that equilibrium condition tailored to the characteristics of the experimental set-up, *i.e.*, sediment scale parameter equal to 0.119m$^{1/3}$ in accordance to the sediment grain size (D_{50}) of the coastal sediment model.

The differences in response of the cross-shore profile to the presence of the structure have been assessed with respect to *(i)* wave reflection off the structure; *(ii)* wave-induced pressure variations; and *(iii)* beach-profile evolution.

The analysis of wave reflection off the structure show that the computed reflection coefficients obtained with Model D, variants 1 and 2, are generally lower than those obtained with the other models. On the contrary, the computed reflection coefficients obtained with Model A and Model E, variants 1 to 4, are higher than those obtained with the dune erosion control systems. The differences in the computed coefficients of wave reflection have been attributed to the specific geometrical conditions of each model, as presumably, the rounded shape of the elements with which is build Model D, and the steps in Model C facilitate the dissipation of some additional wave energy; to the steeper beach-profile in Model A; and to the partial attenuation of the incident waves in Model E, of which a substantive part is reflected from the structure seawards.

In the study of the wave propagation over the beach, the dynamic pressure component was examined with respect to energy spectral balance and cross-shore energy flux gradients. The differences on the energy transfer to higher and lower frequencies were small across models (B to D) even when compared to the reference case. The comparison between the attenuation of wave-induced pore-pressure in the soil based on the laboratory data and that calculated by the theory developed by Mei and Foda (1981) show that the theoretical expression under-predicts the attenuation delivered from measurements. Possible reasons relate to a higher percentage of air/gas content, energy dissipation in the surf zone, and the inadequacy of that comparison given the specific characteristics of model set-up.

With respect to wave-induced pressures on the dune reinforcement results indicate that the structural elements which have had a higher frequency of response than that of the whole structure were those more close to the bottom. They also indicate that significant damping occurs from surface to interior and that the damping effect is lower for the structure with the highest porosity (Model B). The results for the submerged breakwaters indicate a significant attenuation of incident wave-energy, about 40% on average. Wave shoaling and breaking over the structure seemed to be correctly captured but underestimated in some cases possibly due to turbulent entrainment of air.

Lowering of the beach levels, with shoreline retreat as far as the established alignment and identical change in beach-profile shape was observed in front of the passive coastal defence schemes. The beach-profile has respond to change in forcing wave conditions, erosional to accretionary, but the recovery occurs at much smaller rate. It was apparent that sediment transport removal from the beach was controlled by the position and elevation of the nearshore bar and thus, to further investigate this mechanism, submerged structures were tested. These active coastal defence schemes were capable of retaining more sediment at the upper beach with consequent beach widening.

The results from the laboratory measurements indicate that the maximum scour depth under erosional waves decreased with an increase in the water depth at the structure (*i.e.*, is lower in Model E) but increased with waves breaking near the toe of the structure (Model E4). They also suggest that the scour depth is dominated by the mechanisms of wave reflection off the structure and wave downrush flow on the exposed slope, which may be influenced by the bed and water levels at the structure during the period of higher energy forcing. The comparison of the measured scour depth to that calculated from predictors show that these completely underestimated the scour around structures placed landward the shoreline and exposed to wave breaking of increasing intensity due to beach lowering.

5.7. Extrapolation of the model results on the prototype

In this section the extrapolation of experimental results on the prototype is essayed for a case study on Costa da Caparica - Portugal. This case study is extensively described in several publications (see, *e.g.*, Veloso-Gomes *et al.*, 2009a, 2009b, 2006a, 2006b, 2004a and 2004b) from which a concise review is given.

The coastal stretch between Cova do Vapor and Costa da Caparica, on southern bank of the Tagus river inlet, started a new cycle of coastline retreat in the winter of 2000/2001 with serious erosion and overwashes on S. João beach and on the foredune (Veloso-Gomes *et al.*, 2009a). After that winter coastal management authorities realize that this area was very dynamic and vulnerable and that coastal defences were needed for safety reasons, especially during storm events. Several structural options to protect the Costa da Caparica were proposed and discussed (Veloso-Gomes *et al.* 2004a, 2006a, 2006b). The approved option was divided into three phases of which the following actions are being implemented or have been already: *(i)* reshaping the existing structures; and *(ii)* artificial sand nourishment with 3 million m^3; and *(iii)* dune rehabilitation and protection (see, *e.g.*, FEUP/IHRH, 2003, and Veloso-Gomes *et al.*, 2006b). Figure 5.150 shows sediment balance as of November 2008. As can be observed, the nourished sand is moving towards deeper waters.

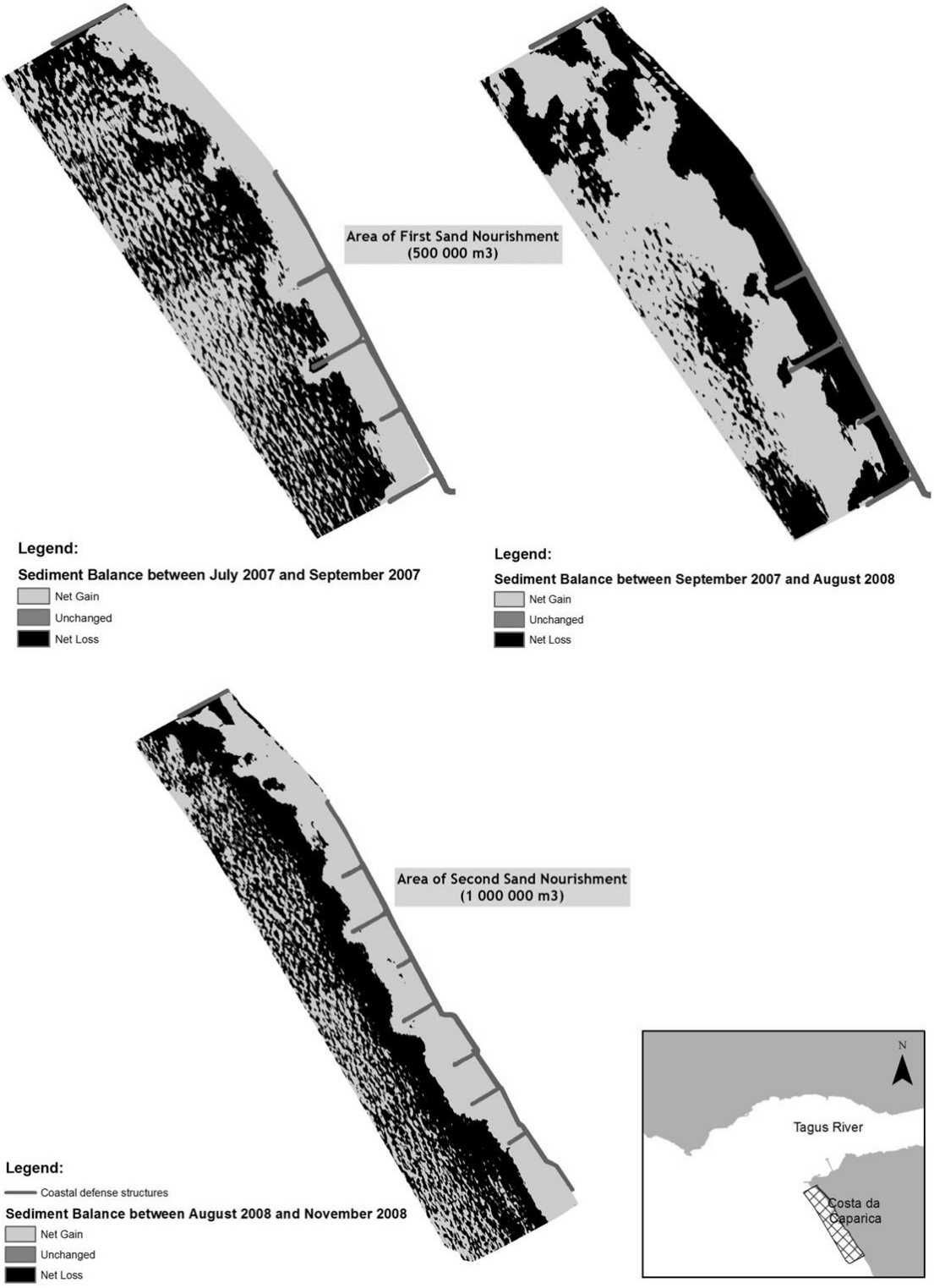

Figure 5.150: Costa da Caparica, sediment balance (Veloso-Gomes *et al.*, 2009a).

The monitoring results indicate substantive cross-shore sediment transport. It also indicates that the artificial sand nourishments have successfully filled the nearshore submerged beach face and have resulted in a moderate beach widening. Yet, it is anticipated that once the beach fill operations stop the continued offshore directed sediment movement to remove a significant part of the added volumes.

To limit the offshore movement of sediment from the upper to the lower beach a detached submerged structure constructed from encapsulated-sand geotextile elements has been proposed to the northernmost part of the stretch. The solution is based on the results obtained from the present experimental work.

Figures 5.151 to 5.153 show beach-profile shapes at different periods, before and after sand nourishment operations, since July 2007 up to May 2010. The equilibrium condition for beach-profiles, as given by Eq. (3.81), with a sediment scale parameter of $0.125 m^{1/3}$ (as recommended for D_{50} of 300μm see, *e.g.*, USACE, 2008) is plotted as well (red dashed-dot line).

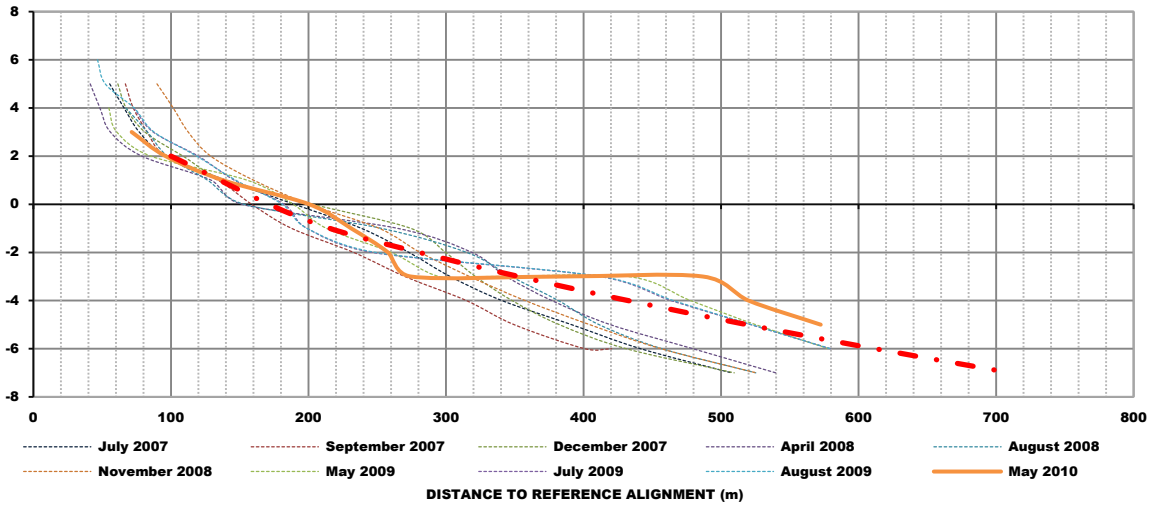

Figure 5.151: S. João beach, profile at the limit of the seawall.

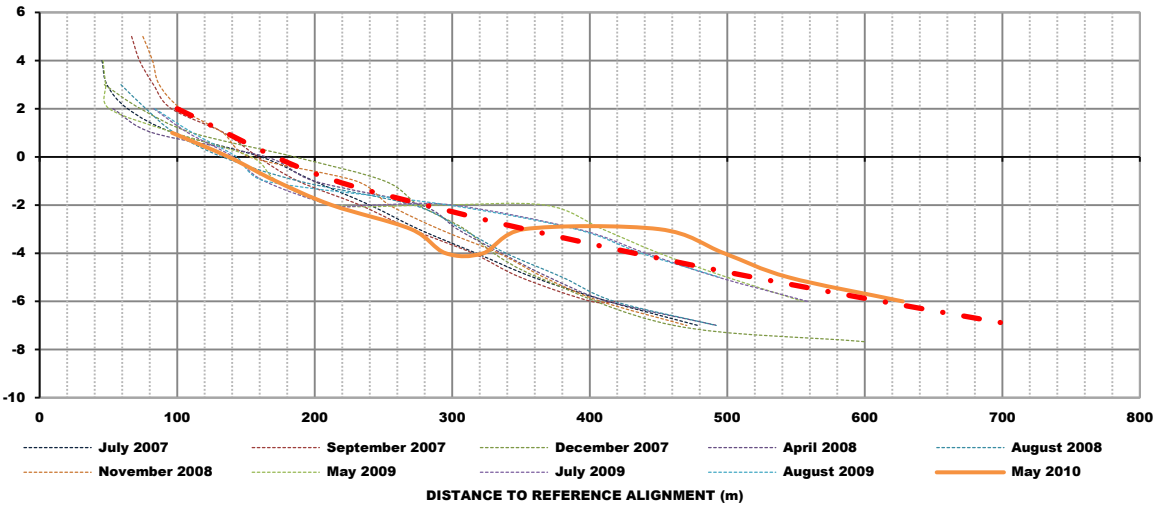

Figure 5.152: S. João beach, intermediate profile between the limit of the seawall and updrift the northernmost groyne.

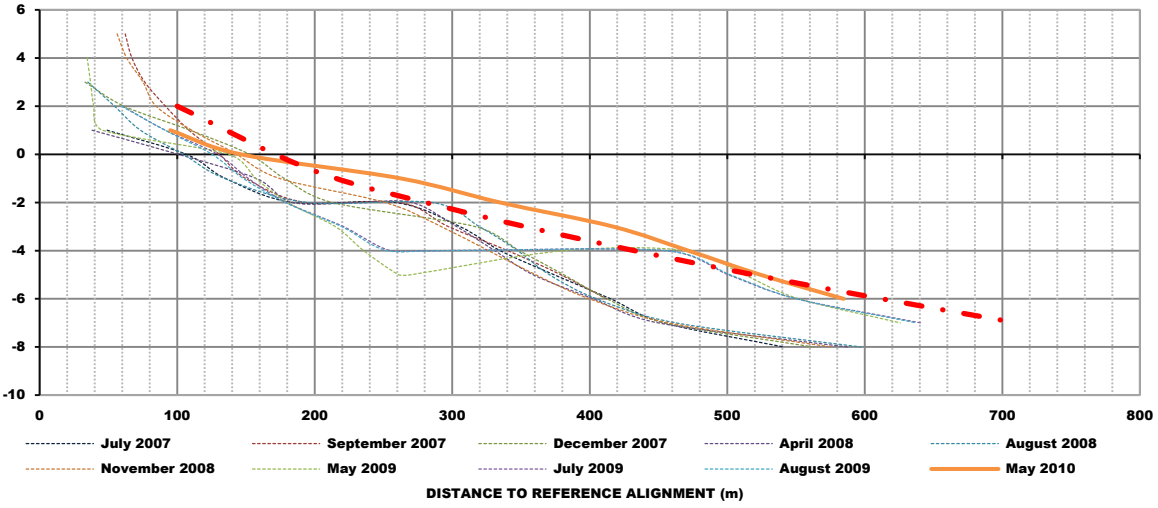

Figure 5.153: S. João beach, profile updrift the northernmost groyne.

It is seen that as of May 2010, the fill material is being transported out the upper beach to deposit within approximately 300 to 600m from the reference alignment. The shoreline has prograde about 50m from the initial shoreline position (*i.e.*, July 2007) except at the intermediate profile, which coincides with the updrift limit of an existing seawall (see Figure 5.150). Figures 5.151 to 5.153 also show that the equilibrium condition for beach-profiles proposed by Dean (1977) – cited in, *e.g.*, USACE, 2008 – describes with reasonable accuracy the most recent beach-profile shapes.

Based on the results from the physical model experiments carried out in the present investigation, it is proposed the installation of sand-filled geotextile tubes as a mean of retarding offshore sand movements. Figure 5.154 is a sketch of the proposed solutions (*i.e.*, the location of the structure). The considered theoretical diameters are Ø1.60m (~1m of height), Ø3.25m (~2m of height), and Ø5.00m (~3m of height) and the crest freeboard is the same and equal to -2m. The distances from the reference alignment vary from *ca.* of 320 to 480m. In regard to scour development, the results indicate that scour holes are likely to appear at both sides of structures S1 and S2 and at the seaside of structure S3. They further indicate that scour depth may be as high as 50% the incident wave-height (refer to Figure 5.148); yet as has been shown in the experiments, scour deepening will decrease with an increase in the water depth at the structure, as such it is anticipated the normalized scour depth (S_d/H_s) to be lower during high-tide even with higher waves reaching the structure.

The implementation of a pilot prototype experiment based on the proposed solutions is being considered for S. João beach. Following the monitoring surveys being carried out, the stretch at the limit of the seawall has been identified as priority and thus the pilot with about 200m in length is to be installed in front of that structure. The choice between the proposed solutions will be based on construction costs and constraints.

Further, there are a number of additional proposals being considered for other coastal stretches along the Portuguese coast, namely along the northwestern at *Esposende*, *Moledo do Minho*, and *Estela*.

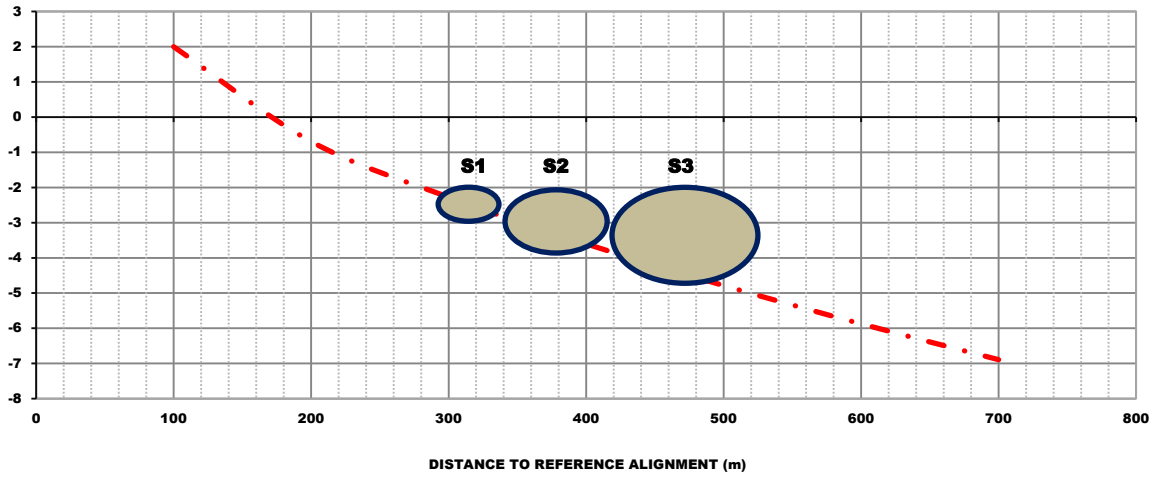

Figure 5.154: S. João beach, sketch of the proposed solutions.

6. CONCLUSIONS AND PERSPECTIVES

The present dissertation documents a systematic experimental study on the stability of geotextile encapsulated-sand systems under wave-loading. The central aim of the study was to provide contributes to the knowledge available on the instability caused by scour development and more widespread beach lowering. Such contributes would in turn provide insights to the efficiency of different geotextile encapsulated-sand systems in maintaining a beach and in protecting the shoreline.

The study was based on the intercomparison of the hydrodynamic and morphodynamic output produced by various coastal defence schemes with focus on wave-reflection off the structure, wave-induced pore-pressures, and response of the bottom profile to the presence of a structure installed at the swash and surf zones. Five perspectives were considered in this assessment *(i)* stability of geotextile encapsulated sand-systems under wave-loading; *(ii)* scour-depth development; *(iii)* storm response; *(iv)* recovery between storms; and *(iv)* coastal evolution. To this end, five models, corresponding to three erosion control systems with two configurations, one nearshore detached breakwater with four configurations and one non-protected beach and dune system as reference were taken for the investigation. The models were submitted to a total of ten different sea-states, combinations of four values of significant wave-height, H_s and four values of peak period, T_p.

The results on change in beach-profile shape have shown identical response across the various models of the bottom profile to the presence of a structure installed at the swash zone. All evidenced sediment removal from the beach face in the vicinity of the original shoreline and development of a break-point bar. The end beach-profile had a much gentler overall slope and the shoreline retreated as far as the alignment fixed by the structure. The beach-profile has respond to change in forcing wave conditions, erosional to accretionary, but the recovery occurred at much smaller rate. It was apparent that sediment transport removal from the beach was controlled by the position and elevation of the nearshore bar.

The response of beach-profile to the presence of detached submerged structures has shown that these have interrupted the offshore sediment transport from the beach. In practically all tests the initial shoreline position was maintained or has prograde seaward.

The results suggest that the scour depth is dominated by the mechanisms of wave reflection off the structure and wave downrush flow on the exposed slope. They further suggest that the geometrical characteristics of the structures (*e.g.*, shape of the elements, and porosity) influence scour development and beach lowering, because of their influence on those two aspects (*i.e.*, wave reflection, and downrush).

The comparison of the measured scour depth to that calculated from predictors have shown that these completely underestimated the scour around structures placed landward the shoreline and exposed to wave breaking of increasing intensity due to shoreline retreat.

In regard to other mechanisms of failure the results indicate that sand-filled containers corresponding to an estimate of 1.5m^3 in prototype, may become unstable (*i.e.*, a significant number of bags being pulled-out and displaced) when exposed to waves with a significant wave-height around 1.80m, and that small tubes of Ø1.60m diameter as crest elements in stacked configurations may become unstable when exposed to waves around that same wave-height (*i.e.*, about 1.80m).

A different but complementary focus of this work has been to sketch the background against which the decision for one type of scheme/material should be made (*e.g.*, hydrodynamic and morphologic conditions, installation, etc), with emphasis on the application of geotextile sand-filled containers at more exposed hydraulic conditions.

For that purpose, case studies selected from the literature were presented over Chapter 2 with the objective of getting past performance indicators out of the most significant projects for which reliable monitoring data is available; in addition to those indicators, some interesting remarks with respect to the generally recognized advantages of easy placement and constructability have been observed from the physical model yielding information that can be extrapolated on the prototype. Most relevant recommendations are summarized hereafter.

For instance, the experimental study show that bigger elements are more stable but also more difficult to handle and more difficult to repair. It also demonstrated that several causes exist for failure of a geotextile structure but are usually related with overturning, sliding, deformation due to local scour, and forcing associated with waves – breaking waves, non-breaking waves, and waves propagating over the structure. Flanking erosion may as well induce instability.

It has become clear that maintenance on a regular basis is anticipated. To expect otherwise may result in failure. It has also become clear that, except may be for very small projects, the installation needs an experienced contractor and/or supervision in order to ensure an optimal quality work. Negligence in materials and site preparation and positioning may lead to tearing of fabric and differential settlements, eventually causing collapse by excessive deflection, slumping and displacements. Seams and overlaps are always weaker than the original, non-connected fabric. They have to be kept to a minimum and pre-fabricated as much as possible.

Smaller elements may also help in keeping damages as localised problems, yet they are significantly less stable. Such lower stability can be enhanced by providing a mechanism that enables individual elements to work together (*e.g.*, in combination with a wrapped around system). The use of smaller elements to prevent sediment removal at the edges of the wrapped around system has proven to be effective, thus it is recommendable the use of those elements in prototype when seams and overlaps exist and at the outer limits of the structure.

Compartmentalisation seems to be significant in the overall stability. A general conclusion is that efficient compartmentalisation is a trade-off between stability and overall vulnerability.

With respect to perspectives of future development it is seen that although this experimental work has improved the knowledge on the scour development and beach lowering at coastal structures constructed from geotextile elements significant research still needs to be performed.

While this work considered the intercomparison of the morphodynamic output produced by each scheme focusing on beach lowering and scour development and consequent hydrodynamic output in that wider spatial scale, the effects of wave-structure interactions, such as wave up- and downrush the structure slope, and sediment transport mechanisms near the structure toe and at the swash zone, and of the geometrical characteristics of each scheme, such as the impact on wave reflection off the structure, were not studied in detail.

The observation that nearshore sandbar behaviour significantly influences the removal of sand from the upper beach, suggests some direction for further research. As such, understanding the mechanisms that cause changes in the location (*i.e.*, position and elevation) of those nearshore bars is an important step for developing coastal protection schemes that are more efficient in maintaining beaches. The present analysis showed that the nearshore sandbars can be constructed from geotextile encapsulated sand-systems with equivalent impact on coastal processes and thus, extending the present research programme to variations of

forcing wave conditions, water depth (*i.e.*, simulating tide amplitude impact), geometrical characteristics of the structures, and distance to shoreline is a natural step forward. The reproduction of this experimental study in 3D would also be a very interesting development, namely to assess the impact of the longshore component of sediment transport.

The long-term behaviour of the nearshore sandbar (or submerged structure) with different forcing wave conditions is also a relevant development. Furthermore, it would be interesting to study the long-term efficiency of the submerged structure under persistent erosional to assess the consequences of scour development and the mechanisms associated with the elements sinking into the sand. Additionally, a more detailed analysis of the mass transport over the structure under accretive conditions with freeboard crest elevation is of relevancy to coastal engineering practice. It would also be interesting to investigate the stability of geotextile encapsulated-sand systems under wave-loading in complement with artificial sand nourishments.

At last, is important to note that a substantive data set on hydrodynamic (accretionary and erosional conditions) and morphodynamic output has been compiled within the current investigation. Such a data set can be used to calibrate numerical simulations and thus, some of the aforesaid developments can be obtained by employing numerical tools.

With respect to topics more related to the geosystem itself investigative efforts should be undertaken to *(i)* provide quantification on interface friction development – as presumably it is the most important factor to stability – scoping *(a)* the interface friction characteristics; and *(b)* the movement of sediment inside and being washed-through the geotextile elements; and *(ii)* assess liquefaction potential of the sediment inside the elements and long-term effect of sediment movement inside the geotextile elements.

To conclude, the application of geotextile sand-filled systems in coastal engineering still poses major challenges to which is justified further research. Overall, it is anticipated that the topics related to long-term performance (impact on coastal processes, and survivability of the geotextile element) to be crucial to the direction of future research.

BIBLIOGRAPHY

Aagaard, T.; and Bryan, K.R. (2003). *Observations of infragravity wave frequency selection*, Continental Shelf Research, Amsterdam: Elsevier Science B.V., Volume 23, Issue 10 (June), pp. 1019-1034, ISSN 0278-4343.

Alvarez, E.; Rubio, R.; and Ricalde, H. (2007). *Beach restoration with geotextile tubes as submerged breakwaters in Yucatan, Mexico*, Geotextiles and Geomembranes, Special Issue on Tsunami Reconstruction with Geosynthetic Containment Systems, Proceedings of the International Symposium on Tsunami Reconstruction with Geosynthetics-Protection, Mitigation and Rehabilitation of Coastal and Waterway Erosion, Amsterdam: Elsevier Science B.V., Issues 4-5 (August-October), pp. 233-241, ISSN 0266-1144.

Artières, O.; Dunand, M.; and Durand, F. (2004). *Coastal protection with filter tube breakwater "Amelie" beach case*, Proceedings of EuroGeo3: Third European Geosynthetics Conference, Munich, Germany, pp. 367-370.

Bailard, J.A.; DeVries, J.W.; and Kirby, J.T. (1992). *Considerations in using Bragg reflection for storm erosion protection*, Journal of Waterway, Port, Coastal and Ocean Engineering, ASCE, Volume 118, Issue 1 (January/February), pp. 62-74, ISSN 0733-950X.

Bakhtyar R.; Yeganeh-Bakhtiary, A.; Ghaheri, A.; and Barry, D.A., (2009). *Process-based model for nearshore hydrodynamics, sediment transport and morphological evolution in the surf and swash zones*, Applied Ocean Research, Amsterdam: Elsevier Science B.V., Volume 31, pp. 44-56, ISSN 0141-1187.

Baldock, T.E. (2006). *Long wave generation by the shoaling and breaking of transient wave groups on a beach*, Proceedings of The Royal Society A: Mathematical Physical and Engineering Sciences, Volume 462, Issue 2070, pp. 1853-1876, ISSN 1364-5021.

Batjes, J.A.; Zitman, T.J.; and Holthuijsen, L.H. (1987). *A reanalysis of the spectra observed in JONSWAP*, Journal of Physical Oceanography, American Meteorological Society, Volume 17, pp. 1288-1295, ISSN 0022-3670.

Battjes, J.A.; Bakkenes, H.J.; Janssen, T.T.; and van Dongeren, A.R. (2004). *Shoaling of subharmonic gravity waves*, Journal of Geophysical Research, American Geophysical Union, Volume 109(C02009), 15p, ISSN 2156-2202.

BBG (2004). *Reabilitação da duna da Leirosa: projecto* (*in Portuguese*).

Bernabeu, A.M.; Medina, R.; and Vidal, C. (2003). *Wave reflection on natural beaches: an equilibrium beach profile model*, Estuarine, Coastal and Shelf Science, Amsterdam: Elsevier Science B.V., Volume 57, Issue 4 (July), pp. 577-585, ISSN 0272-7714.

Bezuijen A.; Oung, O.; Klein Breteler, M.; Berendsen, E.; and Pilarczyk, K.W. (2002a). *Model tests on geocontainers, placing accuracy and geotechnical aspects*, Proceedings of 7th International Conference on Geosynthetics, Nice, France.

Bezuijen, A.; and Vastenburg, E. (2008). *Geosystems, possibilities and limitations for applications*, Proceedings of EuroGeo4: Fourth European Geosynthetics Conference, Edinburgh, Scotland, United Kingdom.

Bezuijen, A.; de Groot, M.B.; Klein Breteler, M. and Berendsen, E. (2004). *Placing accuracy and stability of geocontainers*, Proceedings of EuroGeo3: Third European Geosynthetics Conference, Munich, Germany.

Bezuijen, A.; den Adel, H.; de Groot, M.B.; and Pilarczyk, K.W. (2000). *Research on geocontainers and its application in practice*, Proceedings of 27th International Conference on Coastal Engineering, Sydney, Australia.

Bezuijen, A.; Schrijver, R.R.; Klein Breteler, M.; Berendsen, E.; and Pilarczyk, K.W. (2002b). *Field tests on geocontainers*, Proceedings of 7th International Conference on Geosynthetics, Nice, France.

Black, K. (2004). *Reefs for coastal protection - are they just a fad or a sustainable solution which meet modern shifts in social attitudes and policies?*, Littoral 2004: Delivering Sustainable Coasts: Connecting Science and Policy, D.R. Green *et al.* (ed.), Cambridge, UK: Cambridge Publications, Volume I, pp. 12-24, ISBN 0-9540081-0-4.

Blacka, M.; Anderson, D.; and Mallen Lopez, L. (2008). *Analysis of shoreline variability, seasonability and erosion/accretion trends*: *February - July 2008, Report 18: Northern Gold Coast Coastal Imaging System*, Manly Vale, N.S.W. Australia: Water Research Laboratory, University of New South Wales, Technical Report 2008/27-November.

Bleck, M. (2003). *Hydraulic performance of artificial reefs shown exemplarily for a rectangular structure*, PhD Thesis: Leichtweiß Institut of the Technical University of Braunschweig, Germany (*in German*).

Borrero, J. (2001). *Pratte's reef monitoring report*, prepared for The Surfrider Foundation, January.

Borrero, J. (2002a). *Pratte's reef monitoring report*, prepared for The Surfrider Foundation, February.

Borrero, J. (2002b). *Pratte's reef monitoring report*, prepared for The Surfrider Foundation, December.

Borrero, J.; and Nelsen, C. (2003). *Results of a comprehensive monitoring program at Pratte's reef*, Third International Conference Artificial Surfing Reefs, Raglan, New Zealand.

Breusers, H.; and Raudkivi, A. (1991). *Scouring*, Rotterdam: AA Balkema, 143p, ISBN 90-6191-983-5.

Brodtkorb, P.A.; Johannesson, P.; Lindgren, G.; Rychlik, I.; Rydén, J.; and Sjö, E. (2000). *WAFO - a Matlab toolbox for analysis of random waves and loads*, Proceedings of the 10th International Offshore and Polar Engineering Conference, Seattle, USA.

Buffington, J.M. (1999).*The legend of A.F. Shields*, Journal of Hydraulic Engineering, ASCE, Volume 125, Issue 4 (April), pp. 376–387, ISSN 0733-9429.

Buffington, J.M.; and Montgomery, D.R. (1997). *A systematic analysis of eight decades of incipient motion studies, with special reference to gravel-bedded rivers*, Water Resources Research, American Geophysical Union, Volume 33, Issue 8 (August), pp. 1993-2029, ISSN 0043-1397.

Burcharth, H.F.; and Brorsen, M. (1978). *On the design of gravity structures using wave spectra, Lectures on offshore engineering*, W.J. Graff and P. Thoft-Christensen (ed.), Institute of Building Technology and Structural Engineering Centre, Aalborg University, pp. 185-231.

Cacchione, D.A.; Thorne, P.D.; Agrawal, Y.C.; and Nidzieko, N.J. (2008). *Time-averaged near-bed suspended sediment concentrations under waves and currents: Comparison of measured and model estimates*, Continental Shelf Research, Amsterdam: Elsevier Science B.V., Volume 28, Issue 3, pp. 470-484, ISSN 0278-4343.

Caldeira, L.; and Gonçalves da Silva, M. (2000). *Friction at the soil-structure interface based on direct shear box tests*, VII Congresso Nacional de Geotecnia, pp. 53-62 (*in Portuguese*).

Cao, Z.; Pender, G.; and Meng, J. (2006). *Explicit formulation of the Shields diagram for incipient motion of sediment*, Journal of Hydraulic Engineering, ASCE, Volume 132, Issue 10 (October), pp. 1097-1099, ISSN 0733-9429.

Carneiro, R. (2009). *Durabilidade de materiais geossintéticos em estruturas de carácter ambiental - a importância da incorporação de aditivos químicos*, PhD Thesis: Universidade do Porto, Faculdade de Engenharia, Portugal (*in Portuguese*).

Carpenter, K.E. and Powell, K.A. (1998). *Toe scour at vertical walls: mechanisms and protection methods*, Wallingford, UK: HR Wallingford, Strategic Research Report SR 506.

Chanson, H. (2004). *The hydraulics of open channel flow*, Amsterdam: Elsevier Science B.V., 650p, ISBN 10: 0-7506-5978-5.

Cheng, N.S. (1997). *A simplified settling velocity formula for sediment particle*, Journal of Hydraulic Engineering, ASCE, Volume 123, Issue 2, pp. 149-152, ISSN 0733-9429.

Cheng, N.S.; and Chiew, Y.M. (1999). *Incipient sediment motion with upward seepage*, Journal of Hydraulic Research, London: Taylor & Francis, Volume 37, Issue 5 (September), pp. 665-681, ISSN 1814-2079.

CIRIA (1986). *Seawalls: survey of performance and design practice*, Technical Note 125.

CIRIA, CUR and CETMEF. (2007). *The Rock Manual*, London: C863, 1268p, ISBN 978-0-86017-683-1.

Coastal Frontiers Corporation (2008). *Project description for removal of Pratte's reef*, prepared for Surfrider Foundation.

Coelho, Carlos (2005). *Riscos de exposição de frentes urbanas para diferentes intervenções de defesa costeira*, PhD Thesis: Universidade de Aveiro, Portugal (*in Portuguese*).

Comissão Europeia (2006). *Viver com a erosão costeira na Europa - Sedimentos e espaço para a sustentabilidade*, Luxemburgo: Serviço das Publicações Oficiais das Comunidades Europeias, 40p, ISBN 92-79-02209-1.

Cowell, P.J.; Stive, M.J.; Niedoroda, A.W.; de Vriend, H. J.; Swift, D.J.; and Kaminsky, G.M. (2003a). *The coastal-tract (part 1): a conceptual approach to aggregated modeling of low-order coastal change*, Journal of Coastal Research, West Palm Beach (Florida), Volume 19, Issue 4 (Autumn), pp. 812-827, ISSN 0749-0208.

Cowell, P.J.; Stive, M.J.; Niedoroda, A.W.; Swift, D.J.; de Vriend, H.J.; and Buijsman, M.C. (2003b). *The coastal-tract (part 2): applications of aggregated modeling of low-order coastal change*, Journal of Coastal Research, West Palm Beach (Florida), Volume 19, Issue 4 (Autumn), pp. 828-848, ISSN 0749-0208.

Creed, G.C.; Bodge, K.R.; and Suter, C.L. (2000). *Construction slopes for beach nourishment projects*, Journal of Waterway, Port, Coastal and Ocean Engineering, ASCE, Volume 126, Issue 1 (January/February), pp. 57-62, ISSN 0733-950X.

CUR (2004). *Geotextiele zandelementen*, CUR 214: Stichting CUR, Gouda (*in Dutch*).

CUR (2006). *Ontwerpen met geotextiele zandelementen*, CUR 217: Stichting CUR, Gouda (*in Dutch*).

Dalrymple, R. (1985). *Physical modelling in coastal engineering*, London: Taylor & Francis, 276p, ISBN 10 9061915163.

das Neves L.; Veloso-Gomes F.; and Lopes M.L. (2005). *Coastal erosion control using sand-filled geotextile containers: a case study from the NW coast of Portugal*, Proceedings of the 29th International Conference Coastal Engineering, McKee Smith Jane (ed.), Singapore: World Scientific Publishing Co. Pte. Ltd., Volume 4, pp. 3852-3864, ISBN 978-981-256-298-2.

das Neves Luciana (2003). *Geossintéticos e geossistemas em engenharia costeira*, MSc Thesis: Universidade do Porto, Faculdade de Engenharia, 206p (*in Portuguese*).

Davies, A.G.; and Heathershaw, A.D. (1983). *Surface wave propagation over sinusoidally varying topography: theory and observation*, Wormley, UK: Institute of Oceanographic Sciences, Report no. 159, Part I and II, 181p.

de Rouck, J.; and Troch, P. (2002). *Pore water pressure response due to tides and waves based on prototype measurements*, PIANC Bulletin, Issue 110, pp. 9-30.

Dean, R.; and Zheng, J. (1994). *Cross-shore sediment transport relationships*, University of Florida, 32p.

Dean, R.G.; and Yoo, C.H. (1994). *Beach nourishment in the presence of seawall*, Journal of Waterway, Port, Coastal and Ocean Engineering, ASCE, Volume 120, Issue 3, pp. 302-317, ISSN 0733-950X.

Dey, S. (2003). *Threshold of sediment motion on combined transverse and longitudinal sloping beds*, Journal of Hydraulic Research, IAHR, Volume 41, Issue 4, pp. 405–415, ISSN 1814-2079.

Dronkers, J. (2005). *Dynamics of coastal systems*, Advanced Series on Ocean Engineering – Volume 25, Singapore: World Scientific Publishing Co. Pte. Ltd., 519p, ISBN 981-256-349-0.

Dulou, C.; Belzons, M.; and Rey, V. (2000). *Laboratory study of wave bottom interaction in the bar formation on an erodible sloping bed*, Journal of Geophysical Research, American Geophysical Union, Volume 105(C8), Issue 19, pp. 745-762, ISSN 0148-0227.

Elgar, S.; Herbers, T.H.C.; and Guza R.T. (1994). *Reflection of ocean surface gravity waves from a natural beach*, Journal of Geophysical Research, American Geophysical Union, Volume 100(C5), pp. 8751-8760, ISSN 0148-0227.

Elgar, S.; Raubenheimer, B.; and Herbers, T.H.C. (2003). *Bragg reflection of ocean waves from sandbars*, American Geophysical Union, Volume 30, Issue 1, pp. 16.1-16.4, ISSN 0094-8276.

Elko, N.A.; and Mann, D.W (2007). *Implementation of geotextile T-groins in Pinellas county*, Florida, Shore and Beach, Manhattan, Association American Shore and Beach Preservation, Volume 75, Issue 2, pp. 2-10, ISSN 0037-4237.

Erchinger, H. (1993). *Geotextile tubes filled with sand for beach erosion control North Sea coast, Germany*, Geosynthetics Case Histories, Thirty Five Years of Experience, G.P. Raymond, and J.P. Giroud (ed.), ISSMFE: Committee TC9.

FEUP/IHRH. (2003). Estudo *de reabilitação das obras de defesa costeira e de alimentação artificial na Costa da Caparica*, Porto: Faculdade de Engenharia da Universidade do Porto.

Fowler, J. (1992). *Scour problems and methods for prediction of maximum scour at vertical seawalls*, Vicksburg, MS: U.S. Army Corps of Engineers, Technical Report CERC 92-16 (December), 40p.

Fowler, J. (1993). *Coastal scour problems and methods for prediction of maximum scour*, Vicksburg, MS: U.S. Army Corps of Engineers, Technical Report CERC 93-8 (May), 59p.

Franco, L.; Bellotti, G.; and Macro, G. (2009). *Design of an artificial surf reef at S. Marinella, Rome (Italy)*, Proceedings of the 5th International Conference Coastal Structures, Leopoldo Franco, Giuseppe R. Tomasicchio, and Alberto Lamberti (ed.), Singapore: World Scientific Publishing Co. Pte. Ltd., Volume I, pp. 389-399, ISBN 13 978-981-4280-99-0.

Frigaard, P.; and Lykke Andersen, T. (2010). *Technical background material for the wave generation software AwaSys 5*, Aalborg University: DCE Technical Report, Issue 64, 109p, ISSN 1901-726X.

Gantner (2006). *e.gate / e.pac*, Instruction Manual, 58p.

Gibeaut, J.; Hepner, T.; Waldinger, R.; Andrews, J.; Smyth, R.; and Gutiérrez, R. (2003). *Geotextile tubes along the upper Texas Gulf coast: May 200 to March 2003*, prepared for Texas Coastal Coordination Council pursuant to National Oceanic and Atmospheric Administration, Award Issue NA07OZ0134, under GLO contract Issue 02-493/The University of Texas, Bureau of Economic Geology, 37p+apps.

Gislason, K.; FredsØe, J.; and Sumer, B.M. (2009). *Flow under standing waves (part 2): scour and deposition in front of breakwaters*, Journal of Coastal Engineering, Amsterdam: Elsevier Science B.V., Volume 56, Issue 3 (March), pp. 363-370, ISSN 0378-3839.

Goda, Y. (2000). *Random seas and design of maritime structures*, Advanced Series on Ocean Engineering – Volume 15, Singapore: World Scientific Publishing Co. Pte. Ltd., 443p, ISBN 981-02-3256.

Gögüs, M.; and Defne, Z. (2005). *Effect of shape on incipient motion of large solitary particles*, Journal of Hydraulic Engineering, ASCE, Volume 131, Issue 1 (January), pp. 38–45, ISSN 0733-9429.

Graf, W.H (1984). *Hydraulics of sediment transport*, Water Resources Publications, 511p, ISBN 0-918334-56-X.

Heilman, D.; Perry, M.; Thomas, R.; and Kraus, N. (2008). *Interaction of shore-parallel geotextile tubes and beaches along the upper Texas coast*, Vicksburg, MS: U.S. Army Corps of Engineers, Technical Note ERDC/CHL CHETN-II-51 (January), 18p.

Henderson, S.M.; Guza, R.T.; Elgar, S.; Herbers, T.H.C.; and Bowen, A.J. (2006). *Nonlinear generation and loss of infragravity wave energy*, Journal of Geophysical Research, American Geophysical Union, Volume 111(C12007), 9p, ISSN 0148-0227.

Herbers, T.H.C.; and Burton, M.C. (1997). *Nonlinear shoaling of directionally spread waves on a beach*, Journal of Geophysical Research, American Geophysical Union, Volume 102(C9), Issue 21, pp. 101–114, ISSN 0148-0227.

Herbers, T.H.C.; Russnogle, N.R.; and Elgar, S. (2000). *Spectral energy balance of breaking waves within the surf zone*, Journal of Physical Oceanography, American Meteorological Society, Volume 30, pp. 2723-2737, ISSN 0022-3670.

Hoffmans, G.J.C.M.; and Verheij, H.J. (1997). *Scour manual*, Rotterdam: AA Balkema, 205p, ISBN 90-5410-673-5.

HR Wallingford (2003). *HR WaveMaker wave generation control program*, Software Manual - Report IT 453 (Issue 5).

HR Wallingford (2005). *HR WaveData wave generation control program*, Software Manual - Report IT 453 (Issue 5).

HR Wallingford (2006). *Wave probe monitor*, User Manual - Report IT (August).

HR Wallingford (2007). *Multi-element wave generation system with AC drives and dynamic wave absorption*, User Manual - Report IT CQR 4104 (May).

HR Wallingford (2009). *2D-bed profiler*, User Manual (August).

Hughes, S. (1993). *Physical models and laboratory techniques in coastal engineering*, Advanced Series on Ocean Engineering – Volume 7, Singapore: World Scientific Publishing Co. Pte. Ltd., 550p, ISBN 13: 978-9810215415.

Hughes, S.; and Fowler, J. (1991). *Wave-induced scour prediction at vertical walls*, Proceedings of the International Conference Coastal Sediments, Nicholas C. Kraus, Kathryn J. Gingerich, and David L. Kriebel, (ed.), ASCE, Volume 2, pp. 1886–1899, ISBN 978-0-87262-808-3.

HYDRALAB (2007a). *Guidelines for physical model testing of breakwaters: rubble mound breakwaters*, HYDRLAB III (EC contract Issue 022441) Deliverable NA3.1-2 (August), 38p.

HYDRALAB (2007b). *Guidelines for wave modelling in flumes and basins: hydraulic model testing in waves*, HYDRLAB III (EC contract Issue 022441) Deliverable NA3.1-1 (December), 26p.

HYDRALAB (2008). *Guidelines for physical modelling of sediment dynamics*, HYDRLAB III (EC contract Issue 022441) Deliverable NA3.1-3 (May), 69p.

Inman, D.L.; Elwany, M.H.S.; and Jenkins, S.A. (1993), *Shorerise and bar-berm profiles on ocean beaches*, Journal of Geophysical Research, American Geophysical Union, Volume 98(C10), Issue 18, pp. 181–199, ISSN 0148-0227.

ISO 10318:2005. *Geosynthetics – terms and definitions*.

ISO 10319:2008. *Geosynthetics – wide-width tensile test*.

ISO 10321:2008. *Geosynthetics – tensile test for joints/seams by wide-width strip method*.

ISO 10722:2007. *Geosynthetics – index test procedure for the evaluation of mechanical damage under repeated loading, damage caused by granular material*.

ISO 11058:2010. *Geotextiles and geotextile-related products – determination of water permeability characteristics normal to the plane, without load*.

ISO 12224:2000. *Geotextiles and geotextile-related products – resistance to weathering*.

ISO 12225:2000. *Geotextiles and geotextile-related products – screening test method for determining the microbiological resistance*.

ISO 12236:2008. *Geosynthetics – static puncture test (CBR test)*.

ISO 12447:2001. *Geotextiles and geotextile-related products – screening test method for determining the resistance to hydrolysis*.

ISO 12956:1999. *Geotextiles and geotextile-related products – determination of the characteristic opening size*.

ISO 12957:2005. *Geosynthetics – friction characteristics*.

ISO 12960:1998. *Geotextiles and geotextile-related products – screening test method for determining the resistance to liquids*.

ISO 13253:2000. *Geotextiles and geotextile-related products – characteristics required for use in erosion control works (coastal protection, bank revetments)*.

ISO 13431:1999. *Geotextiles and geotextile-related products – determination of tensile creep and creep rupture behaviour*.

ISO 13433:2006. *Geosynthetics – dynamic perforation test (cone drop test)*.

ISO 13438:2004. *Geotextiles and geotextile-related products – screening test method for determining the resistance to oxidation*.

Jackson, L.; Corbett, B.; and Tomlinson, R. (2004). *Baseline data assessment volume 4: summary of Narrowneck reef monitoring to June 2004*, Griffith, Australia: Griffith Centre for Coastal Management, Research Report no. 38.

Jackson, L.A.; Corbett, B.B.; McGrath, J.E.; and Tomlinson, R. (2007). *Narrowneck reef: review of seven years of monitoring*, Florida, Shore and Beach, Manhattan, Association American Shore and Beach Preservation, Volume 75, Issue 4 (Fall), pp. 67-79, ISSN 0037-4237.

Jiménez, J.A.; and Madsen, O.S. (2003). *A simple formula to estimate settling velocity of natural sediments*, Journal of Waterway, Port, Coastal and Ocean Engineering, ASCE, Volume 129, Issue 2 (March), pp. 70-78, ISSN 0733-950X.

Kamphuis, J. (2000). *Introduction to coastal engineering and management*, Advanced Series on Ocean Engineering – Volume 16, Singapore: World Scientific Publishing Co. Pte. Ltd., 437p, ISBN 981-02-4930-6.

Kamphuis, J. (2009). *Model scaling*, Kingston, Canada: Queen's University, 27 pp.

Kirby, J.T. (1986). *A general wave equation for waves over rippled beds*, Journal of Fluid Mechanics, Cambridge University Press, Volume 162 (January), pp. 171-186, ISSN: 0022-1120.

Koerner, R.M. (1999). *Designing with geosynthetics*, 4th edition, New Jersey: Prentice-Hall, Englewood Cliffs, 816p, ISBN 0-13-726175-6.

Komar, P.D. (1998). *Beach processes and sedimentation.* 2nd Edition, New Jersey: Prentice-Hall, 544p, ISBN-10: 0137549385.

Komarova, N.L.; and Newell, A.C. (2000). *Nonlinear dynamics of sand banks and sand waves.* Journal of Fluid Mechanics, Cambridge University Press, Volume 415 (July), pp. 285-321, ISSN 0022-1120.

Kraus, N.; and McDougal, W. (1996). *The effects of seawalls on the beach (Part I): an updated literature review*, Journal of Coastal Research, West Palm Beach (Florida), Volume 12, Issue 3 (Summer), pp. 691-701, ISSN 0749-0208.

Kraus, N.; and Smith, E. (1994). *SUPERTANK laboratory data collection project*, Vicksburg, MS: U.S. Army Corps of Engineers, Technical Report CERC-94–3 (January), 274p.

Lenze, B.; Heerten, G.; Saathoff, F.; and Stelljes, K. (2002). *Geotextile sand containers - successful solutions against beach erosion at sandy coasts and scour problems under hydrodynamic loads*, Proceedings of the Sixth International Conference LITTORAL 2002, F. Veloso Gomes, F. Taveira Pinto and Luciana das Neves (ed.), Eurocoast-Portugal Association, Volume II, pp. 375-381, ISBN 972-8558-09-0.

Lillycrop, W.; and Hughes, S. (1993). *Scour hole problems experienced by the corps of engineers: data presentation and summary*, Vicksburg, MS: U.S. Army Corps of Engineers, Technical Report CERC-93-2 (March), 80p.

Lopez, F.; and Garcia, M.H. (2001). *Risk of sediment erosion and suspension in turbulent flows*, Journal of Hydraulic Engineering, ASCE, Volume 127, Issue 3 (March), pp. 231–235, ISSN 0733-9429.

Mangor, K. (2004). *Shoreline Management Guidelines*, Hørsholm, Denmark: DHI Water & Environment (DHI), 294p, ISBN 87-981950-5-0.

Marieu, V.; Bonneton, P.; Foster, D.L.; and Ardhuin, F. (2008). *Modeling of vortex ripple morphodynamics*, Journal of Geophysical Research, American Geophysical Union, Volume 113(C09007), 15p, ISSN 2156–2202.

Markle, D. (1986). *Stability of toe berm armor stone and toe buttressing stone on rubble-mound breakwaters and jetties – physical model investigation*, Vicksburg, MS: U.S. Army Corps of Engineers, Technical Report REMR-CO-12 (September), 71p.

Massel, S.R.; Przyborska, A.; and Przyborski, M. (2004). *Attenuation of wave-induced groundwater pressure in shallow water (Part 1)*, Oceanologia, Polska Akademia Nauk, Instytut Oceanologii, Volume 46 (3), pp. 383-404, ISSN 0078-3234.

Massel, S.R.; Przyborska, A.; and Przyborski, M. (2005). *Attenuation of wave-induced groundwater pressure in shallow water (Part 2: theory)*, Oceanologia, Polska Akademia Nauk, Instytut Oceanologii, Volume 47(3), pp. 291-323, ISSN 0078-3234.

Masselink, G. (1998). *Field investigation of wave propagation over a bar and. the consequent generation of secondary waves*, Journal of Coastal Engineering, Amsterdam: Elsevier Science B.V., Volume 33, Issue 1 (March), pp. 1-9, Elsevier Science B.V., ISSN 0378-3839.

McDougal, W.; Kraus, N.; and Ajiwibowo, H. (1996). *The effects of seawalls on the beach: Part II, numerical modeling of SUPERTANK seawall tests*, Journal of Coastal Research, West Palm Beach (Florida), Volume 12, Issue 3 (Summer), pp. 702-713, ISSN 0749-0208.

Mei, C.C. (1985). *Resonant reflection of surface water waves by periodic sandbars*, Journal of Fluid Mechanics, Cambridge University Press, Volume 152, pp. 315-335, ISSN 0022-1120.

Mei, C.C. (1989). *The applied dynamics of ocean surface waves*, Advanced Series on Ocean Engineering – Volume 1, Singapore: World Scientific Publishing Co. Pte. Ltd., 768p, ISBN 978-981-279-605-9.

Mitchener, H.; and Torfs, H. (1996). *Erosion of mud/sand mixtures*, Journal of Coastal Engineering, Amsterdam: Elsevier Science B.V., Volume 29, pp. 1-25, Elsevier Science B.V., ISSN 0378-3839.

Miyamoto, J.; Sassa, S.; and Sekiguchi, H. (2004). *Progressive solidification of a liquefied sand layer during continued wave loading*, Géotechnique, Volume 54, Issue 10, pp. 617-629, ISSN 0016-8505.

Mocke, G.; Jackson, L.; and Smit, F. (2008). *Alternative coastal protection and amenity provision using multi function sand filled geo-containers*, COMPASS 2008.

Myrhaug, D.; and Holmedal, L.E. (2005). *Bottom friction caused by boundary layer streaming beneath random waves for laminar and smooth turbulent flow*, Ocean Engineering, Amsterdam: Elsevier Science B.V., Volume 32, Issue 2 (February), pp. 195-222, ISSN 0029-8018.

Myrhaug, D.; Holmedal, L.E.; and Rue, H. (2004). *Bottom friction and bedload sediment transport caused by boundary layer streaming beneath random waves*, Applied Ocean Research, Amsterdam: Elsevier Science B.V., Volume 26, Issue 5 (July), pp. 183-197, ISSN 0141-1187.

Myrhaug, D.; Holmedal, L.E.; Simons, R.R.; and MacIver, R.D. (2001). *Bottom friction in random waves plus current flow*, Journal of Coastal Engineering, Amsterdam: Elsevier Science B.V., Volume 43, Issue 2 (June), pp. 75-92, ISSN 0378-3839.

NAUE FASERTECHNIK (2000). *Terrafix© brochure*.

Neves, A.C. (2007). *Análise do Campo de Pressões em Quebramares Submersos*, PhD Thesis: Universidade do Porto, Faculdade de Engenharia, Portugal (*in Portuguese*).

NGCBPS (2000). *Nothern Gold Coast beach protection strategy*, July.

Nicholls, R.J.; Wong, P.P. ; Burkett, V.R.; Codignotto, J.O.; Hay, J.E.; McLean, R.F.; Ragoonaden, S.; and Woodroffe, C.D. (2007). *Coastal systems and low-lying areas*, Climate Change 2007: Impacts, Adaptation and Vulnerability. Contribution of Working Group II to the Fourth Assessment Report of the Intergovernmental Panel on Climate Change, M.L. Parry, O.F. Canziani, J.P. Palutikof, P.J. van der Linden, and C.E. Hanson (ed.), Cambridge, UK: Cambridge University Press, pp. 315-356.

Nielsen, P. (2009). *Coastal and estuarine processes*, Advanced Series on Ocean Engineering – Volume 29, Singapore: World Scientific Publishing Co. Pte. Ltd., 343p, ISBN 13 978-981-283-712-7.

Norheim, C.A.; Herbers, T.H.C.; and Elgar, S. (1998). *Nonlinear evolution of surface wave spectra on a beach*, Journal of Physical Oceanography, American Meteorological Society, Volume 28, pp. 1534-1551, ISSN 0022-3670.

O'Donoghue, T. (2001). *N-type sediment bed response under standing wave*, Journal of Waterway, Port, Coastal and Ocean Engineering, ASCE, Volume 127, pp. 245-248, ISSN 0733-950X.

Oh, Y. I.; and Shin, E. C. (2006). *Using submerged geotextile tubes in the protection of the E. Korean shore*, Journal of Coastal Engineering, Amsterdam: Elsevier Science B.V., Volume 53, pp. 879-895, ISSN 0378-3839.

Oliveira, M.M.S.; and Marques, J.P.G. (2005). *Recife artificial para a praia do Castelo do Queijo*, Projecto de Hidráulica: Universidade do Porto, Faculdade de Engenharia, Portugal (*in Portuguese*).

Oumeraci, H. (1993). *Scour in front of vertical breakwaters - review of scaling problems*, Braunschweig, Germany: Leichtweiβ Institute for Hydraulic Engineering and Water Resources, Research Report no. 125, 39p.

Oumeraci, H.; and Recio, J. (2009). *Geotextile sand containers for shore protection*, Handbook of Coastal and Ocean Engineering, Y.C. Kim (ed.), Singapore: World Scientific Publishing Co. Pte. Ltd., pp. 553-600, ISBN 13-978-981-281-929-1.

Oumeraci, H.; Hinz, M.; Bleck, M.; and Kübler, S. (2002). *Großmaßstäbliche Untersuchungen zur hydraulischen Stabilität geotextiler Sandcontainer unter Wellenbelastung*, Braunschweig, Germany: Leichtweiβ Institute for Hydraulic Engineering and Water Resources, Research Report no. 878, unpublished (*in German*).

Pais-Barbosa, J. (2007). *Hidromorfologias e hidroformas costeiras locais*, PhD Thesis: Universidade do Porto, Faculdade de Engenharia, Portugal (*in Portuguese*).

Papanicolaou, A.N. (1997). *The role of turbulence on the initiation of sediment motion*, PhD Thesis: Faculty of the Virginia Polytechnic Institute and State University, USA.

Pape, L. (2010). *Predictability of nearshore sandbar behavior*, PhD Thesis: Faculteit Geowetenschappen Universiteit Utrecht, The Netherlands.

Pilarczyk, K. (2000). *Geosynthetics and geosystems in hydraulics and coastal engineering*, Rotterdam: A.A. Balkema Publications, 913p, ISBN 90-5809-302-6.

Pinho-Lopes, M. (2009). *Estudo dos coeficientes de segurança a Aplicar a estruturas de controlo de erosão e de estabilização de maciços com geossintéticos*, PhD Thesis: Universidade do Porto, Faculdade de Engenharia, Portugal (*in Portuguese*).

Pinho-Lopes, M.; and Lopes, M.L. (2010). *A durabilidade dos geossintéticos*, Porto, Portugal: FEUP edições, 294p (*in Portuguese*).

Powell, K.; and Whitehouse, R. (1998). *The occurrence and prediction of scour at coastal and estuarine structures*, 33rd MAFF Conference of River and Coastal Engineers, Keele University, UK.

Powell, K.; and Lowe, J. (1994). *The scouring of sediments at the toe of seawalls*, Proceedings of the Hornafjordur International Coastal Symposium, G. Viggosson (ed.), Iceland, pp. 749-755.

Raubenheimer, B.; Guza R.T.; Elgar, S.; Kobayashi, N. (1995). *Swash on a gently slope beach*, Journal of Geophysical Research, American Geophysical Union, Volume 100(C5), pp. 8751-8760, ISSN 0148-0227.

Recio, J. (2007). *Hydraulic stability of geotextile sand containers for coastal structures - effect of deformations and stability formulae*, PhD Thesis: Leichtweiβ Institute for Hydraulic Engineering and Water Resources, Germany.

Recio, J.; and Oumeraci, H. (2007a). *Numerical simulations on the stability of coastal structures made of geotextile sand containers (GSC)*, Braunschweig, Germany: Leichtweiβ Institute for Hydraulic Engineering and Water Resources, Research Report no. 942.

Recio, J.; and Oumeraci, H. (2007b). *Permeability of GSC-structures - laboratory tests and results*, Braunschweig, Germany: Leichtweiβ Institute for Hydraulic Engineering and Water Resources, Research Report no. 943.

Recio, J.; and Oumeraci, H. (2007c). *Processes affecting the hydraulic stability of geotextile sand containers - experimental studies*, Braunschweig, Germany: Leichtweiβ Institute for Hydraulic Engineering and Water Resources, Research Report no. 944.

Restall, S.; Jackson, L.; Heerten, G.; and Hornsey, W. (2002). *Case studies showing the growth and development of geotextile sand containers: an Australian perspective*, Geotextiles and Geomembranes, Amsterdam: Elsevier Science B.V., Volume 20, pp. 321-342, ISSN 0266-1144.

Rosa-Santos, P. (2010). *Análise da Interacção de Navios com Dispositivos de Acostagem e Amarração. Estudo em Modelo Físico do Posto "A" do Terminal de Petroleiros do Porto de Leixões*, PhD Thesis, Universidade do Porto, Faculdade de Engenharia, Portugal (*in Portuguese*).

Saathoff, F. (2003). *Geosynthetics in geotecnical and hydraulic engineering*, Chapter 2.13. In U. Smoltczyk (ed.), Geotechnical Engineering Handbook (Volume 2: Procedures), Ernest and Sohn Verlag für Architektur und Technische Wissenschaften Gmbh und Co. KG, Berlin.

Saathoff, F.; Oumeraci, H.; and Restall, S. (2007). Australian *and German experiences on the use of geotextile containers*, Geotextiles and Geomembranes, Amsterdam: Elsevier Science B.V., Volume 25, pp. 251-263, ISSN 0266-1144.

Schäffer, H.A. (1996). *Second-order wavemaker theory for irregular waves*, Ocean Engineering, Amsterdam: Elsevier Science B.V., Volume 23, Issue 1, pp. 47-88, ISSN 0029-8018.

Schäffer, H.A.; and Steenberg, C.M. (2003). *Second-order wavemaker theory for multidirectional waves*, Ocean Engineering, Amsterdam: Elsevier Science B.V., Volume 30, Issue 10 (July), pp. 1203-1231, ISSN 0029-8018.

Schwartz, M. (2005). *Encyclopedia of Coastal Science*, Springer, 1211p, ISBN 13 978-1402019036.

Shin, E.; and Oh, Y. (2007). *Coastal erosion prevention by geotextile tube technology*, Geotextiles and Geomembranes, Special Issue on Tsunami Reconstruction with Geosynthetic Containment Systems, Proceedings of the International Symposium on Tsunami Reconstruction with Geosynthetics-Protection, Mitigation and Rehabilitation of Coastal and Waterway Erosion, Amsterdam: Elsevier Science B.V., Volume 25, Issues 4-5 (August-October), pp. 264-277, ISSN 0266-1144.

Short, A.D. (1999). *Handbook of beach and shoreface morphodynamics*, John Wiley & Sons, Ltd., 379p, ISBN 0 471 96570 7.

Silva, R. (2010). *Avaliação Experimental e Numérica de Parâmetros Associados a Modelos de Evolução da Linha da Costa*, PhD Thesis: Universidade do Porto, Faculdade de Engenharia, Portugal (*in Portuguese*).

Silvester, R.; and Hsu, J. (1997). *Coastal stabilization*, Advanced Series on Ocean Engineering – Volume 14, Singapore: World Scientific Publishing Co. Pte. Ltd., 578p, ISBN 981-02-3137-7.

Sistermans, P.; and Nieuwebhuis, O. (2002). *EUrosion Case Study: Isle of Sylt*, 21p.

Small, C.; and Nicholls, R.J. (2003). *A global analysis of human settlement in coastal zones*. Journal of Coastal Research, West Palm Beach (Florida), Volume 19, Issue 3 (Summer), pp. 584-599, ISSN 0749-0208.

Smit, F.; Mocke, G.; and Jackson, L.A. (2009). *Design and construction methodology of a novel multifunctional artificial reef for Dubai*, Proceedings of the 5th International Conference Coastal Structures, Leopoldo Franco, Giuseppe R. Tomasicchio, and Alberto Lamberti (ed.), Singapore: World Scientific Publishing Co. Pte. Ltd., Volume I, pp. 400-411, ISBN 13 978-981-4280-99-0.

Smith, D.A.; and Cheung, K.F. (2003). *Settling characteristics of calcareous sand*, Journal of Hydraulic Engineering, ASCE, Volume 129, Issue 6 (June), pp. 479-483, ISSN 0733-9429.

Smith, D.A.; and Cheung, K.F. (2004). *Initiation of motion of calcareous sand*, Journal of Hydraulic Engineering, ASCE, Volume 130, Issue 5 (May), pp. 467–472, ISSN 0733-9429.

Smith, E.R.; and Kraus, N. C. (1991). *Laboratory study of wave-breaking over bars and artificial reefs*. Journal of Waterway, Port, Coastal and Ocean Engineering, ASCE, Volume 117, Issue 4 (July/August), ISSN 0733-950X.

Smith, E.R.; Wang, P.; Ebersole, B.A.; and Zhang, J. (2009). *Dependence of total longshore sediment transport rates on incident wave parameters and breaker type*, Journal of Coastal Research, West Palm Beach (Florida), Volume 25, Issue 3, pp. 675-683, ISSN 0749-0208.

Sumer, B.M.; and FredsØe, J. (1997). *Scour at the head of a vertical-wall breakwater*, Journal of Coastal Engineering, Amsterdam: Elsevier Science B.V., Volume 29, Issue 3-4 (January), pp. 201-230, ISSN 0378-3839

Sumer, B.M.; and FredsØe, J. (2000). *Experimental study of 2D scour and its protection at a rubble-mound breakwater*, Journal of Coastal Engineering, Amsterdam: Elsevier Science B.V., Volume 40, pp. 59-87, ISSN 0378-3839.

Sumer, B.M.; and FredsØe, J. (2002). *The mechanics of scour in the marine environment*, Advanced Series on Ocean Engineering – Volume 17, Singapore: World Scientific Publishing Co. Pte. Ltd., 536p, ISBN 981-02-4930-6.

Sumer, B.M.; Fredsøe, J.; Christensen, S.; and Lind, M. (1999). *Sinking/Floatation of pipelines and other objects in liquefied soil under waves*, Journal of Coastal Engineering, Amsterdam: Elsevier Science B.V., Volume 38, pp. 53-90, ISSN 0378-3839.

Sumer, B.M.; Fredsoe, J.; Lamberti, A.; Zanuttigh, B.; Dixen, M.; Gislason, K.; and di Penta, A.F. (2005). *Local scour at roundhead and along the trunk of low crested structures*, Journal of Coastal Engineering, Volume 52, Issues 10-11, November, pp. 995-1025, ISSN 0378-3839.

Sumer, B.M.; Hatipoglu, F.; FredsØe, J.; and Kaan Sumer, S. (2006). *The sequence of sediment behaviour during wave-induced liquefaction*, Sedimentology, International Association of Sedimentologists, Volume 53, Issue 3 (June) pp. 611–629, ISSN 1365-3091.

Sumer, B.M.; Whitehouse, R.; and Tørum, A. (2001). *Scour around coastal structures: a summary of recent research*, Journal of Coastal Engineering, Amsterdam: Elsevier Science B.V., Volume 44, Issue 2, pp. 153–190, ISSN 0378-3839.

Sutherland, J.; Brampton, A.; Obhrai, C.; Dunn, S.; and Whitehouse, R. (2008). *Understanding the lowering of beaches in front of coastal defence structures (Stage 2)*, Rand Technical Report FD1927/TR, DEFRA.

Taveira-Pinto, F. (2001). *Análise das oscilações e dos campos de velocidade nas proximidades de quebramares submersos sob a acção da agitação marítima*. PhD Thesis: Universidade do Porto, Faculdade de Engenharia Engenharia, Portugal (*in Portuguese*).

Taveira-Pinto, F.; Veloso-Gomes, F.; Silva, R.; das Neves, L.; Rosa-Santos, P.; and Guedes-Lopes, H. (2007). *The new wave generation system of the Laboratory of Hydrauics of FEUP*, 2.as Jornadas de Hidráulica, Recursos Hídricos e Ambiente, pp. 1-13, Porto, ISBN 978-989-95557-1-6 (*in Portuguese*).

Terrile, E.; Reniers, J.H.M.; Stive, M.J.F.; Tromp, M.; and Verhagen, H.J. (2006). *Incipient motion of coarse particles under regular shoaling waves*, Journal of Coastal Engineering, Amsterdam: Elsevier Science B.V., Volume 53, pp. 81–92, ISSN 0378-3839.

Thomson, J.M. (2006). *Infragravity waves over topography: generation, dissipation, and reflection*, PhD Thesis: Massachusetts Institute of Technology and the Woods Hole Oceanographic Institution, USA.

Tirindelli, M.; Lamberti, A.; Paphitis, D.; Collins, M.; Vidal, C.; and Hawkins, S. (2000). *Wave action on rubble mound breakwaters: the problem of scale effects*, DELOS EVK3-CT-2000-00041.

TØrum, A. (2007). *Wave-induced pore pressures - air/gas content*, Journal of Waterway, Port, Coastal and Ocean Engineering, ASCE, Volume 133, Issue 1 (January), pp. 83-86, ISSN 0733-950X.

TØrum, A., Kuhnen, F.; and Menze, A. (2003). *On berm breakwaters. Stability, scour, overtopping*, Journal of Coastal Engineering, Amsterdam: Elsevier Science B.V., Volume 49, Issue 3, pp. 209-238, ISSN 0378-3839.

Troch, P. (2001). *Experimental study and numerical modelling of pore pressure attenuation inside a rubble mound breakwater*. PIANC Bulletin, Issue 108, pp. 5-27.

Troch, P.; de Rouck, J.; and van Damme, L. (1998). *Instrumentation and prototype measurements at the Zeebrugge rubble mound breakwater*, Journal of Coastal Engineering, Amsterdam: Elsevier Science B.V., Volume 35, pp. 141-166, ISSN 0378-3839.

Turner, I. (2004). *Analysis of shoreline change: August 2003 - January 2004, Report 9: Northern Gold Coast Coastal Imaging System*, Manly Vale, N.S.W. Australia: Water Research Laboratory, University of New South Wales, Technical Report 2004/07-March.

Turner, I. (2006). *Analysis of shoreline variability, seasonability and erosion/accretion trends: August 2005 - January 2006, Report 13*, Manly Vale, N.S.W. Australia: Water Research Laboratory, University of New South Wales, Technical Report 2006/01-February.

USACE. (2008). *Coastal Engineering Manual*, Vicksburg, MS: U.S. Army Corps of Engineers, Engineer Manual 1110-2-1100.

van Rijn, L. (2006). *Manual of sediment transport measurements in rivers, estuaries and coastal seas*, Aquapublications.

van Steeg, P.; and Breteler, K. (2008). *Large scale physical model tests on the stability of geocontainers*, DELTARES.

van Steeg, P.; and Vastenburg, E. (2010). *Large scale physical model tests on the stability of geotextile tubes*, DELTARES.

Veloso-Gomes, F.; Taveira-Pinto, F.; and Pais-Barbosa, J. (2004a). *Rehabilitation study of coastal defense works and artificial sand nourishment at Costa da Caparica*, Proceedings of the 29th International Conference Coastal Engineering, J. McKee Smith (ed.), Singapore: World Scientific Publishing Co. Pte. Ltd., Volume 4, pp. 3429-3440, ISBN 978-981-256-298-2.

Veloso-Gomes, F.; Taveira-Pinto, F.; das Neves, L.; and Pais-Barbosa, J. (2006a). *EUrosion - a Eropean initiative for sustainable coastal erosion management. Pilot site of river Douro - Cabo Mondego and case studies of Estela, Aveiro, Caparica, Vale do Lobo and Azores*. Porto, Portugal: IHRH/FEUP, 317p+app.

Veloso-Gomes, F.; Taveira-Pinto, F.; Pais-Barbosa, J.; Costa, J.; and Rodrigues, A. (2006b). *Monitoring of the coastal defence Works of Costa do Caparica, Portugal*, Proceedings of the 30th International Conference Coastal Engineering, J. McKee Smith (ed.), Singapore: World Scientific Publishing Co. Pte. Ltd., Volume 5, pp. 5241-5253, ISBN 978-981-270-636-2.

Veloso-Gomes, F.; Costa, J.; Rodrigues, A.; Taveira-Pinto, F.; and das Neves, L. (2009a). *Costa da Caparica artificial sand nourishment and coastal dynamics*, Journal of Coastal Research, West Palm Beach (Florida), Special Issue 56 (Proceedings of the 10th International Coastal Symposium), pp. 678-682, ISSN 0749-0208.

Veloso-Gomes, F.; Taveira-Pinto, F.; and Rosa-Santos, P. (2009b). *Scour on Portuguese coastal defence structures*, Proceedings of the 5th International Conference Coastal Structures, Leopoldo Franco, Giuseppe R. Tomasicchio, and Alberto Lamberti (ed.), Singapore: World Scientific Publishing Co. Pte. Ltd., Volume I, pp. 187-198, ISBN 13 978-981-4280-99-0.

Veloso-Gomes, F.; Taveira-Pinto, F.; das Neves, L.; Pais-Barbosa, J.; and Coelho, C. (2004b). *Erosion Risk Levels at the NW Portuguese Coast: the Douro Mouth - Cape Mondego Stretch*, Journal of Coastal Conservation, Springer, Volume 10: 1-2, January, pp. 43-52, ISSN 1400-0350.

Venis, W.A. (1968). *Behaviour of dumping material when exposed to currents and wave action*, De Ingenieur, Bouw- en Waterbouwkunde (December), pp. 159-167.

Vieira, C. (2009). *Muros e taludes de solo reforçado com geossintéticos: comportamento sísmico e metodologias de dimensionamento*, PhD Thesis: Universidade do Porto, Faculdade de Engenharia Engenharia, Portugal (*in Portuguese*).

WAFO-group (2000). *WAFO – a Matlab toolbox for analysis of random waves and loads (tutorial)*, Lund, Sweden: Mathematical Statistics, Centre for Mathematical Science.

Wallis, M.; Whitehouse, R.; and Lyness, N. (2009). *Development of guidance for the management of the toe of coastal defence structures*, Wallingford, UK: HRPP 413, 14p.

Wang, P.; Ebersole, B.A.; and Smith, E.R. (2003). *Beach-profile evolution under spilling and plunging breakers*, Journal of Waterway, Port, Coastal and Ocean Engineering, ASCE, Volume 129, Issue 1 (January), ISSN 0733-950X.

Wang, P.; and Davis, R.A. Jr. (1998). *A beach profile model for a barred coast: case study from Sand Key, West-Central Florida*, Journal of Coastal Research, West Palm Beach (Florida), Volume 14, Issue 3 (Summer), pp. 981-991, ISSN 0749-0208.

Wang, P.; and Kraus, N.C. (2005). *Beach profile equilibrium and patterns of wave decay and energy dissipation across the surf zone elucidated in a large-scale laboratory experiment*, Journal of Coastal Research – West Palm Beach (Florida), Volume 21, Issue 3, pp. 522–534, ISSN 0749-0208.

Whitehouse, R. (1998). *Scour at marine structures*, Thomas Telford, Ltd., 224p, ISBN 0 7277 2655 2.

Xie, L.; Lei, H.; and Yu, Y. (2009). *Incipient motion of riverbank sediments with outflow seepage*, Journal of Hydraulic Engineering, ASCE, Volume 135, Issue 3 (March), pp. 228-233, ISSN 0733-9429.

Xie, S. (1981). *Scouring patterns in front of vertical breakwaters and their influences on the stability of the foundation of the breakwaters*, MSc Thesis: TU Delft, Faculty of Civil Engineering and Geosciences, Hydraulic Engineering, The Nethwerlands.

Yoshida, A.; Yan, S.; Yamashiro; M.; and Irie, I. (2002). *Wave field behind a double-submerged breakwater*, Proceedings of the 12th International Offshore and Polar Engineering Conference, International Society of Offshore and Polar Engineers, pp. 785-790, ISBN l-880653-58-3.

Yu, J.; and Mei, C.C. (2000a). *Do longshore bars protect the shore?*, Journal of Fluid Mechanics, Cambridge University Press, Volume 404, pp. 251-268, ISSN 0022-1120.

Yu, J.; and Mei, C.C. (2000b). *Formation of sand bars by surface waves*, Journal of Fluid Mechanics, Cambridge University Press, Volume 416, pp. 315-348, ISSN 0022-1120.

Zanke, U.C.E (2003). *On the influence of turbulence on the initiation of sediment motion*, International Journal of Sediment Research, Amsterdam: Elsevier Science B.V., Volume 18, Issue 1, pp. 17-31, ISSN 1001-6279.

Zhang, H.; and Schäffer, H.A. (2007). *Approximate stream function wavemaker theory for highly non-linear waves in wave flumes*, Ocean Engineering, Amsterdam: Elsevier Science B.V., Volume 34, Issue 8-9 (June), pp. 1290-1302, ISSN 0029-8018.

Zheng, J. (1996). *Improved cross-shore sediment transport relationships and models*, PhD Thesis: University of Florida, USA.

Zhiyao, S.; Tingting, W.; Fumin, X. (2008). *A simple formula for predicting settling velocity of sediment particles*, Water Science and Engineering, Volume 1, Issue 1 (March), pp. 37-43, ISSN 1674-2370.

APPENDIX A

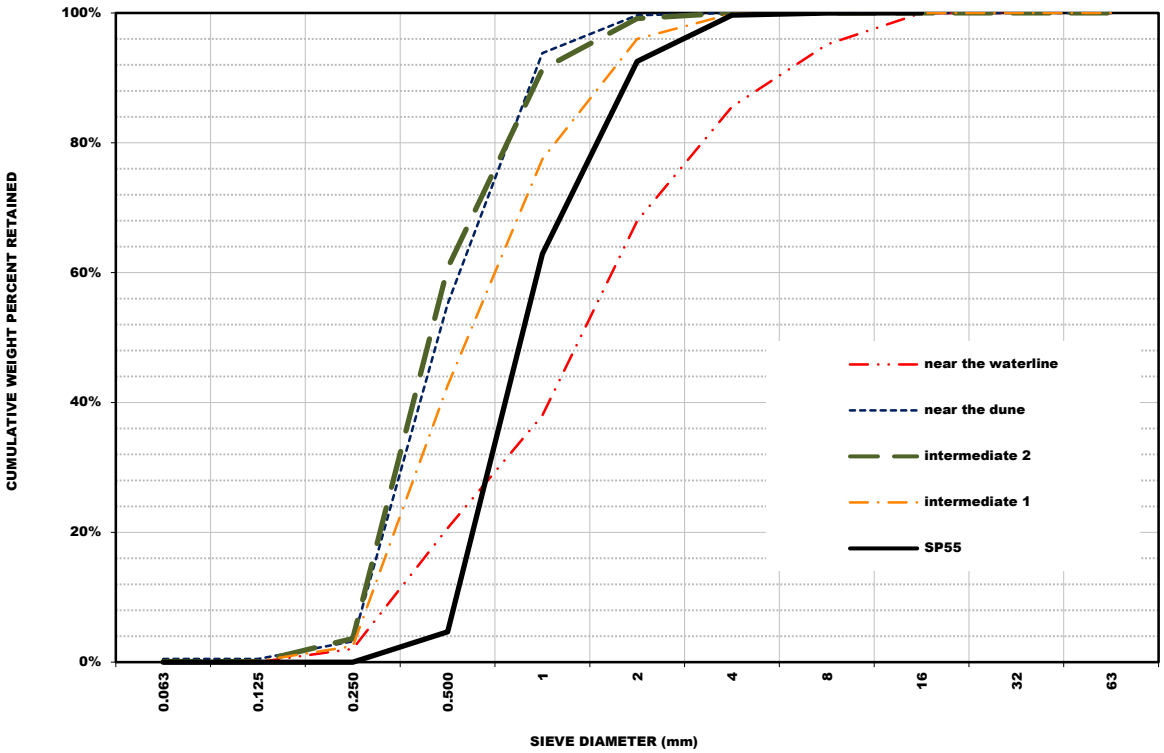

Figure A.1: Prototype and model sediment grain size distributions.

APPENDIX B

Figure B.1: Model B: aspects of the construction and running.

Figure B.2: Model C: aspects of the construction and running.

Figure B.3: Model D: aspects of the construction.

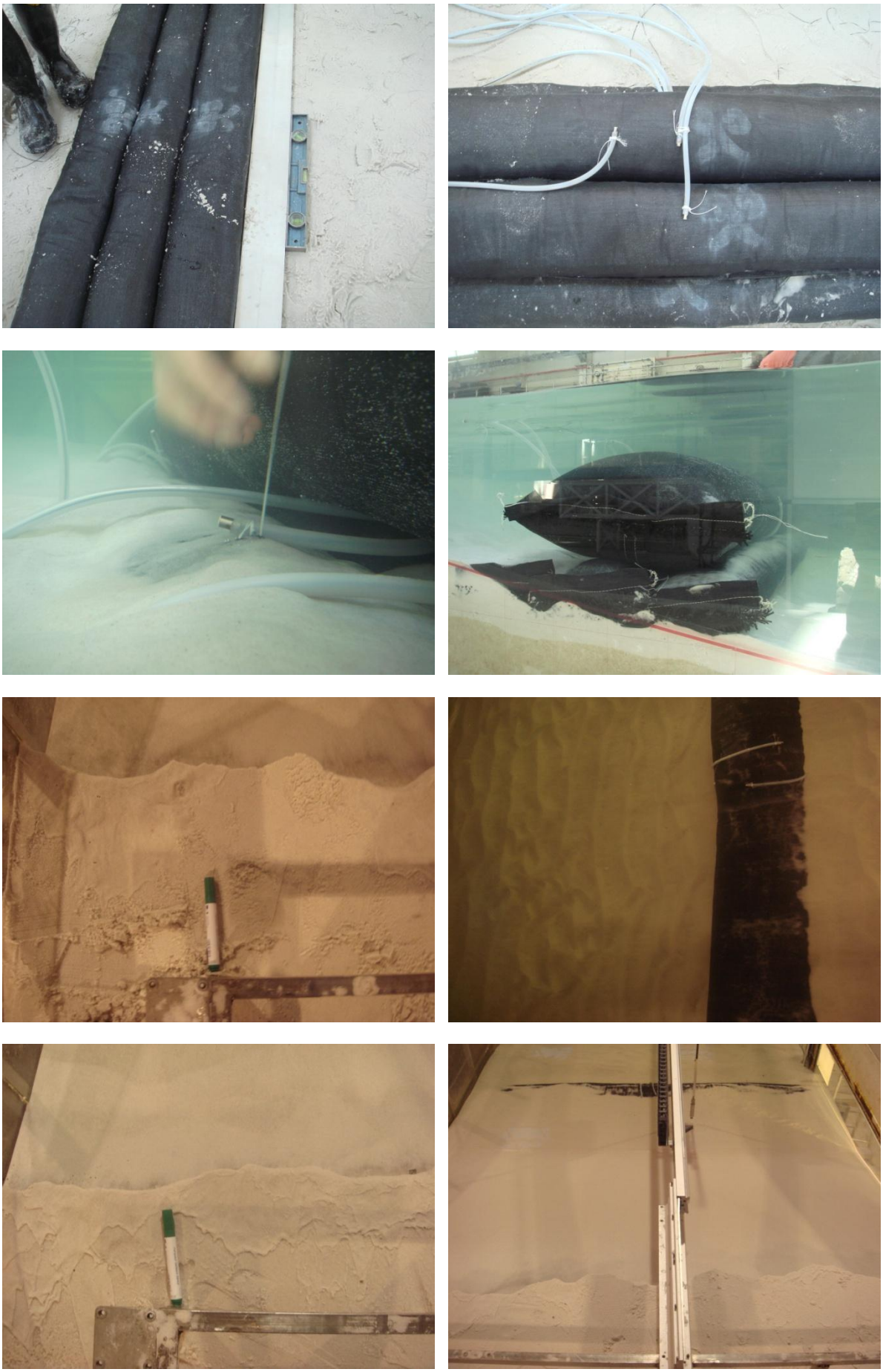

Figure B.3: Model E: aspects of the construction and running.

APPENDIX C

As described in section 4.2, the wave basin of FEUP Hydraulics Laboratory is 28m long, 12m wide but was partitioned to a wave channel of 2.25m wide. The total length from the paddles to the shoreline is 13.60m (9.7m from the paddles to the beach foot, and another 3.9m to the shoreline) in working water depth of 0.58m.

Assuming an enclosed basin, Eq. (C.1) is the expression for the natural free oscillating period of a rectangular basin with vertical sides, significant width as well as length, and uniform depth, on the assumption that water is inviscid and incompressible.

$$T_n = \frac{2\,L_B}{n\sqrt{g\,d}} \tag{C.1}$$

where, T_n is the natural free oscillation period, n is the number of nodes along the long basin axis, L_B is the basin along that axis, g is the acceleration due to gravity, and d is the water depth.

For open basins, the natural free oscillating period is given by Eq. (C.2).

$$T_n = \frac{4\,L_B}{(1+2\,n)\sqrt{g\,d}} \tag{C.2}$$

The estimated natural free oscillating periods, for several modes (n=0, 1, 2, 3), based on both closed and open hypothesis, are given in Table C.I.

Table C.I: Natural free oscillating periods of the basin.

Basin	***n***	$T_{n,m}$ **[s in model]**	$T_{n,m}$ **[s in prototype]**
Closed	1	11.40	39.50
	2	5.70	19.75
	3	3.80	13.17
Open	0	22.81	79.00
	1	7.60	26.33
	2	4.56	15.80
	3	3.26	11.29